DEVELOPMENT OF IMPROVED SOLUTIONS FOR STEEL CATENARY RISER CHALLENGES

by

Achoyamen Michael Ogbeifun

This thesis is submitted for the degree of Doctor of Philosophy

at

The University of Strathclyde

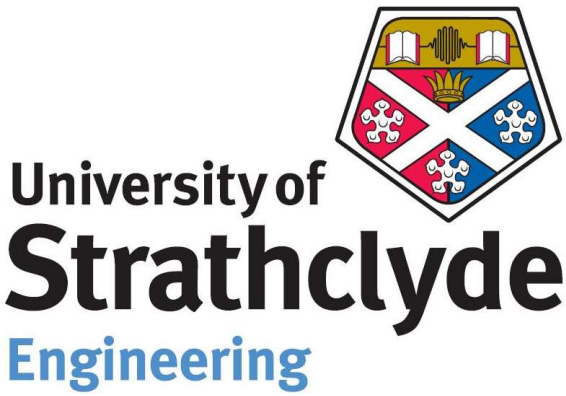

Department of Naval Architecture, Ocean, and Marine Engineering

June 2022

DECLARATION

This dissertation is the result of my own work and includes nothing which is the outcome of work done in collaboration except where specifically indicated in the text. It has not been previously submitted, in part or whole, to any university or institution for any degree, diploma, or other qualification.

Signed:_____

Date: March 15, 2022

Achoyamen Michael Ogbeifun

Department of Naval Architecture, Ocean, and Marine Engineering

University of Strathclyde

DEDICATION

This research is dedicated to:

- My wife, Stella and our little princess (Samantha), who have been the source of love and joy for me throughout this research.
- Dr Selda, Dr Julia, Mr Harit, Dr Dakshina, Dr Subrata, Dr Julie, Mr Eduardo, who have created for me a solid platform to complete this study, and to Dr.Mahdi, who provided me this opportunity.
- God, who gave me the breath of life, strength and wisdom to see this research to successful completion.

ACKNOWLEDGEMENTS

My PhD journey was fascinating, with God at the heart of it all, bringing me to success. Without Him, nothing was possible. He got the best of everyone involved in this research for the greater good –the successful completion of my program. To You, O God be the glory.

I thank my wife for her outstanding support. Without her love and care, this would not have been possible. Sometimes I am home but not home as my study keeps me away from her and our daughter, Samantha. But she was always there to fill in the gaps. Stella, you are God sent. I also thank my entire family (especially Ehimen and his wife) for their support, advice, encouragement, and prayers.

Dr Selda Oterkus was not just a supervisor but a mentor, a sister and a mother. She was always ready to provide me with the support she could get within her power to smoothen my PhD journey. My family and I owe her a debt we cannot repay. A big thanks to Dr Julia Race, whose words of encouragement fueled my research passion throughout the program. Knowing she was there increased my momentum towards the completion of this program. Ross Gilmour was more than an IT staff to me. In times of need on IT matters, he was a friend who provided me with all the IT support needed to ease my research. Ross, thank you very much! Susan, you are not left out, as your administrative presence was evident throughout my research. Thank you very much, Susan, for your support.

My study would not have been possible without the support of McDermot International, which provided the sponsorship and support throughout the program. I thank Harit Naik, Dakshina Moorthy, Subrata Bhowmik, Julie Ingram and Eduardo Decnop for all their technical support and encouragement throughout my study. Without them, this would not have been possible. I also thank Dr Mahdi Khorasanchi, who recruited me and brought me to the UK from Nigeria for this research. He barely stayed when I arrived in the UK. However, I am indebted to him for helping me to start this new phase of my career.

ABSTRACT

The current demand for oil and gas resources persists as no established alternative energy source completely meets the world's high demand for energy. The depleting onshore and shallow-water oil and gas reservoirs are now driving the production of large hydrocarbon reservoirs in deep and ultra-deepwater. Therefore, it is necessary to innovate cost-effective and less risky riser technology for this purpose. The conventional steel catenary risers (SCR) are limited in their application for deep and harsh water environments due to the high stresses and fatigue response at their critical sections. In line with the aim and objective of this research, riser solutions for SCR are developed and investigated in this thesis. These solutions include the branched riser system (BRS), the floating catenary riser system (FCR), the vessel relocation strategy (VRS) and the simulation stage-based pre-trenching technique (SSBPT). Also, the index matching technique (IMT) is developed for the optimisation process of some of the riser solutions.

The IMT is a descriptive rather than an inferential technique that applies statistical operations like indexing, intersection, and sorting to obtain optimal solutions to the optimisation problems. The IMT assigns unique index identities to design points in the optimisation design space and tracks the constraint (feasibility) and performance of the objective functions at those design points using those indices. The objective functions are evaluated at the feasible design points and sorted in ascending or descending order depending on whether the problem is minimised or maximised. The vector of the indices of the design points is rearranged to match the order of the sorted objective function vector. The index at the top of the index columns represents the optimum design point of the problem, from which the design variables and objective functions are mapped. The IMT is demonstrated with the SLWR optimisation problem and is further applied to optimise the BSCR, the FCR and the VRS.

The BRS concept is developed to address the stress and fatigue challenge of the conventional SCR TDZ. Under limited environmental conditions and vessel motion, a small diameter pipe performs better in strength and fatigue response around the touchdown zone (TDZ) than a larger diameter riser pipe. However, the large bore pipe provides benefits of large fluid throughput from the seabed to the host platform, with lower top-side connections than smaller pipe diameter risers. The BRS concept combines these performances by branching the larger bore riser at an optimum water depth via a connecting structure into two small-bore riser pipes, which extend from the branching dept to the seabed. The BRS configuration variants include

the Branched Steel Catenary Riser (BSCR), the Branched Steel Lazy Wave Riser (BSLWR) and the Branched Lazy Wave Hybrid Riser (BLWHR). However, only the BSCR is investigated in this thesis. The BSCR global configuration is developed and analysed to demonstrate its feasibilities. The investigation reveals the stress and fatigue response benefits of the BSCR compared with conventional small bore and large bore SCR. An optimisation methodology was developed to access the optimum BSCR configurations.

The FCR concept is developed to address the tieback challenge of the conventional SCR across the congested or environmentally protected seabed. The FCR, with its double “wave bends”, is engineered to extend the riser touch down point (TDP) far beyond the nominal SCR TDP and away from the congested seabed footprint. The riser sections before the nominal SCR TDP are configured to float by installing buoyancy modules. The multiple wave buoyant sections also allow the FCR to decouple its TDZ from the floating platform motion. This can result in a significant reduction in the stress and fatigue damage around the riser TDP. The FCR global configuration is developed and tested for feasibility and was found to provide a better response than the SCR, in addition to its ability to provide a longer span across congested and protected seabed sections. An optimisation method for the FCR is also developed and applied in the selection of optimum FCR configurations.

The VRS is the vessel’s planned repositioning within the acceptable limit of the riser design storm responses to help spread and reduce the fatigue damage over a more extended riser seabed section. There is a need to obtain an optimum vessel relocation program that best reduces the SCR TDZ fatigue damage and to know the optimum combination of the number of stations along the relocation axis, the vessel offset limits and the direction of relocation. The constraints on the problem are imposed by the stress utilisation, TDZ compression and top tension. The developed approach includes both symmetric and non-symmetric relocation patterns and can be applied to existing SCRs for life extension purposes. The VRS is developed and demonstrated to show the potential significant reduction in the SCR TDZ fatigue damage compared with SCR with no vessel relocation.

The SSBPT is a numerical pre-trenching technique developed to qualify and quantify the trench impact on the SCR TDZ fatigue responses. The method is created using the capabilities of the hysteretic non-linear seabed interaction model, implemented in the OrcaFlex software. The method reveals that the presence of a pre-trench can increase the SCR TDZ fatigue damage. The TDZ damage response depends on several other factors such as the seabed properties, the

SCR configurations, the pre-trench depth, the applied wave loads etc. Hence the pre-trench impact on the SCR TDZ fatigue response should be conducted on a case-by-case basis, based on the available design data for the SCR. The SSBPT provide the opportunities to investigate these complex load scenarios.

As part of the SCR seabed interaction investigation, the influence of seabed slope on the SCR TDZ response is investigated in this thesis. SCR analyses are usually conducted considering flat seabed, neglecting sloped seabed around the SCR TDZ, which could potentially affect the response of the SCR. The impact of seabed slope on the SCR TDZ strength and fatigue response is investigated using a non-linear (NL) riser soil interaction model. The responses of SCRs on positively and negatively sloped seabed are compared with SCRs on the flat seabed. The investigation reveals that the SCR TDZ responses can be over or under-predicted depending on the seabed slope deviation from the flat seabed.

RESEARCH PUBLICATIONS

Several conference and Journal publications directly related with this PhD research work were produced as part of the deliverables of the research. These publications are outlined as follows:

- Ogbeifun, A. M., Oterkus, S., Race, J., Naik, H., Decnop, E., & Dakshina, M. (2019, June). The Branched Riser Systems: Concept Development. In International Conference on Offshore Mechanics and Arctic Engineering (Vol. 58813, p. V05BT04A029). American Society of Mechanical Engineers.

- Ogbeifun Michael, A., Oterkus, S., Race, J., Naik, H., Decnop, E., Moorthy, D., & Bhowmik, S. (2019, October). The Branched Steel Catenary Riser Interference Study. In Offshore Technology Conference Brasil. OnePetro.

- Ogbeifun, A. M., Oterkus, S., Race, J., Naik, H., Moorthy, D., Bhowmik, S., & Ingram, J. (2021). Floating catenary riser system concept for brownfield application. Ocean Engineering, 236, 109549.

- Ogbeifun, A. M., Oterkus, S., Race, J., Naik, H., Moorthy, D., Bhowmik, S., & Ingram, J. (2021). Impact of seabed slope on steel catenary riser touchdown zone response. In IOP Conference Series: Materials Science and Engineering (Vol. 1052, No. 1, p. 012018). IOP Publishing.

- Ogbeifun, A. M., Oterkus, S., Race, J., Naik, H., Moorthy, D., Bhowmik, S., & Ingram, J. (2021). Vessel relocation solution for steel catenary riser touch down fatigue management. Ocean Engineering, 237, 109632.

- Ogbeifun, A. M., Oterkus, S., Race, J., Naik, H., Moorthy, D., Bhowmik, S., & Ingram, J. (2021). A tabular optimisation technique for steel lazy wave riser. In IOP Conference Series: Materials Science and Engineering (Vol. 1052, No. 1, p. 012022). IOP Publishing.

- Ogbeifun, A. M., Oterkus, S., Race, J., Naik, H., Moorthy, D., Bhowmik, S., & Ingram, J. (2021). A Numerical Seabed Trench Initiation Technique for Steel Catenary Riser Touchdown Stress and Fatigue Analysis. "On Ships and Offshore Structures": ICSOS2020_011.

- Ogbeifun, A., Oterkus, S., Race, J., Naik, H., Moorthy, D., Bhowmik, S., & Ingram, J. (2021). Simulation stage-based seabed pre-trenching technique for steel catenary riser touchdown fatigue analysis. Ships and Offshore Structures.
- Ogbeifun, A. M., Oterkus, S., Race, J., Naik, H., Moorthy, D., Bhowmik, S., & Ingram, J. (2021). Vessel relocation strategy for multiple steel catenary riser fatigue damage mitigation. Ocean Engineering.

CONTENTS

LIST OF TABLES

LIST OF FIGURES

1 INTRODUCTION

This chapter presents the relevance of this research and contributions made to both the academic and the riser industry domain. A preliminary background for the research work is presented, where the meaning and use of the deepwater riser systems are highlighted, as well as the challenges of deepwater riser systems and the current riser solution categories. The research background is then followed by the research focus, aims and objectives. Lastly, the thesis chapters' structure, organisation and contents are presented.

The sections in this chapter are as follows:

- 1.1 – Research Background
- 1.2 – Steel Catenary Riser System Challenges
- 1.3 – Research Focus
- 1.4 – Research Aims and Objectives
- 1.5 – Chapter Organisation and Layout
- 1.6 – Chapter Summary

1.1 Research Background

The depletion of hydrocarbon resources in onshore and shallow water reservoirs has resulted in deeper water exploration. Large hydrocarbon reservoirs are now being located and produced

in deepwater and ultra-deepwater, and the associated challenges are increasing with water depths, harsh environmental conditions, and unfriendly fluid properties. Therefore, it is necessary (engineering, environmental, safety and business) to safely and cost-effectively conduct these deepwater operations. The current riser technologies need stretching beyond their current abilities and capacities to achieve safety and cost-effectiveness, requiring innovations in their structural form and design methodologies. With increasing water depth and harsher environmental conditions, the conventional riser systems become limited in their application. For example, higher reservoir pressure and higher hydrostatic collapse pressure associated with deeper water columns become very significant in driving the wall thickness and weight of the riser pipe for burst and collapse resistance, respectively. Also, harsh sea state conditions peculiar to deepwater induce large host floating platform motions, resulting in large stresses and fatigue damage in the critical sections of the risers. As a result, significant research resources have been directed towards building riser systems and developing better design methods for the safe and economical mining of hydrocarbons from deepwater and ultra-deep waters.

A riser is a string of jointed pipe segments used to transport material between seabed pipelines and the floating production platform. Without riser systems, it is impossible to convey oil and gas produced from deepwater offshore reservoirs to the floating production platform and subsequently to onshore processing facilities. Deepwater risers are hosted or held in place by a floating production platform. The unsupported section between the vessel and the seabed is either tensioned externally or under the riser self-weight. In terms of material makeup, risers can be metallic or non-metallic. In terms of application/usage, the deepwater riser can be drilling risers, production/injection risers, Export/import risers and completion/workover risers [1, 2]. In terms of configurations, deepwater riser systems can be either tensioned risers where an additional pull is applied at its top to keep its tension positive or can be free-hanging, where the riser is tensioned under its weight. The free-hanging risers have many variations, as shown in Figure 1-1, with common and widely applied types such as the steel catenary risers (SCR) and the steel lazy wave risers (SLWR).

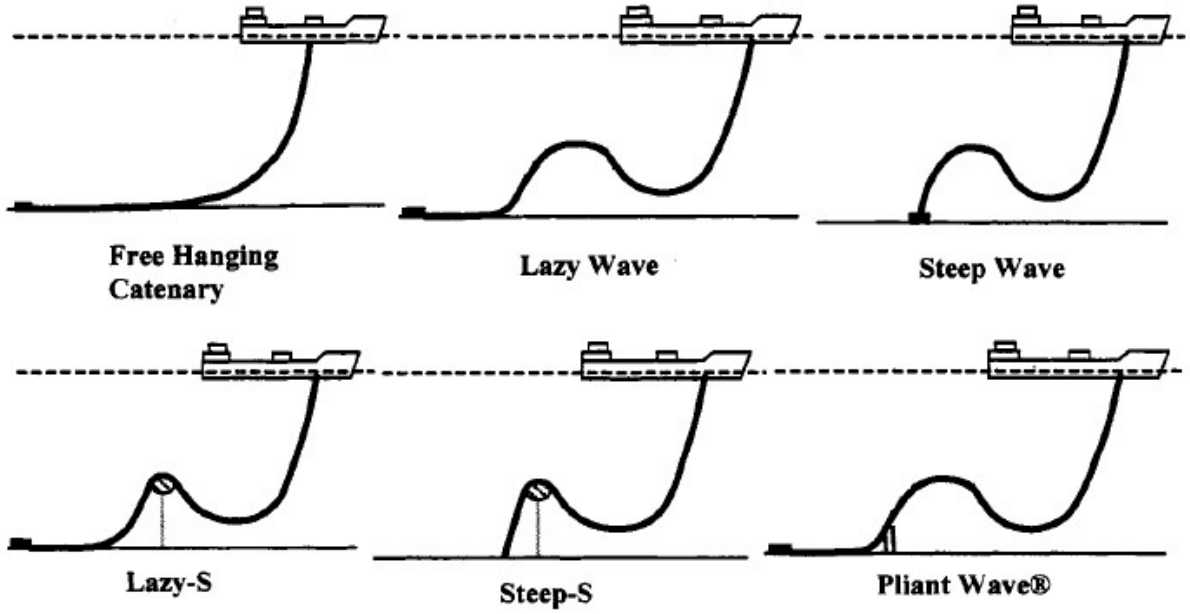

Figure 1-1 – Major variations of free-hanging riser configurations [1]

Deepwater riser systems challenges fall under any of the categories highlighted in Figure 1-2. Any of these challenges or a combination of challenges in Figure 1-2 (a) induce stresses and fatigue damage in the risers, limiting their application for drilling and production. If any or a combination of challenges is not designed out from the riser procurement process, failure of the system can occur when being operated.

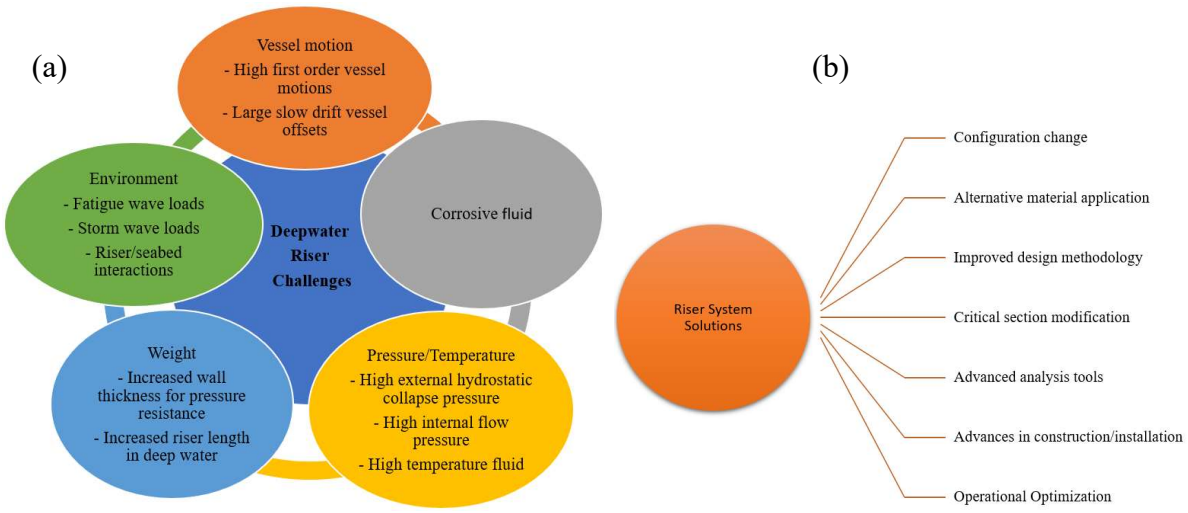

Figure 1-2 – (a) categories of deepwater riser system challenges, (b) categories of deepwater riser system solutions

Failures of deepwater risers can be catastrophic and disastrous to lives and the environment, hence the high safety precautions taken during their design [3, 4]. Fortunately, no available reports in the public domain have indicated significant failures for deepwater production risers. However, some minor failures have been recorded for flexible joints, tapered stress joints and VIV suppression devices, which did not cause injury to people or damage to the environment [5]. Over the years since the inception of deepwater resource exploration, deepwater riser solutions are continuously being developed by offshore industry and academic research institutions to address the riser challenges. Developed solutions can be classified as shown in Figure 1-2 (b). The details of the available solutions in these categories are dynamic in nature and are highly time-dependent, as the business models, safety, and quality requirements by the offshore industry for deepwater operations are ever-changing with higher stringent demands with time. Hence, this research is directed towards contributing knowledge to improve deepwater steel catenary riser systems under these categories of solutions to meet current business and safety standards. The research is driven by the development of cost-effective and efficient deepwater riser systems for optimum oil and gas production from deepwater field development.

1.2 Steel Catenary Risers Systems and Challenges

The riser solutions developed and investigated in this research aim to improve the response and design methodologies for the steel catenary risers (SCR). This can include SCR derivatives obtained by configuration change such as steel lazy wave risers (SLWR) and other new configurations developed during the research. An SCR is a string of jointed steel pipe, maintaining a catenary configuration between the floating production platform (host platform) and the seabed, as shown in Figure 1-3.

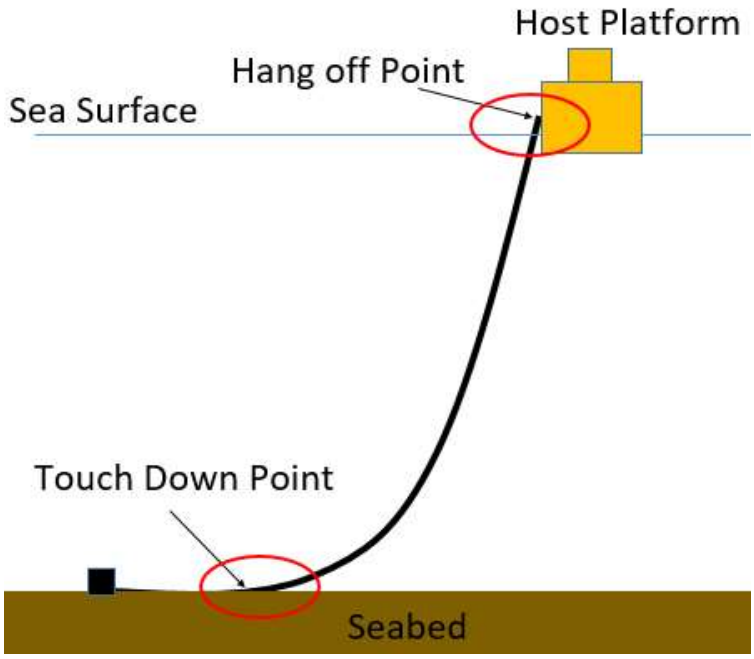

Figure 1-3 – Steel catenary riser configuration.

SCR are the most popular riser among the deepwater riser systems and have been widely adopted for many field developments [6]. This is mainly because of their simplicity [7] and lower delivery cost relative to other riser systems [8]. Although SCRs are considered most attractive [9], a lot of limitations need to be overcome in their development, installation and operation in terms of strength and fatigue issues at their critical sections, which are the hang off (HO) region and the touchdown zone (TDZ) [10] (see Figure 1-3). Due to the limitations highlighted in Figure 1-2 (a), it is challenging to keep the stress and fatigue responses, around the SCR critical sections, below their design limits prescribed in relevant design codes and standards, as they are usually high for harsh environmental conditions. Hence, many research efforts have been directed towards improving the SCR systems to increase their capability and capacity for extended applications in deeper and harsher operating conditions. This research work is a contribution to these efforts.

1.3 Research Focus

Driven by the above preview of SCR challenges, this thesis will focus on specific solutions under four broad areas of SCR solutions summarised in Figure 1-3. These areas are:

- Design and optimisation analysis methodology for SCR and its derivatives
- New riser configurations derived from SCR configuration change

- SCR-seabed interactions (sloped seabed and seabed trench impact)
- Operational optimisation (vessel relocation strategy)

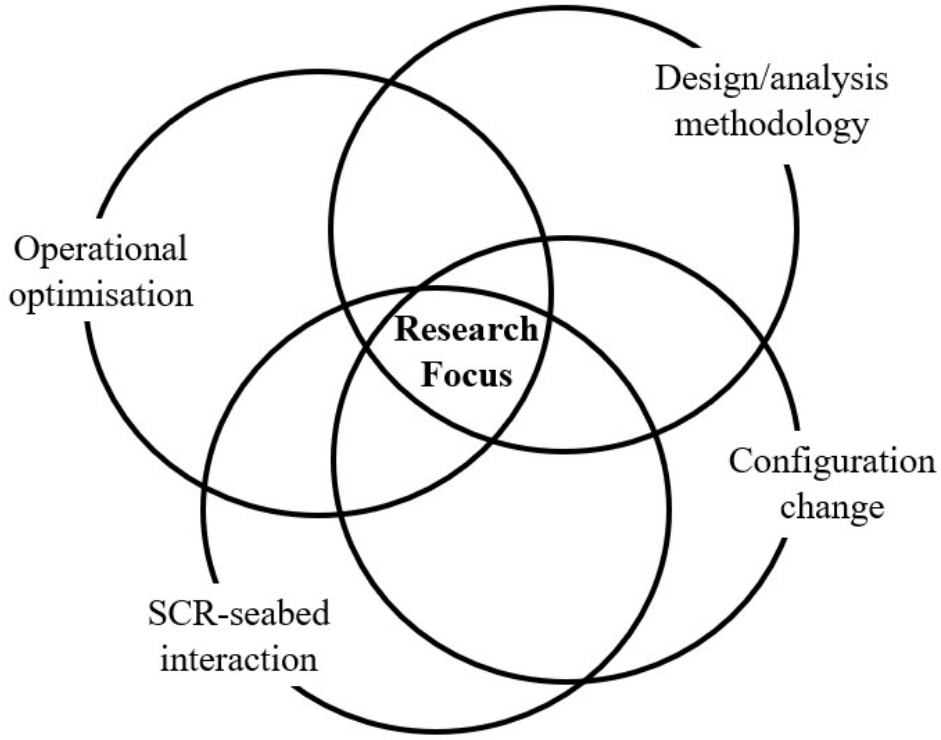

Figure 1-4 – Research focus

The SCR HO section is the region bordering the SCR connection to the host platform. Since this region bears the hanging weight of the SCR, the axial stress and the fatigue damage around it is usually high. The SCR is not directly connected to the host platform but through a structural interface which can either be a flexible joint or stress joint, designed purposely to bear the stresses around the SCR HO. Hence, the SCR HO is not considered to be a primary part of the SCR and is less of a concern in this research. The touchdown zone is the region of the SCR in contact with the seabed, the first point of contact being the touchdown point (TDP), as shown in Figure 1-3. The seabed section of the SCR connects to the subsea pipelines or structures, and the longer this section is, the more static condition it assumes due to the seabed's frictional resistive force. The SCR section around the TDP is most responsive to dynamic conditions and bears the bulk of the stresses and fatigue damage due to the large fluctuating bending response and active(dynamic) boundary conditions with the seabed. The active TDZ response is of

concern in this research since it is a native part of the SCR, and therefore is a focus of the research.

A major approach to mitigating the stress and fatigue damage at the SCR TDZ is to change the SCR configuration. In this regard, solutions such as the SLWR exist. The SLWR was developed from the SCR configuration by including buoyancy modules on the SCR sections close to the seabed [1, 11]. As a result, the buoyancy section is pulled up to give SLWR its unique wave shape. The buoyancy section and induced wave shape respectively reduce the riser's submerged hanging weight and decouples the riser TDZ from the dynamics of the host platform. Hence, the top tension, stresses and fatigue damage along the SLWR is well improved compared with SCR resulting in its implementations for some deepwater field development [12, 13].

Due to additional components to SCR when they are modified, the SLWR and the new riser concepts developed and investigated in this thesis will have associated cost compared with the conventional SCR. By the several design variables required to define any of these configurations, there can be an infinite number of configurations for a given water depth. The riser procurement cost is largely affected by the chosen configuration. Therefore, there is the need to obtain a good balance between configuration change (which provides opportunities to reduce the TDZ stress fatigue responses, etc.) and the riser cost. This is an engineering optimisation problem, which has recently attracted significant interest in the research domain and has also attracted the attention of this research, resulting in the development of the index matching optimisation technique.

The SCR seabed interactions is an area of the SCR being actively developed and investigated in the research domain. As more powerful numerical tools for riser analysis are developed, the complex nonlinear interactive process between the SCR TDZ and the seabed can be modelled and investigated. One area of focus of this research is the impact of sloped and the pre-trenched seabed on the strength and fatigue response of the SCR, an outcome of which led to the development of the simulations stage-based pre-trenching technique – SSBPT.

When the floating production platform hosting SCRs are relocated, the operation results in modifying the SCR TDZ configuration. This modification includes variation in the fatigue hot spot in the TDZ, resulting in spreading and a consequent reduction in fatigue damage. This thesis aims to develop a formal methodology to take advantage of the vessel relocation opportunities through optimisation of the vessel relocation design/operating variables.

1.4 Research Aims and Objectives

This research project aims to develop solutions for rigid catenary shaped risers to help them overcome challenges due to their high responses to vessel motions in extreme and fatigue wave environments. This aims to improve the riser configurations, design methods, and processes to better design output and riser models. To achieve this, the following objectives are set:

1. Acquire an understanding of deepwater riser solutions currently in the market through a literature review
2. Identify challenges and a technological gap in current riser solutions where solutions can be introduced.
3. Develop riser solutions to address some of the challenges while demonstrating their advances and limitation over other readily available solutions.
4. Understand the driver parameters for the proposed solutions through parametric studies.

1.5 Chapter Organisation and Layout

As depicted in Figure 1-5, this thesis is structured in nine (9) chapters. The organisation and contents of these nine chapters are summarised as follows:

- **Chapter 1**: This chapter presents deepwater steel catenary shaped risers and their current challenges. The factors mitigating the design responses and process of these risers are highlighted. The research goals and objectives are presented, and the thesis chapter organisations are outlined.
- **Chapter 2**: This chapter presents a review of the relevant literature for this research. The subject areas reviewed include catenary shaped riser configurations modifications for improved stress and fatigue responses, riser soil interactions challenges and solutions and vessel relocation strategy for riser fatigue mitigation. Proposed solutions to some of the identified challenges are presented, which will subsequently form the basis and focus of other chapters.
- **Chapter 3**: This chapter presents the riser analysis methodologies based on industry design standards and numerical software. This chapter presents a framework for modelling catenary shaped risers to conduct useful investigations on them and acquire knowledge that may not be directly obvious from the simplified analytical solution

process. The data, procedures, design limits, and methods presented in this section are applied across the thesis during the investigations of proposed solutions.

- **Chapter 4:** This chapter presents the index matching optimisation technique developed during this research to provide a straightforward assessment of the design optimisation solutions proposed and investigated in this thesis. The method development, validation, and demonstrated application for SLWR are contained in this chapter. The index matching technique is applied to optimise the proposed riser concepts, which are the branched riser systems (BRS) and the floating catenary risers (FCR). The optimisation technique is also applied for the vessel relocation strategy.

- **Chapter 5**: This chapter presents the branched riser system (BRS) solution concept, development, global analysis, and optimisation. The idea is to combine different sizes of risers to mitigate their challenges and harness their joint beneficial features. The basis for developing this riser configuration solution is the parametric response comparison of small and large-sized pipe risers. This study is also presented in this chapter.

- **Chapter 6:** This chapter presents the floating catenary riser (FCR) solution, concept development, global analysis, and optimisation. This riser solution concept allows new catenary shaped risers to be tied back to a production platform across crowded seabed fields or environmentally protected seabed sections. The FCR stress response, fatigue response, and cost can be affected by its configuration's variables. Hence the assessment of optimum FCR configurations is also conducted in this chapter.

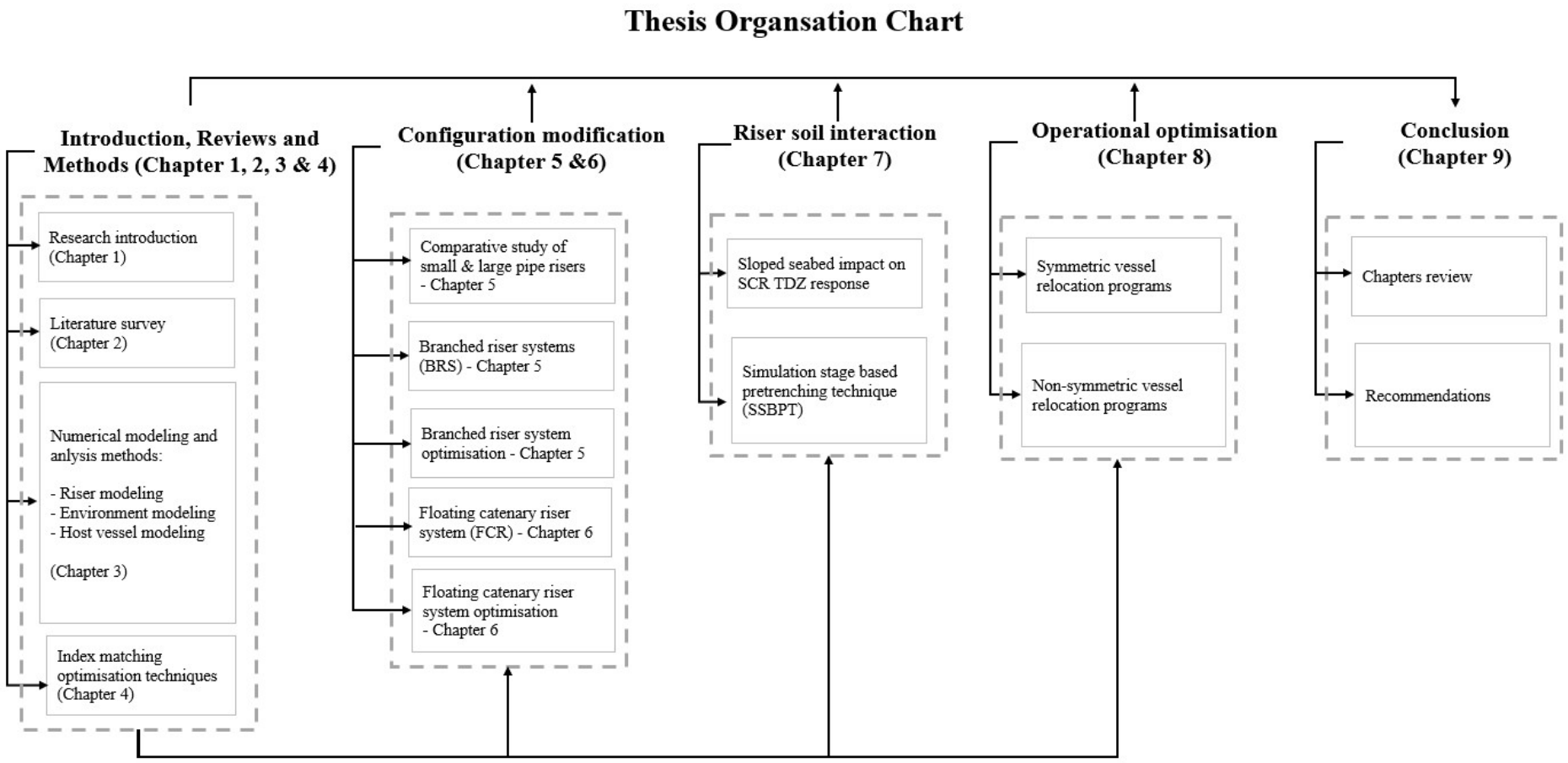

Figure 1-5 – Thesis structure and organisation chart

- **Chapter 7:** This chapter presents the simulation stage-based pre-trenching technique (SSBPT) for conducting fatigue assessment of the SCR TDZ fatigue response in a pre-trench. SCRs are observed from field data to embed themselves into trenches of varying depth shortly after installation (compared with their design lives). It is therefore vital to understand how these trenches affect the fatigue damage of the riser TDZ. The SSBPT is a technique proposed to model design trenches for SCR TDZ fatigue analysis. The method also lends the opportunity to computing SCR TDZ fatigue damage in pre-trench under complex host platform motions and environmental conditions typical of industrial riser design projects. This chapter also contains investigations of the impact of seabed slope on SCR TDZ strength and storm responses.

- **Chapter 8:** This chapter presents the vessel relocation strategy for SCR TDZ fatigue mitigation. Vessel relocation aids the fatigue damage spreading over a longer section of the SCR TDZ, resulting in extended fatigue lives for the risers. However, the procedure to obtain an optimum vessel relocation program is not available now. So, a formal, symmetrical vessel relocation strategy is developed for a single SCR. This technique is further advanced by introducing nonsymmetrical relocation programs for multiple SCR systems.

- **Chapter 9**: This chapter reviews and summarises the work performed in each of the preceding chapters. Also presented in this chapter are the limitations of the proposed solutions and suggested future work or investigations that can be conducted to improve these solutions.

1.6 Chapter Summary

The work in this thesis has been introduced, providing areas of focus for the research. The motivation, objective, and approach for conducting this research have been highlighted. The chapter organisation, structure, and workflow for subsequent chapters in this thesis have also been presented. Publications (Conferences and Journals papers) made over the research period were also presented. This introductory chapter will serve as a basis and guidelines on research work conducted and presented in other chapters.

2 LITERATURE REVIEW

This chapter presents the relevant literature and the basis for the research work conducted in this thesis. The review identifies major motion sources for SCRs, the challenges of SCRs and the available current solutions to those challenges. The technological gaps are highlighted, and new solutions are proposed and briefly introduced, with detailed discussions to come in subsequent chapters of this thesis. The proposed areas of contributed solution are broadly categorised into developing new riser configurations, improving the fatigue assessment methodology for the SCR TDZ interactions with the seabed, and developing operational optimisation techniques for SCR TDZ fatigue mitigation. The chapter sections are as follows:

- Section 2.1 – Riser host production platform and motion characteristics.
- Section 2.2 – Brief history of application and classification of deepwater risers.
- Section 2.3 – Steel catenary riser (SCR) system
- Section 2.4 – Existing solutions to SCRs challenges.
- Section 2.5 - Areas of contributions made by this research.
- Section 2.6 – Chapter summary.

2.1 Riser host production platforms and motion characteristics

Before venturing into the riser subject, it is relevant first to review the riser's major direct source of motions, which is the host vessel platform. As the water depth for riser application gets deeper, the application of fixed or compliant platforms for hosting riser systems becomes impracticable, hence the use of the floating system for hosting deep water risers. Since this research focuses on steel catenary risers (a type of production risers), the floating production platforms (FPP) are discussed. The FPP are the major source of motion for production risers and hence the major source of challenges for SCRs. As a result, the selection of the FPP and the riser systems at the conceptual phase of a deepwater project are very dependent on each other. The FPPs are built to have different forms and motion response features - see different

hull shapes of FPPs in Figure 2-1 [14] and a spectrum of wave energy periods influencing the FPPs in Figure 2-2 [15].

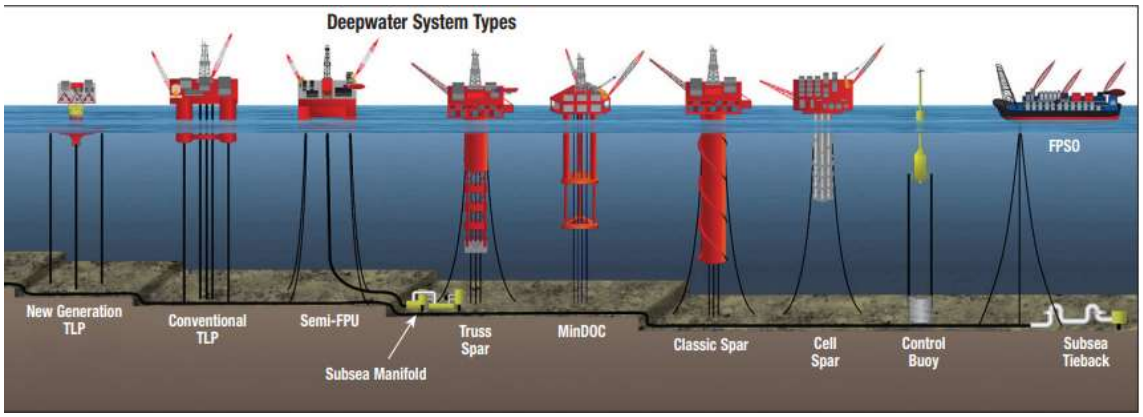

Figure 2-1 – Types of Deepwater Production Systems [14]

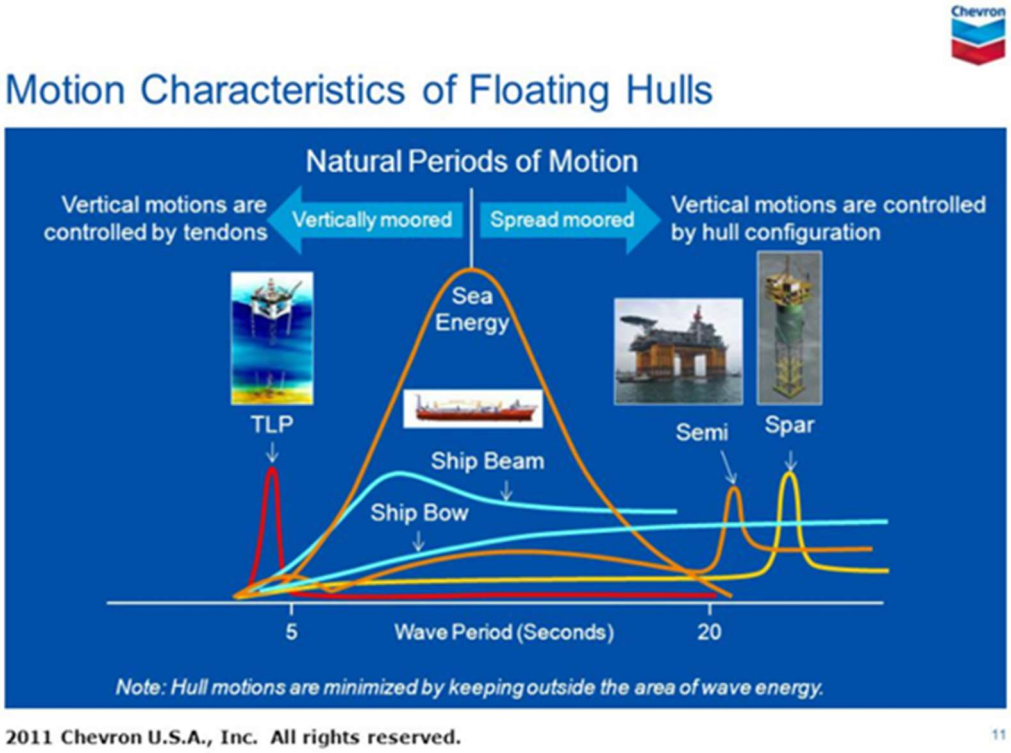

Figure 2-2 – Typical platform response to a spectrum of wave loads [15].

The common FPP used for offshore deepwater oil and gas production include the floating production storage and offloading unit (FPSO), the semi-submersible, the tension leg platform (TLP) and the spar platform. The main considerations for selecting an FPP for oil and gas production depend on the vessel's motion response, storage capacity, and manufacturing,

installation, and maintenance costs. Since FPSO is widely considered for analysis in this thesis, it will be the only FPP discussed.

2.1.1 Floating production storage and offloading unit (FPSO)

The FPSO is a ship-shaped mono haul floating structure used for producing, processing, storing, and offloading hydrocarbons to export systems (tankers or export pipelines). The FPSO houses the topside oil/gas processing equipment for crude hydrocarbons and storage facilities for the processed product. FPSOs have been used for offshore oil and gas production in regions like the North Sea, Offshore Brazil, Asia Pacific, The Mediterranean Sea and Offshore Africa (RIGZONE [16]). Other variations of FPSO include the floating storage and offloading systems (FSOs), the floating production systems (FPSs), the floating drilling production storage and offloading (FDPSO) and the floating liquefied natural gas (FLNG) vessel. FPSO can be reused, i.e., they can be relocated to produce another field when the current reservoir is depleted. The capacity of the FPSO is defined by the size of its hull, which in turn depends on the production rate and the size of the available export systems (Ronalds and Lim [17]). Figure 2-3 shows a typical FPSO in production mode.

Figure 2-3 Floating production storage and offloading unit (Rowles [18])

The FPSO is built onshore (dry dock) and towed to the offshore site. This implies that no offshore deck mating will be required. In deeper water, FPSOs are held to the seabed by mooring systems, which can be either spread or turret mooring systems. Turret mooring

methods can be disconnected in case of extreme environmental events such as hurricanes and cyclones and can be reconnected post-extreme events. The turret mooring method also allows the vessel to weathervane, i.e., align itself with the environment to suppress maximum vessel response in a beam sea. The spread mooring methods require mooring lines symmetrically distributed around the FPSO. Mooring lines are susceptible to wave second-order effects, which may impose large displacement on the FPSO, resulting in high stresses on the riser system. The turret mooring system is quite complex in design than the spreads mooring system and is only attractive for mooring FPSO in regions with extreme environments. On the other hand, disconnection for the purpose of surviving extreme environments or for maintenance at the dry dock while production is ongoing may not be an option for spread moored FPSO. The FPSO motions are typically more severe than other vessels, with the heave response having the most severe impact on the riser response (Sworn [19], Zimmermann, et al. [20]. This is because of its shallow keel and the fact that its response period in roll, pitch, and heave motions fall within the typical frequency range of the wave energy [21], which is between 5 to 20 seconds, as seen in Figure 2-2. The FPSO high response to the extreme environment can limit its application for hosting coupled riser systems like SCR in harsh water. However, they are often preferred over other vessel types for various technical and commercial reasons in mild environments and can be highly functional when equipped with turret [21].

2.1.2 Host vessel response characteristics and suitability for riser systems application

The response of FPPs in various environments and water depth determines their suitability for a given riser system. In Figure 2-2, we presented the typical response of floating platforms in a wave environment. Due to their deep draft, the semi-submersible and the spar have their natural periods higher than the wave energy centre. This is why they are less sensitive to wave environments and are considered good candidates for coupled riser systems in non-mild environments. The TLP, on the other hand, because of the high tendon stiffness, has natural periods in pitch, roll and heave below 5 seconds and are highly restricted or optimised in these degrees of freedom. The FPSO has its period fall within the typical wave energy range. This is the reason FPSO motion response is the most severe of all vessel types, making it very challenging for harsh environments unless the riser systems are decoupled from the FPSO motion. The maximum excursions of riser host platforms depend on the water depth by a constant factor because they depend on the anchoring system’s restoring force. Typically, the

watch cycle radius of TLP is about 10%, the FPSO about 30%, the spar about 15% and the semi-submersible about 20% of water depth [22]. Figure 2-4 presents the riser systems compatibility with the different floating platform types.

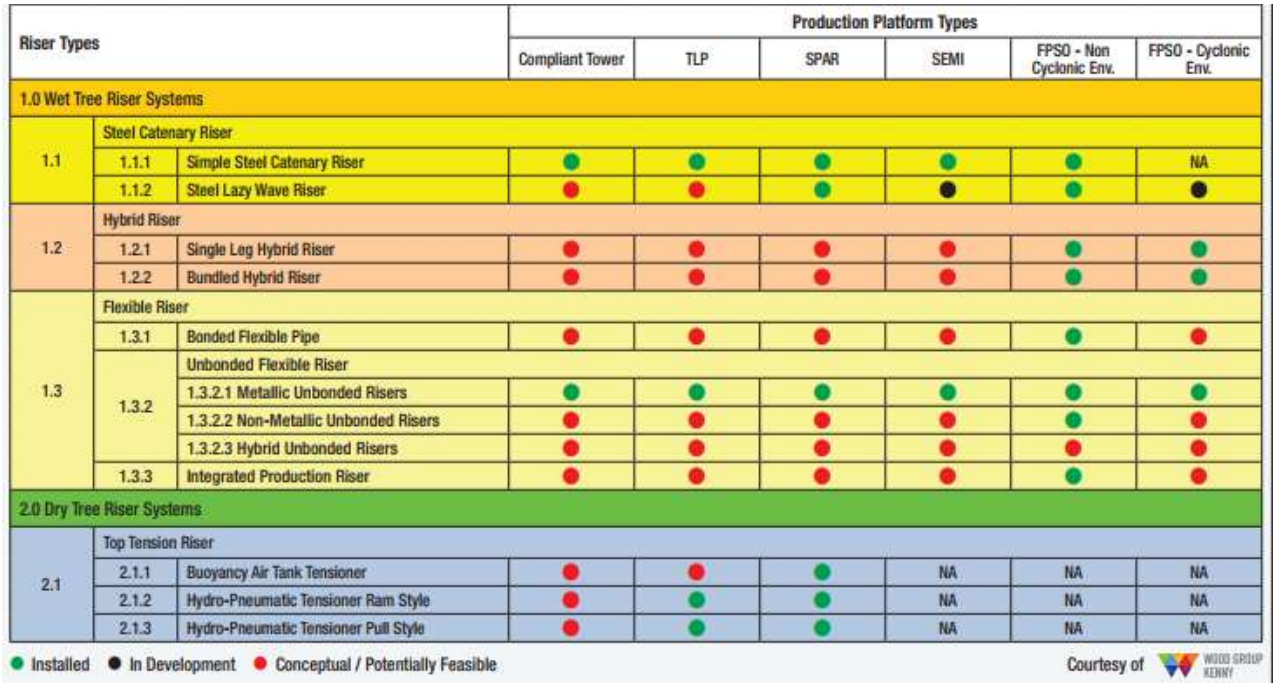

Riser Types			Production Platform Types					
			Compliant Tower	TLP	SPAR	SEMI	FPSO - Non Cyclonic Env.	FPSO - Cyclonic Env.
1.0 Wet Tree Riser Systems								
1.1	Steel Catenary Riser							
	1.1.1	Simple Steel Catenary Riser	●	●	●	●	●	NA
	1.1.2	Steel Lazy Wave Riser	●	●	●	●	●	●
1.2	Hybrid Riser							
	1.2.1	Single Leg Hybrid Riser	●	●	●	●	●	●
	1.2.2	Bundled Hybrid Riser	●	●	●	●	●	●
1.3	Flexible Riser							
	1.3.1	Bonded Flexible Pipe	●	●	●	●	●	●
	1.3.2	Unbonded Flexible Riser						
		1.3.2.1 Metallic Unbonded Risers	●	●	●	●	●	●
		1.3.2.2 Non-Metallic Unbonded Risers	●	●	●	●	●	●
		1.3.2.3 Hybrid Unbonded Risers	●	●	●	●	●	●
	1.3.3	Integrated Production Riser	●	●	●	●	●	●
2.0 Dry Tree Riser Systems								
2.1	Top Tension Riser							
	2.1.1	Buoyancy Air Tank Tensioner	●	●	●	NA	NA	NA
	2.1.2	Hydro-Pneumatic Tensioner Ram Style	●	●	●	NA	NA	NA
	2.1.3	Hydro-Pneumatic Tensioner Pull Style	●	●	●	NA	NA	NA

Figure 2-4 – Riser system options for different production platforms [23]

The FPSO, apart from their motion response limitation in harsh environmental conditions, are mostly favoured by investors for the following reasons [24]:

- They save time and cost in deployment and relocation to other fields development to be reused and are suitable candidates for marginal field production. This provides the opportunities to produce fields that are once classified as non-viable.
- They provide the option of turret mooring systems, which make them safer for disconnections from pipeline /riser networks during large and extreme conditions.
- They provide leasing opportunities, bringing flexibility to the producer, who may not necessarily want to build new vessels for production.
- Because of the ease to create smaller versions of the vessel type and its shallow hull features, FPSO can be applied in very shallow and restricted locations.
- The substantial amount of oil and gas the FPSO can store provides increased commercial viability for marginal fields.

- FPSO is a good candidate for targeted early production, as they can be rolled out within months. This is possible since existing ships can be modified into an FPSO rather than designing one from scratch. Hence, they must not be custom made as their lives do not necessarily start as an FPSO.
- The FPSO provides larger opportunities for retrofitting. Along with its longer hull for riser porch, this increases the desire to extend the vessel life beyond its counterparts.

2.2 A brief history of application and classification of deepwater risers

Marine risers came into existence in 1950 in offshore California, where they were first implemented in drilling activities. They were subsequently used in 1961 in drilling on dynamically positioned barge CUSS1 [2]. Since then, marine risers have been used for drilling, completion/work-over, production and export purposes. Risers designed for production purposes were first seen in the 1970s, and the top tension drilling riser technology inspired these. Subsequently, production risers begin to take other forms such as flexible risers, top tensioned risers, steel catenary risers and hybrid risers, which are a combination of steel and flexible risers [2]. The bundled hybrid riser was the first production riser to be installed on a floating production platform in the Argyle field, the North Sea, in 1975 and was based on the low-pressure drilling riser technology [2]. It comprises a core pipe (functioning as an export riser) and several other satellite risers attached to the core pipe. The bundle riser was again implemented in 1988 in the Placid Green Canyon field in the Gulf of Mexico. The single offset hybrid riser is based on the bundle riser systems technology, except that each riser pipe stands alone and are supported separately by individual buoyancy tank. This provides the advantage of accessing the riser separately for replacement and effecting repair on any of the risers in case of damage while others are still in use. The Flexible riser came into existence as a result of an extraordinary development program in the 1960s. The French petroleum institute attempted to develop a drilling flexible riser system that failed and was abandoned [2]. Subsequently, flexible lines were then applied for other use such as production and export. Flexible risers were used as flow lines in the early 1970s. They were then applied as dynamic risers in 1977 on the Garoupa field offshore Brazil and in the North Sea on the Duncan and the Balmoral fields [2]. The Top Tensioned Risers (TTRs) were first used in 1984 for production/injection and export on the Hutton TLP. The TTRs subsequently were used on other TLP and spars [2]. The Steel Catenary Risers (SCRs) were initially used on a fixed platform for export purposes

in the 1990s on P-18 semi-submersible offshore in Brazil. The first use of SCR for production platforms was on Auger TLP in 1994. Since then, SCRs have been widely used for more severe applications.

Classification of riser systems can be based on function, wellhead location or structure/configuration. Functionally, riser systems can be drilling risers, completion/work-over risers and production risers. Structurally, risers can be coupled or uncoupled riser systems. Coupled riser systems are those directly connected to the host platforms. These include the Steel catenary riser, the flexible riser and the steel lazy wave riser. For these risers, the motion of the vessel directly impacts their response. The uncoupled riser systems are those whose rigid/steel sections (vertical or catenary) are connected through a flexible jumper to the vessel. These riser systems include the Hybrid risers and the Top tensioned risers. The motion of the host vessel does not directly impact these riser systems. Instead, the flexible jumper link absorbs/dampened the vessel motion reaching them. By wellhead location, the riser can be classified as dry tree risers where the wellhead is located on the platform or wet tree risers where the wellhead is located on the seabed. TLP are the common host for dry tree risers, which are top tension risers. Figure 2-5 presents a more inclusive way of grouping the risers. Other new-generation risers have been the product of modifying existing riser systems to enhance performance and overcome technical challenges. These riser systems include Weight-Distributed SCRs, Steel Lazy-Wave Risers (SLWRs), Tethered Catenary Riser (TCR), Catenary Offset Buoyant Riser Assembly (COBRA), Buoy-Supported Risers (BSR) etc.

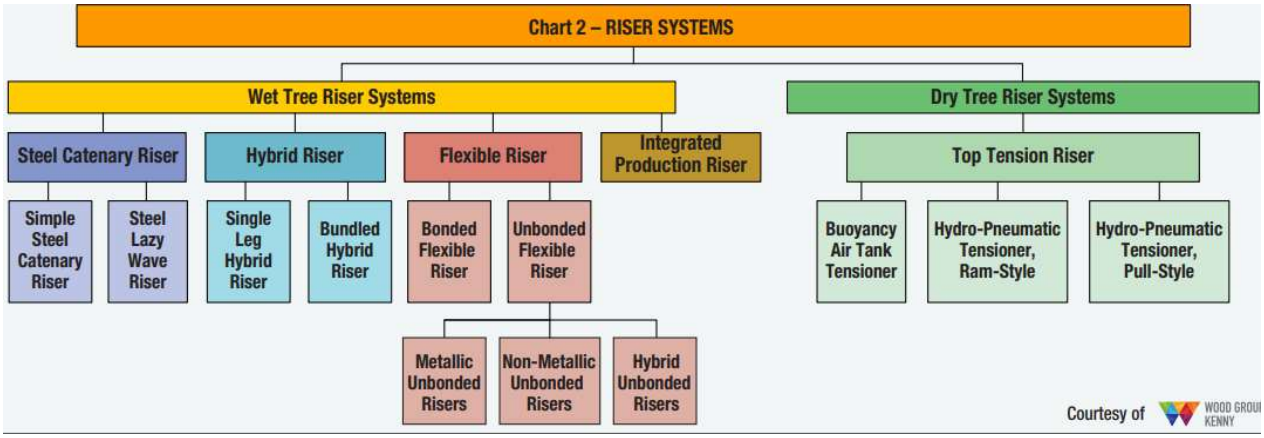

Figure 2-5 - Riser classification by wellhead location [23]

This thesis focuses on the steel catenary riser system, whose features, benefits, challenges, and proposed solutions will be discussed.

2.3 Steel catenary riser (SCR) system

A steel catenary riser (SCR) is a free-hanging string of steel pipes, either welded, maintained in a catenary configuration along the water column. The SCR is usually connected to the host vessel at its hang off (HO) usually through a flex joint or tapered stress joint structure. It makes its first contact on the seabed at the touchdown point (TDP) point, as shown in Figure 2-6 [25]. The active or highly dynamic contacts of the SCR and the seabed is referred to as the touchdown zone (TDZ). SCRs are widely applied on FPSO in regions of the world with benign environments and on heave optimised platforms (e.g. spar) in harsh environments. Different sizes (diameters) of SCRs have been implemented in projects across several water depths, as seen in Figure 2-7 [23]. A notable feature of the SCR is its simplicity, which arguably has contributed to its reduced cost of delivery and maintenance.

The static catenary configuration of SCR is obtained from a balance of its weight and buoyancy force. Assuming the riser global bending stiffness is negligible, the configuration can be roughly estimated mathematically from the basic catenary equations. Figure 2-6 shows the configuration range of the SCR profile relative to water depth and the feasible range of hang-off angles considering the design limits of the hang off connection structures [25]. A well-known challenge with the SCR is its response in strength and fatigue, to extreme and fatigue environments, at the critical sections of the riser (HO and the TDZ). The heave motions of the host production platform are the major source of compressive loads for the SCR TDZ, with the potential to cause global buckling.

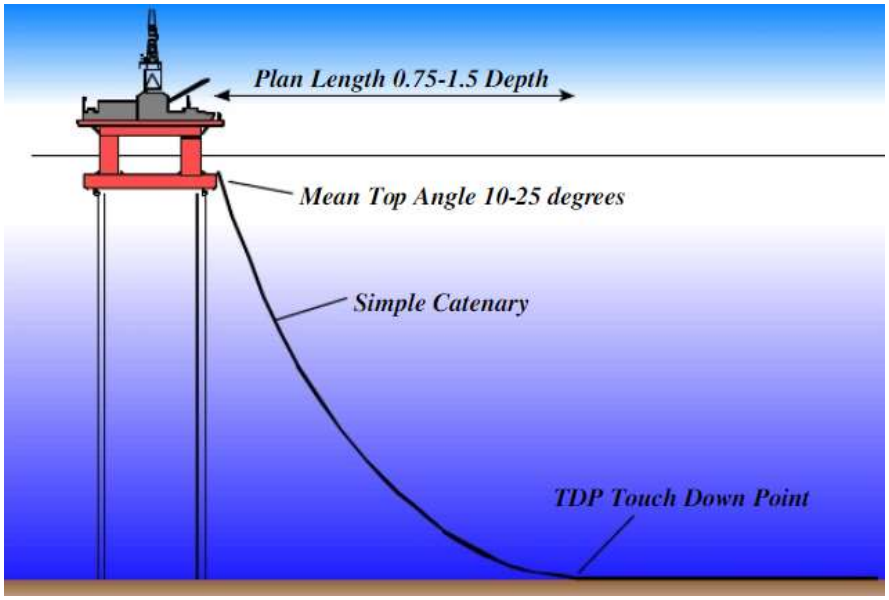

Figure 2-6 – Typical configuration of a steel catenary riser [25].

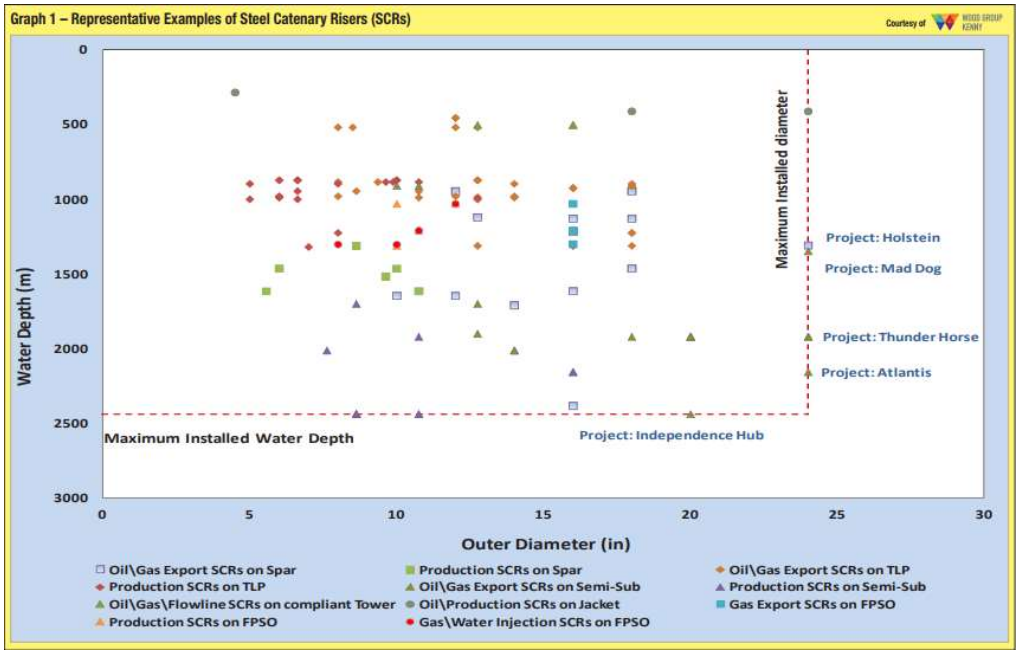

Figure 2-7 – Examples of implemented SCRs for different projects with the riser's outer diameter distributions and water depths [23].

2.3.1 Components of Steel Catenary Risers

The steel catenary riser is the most straightforward system for deepwater oil and gas production with minimum compulsory components. A few other optional components may be specified by the design. The SCR components, in addition to the pipe steel joints, include the following features:

Hang off System: The hang-off system is a structural connector of the SCR to the vessel hull. Functionally, the hang off system must transfer the riser weight to the vessel hull and accommodate riser angle changes due to vessel motions and offsets [22]. There are various connector types available, including the Flexible joint (FJ), the tapered stress joints (TSJ), the I-tube and the J-tube. FJ and the TSJ are primarily used for deepwater applications. The selection of the HO structure depends on the following factors [26]:

- Maximum angular deflection for the SCR in operating and extreme events
- Maximum bending moment in the SCR
- Maximum tension and torsional load to be supported in operation and during installation
- The fatigue capacity of the hang-off system

- Structural and leak integrity of the hang-off system
- Pressure and temperature limit of the material makeup
- Gas absorption ageing of material makeup
- Suitability for sour service and injection chemicals
- Ability to sustain load cracking
- Simplicity in geometry/dimension and ease to repair
- Compatibility with installation vessel facilities – J-lay and S-lay
- Potential to be wet stored
- Cost and lead time for delivery

The flex joint consist of a Flex Joint body, attached flanges, elastomer, reinforcements, extension and cavity. The flex element being the major component which allows relative rotation between the SCR and the host platform [26]. The flex element is a series of spherical steel and elastomer laminates vulcanised together. The TSJ are quite simpler in structure and construction than the FJ. TSJ can be either a titanium tapered stress joint (T-TSJ) or a steel tapered stress joint (S-TSJ). T-TSJ is more flexible than S-TSJ and can be applied for applications requiring large deflection.

- **VIV Suppression Device**: Vortex-Induced Vibration (VIV) strakes are optional components, depending on the design requirement. They are installed on the upper section or along the SCR length to suppress VIV. Current flow across the riser pipe creates vortexes, resulting in fluctuation of the pressure field around the pipe. If the fluctuation frequency is close to the natural frequency of the pipe, it will result in VIV, which contributes to the fatigue life reduction of the SCR. Two major VIV suppression devices are the helical strakes (fixed on the pipe) and fairings (movable parts). The helical strakes have been found to be more user friendly and economical [27].
- **Insulation**: SCR is usually insulated to keep the transported hydrocarbon temperature within the design limits for flow assurance. However, very thick insulations have been found to affect the dynamic response of the SCR. For example, a 50 mm thick thermal insulation coating can increase the TDP peak stress by 15 - 30% [28]. The specification

of insulation, therefore, must be carefully chosen considering the coating density, thickness, and overall heat transfer coefficient vis-à-vis the dynamic global response of the SCR.

- **Corrosion Resistive Alloys (CRA)**: The CRA are optional components specified by the design. It is an alloy material used to cover some internal sections of the riser pipe. The internal lining of the riser pipe with CRA provides the pipe resistance to corrosion and loss of wall thickness. These improve the strength and fatigue life of the riser pipe. CRA can be fitted mechanically or by metallurgy process during the SCR pipe joint manufacturing. The mechanical laid clad type is more cost-effective but less qualified for deepwater application. Generally, pipe joints with CRA are expensive to manufacture and are only required when necessary.

- **Anchoring System**: SCR can be continued from a laid pipeline or terminated on a subsea structure. However, the TDP axial and lateral motion, besides the ratcheting effect developed from cyclic expansion loads, can be high enough to require some means of stability [29]. Therefore, fixed anchoring will be necessary for SCR, where it is determined that the seabed section cannot provide the required stability [7]. The Stab Hinge and Over (SHO) assembly, installed on a seabed pile foundation, is a common termination structure for SCR. It provides the riser with anchorage during installation and operation.

2.3.2 Benefits of Steel Catenary Riser System

The following include the benefits of Steel Catenary Risers:

- **Low delivery cost**: The simplicity in structure, components, and configuration is perceived as cost-reducing factors for SCR delivery compared with other riser types. Cost is usually compared in terms of procurement, design, fabrication, and installation. The delivery cost of SCR could be between 20% - 30% of that of an equivalent flexible pipe and up to half the delivery cost of a hybrid riser [30].

- **Simple interface**: SCR interface with subsea structures and the host vessel (at the SCR porch) are simple; hence simplified installation requirements can be specified compared to hybrid risers.

- **High collapse strength resistance**: SCR being constructed from steel provide high resistance to hydrostatic collapse pressure. As a result, its application can be extended for deeper water development than the flexible riser system.
- **High Temperature and pressure services**: Different steel grades can be specified for the SCR for different production conditions. SCR is known to have good resistance to high temperature and pressure services, which may be technically or commercially challenging with flexible riser pipes.
- **Field-proven technology**: The SCR technology is well established and has been field-proven across different water depths worldwide for various host vessels. This notion increases the understanding of the SCR and the confidence in its application for deepwater projects.
- **Advancement in insulation technology**: SCR allows the extension as a pipe in pipe (PIP) system. The annulus of the PIP system can be filled with dry insulation of different heat resistive capacities. This makes it possible to produce fluid with challenging flow properties.
- **Flowline extension capabilities**: SCR provides the benefit of a combined flowline and riser solution. This means that the installation of the flowline and the SCR can be coupled, resulting in lower installation time and cost.
- **Life extension opportunities**: At the end of the design life of the SCR, residue strength can be amplified by operational modifications to allow its continual usage beyond the design life. Field expansion can benefit from this opportunity offered by SCRs.

2.3.3 Limitation of Steel Catenary Riser System

The following include the limitation of Steel Catenary Risers

- **High top tension:** As the depth of the environment deepens, the SCR length increases. Associated with length increase is the increase in weight, top tension, and stresses at the HO section of the SCR. The SCR top tension can be influenced by other factors such as the grade of steel material used for the riser pipes, the vessel motion, the sea state conditions, the density of the fluid content transported, the riser diameter, and the minimum wall thickness. The minimum wall thickness is driven by the pressure containment and the hydrostatic collapse pressure requirements. The top tension

response of SCR is a vital input variable into the capacity design of the HO structure and cost.

- **High vessel payload**: The SCR host platforms holds several SCRs in place. The number of SCR hosted depends on the required hydrocarbon throughput produced per day from a field's reservoir (s). For large field development, with large reservoir content and high production rate, very many SCRs can be applied. As the water depths and other factors increase the weight of the SCRs, the overall payload capacities of the host platforms for all the SCRs are also increased. The vessel payload capacity has a direct cost implication for a given project. Also, the potential weight increase of the SCR puts additional constraints on the vessel type specification during the riser installation. The type of SCR installation vessel has a direct impact on the overall project delivery cost.

- **Less compatibility with high-motion vessels**: Compared to the flexible riser, the SCR is less compliant to high vessel motion and offsets. As a result, the SCR suffers high bending stresses, compressions, buckling and fatigue damage, especially at the SCR TDZ. This is the major challenge for SCR under dynamic load conditions. The objectives of the solutions proposed and investigated in this thesis are set to address this challenge.

- **Vortex-Induced Vibration (VIV)**: SCR interacts with the current environment resulting in VIV, which can reduce the fatigue life of the riser. VIV causes large fluctuations in the SCR pipe stress and resulting fatigue damage. This interaction is complex and depends on factors such as the riser hang-off angle, the current incident angle, the current flow speed, the pipe diameter, etc. The use of strakes to mitigate VIV impact have also been found to increase drag and significant torque on the riser pipe [28].

- **Complex seabed interaction**: The SCR seabed interactions involve deformation, remoulding, soil liquefaction, sediment transport, trenching, etc. These non-linear interactions characterise the TDZ response as a complex one, which has been simplified as linear during the SCR design analysis. However, these simplifications have been feared to result in under or over conservative SCR design. Further complexities are encountered when trying to qualify or quantify the SCR TDZ fatigue response in trenches dug by the TDZ during its early life. The impact of the trench on the SCR

fatigue response has attracted intensive research interest and have also been a major focus in this research.

- **Welding technology**: SCR installation is susceptible to available welding technologies. This is because SCR weld joints are critical points of fatigue failure and must be subjected to an extensive qualification process. Hence, the quality and performance of SCR welds are limited by the current welding technologies.

- **Spatial Constraint**: Unlike flexible risers and hybrid risers, SCR does not grant the flexibility of being adapted to random field layouts. Field layout must be developed alongside the SCR solution at the select phase of the project. This limitation can significantly impact future field expansion restrictions unless considered during the initial field design. This thesis also focuses on developing a riser configuration solution to address this problem and enable SCR to span across congested or environmentally protected seabed sections.

- **Installation challenges**: Although the installation of SCR is simpler than a hybrid riser system, it may take a longer time than a flexible riser if the lay method other than reel-lay is applied. The S-Lay or Jay-lay nstallation and the SCR HO transfer to the host vessel must be done carefully to keep the steel string within allowable stress and fatigue limit. This operation is highly limited by the environment and the motion response of the installation vessel.

- **Pre-installation challenges**: There is a possibility of installing and wet storing SCR before the arrival of the host vessel. However, the challenges encountered in doing so are still subjects of great concern considering the lay path, crossing of risers, interference with vessel mooring lines and adjacent structures, collapse challenges for the hang-off of the system, etc. As a result, SCR installation still lies in the critical project path, unlike decoupled/hybrid riser systems.

- **Flex Joint pressure and temperature limitation**: The flex joint material selection, structure, design, and fabrication are limited by the service temperature and pressure. This is a challenge for all risers applying FJ. In some HT/HP hydrocarbons applications, FJ application limit may be exceeded and cannot be applied.

- **Disconnection for host platforms**: SCRs cannot be disconnected from the host platform in the event of extreme weather conditions like the hybrid risers. This eliminates the option to use SCR for applications where temporal removal of the vessel from the destructive path of cyclones and hurricanes may be required.
- **Large step-out distance**: To obtain safe bending around the SCR TDZ within the offset allowance of the vessel, the step-out distances of SCR can be large for some water depth. This imposes increased tension at the hang off since more SCR length will be suspended in that water column to maintain a suitable TDZ bending response.

2.4 Existing solutions to SCR challenges

Several efforts have been committed by research institutions and the offshore industries to increase the application of SCRs for deepwater hydrocarbon extraction [31-33]. These solutions include the SCR configuration change such as steel lazy wave and shaped riser solutions [13, 34-51], the alternative material application for SCR design such as high strength material including titanium for the riser pipe joint [31, 52-55], the advancement in riser soil interaction modelling such as the development of non-linear riser soil interaction models [56-58], the decoupling of SCR from vessel motion such as the uncoupled steel catenary riser systems [59-62], the vessel relocation to effect fatigue damage spreading along the SCR TDZ [32, 63-65], the use of upset pipe end and titanium welding connection to improve the life of the riser at welded joints [31, 55, 63-70], the use of hydrodynamic dampers which enhances the damping of stress wave propagated from vessel motion to the SCR TDZ [67], etc.

Generally, we can categorise these current solutions for SCR challenges as follows:

- SCR configuration modification.
- Increased understanding of the SCR seabed interactions.
- Operational optimisation of parameters affecting the SCR response.
- Advancement in fabrication, construction, and installation technology of SCR systems.
- Application of alternative material (high strength) for SCR pipe.
- Improvement in SCR design criteria and analysis methodologies.

This review will focus on areas related to the first three of the above-listed categories of current solutions.

2.4.1 Configuration modification

As oil and gas exploration moves into a deeper, harsher, and more restricted environment, the application of conventional SCR systems becomes complicated. Hence, there is a need to extend the current capabilities of conventional SCRs. Configuration modification of conventional SCR has been a major solution proposed to improve its compliance and hence its response in strength and fatigue. Some of the modified SCR systems have been applied, i.e., field-proven, while others have not, but are available to the market for application or are still in the qualification process. Usually, newly developed riser systems are more technically feasible but can be more expensive than conventional ones. It is typical to see new SCR solutions in tough competition with the traditional SCR at the select stage of the project. Therefore, it is the weighted average of engineering and economics that determines the suitability of the riser systems, i.e., the choice to select either the conventional or modified riser systems. However, there are some scenarios where conventional SCR are prohibitive for application considering its responses. In that case, the developer is left with no choice than new solutions. Some of the solutions developed from configuration modifications of SCRs include:

- Steel lazy wave riser (SLWR) solution
- Weight distributed steel catenary riser (WDSCR) solution
- Tethered catenary riser solutions (TCR)
- Catenary offset buoyant riser assembly (COBRA) solution
- Buoyancy supported risers (BSR)Solutions

Steel lazy wave riser solution - The SLWR is a compliant riser system, considered to be a favourable solution to SCR challenges in harsh and deep water environments [20]. The SLWR is a modified SCR by adding buoyancy modules on sections of the SCR close to the seabed, giving it its characteristic wave bends. The buoyancy module is positioned to be out of the region of intensive current load in the water column. SLWR has an increased length and number of components compared with the conventional SCR and hence will have higher procurement costs than the latter. However, its cost is lower compare to hybrid riser systems [50]. Examples of typical SLWR configurations are presented in Figure 2-8 [30].

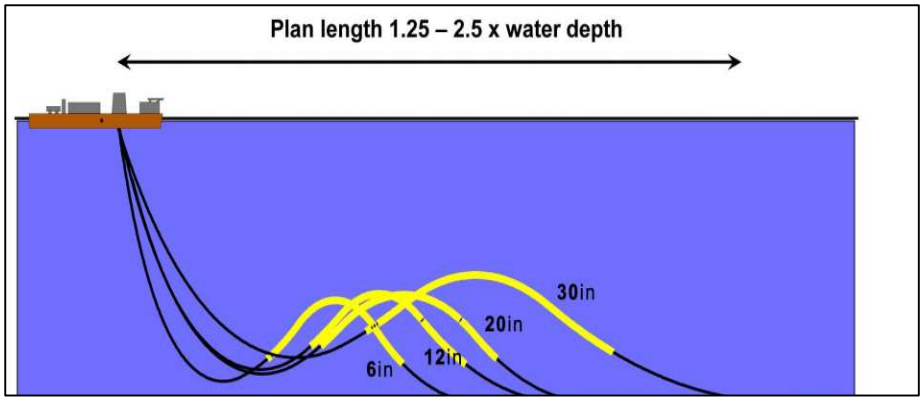

Figure 2-8 – Typical SLWR systems in water depth of 800 m [30]

The compliancy of the SLWR provides it with its ability to absorbs and decouple vessel motions from the riser TDZ. This ability improves the riser strength and fatigue response at the HO and at the TDZ compared to SCR. The variation in the SLWR curvature, water depth of application, arc dimensions and fluid densities can impact its response performance in strength and fatigue (wave and VIV). It has been found that while wave fatigue degradation correlates with the arc geometry, the VIV fatigue degradation correlates with the curvatures along the SLWR, causing maximum VIV damage at the TDZ [50]. Lighter weight SLWR will have a higher response frequency than heavier SLWR and hence will suffer a higher VIV fatigue. However, heavier SLWR will have higher HO tension and greater VIV damage at the HO structure. The vertical distance between the sag point (lowest point on the wave bend) and the hog point (highest point on the wave bend) is an important parameter optimised for the improved response of the SLWR in strength and fatigue. This distance (between the wave bend crest and trough) classifies the SLWR into high arches, mid-arch or low arch configurations. The SLWR configurations depend on the length and amount of the buoyancy system applied. When the section buoyancy is low enough, there is no distinction between the hog and the sag bend, a degenerated SLWR called shaped SCR is formed. The shaped SCR has its lowest elevation coinciding with the highest elevation along the buoyancy catenary.

The components of the SLWR are the same as SCR except with the addition of buoyancy components to generate the sag and arc bend. Though more complicated than SCR, it is simpler than a hybrid riser system. Components and sections of the SLWR are presented in Figure 2-9.

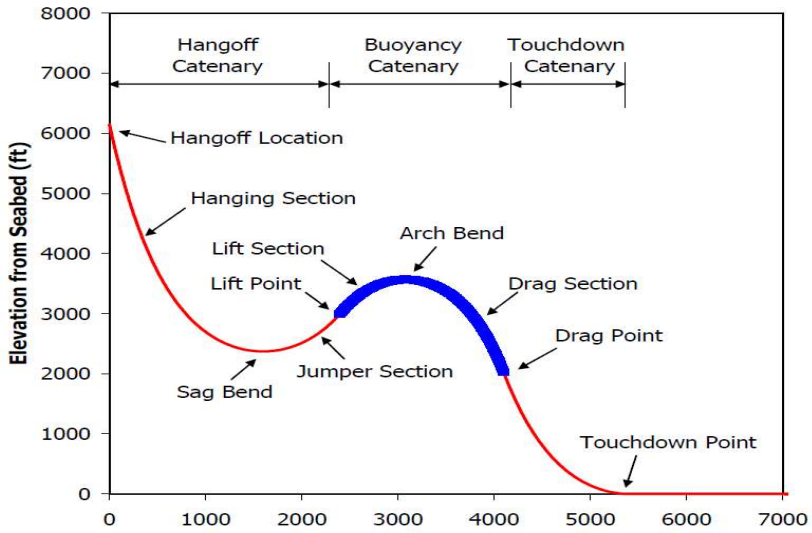

Figure 2-9 – Components and sections of a typical SLWR [71]

The hang-off structure for the SLWR connects it to the host platform and could be the FJ or the TSJ. The hanging catenary section of the SLWR is the double catenary section that extends from the hang-off structure to the start of the buoyancy module. It is the section containing the sag bend of the SLWR. The buoyant section provides the net upthrust to the SLWR system giving it the wave bend profile. The lift is generated from the buoyancy module installed in this section. The optimum configuration (cost and response) of the SLWR is determined by the length and size of the buoyant section. The buoyant section is made up of 2 sections: the lift section, which extends from the first buoyancy module to the wave peak and the drag section, which extends from the wave peak to the end of the buoyancy section. The lower catenary section forms the last buoyancy module to the touchdown point of the SLWR. The seabed section of the SLWR extends from the TDP to the SLWR seabed termination or anchor. The following challenges face the decision to apply SLWR:

- **Configuration optimisation**: The optimisation of SLWR configuration depends on several parameters, including the hang-off angle, the buoyancy capacity, the location and distribution of buoyancy [20]. For such a multi-variable optimisation problem, there is no absolute optimum configuration but one that satisfies the design requirements of the developer.

- **Higher cost than SCR**: The SLWR, an SCR with additional components (buoyancy module), will require an extra cost in manufacturing and installation compared with SCRs.

- **High heave motions**: The lightweight of the SLWR increases its dynamics in the water column. This increases its potential to clash with neighbouring structures like the mooring lines and adjacent riser systems. For relatively shallow water with lower hydrodynamic damping, the vessel motion can result in significant fatigue damage on the SLWR [72].

- **Flow assurance challenge**: The reversed curvature on the SLWR can pose challenges as they are a potential site for slugging to hydrocarbon flow. This can cause serious flow assurance problems.

- **Buoyancy module qualification**: Extensive qualification program of the buoyancy modules of the SLWR is a requirement, especially for deeper water application. This, if not properly planned, can impact the project timelines.

- **Crush load during installation**: The buoyancy modules are subjected to high crushing loads in the stinger during the installation of SLWR. This is a challenge for the lay process where S-lay would be a preferred installation method to J-lay.

Weight distributed steel catenary riser (WDSCR) solution - The WDSCR is a concept solution developed by Subsea 7 and Statoil to address SCR challenges in harsh environments and on non-heave optimised vessels [73]. The WDSCR concept is developed by varying the sectional weight of the SCR to obtain a degenerated SCR, a shape between the SCR and the SLWR. The weight variation can be achieved by using different densities of coating material or by attaching the weight module to the SCR section. Figure 2-10 presents a typical WDSCR configuration. The WDSCR configuration would be like the SLWR except that the section buoyancy is low enough such that there is no distinction between the hog and the sag bend. The light section weight is located close to the seabed, around the TDP, while the heavyweight section is in the straight part of the SCR. The lightweight section close to TDP dampens the motion amplitude at that area, while the heavy section of the straight part reduces the motion of that part since its inertia is increased. The overall effect results in reduced motion at the TDP leading to reduced compression and fatigue damage.

The basic components of the WDSCR are like those of SCR except the variation of sectional weight of the SCR by either using buoyant /weight modules or by using material coating with varying densities. The WDSCR has all advantages of simple SCR in addition to the increased strength and fatigue performance of the riser at the TDP. The advantage of this system over

SCR is that it combines the benefits of SCR and reduces the challenge of TDP compression and fatigue degradation.

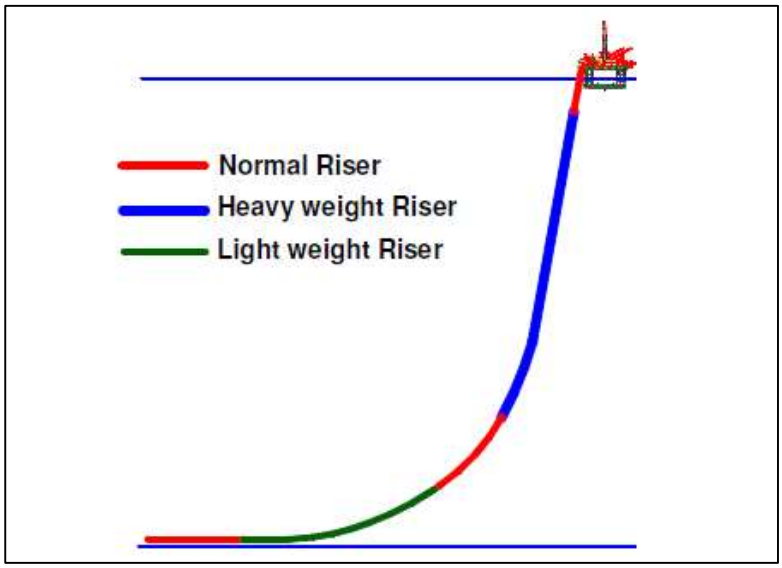

Figure 2-10 – Weight Distributed Steel Catenary Riser [73]

The following include challenges with the WDSCR:

- It is challenging to include in the design and qualification process of the coating material the required buoyancy and resistance to mechanical abrasion, thermal insulation, and resistance to hydrostatic creep (in deep water).
- The WDSCR has not been applied and hence not field-proven.

Catenary offset buoyant riser assembly (COBRA) solution - The COBRA solution is a riser concept developed by subsea 7 to meet the challenges of a harsh and deep environment. The system consists of an SCR section with a long slender buoyancy module on top tethered to the seabed, as shown in Figure 2-11 [60]. The top part of the buoyancy module is connected by a flexible jumper to the vessel, hence decoupling the vessel motion from the rigid SCR. The concept is based on proven technology from the SCR and the hybrid riser to design out their limitations. For instance, the rigid part of the COBRA is decoupled from the vessel motion, which is a major challenge for SCRs. Also, there is no complex bottom assembly like for hybrid risers since the rigid section maintains a catenary profile where the end termination is quite simple. The components of the COBRA are like those of the SCR with additional components such as the buoyancy module, the flexible jumper, the tether, and end connecting structures. The buoyancy tank provides the tension force required to pull the COBRA in place. The flow

pipe goes through the tank and is connected at the top through flexible joints to the flexible jumper. The pair of tethers function as mooring systems, connecting the buoy from below to the seabed. Each tether on each side of the buoy creates a more balanced system compared to the TCR. The tension in the tethers is created by the net upthrust of the buoyancy module. The foundation is a suction pile to which the two tethers are connecting, providing resistive balance force to the upward pull of the buoyancy tank. The gap between the foundation's tether connecting points is the same as that on the buoyancy module interface.

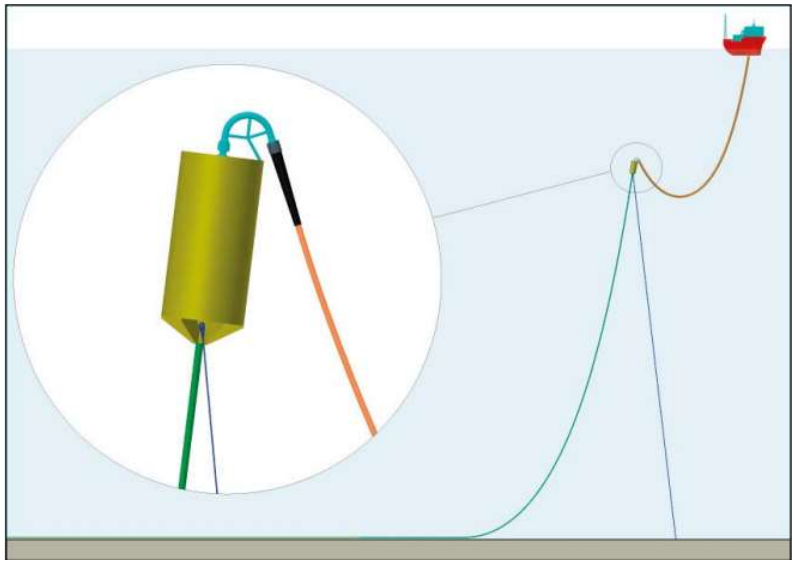

Figure 2-11 – Catenary offset buoyant riser assembly concept [60].

The following are benefits of the COBRA systems

- It has all the benefits of the hybrid riser system, including decoupling from vessel motion, decoupling of the installation from the vessel arrival, good stress and fatigue response, etc.
- The system is less sensitive to the environment since the buoy is below the sea surface, away from wave influence.
- The system bottom connection to the subsea structure is less complex than that of the single hybrid riser system.

The following include challenges of the COBRA system

- Several of the COBRA will be needed to produce a large field development. This amplifies the cost of development for large scale applications.

- The component design and fabrication cost and the conventional base SCR makes it costlier to deliver than SCR.
- The flexible jumper can be limited in capacity to resist HT/HP services and hydrostatic collapse pressure.

Buoyancy supported riser (BSR) solution - The BSR is a concept developed by subsea7 [74]. It consists of several SCRs supported by a subsurface buoy connected to the floating platform through flexible jumpers. The BSR is a hybrid system, and the vessel motion is effectively decoupled from the riser response by the flexible jumpers. A typical configuration of the BSR is presented in Figure 2-12 [74]. The subsurface buoy is placed below the wave zone to remove it from the region of high wave excitations. The buoy is anchored by eight tethers (2 on each corner) via a chain system and a gimballing device to the foundation pile [75]. The buoy's hull is shaped as a closed pontoon with uneven volume to balance asymmetric payloads from the risers and the flexible jumper. Each buoy system, depending on its buoyant capacity, can support several risers. The system's functionality depends on the balance of upthrust and pulls off the mooring lines on the buoy. If the net upthrust is too small, the buoy may lose support capacity resulting in increased hang off angles for the SCRs and the tethers. Lower thrust can also potentially lead to imbalance that can cause the buoy to clash with the vessel mooring lines, and the tethers and sagging movement on the jumpers [74]. If the upthrust is too high, the design requirement of the components (tethers, foundation, and buoy) will be large and would have a high impact on the delivery cost. Therefore, a huge amount of complex system analysis backed by prototype tank testing is required to obtain an acceptable design envelope.

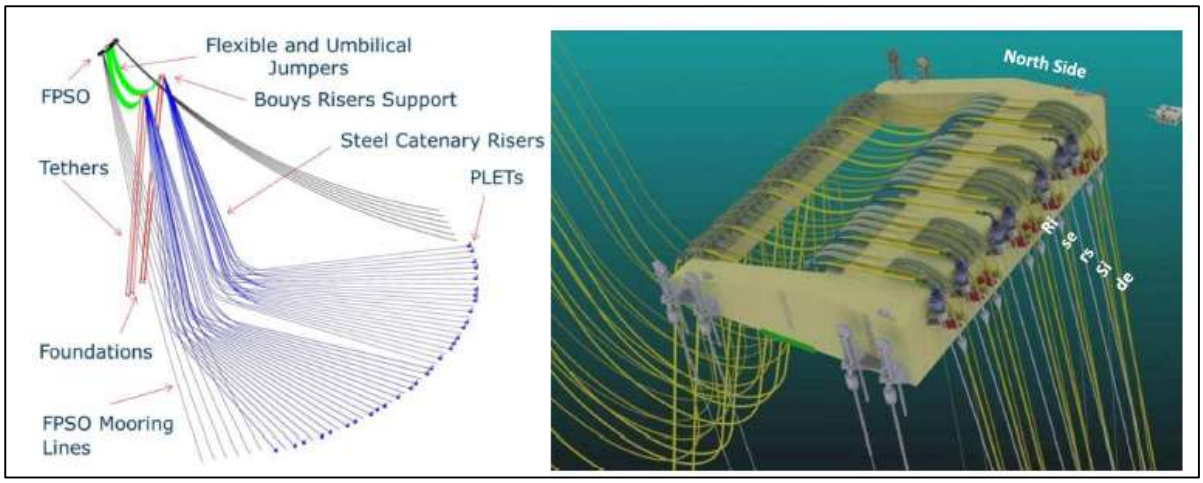

Figure 2-12 - Buoy supporting riser system [74]

The components of the BSR are shown in Figure 2-12. The benefits of the BSR system include all benefits of the SCR (see section 2.3.2) besides the following:

- The system is decoupled from the vessel motion response, resulting in excellent SCR strength and fatigue response.
- The system's installation can be decoupled from the vessel arrival removing its design from the critical project path.
- Since the vessel is not supporting the heavier weight of the system, it enhances cost-effectiveness for the floating platform and the design of its components and makes available vessel payload capacities for another functional requirement.
- The seabed foundation of the SCR is simple, unlike those of the conventional hybrid riser system

The BSR is limited by water depth. As water depth increases, the system capacity to host many risers reduces. If the size of the buoy is increased with water depth, it may result in a very large system with a high vessel spread requirement during installation resulting in a higher cost of installation. Also, the BSR system is far more complex than SCR and requires a higher cost of delivery associated with a lot of components part to design and install. This effectively increases the risk inherent in the system compared with conventional SCR applications.

Tethered catenary riser (TCR) solution - The TCR concept was developed by subsea7 and consist of several SCR and umbilical supported by a subsurface buoy. The subsurface buoy is tethered to the seabed by a single tendon. The risers run uninterrupted from the floating platform to their subsea terminations through the subsurface buoy. The flexible jumper connects the floating vessel and the subsurface buoy, while the SCRs connects the subsurface buoy to the seabed. The TCR is developed to address the motion coupling challenge of the SCR with the host floating platform. The TCR concept is also set to improve existing decoupled riser systems such as the BSR to simplify its tether arrangement and easier installation method. The decoupling of the SCRs is achieved through the flexible jumper. The decoupling reduces the motion excitation of the tethers and the SCRs connected to the subsurface buoy. The system is like the SHR except that the vertical part of the SHR is replaced with SCR, and the buoy system can host serval riser pipes. Figure 2-13 shows a typical configuration of the TCR system.

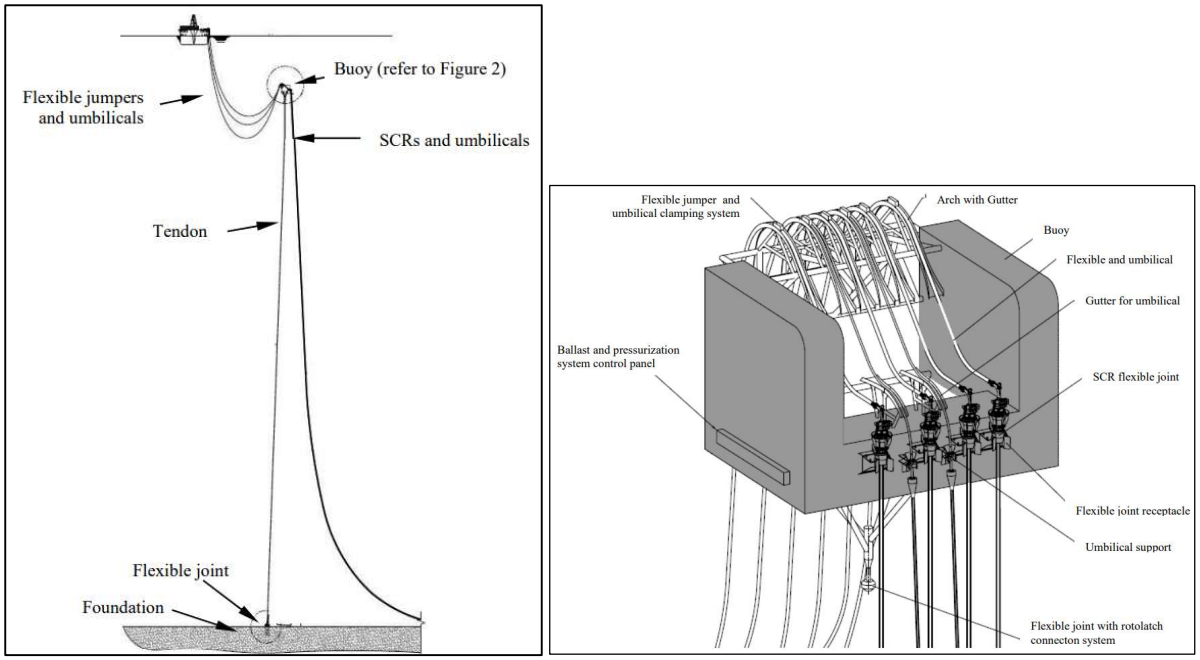

Figure 2-13 – Tethered catenary risers system [76]

The buoy supplies the required buoyancy to support the riser system. Buoyancy can be varied by varying the ballast of the buoy compartments. On the buoy is an arch with gutters through which the flexible jumpers are directed towards the connecting interface to the SCR. It also provides the interface for the flexible jumper and the tether/tendon connection. The tendon is a seamless pipe welded together to provide anchorage to the buoy. It is used to moor the buoy to the seabed, providing restraint against its horizontal and vertical motions. The upper tendon assembly (UTA) connects the tendon to the buoys. It can be a flexible joint or rotor-latch, or tapered stress joint. The lower tendon assembly (LTA) can be a rotor-latch or a flexible joint. It connects the tendons to the seabed foundation. The foundation is a pile structure that transfers the upthrust load from the buoy through the tendons to the seabed. The foundation is like those of hybrid riser systems having receptacles for tendon connection. The TCR system has all benefits a conventional SCR can offer in addition to the following:

- The SCR is decoupled from the vessel's motion, providing it with high performance under fatigue and extreme loads.
- There is no payload constraint on the host platform since a subsurface buoy supports risers.
- The system is less sensitive to the environment since the buoy is located below the sea surface, away from big wave influence.

- The TCR system can be preinstalled before the vessel's arrival, adding value to the project schedule.
- Its design, construction and installation are based on already qualified technology of flexible pipes, catenary risers, hybrid risers, floating buoys, flexible joints, foundations etc.

The following include the limitation of the TCR system

- With each buoy configuration, a small angle of deflection is allowed for the SCR
- The additional components compare to SCR makes it more complex in design and costlier to deliver than the conventional SCR
- The TCR can only host a few SCR numbers and is suitable for one to two drilling centres. For large field development with many drill centres, the system application will not be economical. This also limits it as a good candidate for future field expansion and tiebacks.
- The system loading is non-symmetrical, and its stability is based on the correctness in the buoy compartment ballasting. This, coupled with the tether connecting the floating buoy at just one point, increases the risk of overturning loads in the system about any rotational axis.
- The installation procedure can be complicated considering the extensive ballasting procedure required as loads are gradually applied to the system during installation.
- The system is less economical for very deepwater production with the possibility of a future tieback. As water depth increases, the size of the buoy will also need to increase. Hence, for very deep water, fewer risers can only be hosted, limiting possible future tieback.
- A challenge with the system is its stability in tilting and twisting under external excitations (from the environment and vessel motion) through the flexible, umbilical and SCR, which adds complexity to the system compared with SCR. This can result in unacceptable configuration and instability of the system.
- Although the system is based on qualified technology, it has not been field-proven.

- The flexible jumper can be limited in capacity to resist HT/HP services and hydrostatic collapse pressure.

2.4.2 Increased understanding of the SCR seabed interactions

The strength and fatigue responses of SCR around the TDZ is dependent on its interaction with the seabed. Realistically, the riser-seabed interaction is non-linear, with operative soil stiffness varying with the riser displacement amplitude [77]. However, it is a long design practice in the riser industry to simplify the seabed interaction model as rigid or elastic. This simplistic approach does not sufficiently provide an accurate basis for accessing the fatigue damage around SCR TDZ [57]. The wrong prediction of SCR responses can significantly impact its structural design limit, safety, and cost. It is therefore imperative to increase the understanding of the non-linear interactions of the SCR and the seabed. SCR soil interactions assessment has been a major subject for the riser industry and research institutions [78]. Many kinds of research have been conducted to improve on the riser soil interaction models, resulting in several non-linear (NL) numerical models used to approximate the real riser seabed interactions [56-58]. These NL riser soil interaction models have helped researchers to increase understanding of the SCR TDZ fatigue behaviour.

2.4.2.1 Pipe soil Interaction models

Riser seabed interaction is one aspect of the riser system, which is complex to represent. This is because it is associated with several nonlinear phenomena that are difficult to characterize such as trench formation, soil reconsolidation, hydraulic erosional processes, soil weakening under repetitive cyclic loading, nonlinear soil stiffness, soil suction effect etc. Over a long period, this challenge has been subject to extensive researches that have resulted in some significant findings and understanding of the interactions. Riser soil interaction in the in the past were simplified in design as linear response but more detailed and refined non-linear models are now being developed to model the complex interaction at least close to reality. One of the nonlinear models developed is that of Randolph (R) and Quiggin (Q) and implemented in OrcaFlex - a finite element software developed for the design and analysis of deepwater dynamic systems such as the risers. This report presents a parametric study of the pipe soil response under displacement control loading of different magnitude. Parameters considered for the analysis include pipe properties, soil properties, penetration amplitude, and rate of penetration. This will subsequently help us to obtain better understanding of the capabilities and limitation of the R and Q model in fatigue calculation at the riser touch down point.

A significant challenge with the design of riser system (especially catenary riser system) is the ability to predict its fatigue degradation at the area where it encounters the seabed, popularly known as the touch down zone (TDZ). During and after installation, the riser is expose to dynamic motions directly from the environment and from the host platform (vessel) which is in turn perturbed by the environment. In early times, fatigue prediction was either been conducted considering the soil as rigid or made up of linear springs. Such simplified considerations largely do not consider some complex non-linear interactions associated with the riser soil interface. Recent studies conducted has resulted in identifying significantly contributions of this nonlinear interaction to either increasing or decreasing the fatigue life of the riser system.

From the results obtained from the large scale testing conducted in the STRIDE and CARISIMA JIP, authors found out that the soil stiffness significantly influence the fatigue life of the steel catenary riser[79],[80]. As the soil stiffness increases to higher values, the fatigue damage rendered on the riser at TDZ approaches that which is obtainable when a rigid soil model is used but as the soil stiffness decreases, fatigue lifesaving relative to rigid seabed can be greater than 100% [81]. These extremes of observations based on the variation of soil stiffness places high importance on the need for accurate prediction of the soil stiffness. As a result, risers' designers are considering the rigid and the linear seabed model not sufficient to capture riser soil nonlinear responses especially in situation where the response utilization margin is small. Hence, there is the need to develop appropriate nonlinear seabed models to represent these interactions and predict accurately fatigue life in new riser system and to help extend the life of already existing system built on simplification [78].

There exist a number of nonlinear mathematical model that have been proposed based on data obtained from laboratory and large-scale testing on pipe soil interaction and there is a consensus on the nature of the hysteretic behavior of the soil as observed from experimental data. Some of the popular models proposed are those by Bridge et al [81], Aubeny and Biscontin [58], Randolph and Quiggin [56] and others. Figure -2-14 present a typical hysteretic soil model representing its interaction with the pipe under dynamic loading.

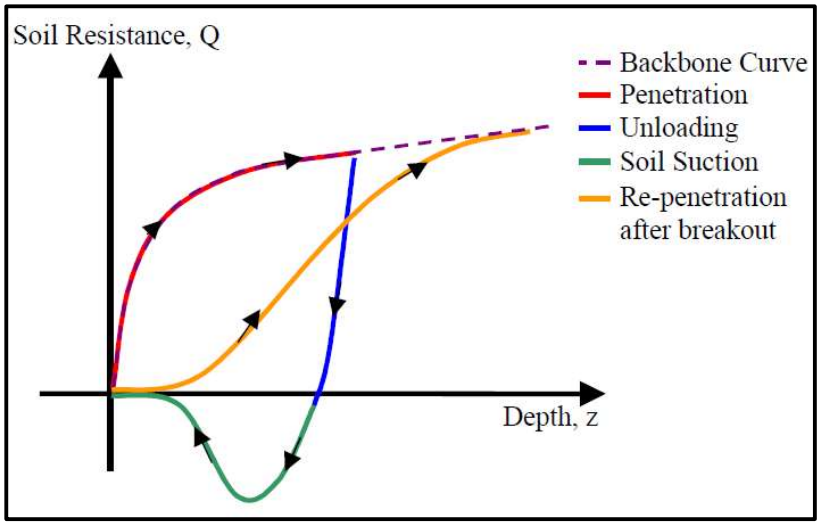

Figure -2-14 – Hysteretic Model for Pipe Soil Interaction [81]

The riser may be modeled as being in contact with the soil at all times during the interaction (in contact model) where it is assumed that the magnitude of the motion amplitude is small or may be considered to have broken out from the soil under large displacement motion (break out model). Such large amplitude loading cycles can be attributed to large vessel displacement associated with failure of mooring systems or/and extreme environmental event. The following represent generally the motion cycle of the pipe in the soil (including the break out cycle) [81].

1. Penetration – The initial penetration cycle represents the pipe movement downward into the soil until an equilibrium point between the soil resistance and the penetration depth. The force displacement curve follows the back bone curve representing plastic deformation

2. Unloading – The unloading cycle represent the upward movement of the pipe from its last equilibrium position resulting in a reduction in the penetration force to 0N within a very small displacement. The soil is swells elastically as it when unloaded during this phase.

3. Soil suction - After the short section of elastic response from step 2, the adhesion between the soil and the pipe continues to increase as the pipe continues its motion vertically upward causing a tensile force resisting the pipe's motion. The adhesion force quickly increases to negative maximum and then reduces to 0N as the pipe moves vertically upwards and out of the trench (break out).

4. Re-penetration - The re-penetration curve represents the reversal of the pipe upward motion back into the existing trench created during the initial penetration. The assumption here is that the pipe on its entrance into the existing trench will experience no resistance force from the soil until it reaches the initial penetration depth where it re-contacts the seabed. At this point, the soil resistance force increases until the curve re-joins the backbone curve at lower depths than the previous penetration and continues along this curve for further penetration.

2.4.2.2 Randolph and Quiggin Model

An example of these NL interaction models is the model proposed by Randolph and Quiggin (RQ) for an SCR TDZ oscillating under dynamic loading conditions [56]. The RQ model has been implemented in OrcaFlex, a dynamic offshore software widely used in the industry and academic domain [82]. The RQ model penetration modes and characteristics are shown in Figure 2-15. The model captures the non-linear behaviour of the soil as it is deformed by the motions of the SCR TDZ travelling through it. The non-linearity captured during the SCR TDZ inversions include soil stiffness degradation under cyclic loading, soil suction resistance and the soil buoyancy force on the SCR TDZ.

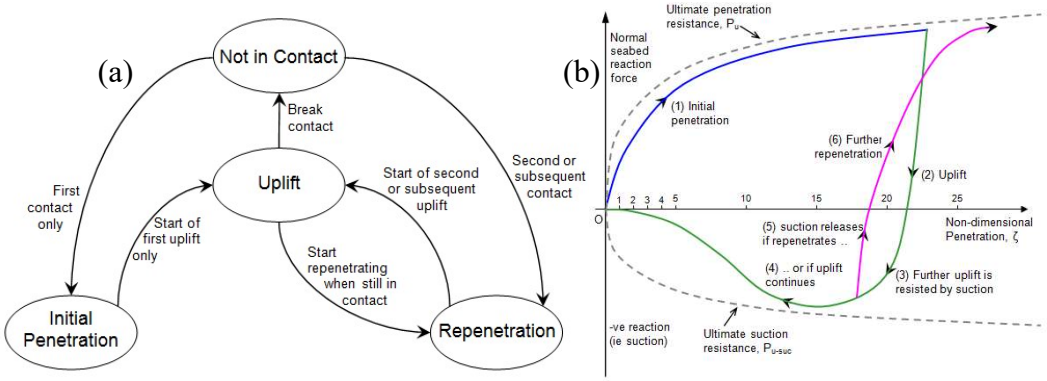

Figure 2-15 – Non-linear hysteretic pipe soil interaction model [56]: (a) penetration modes, (b) characteristics for different modes as modified in [82]

The Randolph and Quiggin (R &Q) non linear riser soil interaction P-y model is based on a hyperbolic secant stiffness formulation such as those proposed by Bridge et al [81] and Aubeny and Biscontin [80]. The model uses four penetration modes namely: Not-contact, Initial penetration, Uplift and Repenetration. In each of the mode, the seabed reaction force per unit pipe length, $P(z)$, is modelled using analyitcal function of non dimensionalised penetration, z/D, where z is the penetration (pipe invert) and D is the pipe diamter. The analytical formula use a term of the hyperbolic form, which provide high stiffness response for small reversal of

motion, but ensures that the resistance, $P(z)$, asymptotically approaches the soil ultimate penetration resistance (for penetration) or ultimate sution resistance (for uplift), as the penetration, z, increases or decreases from its value when the episode of penetration or uplift started [56].

The intial mode (Static configuration) of the pipe can only be represented by either “not in contact” or “initial penetration” mode and whichever of these modes is applied depends on the position of the pipe relative to the sebead. If the pipe is below the sebed, “initial penetration” mode is applied and will remain on this mode for further penetration unless there is reduced pipe invert at which the penatration mode switches to “Uplift”. While in uplift mode, it continues that way until it breaks out from the soil at which point the penetration mode swiches to “not in contact” and subsequent increase in pipe invert swiches the mode to “repenetration”. It should be noted here that “initial penetration” mode is only used once after which the penetration switches among other modes considering whether z has increases or decresed since the previous time step and what wa the last mode in the current pipe episode of displacement.

- For the static analysis where the system initial configuration is established, the position of the pipe node relative to the sebed surface (z) is checked. If this is positive (+ve) i.e below the seabed surface, the “initial penetration” mode is used otherwise if negative (-ve) i.e above the seabed surface, the “not in contact” mode is activated.

- Once the static penetration mode is set, the beginning of the dynamic penetration mode is determined by the last mode from the static analysis. If the static mode was “not in contact”, the dynamic penetration mode switches to “initial penetration” mode. If the static penetration mode was “initial penetration”, the dynamic penetration mode switches to “uplift” mode

- From the uplift mode, the pipe continues to lift up until any of the following happens

    - If the pipe continues to lift up until z is zero i.e break out of pipe from the soil, then the penetation mode swtiches to “not in contcat” mode. Once the pipe breaks out i.e in the “not in cntcet “ mode, the penetartion mode swicthes to “repenetration” mode for reversered motion otherwise it remains in thes “non incontact” mode.

- If during the “Uplift” mode, the pipe motion direction reverses such that the penetration begings to increase, the peentration mode swithches from “uplift” mode to “repenetration” mode. As along as the pipe does not berak out (i.e $z \neq 0$) , the penetration mode can continue to cycle between “uplift” and “repenetrtaion” mode

Note that for the static analysis, initial penetration is considerd pregressive as it does not allow any uplift and repenetration that might have coccured during and after intsallation since this state is not really known.

2.4.2.3 Impact of seabed trench on SCR TDZ fatigue response

The ROV survey conducted during the STRIDE JIP on three fields – Allegheny Green Canyon in the Gulf of Mexico (GoM), Marlin in GoM and P18 Marlim in Compos Basin, showed that stabilised trenches of several riser pipe diameters (OD) were created and that the SCR TDZs were entrenched in them [83]. The embedded section of the SCR TDZ is depicted in Figure 2-16 by the buried zone.

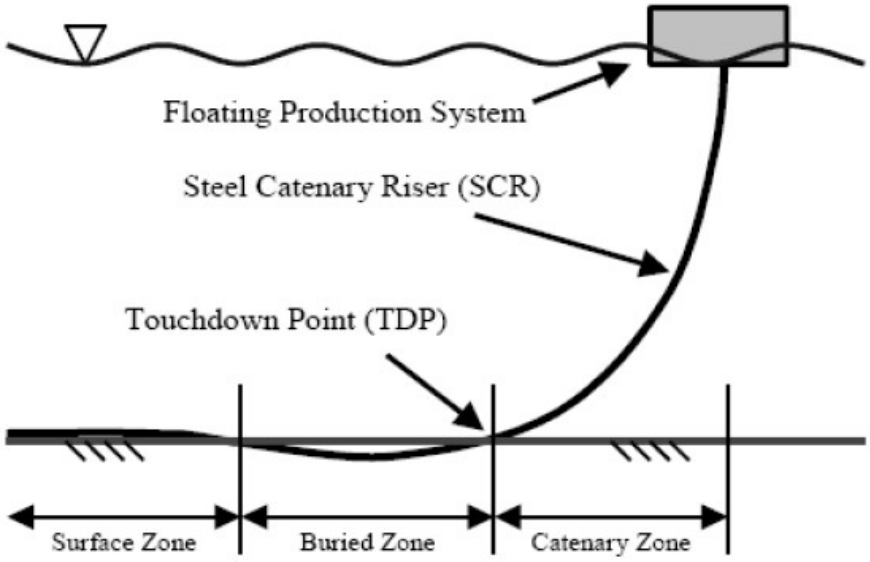

Figure 2-16 –Sections of the SCR interfacing with the seabed [84].

The catenary zone is the section hanging in a catenary configuration. Depends on the vessel offset, the bottom part of the catenary section may be raised from or laid on the seabed. Beyond the buried zone, the SCR rises to the seabed surface, where the line assumes almost a static condition. The periods in which these trenches developed within the buried zone were relatively short compared to the design life cycle of the riser system. Hence, the trench can be

considered as a pre-trench prior to the operational life cycle of the riser system and should be included in the SCR fatigue analysis. Therefore, there is the need to develop robust techniques to create an explicit trench for SCR fatigue analysis.

Some of the authors proposed using some mathematical functions to model the initial trench [77, 85-88]. For example, Langner (2003) investigated the pre-trench impact on the fatigue TDZ response using a circular arc to fit the riser side of the TDZ and a seventh order polynomial to set the boundary conditions for the pipeline side. It was concluded that the trench was positive to the SCR fatigue life. An investigation conducted by Sharma and Aubeny [87] employed the cyclic riser seabed interaction model developed by Aubeny and Biscontin [58] to create pre-trench incrementally. The final numerical trench was then modified using cubic polynomials to fit either side of the trench from the deepest point. The study concluded that the pre-trench has a positive impact on SCR fatigue life. A numerical investigation was conducted by Shiri and Randolph [89], using the RQ model to effect incremental SCR TDZ embedment to an ultimate trench condition in which the SCR TDZ fatigue response was investigated. The results showed that the pre-trench condition increases the SCR TDZ fatigue damage.

From these investigations and many others, conflicting reports exist on the impact of the pre-trench on the SCR TDZ fatigue response. For example, some authors reported that the trench increases fatigue damage [76-79], while others have a contrary conclusion [77, 87, 88, 90, 91]. The major challenge with pre-trench modelling and analysis is the danger of pressure hot spots being generated along the SCR TDZ section in contact with the pre-trench wall, resulting in unrealistic fatigue prediction [77, 92]. This was observed by Shoghi and Shiri [92], who reviewed some existing literature on the subject and attributed the confliction in reports to a possible abnormality in the pre-trenching process. Unrealistic fatigue damage may result from an incompatible trench and the embedded SCR TDZ natural profiles [92]. A comprehensive table developed in [93], showing the different schools of thought on the impact of seabed trench on the SCR fatigue responses, is presented in Table 2-1.

Table 2-1 – A summary review on the impact of trench on SCR TDZ fatigue damage [93].

Analysis type of effect of trench (or penetration)	Published literature	Seabed model	Software for global SCR models	Effect of trench on SCR fatigue life			
				Linear / Rigid seabed		Nonlinear seabed	
				Trench depth	Effect	Trench depth	Effect
Type 1: Effect of gradual trench development (relative to flat seabed)	Chukey et al. (2011)	Centrifuge test					Positive for GoM soil; Negative for Speswhite soil
	Shiri (2014a, b)	Nonlinear (RQ model)	Abaqus	N/A		Up to 5D	Negative
	Kimiaei et al. (2010; 2015)	Nonlinear (RQ model)	OrcaFlex	N/A		Unknown	Negative
Type 2: Effect of pre-formed trench (relative to flat seabed)	Langner (2003)	Rigid seabed	Finite difference	1.8D (rigid)	Decreased bending strain	N/A	
	Leira et al. (2004)	Linear and nonlinear (CARISIMA model)	RIFLEX	2D	Negative generally	2D	Negative generally
	Chukey et al. (2007)	Linear and nonlinear (STRIDE model)	Abaqus	0.5D, D, 2D	Positive	0.5D, D, 2D	Positive
	De Amicis et al. (2008)	Rigid seabed	Flexcom	5D (rigid)	Decreased bending moment	N/A	
	Sharma & Aubeny (2011)	Linear	RIFLEX	3.5D	Positive	N/A	
	Li & Low (2012)	Nonlinear (RQ model)	OrcaFlex	N/A		A series of	Positive
	Li & Low (2014)	Nonlinear (RQ model)	OrcaFlex	N/A		A series of	Positive for wave frequency motions, but mitigated by low-frequency motions
	Wang et al. (2013)	Nonlinear	Abaqus	N/A		0.3D, 0.5D, 0.7D, 0.9D	Positive
	Randolph et al. (2013)	Linear and nonlinear (RQ model)	OrcaFlex	5D	Positive generally	5D	Positive generally
	Shiri (2014b)	Linear	Abaqus	1.5D, 5D	Unpredictable	N/A	
	Wang & Low (2016)	Nonlinear (RQ model)	OrcaFlex	N/A		4D	Positive
	Chukey & Zakeri (2017)	Centrifuge test					Negligible

Several of these investigations have applied regular wave loads and significant simplifications in the analysis process. Therefore, it is essential to advance the pre-trench modelling process to create a more realistic pre-trench envelope for SCR TDZ fatigue investigation. A natural and fully developed pre-trench can be achieved by exciting the SCR TDZ through the vessel's first and second-order wave load and slow vessel drift motion during the lifetime of the SCR [92]. Such a fully developed trench will have a longer span (along the riser plane) and depth to accommodate the SCR TDZ motions.

One of the advanced techniques developed to address the pressure hot spots in the pre-trench profile is the "stepped trench" technique [77]. The technique is a numerical-analytic method, which starts with a base trench profile generated numerically [89] (see Figure 2-17 (a)). The base trench is then modified analytically such that the profile is identical to the riser profile on the pipeline side (see section 1 of Figure 2-17 (b)). On the riser side, the trench profile is made a mirror image of the pipeline side up to the point of inflexion (see section 2 of Figure 2-17 (b)), and then extrapolated linearly beyond (see section 3 of Figure 2-17 (b)). The modifications intend to expand the trench envelope to accommodate all motions of the SCR TDZ resulting from vessel excursions. However, it is not clear if this was achieved throughout the loading cycles of the analysis. With the current capability of OrcaFlex, it may be difficult to replicate the analytically modified trench profile for time-domain fatigue analysis of the SCR.

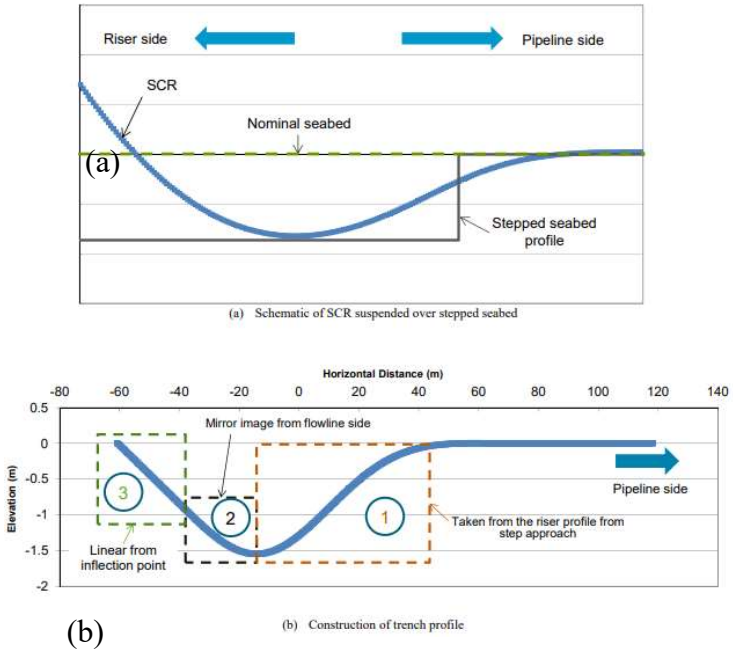

(b)

Figure 2-17 – Stepped trench profile development [77]

There is a need in the riser industry, during SCR design analysis, to be able to initiate a pre-trench and quantify its impact on the SCR TDZ response during the simulation of complex loading conditions in a full-time domain. A new numerical technique is developed in this thesis to address this challenge. This technique is referred to as the simulation stage-based pre-trenching technique (SSBPT).

2.4.3 Operational optimisation of parameters affecting the riser response

Operational optimisation for SCR is set to mitigate the level of fatigue damage in the SCR TDZ. A major example of this is the vessel relocation solution for SCR fatigue management. The fatigue damage in the active SCR TDZ is proportional to its exposure time to the applied fatigue load, which in turn depends on the variation in the SCR global position and configuration. The relocation of the vessel is a planned variation of the riser host platform from its mean position to effect changes in the global riser configuration, resulting in the spatial (arc length) variation of the SCR fatigue hot spots. The wider the variation or spread of the active seabed section, the higher will be the reduction of the fatigue exposure time and the SCR TDZ effective fatigue damage.

The vessel relocation solution for fatigue mitigation in the SCR TDZ has been referenced in literature to have been implemented in real-life projects [32, 63-65]. However, the methodology for investigating and conducting an optimum vessel relocation program is still absent from open literature. There is a need to develop a formal assessment method for vessel hosting SCRs. Considering multiple SCR for such optimisation analysis can be prohibitive numerically. Hence, the formal approach for vessel relocation strategy must be conducted in a way to cut down on the computation requirement of the process while capturing the optimum relocation programs. The development of vessel relocation strategy for SCR in this thesis is set to address this challenge.

2.5 Preview of areas of contributions made by this research

Driven by the SCR challenges presented and discussed in this chapter, this thesis will focus on providing improved SCR solutions by developing novel analysis methods and optimisation procedures to selected aspects of the SCR challenges. The areas of contribution are briefly discussed in this section. Detailed investigation and discussions of these new solutions will be presented in their respective chapters.

2.5.1 Branched riser systems

The branched riser system (BRS) is a concept developed and investigated in this thesis for deepwater application. Possible variants of the BRS include the Branched Steel Catenary Riser (BSCR) System, the Branched Steel Lazy Wave Riser (BSLWR) System and the Branched Lazy Wave Hybrid Riser (BLWHR) Systems. The BRS consists of a large-bore pipe terminated at an optimum water depth at a connecting structure. The larger bore riser pipe is then extended from the connecting structure to the seabed by two smaller riser pipes. The concept draws benefits from the performance of smaller riser bore pipes in strength and fatigue performance in a benign environment over large-bore riser pipes. Also, the BRS benefits from the opportunities provided by larger bore pipes for maximum flow throughput and vessel top decongestion. The BSCR variant of the BRS is focused on in this thesis.

2.5.2 Floating catenary riser (FCR) systems

The expansion of a deepwater brownfield may become necessary to increase the production of hydrocarbons. Such expansion often requires the installation of additional risers to the existing floating production platform. However, the seabed footprint of the production facilities may be congested with existing subsea pipelines and structures or environmentally protected. In scenarios like these, tying back of risers such as steel catenary riser (SCR) to the floating platform becomes challenging. The FCR is a novel riser solution developed in this thesis, with floating bends or ‘waves’ close to the seabed. The FCR is engineered to extend its touch down point (TDP) far beyond the nominal TDP of the SCR and away from the congested or protected seabed footprint. The riser sections before and after the nominal SCR TDP are floated by installing buoyancy modules on them. The multiple wave buoyant sections also allow the FCR to decouple its touch down zone (TDZ) from the floating platform motion. This can result in a significant reduction in the stress and fatigue damage around the riser TDP. A method to obtain the optimum configuration of the FCR has also been developed in this thesis.

2.5.3 Seabed sloped impact on SCR TDZ fatigue damage

Several factors can affect the response of steel catenary risers (SCR) around its touchdown zone (TDZ). These include the stiffness of the soil, the soil suction force on the riser TDZ, the soil degradation with cyclic TDZ loading, etc. Riser strength and fatigue response computation are usually performed considering flat seabed using a rigid or linear (spring) riser soil interaction model. However, bathymetric information obtained for the SCR lay path on the

seabed reveals complex seabed profile variation, indicating that the seabed is far from being flat around the SCR TDZ. In this thesis, the impact of seabed slope on the strength and fatigue responses of the SCR is conducted using a non-linear (NL) riser soil interaction model. The responses of SCRs on positively and negatively sloped seabed (rotated about the static touch down point on the flat seabed) are compared with responses of SCRs on the flat seabed.

2.5.4 Simulation staged based pre-trenching technique (SSBPT)

The development of seabed trench by the SCR TDZ in its early life can be caused by installation loads, direct hydrodynamic loads, and vessel first and second-order motion imposed on the SCR during and after its installation. Several studies have been conducted to investigate the SCR TDZ fatigue response as it progressively trenches itself into the seabed, while other studies have investigated the impact of existing trench or pre-trench on the SCR fatigue response. However, most of these investigations were conducted using a series of regular wave loads through quasi-static simulations. Also, although important information on the trench effect on SCR TDZ fatigue response is known in the research domain, little has been said about incorporating them in the actual SCR design process. In this thesis, the SSBPT is developed to address these gaps. Example analyses are presented to demonstrate the new approach and how the SCR fatigue response can be calculated in the presence of the created pre-trench. This technique makes it possible to conduct a full time-domain, irregular wave simulations of the SCR in the presence of a pre-trench created using the hysteretic non-linear pipe soil interaction model.

2.5.5 Vessel relocation strategy for SCR TDZ fatigue mitigation

This work is focused on developing a formal optimisation approach to the vessel relocation program for the SCR TDZ fatigue management. Vessel relocation is the planned repositioning of the vessel within the acceptable limit of the riser design to help spread and reduce the fatigue damage over the SCR TDZ. There is a need to obtain an optimum vessel relocation program that best reduces the SCR TDZ fatigue damage. Hence, the facility operator will need to know the optimum combination of the number of stations along the relocation axis, the distance limits for the relocation, and the relocation axis direction. The constraints on the problem are imposed by the stress utilisation, TDZ compression and top tension. To demonstrate the approach's suitability, we consider first a single SCR hosted by a production platform. The strategy is then extended for vessels hosting multiple SCRs. The fatigue damage responses of the SCR with

the optimum vessel relocation programs are compared with those without vessel relocation to quantify the magnitude of SCR TDZ fatigue damage reduction through this strategy.

2.6 Chapter summary

In this chapter, the main source of motion for the SCR is reviewed. The SCR, its benefits and limitations during application are discussed. There are different categories of solutions that have been developed in the literature to address SCR challenges. Among these are SCR configuration modification, increased understanding of the SCR seabed interactions and operational optimisation of parameters affecting SCR response. Different riser configuration solutions that have been developed to address the SCR challenges are presented. The spatial field constraint imposed on SCR application is highlighted, especially in regions where a section of the seabed is congested or needs protection. The challenges inherent in the available SCR soil interaction models are discussed, and the knowledge gap in predicting SCR TDZ fatigue damage in a pre-trench condition is highlighted. The operational optimisation in the form of vessel relocation technique for SCR TDZ fatigue mitigation is discussed, and the knowledge gap in developing a formal approach to obtaining optimum vessel relocation programs is highlighted. Finally, the solutions proposed and investigated in this research thesis to address some of these technology gaps for SCR are previewed. These proposed solutions will be the focus of detailed investigation and discussions in subsequent chapters of the thesis.

3 RESEARCH METHODOLOGY

The literature review chapter (Chapter 2) highlighted and briefly discussed proposed solutions to steel catenary riser's challenges. This chapter discusses the methods, procedures, and tools used in the development and simulation process of these proposed solutions. The chapter is sectioned as follows:

- Section 3.1 – Initial configuration development for risers
- Section 3.2 – Riser wall thickness calculation
- Section 3.3 – Software used for riser modelling and analysis
- Section 3.4 – Global strength and fatigue analysis for riser systems
- Section 3.5 – Chapter summary

This chapter presents the methodologies for modelling and analysing the riser solutions across the thesis. While some of these methodologies exist in practice (industry practice, design standards and academic literature), other methods are newly introduced. The newly introduced concept/methodologies are:

- The concept of apparent mass ratio (AMR) used to model the riser buoyancy sections.
- The index matching technique (IMT) applied for the optimisation of the riser solutions

3.1 Initial configuration development for risers

The behaviour of any riser system depends mainly on its global configuration, which implies that the configuration or shape is a significant input for this thesis's numerical modelling of the riser solutions. The initial riser configuration for numerical modelling and analysis are developed based on the analytical catenary equations. The riser solution configurations detailed in this thesis are based on the either the simple catenary or the lazy wave configuration model that are presented in this chapter. The relevant riser system configurations discussed in this section are:

- Steel catenary risers
- Steel lazy wave risers

The following assumptions are made during the development of the shapes of the above risers:

- The bending stiffness of the risers are negligible
- The axial stiffnesses of the risers are infinite
- The seabed approach before the TDP is continuous
- There is no kink or constriction in the riser profile.

Although the above stiffness (axial and bending) assumptions are made, the correct stiffness values based on the cross-section geometric and material properties are captured when the initial calculated configurations are imputed into the numerical software. The analytical shape based on the above assumptions has a negligible impact on the global profile of the risers when compared to the final numerical model with the stiffness applied [2].

3.1.1 The simple catenary riser configuration

The developments of the riser configurations in this thesis are based on the formulation developed for the simple catenary riser. A typical static configuration and variables of a simple catenary riser are presented in Figure 3-1

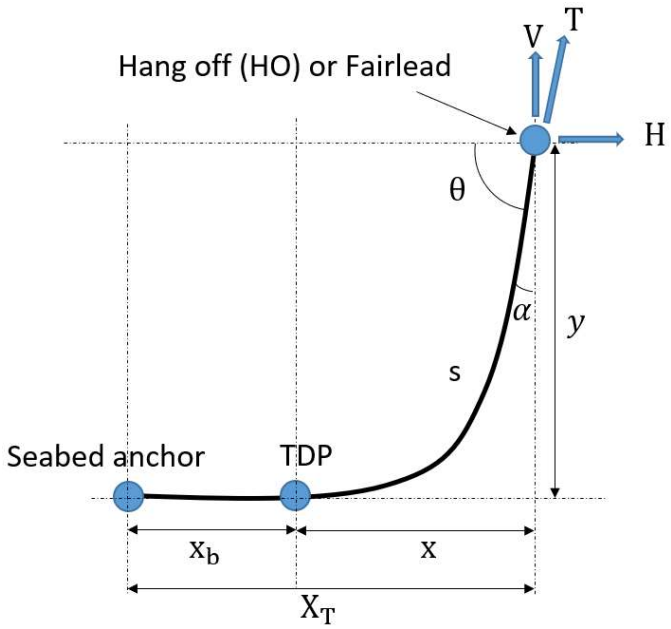

Figure 3-1 – Simple catenary configuration with configuration variables.

Where:

$y =$ height of riser measured from TDP

$x =$ horizontal distance of the catenary measured from the TDP

$X_T =$ Total horizontal distance from the riser anchor to hang off point ($X_T = x + x_b$)

$s =$ Hanging length of the riser (scope of the riser) measured from TDP

$S_T =$ Total riser length ($S_T = s + x_b$)

$\alpha =$ Hang-off angle of the riser with the vertical

$\theta =$ Hang-off angle with the horizontal

$w =$ Submerged unit weight of riser pipe

$H =$ Horizontal tension component at the hang-off

$V =$ Vertical tension component at the hang-off

$T =$ Hang-off tension

A summary of the developed expressions to the catenary problems obtained from [2] is presented in equations (3-1) to (3-6).

$$y = \frac{H}{w}\left(cosh\left(\frac{wx}{H}\right) - 1\right) \tag{3-1}$$

$$s = \frac{H}{w}\left(sinh\left(\frac{wx}{H}\right)\right) \tag{3-2}$$

$$H = T - wy \tag{3-3}$$

$$tan\theta = \frac{V}{H} \tag{3-4}$$

$$T^2 = H^2 + V^2 \tag{3-5}$$

$$V = ws \tag{3-6}$$

When computing the initial SCR configuration, some input design variables must be known. Because the SCR configuration has many configuration variables, different combinations of

the known variable may be available. For example, Table 3-1 presents two options of the configuration design variables. From the known data, other variables and parameters must be calculated in preparation for the numerical modelling. The unknown variables are computed using equations (3-1) to (3-6) or with expressions developed from a combination of at least two of the equations. From experience, most installed SCRs have hang-off angles ranging from 10deg to 18deg, and outer pipe diameters ranging from 8inch to 20inch.

Table 3-1 – Configuration design options for SCR configuration calculation

Options	x	y	s	H	θ
1	-	✓	-	-	✓
2	-	-	✓	-	✓

3.1.1.1 Design catenary configuration input (Option 1)

Consider option 1, where the vertical distance from TDP and the hang-off angle are provided. Other configuration variables can be calculated as follows:

substituting equations (3-3) and (3-4) into equation (3-5), we have

$$(H + wy)^2 = H^2 + (H\,tan\,\theta)^2$$

Expanding and simplifying, we have

$$(H\,tan\,\theta)^2 - 2Hwy + w^2y^2 = 0$$

This is a quadratic equation in variable H, and solving this equation will result in equation (3-7)

$$H = \frac{wy}{(tan\,\theta)^2}\,(1 \pm sec\,\theta) \tag{3-7}$$

Since the horizontal tension must be positive for riser systems, equation (3-7) can be re-written as equation (3-8) to obtain the horizontal tension component.

$$H = \frac{wy}{(tan\,\theta)^2}\,(1 + sec\,\theta) \tag{3-8}$$

Substituting equation (3-2) into equation (3-6), we can obtain the vertical tension component at the catenary point of consideration.

$$V = ws = w \times \frac{H}{w} sinh\left(\frac{wx}{H}\right) = H\, sinh\left(\frac{wx}{H}\right)$$

$$V = H\, sinh\left(\frac{wx}{H}\right) \tag{3-9}$$

Substituting equation (3-9) into equation (3-4), we can obtain the horizontal distance of the catenary from the TDP.

$$tan\,\theta = \frac{V}{H} = \frac{1}{H} \times H\, sinh\left(\frac{wx}{H}\right) = sinh\left(\frac{wx}{H}\right)$$

$$x = \frac{H\, sinh^{-1}(tan\,\theta)}{w} \tag{3-10}$$

Since x and H are now known, we can then calculate s from equation (3-2). With these configuration variables calculated, the catenary solution for option-1 is completed.

3.1.1.2 Design catenary configuration input (Option 2)

Consider option 2 (see Table 3-1) where the catenary length (s) the hang off angle(α or θ) are provided. Substituting equation (3-6) into equation (3-4), we can obtain the horizontal tension component, H.

$$tan\,\theta = \frac{V}{H} = \frac{ws}{H}$$

$$H = \frac{ws}{tan\,\theta} \tag{3-11}$$

From equation (3-2), we can then obtain the horizontal distance from the TDP.

$$x = \frac{H\, sinh^{-1}(tan\,\theta)}{w} \tag{3-12}$$

The vertical distance, y, from the TDP can then be obtained from equation (3-1). Other catenary design configuration options can similarly be derived by combining the provided input variable. However, in this research work, the riser configurations investigated are considered to have a known hang-off angle (θ or α) and a catenary vertical distance, y. Hence, option 1 is implied.

3.1.2 Steel lazy wave riser configuration calculation

The steel lazy wave riser configuration is a modified catenary with buoyancy modules attached to sections closer to the seabed. This helps to effectively decouple the riser TDZ from the motions transmitted from the host floating platform. A typical SLWR configuration can be broken down into five sub-catenaries to aid the application of the simple catenary expression. The five (5) sub catenary sections presented in Figure 3-2 are as follows:

1. The touchdown section (ab) – sub catenary 1
2. The drag section (bc) – sub catenary 2
3. The lift section (cd) – sub catenary 3
4. The jumper section (de) – sub catenary 4
5. The hanging section (ab) – sub catenary 5

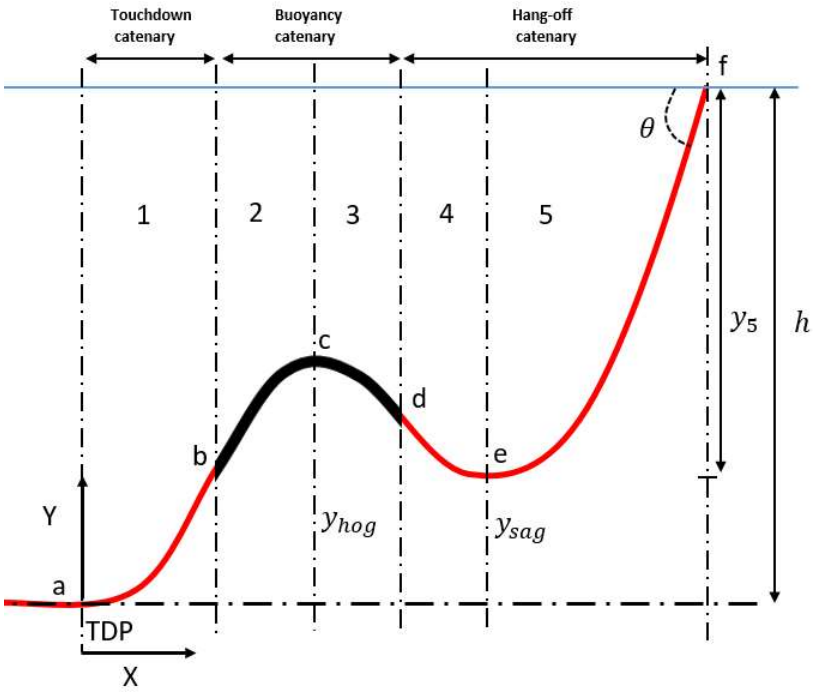

Figure 3-2 – Lazy Wave Configuration

The elevations of the maximum and minimum points of the wave bends (buoyancy section) are referred to as the hog elevation, y_{hog} and the sag elevation, y_{sag}, respectively. The difference between the y_{hog} and y_{sag} is the arc height, Δh, where

$$\Delta h = y_{hog} - y_{sag} \tag{3-13}$$

The following variation in the SLWR configurations are possible:

- For positive values of Δh ($y_{hog} > y_{sag}$) , we have the conventional SLWR configuration.
- For Δh equals zero and $y_{hog} = y_{sag} \neq 0$, the shaped catenary configuration is formed.
- For Δh equals zero and ($y_{hog} = y_{sag} = 0$), the simple catenary configuration is formed.
- For negative values of $\Delta h (y_{hog} < y_{sag})$, the curve is discontinuous, and the catenary equations are not valid.

Like the simple catenary configuration calculation, the SLWR can be defined by different configuration design options. There are two common configuration design options [71], presented in Table 3-2. Other unknown configuration variables will have to be calculated as input to the SLWR numerical modelling for any given options. However, in this thesis, option-1 is adopted to model the SLWR.

Table 3-2 – Design input options for steel lazy wave riser configuration.

Options	y_{hog}	y_{sag}	Section lengths	θ	h
1	✓	✓	-	✓	✓
2	-	-	✓	✓	✓

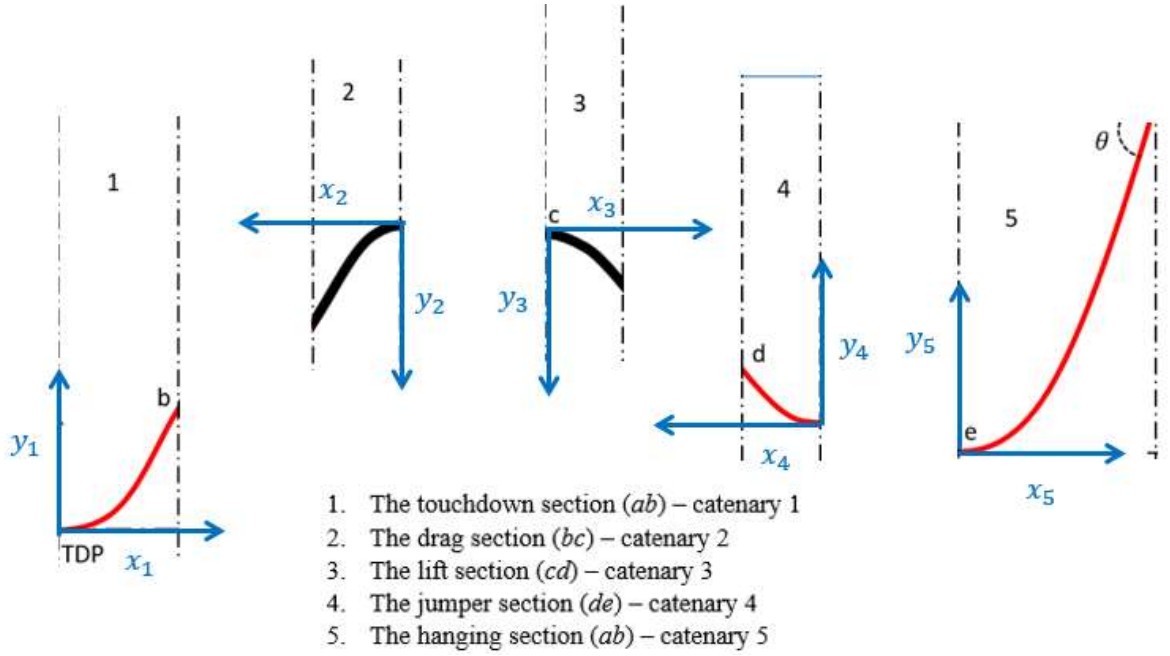

Figure 3-3 – 5 sub catenaries of the lazy wave configuration

3.1.3 Design Lazy Wave Configuration Input – Option 1

Consider the five sub catenaries shown in Figure 3-3 and consider that the y_{sag}, y_{hog} and the submerged weights $(w_1, w_2, w_3, w_4, w_5)$ of lazy wave riser sections are given. Note that the x and y of any of the five sub-catenaries are referenced from their local catenary origin, as indicated in Figure 3-3. A condition for the continuity of curvatures of the SLWR is that the horizontal tension along the riser, H, must be constant all through the riser profile and at points a, b, c, d, e as expressed in equation (3-14)

$$H_1 = H_2 = H_3 = H_4 = H_5 = H \tag{3-14}$$

For homogenous pipe, the submerged unit weight of sub-catenaries 1, 4 and 5 are equal, and the submerged weight of sub-catenaries 2 and 4 (buoyancy section) are equal i.e.,

$$w_1 = w_4 = w_5 = w \tag{3-15}$$

$$w_2 = w_3 = w' \tag{3-16}$$

We can derive the catenary model for the SLWR, starting with the upper sub-catenary (sub-catenary-5).

Sub catenary five (5)

$$y_5 = h - y_{sag} \tag{3-17}$$

The horizontal tension component can be obtained using equation (3-18)

$$H = \frac{wy_5}{(tan\,\theta)^2}(1 + sec\,\theta) \tag{3-18}$$

The horizontal catenary distance from TDP can be obtained using equation (3-1).

$$x_5 = \frac{H}{w} cosh^{-1}\left(\frac{wy_5}{H} + 1\right) \tag{3-19}$$

The length (arc length from TDP) of sub-catenary five can be obtained using equation (3-2).

$$s_5 = \frac{H}{w} sinh\left(\frac{wx_5}{H}\right) \tag{3-20}$$

Sub catenary four (4)

The tension *T*, the horizontal tension component *H*, the vertical span, *y*, and the unit weight of the catenary section *w,* are related by equation (3-3) as follows:

$$T = H + wy$$

Since the tension, T, at point d and the horizontal tension, H, across catenary 3 and 4 boundaries are equal, the following expressions can be obtained using equation (3-3).

$$w'y_3 = wy_4$$

$$y_3 = y_4 \frac{w}{w'} \tag{3-21}$$

Also, from Figure 5-9,

$$y_3 + y_4 = y_{hog} - y_{sag} \tag{3-22}$$

Substituting y_3 from equation (3-21) into equation (3-22)

$$y_4 + \frac{wy_4}{w'} = y_{hog} - y_{sag}$$

$$y_4 \frac{(w' + w)}{w'} = y_{hog} - y_{sag}$$

$$y_4 = \frac{w'}{(w + w')}(y_{hog} - y_{sag}) \quad (3\text{-}23)$$

The horizontal span of sub catenary 4 can then be obtained using (3-1).

$$x_4 = \frac{H}{w} cosh^{-1}\left(\frac{wy_4}{H} + 1\right) \quad (3\text{-}24)$$

The length span (arc length) of sub catenary 4 is obtained using equation (3-2).

$$s_4 = \frac{H}{w} sinh\left(\frac{wx_4}{H}\right) \quad (3\text{-}25)$$

Sub catenary three (3)

Substituting equation (3-23) into equation (3-21), we can obtain the vertical dimension of sub-catenary 3 as follows:

$$y_3 = \frac{w'}{(w + w')}(y_{hog} - y_{sag})\frac{w}{w'} = \frac{w}{(w + w')}(y_{hog} - y_{sag})$$

$$y_3 = \frac{w}{(w + w')}(y_{hog} - y_{sag}) \quad (3\text{-}26)$$

Equation (3-1) is then applied to obtain the horizontal span of sub catenary 3 as follows:

$$x_3 = \frac{H}{w'} cosh^{-1}\left(\frac{w'y_3}{H} + 1\right) \quad (3\text{-}27)$$

We can then derive the arc length (from TDP) from equation (3-2) as follows:

$$s_3 = \frac{H}{w'} sinh\left(\frac{w'x_3}{H}\right)$$

Catenary two (2)

Like the relationship between sub catenaries 3 and 4, sub catenaries 1 and 2 are related through their equal tension, T, at point b and horizontal tension component across the sub catenary section. Hence, using equation (3-3).

$$wy_1 = w'y_2$$

$$y_1 = y_2 \frac{w'}{w} \tag{3-28}$$

Also, the sum of the vertical span of sub catenary 1 and 2 is the arch bend height from the seabed

$$y_{hog} = y_1 + y_2 \tag{3-29}$$

Substituting equation (3-28) into equation (3-29)

$$y_{hog} = \frac{w'y_2}{w} + y_2$$

$$y_{hog} = y_2 \frac{(w' + w)}{w}$$

$$y_2 = \frac{w}{(w + w')} y_{hog} \tag{3-30}$$

The horizontal span of sub catenary 2 is obtained using equation (3-1).

$$x_2 = \frac{H}{w'} cosh^{-1}\left(\frac{w'y_2}{H} + 1\right) \tag{3-31}$$

The length span (arc length) of the sub catenary is obtained using equation (3-2).

$$s_2 = \frac{H}{w'} sinh\left(\frac{w'x_2}{H}\right) \tag{3-32}$$

Sub catenary one (1)

Substituting equation (3-30) into equation (3-29), the vertical span of sub catenary 1 is obtained.

$$y_1 = y_{hog} - y_2 = y_{hog} - \frac{w}{(w + w')} y_{hog} = y_{hog} \frac{w'}{(w + w')}$$

$$y_1 = y_{hog}\frac{w'}{(w+w')} \tag{3-33}$$

The horizontal span of sub catenary 1 is then obtained using equation (3-1).

$$x_1 = \frac{H}{w}cosh^{-1}\left(\frac{wy_1}{H}+1\right) \tag{3-34}$$

The length span (arc length) of sub catenary 1 is obtained using equation (3-2)

$$s_1 = \frac{H}{w}sinh\left(\frac{wx_1}{H}\right) \tag{3-35}$$

Global or complete lazy wave configuration

Once each sub catenary configuration is determined, they can be combined to form the global steel lazy wave configuration, relating their local origins to the global origin (TDP). The overall vertical, horizontal and length span of the lazy wave configuration referenced from the TDP will be:

$$X = \sum_{i=1}^{5} x_i = x_1 + x_2 + x_3 + x_4 + x_5 \tag{3-36}$$

$$Y = h = \sum_{i=1}^{5} y_i = y_1 + y_2 - y_3 - y_4 + y_5 \tag{3-37}$$

$$S = \sum_{i=1}^{5} s_i = s_1 + s_2 + s_3 + s_4 + s_5 \tag{3-38}$$

3.1.4 Apparent mass ratio concept

In this thesis, There are two choices of numerical modelling of the buoyancy systems on risers, as shown in Figure 3-4. These are the discrete and the smeared buoyancy system modelling approach. The discrete modelling approach directly represents the actual discrete buoyancy sections. In contrast, the smeared buoyancy system approach converts the discrete modules to an equivalent smeared or continuous buoyancy section with an equivalent diameter. The smeared buoyancy option is used in this thesis since this approach has fewer numerical modelling parameters and fewer steps to modelling. Also, for preliminary analyses of risers

with uplifted sections (wave bends), one does not face the challenge of the "curtain railing" effect when the second option is adopted. The "curtain railing" effect is the sharp changes in the profile or curvatures of the buoyancy section caused by the riser beam sagging between two discrete buoyancy modules, as seen in Figure 3-5. Note that the derived buoyancy section from both approaches is interconvertible, as depicted in Figure 3-6, considering volume (displacement) equivalence. Hence, we can take advantage of the simplified smeared buoyancy section at the preliminary design stage of the riser and then convert it to the actual discrete buoyancy section for the final evaluation of the system response.

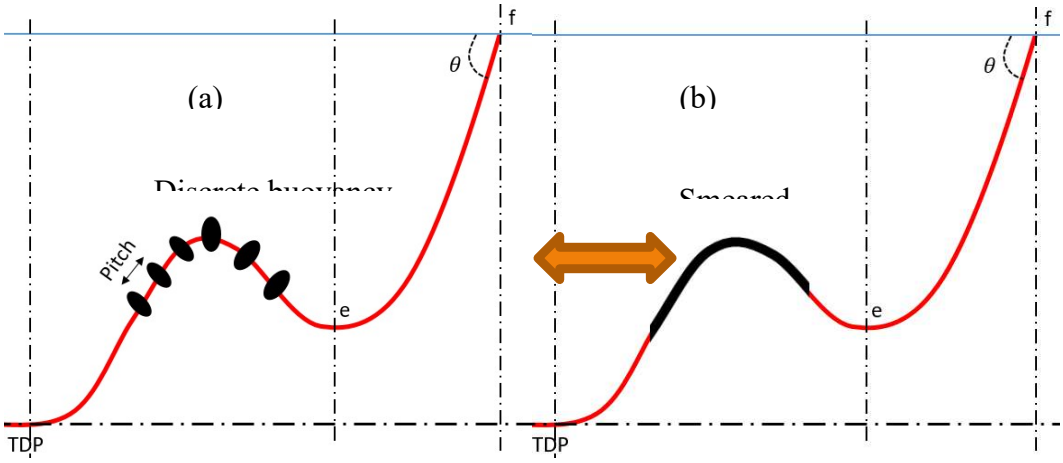

Figure 3-4 – Discrete and smeared buoyancy modules

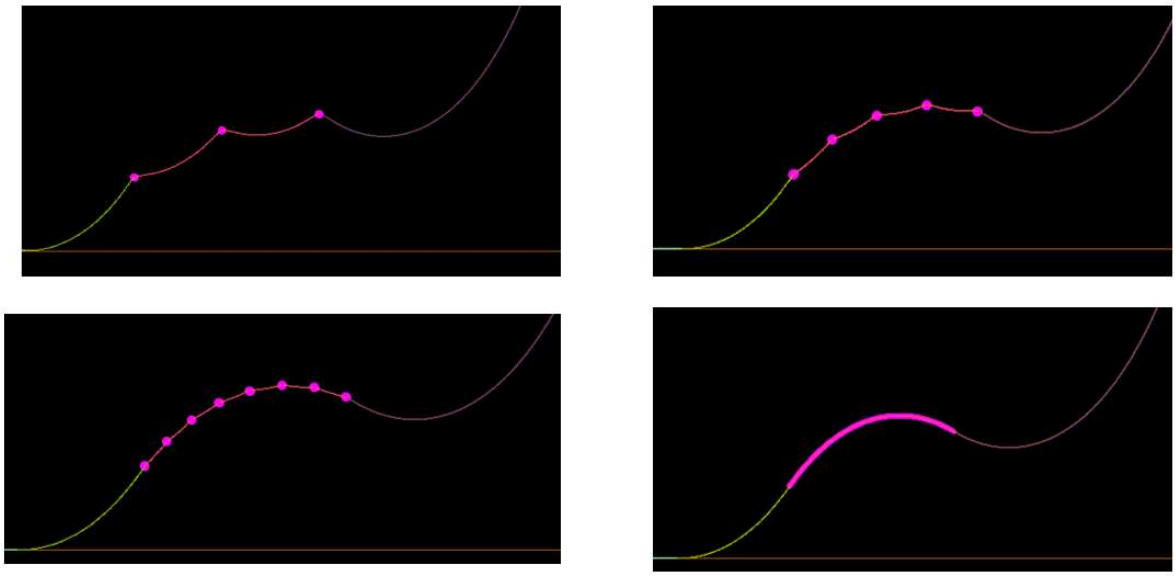

Figure 3-5 – Numerical influence of discrete buoyancy system as the number of discrete buoys increases from 3 to a continuous (smeared) buoyancy system.

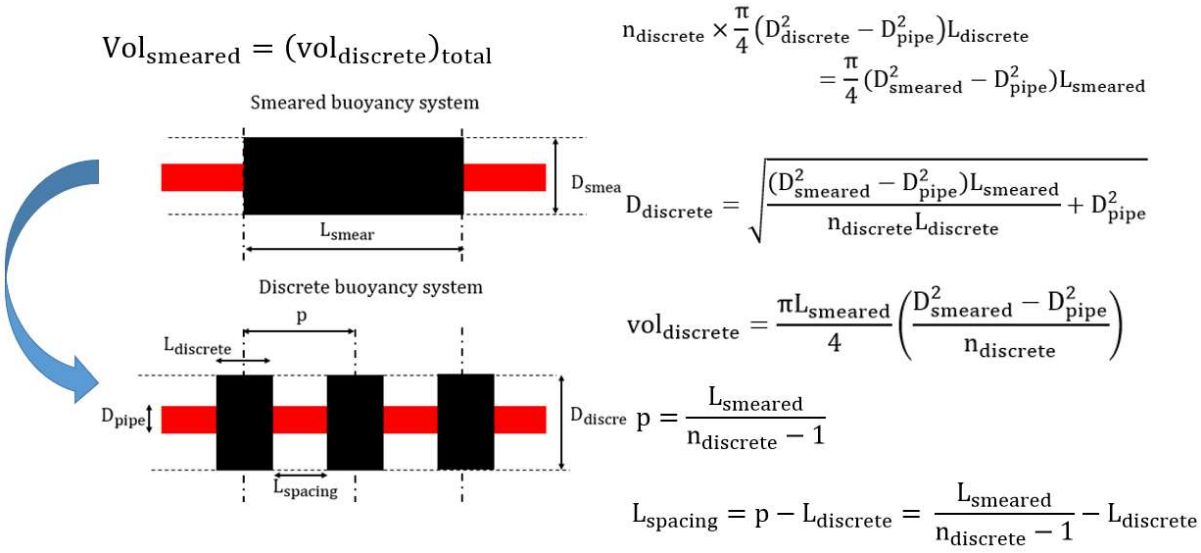

$$Vol_{smeared} = (vol_{discrete})_{total}$$

$$n_{discrete} \times \frac{\pi}{4}(D^2_{discrete} - D^2_{pipe})L_{discrete} = \frac{\pi}{4}(D^2_{smeared} - D^2_{pipe})L_{smeared}$$

$$D_{discrete} = \sqrt{\frac{(D^2_{smeared} - D^2_{pipe})L_{smeared}}{n_{discrete}L_{discrete}} + D^2_{pipe}}$$

$$vol_{discrete} = \frac{\pi L_{smeared}}{4}\left(\frac{D^2_{smeared} - D^2_{pipe}}{n_{discrete}}\right)$$

$$p = \frac{L_{smeared}}{n_{discrete} - 1}$$

$$L_{spacing} = p - L_{discrete} = \frac{L_{smeared}}{n_{discrete} - 1} - L_{discrete}$$

Figure 3-6 – Equivalent smeared and discrete buoyancy system

Where:

p = The distance between centres of discrete modules (pitch).

$L_{spacing}$ =The gap between two discrete buoyancy modules.

L_{smear} = Length of the smeared buoyancy section

D_{smear} = Diameter of the equivalent smeared buoyancy section.

$D_{discrete}$ = Diameter of the discrete smeared buoyancy module.

D_{pipe} = Diameter of the steel pipe on which the modules are installed.

$n_{discrete}$ = Number of discrete buoyancy modules.

vol_{smear} = Volume of smeared buoyancy section.

vol_{smear} = Volume of the discrete buoyancy section.

The required capacity of the smeared buoyancy system depends on the unit weight of the uplifted riser section and the wave bend elevations. Therefore, it is relevant to know what buoyancy capacity and distribution are needed to achieve the desired wave bend configuration. Given the buoyancy material density, we can calculate the thickness of the smeared buoyancy module to arrive at a required buoyancy capacity (upthrust). This is achievable in this thesis using the apparent mass ratio concept, AMR. The AMR is a single parameter used to model both the Diameter of the smeared buoyancy sections and the length (distribution) of the

sections, providing an advantage in the number of variable reductions during the optimisation of these riser systems. The AMR is taken to be the ratio of the apparent or submerged weight of the buoyant section, w_b, to the apparent or submerged weight of the bare pipe section, w

$$AMR = \frac{w_b}{w} = \frac{w_p + w_c + w_m - B_b}{w_p + w_c - B_p} \tag{3-39}$$

Where w_p, w_c, w_m, B_b and B_p are respectively the unit weight of bare pipe, unit weight of riser content, unit weight of buoyancy material, unit buoyancy force provided by the buoyant section and unit buoyancy force provided by the bare pipe section. The expansion of equation (3-39) can be summarised as follows:

$$AMR = \frac{\frac{\pi}{4}(D_o^2 - D_i^2)\rho_s g + \frac{\pi}{4}D_i^2\rho_c g + \frac{\pi}{4}((D_o + 2t_b)^2 - D_o^2)\rho_b g - \frac{\pi}{4}(D_o + 2t_b)^2\rho_w g}{\frac{\pi}{4}(D_o^2 - D_i^2)\rho_s g + \frac{\pi}{4}D_i^2\rho_c g - \frac{\pi}{4}D_o^2\rho_w g}$$

$$AMR = \frac{\rho_s(D_o^2 - D_i^2) + \rho_c D_i^2 - D_o^2\rho_w + 4t_b D_o(\rho_b - \rho_w) + 4t_b^2(\rho_b - \rho_w)}{\rho_s(D_o^2 - D_i^2) + \rho_c D_i^2 - \rho_w D_o^2}$$

$$\begin{aligned} 4t_b^2(\rho_b - \rho_w) + 4t_b D_o(\rho_b - \rho_w) + \rho_s(D_o^2 - D_i^2) + \rho_c D_i^2 - D_o^2\rho_w \\ - AMR(\rho_s(D_o^2 - D_i^2) + \rho_c D_i^2 - \rho_w D_o^2) = 0 \end{aligned} \tag{3-40}$$

Where:

D_o and D_i $=$ External and internal diameters of the bare pipe, respectively

t_b $=$ Smeared buoyancy material thickness

ρ_b , ρ_c and ρ_w $=$ Density of buoyancy material, content, and seawater densities, respectively

Let

$$A = 4(\rho_b - \rho_w) \tag{3-41}$$

$$B = 4D_o(\rho_b - \rho_w) \tag{3-42}$$

$$\mathrm{C} = \rho_s(D_o^2 - D_i^2) + \rho_c D_i^2 - D_o^2\rho_w - AMR(\rho_s(D_o^2 - D_i^2) + \rho_c D_i^2 - \rho_w D_o^2)$$

$$C = (1 - AMR)\left(D_o^2(\rho_s - \rho_w) - D_i^2(\rho_s - \rho_c)\right) \quad (3\text{-}43)$$

Then, equation (3-40) can be expressed as equation (3-44), which provides a relationship between the AMR, the buoyancy material density (ρ_b) and the smeared buoyancy material thickness (t_b). The positive real roots of equation (3-44) gives the required, t_b for a given AMR and ρ_b. If the pipe section does not have buoyancy systems installed, $t_b = 0$. For this case, $C = 0$ from equation (3-44) and $AMR = 1$ from equation (3-43).

$$At_b^2 + Bt_b + C = 0 \quad (3\text{-}44)$$

3.2 Riser wall thickness calculation

For the analyses conducted across this thesis, the grade of the riser steel pipe is selected from the range: X60 to X70. Typically, from experience, pipe grade for riser design falls within this range. The higher the grade of steel pipe, the lighter its weight and reduced payload on the vessel. The unit weight of the riser pipe section (steel in this research) is dependent on the wall thickness of the pipes to resist burst pressure, collapse pressure, stresses and fatigue damage under various loading conditions. It is the industry tradition to calculate the minimum required wall thickness of the riser pipe considering collapse and burst pressure loads and then progress with dynamic loading conditions to test if the minimum specified wall thickness is sufficient. Hence, the specified minimum wall thickness of the riser pipe will be driven by the internal pressure of transported material and the external hydrostatic pressure. The minimum riser wall thickness can be obtained using different design standards such as API-STD-2RD [94] and DNV-OS- F201 [95]. In this thesis, the approach prescribed by DNV- OS-F201 is applied for the riser pipe minimum wall thickness calculation. The DNV approach is based on the load resistance factor design, where load effects contributions to the overall load are quantified using appropriate safety factors. An explicit form of the required minimum wall thickness based on burst and the collapse pressure criteria are developed for use in this thesis.

3.2.1 The explicit form of minimum wall thickness for burst pressure

The limit state condition required for steel riser pipes under internal pressure loads (burst pressure) is presented in equation (3-45).

$$p_{li} - p_e \leq \frac{p_b}{\gamma_m \gamma_{SC}} \tag{3-45}$$

where:

$$p_b = \frac{4 t_b f_{min}}{\sqrt{3}(D - t)},\ f_{min} = min\left(f_y, \frac{f_u}{1.15}\right) \tag{3-46}$$

$$p_{li} = p_{ld} + 0.1 p_d = \ p_d + \rho_i g h \ + 0.1 p_d = 1.1 p_d + \ \rho_i g h = \ 1.1 p_d + \ p_i \tag{3-47}$$

Where:

p_{li} = Local incidental pressure

p_e = External pressure

p_{ld} = Local internal design pressure

p_d = Design pressure at the reference point

p_b = Burst resistance pressure

p_i = Internal pressure

γ_m = Resistance factor to consider uncertainties in material properties

γ_{SC} = Resistance factor dependent on safety class

t_b = Pipe wall thickness required for burst resistance

D = Nominal diameter

f_y = Yield strength to be used in the design

f_u = Tensile strength to be used in the design

ρ_i = Density of internal fluid (contents)

g = Gravity acceleration

h = Height from the riser section to the reference point for design pressure

Combining equations (3-45), (3-46) and (3-47), we obtain the exact minimum wall thickness expression, which satisfies the burst design criteria in equation (3-45).

$$t_b = \frac{\sqrt{3} \times D\gamma_m\gamma_{SC}(1.1p_d - p_e + p_i)}{\sqrt{3} \times \gamma_m\gamma_{SC}(1.1p_d - p_e + p_i) + 4f_{min}} \quad (3\text{-}48)$$

3.2.2 The explicit form of minimum wall thickness for collapse pressure

The limit state condition to be satisfied for steel riser pipes under external pressure loads (collapse pressure) is presented in equation (3-49).

$$p_e - p_{min} \leq \frac{p_c}{\gamma_m\gamma_{SC}} \quad (3\text{-}49)$$

Where:

$$(p_c - p_{el})(p_c^2 - p_p^2) = p_c p_{el} p_p f_o \frac{D}{t_c} \quad (3\text{-}50)$$

$$p_{el} = \frac{2E\left(\frac{t_c}{D}\right)^3}{1 - v^2}, \quad p_p = 2\left(\frac{t_c}{D}\right) f_y \alpha_{fab} \quad (3\text{-}51)$$

Combining equations (3-49), (3-50) and (3-51), we obtain a polynomial expression in terms of the riser pipe wall thickness as presented in equation (3-52).

$$A_1 t_c^5 + A_2 t_c^3 + t_c^2 + A_4 = 0 \quad (3\text{-}52)$$

Where:

$A_1 = -8E\alpha_{fab}^2 f_y^2$

$A_2 = 2D^2 E\gamma_m\gamma_{SC}(p_e - p_{min})\left(2\alpha_{fab} f_y f_o + \gamma_m\gamma_{SC}(p_e - p_{min})\right)$

$A_3 = 4D^3\alpha_{fab}^2 f_y^2 \gamma_m\gamma_{SC}(p_e - p_{min})(1 - v^2)$

$A_4 = -D^5\gamma_m^3\gamma_{SC}^3(p_e - p_{min})^3(1 - v^2)$

The positive real roots of equation (3-52) provide the minimum pipe wall thickness to satisfy the collapse design criteria.

Where:

E = Young's Modulus

α_{fab} = Manufacturing process reduction factor

p_{el} = Elastic collapse pressure

p_c = Collapse pressure

p_p = Plastic collapse pressure

f_o = Ovality

v = Poisson's ratio

p_{min} = Local minimum internal pressure

t_c = Pipe wall thickness required for collapse resistance

3.2.3 Minimum wall thickness analysis example

Once the minimum required burst and collapse wall thickness are computed, the risers' design thickness will be the maximum of the two thicknesses as expressed in equation (3-53). In the calculation of these wall thicknesses in this thesis, no corrosion allowance is considered. Considering the internal burst pressures (typically 10 ksi) and the water depths (typically 1500m) investigated for the riser solutions in this thesis, the burst criteria is found to be the driver of the wall thickness design. This means that the wall thickness required to resist the burst pressure are higher than those required to withstand the collapse pressure. However, for deeper water, this may not be the case.

$$t_{min} = max\ (t_b, t_c) \tag{3-53}$$

Examples of variations of the burst and collapse wall thickness are presented in Figure 3-7. It could be seen in Figure 3-7 (b), (c), (d) that the collapse pressure increases with the water depth until it cancels out the internal pressure and become the driver of the wall thickness design. It could also be observed that the water depth at which the collapse pressure drives the design of the riser pipe wall thickness depends on the magnitude of the internal pressure.

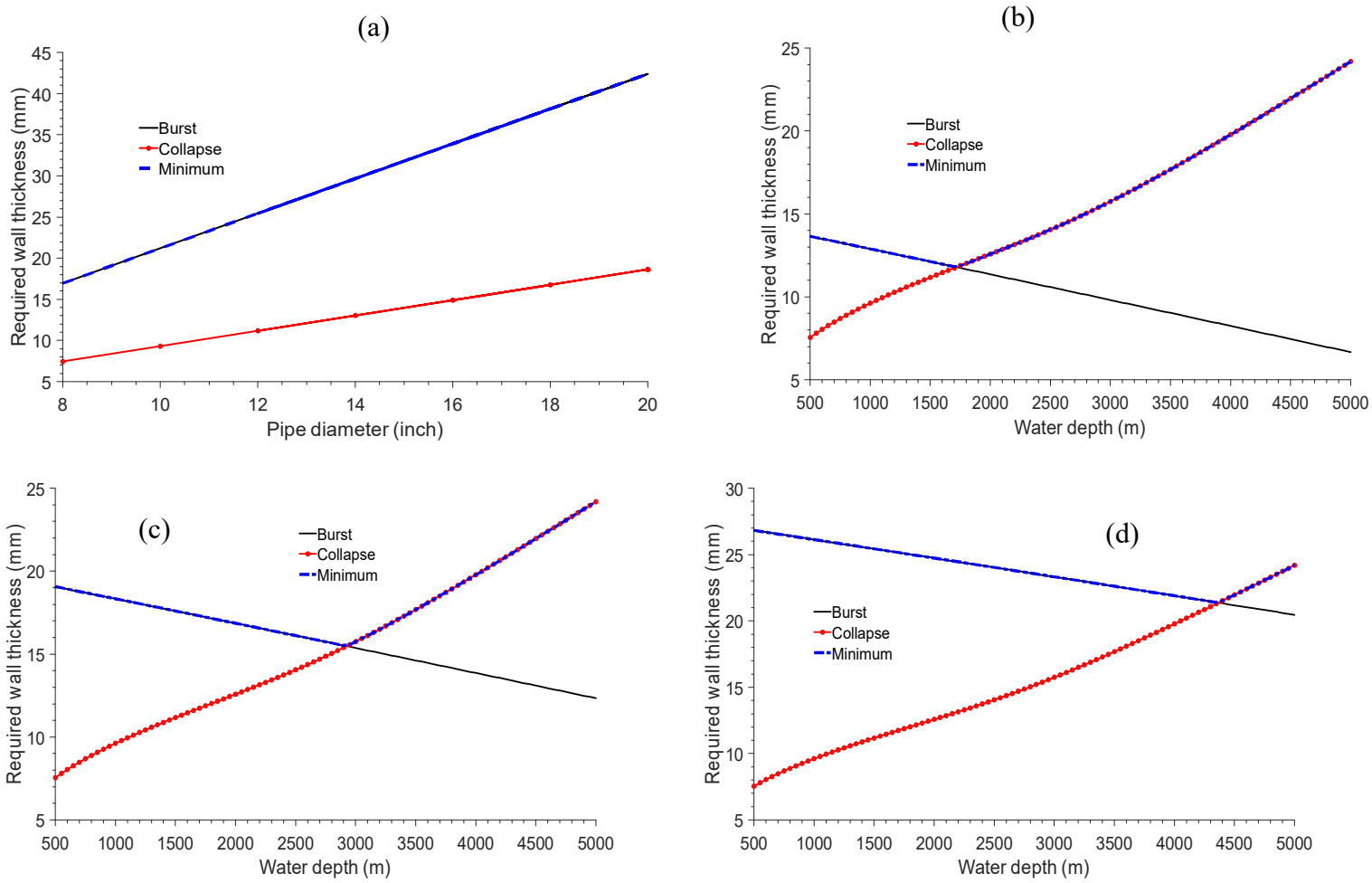

Figure 3-7 (a)- Required pipe wall thickness for riser pipe: Outer diameter (OD) = 12inch, Design pressure (DP) = 10ksi, Water depth = 1500m; Wall thickness requirement for 12 inch riser pipe in 1500 m water depth (b) design pressure (DP) = 5 ksi, (c) design pressure (DP) = 7 ksi, (d) design pressure(DP) = 10 ksi.

3.3 Software used for riser modelling and analysis

3.3.1 Introduction to riser analysis software's

Many popular commercial tools are available for the numerical modelling and analyses of dynamic offshore flexible systems. However, in this research work, OrcaFlex software is employed. OrcaFlex is one of the world's leading packages for the dynamic analysis of offshore marine systems, including risers. It is known academically and industrially for its breadth of technical capability and user-friendliness. OrcaFlex also has the unique feature as a library, allowing a host of automation possibilities and easy integration into 3rd party software such as MATLAB, PYTHON, C++, etc. OrcaFlex software provides analysis in the time domain and frequency domain. It can compute environments and vessel motion loads on the riser systems and the riser interaction with the seabed. In OrcaFlex, the user can choose either using a linear or specialised non-linear riser soil interaction model. The calculable responses for the riser in OrcaFlex include but are not limited to the axial, shear, bending, torsional responses and motions. Other important post-processed responses include the stresses, stress range and fatigue damage. The forces and moments calculated by OrcaFlex take into consideration the riser weight, buoyancy, hydrodynamic drag, hydrodynamic added mass effects, tension, and shear, bending and torque, seabed reaction and friction.

OrcaFlex calculations are performed in both the time and frequency domain. The time domain is fully non-linear and uses the static analysis as its initial configuration. Mass, damping, stiffness, loading etc., are evaluated at each time step, considering the instantaneous time-varying geometry of the risers. There are two (2) time-domain integration schemes used in OrcaFlex, namely the implicit and the explicit time integration schemes. Both schemes use a numerical time-stepping algorithm to solve the equation of motion in the time domain. The equation of motion is generally cast as:

$$M(p,a) + C(p,v) + K(p) = F(p,v,t) \tag{3-54}$$

where:

$M(p,a) =$ The system inertia load

$C(p,v) =$ The system-damping load

$K(p) =$ The system stiffness load

$F(p, v, t) =$ The external load

$p, v\ and\ a =$ Position, velocity and acceleration vectors, respectively

$t =$ The simulation time

The solution to the EOM includes the positions velocity and accelerations of the line nodes. With these, other required line results can be calculated.

3.3.2 Theories of OrcaFlex object used for riser system modelling

There are many objects in OrcaFlex used to model real-life objects. These include the line objects, the 3D buoy object, 6D buoy object, the vessel object, the environment object, the link object, the constraint object, the winch object, the turbine object, and the shape object. However, in this thesis, the relevant OrcaFlex objects used are the line object for modelling the riser system; the vessel object for modelling the host floating platform motions; and the environment object for modelling the seawater environment including the wave loads, the current loads, the wind loads and the seabed interactions.

3.3.2.1 Line object modelling

The line object is used to model flexible systems such as risers, mooring, umbilical, cables, etc., and it's the OrcaFlex object used to model the riser system in this thesis. The OrcaFlex line object is divided into segments and nodes, as seen in Figure 3-8 (a). The segments are straight and massless, and the nodes model their masses, weight, buoyancy, drag, etc. This means each node will represent half of the properties of the segments connected to it. The segments model the axial and torsional properties of the line. Forces and moments on the line are applied at nodes, and where a segment pierces the sea surface, all fluid-related forces are calculated, allowing for varying wetted lengths up to the instantaneous water surface level. A segment is made up of two co-axial telescoping rods connected by axial and torsional spring-dampers, as seen in Figure 3-8 (b). The rotational spring-dampers are used to model the bending properties of the line at each end.

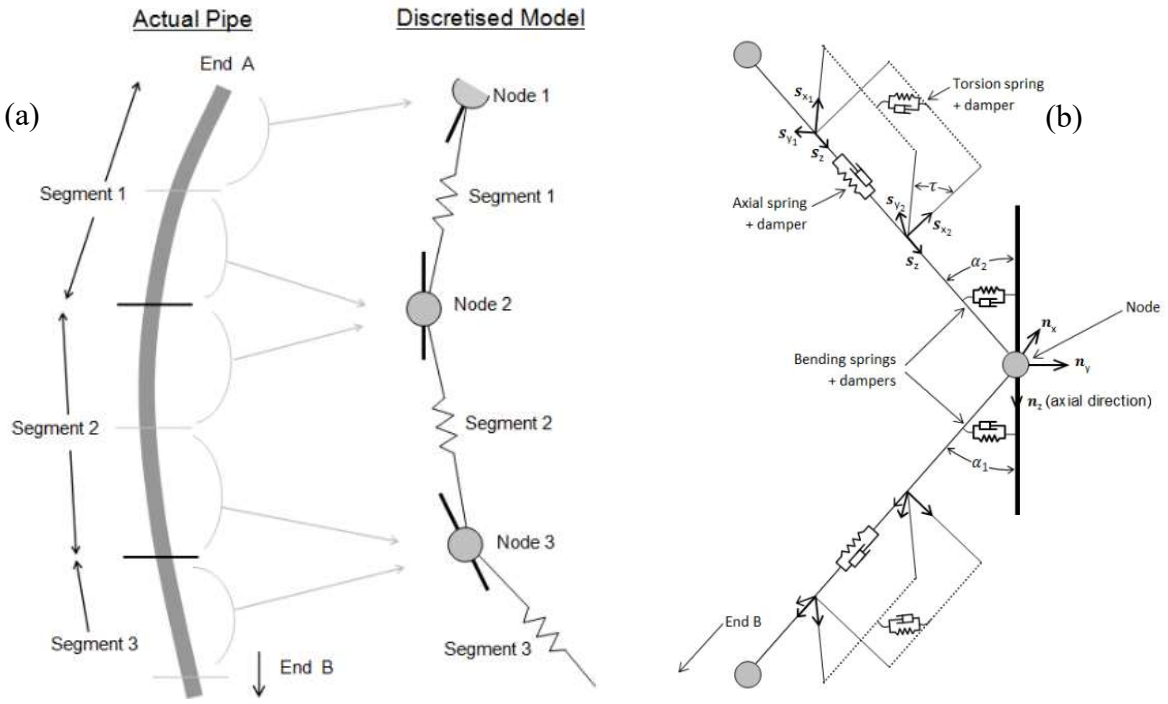

Figure 3-8 – (a) OrcaFlex line model, (b) Detailed of OrcaFlex line model structure [82]

3.3.2.2 Vessel object modelling

The riser system has two connecting interfaces: the vessel and the seabed, as shown in Figure 3-9. The vessel is the host floating platform, which holds the riser in place, while the seabed provides interface support for the riser as it connects to the subsea facilities. The vessel responds to the environment and imposes the resulting motions on the risers through the riser-vessel connecting interface. The risers can also experience direct load impacted on it by the environment. These motions imposed on the risers are the major causes of the risers' forces, stresses, and fatigue damage. Hence, it is important to accurately model this motion so that the riser response predictions are correct. The response amplitude operators (RAOs) define the vessel response motions to first-order wave load, and the quadratic transfer functions (QTFs) define the motion response to second-order wave loads, as depicted in Figure 3-9. The RAO, the QTF and other diffraction data for the vessel can be calculated outside the OrcaFlex program and imported into it for analysis. Other vessel responses to static-like loads, such as current and wind loads, are modelled as static offsets of the vessel. Alternatively, the vessel motion can be defined from data sources such as time histories, prescribed motions, harmonic motions or motions calculated externally using function based on changing values of one or more variables as the simulation proceeds.

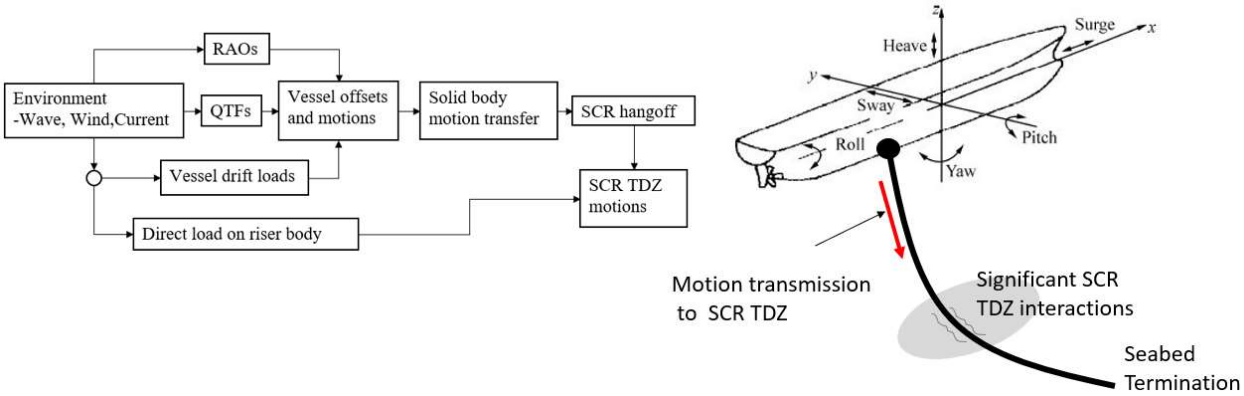

Figure 3-9 – Sources of motion for the riser system.

The OrcaFlex vessel object is applied to model rigid bodies that are large enough to radiate waves. The floating production storage and offloading unit (FPSO), the primary vessel type used in this thesis, is modelled with the OrcaFlex vessel object using the vessel RAO imported from third-party diffraction software. In some analyses, time history data sources are used. In other studies, the riser extreme offsets conditions are modelled by imposing static vessel offsets expressed as a percentage of the water depth. Other analyses require the vessel damaged condition, which is modelled by imposing static heal on the vessel dynamic motions. Other vessels that can be modelled with the OrcaFlex vessel object include the ships, barges, tension leg platforms (TLPs), spar platforms and semisubmersibles. The vessel data applied for a given analysis will be described and presented in the thesis section where the investigation is conducted.

3.3.2.3 Environment modelling

The OrcaFlex environment object is used to model the conditions around the riser and the host platform. The components of the environment object in OrcaFlex include the wave loads, the current load, the wind loads, the seawater and the seabed, as depicted in Figure 3-10. Wave loads can be design waves defined by the wave height, period and directions or storm wave loads defined by the wave spectrum. The JONSWAP spectrum [96] is used in this thesis whenever the irregular wave loads are to be modelled. The current loads are modelled using the current profile variation with water depth. Typical current profiles used in this research during the investigation of riser systems are the constant and varying velocity profiles. The wave load and current data applied during the analysis will be presented in the thesis section for the study.

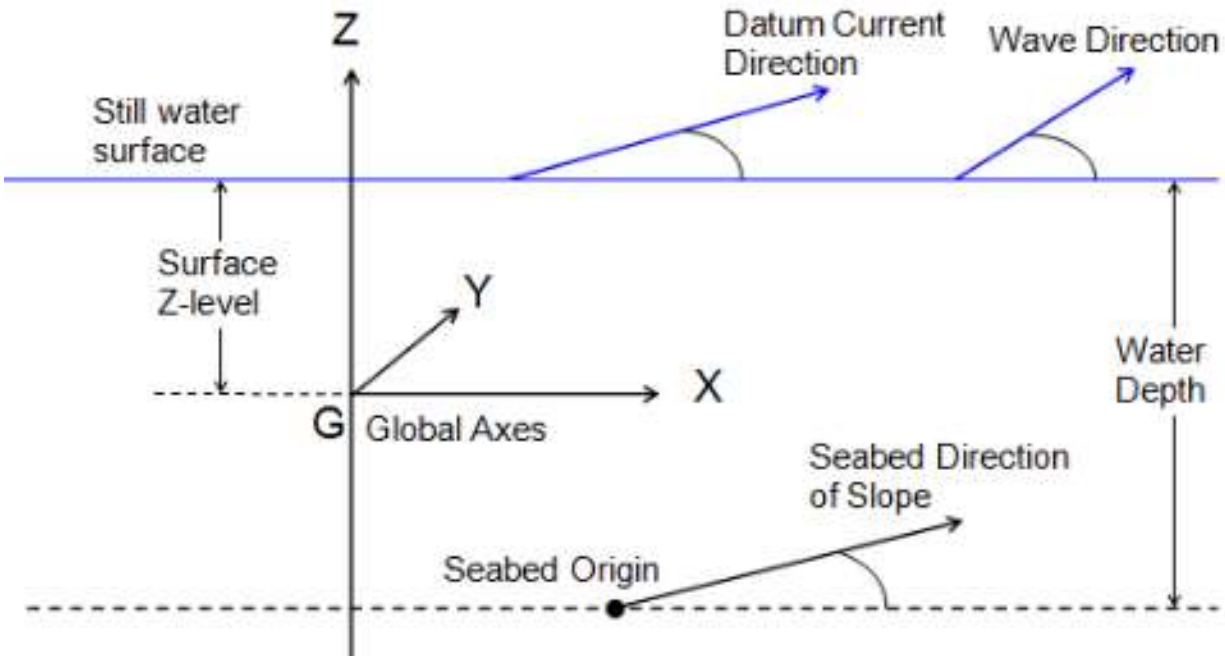

Figure 3-10 – OrcaFlex environment

During the investigation of riser solutions in this thesis, there are cases where parametric studies are conducted using design wave loads characterised by wave height (H) and period (T). In these cases, the combination for the H and T must satisfy the breaking limit for the wave. The wave breaking limit curve is presented in Figure 3-11. This curve is informed by the relations available in [4].

The seabed can be modelled in OrcaFlex using the seabed object. The OrcaFlex seabed object includes both linear and non-linear hysteretic models. The linear model, also known as the spring model, provide a linear relationship between the load exerted by the riser on the seabed and the seabed deformation, as seen in Figure 3-12 (a). The non-linear model does not follow the linear relation but is affected by the hysteretic deformation behaviour of the seabed under the riser loading, as shown in Figure 3-12 (b). The linear soil model (spring model) is more conservative but less computationally expensive to simulate for deepwater SCRs. To reduce computational cost at the early or preliminary stage of the SCR design, where several riser configurations may be investigated or screened, linear soil model can be used. Once a suitable SCR configuration has been selected, it can then be subjected to detailed analysis using a non linear riser soil interaction model. Details of the hysteretic riser-soil interaction model have been discussed in Chapter 2

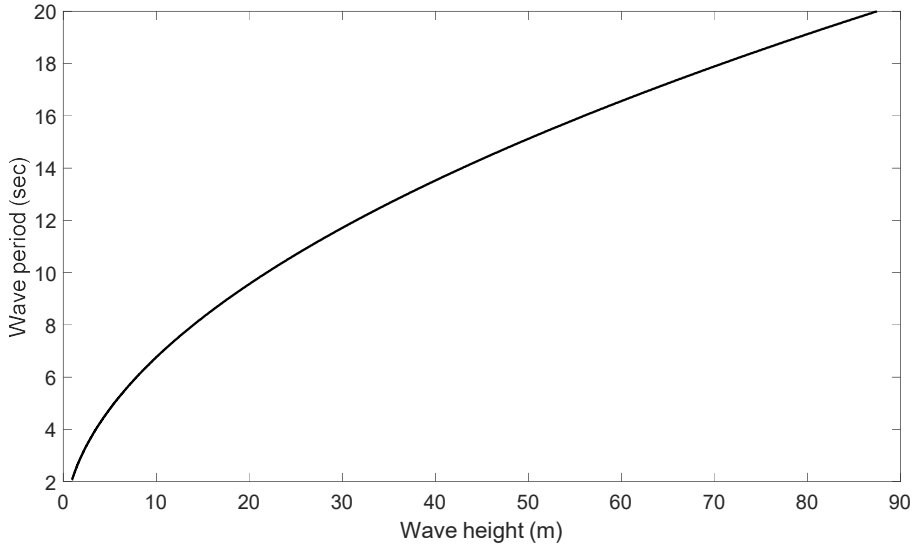

Figure 3-11 – Breaking wave limit curve for regular wave loads

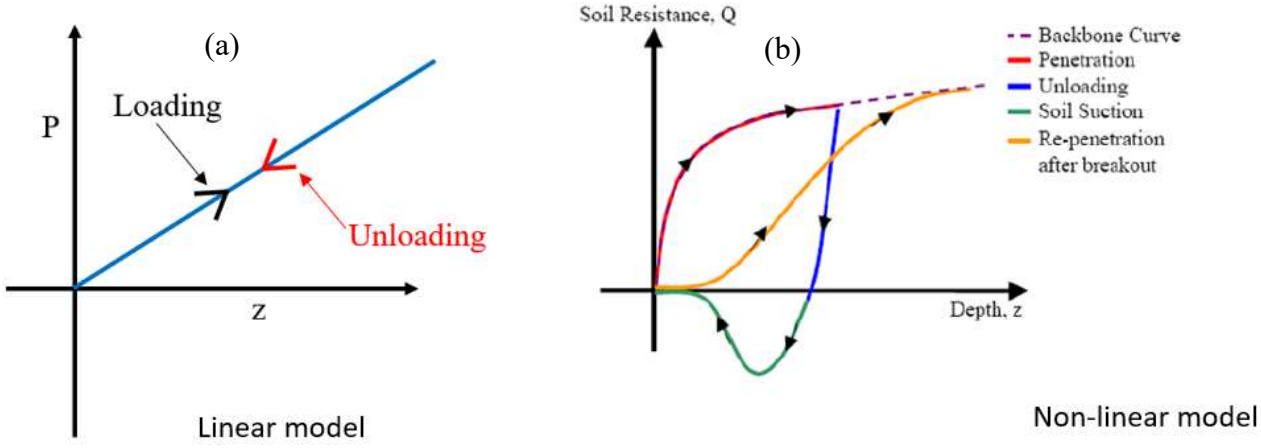

Figure 3-12 –Typical response for (a) the linear soil model, (b) the non-linear hysteretic soil model

3.3.3 MATLAB routine for numerical modelling in OrcaFlex

Across the analyses in this thesis, modelling is conducted using many data that need to be inputted correctly. These data include:

- The riser configuration data
- The hydrodynamic riser data, boundary conditions, etc.
- Environmental data including wave loads, current profiles, seabed model

- Vessel data, including its motion data, position, orientation, etc

During the optimisation analysis of the risers, hundreds to thousands of models need to be created from unique combinations of the optimisation design variables. Manually conducting the OrcaFlex modelling for these analyses will cost a significant amount of time and prone to mistakes. Hence, there is the need to automate these modelling processes (pre-processing) and post-processing of results through a programming interface. OrcaFlex provides a programming platform for several programming languages such as MATLAB, PYTHON, C++, etc. However, in this thesis, the MATLAB program is employed. The MATLAB-OrcaFlex interface is a set of M-files and a MATLAB Mex file that provide access to the OrcaFlex API from within the MATLAB environment. Several MATLAB program routines were developed during this research for the investigation of different riser solutions. Figure 3-12 presents the interactions between the MATLAB routines with the OrcaFlex software.

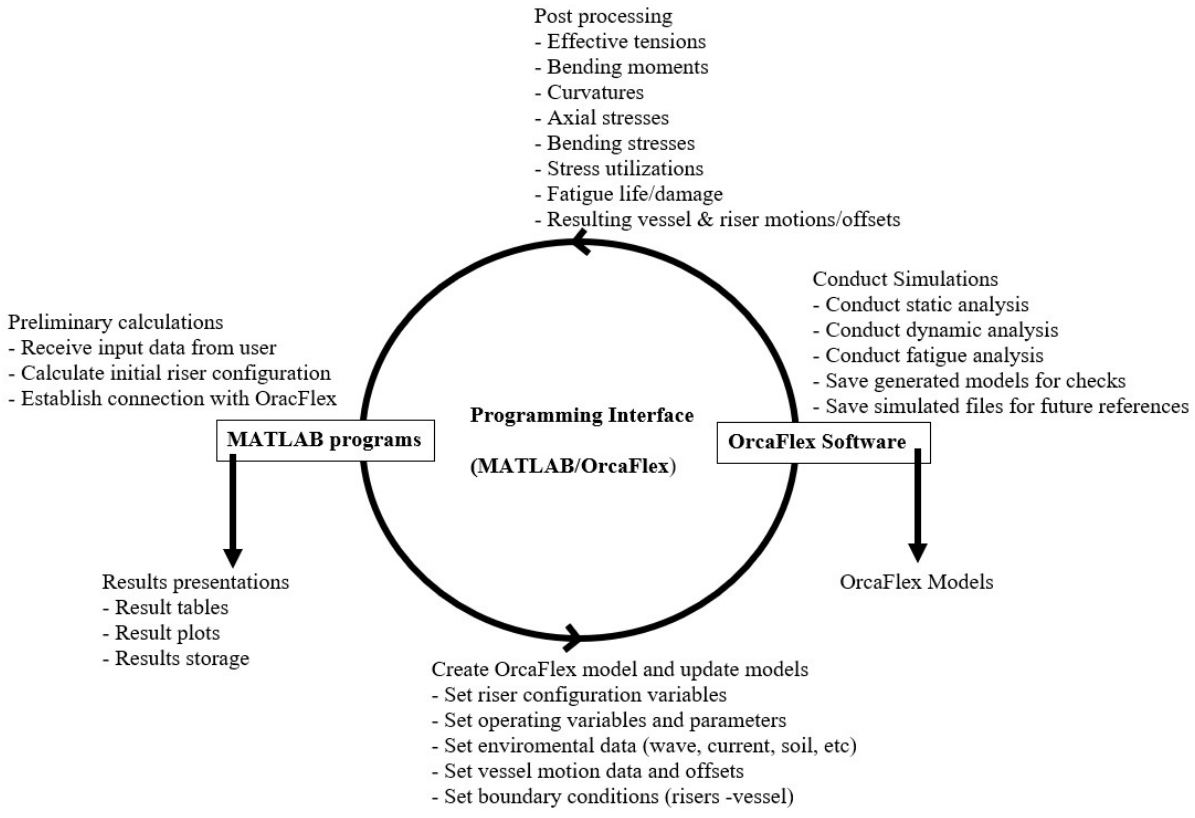

Figure 3-13 – OrcaFlex modelling, simulation, and post-processing flow chart process using MATLAB routines

3.4 Global strength and fatigue analysis for risers

The riser solutions' investigations in this thesis are conducted globally, hence the need for global riser analyses. For global riser studies, the industry design standards have criteria that guides and limit the responses of the riser system. In this thesis, stress utilisation and fatigue damage are the two most crucial post-processed riser responses on which the riser performance is measured. In this regard, we present here the stress utilisation and the fatigue damage calculation methods. The stress utilisation calculations included other strength responses such as bending stress due to bending moments, axial stress due to tensions, and torsional stress due to twisting. In some analyses, bending moments can be post-processed to compare riser systems under different load case scenarios. In other cases, the maximum and the minimum effective tensions are required to optimise some riser solutions. While the maximum tension at the riser hang-off points limits the load-bearing capacity of the connecting structure and the riser pipe itself, the effective minimum tension is used to measure the riser compressions at the TDZ. As the minimum effective tension gets less positive, the riser is said to be increasing in compressions.

3.4.1 Combined load criteria for stress utilisation calculations

The DNV-OS-F201 [4] is used for the calculations of the riser stress utilisation. DNV-OS-F201 F201 is a riser standard developed based on the limit state or load resistance factor design (LRFD), which relates allowable loads to the material's ultimate strength. The standard provides criteria, requirements, and guidance on structural design and analysis of riser systems when exposed to static and dynamic loading conditions. The DNV-OS-F201 ensures that the factored load effect is less than the factored design resistance for any limit states. This implies that the failure probability, i.e., probabilities exceeding a limit state, is kept below a certain value. The limit state is the design state beyond which the riser or part of the riser no longer satisfies the requirements defined for its performance or operation. When the limit state is exceeded, the riser is said to have failed either structurally or functionally. The LRFD is distinguished into the pressure load effect (static), the functional load effect (static), the environmental load effect (mainly dynamic) and the accidental load effect. The categories of limit states covered by DNV-OS-F201 are:

- Ultimate Limit State (ULS) – corresponding to the ultimate resistance for carrying loads
- Fatigue Limit State (FLS) – relates to the possibility of failure because of cyclic load

- Accidental Limit State (ALS) – corresponds to damage to components due to an accidental event or operational failure
- Serviceability Limit State (SLS) – corresponding to the criteria applicable to normal use or durability

The DNV F201 provides design methods, including the load resistance factor design (LRFD) method, the working stress design (WSD) method, the reliability analysis, and the design testing method. The LRFD method separates the influence of uncertainties and variability using partial safety factors. The WSD method is adopted for simplicity and is more conservative than the LRFD. It addresses the same limit state as the LRFD but uses a single usage factor to account for uncertainties in the design. Hence, the LRFD provides more flexibility than the WSD. The reliability analysis is applied for special case designs, where limited experience exists for the system and for design scenarios where the safety or usage factor need to be recalibrated. The experimental approach applies valid experimental methods to verify riser systems load effects, structural response, and resistance against material degradation.

The ultimate and the fatigue limit state is considered for the global riser analysis in this thesis. Also, the LRFD is applied, where partial safety factors are used to specify contributions of various loads to the overall load effect and structural responses. For design criteria where the load and resistance can be separated, the LRFD format can be expressed as:

$$S_d\left(S_p; \gamma_F . S_F; \gamma_E . S_E; \gamma_A . S_A; \right) \leq \frac{R_K}{\gamma_{Sc} \cdot \gamma_m \cdot \gamma_c} \tag{3-55}$$

Where:

S_P = pressure load

S_F = load effect from functional load

S_A = load effect from accidental load

γ_F = load effect factor for functional loads

γ_E = Load effect factor from environmental loads

γ_A = load effect factor from for accidental loads

R_k = generalised resistance

γ_{Sc} = resistance factor to take into account the safety class (i.e. failure consequences)

γ_m = Resistance factor o account for material and resistance uncertainties

γ_c= Resistance factor to account for special condition

Note that the load effect factor accounts for the natural variability in loads and model uncertainties caused by incomplete knowledge or models leading to possible inaccurate calculation of load effects. The resistance factors account for variability in strength and basic variables, including the effect of dimensional tolerances and model uncertainties due to an incomplete resistance model. As discussed earlier, the dynamic boundaries for the risers systems are caused by direct load on the riser or motions imposed by the host platform as it responds to the environment. The DNV combined load resistance factor design criteria for internal and external pressure conditions are expressed in equations (3-56) and (3-57). The left-hand side of the equation is the stress utilisation of the riser pipe.

$$\gamma_{SC}\cdot\gamma_m \left[\left(\frac{|M_d|}{M_k}\cdot\sqrt{1-\left(\frac{p_{ld}-p_e}{p_b(t_2)}\right)^2}\right)+\left(\frac{T_{ed}}{T_k}\right)^2\right]+\left(\frac{p_{ld}-p_e}{p_b(t_2)}\right)^2 \leq 1 \qquad (3\text{-}56)$$

$$(\gamma_{SC}\cdot\gamma_m)^2 \left[\left(\frac{|M_d|}{M_k}+\left(\frac{T_{ed}}{T_k}\right)^2\right)^2\right]+(\gamma_{SC}\cdot\gamma_m)^2\left(\frac{p_e-p_{min}}{p_c(t_2)}\right)^2 \leq 1 \qquad (3\text{-}57)$$

Where:

$$M_d=\gamma_F M_F+\gamma_E M_E;\ T_{ed}=\gamma_F T_{eF}+\gamma_E T_{eE} \qquad (3\text{-}58)$$

$$M_k=f_y\alpha_c(D-t_2)^2;\ T_k=f_y\alpha_c\pi(D-t_2)t_2 \qquad (3\text{-}59)$$

M_F = Bending moment from functional loads

M_E = Bending moment from environmental loads

T_{eF} = Effective tension from functional load

T_{eE} = Effective tension from environmental load

M_d = Design bending moment

T_{ed} = design effective tension

p_{ld} = Local internal design pressure

p_e = Local external pressure

p_c = Collapse resistance

p_b = Burst resistance

p_i = Internal pressure

p_{li} = Local incidental pressure

p_{inc} = Lincidental pressure

p_d = Design pressure at the reference point

p_{min} = Local minimum internal pressure = 0

M_k = Plastic bending moment resistance

T_k = Plastic axial force resistance

$p_b(t_2)$ =Burst resistance

f_y = Yield strength to be used in the design

f_u = Tensile strength to be used in the design

t_2 = Nominal walls thickness less corrosion allowance

α_c = Flow stress parameter accounting for strain hardening =1.2

D = Nominal Outside Diameter

In this thesis, some of the main DNV factors considered for analysing the riser solutions are presented in

Table 3-3.

Table 3-3 – Examples of double wave configurations and their derivatives.

Symbol	Value	Note
γ_m	1.15	For ULS/ALS
γ_{SC}	1.14	
γ_c	1.05	For normal condition
γ_E	1.3	
γ_F	1.1	
α_{fab}	1	
α_u	0.96	
f_y	SMYS	Derated values
f_u	SMTS	Derated values
f_o	0.005	

Note: ULS – ultimate limit state, ALS – accidental limit state

3.4.2 Global fatigue response analysis for riser systems

Fatigue is a process of material degradation or failure caused by cumulations of damage due to the repetitive application of loads. The loads causing the failure may be well below the yield point. This implies that a single application of such loads may not result in failure, but a repetition of the load over an extended period can cause fatigue failure. Possible sources of fatigue load include construction loads, transportation loads, installation loads, pressure variations, vortex-induced vibrations, weight variations, temperature variations, etc. However, the major source of fatigue damage for risers is the wave load. This is referred to as wave

induce fatigue load. Sometimes, fatigue damage due to VIV may dominate the riser fatigue damage in an environment with intensive current flow. In this thesis, only fatigue damage due to wave loads is considered in the analysis of riser solutions.

Figure 3-14 is a typical representation of variation in the stresses generated when a regular cyclic load is applied to the riser systems. The maximum stress level characterises the stress cycle (σ_{max}) and the minimum stress level (σ_{min}). The stress range, $\Delta\sigma$ is the diffrnec between these stress levels, i.e. $\Delta\sigma = \sigma_{max} - \sigma_{min}$. The stress ratio, R, is the ratio of the maximum and minimum stress levels, i.e., $R = \sigma_{max}/\sigma_{min}$, the stress ratio provide information about the deviation of mean stress of the stress cycle from the mean zero stress. For fully reverse stress cycle, R = -1. for static loading, R = 1. The zero mean stress approach is considered throughout this thesis during the fatigue damage post-processing. The S-N curve provides the relationship between the stress range and the number of cycles to failure as obtained from experiments. The S-N curve is typical obtained dorm experiments applying the zero mean to stress approach. In this thesis, the DNV D-curve [97] is mostly applied for riser analysis. Where this is not the case, additional information about the S-N curve used will be provided.

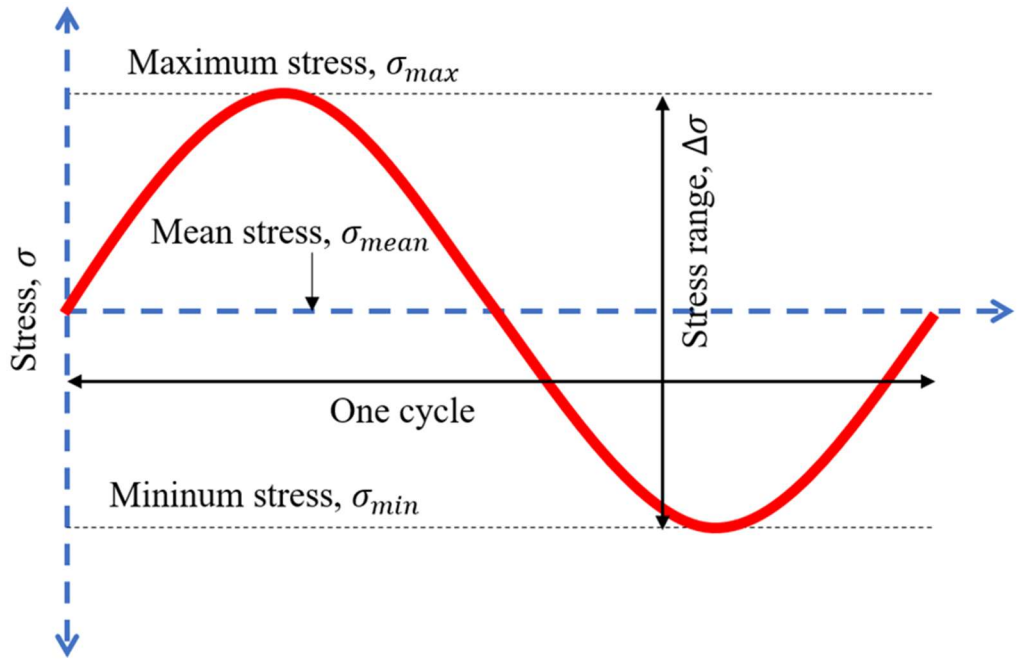

Figure 3-14 – Characteristics stress level of a regular load cycle

The fatigue damage is calculated from the stress range in the riser. The stress range in risers are taken to be the stress variation of the axial stress σ_{zz} , which is a combination of direct stress and bending stress as follows:

$$\sigma_{zz} = \sigma_{direct} + \sigma_{bending\ stress} \tag{3-60}$$

where:

$$\sigma_{direct} = \frac{T_w}{a_{stress}}$$

$$\sigma_{bending\ stress} = c_2 r I_{xy}(m_x \sin\theta - m_y \cos\theta)$$

T_w is the wall tension, c_2 is the bending stress loading factor, r and θ are the radial and theta positions corresponding with the point on the riser cross-section at which the stress response is computed, as shown in Figure 3-15. The stress range is therefore expressed as (3-61).

$$\Delta\sigma_{zz} = max(\sigma_{zz}) - min\ (\sigma_{zz}) \tag{3-61}$$

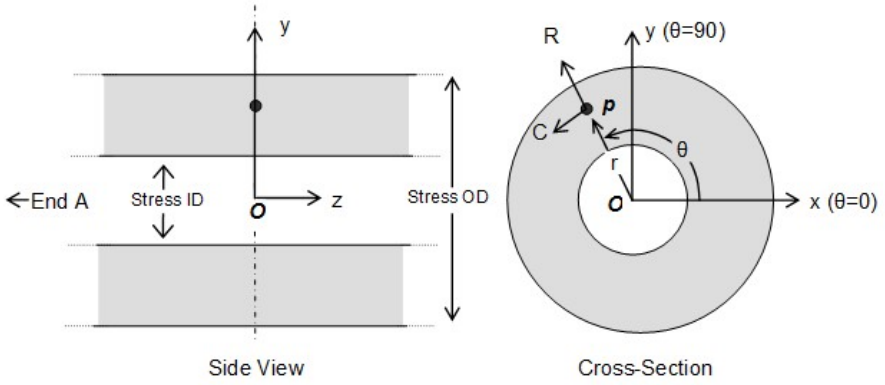

a

Figure 3-15 – Frame of reference for stress calculation [82]

Stresses in the physical riser systems are not regular. Hence, other methods such as the Rain flow counting technique [98] will be used to reduce the spectrum of varying SCR stress response obtained for each fatigue wave load into an equivalent set of simple stress reversals. The Miner's rule will then be applied to compute the simple stress reversals to compute the overall cumulative damage contribution as presented in equation (3-62), where n_i is the ith stress range amplitude components of the stress range histogram, N_i is the number of cycles to failure associated with the ith stress range as obtained from the S-N curve [97] and p_i is the probability of occurrence.

$$\sum_i \frac{n_i}{N_i} p_i \tag{3-62}$$

3.5 Chapter summary

This chapter presents the methods applied across the thesis for the development and investigation of the riser solutions. The need often arises to calculate the initial configurations of riser solutions as input to their numerical modelling processes. In this thesis, the initial configurations for the riser solutions are calculated based on the simple catenary relations. The global configurations are decomposed into sub-catenaries, to which the catenary relations are applied. The developed sub-catenary equations can then be composed to obtain the global riser configuration. The configurations presented are for the simple catenary risers (SCR), the steel lazy wave riser (SLWR), the branched riser system (BRS) and the floating catenary system (FCRS). These are the riser configuration discussed in this thesis. The concept of the apparent mass ratio (AMR) is introduced, which is applied to calculate the required amount of buoyancy on lifted sections of the risers. When the AMR is incorporated into the catenary relations derived for the risers, the smeared buoyancy thickness required to provide buoyancy for the rise to achieve a given elevation can be calculated. The AMR and the riser configuration relations can significantly simplify the modelling of the riser solutions, especially for the optimisation processes where hundreds to thousands of models are to be built quickly. The explicit forms of the DNV wall thickness formulations based on burst and collapse are developed and presented. It could be seen that for the internal design pressure and water depth considered across the work in this thesis, the burst design criteria drive the wall thickness sizing for the riser solutions. The wall thickness formulation can be integrated into the MATLAB routine for the numerical modelling of the riser pipe.

For the analyses conducted across this thesis, the OrcaFlex software is used to simulate the risers' solutions. The major objects in OrcaFlex used for the riser system modelling are the line, vessel, environment and seabed objects. The line object models the riser string, the vessel object models the top boundary condition of the riser, the environment object models the riser's surrounding conditions, and the seabed object models the linear and non-linear-hysteretic riser-seabed boundary conditions. Automating the pre-processing, modelling, simulation and post-processing in OrcaFlex is essential for effective conduction of the analyses, especially for complex model updating, parametric modelling and optimisation processes. MATLAB is used

to provide the automation capabilities during the modelling process with OrcaFlex. The global riser strength and fatigue analyses in this thesis are conducted based on the DNV F201 criteria. The stress utilisation for the riser solution will be calculated based on the LRFD approach, where uncertainties and variability in the design load and effect are represented using partial safety factors. The stress utilisation represents the effect of pressure (internal and external), axial and bending stresses on the risers and provides how much the riser material is used up. Other riser responses of interest by which riser solutions are compared include compressions at the riser bends, top tension, bending moments, and the variables of the riser configurations. Fatigue is the accumulated damage for several cycles of loads, typically of varying stress amplitudes. However, there are analysis cases where regular wave loads are applied. For such cases, the direct application of Miner's rule is applied to cumulate the fatigue damage using the S-N curve. However, the Rain flow counting technique will be applied for irregular wave fatigue analysis to convert the stress spectrum to a histogram of regular stress amplitudes before applying Miner's rule.

4 INDEX MATCHING TECHNIQUE

Many optimisation tools are available in the literature to solve riser optimisation problems, with different levels of limitations and robustness. However, in this thesis, a new optimisation technique is developed and presented: the index matching technique (IMT). The IMT is developed in-house and used in this thesis as it provides the flexibility needed to handle the nature of the problems. The technique assigns indices to the design points in the optimisation space. It then tracks the objective and constraint functions associated with these indices for performance measurement through sorting and intersections operations. The index matching technique is validated through examples from the literature and demonstrated in this chapter to solve the SLWR optimisation problem. The method is developed using the brute force approach, where it is required to evaluate the constraint and objective functions at every design point in the optimisation design space. This is a limitation since the computation resource needed can be significant for large problems. However, for large optimisation problems in this thesis, the design space is selected carefully through screening analysis to reduce the optimization space and remove the need to evaluate functions at impractical design points.

The sections in this chapter are as follows:

- Section 4.1 – Background to engineering optimisation problems
- Section 4.2 – Index matching optimisation technique
- Section 4.4 – Multi-objective optimisation problems
- Section 4.3 – Demonstrating SLWR optimisation using the index matching technique
- Section 4.5 – Chapter summary

4.1 Background to engineering optimisation problem

A general engineering optimization problem layout can be stated as follows, where $f(\mathrm{X})$ is a system of objective functions, $g_j(\mathrm{X})$ is the system of constraints and X is the vectors of the independent design variables:

Minimize:

$$\mathrm{f(X)} = \begin{Bmatrix} f_1(\mathrm{X}) \\ f_2(\mathrm{X}) \\ . \\ . \\ . \\ f_n(\mathrm{X}) \end{Bmatrix}$$

Subject to the following constraints: $\boldsymbol{g_j(\mathrm{X}) \leq b_j,\ j = 1, 2, 3 \ldots, p}$ (4-1)

Where:

$$\mathrm{X} = \{x_1, x_2, x_3, \ldots, x_p\}^{\mathrm{T}}$$

For riser solutions that are optimised in this thesis, the objective function can be the fatigue damage response or the cost function, or a combination of these. The constraint functions can be the top tension, riser compression at riser sections with large curvature, or the stress utilization. It will be seen across the thesis that some of the listed constraint functions can be considered as objective functions. The nature of the problem drives this decision.

4.2 Index matching technique (IMT)

A variation of the IMT, called the tabular optimisation method is developed from the index matching technique. This approach reduces the multidimension problem to sets of 2D problems, which provides significant reduction in the computation resource required. In this chapter, the application of the multidimensional IMT will be referred to as the "direct application of the IMT", while the derived 2-D approach will be referred to as the application of the "tabular optimisation" technique.

4.2.1 Development of the IMT

Given a general engineering optimisation problem:

$$\textbf{Minimise}: \boldsymbol{f(\mathrm{X})} = \begin{Bmatrix} \boldsymbol{f_1(\mathrm{X})} \\ \boldsymbol{f_2(\mathrm{X})} \\ . \\ . \\ . \\ \boldsymbol{f_n(\mathrm{X})} \end{Bmatrix} \quad (4\text{-}2)$$

subject to the following constraints:

$$\mathrm{g_j(X)} \leq \mathrm{b_j}, \qquad j = 1,2,3 \ldots, r$$

Where:

$$\mathrm{X} = \left\{\mathrm{x_1}, \mathrm{x_2}, \mathrm{x_3}, \ldots, \mathrm{x_p}\right\}^{\mathrm{T}}$$

Where:

$f(X)$ = a set of objective functions to be optimised.

$g_j(X)$ = a set of constraint function.

X = a set of the design variable vectors

The design space can be defined by a unique combination of elements from each vector in **X**. For k such combinations (design points) at which the objective and the constraint functions are evaluated, there will be k elements in each objective function. Let the collection of index vectors, **I**, each containing k indices be assigned to represent the k elements in each of the functions in $f(\mathbf{X})$ as depicted in Figure 4-1, where **I** is expressed as:

$$\mathbf{I} = \begin{Bmatrix} \boldsymbol{I_1} \\ \boldsymbol{I_2} \\ . \\ . \\ . \\ \boldsymbol{I_n} \end{Bmatrix} \tag{4-3}$$

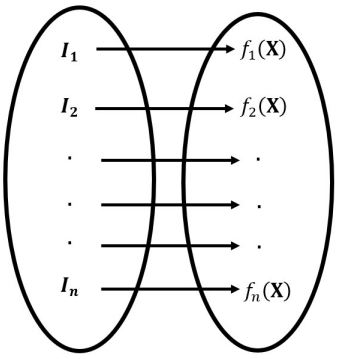

Figure 4-1. Index system of vectors representing elements in each objective function.

The feasible design space, $\mathbf{X_{FDS}}$, is the region where the constraint functions are satisfied. The objective functions' values at the feasible design points can be obtained by evaluating them at $\mathbf{X_{FDS}}$ as shown in equation (4-4). The corresponding feasible set of index system, $\mathbf{I_{FDS}}$, which is a subset of $\mathbf{I}$ is expressed as shown in equation (4-5).

$$\mathbf{Y} = \{f(\mathbf{X_{FDS}})\} = \begin{Bmatrix} f_1(\mathbf{X_{FDS}}) \\ f_2(\mathbf{X_{FDS}}) \\ . \\ . \\ . \\ f_n(\mathbf{X_{FDS}}) \end{Bmatrix} \tag{4-4}$$

$$\mathbf{I_{FDS}} = \{\mathbf{I}(\mathbf{X_{FDS}})\} = \begin{Bmatrix} \boldsymbol{I_1}(\mathbf{X_{FDS}}) \\ \boldsymbol{I_2}(\mathbf{X_{FDS}}) \\ . \\ . \\ . \\ \boldsymbol{I_n}(\mathbf{X_{FDS}}) \end{Bmatrix} \tag{4-5}$$

If the columns of $\mathbf{Y^T}$ are sorted in ascending order (for minimisation) problem or descending order for maximisation problem, we will have $\mathbf{Y'}$ as presented in equation (4-6). We can then rearrange elements in the vectors of $\mathbf{I_{FDS}}$ such that their orders match the previous element they represented in vectors of $\mathbf{Y}$ before they were sorted. The re-ordered $\mathbf{I_{FDS}}$ is expressed in equation (4-7).

$$\mathbf{Y'} = \text{sort}\{\mathbf{Y}^{\mathrm{T}}\} \tag{4-6}$$

$$\mathbf{I'} = (\mathbf{I_{FDS}})_{\text{reordered}} = \begin{Bmatrix} \boldsymbol{I'}_1 \\ \boldsymbol{I'}_2 \\ . \\ . \\ . \\ \boldsymbol{I'}_n \end{Bmatrix} \tag{4-7}$$

The intersection of the indices in the first q rows and across all columns of $(\mathbf{I'})^{\mathbf{T}}$ gives a family of index numbers that represent or point to the sets of optimum design points, i.e.:

$$\mathbf{I_{opt}} = \bigcap_{1}^{q}\{(\mathbf{I}')^{\mathrm{T}}\} \tag{4-8}$$

The family of optimum design variables, $\mathbf{X_{opt}}$, and the corresponding optimum values of the objective functions, $\mathbf{Y_{opt}}$, can then be obtained through the following matching:

$$\mathbf{X_{opt}} = \mathbf{X}(\mathbf{I_{opt}}) \tag{4-9}$$

$$\mathbf{Y_{opt}} = \mathbf{Y}(\mathbf{I_{opt}}) \tag{4-10}$$

The flow chart for the index matching optimisation technique is presented in Figure 4-2 A summary of the index matching technique procedure is as follows:

- Assemble all possible combinations of the design variables.
- Run numerical analyses (for each combination) to determine the values of the constraints.
- Run numerical analyses (for each combination) to determine the values of the objective function.
- Eliminate combinations that do not satisfy the constraints.
- Order the remaining combinations in ascending order of the objective function to find the combination that minimises the objective function while satisfying the constraints.

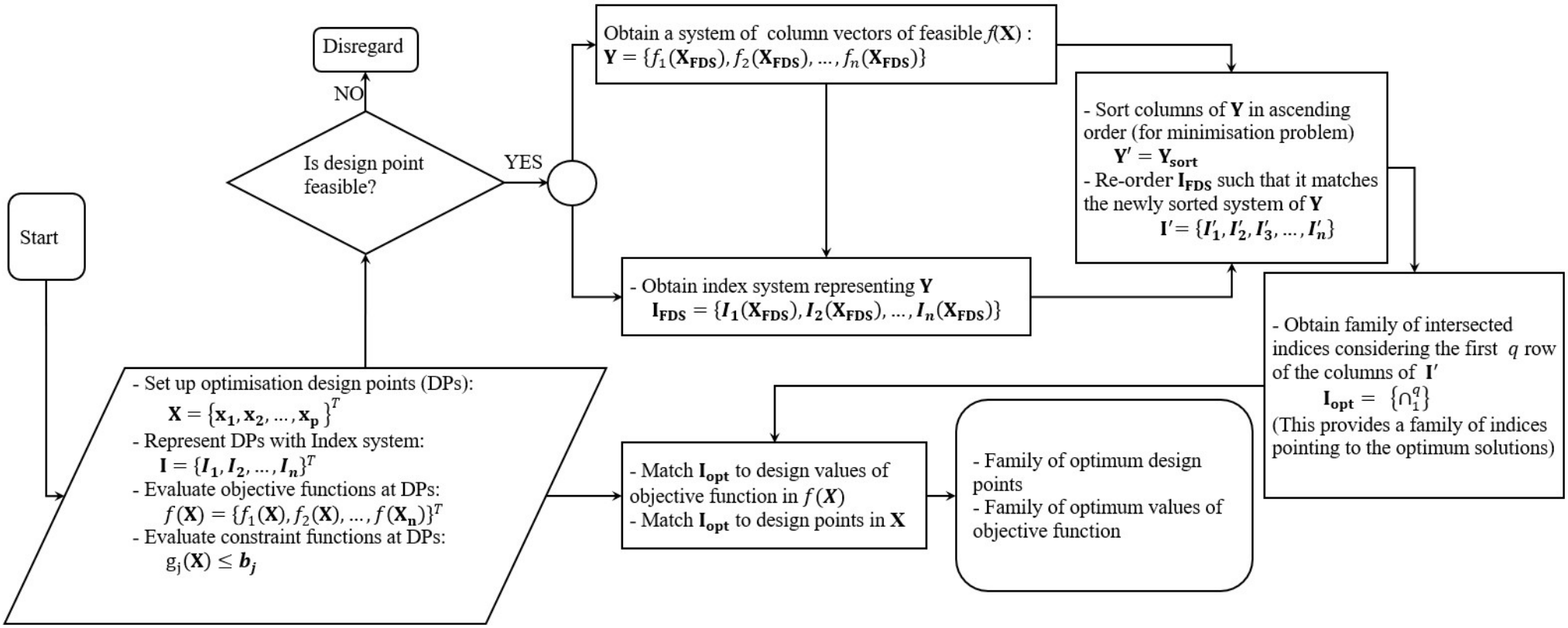

Figure 4-2. Index matching optimisation technique flowchart.

4.2.2 Validation of the IMT

To validate the IMT, we apply the technique to solve the following example in [99]: The optimal design of the three-bar truss is considered using different objectives with design variables as the cross-sectional area A_1 of members 1 (and 3) and A_2 for member 2. The truss bar system is presented in Figure 4-3.

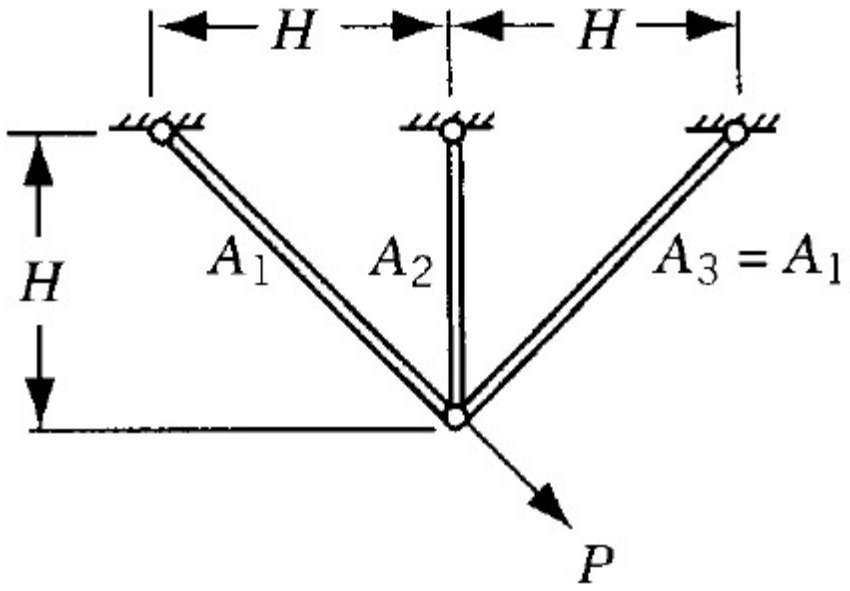

Figure 4-3 – Three truss bar design problem

The design vector is given as

$$\mathbf{X} = \begin{Bmatrix} x_1 \\ x_2 \end{Bmatrix} = \begin{Bmatrix} A_1 \\ A_2 \end{Bmatrix} \tag{4-11}$$

The objective functions are given as follows, where $f_1(\mathbf{X})$ is the weight and $f_2(\mathbf{X})$ is the vertical deflection of loaded joint.

$$f_1(\mathbf{X}) = 2\sqrt{2}x_1 + x_2 \tag{4-12}$$

$$f_2(\mathbf{X}) = \frac{PH}{E}\frac{1}{x_1 + \sqrt{2}x_2} \tag{4-13}$$

The constraints are provided as follows:

$$\sigma_1(\mathbf{X}) - \sigma^{(u)} \leq 0$$

$$\sigma_2(\mathbf{X}) - \sigma^{(u)} \leq 0 \qquad (4\text{-}14)$$

$$\sigma_3(\mathbf{X}) - \sigma^{(l)} \leq 0$$

$$x_i^{(l)} \leq x_i \leq x_i^{(u)}, \qquad i = 1, 2$$

Where σ_i is the stress induced in member i, $\sigma^{(u)}$ is the maximum permissible stress in tension, $\sigma^{(l)}$ the maximum permissible stress in compression, $x_i^{(l)}$ is the lower bound on x_i, and $x_i^{(u)}$ is the upper bound on x_i. The stresses are given by:

$$\sigma_1(\mathbf{X}) = P\frac{x_2 + \sqrt{2}x_1}{\sqrt{2}x_1^2 + 2x_1x_2}$$

$$\sigma_2(\mathbf{X}) = P\frac{1}{x_1 + \sqrt{2}x_2} \qquad (4\text{-}15)$$

$$\sigma_3(\mathbf{X}) = -P\frac{x_2}{\sqrt{2}x_1^2 + 2x_1x_2}$$

The design parameters are:

$\sigma^{(u)} = 20,\ \sigma^{(l)} = -15,\ x_i^{(l)} = 0.1\ (i = 1, 2),\ x_i^{(u)} = 5.0\ (i = 1, 2),\ P = 20,\ H = 1$, and $E = 1$

The solutions to this problem are:

$$\mathbf{X}_1^* = \begin{Bmatrix} 0.78706 \\ 0.40735 \end{Bmatrix}, \qquad f_1^* = 2.6335$$

$$\mathbf{X}_2^* = \begin{Bmatrix} 5.0 \\ 5.0 \end{Bmatrix}, \qquad f_2^* = 1.6569 \qquad (4\text{-}16)$$

Note that the problem consists of the independent optimisation of two objective function, $f_1(\mathbf{X})$ and $f_2(\mathbf{X})$, both subjected to same sets of constraint functions. Also note that there are two design variables for each of the problems, as seen in equation (4-11). The values of f_1^* and f_2^*

given in equation (4-16) are the best or optimum respective values of the two objective functions obtained by the substitution of the optimum design A_1 or x_1 and A_2 or x_2 into the objective functions in equations (4-12) and (4-13).

Table 4-1 – Results obtained from the index matching technique

S/N	$[x_1, x_2]$ (For f_1)	$[x_1, x_2]$ (For f_2)	f_1	f_2
1	[0.79200,0.39900]	[5,5]	2.639114283	1.656854249
2	[0.78600,0.41600]	[4.9990,5]	2.63914372	1.656991519
3	[0.79100,0.40200]	[5,4.9990]	2.639285856	1.657048385
4	[0.78500,0.41900]	[4.9980,5]	2.639315293	1.657128812
5	[0.79600,0.38800]	[4.9990,4.9990]	2.639427991	1.657185687
6	[0.79000,0.40500]	[5,4.9980]	2.639457429	1.657242566
7	[0.78400,0.42200]	[4.9970,5]	2.639486866	1.657266127
8	[0.79500,0.39100]	[4.9980,4.9990]	2.639599564	1.657323011
9	[0.78900,0.40800]	[4.9990,4.9980]	2.639629001	1.6573799
10	[0.78300,0.42500]	[4.9960,5]	2.639658439	1.657403465
11	[0.79400,0.39400]	[5,4.9970]	2.639771137	1.657436792
12	[0.78800,0.41100]	[4.9970,4.9990]	2.639800574	1.657460359
13	[0.78200,0.42800]	[4.9980,4.9980]	2.639830012	1.657517256
14	[0.79900,0.38000]	[4.9950,5]	2.639913273	1.657540825
15	[0.79300,0.39700]	[4.9990,4.9970]	2.63994271	1.657574158
16	[0.78700,0.41400]	[4.9960,4.9990]	2.639972147	1.657597729
17	[0.78100,0.43100]	[5,4.9960]	2.640001584	1.657631064
18	[0.79800,0.38300]	[4.9970,4.9980]	2.640084846	1.657654636
19	[0.79200,0.40000]	[4.9940,5]	2.640114283	1.657678209
20	[0.78600,0.41700]	[4.9980,4.9970]	2.64014372	1.657711547

The index matching technique is applied to solve this problem following the methodology presented in Figure 4-2. The discretization of the design space along each of the x_1 and x_2 are 0.001. This will result in the evaluation of 24,019,801 design points evaluated within the boundaries of optimisation design space defined by A_1 and A_2. The results obtained for the best

first 20 members of the optimum groups from the IMT is provided in the truncated The design vector is given as

$$\mathbf{X} = \begin{Bmatrix} x_1 \\ x_2 \end{Bmatrix} = \begin{Bmatrix} A_1 \\ A_2 \end{Bmatrix} \tag{4-11}$$

The objective functions are given as follows, where $f_1(\mathbf{X})$ is the weight and $f_2(\mathbf{X})$ is the vertical deflection of loaded joint.

$$f_1(\mathbf{X}) = 2\sqrt{2}x_1 + x_2 \tag{4-12}$$

$$f_2(\mathbf{X}) = \frac{PH}{E}\frac{1}{x_1 + \sqrt{2}x_2} \tag{4-13}$$

The constraints are provided as follows:

$$\sigma_1(\mathbf{X}) - \sigma^{(u)} \leq 0$$

$$\sigma_2(\mathbf{X}) - \sigma^{(u)} \leq 0 \tag{4-14}$$

$$\sigma_3(\mathbf{X}) - \sigma^{(l)} \leq 0$$

$$x_i^{(l)} \leq x_i \leq x_i^{(u)}, \qquad i = 1, 2$$

Where σ_i is the stress induced in member i, $\sigma^{(u)}$ is the maximum permissible stress in tension, $\sigma^{(l)}$ the maximum permissible stress in compression, $x_i^{(l)}$ is the lower bound on x_i, and $x_i^{(u)}$ is the upper bound on x_i. The stresses are given by:

$$\sigma_1(\mathbf{X}) = P\frac{x_2 + \sqrt{2}x_1}{\sqrt{2}x_1^2 + 2x_1x_2}$$

$$\sigma_2(\mathbf{X}) = P\frac{1}{x_1 + \sqrt{2}x_2} \tag{4-15}$$

$$\sigma_3(\mathbf{X}) = -P\ x22x12{+}2x1x2$$

The design parameters are:

$\sigma^{(u)} = 20,\ \sigma^{(l)} = -15,\ x_i^{(l)} = 0.1\ (i = 1,2),\ x_i^{(u)} = 5.0\ (i = 1,2),\ P = 20,$
H =1, and E=1

The solutions to this problem are:

$$\mathbf{X_1^*} = \begin{Bmatrix} 0.78706 \\ 0.40735 \end{Bmatrix}, \qquad f_1^* = 2.6335$$
$$\mathbf{X_2^*} = \begin{Bmatrix} 5.0 \\ 5.0 \end{Bmatrix}, \qquad f_2^* = 1.6569 \tag{4-16}$$

Note that the problem consists of the independent optimisation of two objective function, $f_1(\mathbf{X})$ and $f_2(\mathbf{X})$, both subjected to same sets of constraint functions. Also note that there are two design variables for each of the problems, as seen in equation (4-11). The values of f_1^* and f_2^* given in equation (4-16) are the best or optimum respective values of the two objective functions obtained by the substitution of the optimum design A_1 or x_1 and A_2 or x_2 into the objective functions in equations (4-12) and (4-13).

Table 4-1. The technique provides the family of optimum solutions in order of performance (minimum at the top to maximum at the bottom). The first two columns are sets of design variables which provide optimum values of the respective objective functions within the constrained design space for the problems. The last two columns provide the values of the respective objective function. It could be seen that these results match closely with the results the literature presented in equation (4-16). One could see that the technique can provide a family of good solutions for the problem, from which the user can decide on which solutions to select for further analysis or decision making. The results are indications of the suitability of the IMT to capture families of optimum configurations for an engineering problem, and hence can be adapted for solving the riser problems in this thesis.

4.2.3 Tabular optimization technique

The tabular optimization technique is a 2-D type of the index matching where the multiple dimensions of the problem are reduces to sets of two-dimensional problem. To understand the basis on which the tabular optimization technique is based, we present a simple example, where key terminology and operations are explained and presented. Consider system **Y** of two (n =

2) objective functions, $\mathbf{Y_1}$ and $\mathbf{Y_2}$, that are to be evaluated in a three-dimensional design space defined by a set of independent input design variables $\mathbf{X}$,

$$\mathbf{Y} = \{\mathbf{Y_1}, \mathbf{Y_2}\} \tag{4-17}$$

$$\mathbf{X} = \{\mathbf{X_1}, \mathbf{X_2}, \mathbf{X_3}\} \tag{4-18}$$

Where in this demonstrated example, we have assigned three values each to the input design variables:

$\mathbf{X_1} = \{x_{11}, x_{12}, x_{13}\}^{\mathrm{T}}$; $\mathbf{X_2} = \{x_{21}, x_{22}, x_{23}\}^{\mathrm{T}}$; $\mathbf{X_3} = \{x_{31}, x_{32}, x_{33}\}^{\mathrm{T}}$

This means there will be 27 design points in the design space. Let us say we evaluate each of the objective functions $\mathbf{Y_1}$ and $\mathbf{Y_2}$ at the 27 design points, and obtained results stored in a 3×3 array or tables as shown in Figure 4-2, where the row is the first dimension ($\mathbf{X_1}$), the column is the second dimension ($\mathbf{X_2}$) and the page is the third dimension ($\boldsymbol{X_3}$)

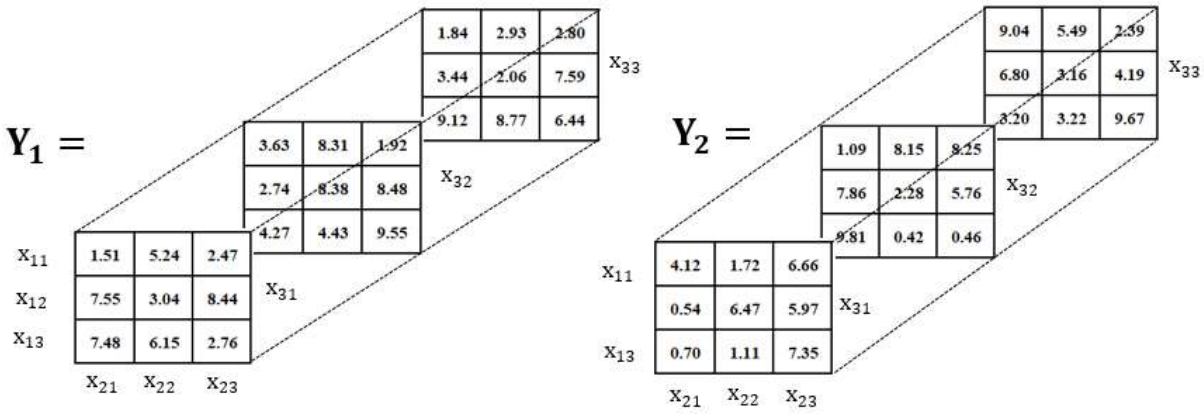

Figure 4-4 – Design space and design output variables.

Table 4-2 – Design points, design output variables, design point indices

Design points	Y_1	I_1	Y_2	I_2		Y'_1	I'_1	Y'_2	I'_2	I'_1	I'_2
(x_{11}, x_{21}, x_{31})	1.51	1	4.12	1		1.51	1	0.42	15	1	15
(x_{12}, x_{21}, x_{31})	7.55	2	0.54	2		1.84	19	0.46	18	19	18
(x_{13}, x_{21}, x_{31})	7.48	3	0.70	3		1.92	16	0.54	2	16	2
(x_{11}, x_{22}, x_{31})	5.24	4	1.72	4		2.06	23	0.70	3	23	3
(x_{12}, x_{22}, x_{31})	3.04	5	6.47	5		2.47	7	1.09	10	7	10
(x_{13}, x_{22}, x_{31})	6.15	6	1.11	6		2.74	11	1.11	6	11	6
(x_{11}, x_{23}, x_{31})	2.47	7	6.66	7		2.76	9	1.72	4	9	4
(x_{12}, x_{23}, x_{31})	8.44	8	5.97	8		2.80	25	2.28	14	25	14
(x_{13}, x_{23}, x_{31})	2.76	9	7.35	9		2.93	22	2.39	25	22	25
(x_{11}, x_{21}, x_{32})	3.63	10	1.09	10		3.04	5	3.16	23	5	23
(x_{12}, x_{21}, x_{32})	2.74	11	7.86	11		3.44	20	3.20	21	20	21
(x_{13}, x_{21}, x_{32})	4.27	12	9.81	12	Sort Y_1 & Y_2	3.63	10	3.22	24	10	24
(x_{11}, x_{22}, x_{32})	8.31	13	8.15	13		4.27	12	4.12	1	12	1
(x_{12}, x_{22}, x_{32})	8.38	14	2.28	14		4.43	15	4.19	26	15	26
(x_{13}, x_{22}, x_{32})	4.43	15	0.42	15		5.24	4	5.49	22	4	22
(x_{11}, x_{23}, x_{32})	1.92	16	8.25	16		6.15	6	5.76	17	6	17
(x_{12}, x_{23}, x_{32})	8.48	17	5.76	17		6.44	27	5.97	8	27	8
(x_{13}, x_{23}, x_{32})	9.55	18	0.46	18		7.48	3	6.47	5	3	5
(x_{11}, x_{21}, x_{33})	1.84	19	9.04	19		7.55	2	6.66	7	2	7
(x_{12}, x_{21}, x_{33})	3.44	20	6.80	20		7.59	26	6.80	20	26	20
(x_{13}, x_{21}, x_{33})	9.12	21	3.20	21		8.31	13	7.35	9	13	9
(x_{11}, x_{22}, x_{33})	2.93	22	5.49	22		8.38	14	7.86	11	14	11
(x_{12}, x_{22}, x_{33})	2.06	23	3.16	23		8.44	8	8.15	13	8	13
(x_{13}, x_{22}, x_{33})	8.77	24	3.22	24		8.48	17	8.25	16	17	16
(x_{11}, x_{23}, x_{33})	2.80	25	2.39	25		8.77	24	9.04	19	24	19
(x_{12}, x_{23}, x_{33})	7.59	26	4.19	26		9.12	21	9.67	27	21	27
(x_{13}, x_{23}, x_{33})	6.44	27	9.67	27		9.55	18	9.81	12	18	12

The two objective functions ($\mathbf{Y_1}$and $\mathbf{Y_2}$) table of values presented in Figure 4-4 can be arranged in column vector form, and a corresponding index system ($\mathbf{I}$) of the same dimension as $\mathbf{Y_1}$ and $\mathbf{Y_2}$ created to represent them as shown in Figure 4-4 – Design space and design output variables.

Table 4-2, where $\mathbf{I_1}$ and $\mathbf{I_2}$ are respectively column vectors of index system for $\mathbf{Y_1}$ and $\mathbf{Y_2}$ respectively. For minimization problems, we sort each of the objective functions in ascending order and then re-arranged the index system such that the row of the previous index numbering prior to sorting matches the new positions of the values in the sorted objective function column vectors. The sorted objective functions are demoted as $\mathbf{Y'_1}$ and $\mathbf{Y'_2}$, and the corresponding index

system column vectors are denoted $\mathbf{I_1'}$ and $\mathbf{I_2'}$. The columns vectors of $\mathbf{I_1'}$ and $\mathbf{I_2'}$ are important to determining the optimum design point for the example, hence we conduct the intersect operations across the columns and down their rows.

The intersection of two or more sets is the mathematical elements common to all the sets. However, the intersection of a set and itself will be the set itself if all elements in it is considered. In other words, a set can intersect with itself, but the values in the intersection will depend on how many elements is considered and in what order they are considered. For example, consider $\mathbf{I_1'}$ and $\mathbf{I_2'}$ from Figure 4-4 – Design space and design output variables.

Table 4-2. Each column contains 27 elements (i.e. $p = 1,2,3, \dots, 27$ rows) as shown in the first column of

Table 4-3. From

Table 4-3, it could be observed that as p increases from 1 towards 27, the intersected set of values in $\mathbf{I_1'}$ in second column and $\mathbf{I_2'}$ in third column increases until p =27 where each set of $\mathbf{I_1'}$ and $\mathbf{I_2'}$ intersect with themselves fully. Another way of viewing this is the progressive expansion of the sets of $\mathbf{I_1'}$ and $\mathbf{I_2'}$ as p increases from 1 to 27. The fourth column ($\mathbf{I_{pn}'}$) is the

intersection down the p −rows and across the n −columns which are columns of $\mathbf{I}_1'$ for $n =$ 1 and $\mathbf{I}_2'$ for = 2, where n is the number of objective functions.

Since the column vectors of $\mathbf{I}_1'$ and $\mathbf{I}_2'$ represent the values of $\mathbf{Y_1}$ and $\mathbf{Y_2}$ sorted in asceding order. It means that the first element in $\mathbf{I}_1'$ and $\mathbf{I}_2'$ represent respectively the minimum values in $\mathbf{Y_1}$ and $\mathbf{Y_2}$ and gives to the design point at which these minimums occur. As you go down the columns of each $\mathbf{I}_1'$ and $\mathbf{I}_2'$, e.g. p = 1,2,3,…, 27, the items in the self-intersection or expanded set of $\mathbf{I}_1'$ and $\mathbf{I}_2'$ increases with each row providing a family of minimum values of $\mathbf{I}_1'$ and $\mathbf{I}_2'$. The first index number appearing in $\mathbf{I}_1'$, which represents the first objective function (i.e. n =1) is 1 and this number points to the design point which minimizes $\mathbf{Y_1}$. Similarly, the first index number appearing in $\mathbf{I}_2'$, which represents the second objective function (i.e. n =2) is 15 and this number points to the design point which minimizes $\mathbf{Y}_1'$. The joint intersection of rows of $\bigcap(\mathbf{I_{p1}'})$ and $\bigcap(\mathbf{I_{p2}'})$ is $(\mathbf{I_{pn}'})$ and the first element in it occurs at p =9 where index number 25 appears as a common index or intersect of columns 2 and 3. This index number points to the design point which jointly minimizes the two objective functions $\mathbf{Y}_1'$ and $\mathbf{Y}_2'$ corresponding with n =1 and 2. For values of p increasing beyond 9, more index intersection are observed such as 23, 10, 1, 15, etc.

Table 4-3 – Intersection of the first $\boldsymbol{q}$ = 16 design point indices

p	$\cap(I'_1)$	$\cap(I'_2)$	$\cap(I'_{pn})$
1	1	15	-
2	1,19	15,18	-
3	1,19,16	15,18,2	-
4	1,19,16,23	15,18,2,3	-
5	1,19,16,23,7	15,18,2,3,10	-
6	1,19,16,23,7,11	15,18,2,3,10,6	-
7	1,19,16,23,7,11,9	15,18,2,3,10,6,4	-
8	1,19,16,23,7,11,9,25	15,18,2,3,10,6,4,14	-
9	1,19,16,23,7,11,9,25,22	15,18,2,3,10,6,4,14,25	25
10	1,19,16,23,7,11,9,25,22,5	15,18,2,3,10,6,4,14,25,23	23,25
11	1,19,16,23,7,11,9,25,22,5,20	15,18,2,3,10,6,4,14,25,23,21	23,25
12	1,19,16,23,7,11,9,25,22,5,20,10	15,18,2,3,10,6,4,14,25,23,21,24	10,23,25
13	1,19,16,23,7,11,9,25,22,5,20,10,12	15,18,2,3,10,6,4,14,25,23,21,24,1	1,10,23,25
14	1,19,16,23,7,11,9,25,22,5,20,10,12,15	15,18,2,3,10,6,4,14,25,23,21,24,1,26	1,10,15,23,25
15	1,19,16,23,7,11,9,25,22,5,20,10,12,15,4	15,18,2,3,10,6,4,14,25,23,21,24,1,26,22	1,4,10,15,22,23,25
16	1,19,16,23,7,11,9,25,22,5,20,10,12,15,4,6	15,18,2,3,10,6,4,14,25,23,21,24,1,26,22,17	1,4,6,10,15,22,23,25

With these indices' intersections, we can obtain the optimum values of the objective functions as well as the design points at which the optimum values occur. To do this, we match the family of index numbers with the design space presented in the first column of Figure 4-4 – Design space and design output variables.

Table 4-2. The optimum design data for the individual objective functions and the optimum design point for the joint objective functions are presented in Table 4-4. Following this approach, one could observe that irrespective of the number of objective functions available to be optimized, an optimum design point can be obtained for a joint subset of the objective function. However, it should be noted that because the optimisation space is reduced to a 2-D space, multiple mapping will be required from the optimum indices to the sets of 2-D spaces.

Table 4-4 – Optimum design point data

Objective function (n)	**Optimum Index**	**Design point**	Y_1	Y_2

1	1	x_{11}, x_{21}, x_{31}	1.51	4.12
2	15	x_{13}, x_{22}, x_{32}	4.43	0.42
Joint	25	x_{11}, x_{23}, x_{33}	2.80	2.39

4.3 Multi objective optimisation

Riser problems often are multi-objective optimisation problems. Hence, there is a need to determine the optimal global solutions for the multi-objectives. There are two methods applied in this thesis to solve multi-objective problems, both based on the index matching technique.

4.3.1 Method 1 - Constructing a global objective function

The global objective function, F, is created through a linear combination of the objective functions, weighted by their contributions to F. This is expressed in equation (8-23), where j is the number of the objective functions.

$$F = \sum_{j=1}^{6} a_j f_j \tag{4-19}$$

The objective functions must have the same unit for equation (8-23) to be applied. Hence, there is the need to standardise or normalize the values of the objective functions computing their linear sum, to obtain the normalised joint objective function, F^{nom}. The following are steps taken to obtain F^{nom}:

- Evaluate the objective functions for the feasible design points, f_j
- For each objective function, obtain the maximum and minimum values are f_j^{max} and f_j^{min} respectively.
- Obtain the normalised or standardized f_j using equation (8-24).

$$f_j^{nom} = \frac{f_j - f_j^{min}}{f_j^{max} - f_j^{min}} \tag{4-20}$$

- Obtain the weight contributions, a_j, of each objective functions based on the maximum, minimum or mean values. For example, f_j calculated based on the f_j^{max} and f_j^{min} are presented in equations (8-25) and (8-26). Consider for example the weight, a_j calculated based on the f_j^{max}, this means that the higher the values of the objective function, the higher will be its weight contributions to the global function F, and the less favourable its contributions will be to the minimisation of the objective function f_j.

$$a_j = a_j^{max} = \frac{f_j^{max}}{\sum_{j=1}^{N} f_j^{max}} \tag{4-21}$$

$$a_j = a_j^{min} = \frac{f_j^{min}}{\sum_{j=1}^{N} f_j^{min}} \tag{4-22}$$

- The combined normalised F i.e., F^{nom} is then obtained using equation (8-27).

$$F^{nom} = \sum_{j=1}^{6} a_j f_j^{nom} \tag{4-23}$$

The index optimisation technique can then be applied to obtain the optimum solutions for this single global objective function, F.

4.3.2 Method 2 – Intersection of the index systems of the Ideal solutions

The individual ideal solutions are the family of optimum relocation programs obtained considering each objective function exclusively. This means, within the feasible design space, the optimum members of any objective functions are obtained without considering the influence on the other objective functions. Recall from equation (4-7), that the reordered index system representing each of the objective functions can be written as:

$$\mathbf{I}' = (\mathbf{I_{FDS}})_{\text{reordered}} = \{\boldsymbol{I}_1', \boldsymbol{I}_2', \dots, \boldsymbol{I}_6'\}^{\mathrm{T}} \tag{4-24}$$

A direct intersection of the columns of $\mathbf{I}'$, taken q rows at a time, provides the family of joint optimum solutions for the objective functions. Figure 8-29 (a) shows a common region where

the family of global optimum solutions lie, while Figure 8-29 (b) demonstrates the intersection operation process for the columns of $\mathbf{I}'$ taken q rows at a time. The first values of q, may yield no intersected indices, resulting in an empty set. However, as q increases i.e., as we go further down the columns, the number intersected indices increase. The maximum value of q, denoted as Q in Figure 8-29 (b), is the number of feasible design points within the optimisation designs space.

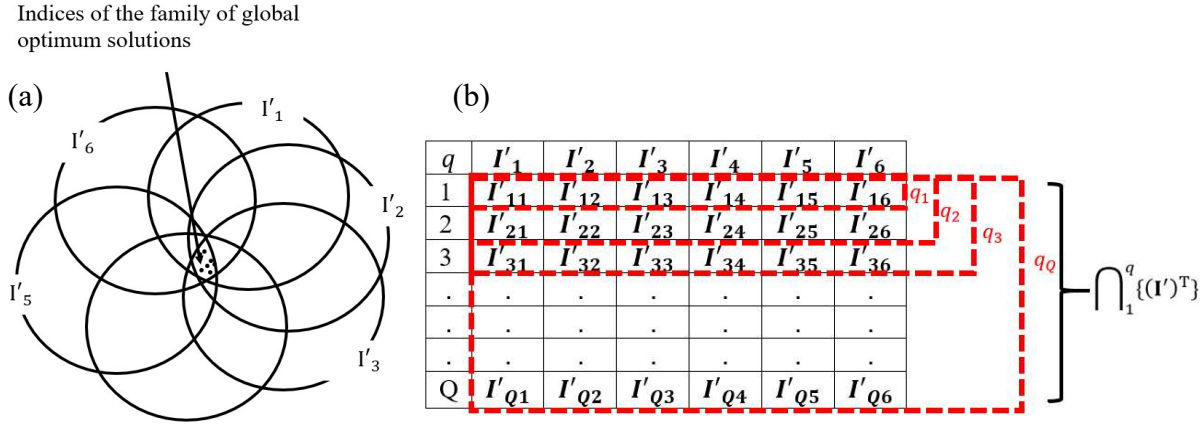

Figure 4-5. (a) Intersection region containing the family of global optimum for the objective functions (b) Conducting intersection operation on the index columns of the ideal solutions, $\boldsymbol{q}$ row at a time.

4.4 Demonstrating SLWR optimisation with the IMT

In this demonstration, the 2-D version of the index matching technique i.e., the tabular optimisation is applied. For the tabular optimisation technique, two design variable are allowed to change while the other are fixed to an arbitrary reasonable value. The SLWR riser configuration was developed in chapter 3 and will be used to define initial configuration for the SLWRs corresponding to the design points optimisation space. Recall that the SLWR configuration variables are the sag elevation, y_{sag}, the hog elevation, y_{hog}, the arc height, Δh, and the apparent mass ratio, AMR. The AMR concept was developed also in chapter 3 and is a parameter used to define the length and thickness of the smeared buoyancy section of the SLWR. The optimum results obtained form the tabular optimisation technique are compared with those obtained using the direct application of the IMT, where all design variables are allowed to vary over the optimisation design space. Further analysis are then conducted on a few selected optimum configurations and randomly selected configuration to demonstrate the suitability of the optimum solutions.

4.4.1 Tabular optimisation approach for SLWR optimisation

Consider a SLWR with hang off angle with the horizontal, θ and the height of the SLWR, h, let X be the vector of design input variables i.e. $X_1 = y_{sag}$, $X_2 =$ AMR, and $X_3 = \Delta h$. Let Y be the design output variables to be optimised i.e. $Y_1 = U_{bend}$, $Y_2 = T_{top}$, $Y_3 = \Delta\sigma_{bend}$, $Y_4 = s_b$, $Y_5 = t_b$ and $Y_6 = S_T$. The optimization problem can be expressed as follows:

$$\text{find X} = \begin{Bmatrix} AMR \\ y_{sag} \\ \Delta h \end{Bmatrix} \text{ which minimizes Y} = \begin{Bmatrix} U_{bend} \\ T_{top} \\ \Delta\sigma_{bend} \\ s_b \\ S_T \\ t_b \end{Bmatrix} \tag{4-25}$$

Subject to the following constraints:

$$AMR < 0, y_{sag} > 0, \Delta h \geq 0$$

Where AMR is the apparent mass ratio of the buoyant sections, y_{sag} is the sag height elevation from the seabed, Δh is the arc height, U_{bend} is the stress utilization in the riser bends, T_{top} is the top tension, $\Delta\sigma_{bend}$ is the stress range in the riser bends (representative of the fatigue damage), s_b is the smeared buoyant section length, S_T is the total hanging length of the SLWR, and t_b is the smeared buoyant section thickness. Note that for this example, geometric or side constraints are applied where the constraints are defined on the design variables AMR, y_{sag} and Δh. All other variables are considered as part of the objective function.

From the optimization problem layout, there are three independent design input variables (m =3) and six design output variables (p = 6). The 2D tabular approach presented in this study requires the joint variation of two (2) variables, while the third is set to an arbitrary practical value. Hence, there will be three combination pairs ($n = \mathrm{C}(m, 2) = \mathrm{C}(3,2) = 3$), referred to as the design configurations groups. The number of result tables (denoted as $Y_{p,n}$) will then be $p \times n$. A system of index tables (denoted as $I_{p,n}$) is created of equal dimension with $Y_{p,n}$ to represent the index locations of all results in the tables of $Y_{p,n}$. The layout of the results tables, $Y_{p,n}$ and the index system tables, $I_{p,n}$ are presented in Table 4-5 and Table 4-6, respectively. For numerical convenience, each table in $Y_{p,n}$ and $I_{p,n}$ can be converted to columns or vectors,

and from this point on can be interchangeably referred to as *result columns* and *index columns* in $Y_{p,n}$ and $I_{p,n}$ respectively.

Table 4-5. Result tables in each configuration groups.

Configuration group		Output variable tables or columns ($Y_{p,n}$)					
		U_{bend}	T_{top}	$\Delta\sigma_{bend}$	s_b	S_T	t_b
y_{sag}, AMR	$Y_{p,n=1}$	$Y_{1,1}$	$Y_{2,1}$	$Y_{3,1}$	$Y_{4,1}$	$Y_{5,1}$	$Y_{6,1}$
$\Delta h, AMR$	$Y_{p,n=2}$	$Y_{1,2}$	$Y_{2,2}$	$Y_{3,2}$	$Y_{4,2}$	$Y_{5,2}$	$Y_{6,2}$
$y_{sag}, \Delta h$	$Y_{p,n=3}$	$Y_{1,3}$	$Y_{2,3}$	$Y_{3,3}$	$Y_{4,3}$	$Y_{5,3}$	$Y_{6,3}$

Table 4-6. Index tables system.

Configuration groups		Index system tables or columns ($I_{p,n}$)					
		U_{bend}	T_{top}	$\Delta\sigma_{bend}$	s_b	S_T	t_b
y_{sag}, AMR	$I_{p,1}$	$I_{1,1}$	$I_{2,1}$	$I_{3,1}$	$I_{4,1}$	$I_{5,1}$	$I_{6,1}$
$\Delta h, AMR$	$I_{p,2}$	$I_{1,2}$	$I_{2,2}$	$I_{3,2}$	$I_{4,2}$	$I_{5,2}$	$I_{6,2}$
$y_{sag}, \Delta h$	$I_{p,3}$	$I_{1,3}$	$I_{2,3}$	$I_{3,3}$	$I_{4,3}$	$I_{5,3}$	$I_{6,3}$

Every table (or result column) in $Y_{p,n}$ are sorted in ascending order (for minimisation problem) or descending order for maximisation problems. The corresponding tables (or index columns) in $I_{p,n}$ are likewise re-arranged accordingly to match the repositioned output variable values in the sorted tables in $Y_{p,n}$. Intersection operation is carried out on the re-arranged index columns, and the first user-specified number of index intersections, k, point to a family of optimum SLWRs configurations. The k indices of the optimum SLWR configurations can be generally expressed as equation (4-26) and depicted in Figure 8-3, where P is the total number of output variables and N is the total number of pair combinations of the input variables.

$$\bigcap\left(I_{p,n}\right)_k, 1 \le p \le P \text{ and } 1 \le n \le N \tag{4-26}$$

A subset of the intersection in equation (4-26) can also be searched for. For example, if there is need to know what configurations optimizes U_{bend} (p =1) and s_b (p =4), then equation (4-27) applies.

$$\bigcap(I_{p,n}), p = 1,4 \text{ and } 1 \leq n \leq 3 \quad (4\text{-}27)$$

The k indices of optimum family members obtained can then be matched to the design and result space to determine the corresponding optimum design variables, which are the AMR, y_{sag} and Δh, and the corresponding values of the design output variable, which are U_{bend}, T_{top}, $\Delta\sigma_{bend}$, s_b, S_T and t_b.

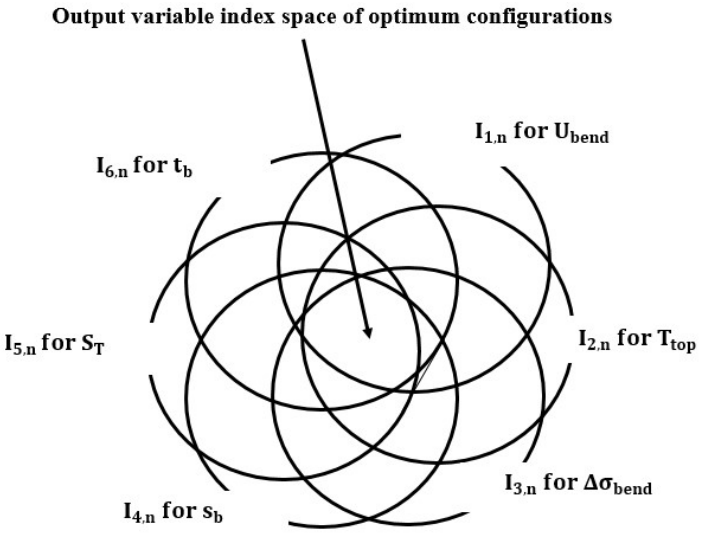

Figure 4-6. Optimum configuration index space intersections.

4.4.2 Analysis data

The SLWR used for this study is made up of a string of 12-inch X70 grade pipes. It is hosted by a generic floating production, storage, and offloading (FPSO) unit at an azimuth of 90deg to the vessel heading. The minimum wall thickness required for burst and collapse pressure resistance was calculated using DNV-OS-F201 criteria [4]. Table 4-7 presents the design data for the riser. The design range of values for each of the design input variables consist of 14 entries (design points) presented in Table 4-8.

Two irregular wave loads for the combined load and fatigue analysis are presented Table 4-6. The optimisation stage is a screening process where hundreds of FE models are simulated to search for a family of optimum configurations. Applying irregular wave loads for the combined

load and fatigue analysis during the optimisation process may be prohibitive as huge computation resources will be required to do so. Hence, the equivalent regular wave load data are used during the optimisation stage. Once a family of the optimum SLWR configurations are obtained, the selected optimum configurations will be subjected to the irregular wave analysis for a minimum of 3hrs period.

Table 4-7. Riser data.

SLWR data	Values
Pipe size	12 inch
Internal Design pressure	10 ksi
Pipe thickness (fixed)	27.5 mm
Hang off angle with the vertical (fixed)	$(90 - \theta) = 12^o$
Content density	600 kg/m3
Hang off stiffness (linear)	12 kN.m/deg
Buoyancy material density	500 kg/m^3
Water depth	1500 m
Buoyant section length	Vary (m) (based on varying AMR)
Smeared buoyancy thickness	Vary (m) (based on varying AMR)
Total riser length	Vary (m)

Table 4-8. Design input variable space.

y_{sag}(m)	AMR	Δh(m)	y_{sag}(m)	AMR	Δh(m)
10	-0.10	0	430	-1.75	280
70	-0.25	40	490	-2.00	320
130	-0.50	80	550	-2.25	360
190	-0.75	120	610	-2.50	400
250	-1.00	160	670	-2.75	440
310	-1.25	200	730	-3.00	480
370	-1.50	240	790	-3.25	520

The equivalent regular wave loads are calculated from the irregular wave loads using equations (4-28) and (4-29), where T is the regular wave period, H_{max} is the probable maximum wave height, T_z is the irregular wave zero up crossing period, T_p is the wave peak period and γ is the wave peak shape parameter. Both equations are valid for the JONSWAP spectrum with

wave peak shape parameter in the range $1 \leq \gamma < 7$ [100]. All wave loads are considered Beam Sea to impact maximum roll motions on the vessel, which translates to higher heave motions for the SCR. Current loads are excluded for simplification purposes because the current load being steady will have a negligible impact on the fluctuating (dynamic) components of the SCR responses.

$$H_{max} = 1.86H_s, T = T_z \tag{4-28}$$

$$T_z = T_p(0.6673 + 0.05037\gamma - 0.006230\gamma^2 + 0.0003341\gamma^3) \tag{4-29}$$

A generic response amplitude operator (RAOs) for the FPSO is implemented. The nonlinear hysteretic riser soil interaction model is used. Details of the default riser soil interaction model data used can be found in [56].

Table 4-9. Wave load data.

Analyses	Wave type	Data	Values
Combined	Irregular wave	H_s(m)	8
		T_p(sec)	13
		γ	1.6
	Equivalent regular wave	H_{max}(m)	14.9
		T(sec)	9.5
Fatigue	Irregular wave	H_s(m)	4.5
		T_p(sec)	9.5
		γ	1.8
	Equivalent regular wave	H_{max}(m)	8.4
		T(sec)	7

4.4.3 Analysis, results, and discussion

As presented in Table 4-8, each of the three design variables has 14 entries. There are $n = 3$ combination pairs or configuration groups of the design variables presented in Table 4-10, resulting in a total number of $2 \times 14 \times 14$ =588 design points. For each of the configuration group, an arbitrary practical value for the third variable is set. As seen in Table 4-10, $\Delta h = 50m$ for group 1, $y_{sag} = 100m$ for group 2 and $AMR = -1$ for group 3. FE model for each of the 588 design points are built and simulated for both the combined and the fatigue regular wave loads. The numerical simulations of the models were conducted using the OrcaFlex FE

software package[101]. Modelling, pre-processing, post-processing, result organisation in tables of $Y_{p,n}$ and the setting up of the corresponding index tables in $I_{p,n}$ are automated using MATLAB/PYTHON programs integrated with OrcaFlex programming interface (OrcFxAPI [102]). The program generates the OrcaFlex models using the steel lazy wave configuration model (equations) developed in section 3.1.3 to define the SLWRs initial configurations.

For each model, the output variables: the stress utilization (U_{bend}), the top tension (T_{top}), the stress range ($\Delta\sigma_{bend}$) and the SLWR geometry or dimension (t_b, S_T and s_b) are obtained. Note that stress utilization is calculated based on DNV-OS-F201, considering the combined load resistance factor design criteria for internal and external overpressure conditions [4]. The output ($p = 6$) variables are post-processed, and their extreme or maximum values are obtained and organised in tables in $Y_{p,n}$. The number of result tables or columns in $Y_{p,n}$ will be $n \times p = 18$ (see Table 4-8). The corresponding system of index tables $I_{p,n}$ will also contain 18 tables or result columns. Figure 4-9 (a), (b) and (c) present the 2D spatial representation of Table 4-10, showing the design space index of the three-design variable combination or configuration groups. The design variable values are shaded in 'blue'.

Recall from Table 4-5 that each of the ($n = 3$) configuration group contains six result tables or columns, corresponding to each of the ($p = 6$) design output variables. This gives 18 result columns in $Y_{p,n}$. Similarly, there will be 18 associated index tables or columns in $I_{p,n}$ as seen in Table 4-6. First, the 18 index tables or columns in $I_{p,n}$ are sorted in ascending order, and the associated index tables in $I_{p,n}$ are rearranged accordingly.

Table 4-10. Input variable combination (Configuration groups).

Conf. Group1		Conf. Group2		Conf. Group3	
$\Delta h = 50$m		$y_{sag} = 100$m		AMR = -1	
y_{sag}(m)	AMR	Δh(m)	AMR	y_{sag}(m)	Δh(m)
10	-0.10	0	-0.10	10	0
70	-0.25	40	-0.25	70	40
130	-0.50	80	-0.50	130	80
190	-0.75	120	-0.75	190	120
250	-1.00	160	-1.00	250	160
310	-1.25	200	-1.25	310	200
370	-1.50	240	-1.50	370	240
430	-1.75	280	-1.75	430	280

490	-2.00	320	-2.00	490	320
550	-2.25	360	-2.25	550	360
610	-2.50	400	-2.50	610	400
670	-2.75	440	-2.75	670	440
730	-3.00	480	-3.00	730	480
790	-3.25	520	-3.25	790	520

AMR

$\mathbf{y_{sag}(m)}$	-0.1	-0.25	-0.5	-0.75	-1	-1.25	-1.5	-1.75	-2	-2.25	-2.5	-2.75	-3	-3.25
10	1	15	29	43	57	71	85	99	113	127	141	155	169	183
70	2	16	30	44	58	72	86	100	114	128	142	156	170	184
130	3	17	31	45	59	73	87	101	115	129	143	157	171	185
190	4	18	32	46	60	74	88	102	116	130	144	158	172	186
250	5	19	33	47	61	75	89	103	117	131	145	159	173	187
310	6	20	34	48	62	76	90	104	118	132	146	160	174	188
370	7	21	35	49	63	77	91	105	119	133	147	161	175	189
430	8	22	36	50	64	78	92	106	120	134	148	162	176	190
490	9	23	37	51	65	79	93	107	121	135	149	163	177	191
550	10	24	38	52	66	80	94	108	122	136	150	164	178	192
610	11	25	39	53	67	81	95	109	123	137	151	165	179	193
670	12	26	40	54	68	82	96	110	124	138	152	166	180	194
730	13	27	41	55	69	83	97	111	125	139	153	167	181	195
790	14	28	42	56	70	84	98	112	126	140	154	168	182	196

Vectorized indices

Figure 4-7. Conf. Group 1: Joint variation of $\mathbf{y_{sag}}$ and AMR.

AMR

$\mathbf{\Delta h(m)}$	-0.1	-0.25	-0.5	-0.75	-1	-1.25	-1.5	-1.75	-2	-2.25	-2.5	-2.75	-3	-3.25
0	1	15	29	43	57	71	85	99	113	127	141	155	169	183
40	2	16	30	44	58	72	86	100	114	128	142	156	170	184
80	3	17	31	45	59	73	87	101	115	129	143	157	171	185
120	4	18	32	46	60	74	88	102	116	130	144	158	172	186
160	5	19	33	47	61	75	89	103	117	131	145	159	173	187
200	6	20	34	48	62	76	90	104	118	132	146	160	174	188
240	7	21	35	49	63	77	91	105	119	133	147	161	175	189
280	8	22	36	50	64	78	92	106	120	134	148	162	176	190
320	9	23	37	51	65	79	93	107	121	135	149	163	177	191
360	10	24	38	52	66	80	94	108	122	136	150	164	178	192
400	11	25	39	53	67	81	95	109	123	137	151	165	179	193
440	12	26	40	54	68	82	96	110	124	138	152	166	180	194
480	13	27	41	55	69	83	97	111	125	139	153	167	181	195
520	14	28	42	56	70	84	98	112	126	140	154	168	182	196

Vectorized indices

Figure 4-8. Conf. Group 2: Joint variation of $\mathbf{y_{sag}}$ and $\mathbf{\Delta h}$.

Δh(m)

$\mathbf{y_{sag}(m)}$	0	40	80	120	160	200	240	280	320	360	400	440	480	520
10	1	15	29	43	57	71	85	99	113	127	141	155	169	183
70	2	16	30	44	58	72	86	100	114	128	142	156	170	184
130	3	17	31	45	59	73	87	101	115	129	143	157	171	185
190	4	18	32	46	60	74	88	102	116	130	144	158	172	186
250	5	19	33	47	61	75	89	103	117	131	145	159	173	187
310	6	20	34	48	62	76	90	104	118	132	146	160	174	188
370	7	21	35	49	63	77	91	105	119	133	147	161	175	189
430	8	22	36	50	64	78	92	106	120	134	148	162	176	190
490	9	23	37	51	65	79	93	107	121	135	149	163	177	191
550	10	24	38	52	66	80	94	108	122	136	150	164	178	192
610	11	25	39	53	67	81	95	109	123	137	151	165	179	193
670	12	26	40	54	68	82	96	110	124	138	152	166	180	194
730	13	27	41	55	69	83	97	111	125	139	153	167	181	195
790	14	28	42	56	70	84	98	112	126	140	154	168	182	196

Vectorized indices

Figure 4-9. Conf. Group 3: Joint variation of AMR and Δh.

The intersection of the index columns for each configuration group is then obtained. The second, third and fourth columns of Table 4-11 present the intersections of tables or index columns in each of the three configuration group. They are respectively $\bigcap(I_{p,1})$, $\bigcap(I_{p,2})$ and $\bigcap(I_{p,3})$. The configuration indices in these columns are pointers to optimum SLWR

configurations for the groups. The fifth column presents the combined intersection of the three configuration groups, i.e.:

$$\cap(\boldsymbol{I_{p,n}}) = \cap(\boldsymbol{I_{p,1}}, \boldsymbol{I_{p,2}}, \boldsymbol{I_{p,3}}), \qquad \boldsymbol{1 \leq p \leq 6} \tag{4-30}$$

Table 4-11. Index numbers intersection (pointers) to optimum configurations.

N	Conf. group 1	Conf. group 2	Conf. group 3	Combined
92	[]	[]	[]	[]
93	[]	[]	[]	[]
94	[]	[]	78	[]
95	[]	[]	78	[]
96	[]	[]	[78;92]	[]
97	[]	[]	[78;92]	[]
98	[]	[]	[78;92]	[]
99	[]	[]	[78;91;92]	[]
100	[]	[]	[77;78;91;92]	[]
101	[]	[]	[77;78;91;92]	[]
102	[]	[]	[77;78;91;92]	[]
103	[]	[]	[63;77;78;91;92]	[]
104	[]	[]	[63;77;78;91;92]	[]
105	[]	[]	[63;64;77;78;91;92]	[]
106	[]	86	[63;64;77;78;91;92]	[]
107	[]	[73;86;107]	[63;64;77;78;91;92]	[]
108	[]	[73;86;107]	[63;64;77;78;91;92]	[]
109	[]	[73;86;101;107]	[63;64;77;78;91;92]	[]
110	[]	[73;86;87;101;107]	[63;64;77;78;91;92;106]	[]
111	[]	[73;86;87;101;107]	[63;64;77;78;79;91;92;106]	[]
112	[]	[73;86;87;101;107]	[63;64;77;78;79;91;92;93;106]	[]
113	91	[73;86;87;101;107]	[63;64;77;78;79;91;92;93;105;106]	[]
114	91	[73;86;87;101;107;108]	[63;64;77;78;79;90;91;92;93;105;106]	[]
115	91	[73;86;87;92;101;107;108]	[48;63;64;77;78;79;90;91;92;93;105;106;107]	[]
116	[91;107]	[73;86;87;92;101;107;108]	[48;63;64;77;78;79;90;91;92;93;105;106;107]	107
117	[91;107]	[73;86;87;92;101;107;108]	[48;63;64;77;78;79;90;91;92;93;105;106;107]	107
118	[91;107]	[73;86;87;92;101;107;108]	[48;62;63;64;77;78;79;90;91;92;93;105;106;107]	107
119	[91;94;107]	[73;86;87;92;93;101;107;108]	[48;62;63;64;77;78;79;90;91;92;93;104;105;106;107]	107
120	[91;94;107]	[73;86;87;92;93;101;107;108]	[48;62;63;64;76;77;78;79;90;91;92;93;104;105;106;107]	107
121	[91;94;107]	[73;86;87;92;93;101;107;108;121]	[48;62;63;64;76;77;78;79;90;91;92;93;104;105;106;107]	107
122	[91;94;95;107;108]	[73;86;87;92;93;101;107;108;115;121;122]	[48;62;63;64;76;77;78;79;90;91;92;93;104;105;106;107]	107
123	[91;92;94;95;107;108]	[73;86;87;92;93;101;107;108;115;121;122]	48;62;63;64;76;77;78;79;90;91;92;93;104;105;106;107;108	[92;107;108]
124	[91;92;94;95;107;108]	3;86;87;92;93;101;107;108;115;121;122;12	;62;63;64;76;77;78;79;90;91;92;93;104;105;106;107;108;1	[92;107;108]

.From Table 4-11, the following points should be noted:

- Configuration index 91 appears as the first configuration, which optimises all six output variables in configuration group 1. In Figure 4-7, Index 91 matches SLWR configuration with AMR = -1.5 and y_{sag} =370m. Index 91 occurs in the first k = 113 row search across the six index columns of configuration group 1 ($Y_{p,1}$). As k increases beyond 115, more configurations index such as 107, 94, 95, 108, etc. is included in the family of optimum SLWR in configuration group 1.

- Configuration index 86 appears as the first configuration, which optimises all six output variables in configuration group 2. In Figure 4-8, Index 86 matches SLWR configuration with AMR = -1.5 and Δh =40m. Index 86 occurs in the first k = 106 row search across the six index columns of configuration group 2 ($Y_{p,2}$). As k increases beyond 106, more configurations index such as 73, 107, 87,101, etc. is included in the family of optimum SLWR in configuration group 2.

- Configuration index 78 appears as the first configuration, which optimises all six output variables in configuration group 3. In Figure 4-9, Index 78 matches SLWR configuration with Δh = 200 and y_{sag} =430m. Index 78 occurs in the first k = 94 row search across the six index columns of configuration group 3 ($Y_{p,3}$). As k increases beyond 95, more configurations index such as 92, 91, 77, 63, etc. is included in the family of optimum SLWR in configuration group 3.

- Configuration index 107 appears as the first configuration, which optimises all six output variables in all three configuration groups (Group 1, 2 and 3). Index 107 occurs in the first k = 116 row search across the six index columns vectors of all three configuration groups as indicated by equation (4-30). Since index 107 is a result of the intersection of the index columns across the three groups, we must therefore match it against the three configuration group design spaces presented respectively in Figure 4-7, Figure 4-8 and Figure 4-9. By doing so, we find out that index 107 matches with the SLWR configurations with y_{sag} = 490m, AMR = -1.75, Δh =320m, 280m. Note that two Δh values occur since Δh appears as the row header in Figure 4-8 and the column header Figure 4-9. As k increases beyond 122, more configurations such as 92, 108, etc. are observed to be included in the family of problem's optimum configurations.

For further analysis, the first two members of the joint intersection of the three groups i.e. from the last column of Table 4-11. These are indices 92 and 107. These configurations will be checked against the randomly selected configurations 33 and 195. The four configuration indices (92, 107, 33 and 195) are matched against the configuration group design spaces in Figure 4-7, Figure 4-8 and Figure 4-9 to derive Table 4-12. Table 4-13 is developed by re-arranging Table 4-12, such that each row represents a unique SLWR configuration. The randomly selected configurations are highlighted in red.

Table 4-12. Selected configuration design variable table.

Conf. index	**Conf. group 1**			**Conf. group 2**			**Conf. group 3**		
	y_{sag}(m)	AMR	Δh(m)	y_{sag}(m)	AMR	Δh(m)	y_{sag}(m)	AMR	Δh(m)
92	430	-1.5	-	-	-1.5	280	430	-	240
107	490	-1.75	-	-	-1.75	320	490	-	280
33	250	-0.5	-	-	-0.5	160	250	-	80
195	730	-3.25	-	-	-3.25	480	730	-	520

Table 4-13. Expanded configuration table.

S/N	**Conf. ID**	**Configurations input variables**		
		y_{sag}(m)	AMR	Δh(m)
1	92a	430	-1.5	280
2	92b	430	-1.5	240
3	107a	490	-1.75	320
4	107b	490	-1.75	280
5	33a	250	-0.5	160
6	33b	250	-0.5	80
7	195a	730	-3.25	480
8	195b	730	-3.25	520

4.4.4 Comparison of tabular optimisation results with direct application of IMT

In the direct application of the IMT, the three independent variables are allowed to vary across the design space at the same time. None of the variable is fixed in the process as was done for

the tabular (2D) optimization approach. For the direct application of the IMT, each input design variable space is discretised into 14 points, like the tabular optimisation approach. This will result in $14\times 14 \times 14 = 2744$ number of configurations or design points to be simulated for the optimisation problem. Recall that for tabular technique, there were C (3,2) ×196 = 588 configurations or design points simulated. This implies a huge reduction in computation resource if the tabular method can provide same results as the direct IMT. The direct IMT is applied following the procedure presented in. Each of the columns of the results obtained are sorted (according to the procedure) to obtain ideal solutions for each objective function. Note that the ideal solution is the family of optimum solution for an objective function independent on other objective functions. However, the problem is a multi-objective optimisation problem, hence a joint intersection of the columns of the indices representing the sorted values of each objective function will be taken, following the procedure presented in section 8.2.3.3.2. The joint intersections of the index columns of the sorted values objective functions are presented in Table 4-5 (a). Note that this is truncated table, indicating that the first intersection was obtained at the 1409th row of the table, which range from 1 to 2744. The indices for the first three optimum members with the corresponding design points are highlighted in "blue" in Table 4-5 (b). The first 3 configurations from the direct IMT are compared with against the first set of optimum configurations from the tabular optimisation technique in Table 4-12. It could be observed that the optimum configurations of both technique match. This indicate that we can either apply the index matching technique or the tabular optimisation technique for analysis of risers in this thesis. Because the tabular technique reduces the three-dimensional space to two-dimensional space, the computational effort and storage requirements are significantly reduced compared with the index matching techniques. However, more programming effort is required for the tabular optimisation technique than for the direct index matching technique. For this example, the computational time and disc space for the direct IMT is higher by 78.5%. Since the 2D approach presents a huge reduction in the computational resource requirement, it can become very useful and advantageous for quick search of optimum SLWR configuration solution and for any riser optimization problems with more than two input design variable space.

Table 4-14 – Results obtained from direct application of IMT, (a) Intersection column showing the first three members of the family of optimum configuration, (b) The configuration name showing the values of the design variables corresponding to the optimum points (highlighted in blue) intersection column for the summarized configuration solution from 3D Tabular optimization approach

N	Conf Index
1409	1072
1410	1072
1411	[1072;1073]
1412	[1072;1073]
1413	[1072;1073]
1414	[1072;1073]
1415	[1072;1073]
1416	[1072;1073]
1417	[1072;1073]
1418	[1072;1073]
1419	[1072;1073]
1420	[1072;1073]
1421	[1072;1073]
1422	[1072;1073]
1423	[1072;1073]
1424	[1072;1073]
1425	[1072;1073]
1426	[1072;1073]
1427	[1072;1073]
1428	[1072;1073]
1429	[1072;1073]
1430	[1072;1073]
1431	[1072;1073]
1432	[1072;1073]
1433	[1072;1073]
1434	[1072;1073]
1435	[1072;1073]
1436	[1072;1073]
1437	[1072;1073]
1438	[1072;1073]
1439	[1072;1073;1267]
1440	[1072;1073;1267]

(a)

Configuration index	$y_{sag}, AMR, \Delta h$
1066	70,-1.5,200
1067	130,-1.5,200
1068	190,-1.5,200
1069	250,-1.5,200
1070	310,-1.5,200
1071	370,-1.5,200
1072	430,-1.5,200
1073	490,-1.5,200
1074	550,-1.5,200
1075	610,-1.5,200
1076	670,-1.5,200
1077	730,-1.5,200
1078	790,-1.5,200

(b)

1263	130,-1.5,240
1264	190,-1.5,240
1265	250,-1.5,240
1266	310,-1.5,240
1267	370,-1.5,240
1268	430,-1.5,240
1269	490,-1.5,240
1270	550,-1.5,240
1271	610,-1.5,240

(c)

Conf. index	**Configurations**		
	y_{sag}(m)	AMR	Δh(m)
1072	430	-1.5	200
1073	490	-1.5	200
1267	370	-1.5	240

4.4.5 Further analysis of optimum configurations

The static configurations of the SLWRs presented in Table 4-13 are shown in Figure 4-10. The selected optimum configurations (92a, 92b, 107a, 107b) are observed to cluster around each other. On the other hand, the profiles of the randomly selected configurations (conf. 33a, conf.33b, conf. 195a, conf. 195b) are found to deviate widely from those of the optimum solution cluster. Bar plot of the geometric output variable (s_b and S_T) of the configurations are presented in Figure 4-11. The s_b and S_T values of the randomly selected configurations are observed to be higher than those of the optimum configurations, except s_T of conf 33b and s_b of configuration 195a and 195b. Numerical values are presented in Table 4-15.

One of the cost drivers of the SLWR is the buoyancy material volume of the buoyant section. The smeared volume, vol_b, can be expressed in terms of t_b, s_b, as shown in equation (4-31). Recall from equation (4-31) that t_b and s_b are part of the design output variables to be optimised. Hence, optimising t_b and s_b implies optimization of vol_b.

$$\boldsymbol{vol_b = \pi t_b s_b (OD + t_b)} \tag{4-31}$$

The bar plot of vol_b is presented in Figure 4-12. While the smeared buoyancy of configuration 195 requires a higher volume to achieve higher wave bend elevation, configuration 33 require lower buoyancy volume because of its lower wave bend elevation, compared with the selected optimum configurations. However, the problem is set to optimise six output variables (not just s_b and S_T), it will therefore be comprehensive to examine the suitability of the selected optimum configurations in terms of all the six variables.

The irregular wave loads for combined and fatigue were simulated on the selected SLWR configurations. Figure 4-13, Figure 4-14 and Figure 12 respectively present the U_{bend} , the T_{top} and minimum fatigue life of the selected SLWR configurations. Table 4-15 offers a comparison of maximum values for the design output variables.

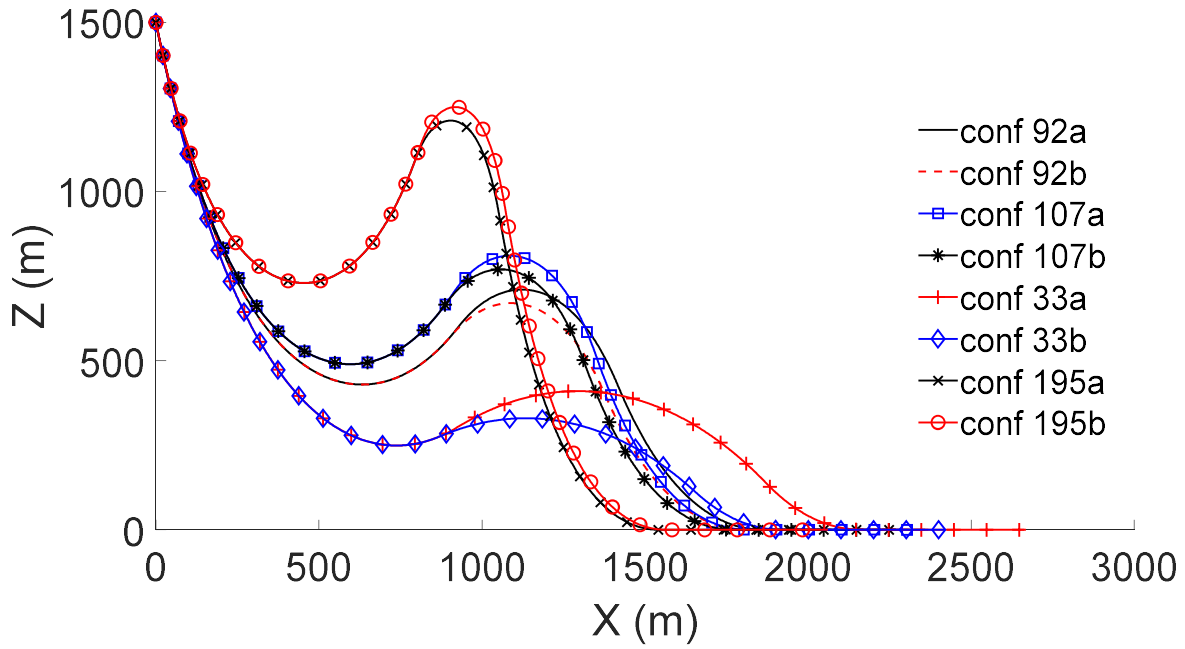

Figure 4-10. Static configuration of selected SLWRs.

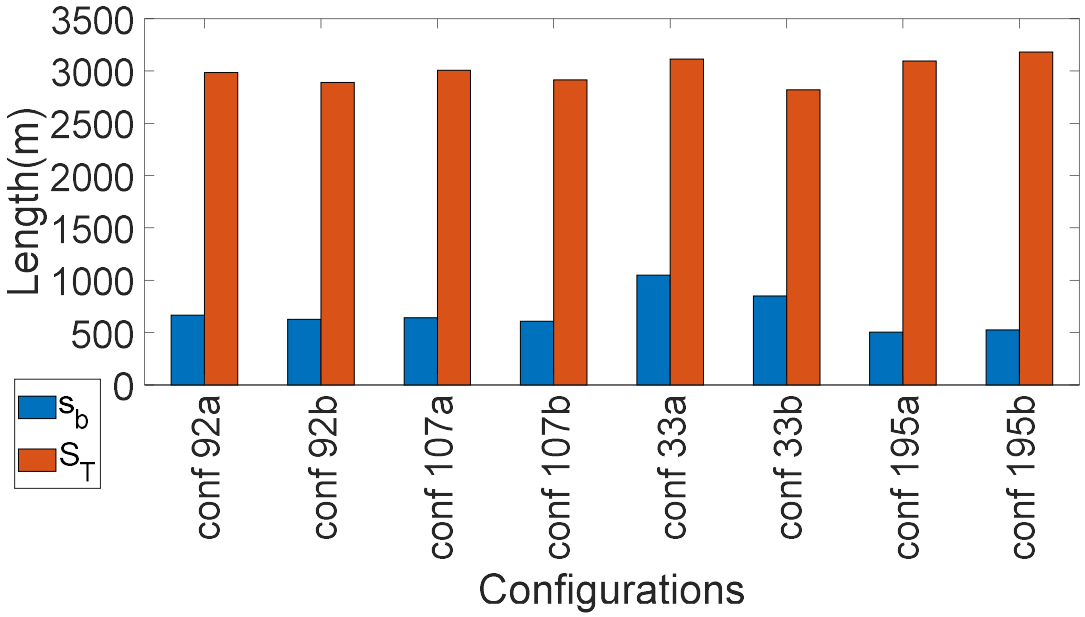

Figure 4-11. Comparing SLWR hanging length ($\mathbf{s_T}$) and smeared buoyancy section length ($\mathbf{s_b}$).

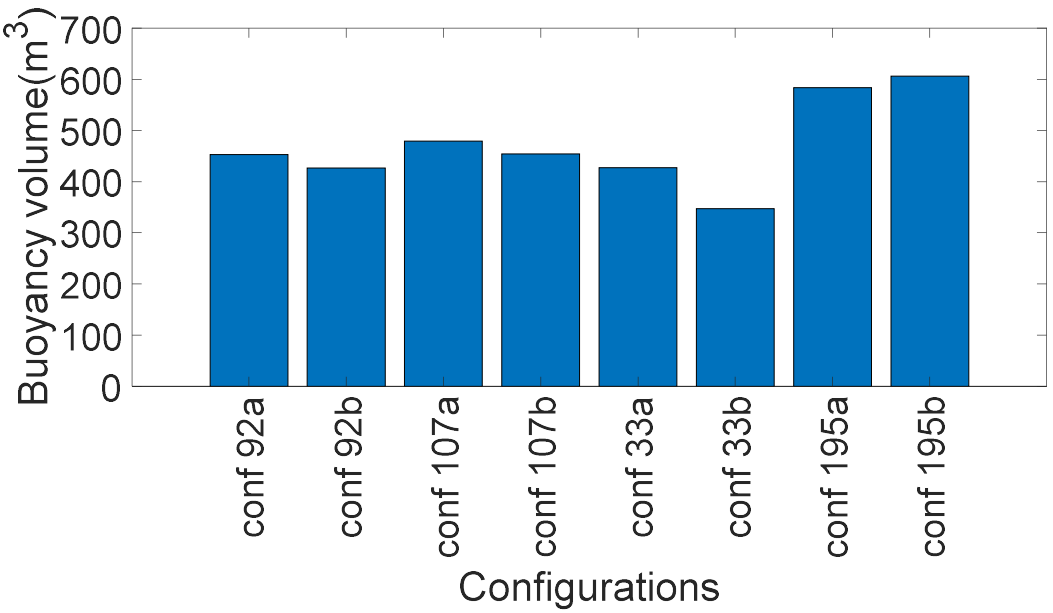

Figure 4-12. Comparing the volume of SLWRs buoyancy section.

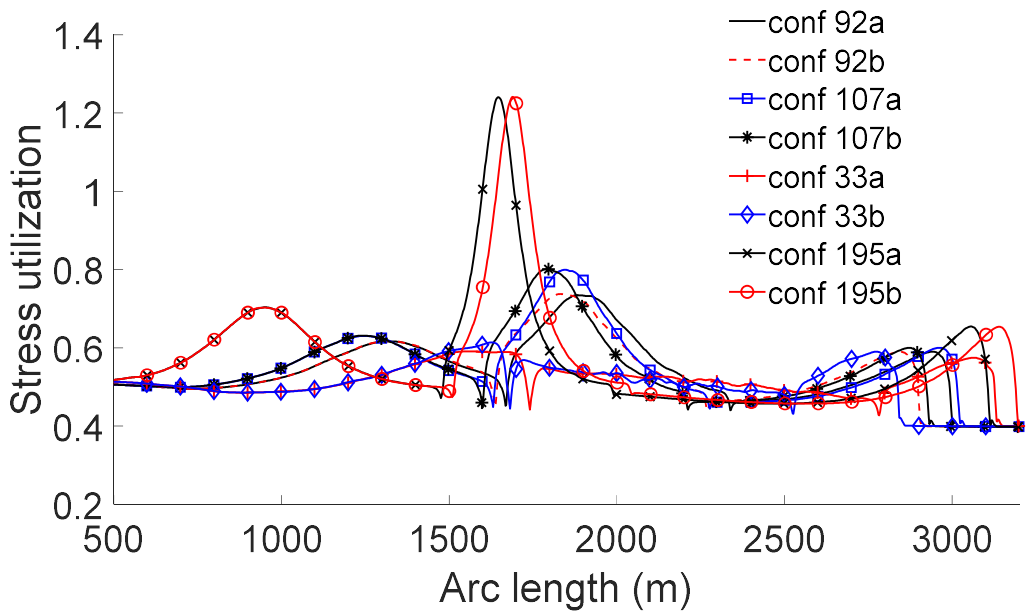

Figure 4-13. Maximum stress utilization at bends.

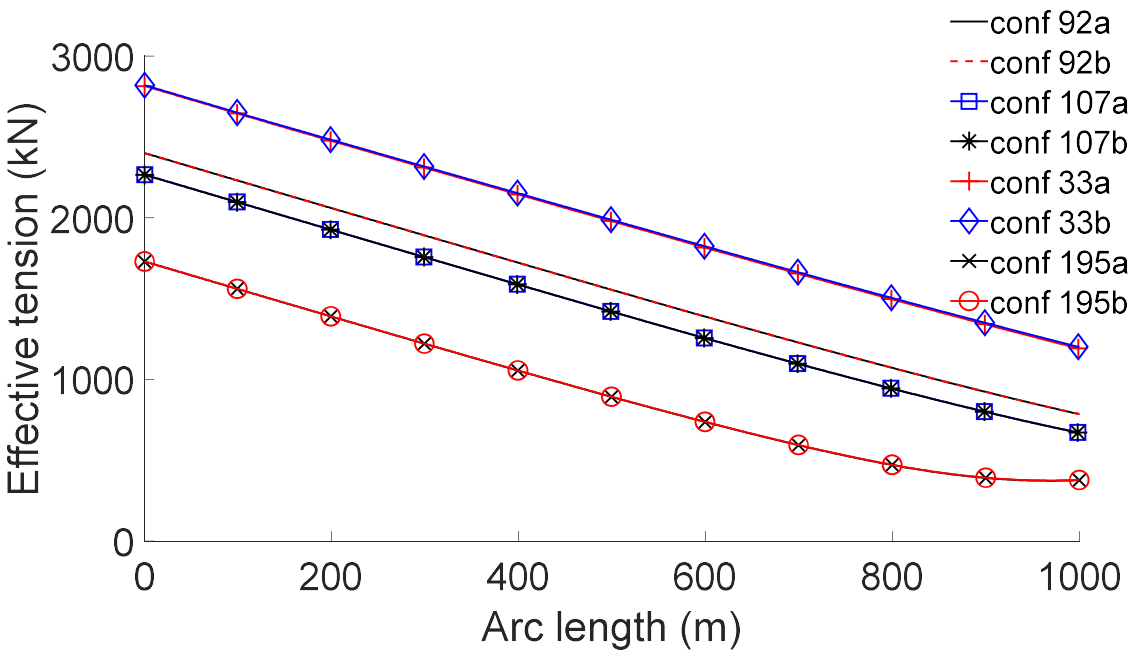

Figure 4-14. Maximum top tension.

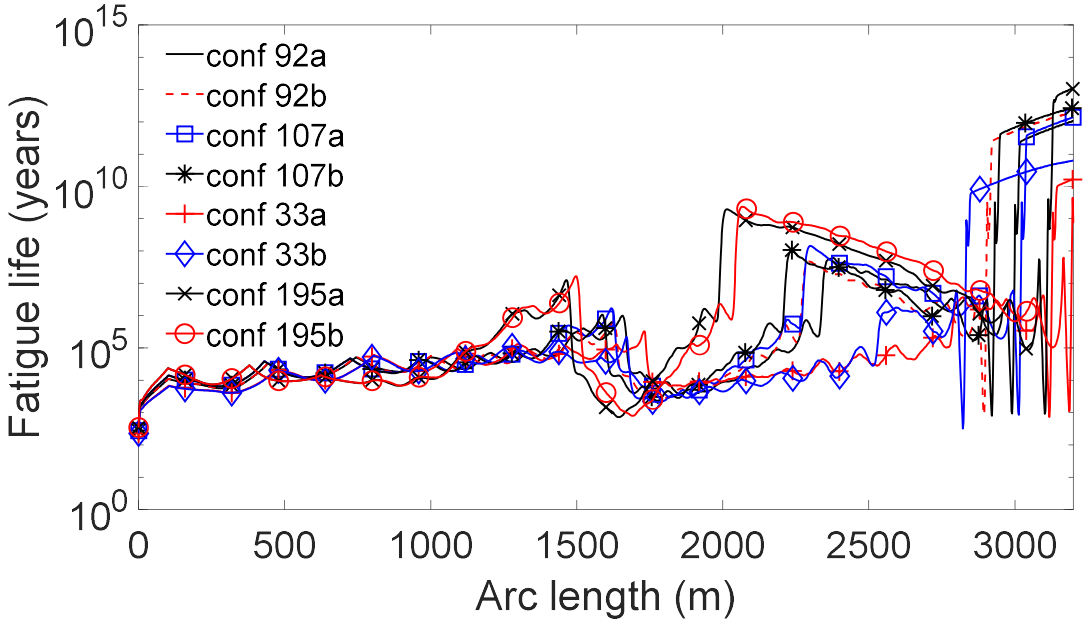

Figure 4-15. Maximum stress range around SLWR bends.

Table 4-15. Summary of the configurations output variable.

Conf. ID	Independent Input design variables			Critical values of design output variables						
	y_{sag}(m)	AMR	Δh(m)	U_{bend}	T_{top} (MN)	Min. Life (years)	s_b (m)	S_T (m)	t_b(m)	Vol_b (m^3)
92a	430	-1.5	280	0.75	2400.12	254.68	665.87	2986.01	0.34	452.76
92b	430	-1.5	240	0.75	2399.38	256.31	627.47	2890.03	0.34	426.66
107a	490	-1.75	320	0.80	2266.57	277.88	640.42	3008.41	0.36	479.01
107b	490	-1.75	280	0.80	2265.41	277.87	607.04	2916.61	0.36	454.04
33a	250	-0.5	160	0.77	2815.55	226.24	1047.43	3114.76	0.24	427.32
33b	250	-0.5	80	0.77	2820.92	226.13	850.52	2819.41	0.24	346.99
195a	730	-3.25	480	1.24	1728.75	346.59	504.99	3097.08	0.47	583.74
195b	730	-3.25	520	1.24	1729.24	344.97	524.58	3180.36	0.47	606.38

Table 4-16. Percentage change in critical values of the randomly selected configuration relative to the mean of the optimum configuration.

Conf. ID	Independent Input design variables			% change						
	y_{sag}(m)	AMR	Δh(m)	U_{bend}	T_{top}	Min. Life	s_b	S_T (m)	t_b	Vol_b
33a	250	-0.5	160	-0.6	20.7	-15.2	64.9	5.6	-31.4	-5.7
33b	250	-0.5	80	-0.6	20.9	-15.2	33.9	-4.4	-31.4	-23.4
195a	730	-3.25	480	60.0	-25.9	30.0	-20.5	5.0	34.3	28.8
195b	730	-3.25	520	60.0	-25.9	29.4	-17.4	7.8	34.3	33.8

Note: Positive percentages means that the value of the randomly selected configuration output variables is higher than the mean of the values of the optimum configurations. The reverse is the case for negative values.

For easy comparison of the performances of the optimum configurations, the values of the output variable for the randomly selected configurations are compared with the mean values of the optimum configuration. The comparison is expressed in percentages presented in Table 4-16. Positive percentages mean that the value of the randomly selected configuration output variables is higher than the mean of the values of the optimum configurations. The reverse is the case for negative values. The results show that the 2D optimisation technique balances the interest of all six output variables in the selected optimum configurations. For example, while the mean of the fatigue lives of the optimum configurations is lower than those of the randomly selected configuration 33a and 33b by 15%, the top tension of configuration 33a and 33b are higher by 21%. On the other hand, the randomly selected configuration 195a and 195b have stress utilization higher than the mean stress utilization of the optimum configuration by 60%, but with fatigue life higher by about 30% and a reduction in top tension by about 26%. The results indicate the challenges inherent in solving a multi-objective optimisation problem. A unique decision would be possible for a single-objective optimisation problem. However, for a multi-objective problem, with additional considerations from the designer, a given optimum configuration can be selected from the family of optimum solutions. For example, if the design interest is majorly the cost of the SLWR, the total riser length and volume of buoyancy material will be of interest and configuration 195a and 195b will be seen to be more expensive relative to the current sets optimum configurations. If the designer's major interest is the top tension capacity of the supporting structure for the riser, then configuration 33a and 33b will be seen to provide higher top tension relative to the current sets of optimum configurations. However, for the above two conditions specified, the 2D tabular technique can be reapplied for the subset of considerations and new sets of optimum configurations can be derived for the problem (see the example presented by equation (4-27)).

4.5 Chapter summary

A 2D tabular and index matching optimisation technique is presented in this chapter. The tabular optimisation technique reduces a higher dimensional design space of a problem to sets of two-dimensional design spaces. It then assigns indices (identifiers) to every design point or configuration in the 2D design spaces. The optimum design points are then tracked through index matching, using techniques such as data sorting and intersection operations.

The technique is demonstrated by its application to solve the SLWR riser optimisation problem. For the SLWR example, there are three independent design input variables: y_{sag}, AMR and

Δh. The output variables to be optimised are T_{top}, U_{bend}, s_b, S_T, t_b and $\Delta\sigma$ or fatigue damage. Design points or configurations in the 2D design spaces are simulated with the combined and fatigue wave loads. The design output results are post-processed and organized in a system of result tables or columns, $Y_{p,n}$. A corresponding system of index tables or columns, $I_{p,n}$ is set up, which serve as identifiers for results tables in $Y_{p,n}$. The results columns are sorted in ascending order (for minimisation problem), while the system of index tables is re-arranged accordingly to match the new positions for design points in the sorted result columns. The intersection operation is carried out on the index table system, and the first sets of intersected indices indicate the sets of design points or configuration which optimises the design output variables. A few numbers of selected optimum SLWR configurations, along with some randomly selected configurations, were simulated for 3hrs, using the irregular combined and fatigue wave loads. This is conducted to demonstrate the potential of the technique to capture optimum design configuration for the problem. The results showed that the 2D tabular technique could take into consideration a balance of the interest of all output variables, by reporting indices for configurations, which equally optimises the design output. The 2D tabular method is also able to report new sets of configuration candidates if the search criteria or the set of design output variables to be optimised is changed. The tabular approach has robust potentials to cut down computation resources required for a higher dimensional problem. It can also accommodate additional load scenarios and other external design constraints that may be imposed on the optimization process.

In the SLWR optimisation example demonstrated in this chapter, the tabular optimisation technique reduces the three-dimensional problem to two dimensions. A potential limitation with the technique is with the reduction of higher dimensional space to that of two dimensions, a transformation which needs further investigation. Future work will be to extend this technique to higher dimensional riser optimisation problems. This could significantly improve the efficiency in the riser optimisation computation.

5 BRANCHED RISER SYSTEM

The branched riser system (BRS) concept is discussed and investigated in this chapter. The BRS system consists of a large bore riser pipe in a catenary configuration and terminated in a connecting structure (connector) at some water depth. Two small bore riser pipes take off from the connector to the seabed either in catenary or lazy wave configurations. The system is expected to provide improved global strength and fatigue response at the SCR TDZ compared with the conventional risers.

This chapter is structured as follows:

- Section 5.1 – Background to branched risers systems
- Section 5.2 – The branched riser system configuration development
- Section 5.3 – BSCR optimisation
- Section 5.4 – BSCR interference study
- Section 5.5 – Chapter summary

5.1 Background to branched riser systems

5.1.1 Comparative study of small and large bore pipe risers

This section presents additional results on the comparative study of SCRs with different bore sizes (OD) and hang-off angles (HO). The following considerations are made for this investigation:

- Pipe diameter of 8inch, 12inch, 16inch and 20inch are investigated
- The hang-off angles for the SCR explored are 10deg, 14deg and 18deg

Note that the different combinations of different values of OD and HO result in different SCR configurations. The combinations of the OD and the HO are provided in

Table 5-1

Table 5-1. Combinations of riser pipe diameter and hang off angles

		Hang-off angle (degrees)		
		10	14	18
Diameters (inch)	8	8,10	8,14	8,18
	12	12,10	12,14	12,18
	16	16,10	16,14	16,18
	20	20,10	20,14	20,18

Table 5-2. Wave scatter investigated

Wave height, H (m)	**Associated wave period, T(sec)**														
1	4	5	6	7	8	9	10	11	12	13	14	15	16	17	18
2	5	6	7	8	9	10	11	12	13	14	15	16	17	18	19
3	5	6	7	8	9	10	11	12	13	14	15	16	17	18	19
4	6	7	8	9	10	11	12	13	14	15	16	17	18	19	20
5	6	7	8	9	10	11	12	13	14	15	16	17	18	19	20
6	7	8	9	10	11	12	13	14	15	16	17	18	19	20	21
7	7	8	9	10	11	12	13	14	15	16	17	18	19	20	21
8	8	9	10	11	12	13	14	15	16	17	18	19	20	21	22
9	8	9	10	11	12	13	14	15	16	17	18	19	20	21	22
10	8	9	10	11	12	13	14	15	16	17	18	19	20	21	22
11	9	10	11	12	13	14	15	16	17	18	19	20	21	22	23
12	9	10	11	12	13	14	15	16	17	18	19	20	21	22	23
13	9	10	11	12	13	14	15	16	17	18	19	20	21	22	23
14	9	10	11	12	13	14	15	16	17	18	19	20	21	22	23
15	10	11	12	13	14	15	16	17	18	19	20	21	22	23	24

The wave loads applied during the investigation is a wave scatter, consisting of the wave height ranging from 1m to 15m, with a series of incremental wave periods starting with the breaking wave period limit. There is 15 number of these incremented periods associated with each wave height. The derived wave scatters are presented in Table 5-2. Note that the starting period is the next integer approximations from the exact values of the breaking wave period limits for any given wave height. Hence, there are 225 wave bins simulated for the study. From these input data sets, one could see that a large amount of result data can be obtained for the

comparative study. However, for brevity's sake, a few of the results data are presented to demonstrate the performances of SCRs with different bore sizes. The main region of interest of the SCR for this comparison is the TDZ. The following responses are post-processed around the SCR TDZ:

- Stress utilization (TDZ)
- Compression (TDZ)
- Fatigue damage (TDZ)

These three responses are considered for increasing wave height and period values, with the wave loads acting along the beam sea direction for which the vessel responses are highest.

It could be seen from Figure 6-4 that the stress utilization performance are higher for smaller pipe OD than larger pipe OD from wave height of 1m to 9m. For wave heights higher than 9m, e.g. 12m. this increased performance can no longer be guaranteed. This is caused by excessive compressions being experienced by the smaller bore risers with increasing wave heights compared to those of the large bore risers, as seen in Figure 5-2. In general, small-bore risers have higher TDZ compression tendencies than large bore risers, as seen in Figure 5-2. However, for as long as this compression magnitude is not excessive, the smaller bore risers will continue to perform better in stress utilization than larger bore risers. Once the compression magnitude becomes significant, the performance of the small-bore risers can no longer be guaranteed over those of the larger bore risers. For higher wave heights, 12sec is seen to be a challenging wave period for the smallest bore (8inch) SCRs. This could be attributed to the response period matching one of the modal periods of the riser. This indicates that although small-bore SCR performs better in stress utilization than larger bore risers, this increased performance can be negatively affected by the wave period of considerations.

Similar behaviours are observed for the fatigue damage responses presented in

Figure 5-3. Fatigue wave loads are typically lower than the extreme wave loads, with higher wave loads having negligible probabilities of occurrences. Since the smaller bore SCR have higher performance for the fatigue wave load dominated by smaller wave heights from 1m to 6m, it could be certain that the smaller bore CR will not have fatigue performance higher than those of the larger bore SCRs. As observed for the stress utilization, the fatigue damage for the 8icnh SCR can be impacted negatively at 12sec.

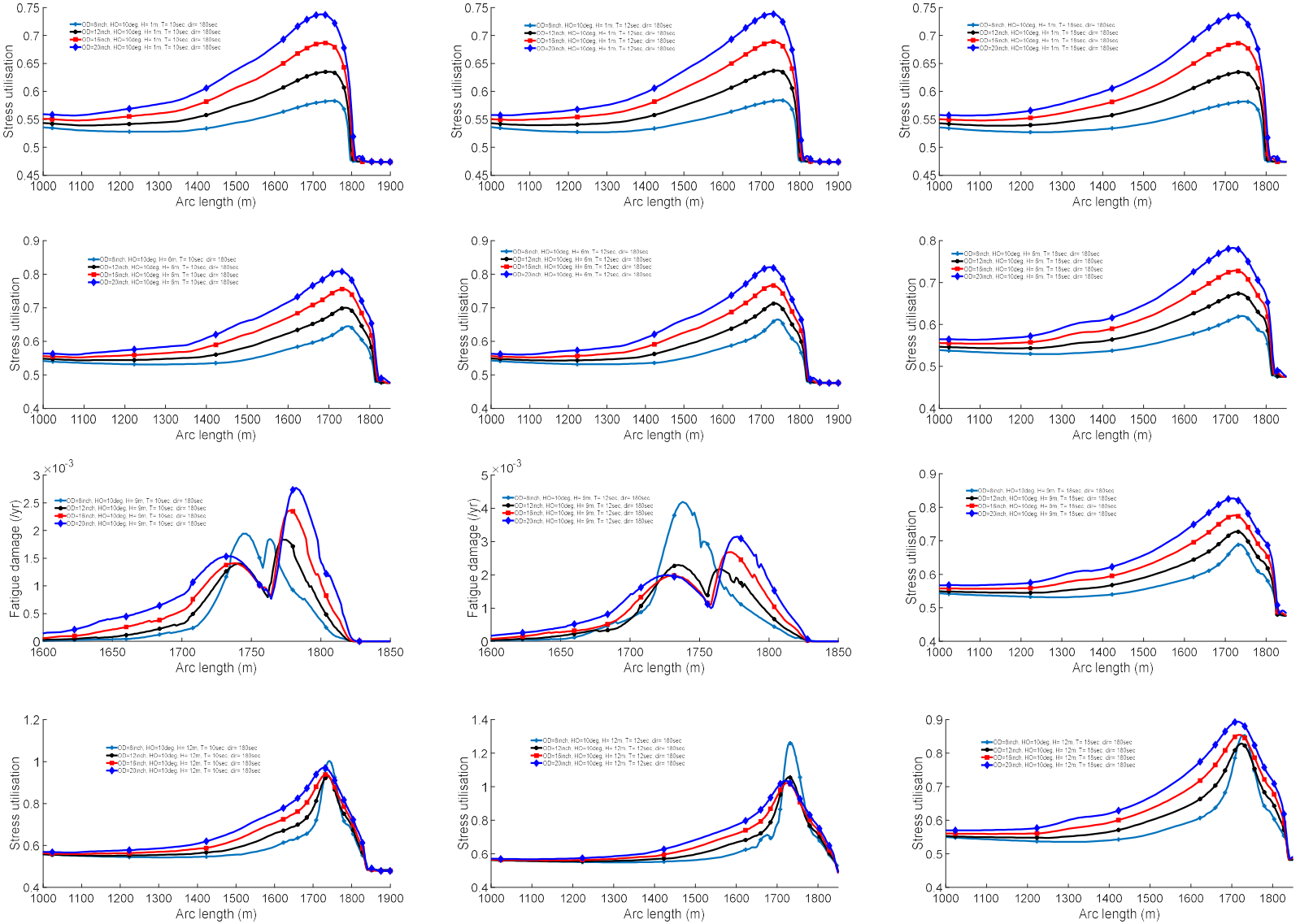

Figure 5-1. SCR TDZ stress utilization for varying wave heights and periods

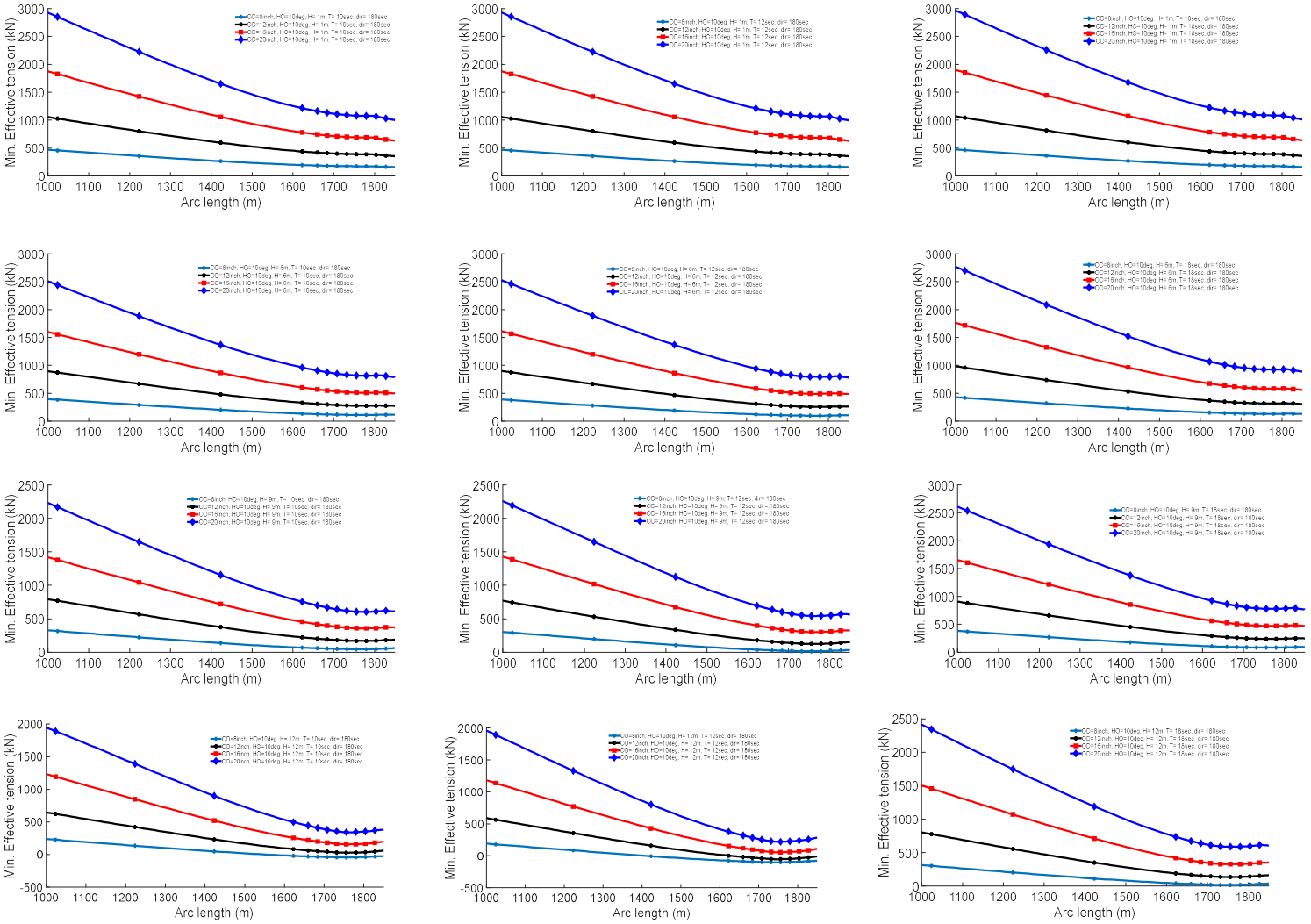

Figure 5-2. SCR TDZ compressions (measured by the negativity of the minimum effective tension) for varying wave heights and periods

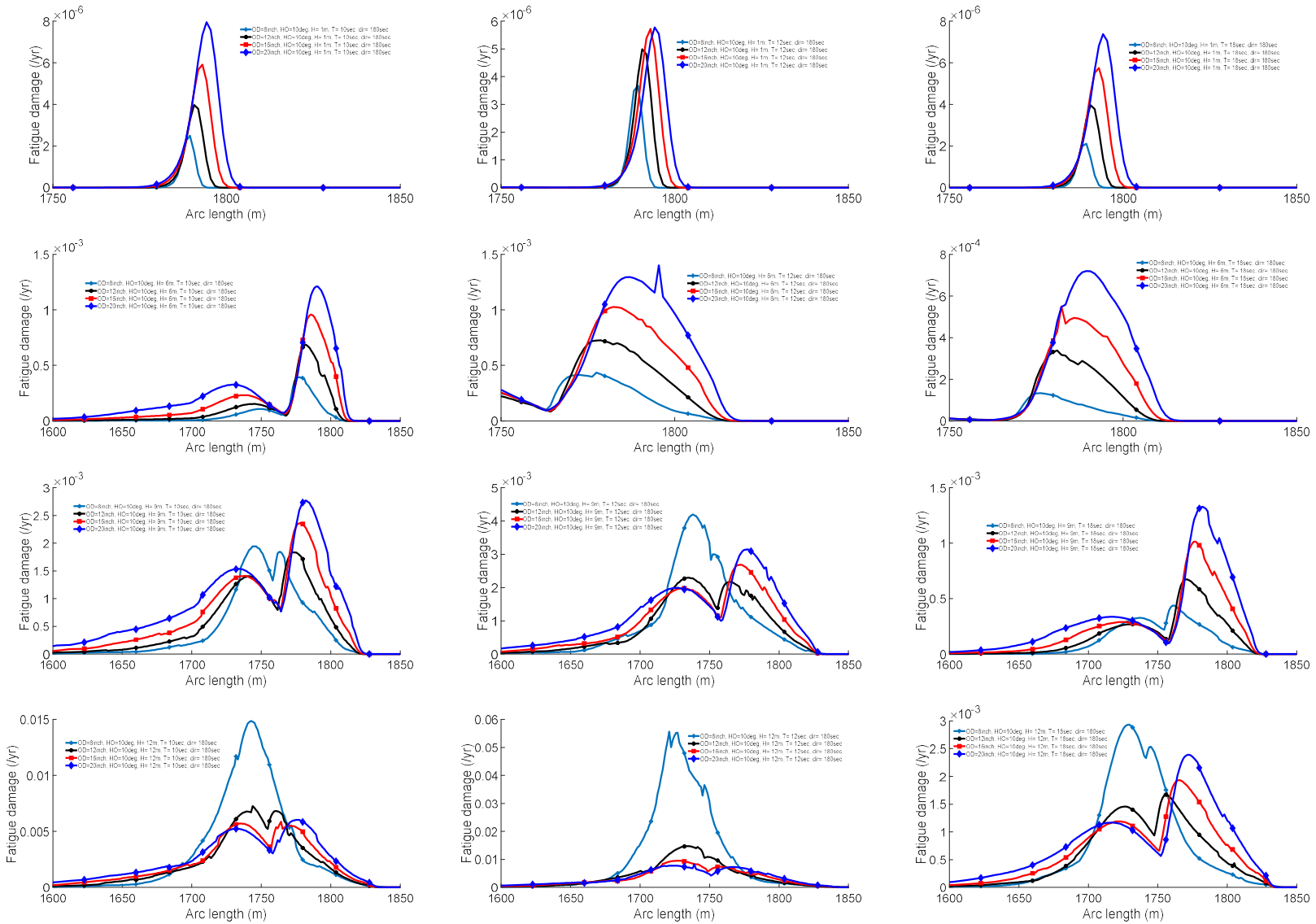

Figure 5-3. SCR TDZ fatigue damage for varying wave heights and period

5.1.2 Branched Riser System Proposition

From the strength and fatigue results obtained in the previous section, It can be seen that the larger the bore of the riser pipe, the higher the stress utilization and the fatigue damage at the TDZ due to high fluctuations bending stress in these regions. For large fields where it is the interest of the producer to convey as much product as possible, larger bore risers will be preferred but with a higher damage around the TDZ. Selecting smaller bore riser in preference to larger bore risers will require more than one smaller pipe to be implemented to conduct same amount of material that a single larger riser pipe will transport. This can result in many tiebacks and associated costs and highly congested vessel-riser interface as illustrated in the example layout in Figure 5-4 (portside).

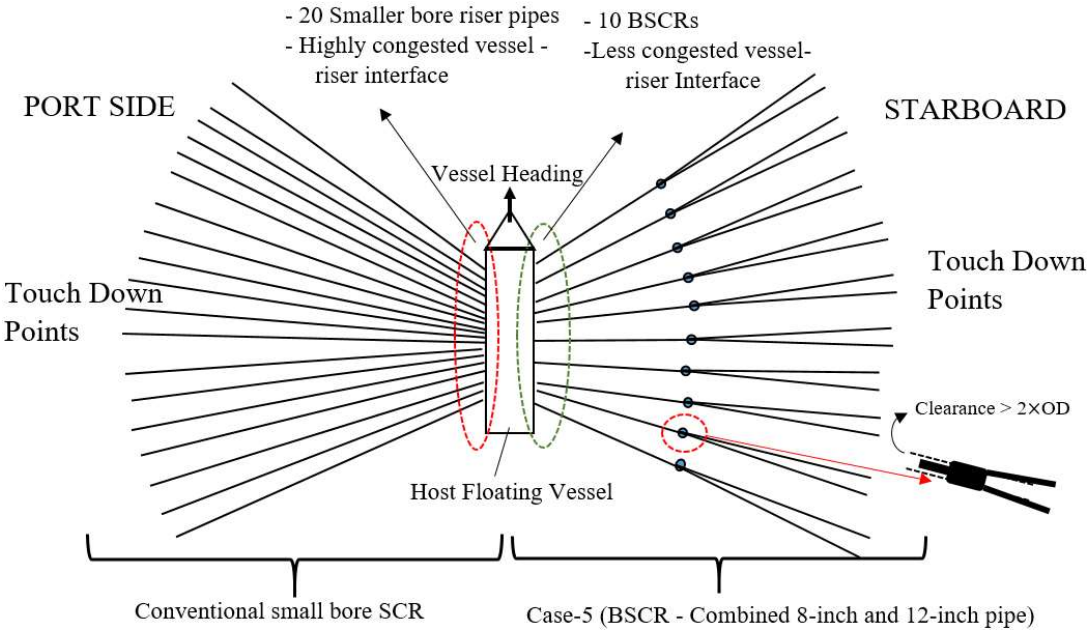

Figure 5-4 – Riser porch connection density (Plan View)

Results from the comparative study suggest benefits of combining advantages of smaller and larger riser pipes considering stress utilization, fatigue damage, flow throughput requirement and vessel top congestion. The smaller riser pipe in contact with the seabed will provide higher resistance to stress and fatigue damage around the TDZ and the larger riser pipe in combination with two smaller pipes will provide opportunities for optimized flow throughput, lesser tiebacks, and vessel top decongestion. This is an idea behind the development of the branched risers systems.

5.1.3 Overview of the branched riser systems configuration types

The branched riser system consists of a large bore pipe, which terminates at a water depth referred to here as the cut off depth. This depth can be determined considering required minimum wall thickness for burst and collapse resistance criteria, and the resulting riser weight. From this cut off depth, the system extends to the seabed by two smaller riser pipes via a connecting component referred to as the connector. The new concept attempts to improve on the requirement for larger bore pipe for high design and collapse pressure, stress and fatigue response experienced at the HO and TDP. The Branched riser systems is of three types namely:

- The Branched Steel Catenary Riser System,
- The Branched Steel Lazy Wave Riser System
- The Branched Lazy Wave Hybrid Riser Systems

5.1.3.1 Branched Steel Catenary Riser (BSCR)

The BSCR consist of a large and two small-bore riser pipes connected together by the connector at the cut off depth. The large bore pipe spans a catenary path between the vessel and the connector while the two small-bore riser extend from the cut off depth to the seabed, also in catenary configurations (Figure 5-5).

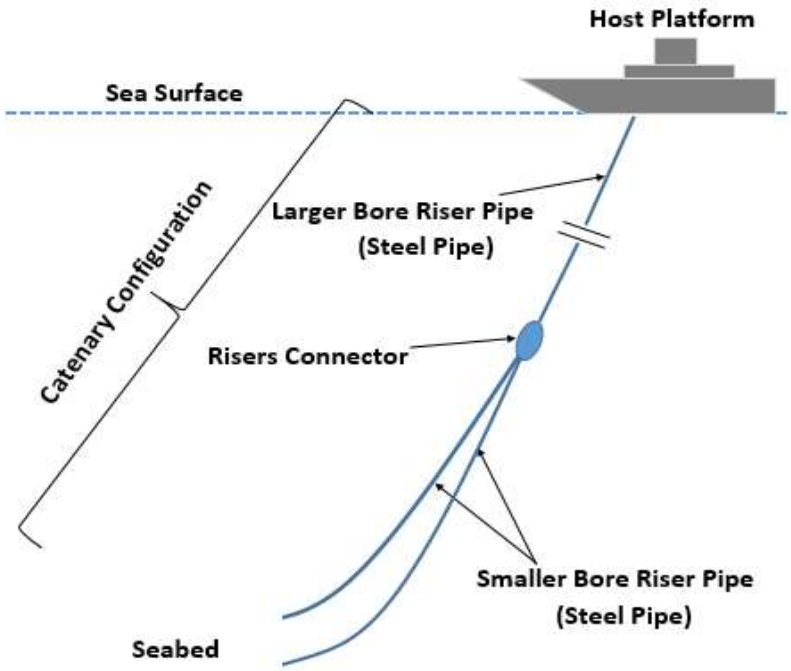

Figure 5-5 – BSCR configuration

5.1.3.2 Branched Steel Lazy Wave Riser (BSLWR)

The BSLWR can be derived from the BSCR by the inclusion of buoyancy modules on sections of the smaller riser pipe close to the seabed as shown in Figure 5-6 . The large bore riser pipe spans a catenary path between the vessel and the connector while the two small-bore pipes assumes lazy wave configurations from the connector to the seabed. The three pipes are metallic and the hanging lengths of the smaller bore pipes will be longer than that of the BSCR in order to accommodate the lazy wave configuration. The addition of buoyancy modules will potentially result in weight reduction and better strength and fatigue response at the TDZ.

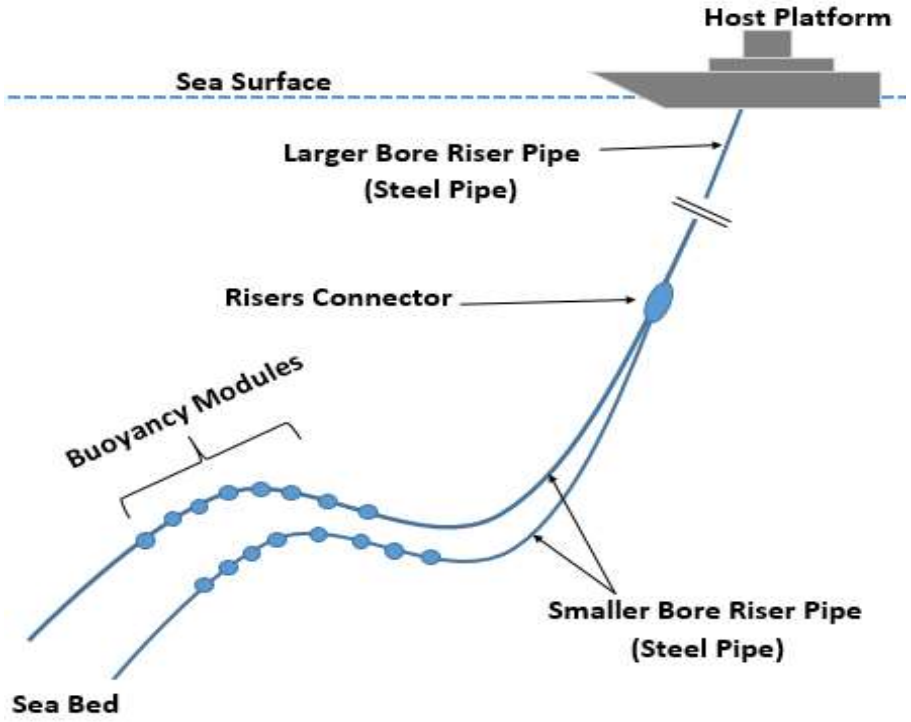

Figure 5-6-BSLWR configuration

5.1.3.3 Branched Lazy Wave Hybrid Riser (BLWHR)

The BLWHR has same configuration as the BSLWR but with its riser components sections made up of a different material. While the large bore riser section is metallic, the smaller bore riser sections is of composite material such as flexible pipes as shown in Figure 5-7. Composite pipe system can provide some benefits over steel pipe such as lightness in weight and good response to fatigue damage [103].

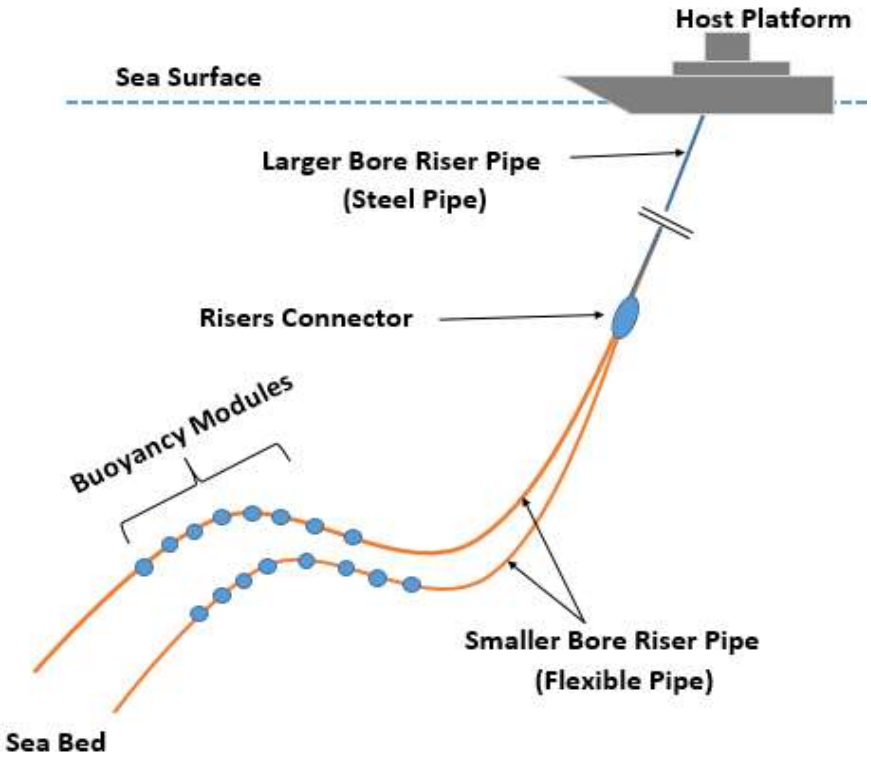

Figure 5-7 – BLWHR configuration

Studies conducted have shown that with proper design and fabrication, composite pipes can provide significant advantages over steel [104], These include but not limited to better response to external excitation because of their global compliant features, ability to attain smaller curvature radius and ease of installation. Unfortunately, larger bore flexible pipe are limited by water depth as the hydrostatic collapse strength requirement gets higher for deeper water and hence make them less attractive for deep-water application. However, smaller bore flexible pipes have been qualified for water depth up to 4,000m [23].

5.2 The branched riser system configuration development

The branched riser system (BRS) is a concept developed for deep-water application in this thesis. Possible variants of the BRS include the Branched Steel Catenary Riser (BSCR) System, the Branched Steel Lazy Wave Riser (BSLWR) System and the Branched Lazy Wave Hybrid Riser (BLWHR) Systems. However, only the BSCR is focused on in this thesis and is detailed in Chapter 5. The BRS consists of a large-bore pipe terminated at an optimum water depth at a connecting structure. The larger bore riser pipe is then extended from the connecting structure to the seabed by two smaller riser pipes. Typical configurations of the BSLWR and the BSCR are presented in Figure 5-8 (a) and (b).

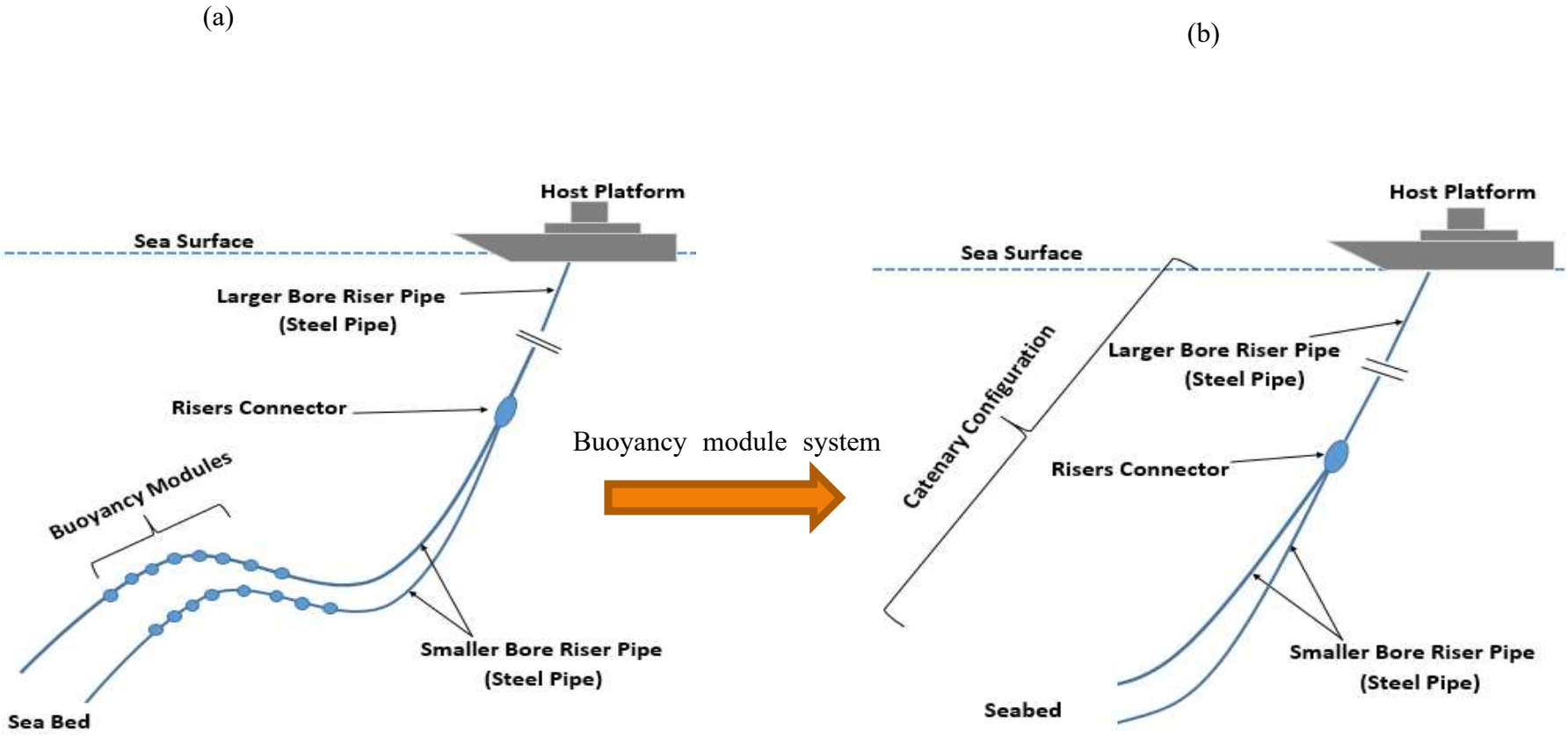

Figure 5-8 –Schematics of branched riser systems: (a) – Branched stell lazy wave riser (BSLWR), (b) Branched steel catenary riser (BSCR).

Since there are different possible configuration types of the BRS, it is better to develop a generic BRS configuration from which other configuration types can be derived. It can be seen from Figure 5-8 that the BSLWR is a BSCR with buoyancy modules installed. This implies that the BSCR is a degenerated BSLWR, with buoyancy modules removed. Therefore, once the configuration of the BSLWR is developed, the configuration of the BSCR can be obtained from it by eliminating the buoyancy components from the configuration expressions. The generic BSLWR configuration expressions can be developed using the expressions already presented and developed for simple catenary configuration in section 3.1.1.

The following considerations and assumptions are made during the BSLWR configuration calculation:

- All assumptions made for the simple catenary configuration development on the axial and bending stiffness apply.
- The vertical axis is taken as z; the horizontal axis is taken as x and the y-axis into the x-z plane.
- The length of the connector is small relative to the length of the sub catenaries and hence considered as a point.
- The hang-off angles with the horizontal of the branched and the stem (large bore pipe) equal, i.e., the transition from the stem to the branches are smooth on the x-z plane as can be seen in Figure 5-9 (a).
- All sub catenary configurations are calculated in their local coordinate systems and then assembled in the global coordinate system referencing the supposed TDP for conventional SLWR (see Figure 5-9 (b)).
- The branches are equal in length, cross-section, and weight. The joint weight of both branches is equal to the weight of the stem, i.e., $2w_S = w_L$. This assumption is made to introduce simplicity in the derivation process. However, a comparison of the weight of the large and the joint weight of the small pipe is comparable. Note that the flow area of the large pipe must equal the combined internal area of the small pipe for an equal volume of fluid transported. The wall thickness of the small and large pipes will depend on the minimum wall thickness required for burst and collapse resistance.

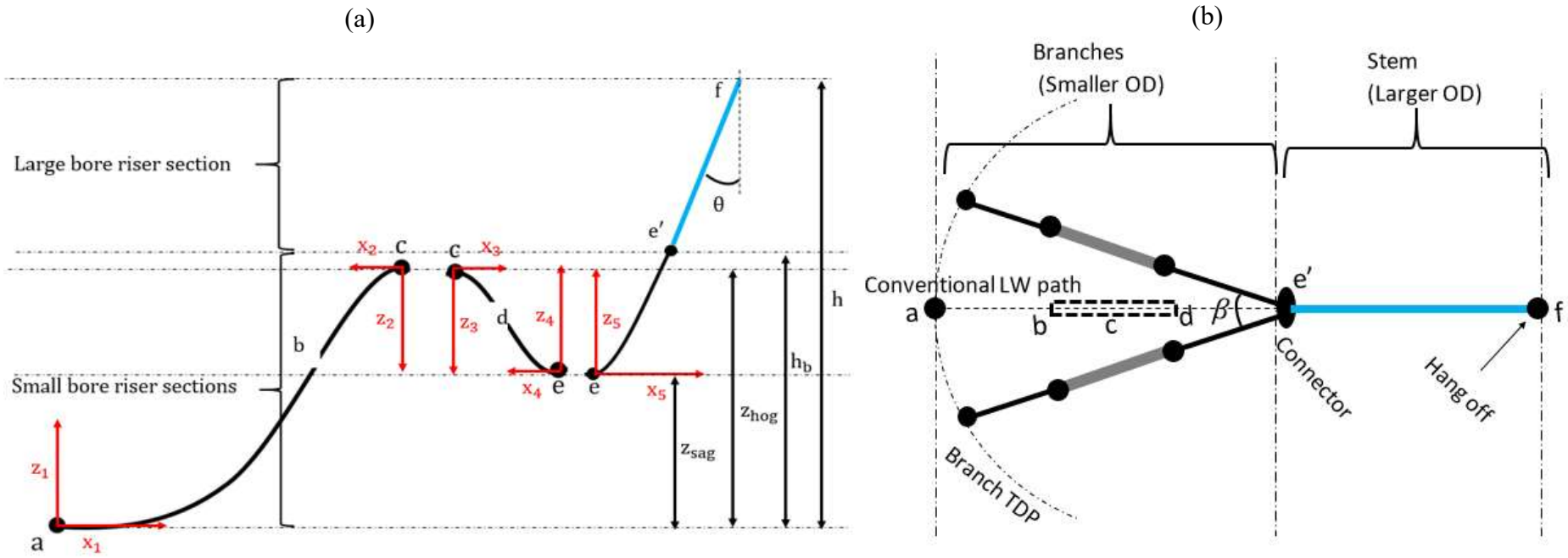

Figure 5-9 – Schematic of the branched steel lazy wave riser (BSLWR), showing basic sub catenary components: (a) - Front view, (b) - Plan view.

As shown in Figure 5-9, the BSLWR is characterised by the branched water depth, h_b and the branch angle, β, which is the angle between the branches or $\beta/2$ which is the angle between each branch and the vertical plane of the larger bore riser (stem). The branched depth is the vertical height of the connector from the seabed. Other configuration variables are like those of the SLWR already presented in 3.1.3, such as the sag elevation, z_{sag}, the hog elevation, z_{ho} and the arc height, $\Delta h = z_{hog} - z_{sa}$.

Each branch of the BSLWR can be considered as a conventional SLWR in the large riser bore plane (i.e., un-rotated) with a hang-off point at the connector. Once the small-bore lazy wave configuration is obtained, it can then be rotated in the z-y plane about the connector point by $\pm\beta/2$, where β is the angle between the branches viewed on the horizontal plane (top view). Figure 5-9 (a) is the front view of the branch consisting of catenaries ab, bc, cd, de and ee' are sub catenaries. $e'f$ is a truncated catenary of the large diameter pipe section.

First, we calculate the configuration of the truncated catenary section of the large bore riser $e'f$. This can be achieved by subtracting catenary ee' from catenary ef, with both calculated using the weight of the larger bore riser section, w_L. From Figure 5-9, the following expressions can be obtained.

$$\begin{cases} z_{ef} = h - z_{sag} \\ z_{ee} = h_b - z_{sag} \\ z_{e'f} = h - h_b \end{cases} \tag{5-1}$$

Applying equations (3-1) and (3-2) to sub catenaries ef, ee' and $e'f$, the following can be obtained:

$$\begin{cases} H_{ef} = \dfrac{w_L z_{ef}}{(tan\,\theta)^2}(1 + sec\,\theta) \\ x_{ef} = \dfrac{H_{ef}}{w_L} cosh^{-1}\left(\dfrac{w_L z_{ef}}{H_{ef}} + 1\right) \\ s_{ef} = \dfrac{H_{ef}}{w_L} sinh\left(\dfrac{w_L x_{ef}}{H_{ef}}\right) \end{cases} \tag{5-2}$$

$$\begin{cases} x_{ee\prime} = \dfrac{H_{ef}}{w_L} cosh^{-1}\left(\dfrac{w_L z_{ee\prime}}{H_{ef}} + 1\right) \\ x_{e\prime f} = \dfrac{H_{ef}}{w_L} cosh^{-1}\left(\dfrac{w_L z_{e'f}}{H_{ef}} + 1\right) \\ s_{ee'} = \dfrac{H_{ef}}{w_L} sinh\left(\dfrac{w_L x_{ee'}}{H_{ef}}\right) \\ s_{e\prime f} = s_{ef} - s_{ee\prime} \end{cases} \quad (5\text{-}3)$$

where:

$H_{ef} =$ Horizontal tension component along sub catenary ef

$x_{ef} =$ Horizontal distance from e to f

$x_{ee'} =$ Horizontal distance from e to e′

$x_{e'f} =$ Horizontal distance from e′ to f

$z_{ef} =$ Vertical distance from e′ to f

$z_{e'f} =$ Vertical distance from e′ to bottom f ($z_{e\prime} \leq z_{e'f} \leq z_f$)

$s_{ef} =$ Length of riser section from e to f

$s_{e'f} =$ Length of riser section from e′ to f

$w_L =$ Submerged unit weight of large pipe section (N/m)

$\theta =$ Hang-off angle measures from the horizontal

The declination angle with the horizontal at the connector (e') can be obtained using sub catenary ee', whose local height is $\left(h_b - z_{sag}\right)$. The tension ($T_{e\prime}$) is obtained using equation (3-3), the vertical tension component ($V_{e\prime}$) is obtained using equation (3-5), and the hang-off angle ($\theta_{e\prime}$) is obtained using equation (3-4).

$$T_{e\prime} = H_{ef} + w_L(h_b - z_{sag}) \quad (5\text{-}4)$$

$$V_{e\prime} = \sqrt{T_{e\prime}^2 - H_{ef}^2} \quad (5\text{-}5)$$

$$\theta_{e\prime} = tan^{-1}\left(\frac{V_{e\prime}}{H_{ef}}\right) \tag{5-6}$$

This value of $\theta_{e\prime}$ is assumed to be continuous at the connector interface and equal the hang-off angle of the branches with the horizontal. The horizontal tension components at each un-rotated branch's small-bore riser–connector interface can be calculated using equation (5-7).

$$H_{e\prime} = \frac{w_S(h_b - z_{sag})}{(tan\,\theta_{e\prime})^2}(1 + sec\,\theta_{e\prime}) \tag{5-7}$$

where w_S is the unit submerged weight of the small-bore pipe, and h_b is the height of the connector from the seabed. With the horizontal tension component ($H_{e\prime}$) and the hang off angle ($\theta_{e\prime}$) known, the sub catenaries composing each branch's configurations can be calculated following similar expressions patterns for SLWR in section 0. These include catenary-1 (ab), catenary-2 (bc), catenary-3 (cd), catenary-4 (de) and catenary-5 (ee'), where x_i, z_i and s_i are the repective horizontal distances, vertical distances and arc lengths of each sub catenary, with subscripts corresponding to the respective sub catenaries as presented in Figure 5-9. Equation (5-13) is the assembling expression of all the sub catenaries to obtain the total horizontal distance (X_T) and the total arc length (S_T).

$$\begin{cases} z_5 = h_b - z_{sag} \\ H_{e\prime} = \dfrac{w_S z_5}{(tan\,\theta_{e\prime})^2}(1 + sec\,\theta_{e\prime}) \\ x_5 = \dfrac{H_{e\prime}}{w_S} cosh^{-1}\left(\dfrac{w_S z_5}{H_{e\prime}} + 1\right) \\ s_5 = \dfrac{H_{e\prime}}{w_S} sinh\left(\dfrac{w_S x_5}{H_{e\prime}}\right) \end{cases} \tag{5-8}$$

$$\begin{cases} z_4 = \dfrac{w_b}{w_S + w_b}\left(z_{hog} - z_{sag}\right) \\ x_4 = \dfrac{H_{e\prime}}{w_S} cosh^{-1}\left(\dfrac{w_S z_4}{H_{e\prime}} + 1\right) \\ s_4 = \dfrac{H_{e\prime}}{w_S} sinh\left(\dfrac{w x_4}{H_{e\prime}}\right) \end{cases} \tag{5-9}$$

$$\begin{cases} z_3 = \dfrac{w_S}{w_S + w_b}\left(z_{hog} - z_{sag}\right) \\ x_3 = \dfrac{H_{e\prime}}{w_b} cosh^{-1}\left(\dfrac{w_b z_3}{H_{e\prime}} + 1\right) \\ s_3 = \dfrac{H_{e\prime}}{w_b} sinh\left(\dfrac{w_b x_3}{H_{e\prime}}\right) \end{cases} \tag{5-10}$$

$$\begin{cases} z_2 = \dfrac{w_S}{w_S + w_b} z_{hog} \\ x_2 = \dfrac{H_{e\prime}}{w_b} cosh^{-1}\left(\dfrac{w_b z_2}{H_{e\prime}} + 1\right) \\ s_2 = \dfrac{H_{e\prime}}{w_b} sinh\left(\dfrac{w_b x_2}{H_{e\prime}}\right) \end{cases} \tag{5-11}$$

$$\begin{cases} z_1 = \dfrac{w_b}{w_S + w_b} z_{hog} \\ x_1 = \dfrac{H_{e\prime}}{w_b} cosh^{-1}\left(\dfrac{wz_1}{H_{e\prime}} + 1\right) \\ s_1 = \dfrac{H}{w_S} sinh\left(\dfrac{wx_1}{H_{e\prime}}\right) \end{cases} \quad (5\text{-}12) \qquad \begin{cases} X_T = x_{e\prime f} + \sum_{i=1}^{5} x_i \\ h = z_{e\prime f} + \sum_{i=1}^{5} z_i \\ s_2 = s_{e\prime f} + \sum_{i=1}^{5} s_i \end{cases} \quad (5\text{-}13)$$

Where:

$$\sum_{i=1}^{5} x_i = x_1 + x_2 + x_3 + x_4 + x_5$$

$$\sum_{i=1}^{5} z_i = z_1 + z_2 - z_3 - z_4 + z_5$$

$$\sum_{i=1}^{5} s_i = s_1 + s_2 + s_3 + s_4 + s_5$$

On assembling the sub catenaries to form the global branch lazy wave configuration along the stem's $z - x$ plane, the branch is duplicated and both rotated (in the opposite direction) about the $z - x$ plane at the connector point (e') by $\pm\beta/2$.

Note that the above expressions have been developed considering the conventional SLWR configuration along the large bore pipe (stem) plane referenced at the TDP, a. However, the SLWR configuration along this path must be duplicated and rotated about the large bore pipe axis and at e', to obtain the branches in their correct planes specified by β as seen in Figure 5-9. Hence, the rotational angle of each branch from the centre axis will be $\pm\beta/2$. The resulting rotated coordinates of the two branches (XX^{+}_{rot} and XX^{+}_{rot}) can be obtained using equation (5-14). Note that the axis about which the rotation is conducted aligns with the y-axis in this case. Hence the y is 0.

$$\mathbf{XX^{+}_{rot}} = \mathbf{T_2 R^{+} T_1}\left(\sum_{\mathbf{i=1}}^{\mathbf{5}} \mathbf{x_i}, \mathbf{0}, \sum_{\mathbf{i=1}}^{\mathbf{5}} \mathbf{z_i}\right)^{\mathbf{T}} \quad (5\text{-}14)$$

$$\mathbf{XX_{rot}^{-}} = \mathbf{T_2 R^{-} T_1} \left(\sum_{\mathbf{i=1}}^{\mathbf{5}} \mathbf{x_i}, \mathbf{0}, \sum_{\mathbf{i=1}}^{\mathbf{5}} \mathbf{z_i} \right)^{\mathbf{T}}$$

The expression is equation (5-14) used to achieve the branches' rotations are explained thusTranslate the coordinates of the branch referencing the origin $a(0,0)$ to the centre of rotation (e'), by the translation matrix T_1

- Effect the rotation of the coordinates at e' using R_1^+ for first branch and R_1^- for the second branch.
- Translate the rotated coordinates of the branches back to a' using matrix T_2

The complete initial branched lazy wave configuration is solved by providing any of the design input options presented in Table 5-3 along with the submerged weights of the sections. The input design option-1 has been considered for the above derivation and used in this thesis.

Table 5-3 - Design input option for lazy wave configuration calculation

Options	$\mathbf{z_{hog}}$	$\mathbf{z_{sag}}$	Section lengths	$\boldsymbol{\theta}$	h	$\boldsymbol{\beta}$
1	✔	✔	-	✔	✔	✔
2	-	-	✔	✔	✔	✔

From the equations presented for the generic BRS (BSLWR), it could be seen that for a given combination of small and large riser diameter pipes, the important configuration variables that influence the configurations of the BRS are:

- The hang-off angle, θ
- The branched angle, β
- The branched height, h_b
- The sag or the elevations, z_{sag} or z_{ho} , which are equal to zero for BSCR
- The arc height, $\Delta h = z_{hog} - z_{sag}$, which is equal to zero for BSCR

Since only the branched steel catenary riser (BSCR) is investigated in this thesis, the first three variables will be the relevant configuration determinants for the BSCR in Chapter 0. An example of the BSLWR configuration calculated using the MATLAB program developed

based on the above-developed expressions is presented in Figure 6. A typical BSCR configuration modelled in OrcaFlex is shown in Figure 5-11.

$$z_{hog} = 300m, z_{sag} = 200m, \theta = 78^o, h = 1500m, \beta = 1^0,$$

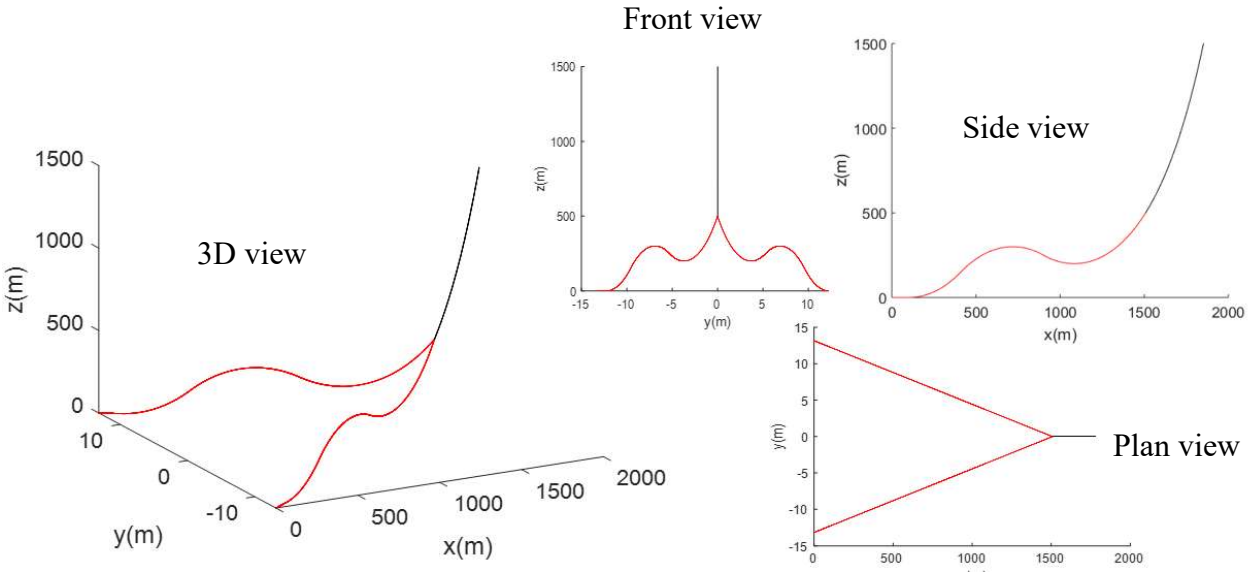

Figure 5-10 – Example of the BSLWR configuration obtain using MATLAB program.

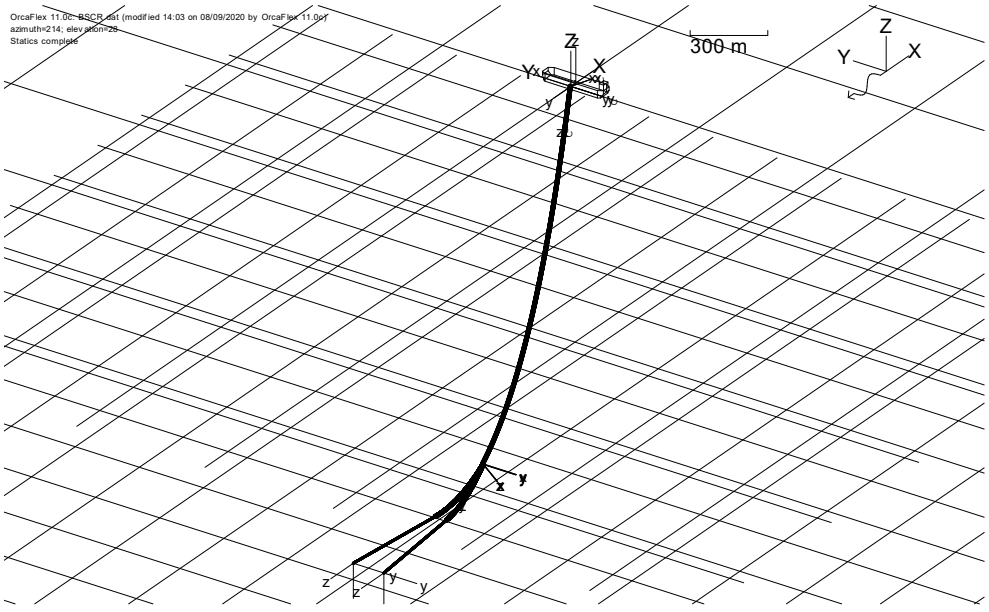

Figure 5-11 – OrcaFlex Model of the BSCR,$h = 1500m, \theta = 12^o,\ \beta = 5.2^o, h_b = 110m$

5.3 BSCR optimisation

The large-bore catenary riser section of the BSCR extends from the hang-off point to the branching height, where it connects through a connecting structure to two smaller bore catenary risers. The divergence of the branches as they approach the seabed from the branching height depends on the branching angle between the small-bore risers relative to large pipe riser plane. The benefits of the BSCR over a single large bore SCR and multiple small SCRs depend on an appropriate combination of the branching angle and the branching height. For a given water depth and a hang off-angle, a combination of the branching angle and the branching height can result in several configurations, necessitating the need for an optimisation technique to obtain an optimum BSCR.

5.4 BSCR interference study

5.4.1 Background

When adjacent risers are closely arranged from one another, they interfere through modification of the flow fields around them. The flow field changes can be slowly or largely dependent on time and can result in complex and highly nonlinear hydrodynamic interactions between a riser and its neighbouring risers through solid fluid coupling. In some situation, the risers' response to these interactions can result in large and relatively differential deflections or displacements that can bring them closer or in contact (clashes) with each other. Understanding this phenomenon is important in the design and arrangement of adjacent risers, which in most design requirement, are not allowed to clash.

The branches of the BRS are of equal geometry and expected weight, and are separated at the connector interface by a distance (clearance) greater than twice their outer diameter. Each branch diverges out from the stem plane, at the connector interface, to the seabed at an angle, β, referred to as the half branch angle as shown in Figure 5-12.

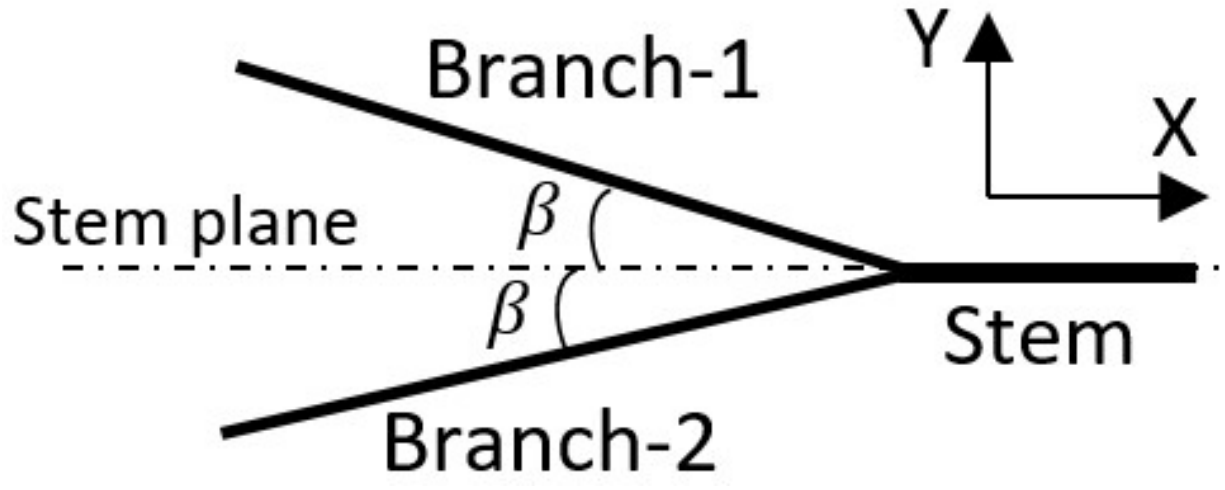

Figure 5-12 : Half branch angle for the BRS branches.

Under direct environmental loading, vessel motions and VIV conditions, there are possibilities of the two BRS branches clashing with each other. In this study, the BSCR is subjected to various static and dynamic conditions to investigate the global and vibrational displacement response of the branches and to ascertain if this novel riser system type is feasible considering interference criteria. The guiding criteria for this study are based on the 'no clash criteria' prescribed in [105] and presented in equation (5-15), which requires that the minimum clearance between the two risers must be equal or greater than the sum of their outer diameters

$$min.clearance \geq OD_{branch-1} + OD_{branch-2} \tag{5-15}$$

5.4.1.1 Drag force

The drag force given by Morison, presented in equation (5-16), is the force resulting from the shear boundary layer between the flow and the riser pipes. It depends on the flow velocity u_c, the riser pipe velocity u, the fluid density ρ, the riser pipe unit projected area normal to flow direction D, and the drag coefficient C_d.

$$F_D = \frac{1}{2}\rho C_d D(u - u_c)|u - u_c| \tag{5-16}$$

Current flow across the riser pipe is generally considered to be time-invariant, and its effect on the structure is represented by its mean value [106]. The global displacement or deflection of the riser relates linearly with pipe's hydrodynamic diameter and the drag coefficient, but quadratically with the relative velocity between the riser and the current flow. The drag

coefficient (C_d) depend on the riser pipe surface roughness and the Reynolds number ($Re = \rho UD/\mu$) where μ is the dynamic fluid viscosity. For a smooth pipe, the relationship between the C_d and Re can be modelled analytically as follows [107] with some appreciable level of accuracy:

$$log(C_d) = 1.0444\, log\left(\frac{Re^{0.246}}{10} log\frac{Re^{0.318}}{10}\right), 0.1 \leq Re \leq 10^5 \tag{5-17}$$

$$C_d = 1.2, 10^5 \leq Re \leq 4 \times 10^5 \tag{5-18}$$

$$C_d = 0.6 + \left(\frac{0.873}{log(Re) - 4.7}\right)^{12} - \left(\frac{0.873}{log(Re) - 4.7}\right)^{2.923}, \quad 4 \times 10^5 \leq Re \leq 8 \times 10^5 \tag{5-19}$$

5.4.1.2 Vortex induced vibration (VIV)

When a riser is placed in a current cross flow, flow separation occurs around it, creating fluctuating velocity and differential pressure field around the riser pipe. Fluctuating pressure field around the riser induces transverse oscillatory force (lift) on the pipe known as vortex-induced vibration (VIV) as shown in Figure 5-13. VIV can effectively increase the in-line drag force on the riser pipe since the projected pipe area to the current flow direction is effectively increased.

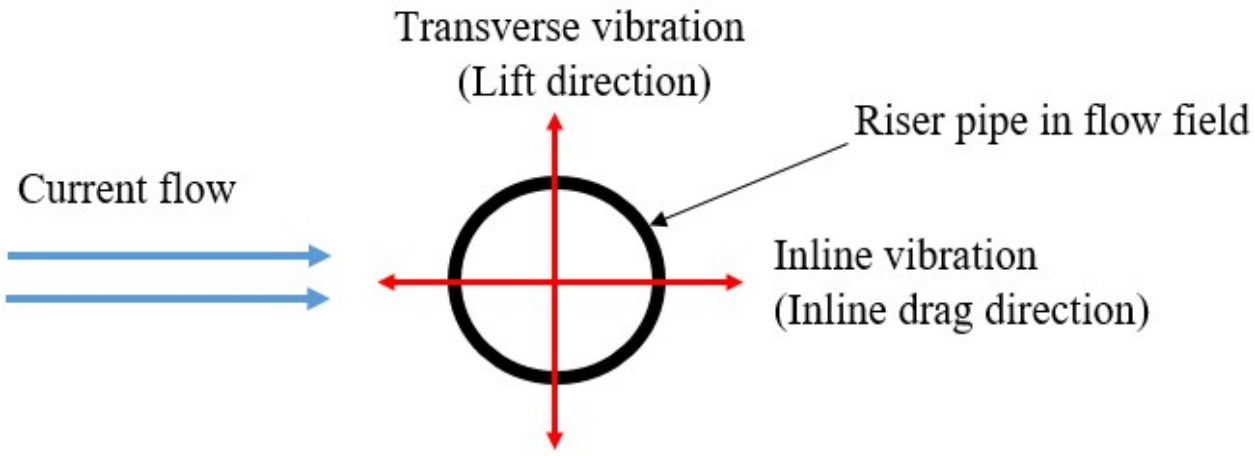

Figure 5-13 – Pipe transverse vibration in a current cross flow

When the shedding or Strouhal frequency approaches the structures natural frequency ('lockin'), resonance occurs and the oscillations (strumming oscillations) can result in

maximum transverse displacement (amplitude) of the riser pipe. In 'lockin' condition, Vandiver presented an empirical relation, presented in equation (5-20), to relate the amplified drag coefficient C_d', the nominal drag coefficient C_d and the VIV amplitude to diameter ratio (A/D)

$$C'_d = C_d\left(1 + 1.043\left(\frac{A}{D}\sqrt{2}\right)^{0.65}\right) \tag{5-20}$$

Riser VIV can be computed empirically or by computational fluid dynamics (CFD). The empirical methods include the frequency and time domain models developed based on acquired experimental data. The numerical VIV model used in this study is the time domain wake oscillator model developed by Iwan and Blevins [108].

5.4.1.3 Iowan and Blevins wake oscillator

Wake oscillators (WO) are developed heuristically to ascribe qualitative characteristics to them similar to those of VIV behaviour such as oscillatory, self-starting and self-limiting features. WO are parameterized by calibration to match empirical results. The Iwan and Blevins (I&B) wake oscillator is a time-domain based oscillator developed from momentum equation, considering a hidden wake single degree of freedom term (in the cylinder transverse direction) representing the fluid wake characteristic. The I&B WO takes the form of the van der Pol equation, a second-order differential equation known to have VIV characteristics such as 'lockin'. Model parameters for I&B WO model were obtained (by authors) through the calibration of a spring-mounted cylinder model with experimental fixed and forced cylinder in a steady-state condition. The coupled fluid oscillator and the elastically mounted cylinder response to the fluid are respectively presented in equation (5-21) and (5-22) as follows[108]:

$$\ddot{z} + K'\frac{u_t}{D}\omega_s z = (a'_1 - a'_4)\frac{U}{D}\dot{z} - a'_2\frac{\dot{z}^3}{UD} + a'_3\ddot{y} + a'_4\frac{U}{D}\dot{y} \tag{5-21}$$

$$\ddot{y} + 2\xi_T\omega_n\dot{y} + \omega_n^2 y = a''_3\ddot{z} + a''_4\dot{z}\frac{U}{D} \tag{5-22}$$

Where:

$$K' = K/(a_0 + a_3)$$

$$a_i' = a_i/(a_0 + a_3\ );\ i = 1,2,3,4$$

$$a_i'' = \ \rho D^2 a_i/(m + a_3 \rho D^2);\quad i = 3,4$$

$$\omega_n = \sqrt{(k/m)}/(1 + a_3 \rho D^2/m);\quad \omega_s = K'(u_t/U)(U/D\ ) \approx 2\pi S(U/D)$$

$$\xi_T = (\xi_s \sqrt{(k/m)}/\omega_n + \xi_f)/(1 + a_3 \rho D^2/m)$$

$$\xi_s = c/(2\sqrt{km}),\quad \xi_f = a_4 \rho DU/(2m\omega_n)$$

where m is the unit mass of cylinder, D is the cylinder hydrodynamic diameter, k is the unit support stiffness, c is the unit damping, ξ_T is the total effective damping coefficient consisting of structural viscous damping (ξ_s) and viscous fluid damping (ξ_s), ω_s is the natural frequency of the fluid oscillator (i.e. Strouhal frequency), ω_n is the natural frequency of the cylinder structure, ρ is the fluid density, U is the free stream flow velocity normal to the cylinder axis, S is the Strouhal number (usually 0.2), y is the cylinder displacement normal to the cylinder axis and flow direction, z is the "hidden" fluid variable which is the transverse component of the flow, and u_t is the translational velocity of the vortex street. The model parameters a_o =0.48, a_1 = 0.44, a_2 = 0.2, a_3 = 0, and a_4 = 0.38 are default values obtained by authors from experimental calibration [108]. Note that experimental value for S and u_t/U gives the parameter K′. 'Locking' condition is said to have occurred when ω_n is close to ω_s. The I&B WO is implemented in OrcaFlex FE software package and can be modelled by associating to each line node the wake oscillator [101]. The nodal oscillators coupled with each other through the structure (not the wakefield) and their responses are modelled by the numerical solutions to the nonlinear coupled differential equations (5-21) and (5-22). The fluid velocity, which is a required input at each line node, is filtered to eliminate VIV motions, preventing them from feeding back as input into wake oscillator, but allowing only the non-VIV motions at the node as input for the VIV calculation. The model needs to be run for a sufficiently long period of time to achieve a steady-state VIV response. Solutions of the I&B WO at each node include the VIV force on the cylinder, the transverse VIV offset and the VIV transverse A/D ratio, with which the amplified inline drag is computed.

5.4.1.4 Drag to apparent weight ratio (DAW)

The ratio of the drag force to the submerged weight is here referred to as the drag-to-apparent-weight (DAW) ratio. The DAW ratio describes the static/dynamic response of the riser pipe due to drag force acting on it. It is noted that the DAW ratio can be influenced greatly by marine growth and that riser with equal or close DAW ratio deflects comparatively [105]. It is, therefore, a good practice to group together adjacent risers with similar DAW ratio to maintain clearance between them, under loaded condition, similar to that in the unloaded condition. This is one of the recommended mitigation for riser clashes [105].

5.4.2 Model Data

5.4.2.1 Riser model description

In this study, the BSCR is composed of X65 steel grade 16-inch stem and 10-inch branches, hosted by a floating production, storage and offloading unit (FPSO) in a water depth of 1500m. The riser wall thicknesses were sized based on API 2RD ST burst and collapse criteria [3] for a fluid density of 600kg/m^3, with an internal design pressure of 10ksi. The BSCR was branched at 750m water depth with half branch angles of 0.1deg, 0.5deg and 1deg. The BSCR hang off angle at the vessel interface is 15deg. The clearance between the branches at the connector interface is ≈1.3m, and the connector length along the stem configuration path is 2m. Depends on the scenario, riser pipes are either filled or empty. Connection stiffness between the risers and vessel, and between the risers and connector interface is 12 kN.m/deg.

5.4.2.2 Environmental Data

Three different current profiles (profile-1, 2 and 3) shown in Figure 5-14 (A), is imposed on the BSCR from 0deg (BSCR near direction) in increments of 45deg as shown in Figure 5-14 (C). While profile-1, a slab current profile, is constant through the water column, profile-2 and profile-3 are sheared current profile respectively typical of west of Africa (WoA) and Gulf of Mexico (GoM). For the dynamic analysis, regular wave loads of maximum wave height of 10m, with the corresponding period of 12sec, is imposed in directions depicted in Figure 5-14 (B). The wave velocity profile, modelled using the Dean Stream theory [96], is presented in Figure 5-14B. It could be seen that the wave velocity profile decreases exponentially from the free surface to the seabed and equals zero at 750m water depth, which is the connector location (branching depth). Note that for the cases where the current and wave loads are imposed, both of them act collinearly in the directions indicated in Figure 5-14 (C).

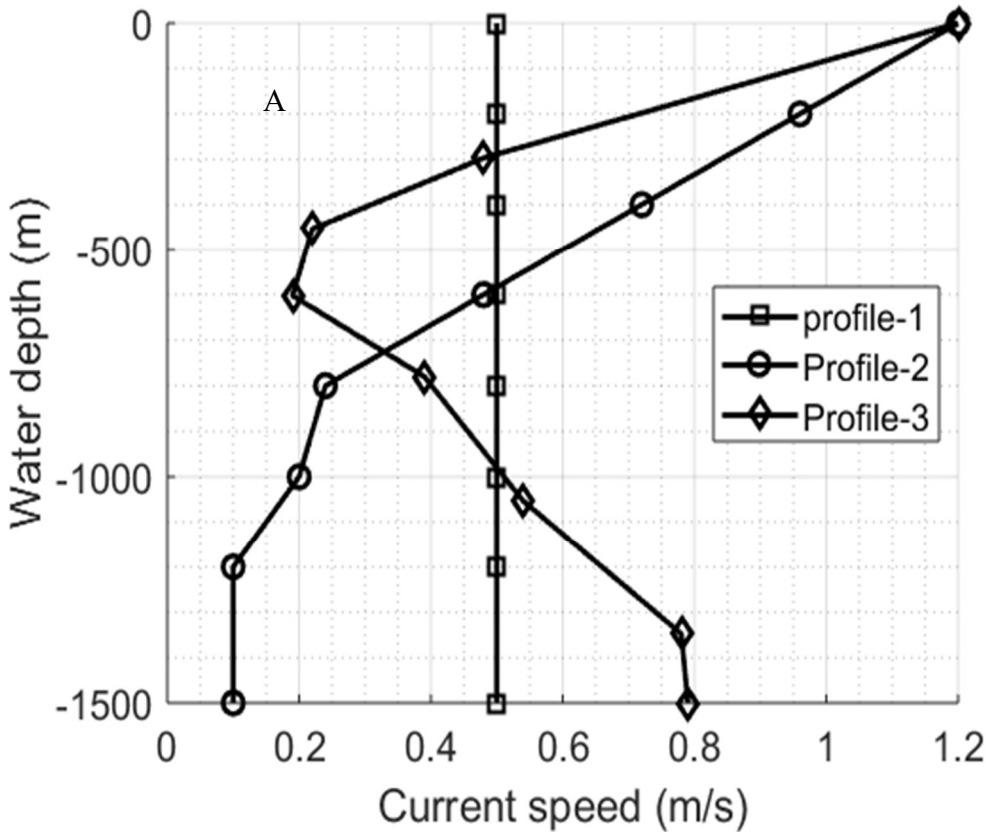
A
0
-500
-1000
-1500
Water depth (m)
0
0.2
0.4
0.6
0.8
1
1.2
Current speed (m/s)
profile-1
Profile-2
Profile-3

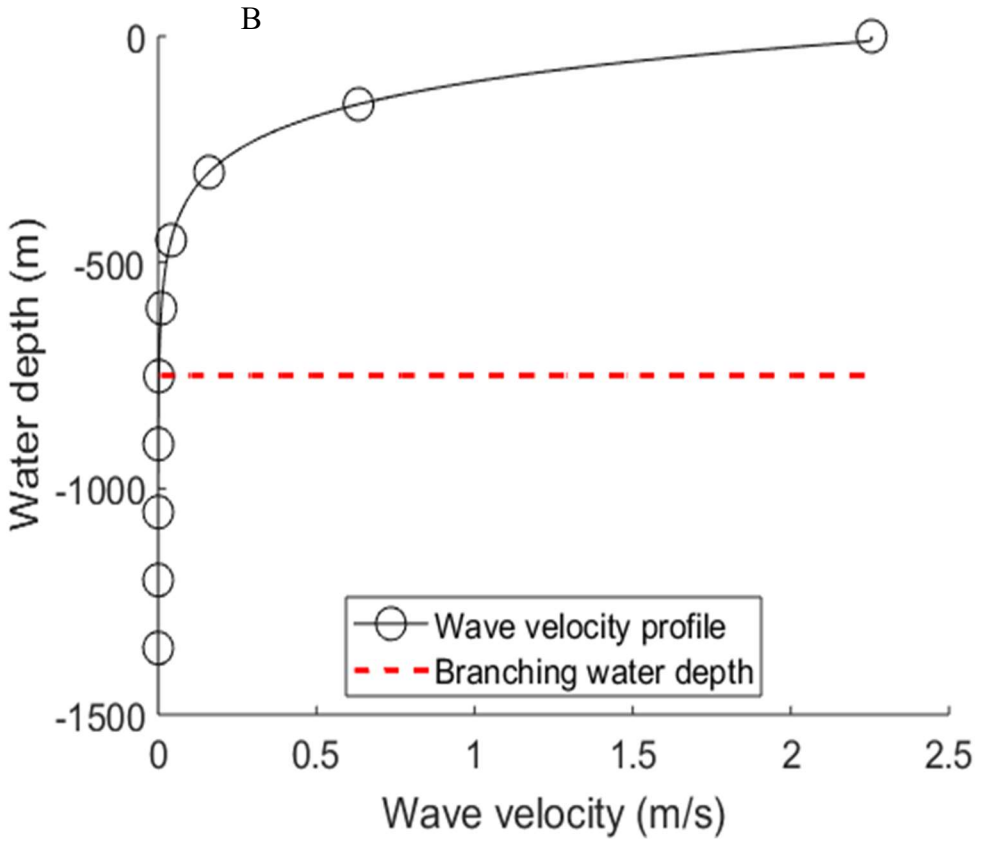
B
0
-500
-1000
-1500
Water depth (m)
0
0.5
1
1.5
2
2.5
Wave velocity (m/s)
Wave velocity profile
Branching water depth

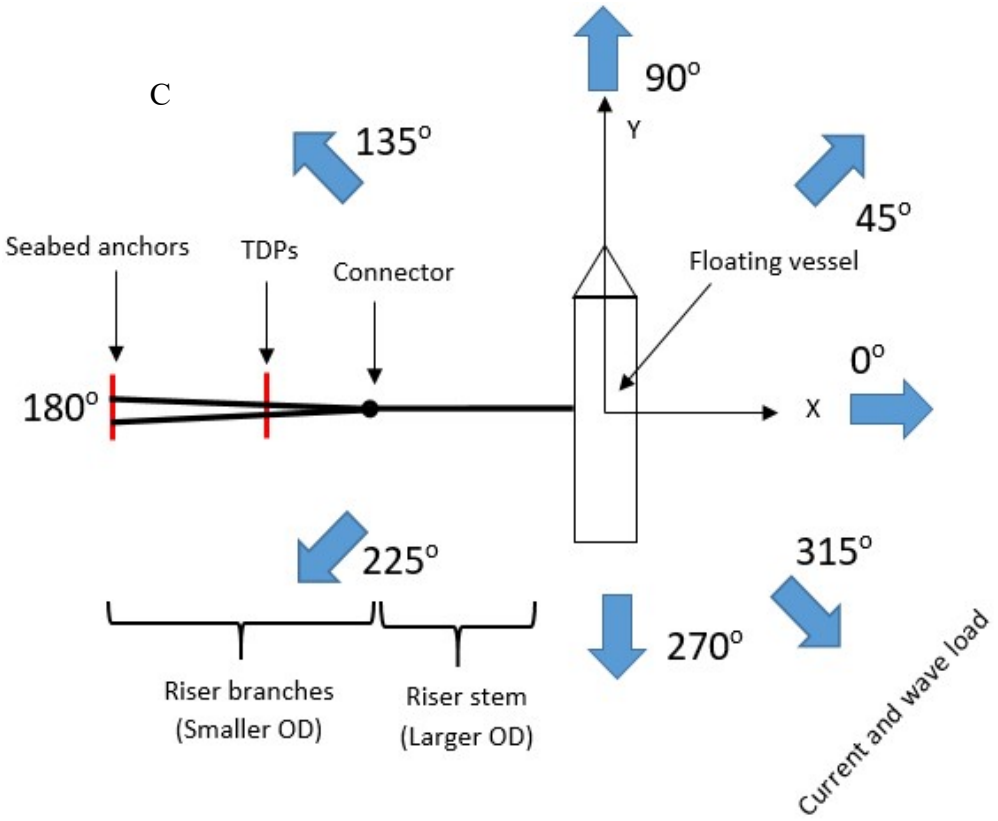

Figure 5-14: (A) – Current velocity profiles (B) – Wave velocity profile, (C) – Current and wave directions

5.4.2.3 Vessel offsets and motion data

The combined second-order drift response (offset) of the vessel was taken to be 10% of the water depth (150m). The vessel offset is imposed on the BSRC in the far, near and transverse directions. Figure 5-15 (A) and (B) presents the vessel RAO (at 50% draft). The RAOs are symmetric about the vessel's longitudinal and transverse axes.

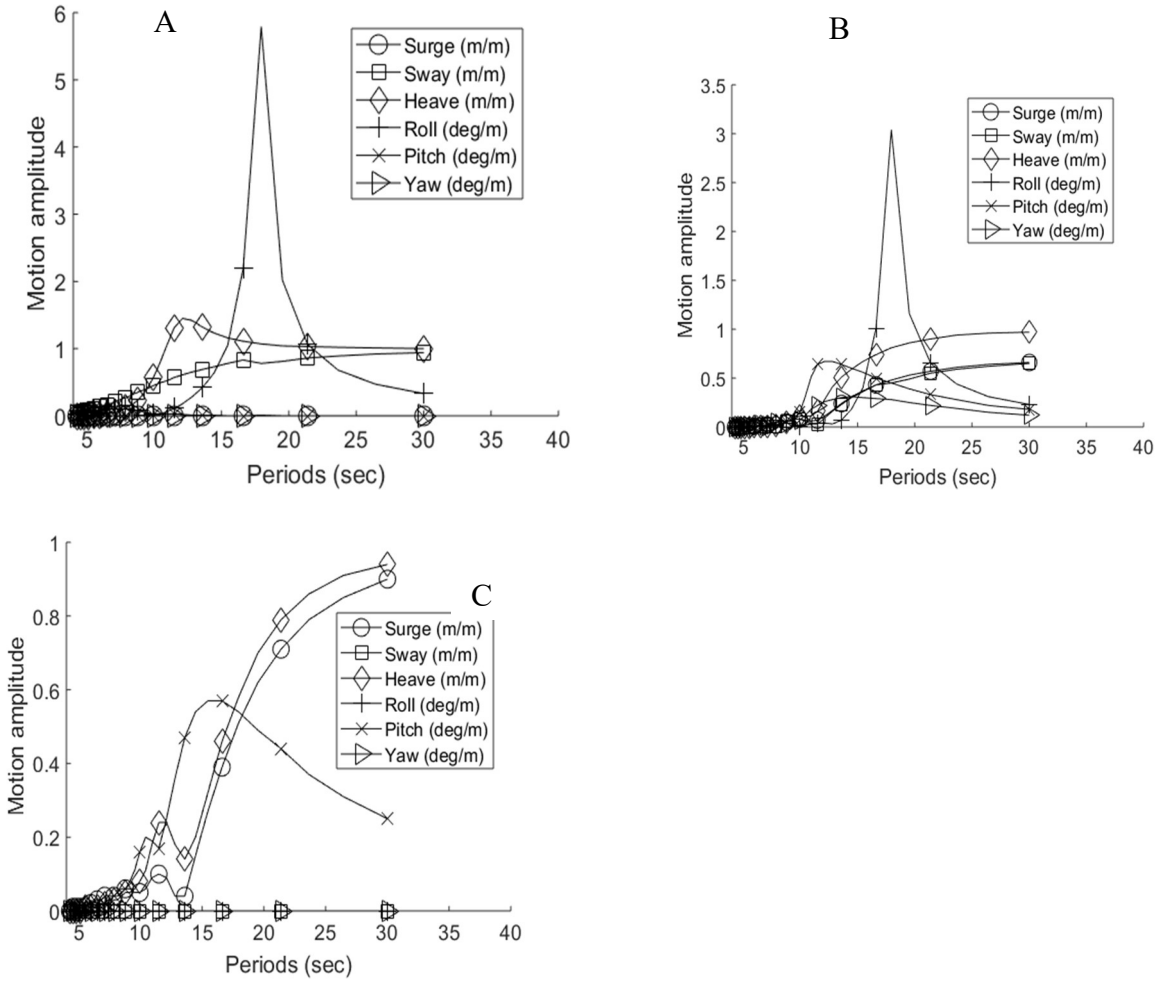

Figure 5-15 – Vessel RAOs: (A) – 0, 180deg wave direction, (B) – 45,135, 225, 315deg wave direction, (C) – 90, 270deg wave direction

5.4.3 Analysis methodology

5.4.3.1 Finite element modelling

OrcaFlex, a suitable FE software package for performing global response calculation of slender structures is used. The MATLAB program developed to calculate the initial BSCR configuration is parameterized by the water depth (h = 1500m), the hang off angle at the vessel interface ($\theta = 15\text{deg}$) , the half branch angle at the connector interface ($\beta = 0.1, 0.5\text{deg}, 1\text{deg}$), the branching water depth (750m) and the connector (2m length). The calculated configuration is modelled in OrcaFlex as the initial BSCR configuration. Environmental conditions (wave and current profiles), the Re-Cd relationship (equations (5-17), (5-18) and (5-19)) and the inline drag amplification model (equation (5-20)) are modelled as well. Loading conditions are developed based on the riser weight, current, vessel offset and wave loads. The load scenarios investigated include current load on BSCR in

nominal position, vessel offsets condition, critical current loads superimposed on the critical vessel offsets, weight variation of BSCR branches, wave loads and drag amplification due to VIV. Modelling, generation of load cases, and results post-processing are enhanced using MATLAB scripts implemented on the OrcaFlex high-level programming interface [102].

5.4.4 Results and discussions

5.4.4.1 Scenario 1 – Unloaded condition

Three configurations of the BSCR characterized by different half branch angle ($\beta = 0.1$deg, 0.5deg and 1deg) were investigated in this study. Figure 5-16 (A1-A3) presents the BSCR nominal configuration (empty, no current loading, no vessel offsets) and Figure 5-16 (A4) presents the clearance between the branches in this configuration. For the nominal configuration, it can be seen that the clearance for all BSCR configurations is minimum at the connector interface where it is $\approx$1.3m, and the rate of clearance divergence, down to the seabed, is dependent on the branching angle. This makes BSCR ($\beta = 0.1\text{deg}$) the most critical configuration among the three, in terms of clash probability. The seabed anchor distance between the branches is dependent on the branching water depth, the branching angle and the length of the branch section on the seabed. Minimizing the anchor distance requires a smaller branch angle. However, the lower bound limit of the branch angle is dictated by the branches' clearance under loaded conditions. The nominal configurations and clearance (Figure 5-16) are comparative bases for other scenarios.

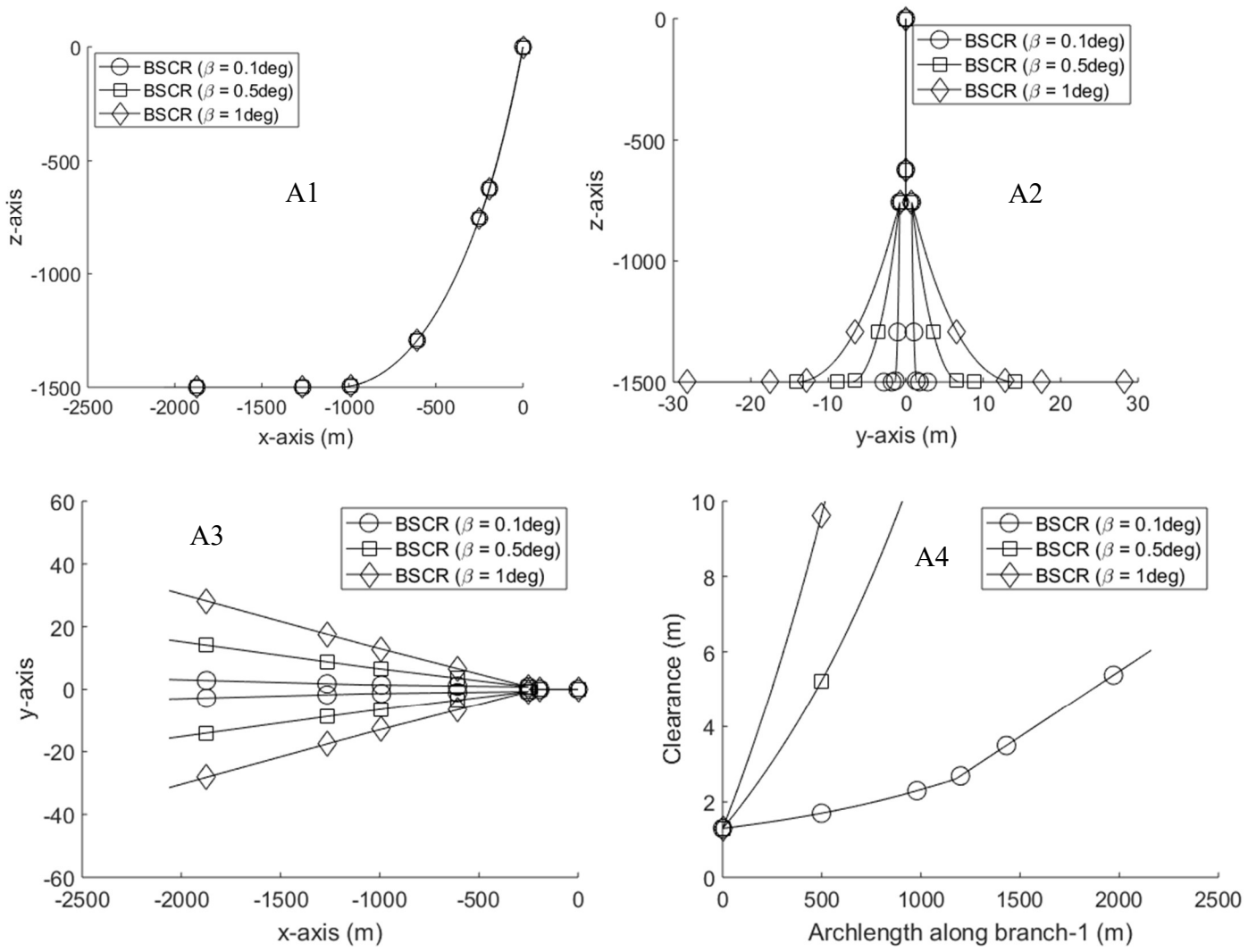

Figure 5-16: (A1)- BSCR configuration in the x-z plane, (A2)- BSCR configuration in the y-z plane, (A3) - BSCR configuration in the x-y plane, (A4) – Clearance between branches 1 and 2 measured along branch 1 from connector interface to the seabed anchor

5.4.4.2 Scenario 2 - Current load on BSCR in the nominal position

First, we reduce the amount of simulation by screening the three current profiles using the BSCR ($\beta = 1\text{deg}$) in its nominal position (no vessel offsets). Each of the three current profiles is imposed on the BSCR in five directions - 0deg, 45deg, 90deg, 135deg and 180deg, as shown in Figure 5-17.

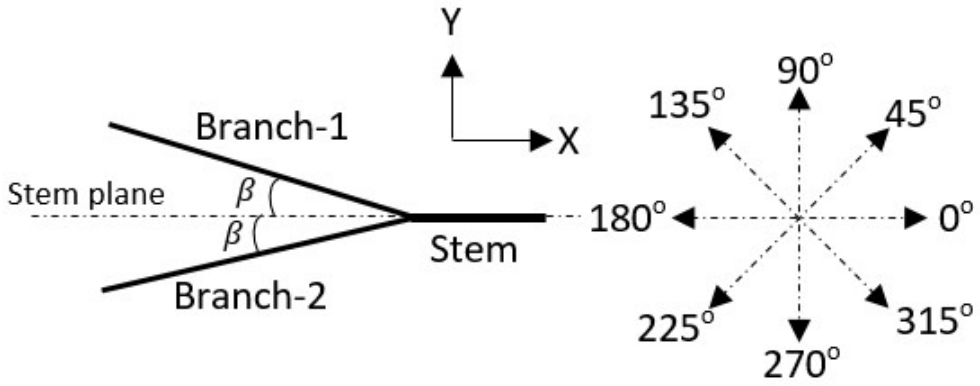

Figure 5-17: Current directions on BSCR

Note that the response of branch-1 in 45deg, 90deg and 135deg directions are respectively mirror response of branch-2 in 315deg, 270deg and 225deg directions and hence the results for the later set of angles are not presented. The deflections under the three current profile-1, 2 and 3, are presented in Figure 5-18 (A1), (A2) and (A3) and clearance response in Figure 5-18 (B1), (B2) and (B3) respectively.

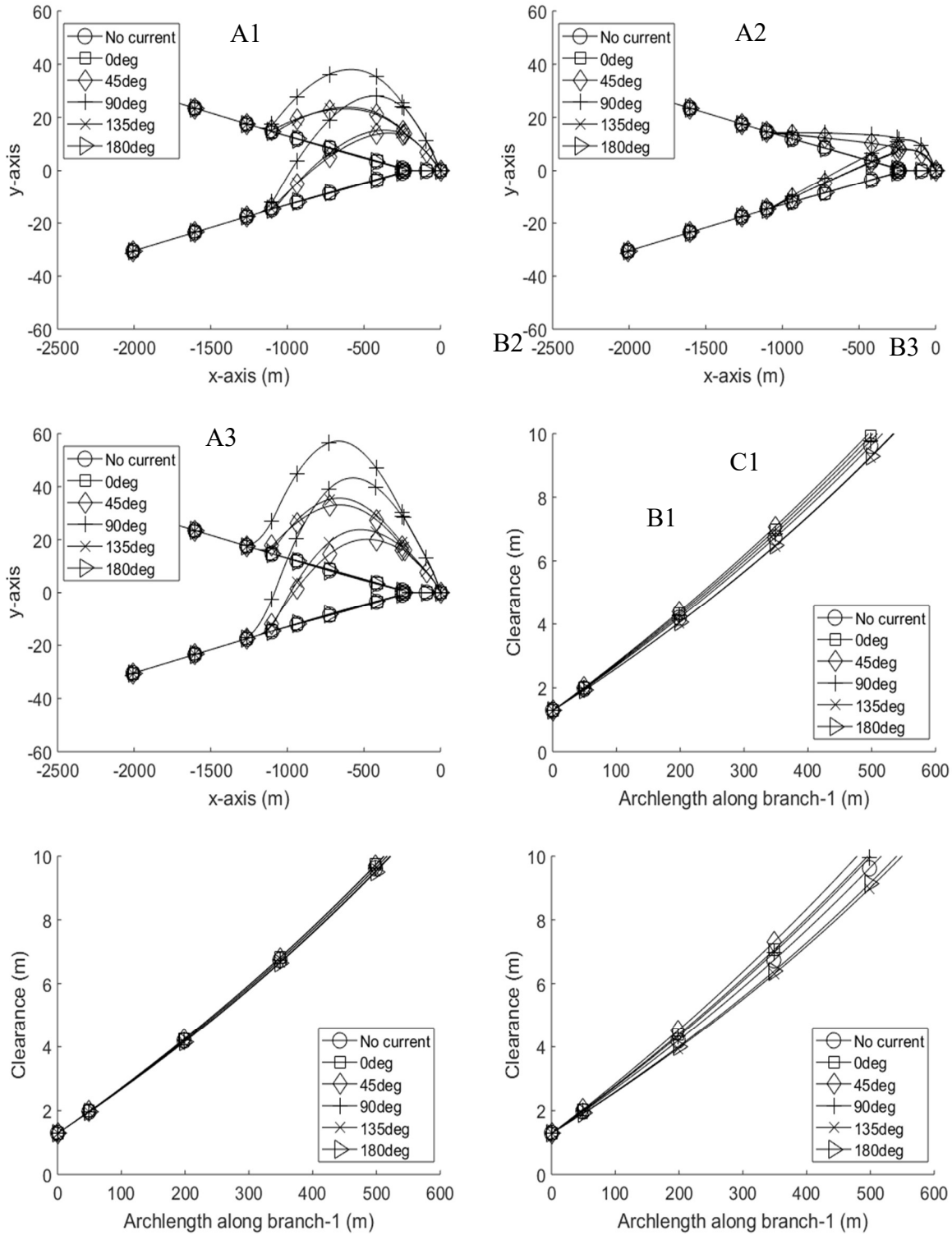

Figure 5-18 - BSCR ($\beta = 1deg$) deflection under current profile – 1 (A1), current profile-2 (A2), current profile -3 (A3). (B1), (B2), (B3) - Corresponding clearance response for A1, A2, A3 respectively.

It is observed that current profile-3 resulted in the largest deflection of the branches, as shown in Figure 5-18 (A3). This is because the current loads imposed on the branches below the connector interface to the seabed is largest for current profile-3 presented as presented in Figure 5-14 (A). It can also be observed from Figure 5-18 (A1, A2 and A3) that the most critical current direction for all current profile, in terms of the deflection of the branches, is that which is perpendicular to the BSCR stem plane (90deg) (see Figure 5-17). However, the current profile resulting in the critical clearance response along the branches is not in 90deg but in 135deg direction. This is attributed to the relatively larger drift load on branch-2 (upstream riser) than branch-1 (downstream riser) when the 135deg current load are resolved perpendicular to the branches' azimuth, i.e. higher DAW ratio for branch-2. The clearances are not very distinguishable with the lower current profile (profile-2) acting in a different direction on the branches (Figure 5-18 (B2)) but appear to gain observable difference for higher current profile (1 and 3) as shown in Figure 5-18 (B1 and B3).

The critical current profile (profile-3) being identified, is then imposed on the most critical BSCR configuration ($\beta = 0.1\text{deg}$) for the empty (0kg/m^3) and filled (600kg/m^3) case. It is observed that though higher deflections occur for the empty case than the filled case, comparing Figure 5-19 (A1) and (B1), the clearance response for the two cases (empty and filled) for each current direction are comparable (see Figure 5-19 (A2) and (B2)). This is because, for the same current profile acting in the same direction on empty and filled cases, the DAW ratios of the branches in each case relate in the same proportion. Hence the clearance for the two cases will be similar.

The above argument is valid when comparing bare riser pipe case with the case where there are marine growth deposits on the BSCR branches. Note that the BSCR branches take off at water depth of 750m and at this depth, marine growth is negligible on the branches and can only be significant on the BSCR stem. However, if marine growth deposited on the branches are significant, the growth may be similar on the branches, and both may likely have same geometry, weight and surface roughness as both are located in the same water column. Although the branches will incur higher deflection since their projected area normal to the current direction and the riser surface roughness have increased due to the marine growth, the clearance will be less affected compared to those of bare riser pipe. This is because, the branches in the marine growth case will have DAW relationship similar to that in the bare pipe case, considering any current profile direction. Note that for this scenario, using the most

critical BSCR configuration ($\beta = 0.1\text{deg}$) and the most critical current profile (profile-3), the minimum clearance occurs at the connector interface, which is above twice OD of each of the branches.

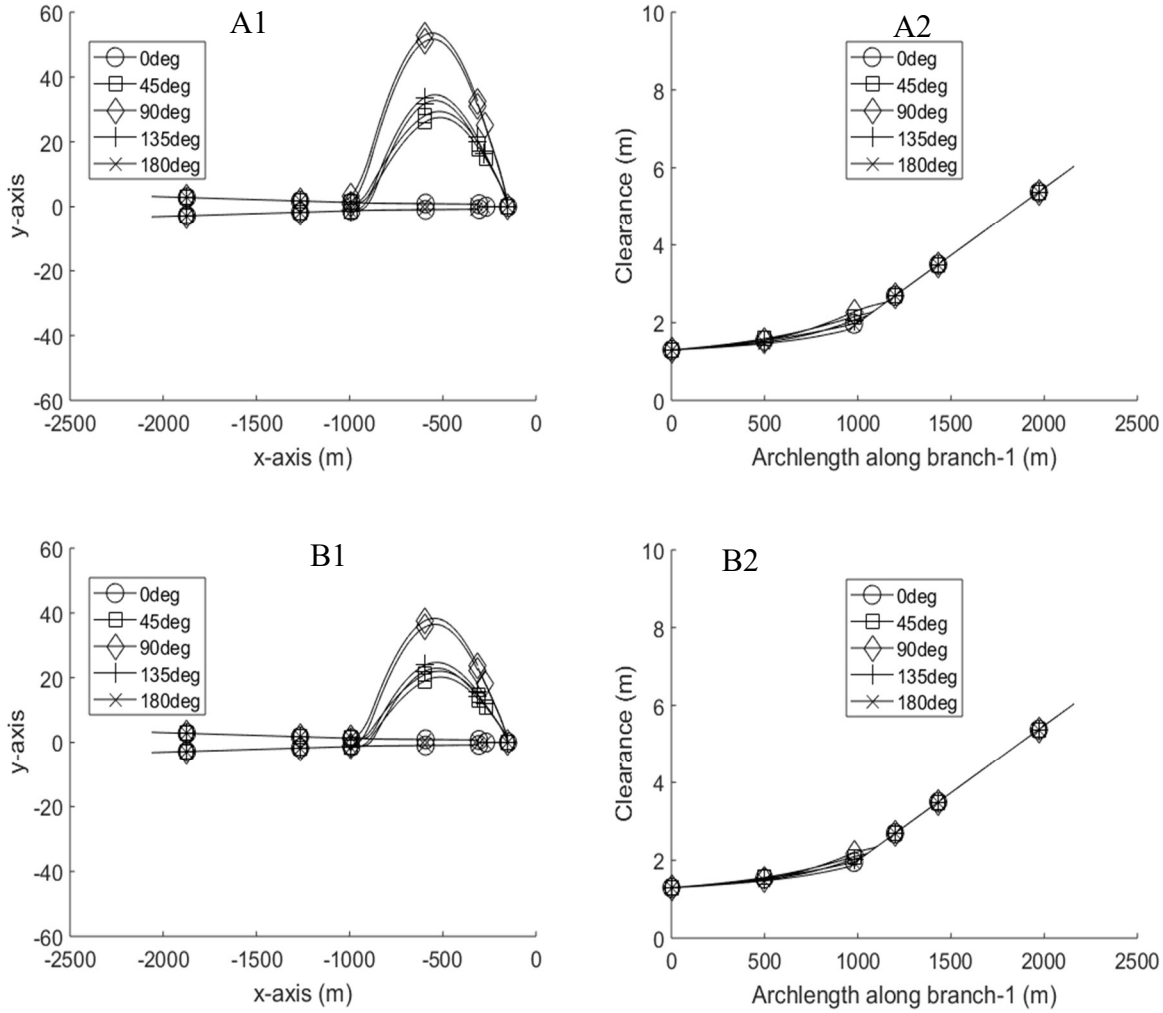

Figure 5-19: (A1, B1) – BSCR ($\beta = 0.1\text{deg}$) deflection under current profile –3 for empty and filled case respectively, (A2, B2) –Corresponding clearance response between branches 1 and 2.

5.4.4.3 Scenario 3 - Vessel offsets

Host platform offsets imposed large displacement on hosted risers. Vessel offsets are caused by wind, current and second-order wave loads imposed on the vessel, besides response to mooring systems motions. In this scenario, vessel offsets of 10% of the water depth (150m) are imposed on the three BSCR configurations ($\beta = 0.1\text{deg}, 0.5\text{deg}, 1\text{deg}$) in the far (0deg), near (180deg), and the transverse directions (90deg and 270deg). No current profile is imposed in this scenario, and the BSCRs are empty. The respective BSCR configurations' displacement is presented in Figure 5-20 (A1, A2, and A3) and the corresponding branches' clearances in

Figure 5-20 (B1, B2, and B3). The clearance response to the vessel offsets in surge directions, although resulted in the largest riser displacements, is comparable with that of the nominal configuration, while the far offset resulted in the least critical clearance response for all BSCR configurations. It is also observed that the most critical clearance between branches along their arch lengths occurs for the vessel near offset (180deg). This can be explained from the fact that as the vessel moves towards the BSCR TDP, shorter riser sections are hanging, the branches become slacker and the tension in them reduced. As a result, a new equilibrium configuration is sorted for by the pulling of the branches towards the centre of symmetry (BSCR stem plane), hence making them closer to each other. For the far offset, the tension in the risers are higher, and the branches are stiffer and more resistant to the pull towards the stem plane. For all BSCR configurations, the clearance response is less affected by the absolute displacement of the branches, but their relative displacement and the smallest clearance occur at the connector interface (≈1.3m), which is greater than the minimum requirement (2 × branches OD)

5.4.4.4 Scenario 4 – Critical current load superimposed on critical vessel offset

From the current load and vessel offset scenarios, it was observed that current profile-3 and the near vessel offset (180deg) resulted in the most critical clearance response along the branches. In this scenario (4), these two worse conditions are superimposed, with the current acting on the BSCR($\beta = 0.1\text{deg}, 0.5\,\text{deg}\,\text{and}\,1\text{deg}$) in the chosen five current directions. Figure 5-21 (A1, A2 and A3) respectively presents the configuration layout and Figure 5-21 (B1, B2 and B3) present the respective branches' clearance for these BSCRs. The most critical clearance response, as expected, occurs for the BSCR ($\beta = 0.1\text{deg}$) and worse current direction (135deg). For the three BSCR configurations ($\beta = 0.1\text{deg}, 0.5\text{deg}, 1\text{deg}$), the minimum clearance along the branches met the clearance requirement of at least $2 \times \text{OD}_{\text{branch}} \approx 0.5\text{m}$ under the worse vessel offset and critical current conditions.

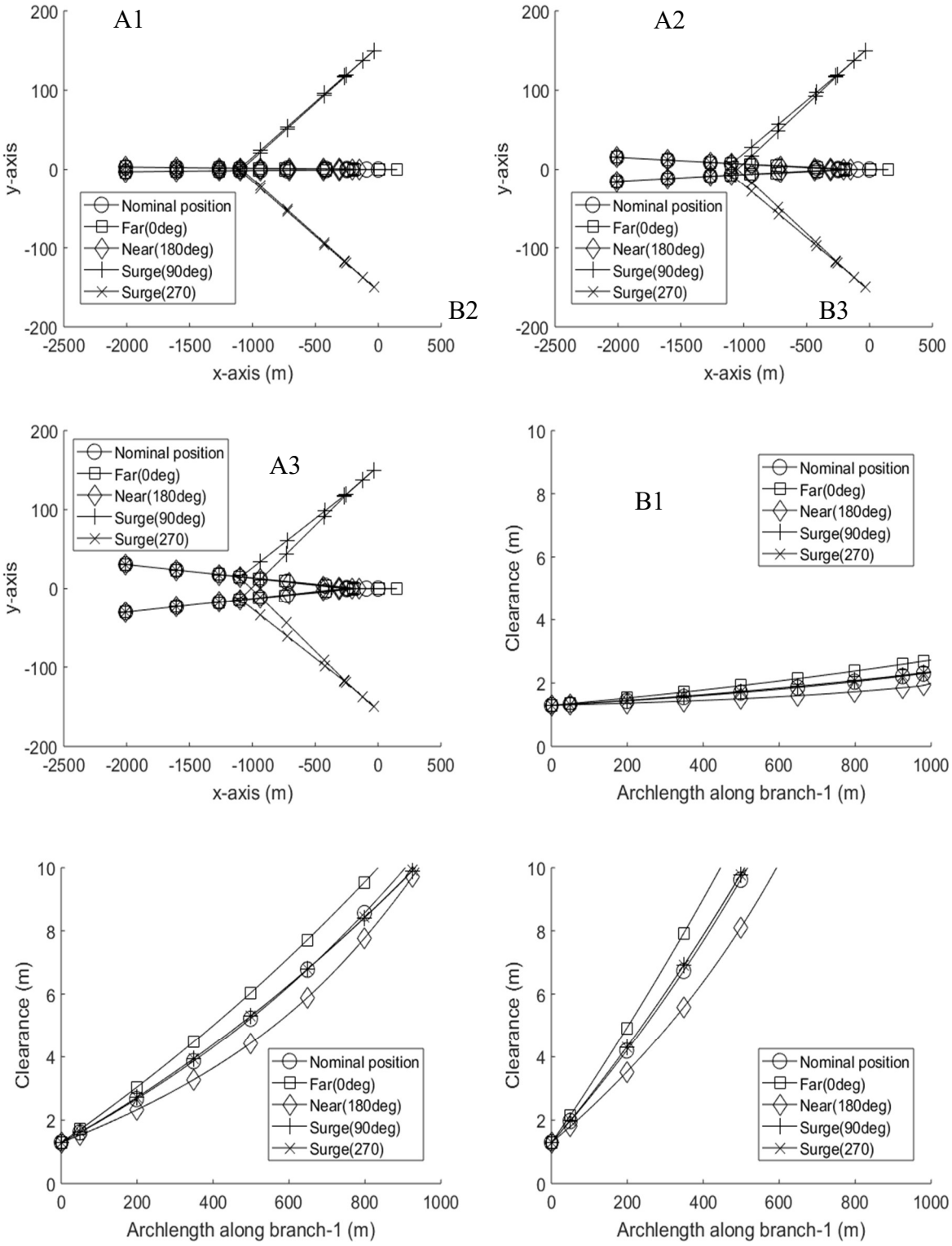

Figure 5-20: BSCR deflection under vessel offset: (A1) - BSCR (β = 0.1deg), (A2) - BSCR (β = 0.5deg), (A3) - BSCR (β = 1deg), (B1,B2,B3) – Corresponding branch clearance for A1, A2, A3 respectively.

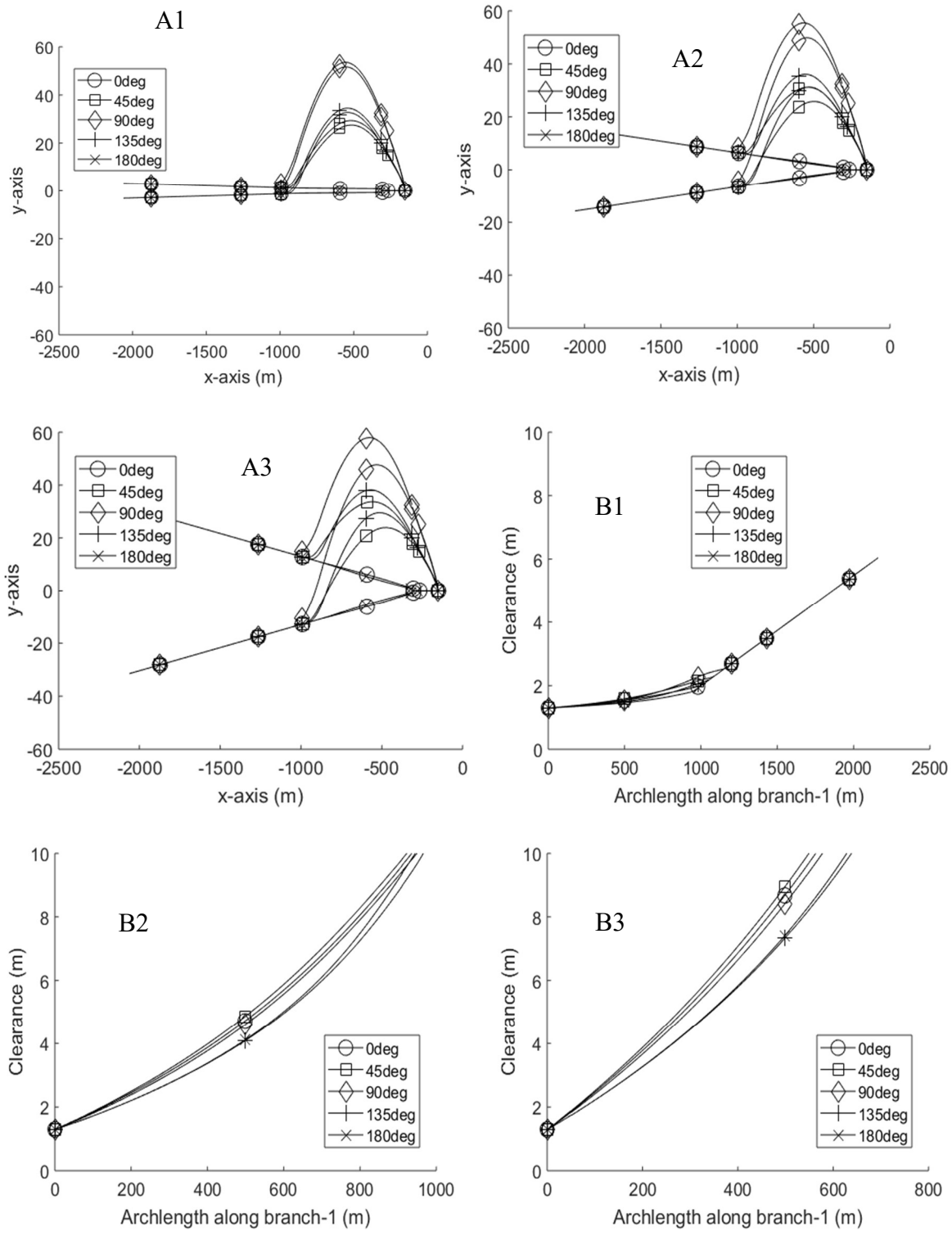

Figure 5-21: BSCR deflection under worse vessel offset and worse current profile (profile-3). (A1) - BSCR (β = 0.1deg), (A2) - BSCR (β = 0.5deg), (A3) - BSCR (β = 1deg), (B1, B2,B3) – Corresponding clearance response for A1,A2,A3 respectively.

5.4.4.5 Scenario 5 - Weight variation of branches

The BSCR branches can be conducting fluid from different wells with different fluid density. This can cause a difference in branches' weights and magnitude of deflection under current loads. This scenario is illustrated using the BSCR configurations ($\beta = 0.1\text{deg}, 0.5\text{deg}, 1\text{deg}$), in the critical offset condition (near position), with the critical current profile (profile-3) acting in the 5-directions and considering fluid content density variation of up to 10% in both branches. In case-1, all BSCR component risers are filled with a fluid of density 600kg/m^{3,} and the clearance between branches for the respective BSCR configurations are presented in Figure 5-22 (A1), (B1) and (C1). In case-2, the content density of branch-2 is reduced by 10% making it lighter than branch-1, and the clearance between branches for the respective BSCR configurations are presented in Figure 5-22 (A2), (B2) and (C2). In case-3, the content density of branch-1 is reduced by 10% making it lighter than branch-2, and the clearance between branches for the respective BSCR configurations are presented in Figure 5-22 (A3), (B3) and (C3). In both case-2 and case-3, the stem content density is averaged at 570kg/m^3. The critical clearance response can be seen for BSCR ($\beta = 0.1\text{deg}$) subjected to current in 90deg direction as shown in Figure 5-22 (A2), where clearance between branches at around 558m arch length reduces to 0.9m. This is resulted from higher DAW ratio for branch-2 (upstream riser for 90deg current direction) relative to branch-1(downstream riser), causing highest differential deflection between the two branches. Conversely, Figure 5-22 (A3) shows an increase in branches' clearance by the current in 90deg direction. This is because, for this case, branch-1 (downstream riser) has higher DAW ratio since it is lighter. When the DAW ratio of the upstream riser is lower than that of the downstream riser, the current load causing the largest deflection (normal to riser plane) gives the most critical branch clearance. For close or equal DAW ratios, the current causing largest deflection (perpendicular to riser plane) has minimum impact on the clearance, while for cases where the downstream riser has higher DAW ratio, clearance responses are higher. The impact of weight variation on branches' clearance is barely noticeable for BSCRs with higher branch angles ($\beta = 0.5\text{deg}, 1\text{deg}$). Note that in this scenario, all BSCR satisfy the minimum clearance requirement.

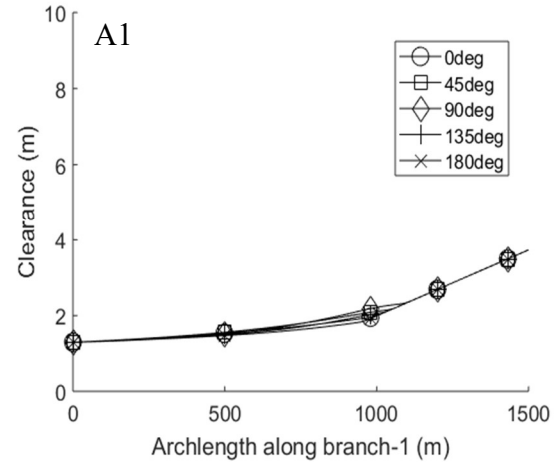
A1
0deg
45deg
90deg
135deg
180deg
Clearance (m)
Archlength along branch-1 (m)

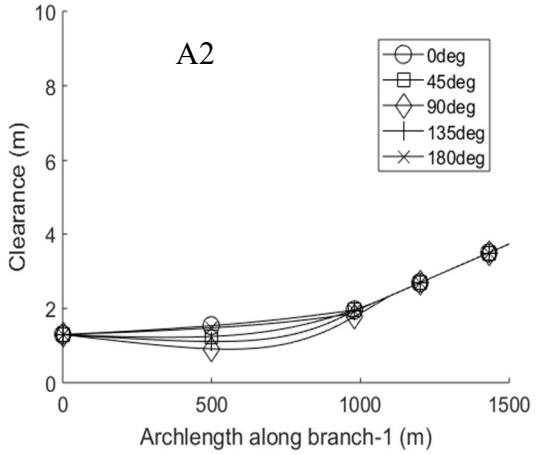
A2
0deg
45deg
90deg
135deg
180deg
Clearance (m)
Archlength along branch-1 (m)

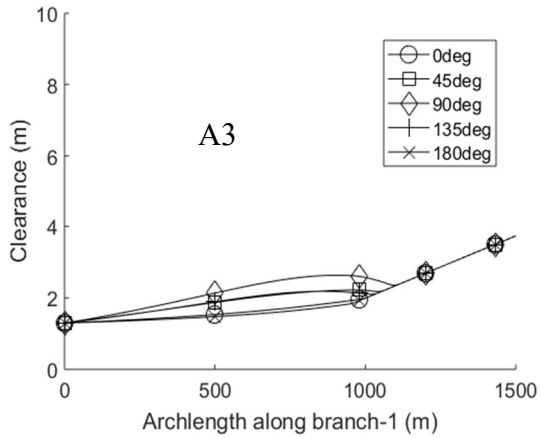
A3
0deg
45deg
90deg
135deg
180deg
Clearance (m)
Archlength along branch-1 (m)

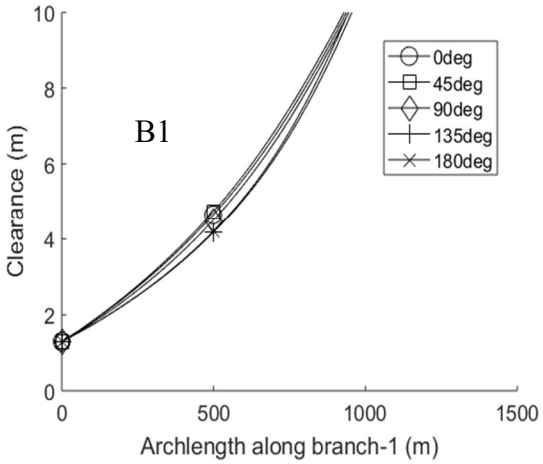
B1
0deg
45deg
90deg
135deg
180deg
Clearance (m)
Archlength along branch-1 (m)

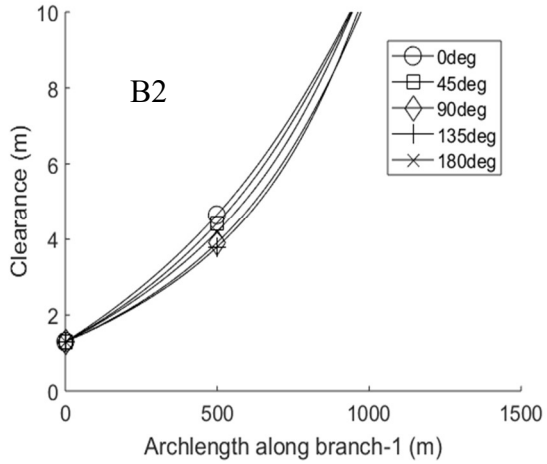
B2
0deg
45deg
90deg
135deg
180deg
Clearance (m)
Archlength along branch-1 (m)

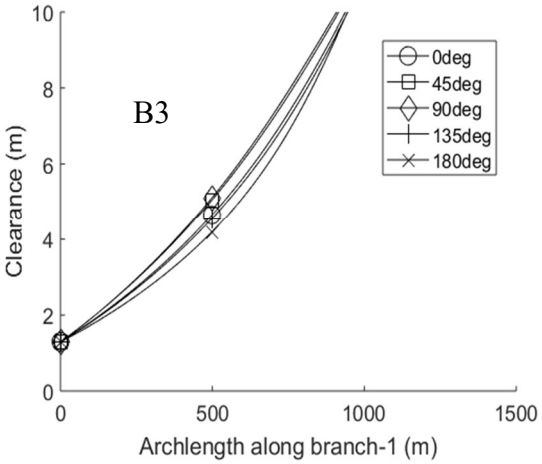
B3
0deg
45deg
90deg
135deg
180deg
Clearance (m)
Archlength along branch-1 (m)

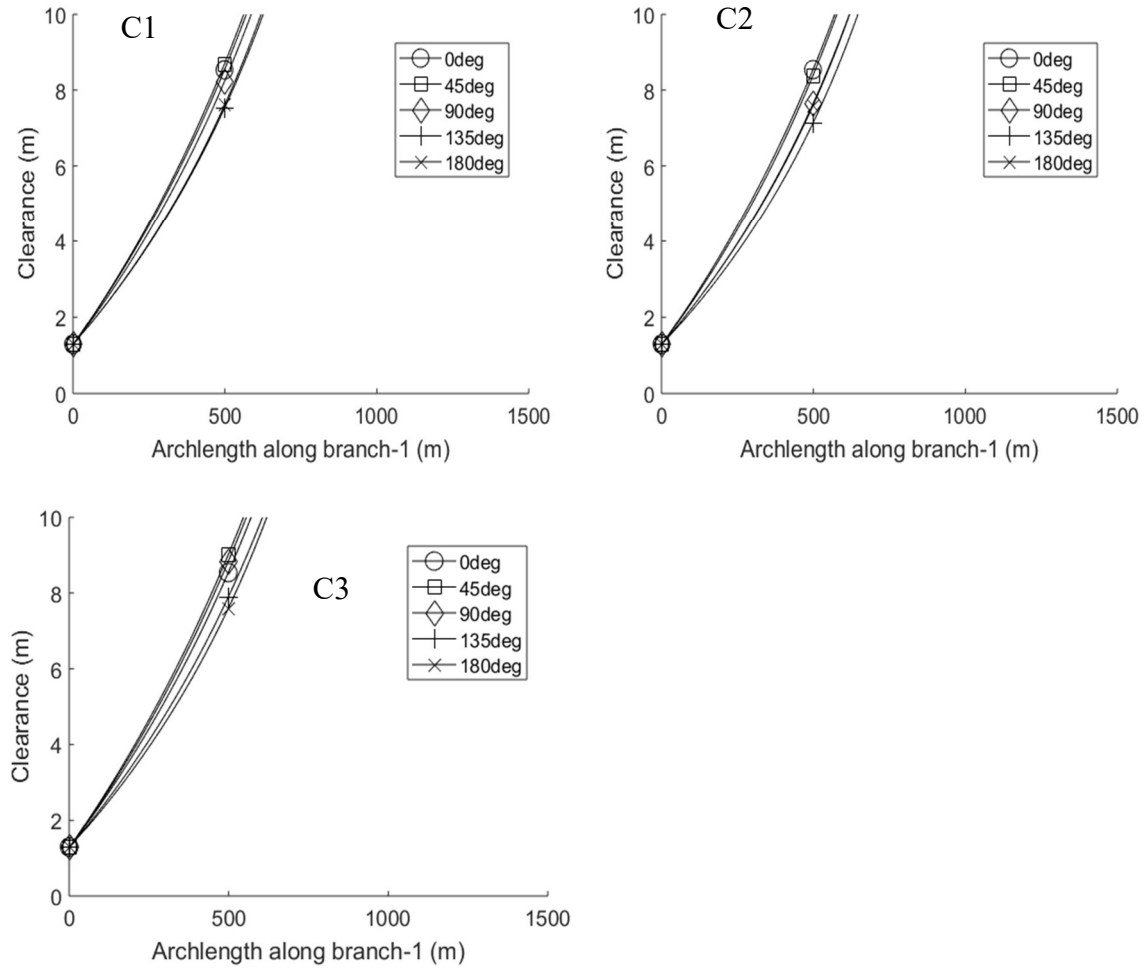

Figure 5-22: Case1 (A1, B1, C1) - Branch-1 (600kg/m^3), Branch-2 (600kg/m^3) for BSCR (β =0.1deg, 0.5deg and 1deg) respectively; Case2 (A2, B2, C2) - Branch-1 (600kg/m^3), Branch-2 (540kg/m^3) for BSCR (β =0.1deg, 0.5deg and 1deg) respectively; Case3 (A3, B3, C3) - Branch-1 (540kg/m^3), Branch-2 (600kg/m^3) for BSCR (β =0.1deg, 0.5deg and 1deg) respectively

5.4.4.6 Scenario 6 – Wave loading

From scenario-5, it was observed that BSCR ($\beta = 0.1$ deg) was more critical with upstream branch higher in weight by 10% compared with the downstream branch, under the worse current profile in 90deg direction, and under the critical vessel offset (near offset – 180deg). The clearance between the branches for the combined condition was 0.9m occurring at 558m arch-length along the branches. In this scenario, this critical combination of conditions on BSCR ($\beta = 0.1$deg) is further subjected to a regular wave load (H = 10m, T = 12sec). Since the vessel RAO is symmetrical about the longitudinal and the transverse axis, the wave direction of 0deg, 45deg, 90deg would have been sufficient for this scenario, except for the direct wave impact on the BSCR stem. Therefore, wave directions selected for this scenario are 0deg, 45deg, 90deg, 135deg and 180deg, based on the same argument posed in the selection

of current directions in scenario-2. For deep water, the wave velocity decreases exponentially and gets to zero from the connector interface down to the seabed (Figure 5-14B). Hence, the wave motions experienced by the branches are not direct wave loads on them but in response to the stem's and vessel's responses induced by the wave load. As shown in Figure 5-23 (A), the different wave loads in the five (5) wave directions were found to have a negligible impact on the branches' clearance when compared with the static case result in Figure 5-22 (A2). In fact, the wave load only changes the clearance from 0.9m to 0.89m, i.e. by 1%.

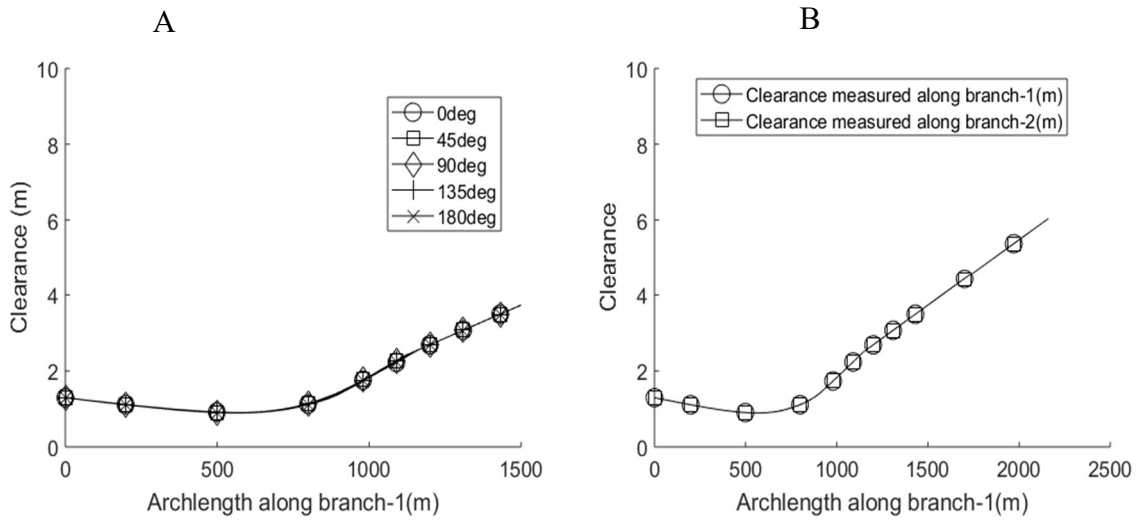

Figure 5-23: (A) – Range graph minimum clearance response under wave loads in five directions on critical static condition (B) – Range graph minimum clearance measured respectively from branch-1 and branch-2 under wave load

It can be seen from Figure 5-23 (B) that the clearance measurement between branches along branch-1, matches with the measurement along branch-2. This means that the shortest distance between the branches (clearance) occur at equal length along branch-1 and branch-2, measured from the connector interface. This also implies that the point (558m), where the smallest clearance occurs, is common for both branches. The time history of heave motion of this point on the two branches, in the five (5) different wave directions, and the clearance response are then obtained and presented in Figure 5-24 (A), (B), and (C) respectively. One can observe from the plots (A and B) that the dynamic heave response of this point on the two branches are in phase. It can also be seen that though this point (558m) on the branches are oscillating vertically with amplitude comparable with the vessel's heave motion, the clearance between branches is negligibly affected, with the minimum(0.89m) occurring for wave load acting in

180deg direction (see Figure 5-24C). The downward vessel heave, roll and sway motions towards the BSCR TDP can result in reduced tension in the lines and a corresponding reduction in the clearance, similar to that observed for near vessel offset in scenario-3. The clearance response can also be observed to be less sensitive to wave load acting in directions out of the riser plane. Results from this scenario indicate that the clearance between the branches is less affected by the wave excitation. This may not be the case for BSCR were the wave velocity is significant on the branches. From these results, the minimum clearance (≈ 0.5m) are satisfied.

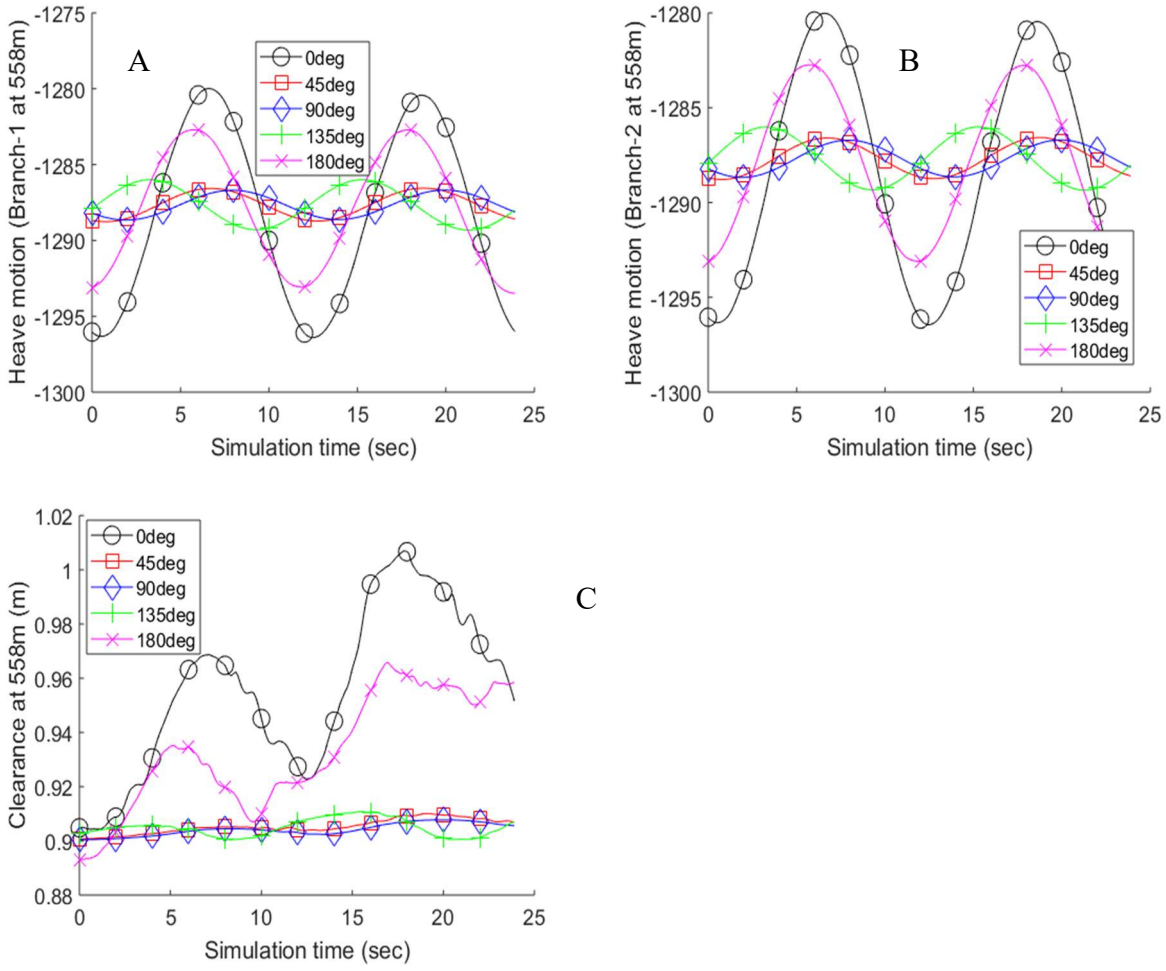

Figure 5-24: (A) – Dynamic heave response of point 558m on branch-1, (B) – Dynamic heave response of point 558m on branch-2, (C) clearance response between branch-1 and branch-2 at point 558m on branch-1.

5.4.4.7 Scenario 7- Drag amplification condition (VIV)

VIV conditions may cause a significant difference in the DAW ratios of the two branches if their in-plane vibration amplitudes are significantly different, resulting in a difference in the current-in-line drag force on them, especially for current profiles nearly perpendicular to the

branches' planes. A 'brute force' approach will be to arbitrarily set up four limiting cases of the branches' Cd values : (1) None of the branches is undergoing VIV, (2) Both branches are undergoing VIV, (3) Only branch-1 is undergoing VIV, and (4) only branch-2 is undergoing VIV. Example result of such arbitrary Cd combinations for the BSCR with branch angles, $\beta = 0.1\text{deg}, 0.5\text{deg}$ and 1deg, using current profile-1 (slab profile), acting perpendicular to the stem plane (90deg), are presented in Figure 5-25 (A), (B) and (C) respectively. Clashes of branches (zero clearance) or clearance below the required minimum are seen to occur for cases where the branch-2 (upstream riser) has higher DAW ratio relative to branch-1 (downstream riser). For equal DAW for the two branches or for higher DAW ratio for branch-1 relative to branch-2, the clearance is higher. The probability of clashing is higher for the most critical BSCR configuration ($\beta = 0.1\text{deg}$) seen in Figure 5-25 (A). However, the above arbitrary combinations of Cd values of the branches are not representative of the actual VIV conditions of the BSCR. In this scenario, the interference feasibility of the BSCR under VIV conditions is investigated using the I&B WO model.

VIV analysis is first performed with the empty BSCR ($\beta = 1\text{deg}$) in nominal offset condition, subjected to the three current profiles (1, 2 & 3) in all five (5) current directions. The results obtained are presented in Figure 5-26, where (A1), (B1) and C1) are the range-graph transverse A/D responses of branch-1 to current profile-1, 2 and 3 respectively; (A2), (B2) and C2) are the range-graph transverse A/D responses of branch-2 to current profile-1, 2 and 3 respectively; and (A3), (B3) and C3) are the range-graph clearance responses between the branches to current profile-1, 2 and 3 respectively. The results are representative of 'lockin' conditions under VIV, over a VIV simulation period of 600sec. It can be seen from Figure 5-26 (B1) and (B2) that current profile-2 (typical of WoA) resulted in smallest transverse A/D ratio of the branches, while the slab current profile-1 (slab current profile) resulted in the highest transverse A/D ratio of the branches as seen in Figure 5-26 (A1) and (A2).

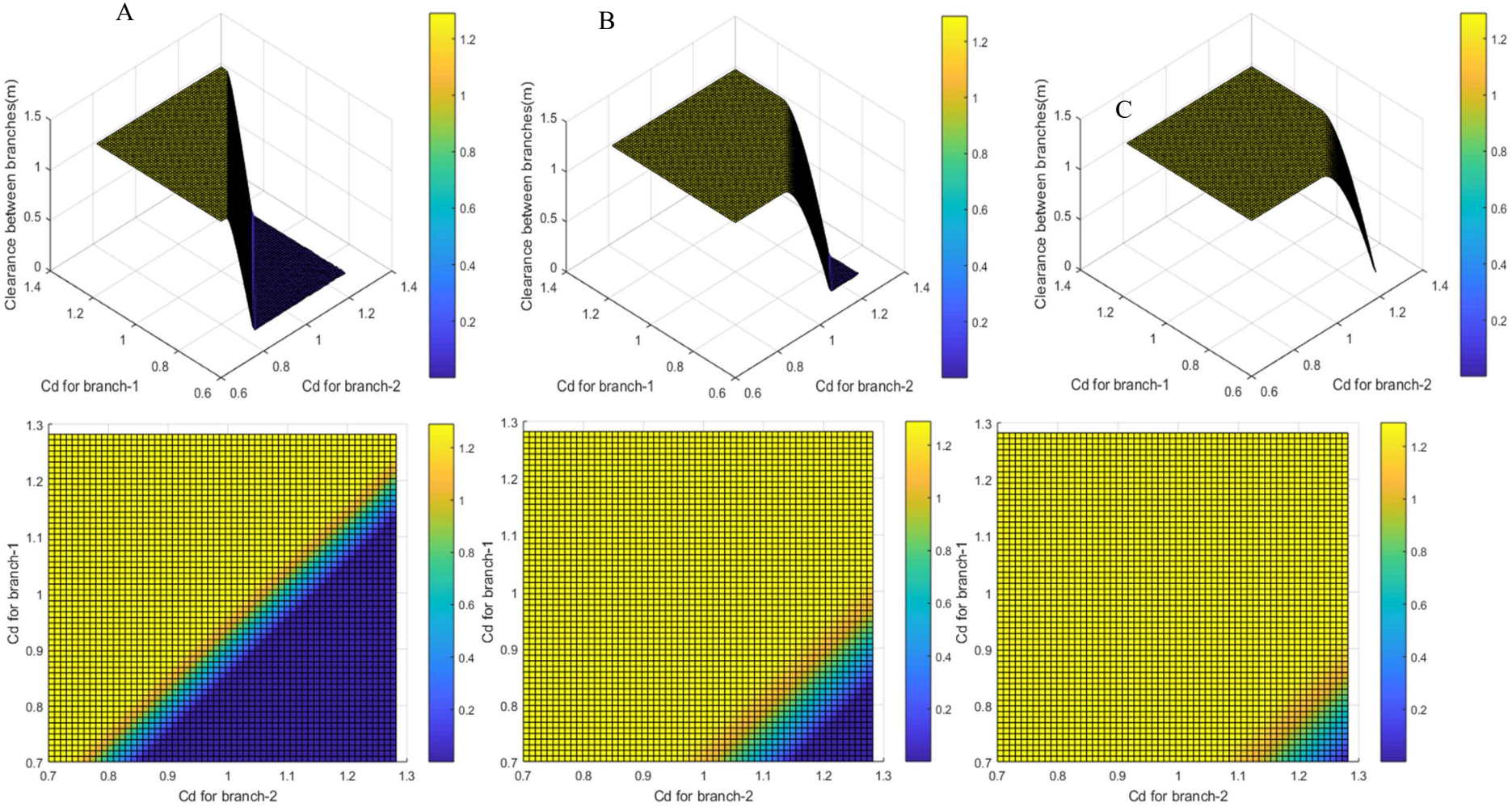

Figure 5-25: Minimum clearance response for BSCR : (A) - $\beta = 0.1\text{deg}$, , (B) - $\beta = 0.5\text{deg}$, (C) - $\beta = 1\text{deg}$, under different drag coefficients for branch-1 and branch-2

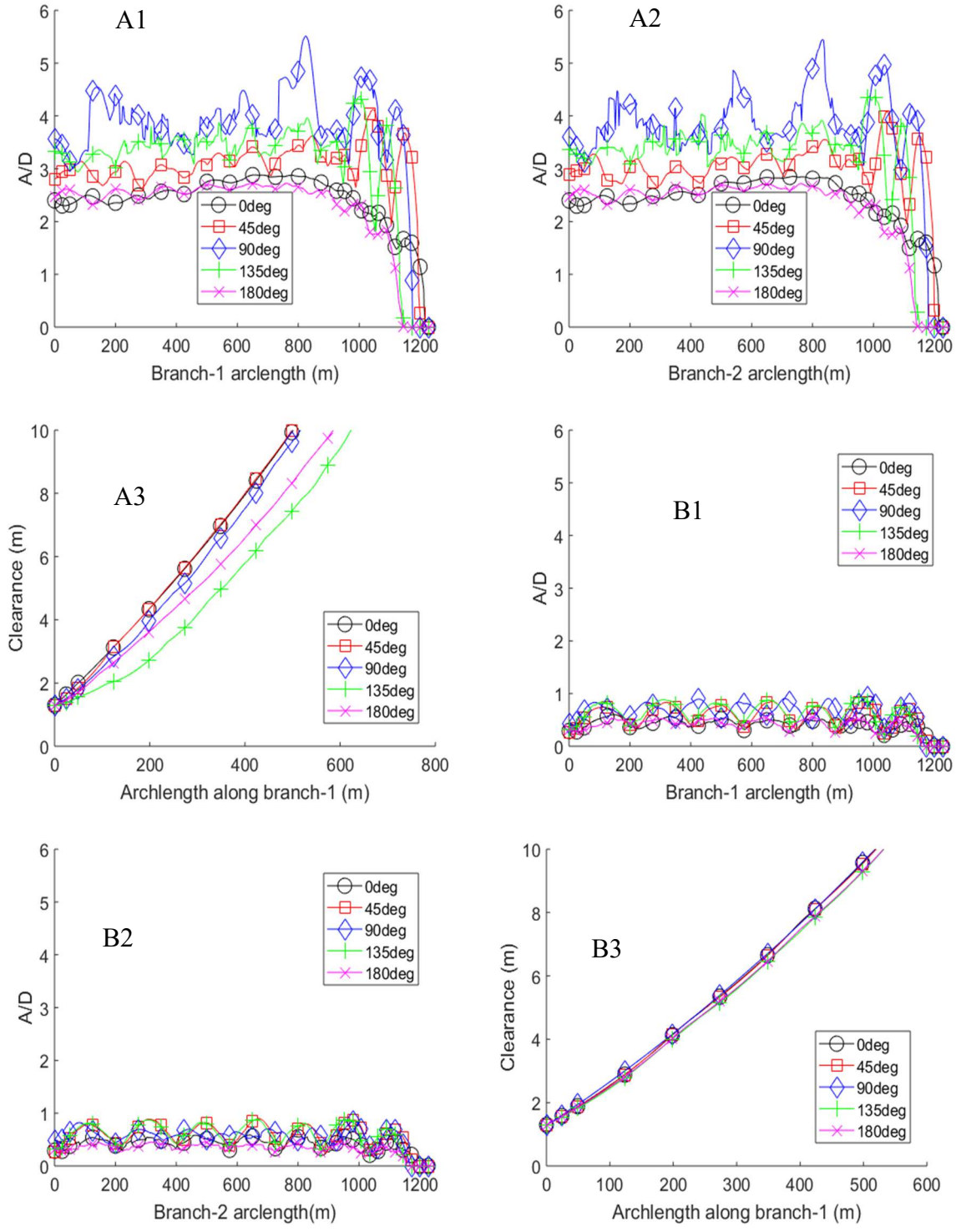
A1
A/D
Branch-1 arclength (m)
0deg
45deg
90deg
135deg
180deg
A2
A/D
Branch-2 arclength(m)
A3
Clearance (m)
Archlength along branch-1 (m)
B1
A/D
Branch-1 arclength (m)
B2
A/D
Branch-2 arclength(m)
B3
Clearance (m)
Archlength along branch-1 (m)

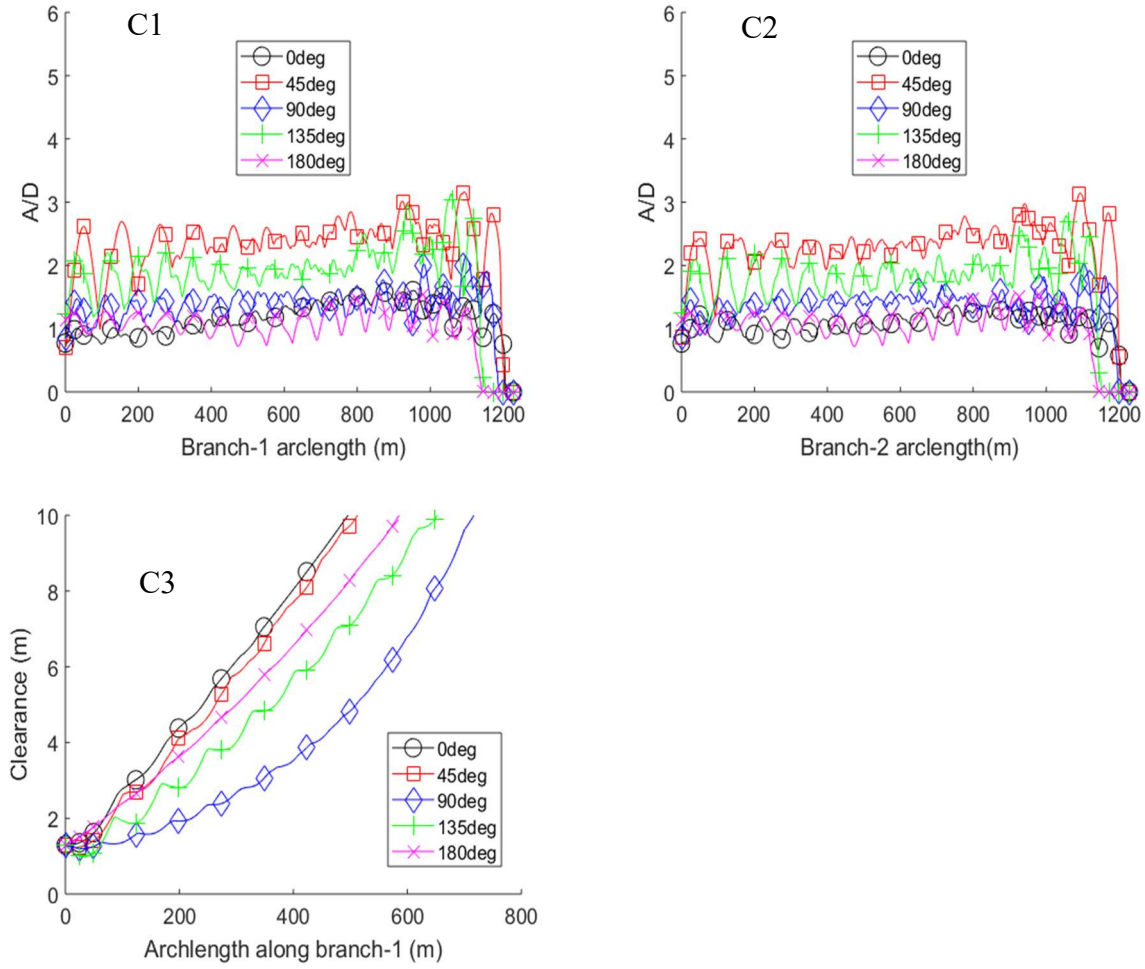

Figure 5-26: BSCR(β = 1deg) (A1, B1, C1) –Range graph maximum for A/D of branch-1 under current profile - 1, 2 and 3 respectively (A2, B2, C2) –Range graph maximum for A/D of branch-2 under current profile - 1, 2 and 3 respectively (A3, B3, C3) –Range graph clearance between branches under current profile – 1, 2 and 3 respectively.

Although the current intensity of profile-3 on the BSCR branches is known to be higher than that of current profile-1 (see Figure 5-14A), the traverse A/D for profile-1 is highest for the branches (1 and 2) as seen in Figure 5-26 (A1) and (A2) compared with Figure 5-26 (C1) and (C2) respectively, for current acting in 90deg direction. This is an indication that VIV response intensity decreases with an increase in current profile sheerness. The range-graph maximum and minimum of the Strouhal (Str) period for current profile-1(slab or constant current profile) across the diameters and over the lengths of branch-1, branch-2 and the stem are respectively presented in Figure 5-27 (A1), (A2) and (A3). Similarly, the range-graph maximum and minimum of the Strouhal (Str) period for current profile-3 (typical of GoM) across the diameters and over the lengths of branch-1, branch-2 and the stem are respectively presented in Figure 5-27 (B1), (B2) and (B3). The global mode number and corresponding periods obtained from coupled Eigen analysis of the BSCR are also included in the plots. Figure 5-27

(C1), (C2) and (C3) present respectively the mode shape (m) in X, Y and Z degree of freedom (DOF), of branch-1, branch-2 and stem (combined in each plot) corresponding with the mode numbers. It could be seen from Figure 5-27(A1) – branch-1, and Figure 5-27(A2) – branch-2, that the Strouhal (Str) period closely matches the global BSCR modal periods at multiple points along their lengths (green dotted lines). This can excite modes between 20 and 40 (occurring between 600m and 1200m - Figure 5-27 (A1 and A2)) that can cause higher transverse A/D response as can be seen in Figure 5-27(C3). When this is compared using profile-3 as seen in Figure 5-27 (B1, B2 and B3), the Strouhal period locks in with the Eigen period at mode 35 and 50. Mode 50 is excited at a point along the branches resting on the seabed and does not have any impact on the vibration of the hanging section. Mode 35 occur around point 1250m. Although this mode (35) can result in higher transverse A/D response (Figure 5-27 C3), it occurs around a very short length (Figure 5-27 B1 and B2) when compared response with the case of current profile-1 for which Strouhal number synchronizes with mode shapes at multiple points and over longer hanging section of the branches (Figure 5-27 A1 and A2). This is in agreement with past studies, where current with slab profiles was observed to cause intensive VIV synchronizing over the entire riser length [109]. The transverse A/D response of the stem (though not presented here) are small. This from the above explanation could be because of the Strouhal period ‘locks in’ with the mode period in mode-25 at just one point (340m) which may not have a significant impact on the overall length of the stem.

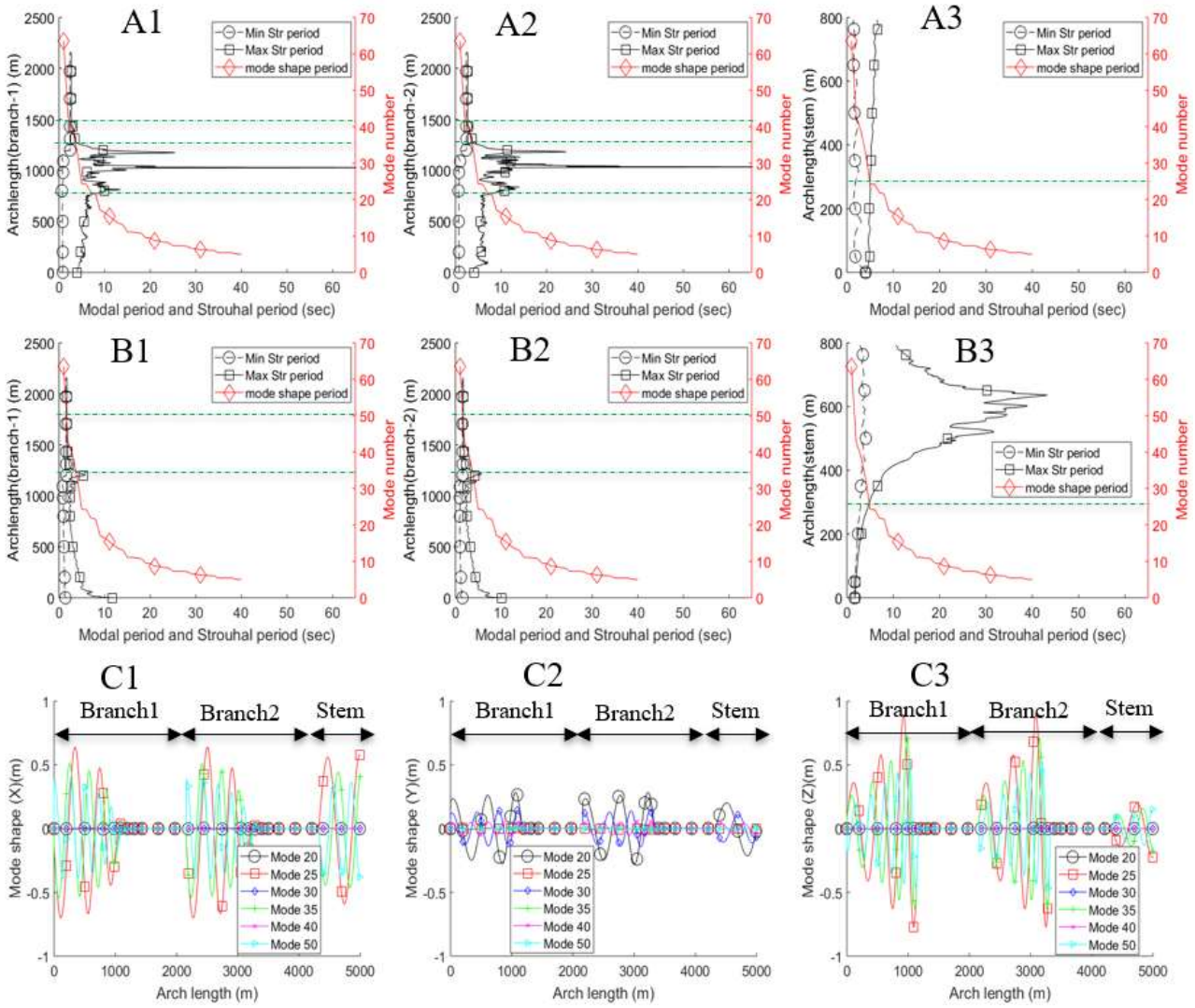

Figure 5-27: (A1, A2, A3) –Strouhal period (Current profile -1) along branch-1, branch-2, and stem with BSCR Eigen number & periods. (B1, B2, B3) –Strouhal period (Current profile -3) along branch-1, branch-2, and stem with BSCR Eigen Number & periods. (C1, C2, C3) –Likely excited branch-1, branch-2 and stem mode shapes in X, Y and Z DOF respectively

For the current profile-1(slab current profile) causing higher transverse A/D, this will induce higher amplification on the inline drag force on the branches and hence the riser deflection under current profile-1 will be higher compared with deflection under other profile-2 and profile-3 under VIV 'lockin' condition. When the BSCR is filled with fluid (600kg/m3), the additional weight dampens the transverse A/D response as seen for branch-1 and branch-2 in Figure 5-28 (A1) and (A2) when compared with the empty BSCR case results presented in Figure 5-26 (C1) and (C2), considering the current direction of 90deg. This indicates that heavier pipes are less susceptible to higher vibration under VIV condition. A reduction in the transverse A/D reduces the magnitude of the inline drag force on the branches, resulting in improved (increase) clearance between them, as shown in Figure 5-28 (A3.)

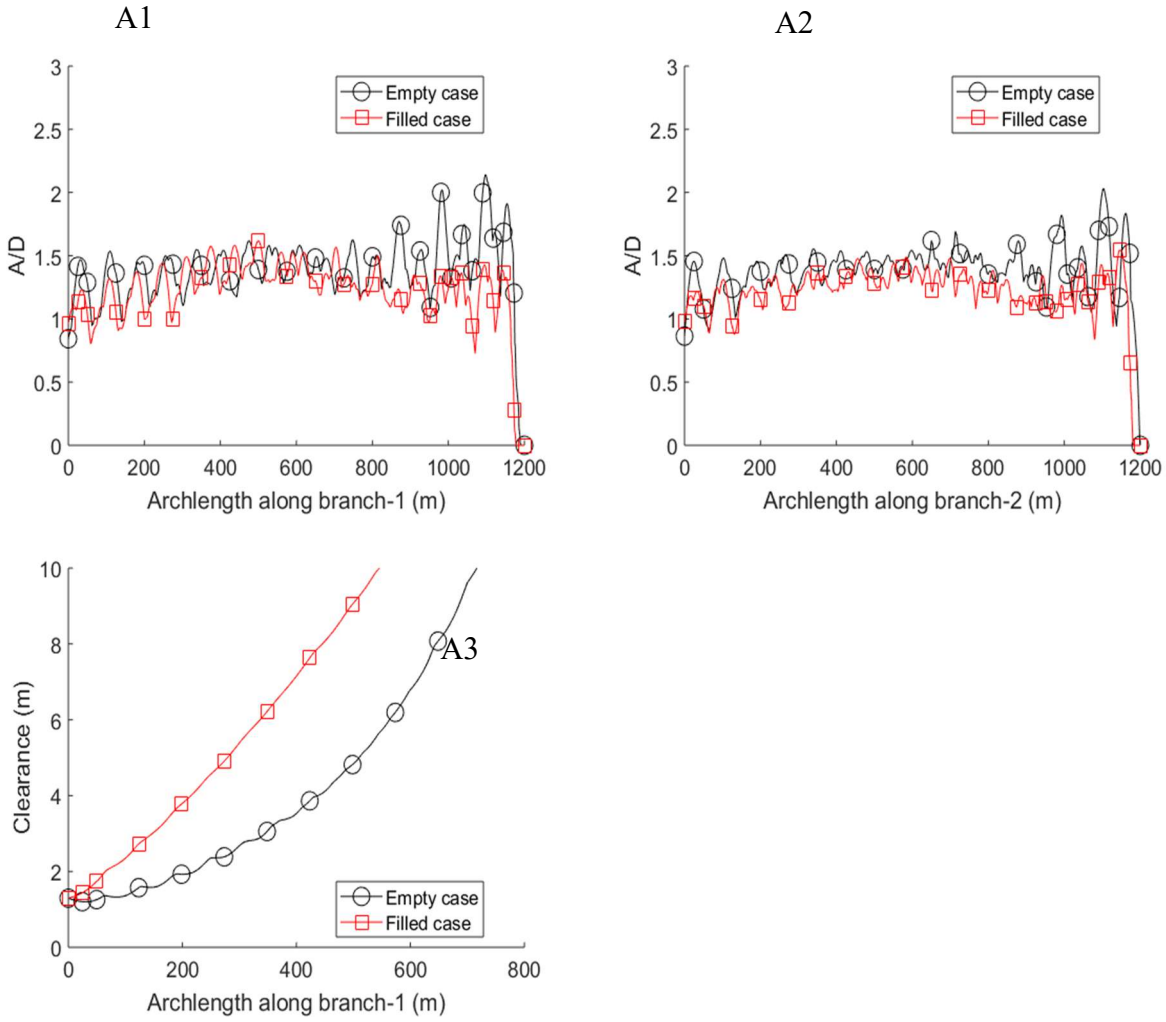

Figure 5-28: BSCR (β =1deg), (A1) – Branch-1 transverse A/D for filled and emty BSCR, (A1) – Branch-2 transverse A/D for filled and empty BSCR, (A3) – Clearance between branches for filled and empty BSCR.

Finally, VIV analysis was conducted for the BSCR ($\beta = 0.1\text{deg}$), which is the most critical among the three BSCR configurations in this study, using current profile-1, 2 and 3 acting on the BSCR in all five(5) current directions. From the VIV analyses result obtained, we can see that BSCR clearance with half branch angle, $\beta = 0.1\text{deg}$, is feasible under current profile-1 and profile-2, but not with current profile-3 (see Figure 5-29 (A3), (B3) and (C3)). The BSCR configuration failed to satisfy the interference criteria under current profile-3 (typical of GoM), indicating that the differential deflection between the branches is sufficiently greater than the clearance, hence the clashes of the branches as seen in Figure 5-29 (C3). This indicates that the half branch angle for BSCR ($\beta = 0.1\text{deg}$) is not sufficient and has to increase during design to make it feasible (under VIV) for current profiles similar to those in GoM.

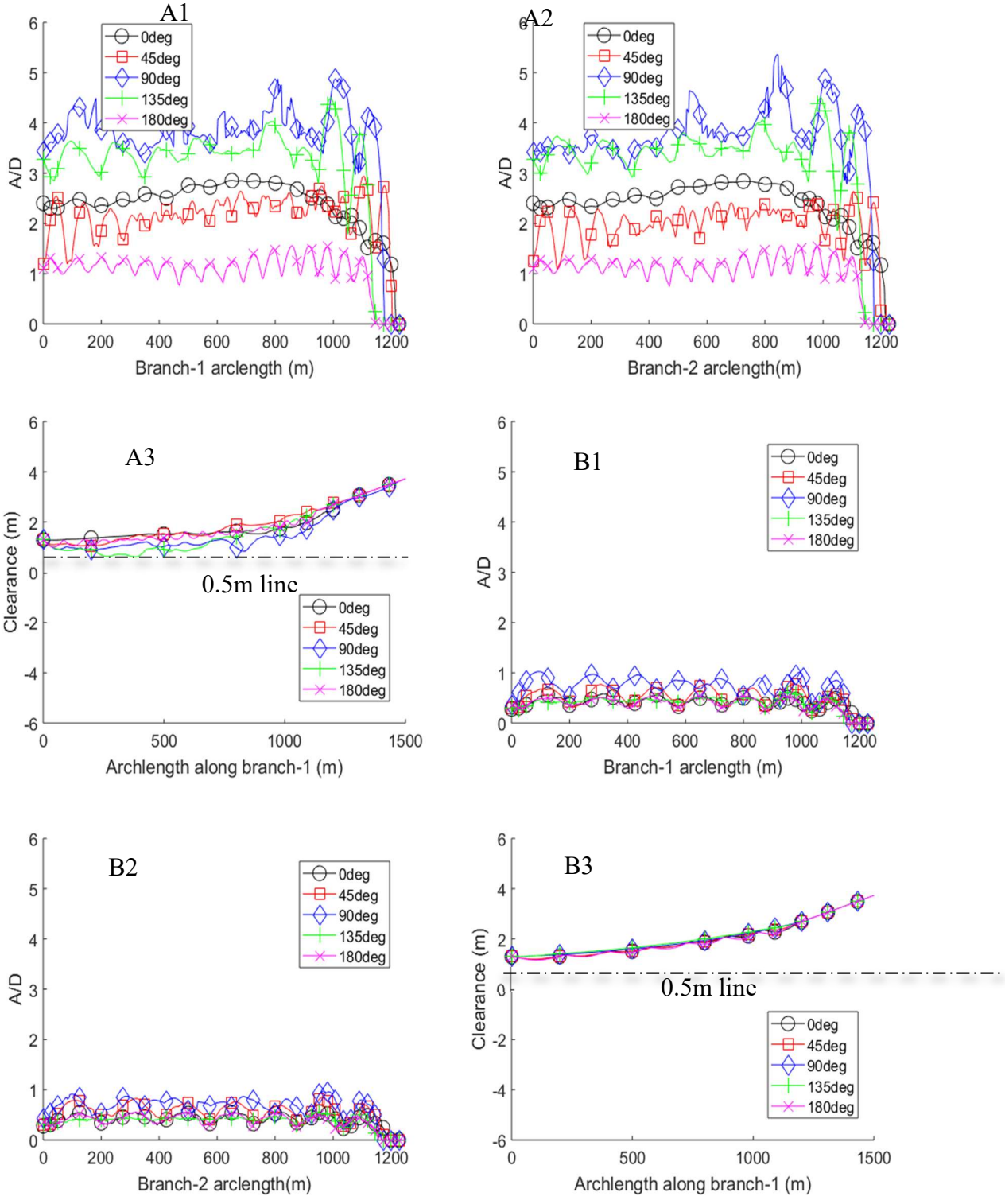
A1
A/D
Branch-1 arclength (m)
A2
A/D
Branch-2 arclength(m)
A3
Clearance (m)
0.5m line
Archlength along branch-1 (m)
B1
A/D
Branch-1 arclength (m)
B2
A/D
Branch-2 arclength(m)
B3
Clearance (m)
0.5m line
Archlength along branch-1 (m)
0deg
45deg
90deg
135deg
180deg

C2

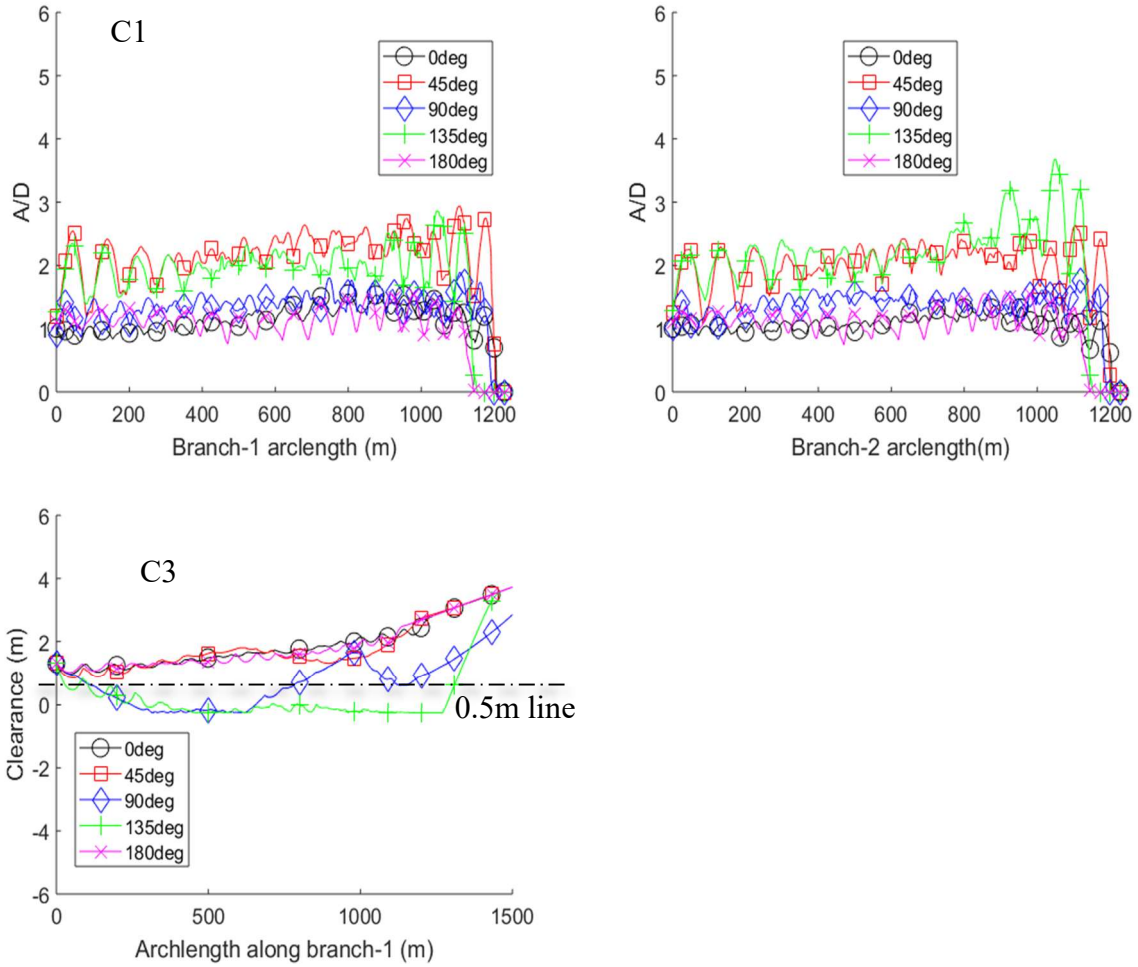

Figure 5-29: BSCR(β = 0.1deg) (A1, B1, C1) –Range graph maximum for A/D of branch-1 under current profile - 1, 2 and 3 respectively (A2, B2, C2) –Range graph maximum for A/D of branch-2 under current profile - 1, 2 and 3 respectively (A3, B3, C3) –Range graph clearance between branches under current profile – 1, 2 and 3 respectively.

5.4.4.8 Concluding remarks on the BSCR interference study

This section presents findings from the investigation of the interference response of the branches of the BSCR with different half branch angles (β =0.1deg, 0.5deg and 1deg), branched at 750m water depth and hosted by FPSO in a water depth of 1500m. The BSCRs were subjected to different loading conditions including current loads, vessel offsets, variation in branch weight, wave loads and drag amplification due to VIV.

Under the non-VIV conditions (current load, vessel offsets, weight variation and critical combinations of them), the drag force on the branches are nominal and are not amplified, the three configurations of the BSCR (β =0.1deg, 0.5deg and 1deg) passed the interference criteria, indicating that half branch angles of 0.1deg, 0.5deg and 1deg are sufficient for BSCR design in these conditions. With wave loads of 10m wave height and 12sec period imposed on

the critical static configurations of the risers, the BSCRs were still found to satisfy the interference criteria. This indicates that wave excitations may have a negligible impact on the BSCR clearance response. For VIV scenarios, the riser vibrates transversely in the riser plane. When a Strouhal period matches closely with a natural period of the BSCR, 'lockin' condition is reached, were higher transverse amplitude to diameter (A/D) is observed. The A/D ratio is highest for constant current profile (profile-1) but does not necessarily result in significant differential deflection and clashes of the branches. Considering a current profile typical of GoM (profile-3), the BSCR need to be designed with sufficiently high half branch angles to prevent the branches from clashing. The results from this study showed that BSCR with very small half branch angle ($\beta = 0.1$deg) failed the interference criteria under 'lockin' condition with current profile-3. For current profile typical of WoA (profile-2), all BSCR configurations ($\beta = 0.1$deg, 0.5deg and 1deg) were found to be feasible in terms of interference checks.

Note that in this study, conservative approaches were employed such as the use of conservative nominal Cd values for the component risers in the BSCR, which were interpolated from approximate analytical expressions, and the use of extreme current profiles for the VIV analysis. Typical nominal values for a bare circular pipe can be chosen within 0.7 to 1.0 [110], and typical current profiles for VIV analysis are usually smaller in magnitude than extreme current profiles used in this study. In addition, no strakes were installed on the branches' sections prone to higher VIV transverse A/D to mitigate vibration amplitude. With actual or more realistic field data used, less conservative deflection and clearance can be achieved.

5.5 Chapter summary

The motivation behind the development of the branched riser system (BRS) has been presented in this chapter. The BSCR is made up of a larger pipe section that connects to the host platform and two branches of smaller bore SCR. The braches extend from the connecting point to the large bore pipe to the seabed. Although different variants of the BRS were introduced, only the BSCR is investigated in this chapter and thesis.

The small-bore pipe SCRs tend to have better stress and fatigue damage responses at the TDZ than large bore pipe SCR as observed from the comparative analysis study conducted for SCR of different bore sizes under different wave load conditions. Based on this finding, the branch riser system (BSCR) concept was developed to take advantage of this improved small-bore SCR TDZ response and, at the same time, take advantage of fewer topside connections. Since

the BSCR configuration is defined by a combination of the branch angle and the branched water height, there is a need to employ an optimisation technique to determine the optimum combination of these design variables for an optimum BSCR configuration. The index matching optimisation technique was employed to demonstrate this process, indicating that for any given field development data, the technique demonstrated here in this chapter can be employed to obtain a suitable BSCR configuration replacement for conventional SCRs.

A potential challenge of the BSCR is the interference of the branches. If the branch angles are small, and the current load environment and lateral riser oscillations are severe, then the BSCR face the potential of its branches clashing with each other. However, from the interference study conducted in this chapter for a set of given BSCR configurations with different branching angles, it could be seen that the BSCR will potentially be feasible for branch angles beyond a given minimum. This critical branch angle must be determined during its design following a similar procedure applied for the BSCR interference study.

6 FLOATING CATENARY RISER SYSTEM

The expansion of a deepwater brownfield may become necessary to increase the production of hydrocarbons. Such expansion often requires the installation of additional risers to the existing floating production platform. However, the seabed footprint of the existing facilities may be congested with existing subsea pipelines and structures. Tying back of risers such as steel catenary riser (SCR) to the floating platform becomes challenging. Floating catenary riser (FCR) is a novel riser solution with floating bends or 'waves' close to the seabed. The FCR is engineered to extend its touch down point (TDP) far beyond the nominal TDP of the SCR and away from the congested seabed footprint. The riser sections before the nominal SCR TDP is configured to float by installing buoyancy modules. The multiple wave buoyant sections also provide the FCR with the capability to decouple its touch down zone (TDZ) from the floating platform motion. This can result in a significant reduction in the stress and fatigue damage around the riser TDP. The configuration development of the FCR has been detailed in section 6.2. In this chapter, the FCR global analysis and optimisation are presented.

The chapter is structured as follows:

- Section 6.1 – Background to FCR concept development
- Section 6.2 - The floating catenary riser system configuration development
- Section 6.3 - Global response study of FCR
- Section 6.4 - Global optimisation of FCR
- Section 0 – Chapter Summary

6.1 Background to the FCR concept development

The floating catenary riser (FCR) is a new riser solution with a double wave bend close to the seabed, providing its characteristic long span feature over congested or environmentally protected seabed section. It is not easy to achieve this long seabed span with SCR and steel

lazy wave risers (SLWR). The FCR concept is proposed in this study to solve such SCR tieback challenges, as depicted in Figure 6-1. The FCR is created by modifying the SCR configuration by installing buoyancy modules on its seabed section. The installed buoyancy system produces multiple wave bends (two-wave bends in this study). The modification is performed while ensuring that the wave bends are close to the seabed as permissible by the design requirements. The elevation from the seabed of the highest points on the wave bends is the hog elevation (y_{hog}), while the elevation from the seabed of the lowest points in the wave bends is the sag elevations (y_{sag}). The arc height, Δh, is the difference between the y_{hog} and y_{sag} i.e. $(\Delta h = y_{hog} - y_{sag})$.

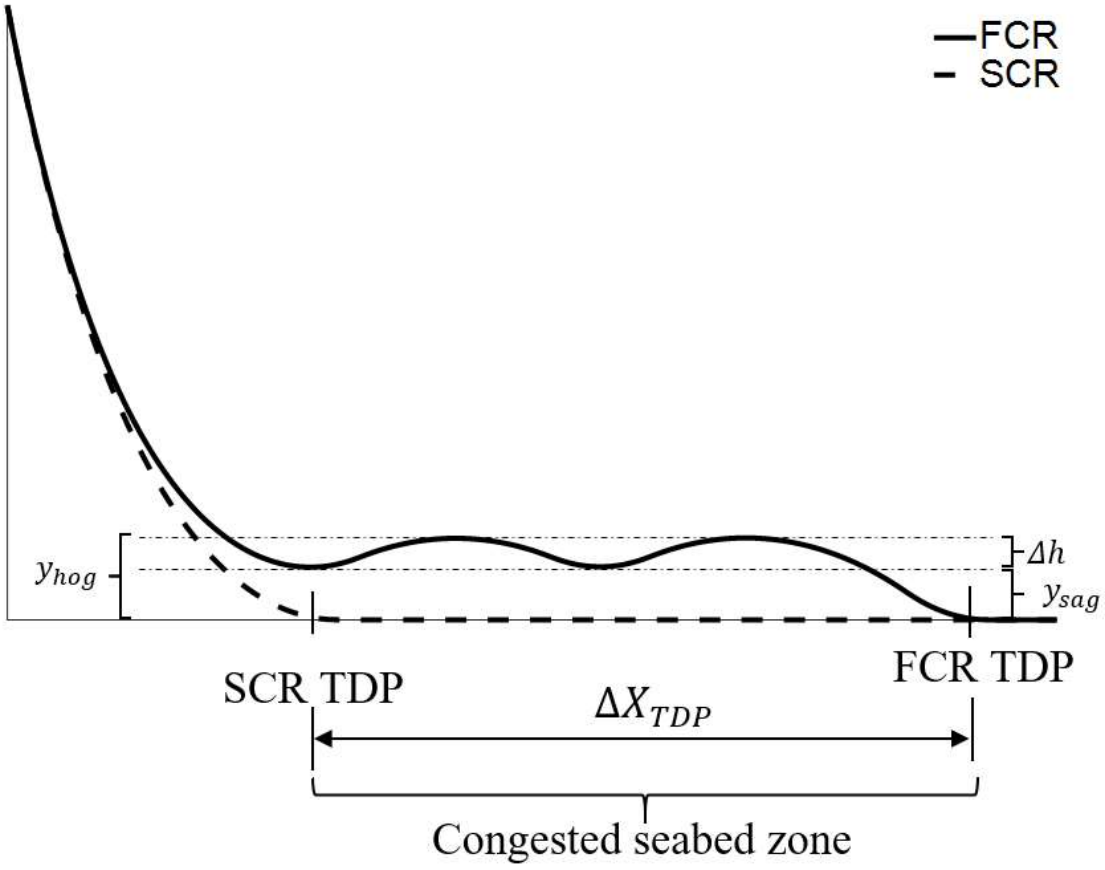

Figure 6-1. Floating catenary and steel catenary riser configuration

The multiple wave buoyant sections also provide the FCR with the capability to decouple its touch down zone (TDZ) from the floating platform motion, a feature typical of steel lazy wave riser (SLWR). This can result in reduced stress and fatigue damage around the touchdown zone (TDZ) when compared with SCR [111]. The configuration development of the FCR was detailed in section 6.2. The buoyancy section is modelled based on the apparent mass ratio concept.

6.2 The floating catenary riser system configuration development

The FCR concept presented in Figure 6-1 is a specific type of the double wave riser configuration shown in Figure 6-2, where the arc heights of the two bends are equal, i.e. Δh ($\Delta h_1 = \Delta h_2$), and the sag elevations are equal, i.e. y_{sag} ($y_{sag1} = y_{sag2}$). One approach to developing the initial configuration of the double wave riser for numerical modelling is by decomposing the riser profile into nine (9) basic catenaries, each having its own local origin, as shown in Figure 6-2 (b). Each of the sub catenaries is calculated, referencing their local coordinate systems and origins. They can all be assembled to form the global riser configuration with the global origin at the TDP (point a). The length of the first and second smeared buoyancy sections are $sb_1 = s_2 + s_3$ and $s_{b2} = s_6 + s_7$, where the total buoyant section length is $S_b = s_{b1} + s_{b2}$. Given the configuration height (h_d), the hang-off angle with the horizontal (θ), the sag elevations (y_{sag} and y_{sag2}) and the hog elevations (y_{hog1} and y_{hog2}), equation (6-1) to equation (6-11) can be developed from the catenary equations presented in 3.1.1, for each of the sub catenaries. The horizontal tension component (H) along the profile is constant to ensure continuity of line curvatures across the boundaries of the sub-catenaries. The configuration variables x_i, y_i and s_i are the horizontal distances, the vertical distances, and arc lengths of each sub catenaries $i = 1, 2, \dots, 9$ from a towards the hang-off. The submerged weight of the bare riser pipe is w and w_{b1} and w_{b2} are the submerged weights of the two buoyancy sections. Equation (6-12) is the assembling equation of all sub catenaries expressions.

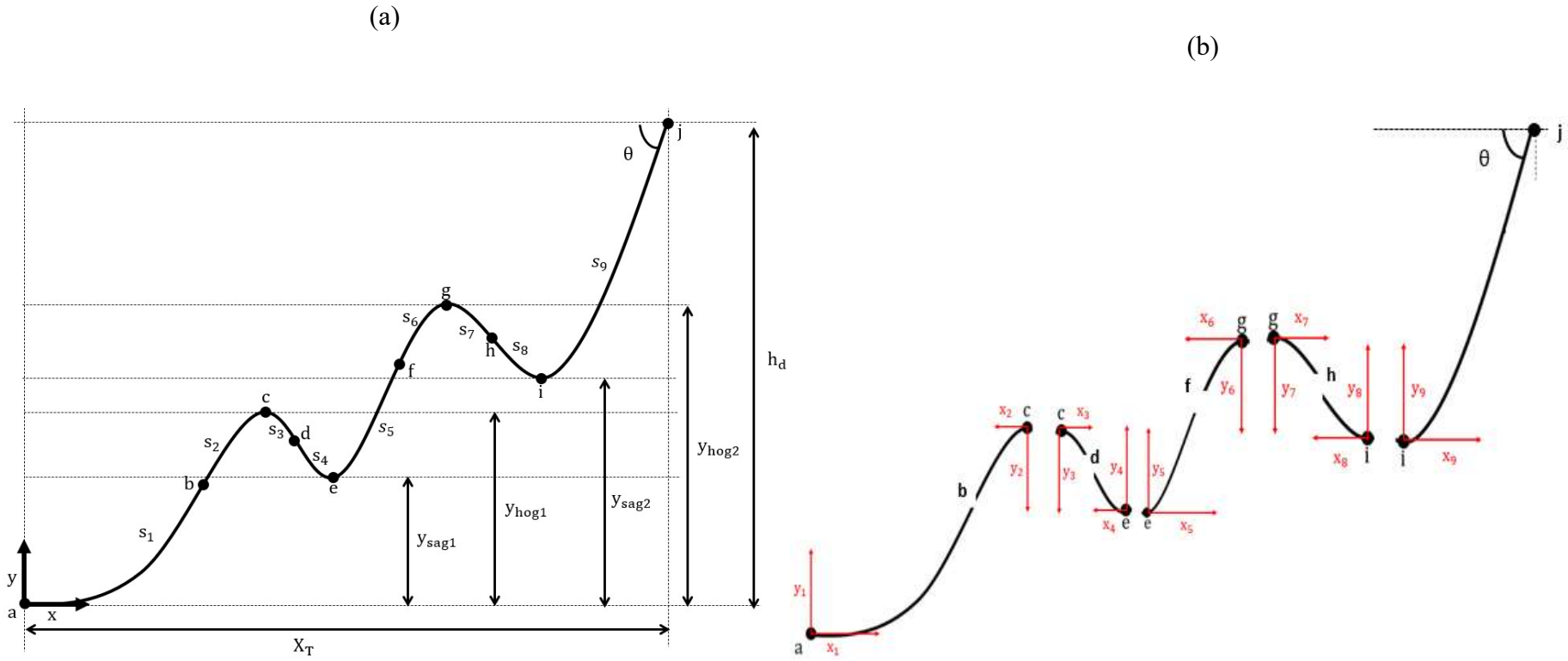

Figure 6-2. (a) - A generic two-wave configuration, (b) – component catenaries of the double wave configurations

$$\boldsymbol{y_9 = h_T - y_{sag2}} \tag{6-1}$$

$$H = H_9 = \frac{wy_9}{(tan\,\theta)^2}(1 + sec\,\theta) \tag{6-2}$$

$$\begin{cases} x_9 = \dfrac{H}{w} cosh^{-1}\left(\dfrac{wy_9}{H} + 1\right) \\ s_9 = \dfrac{H}{w} sinh\left(\dfrac{wx_9}{H}\right) \end{cases} \tag{6-3}$$

$$\begin{cases} y_8 = \dfrac{w_{b2}}{(w + w_{b2})}\left(y_{hog2} - y_{sag2}\right) \\ x_8 = \dfrac{H}{w} cosh^{-1}\left(\dfrac{wy_8}{H} + 1\right) \\ s_8 = \dfrac{H}{w} sinh\left(\dfrac{wx_8}{H}\right) \end{cases} \tag{6-4}$$

$$\begin{cases} y_7 = \dfrac{w}{w_{b2}} y_8 \\ x_7 = \dfrac{H}{w_{b2}} cosh^{-1}\left(\dfrac{w_{b2}y_7}{H} + 1\right) \\ s_7 = \dfrac{H}{w_{b2}} sinh\left(\dfrac{wx_7}{H}\right) \end{cases} \tag{6-5}$$

$$\begin{cases} y_6 = \dfrac{w}{(w + w_{b2})} y_{hog2} \\ x_6 = \dfrac{H}{w_{b2}} cosh^{-1}\left(\dfrac{w_{b2}y_6}{H} + 1\right) \\ s_6 = \dfrac{H}{w_{b2}} sinh\left(\dfrac{w_{b2}x_6}{H}\right) \end{cases} \tag{6-6}$$

$$\begin{cases} y_5 = \dfrac{w_{b2}}{(w + w_{b2})} y_{hog2} \\ x_5 = \dfrac{H}{w} cosh^{-1}\left(\dfrac{wy_5}{H} + 1\right) \\ s_5 = \dfrac{H}{w} sinh\left(\dfrac{wx_5}{H}\right) \end{cases} \tag{6-7}$$

$$\begin{cases} y_4 = \dfrac{w_{b1}}{w + w_{b1}}\left(y_{hog1} - y_{sag1}\right) \\ x_4 = \dfrac{H}{w} cosh^{-1}\left(\dfrac{wy_4}{H} + 1\right) \\ s_4 = \dfrac{H}{w} sinh\left(\dfrac{wx_4}{H}\right) \end{cases} \tag{6-8}$$

$$\begin{cases} y_3 = \dfrac{w}{w + w_{b1}}\left(y_{hog1} - y_{sag1}\right) \\ x_3 = \dfrac{H}{w_{b1}} cosh^{-1}\left(\dfrac{w_{b1}y_3}{H} + 1\right) \\ s_3 = \dfrac{H}{w_{b1}} sinh\left(\dfrac{w_{b1}x_3}{H}\right) \end{cases} \tag{6-9}$$

$$\begin{cases} y_2 = \dfrac{w}{w + w_{b1}} y_{hog1} \\ x_2 = \dfrac{H}{w_{b1}} cosh^{-1}\left(\dfrac{w_{b1}y_2}{H} + 1\right) \\ s_2 = \dfrac{H}{w_{b1}} sinh\left(\dfrac{w_{b1}x_2}{H}\right) \end{cases} \tag{6-10}$$

$$\begin{cases} y_1 = \dfrac{w_{b1}}{w + w_{b1}} y_{hog1} \\ x_1 = \dfrac{H}{w} cosh^{-1}\left(\dfrac{wy_1}{H} + 1\right) \\ s_1 = \dfrac{H}{w} sinh\left(\dfrac{wx_1}{H}\right) \end{cases} \tag{6-11}$$

$$X_T = \sum_{i=1}^{9} x_i \,; h_T = \sum_{i=1}^{9} y_i \,; S_T = \sum_{i=1}^{9} s_i \tag{6-12}$$

In this thesis, only the case where $y_{sag1} = y_{sag2} = y_{sag}$ and $\Delta h_1 = \Delta h_2 = \Delta h$ is considered, which is the floating catenary riser (FCR). Interestingly, the derived double wave bend configuration expressions can degenerate to simple catenary and lazy wave risers by the appropriate setting of the configuration variables, as seen in Table 6-1 is derived from a double wave configuration in a water depth of 1500 m, having a hang-off at the mean sea level and an angle of 12 deg with the vertical. These configurations in Table 6-1 are calculated with one of the MATLAB subroutines developed and are presented in Figure 6-3.

Table 6-1 – Examples of double wave configurations and their derivatives.

ID	Configuration	Configuration variable (m)					
		y_{sag1}	y_{sag2}	y_{hog1}	y_{hog2}	Δh_1	Δh_2
a	Steel catenary riser	0	0	0	0	0	0
b	Steel lazy wave riser	0	200	0	300	0	100
c	Double wave riser	200	900	300	900	100	0
d	Double wave riser	200	800	300	900	100	100
e	Double wave riser	200	600	200	700	0	100
f	Double wave riser	100	900	100	900	0	0
g	Double wave riser (FCR)	100	100	300	300	100	100
h	Double wave riser (FCR)	600	600	700	700	100	100

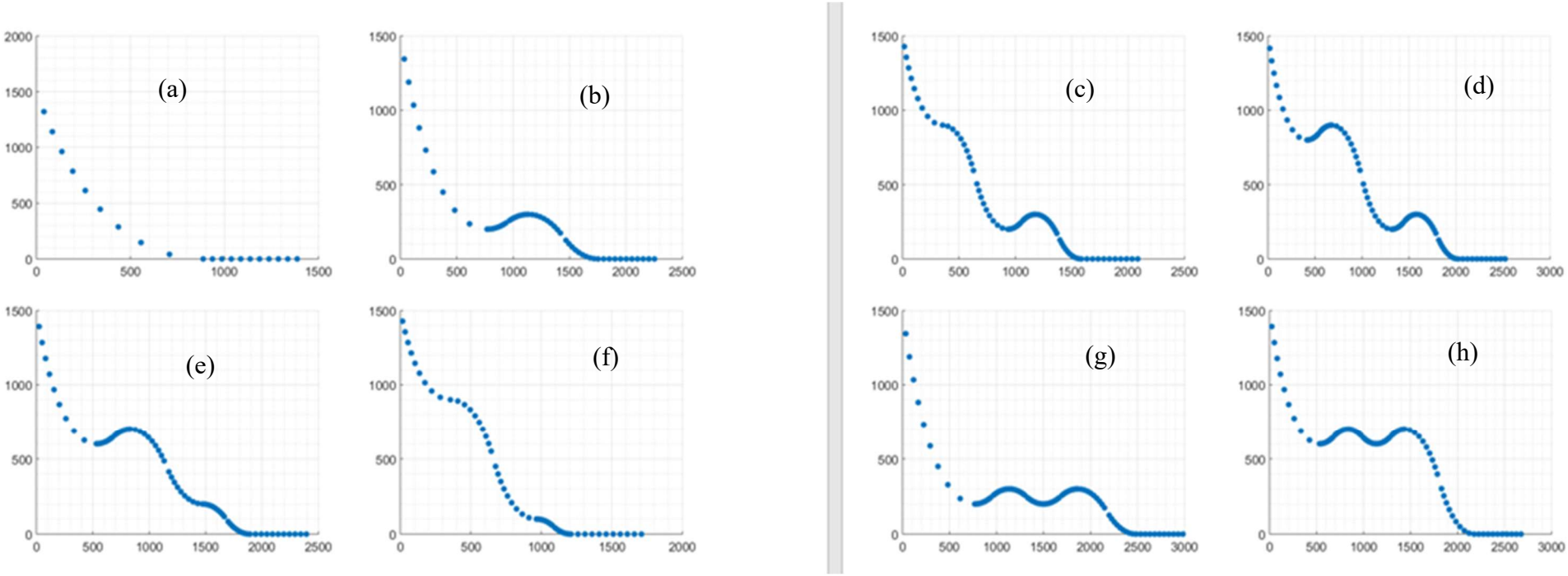

Figure 6-3. Double wave configurations and derivatives calculated from a MATLAB program based on the derived FCR configuration expressions.

6.3 Global response study of FCR

6.3.1 Analysis data and methodology

The risers investigated in this study are of 12-inch X70 grade pipes. X70 grade pipe are selected as they provide reduced payload on the vessel. They are hosted by a generic floating production, storage, and offloading unit at azimuths of 90deg to the vessel heading. The minimum required pipe wall thickness are calculated using DNV-OS-F201 burst and collapse resistance criteria [4]. Table 4-7 presents the riser data. A generic response amplitude operator (RAOs) for the floating production unit is implemented. Details of the default nonlinear hysteretic riser soil interaction model applied for the analyses can be found in [56]. The two current profiles investigated for the riser systems are presented in Figure 6-4. The direction of the current is perpendicular to the riser plane to impose the highest lateral drift effect on the risers. The two irregular beam wave loads simulated for the combined load and fatigue analysis are presented in Table 6-3. The peakedness parameter, γ, is calculated based on [96]. The drag coefficients presented in Table 4-7 are chosen with reference to the smooth pipe outer diameter. For practical purposes, this value ranges between 0.7 and 1.0 [112], and a value of 0.7 is selected for the bare pipe section in this study. However, due to the increased diameter of the smeared buoyancy system over the bare pipe section, a conservative drag coefficient of 1.2 is applied for the buoyancy section. The storm wave load selected for the study is typical with Brazil (Campos Basin) 100years return period sea state condition [113]. One of the dominating fatigue sea state condition obtained from fatigue wave scatter is applied for the fatigue analysis, with a probability of occurrence taken as 1. The selected current profile-2 is a 10years return period current with a surface velocity of 1.6m/s [113]. This decreases to 0.1m/s close to the seabed. The constant current profile-1 is theoretical and is only applied to investigate the FCR behaviour under constant current drag load acting on it throughout the water column.

The initial configurations for the risers are developed for the FE models using the catenary expressions presented earlier and simulated for the static vessel offset condition, vessel-current load conditions, vessel-current-wave load conditions, and fatigue wave load condition. The numerical simulations of the models are conducted using the OrcaFlex software package. The model pre-processing and post-processing are carried out using MATLAB programs integrated with the OrcaFlex programming interface (OrcFxAPI [82]). The program is used to generate the initial riser configuration for the OrcaFlex models using the FCR equations developed in

6.2. The riser stress utilisations are calculated using the DNV-OS-F201 combined load resistance factor design [4]. The fatigue damage is computed using the rain flow counting technique [98], implementing the S-N D curve for seawater [97].

Table 6-2. Riser data.

Riser data	**Values**
Pipe size (D_o)	12inch
Internal Design pressure	10ksi
Pipe thickness	27.5mm
Hang off angle with the vertical (90 – θ)	12^o
Content density	600kg/m^3
Buoyancy material density (ρ_b)	500kg/m^3
Water depth (h_T)	1500m
Drag coefficient for the bare pipe section	0.7
Drag coefficient for the smeared buoyant section	1.2
Sag elevation (y_{sag})	Vary
Arc height (Δh)	Vary
Apparent mass ratio (AMR)	Vary

Table 6-3. Combined and fatigue wave load data.

Analyses	**Wave type**	**Data**	**Values**
Storm	Irregular wave	H_s(m)	8
		T_p(sec)	13
		γ	1.6
Fatigue	Irregular wave	H_s(m)	4.5
		T_p(sec)	9.5
		γ	1.8

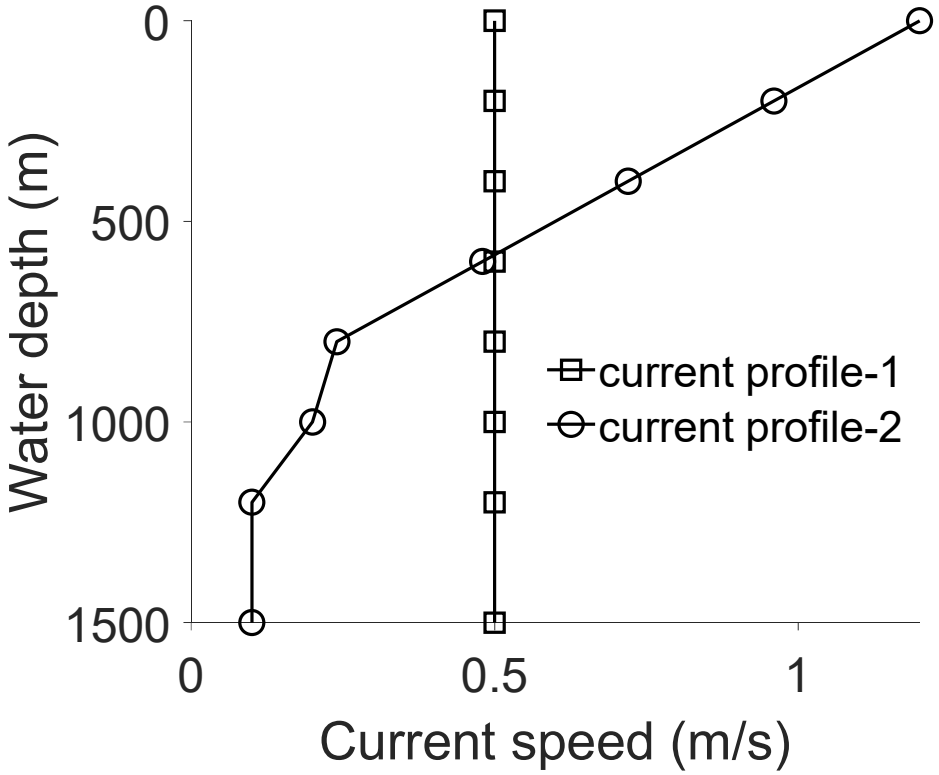

Figure 6-4. Current load profile for analysis.

6.3.2 Analysis results and discussions

6.3.2.1 Controlling the FCR buoyant section geometry with AMR

The AMR can serve as a single parameter used to vary the geometry (length, thickness, and diameter) of the smeared buoyancy section. To briefly demonstrate the variation of s_{b1}, s_{b2}, S_b and t_b with AMR, an example of FCR with y_{sag} =100m and Δh = 70m is presented in Figure 6-5. It could be observed that increasing (or decreasing negative) values of AMR provide smaller t_b and a corresponding longer smeared buoyancy section to achieve a given buoyancy capacity. It can also be observed from Figure 6-5 that the buoyancy section 1, $s_{b1} = s_2 + s_3$ is longer than the buoyancy section 2, $s_{b2} = s_6 + s_7$ for a given AMR. This is expected since the length of the section of the FCR that is lifted by s_{b1} is longer than that lifted by s_{b2}. Hence, the higher required buoyancy capacity of s_{b1} than s_{b2} (both having equal t_b from equal AMR) is compensated by the increased length of the buoyancy section of s_{b1}.

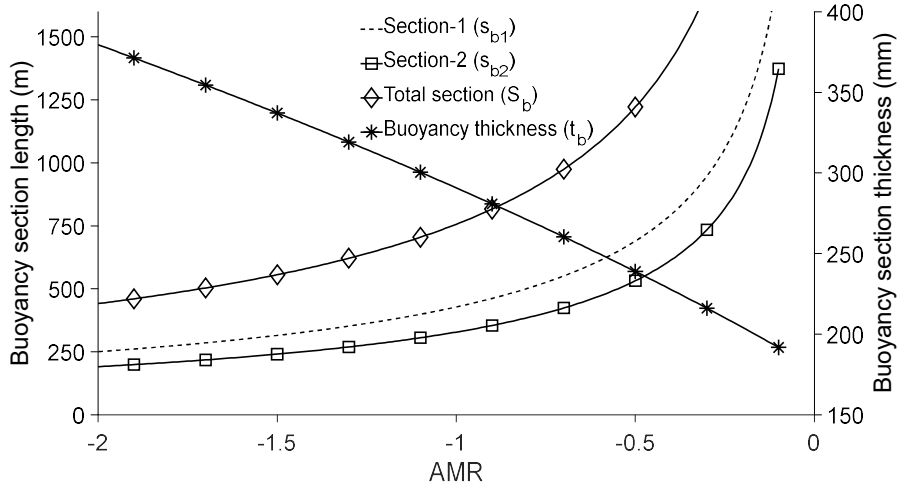

Figure 6-5. Influence of AMR on buoyancy section geometry.

In this sub-section, we demonstrate the influence of $y_{sag}, \Delta h,$ and θ on the FCR configurations and how these affect the desired ΔX_{TDP}. Six pairs of y_{sag} and Δh, which are {(70m, 10m), (70m, 50m), (70m, 70m), (100m, 10m), (100m, 50m), (100m, 70m)} are simulated for varying values of AMR from -0.15 to -2.00. The considered water depth is 1500m, and the FCRs hang off angle with the vertical (90 - θ) is 12deg. For the same water depth and hang-off angle, a base SCR configuration is calculated and its TDP relative with the FCR TDPs (ΔX_{TDP}), is then obtained. The resulting configuration curves are presented in Figure 6-6 (a). For all six combinations of y_{sag} and Δh, the ΔX_{TDP} increases with increasing (or decreasing negativity) AMR. It could be observed from the curves that in terms of a given AMR, it is easier to achieve a desired ΔX_{TDP} for configurations having higher Δh. In fact, increasing the y_{sag} for a given AMR, will have little contribution to the enhancement of ΔX_{TDP}. For example, comparing the configuration corresponding with $(y_{sag}, \Delta h) =$ (70m, 10m), and (100m, 10m), the resulting ΔX_{TDP} are close match. However, for configuration corresponding to $(y_{sag}, \Delta h) =$ (70m, 10m), and (70m, 50m), the ΔX_{TDP} can be increased by more than 500m for a given AMR. Hence, Δh is seen to be a significant influencer of the magnitude of the span that can be achieved for the FCRs for a given AMR. Although in this study, a fixed value of hang off angle (12deg) with the vertical is considered, it may be obvious that ΔX_{TDP} can be increased with increasing hang off angle.

From Figure 6-6 (a), there are an infinite number of FCR configurations that can be derived from the curves, i.e., from different combinations of the FCR configuration variables - $y_{sag}, \Delta h$ and AMR. However, the key idea behind the FCR concept development is to provide

the desired span over the congested section of the seabed. If, for example, ΔX_{TDP} = 1.2km (1200m) is desired, a horizontal line drawn through this point on the ordinate axis intersects the curves at six points, giving six FCR configurations from Figure 6-6(a). The global configurations of these six FCRs and the base SCR configurations have been presented in Figure 6-6 (b). A common X_{TDP} and ΔX_{TDP} can be observed for the FCR configurations. However, the configurations are different since unique combinations of the FCR variables resulted in them. Additional configuration details such as the length of the smeared buoyancy sections (s_{b1} and s_{b2}), The overall riser hanging section length (S_T) (see equation (6-12)), the thickness of the smeared buoyancy material (t_b)(see equation (3-44), the displacement per unit length of s_{b1} and s_{b2} sections (∇_b) and the overall displacement of s_{b1} and s_{b2} sections ($\nabla_{b_T} = \nabla_b(s_{b1} + s_{b2})$) are presented in Table 6-4. Note that the outer diameter of the smeared buoyancy section, D_b is $D_o + 2t_b$, where D_o is the outer diameter of the bare pipe. The total displacem`ent of the buoyant sections is seen to be higher for higher Δh values since higher buoyancy capacity is required for higher uplift of the riser hog elevation (y_{hog}). As will be seen shortly, the stress and fatigue response of the FCRs decreases with increasing compliance of the FCR. The compliancy of the FCR is their ability to accommodate stress and fatigue responses, and this requires increased Δh and, consequently, increased ∇_{b_T}.

Recall from Figure 6-5 that t_b decreases with increasing AMR, resulting in shorter lengths (S_b) of the buoyancy section to provide a given buoyancy capacity, as seen in Table 6-4. The converse is the case for decreasing values of the AMR. The total hanging length, S_T, of the FCR is jointly affected by the y_{sag}, AMR, Δh and θ for a fixed water depth h. It is interesting to note that the SCR length from the hang off to the common TDP of the FCRs is not significantly different from those of the FCRs (see S_T values in Table 6-4). This may be attributed to the SCR taking a longer path in its seabed approach compare with the FCRs, although long paths are also seen for the FCRs caused by their wave bend paths. One of the optimisation objectives of the FCR system should be to ensure a minimum difference in S_T of the SCR and the optimum FCR. The lateral deflection, seabed clearance, stress and fatigue damage responses of the six unique FCR configurations in Figure 6-6 (b) will now be investigated under extreme vessel offsets, current loads, combined loads, as well as fatigue wave load, to demonstrate the FCR global feasibility

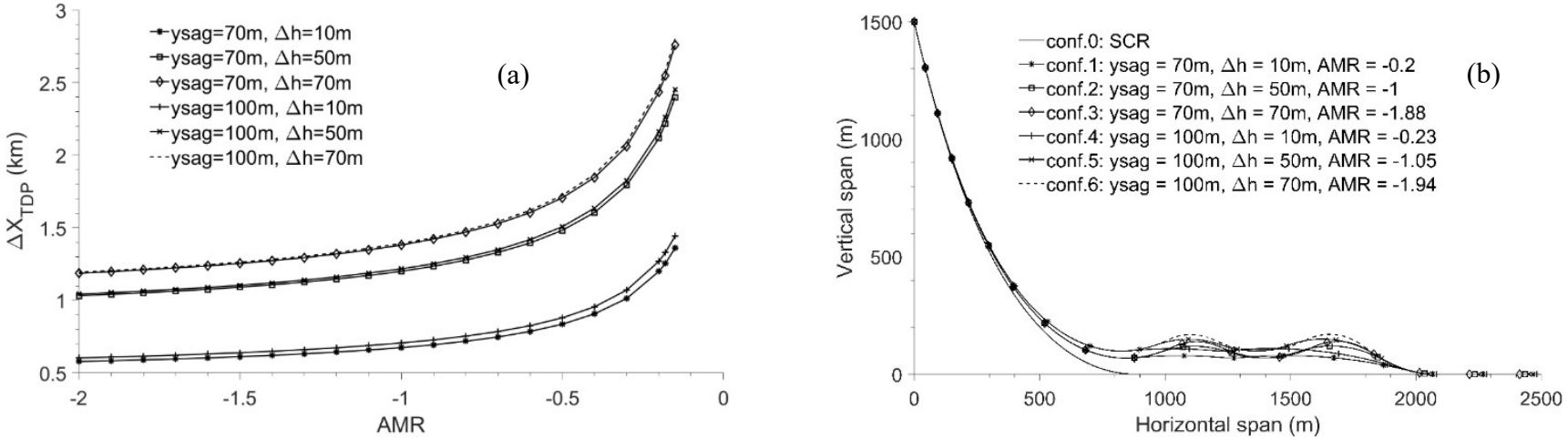

Figure 6-6. (a) – Influence of FCR configuration variables on $\boldsymbol{\Delta X_{TDP}}$, (b) – Selected six configurations that provide $\boldsymbol{\Delta X_{TDP}}$ =1.2km.

Table 6-4. Selected FCRs configuration details.

Conf	Riser type	y_{sag} [m]	Δh [m]	AMR [-]	s_{b1} [m]	s_{b2} [m]	S_b [m]	t_b [m]	D_b [m]	∇_b [te/m]	∇_{b_T} [te]	S_T^* [m]	X_{TDP}^{**} [m]	ΔX_{TDP}^{**} [m]
0	SCR	-	-	-	-	-	-	-	-	-	-	3053.00	885.44	0
1	FCR	70	10	-0.20	681.72	354.11	1035.83	0.20	0.70	0.40	414.22	3014.25	2085.44	1200.00
2	FCR	70	50	-1.00	359.81	278.52	638.32	0.29	0.88	0.63	402.30	3046.26	2085.31	1199.87
3	FCR	70	70	-1.88	249.03	202.94	451.97	0.37	1.04	0.88	397.18	3071.86	2085.70	1200.26
4	FCR	100	10	-0.23	703.39	322.77	1026.16	0.21	0.72	0.42	433.98	2996.61	2082.00	1196.56
5	FCR	100	50	-1.05	370.76	265.84	636.60	0.30	0.90	0.66	419.55	3038.01	2086.69	1201.25
6	FCR	100	70	-1.94	256.81	195.83	452.64	0.37	1.04	0.88	397.77	3063.50	2085.17	1199.73

6.3.2.2 Extreme vessel offsets analysis

One of the most critical design variables to be observed for the extreme vessel offsets of the FCRs is the minimum seabed clearance of the wave bends sections depicted in Figure 6-7. The minimum seabed clearance is taken to be the minimum vertical distance between the bottom section of the FCR wave bends and the seabed. The feasibility of the FCR depends on its configuration performance in extreme offsets conditions, especially the near offset condition, which can result in a significant reduction in the nominal seabed clearance, hence defeating the FCR application need.

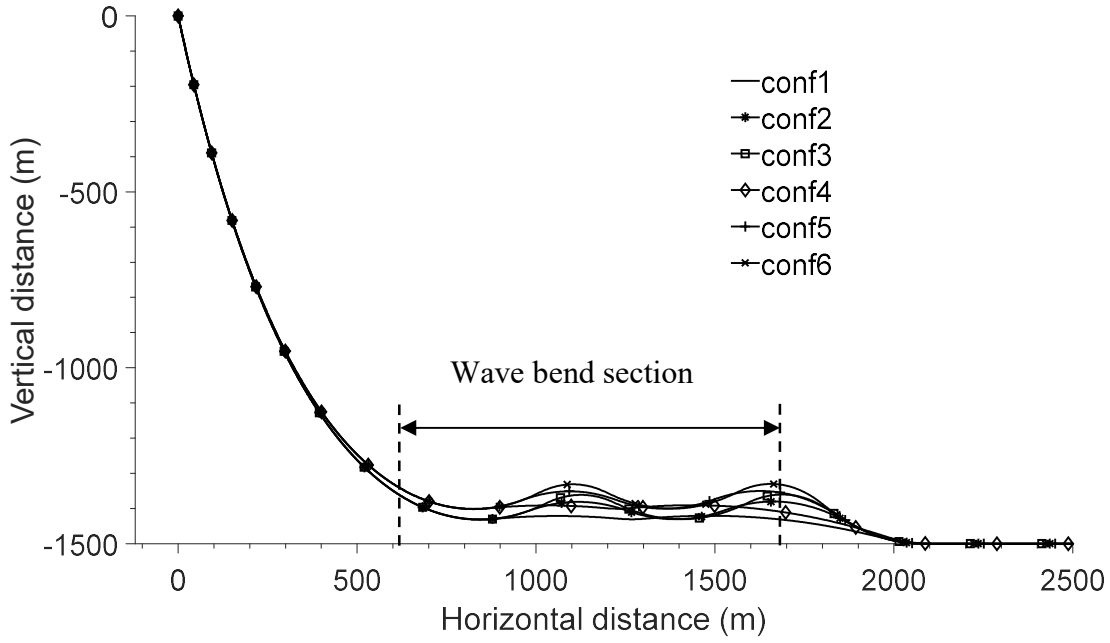

Figure 6-7. Wave bend section for which critical seabed clearance should be checked in extreme vessel far and near offsets.

A vessel offsets of 8% of the water depth ($h = 1500$m) in the near direction (towards the risers' seabed anchor) and the far direction (away from the risers' seabed anchor) are imposed on the FCRs. The resulting global configurations for the near and far offsets are respectively presented in Figure 6-8 (a) and (b). The criticality of the seabed clearance can be seen for the extreme near configurations in Figure 6-8 (a) around the wave bend on the vessel side, caused by the global compression of the FCRs. The far configuration resulted in the increase of the nominal seabed clearance, as seen in Figure 6-8 (b), caused by the stretching of the global riser configuration. A comparison of the seabed clearance for the nominal, the near and far vessel offset configurations are presented in Figure 6-8 (c). Figure 6-8 (d) shows the percentage difference of the FCRs seabed clearances in their offsets positions relative to the nominal

seabed clearance. For all the six FCR configurations considered in this analysis, the nominal clearance can be reduced by more than 40% compared with the nominal configuration. The clearance reduction can be as high as 85% for conf-1, which has the smallest y_{sag} and Δh as seen in Figure 6-8 (d). Considering the FCR configurations of equal y_{sag}, increasing Δh will result in little improvement of the resulting minimum clearance for the FCRs in their near configuration. For example, for conf-2 and conf-3 with equal y_{sag} of 70m, but with respective Δh of 10m and 50m, the seabed clearance for conf-3 in the near configuration is around 10% higher than conf-2. The reverse is the case for the far configuration where increasing values of Δh for fixed y_{sag} performs less in terms of the minimum seabed clearance, although these clearances are still higher than those of the nominal configuration. Significant performance in the seabed clearance can be achieved in the FCR near configurations, for higher y_{sag} values. For example, comparing conf-1 and conf-4, with equal $\Delta h = 10m$ and different y_{sag} of 70m and 100m respectively, conf-4 can perform more than conf-1 up to 30%. These seabed clearance behaviours of the FCRs indicate that clearance performance in the extreme near configuration can be jointly improved by increasing y_{sag} and Δh. However, these increases will imply an increase in the required buoyancy capacity. Hence, there is a need to strike a balance between the FCR performance in terms of the minimum seabed clearance in the extreme near offset condition and the cost associated with the buoyancy capacity required for the configuration.

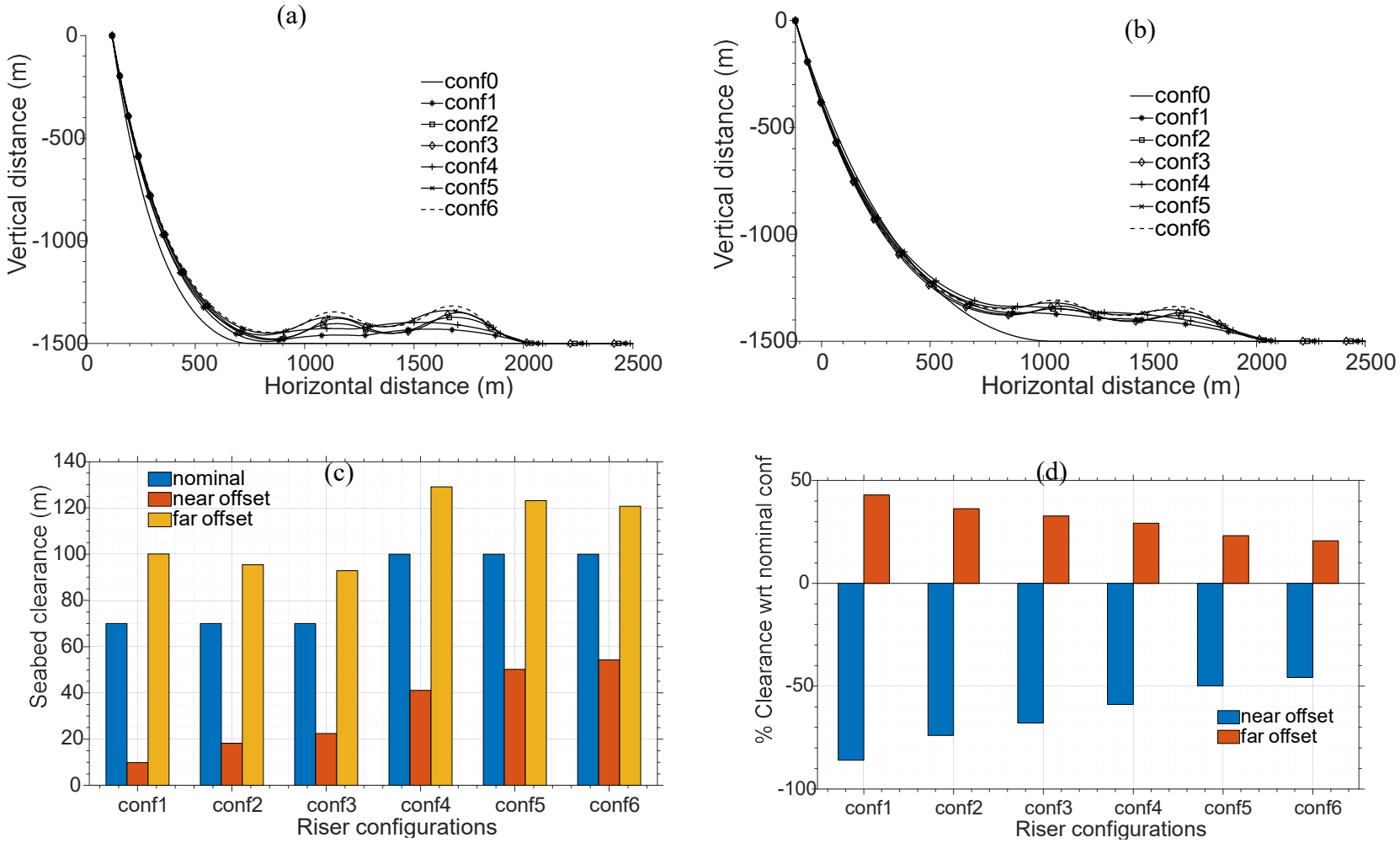

Figure 6-8. (a) risers' configurations in the vessel's extreme near offset condition, (b) risers' configurations in the vessel's extreme far offset condition, (c) minimum seabed clearance of the FCRs in the vessel's extreme nominal, near and far offset conditions, (d) minimum eabed clearance relative to the nominal seabed clearance expressed in percentages.

6.3.2.3 Current loading analysis

Current loads impose statical drift effects on the risers, causing them to deflect globally. The risers' lateral deflections are of more importance since excessive deflection in this direction can result in functional failure of the riser systems as well as interference with other neighbouring systems. The magnitude of the lateral deflection is dependent on the current profile velocities, the drag coefficients of the riser section, the projected drag area of the riser to the current flow direction, and the global stiffness of the riser, which depends on effective tension distribution. The projected hydrodynamic areas of the risers are presented in Figure 6-9, for the bare pipe, the buoyancy, and the sum of both the bare pipe and the buoyancy sections. It could be seen that the projected areas of the smeared buoyancy sections for all FCR configurations, except conf-1 and conf-4, are larger than the projected area of the bare pipe sections. Also, the drag coefficient of the smeared buoyancy section can be higher than that of the bare pipe section. In this work, the drag coefficients for the smeared buoyant section and the bare pipe section are taken to be 1.2 and 0.7, respectively (see Table 4-7).

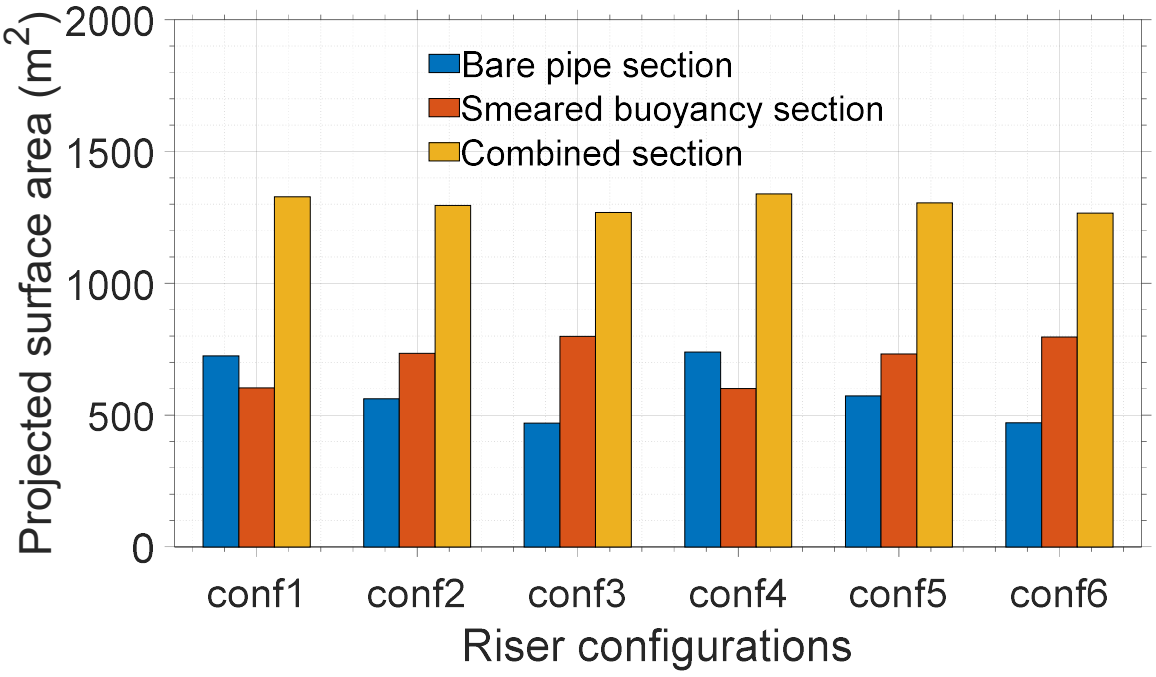

Figure 6-9. Projected surface areas of FCRs to current cross flow

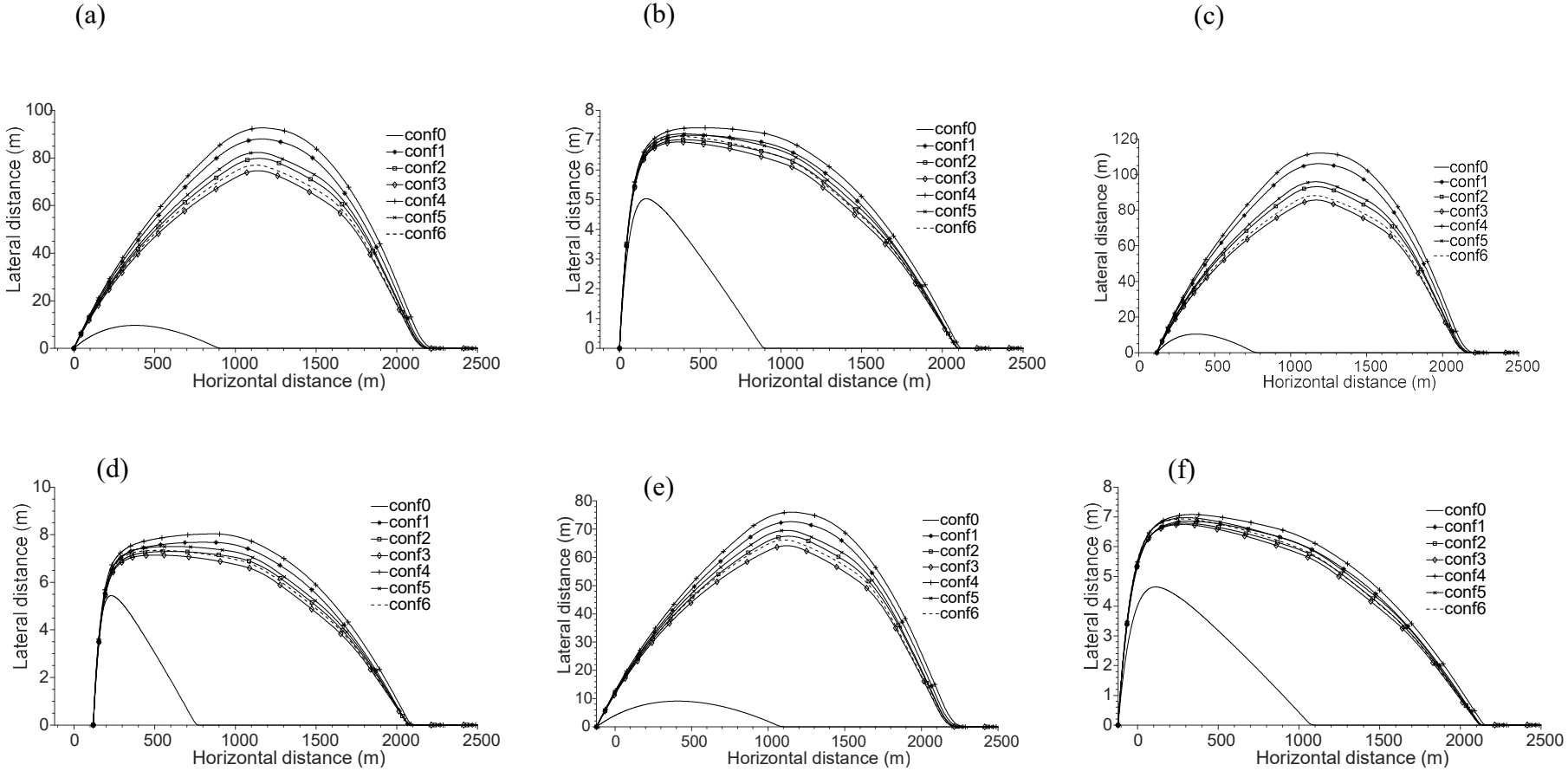

Figure 6-10. Minimum seabed clearance for FCRs under (a) nominal offset condition plus current profile-1, (b) nominal offset condition plus current profile-2, (c) near offset condition plus current profile-1, (d) near offset condition plus current profile-2, (e) far offset condition plus current profile-1, (f) near offset condition plus current profile-2

The two current profiles (profile-1 and profile-2) are imposed on the risers in the nominal, near and far vessel offset conditions. The static lateral deflection responses of the risers under current loads and vessel offsets are presented in Figure 6-10. The current load intensity of current profile-1, being more intensive than current profile-2, resulted in the highest lateral deflections for the same vessel offset conditions. This is observed when Figure 6-10 (a), (c) and (e) are respectively compared side by side with Figure 6-10 (b), (d) and (f). The near vessel offset is the most critical offset condition for which the riser being in global compression (increased slackness) has reduced global stiffness to the current load. The highest lateral deflections of the risers under current profile-1, in the near offset condition, is observed to be about 120m. On the other hand, the maximum deflection under current profile-2 in the near vessel offset condition is about 8m. However, it should be noted that the constant velocity profile-1 is unrealistic but can be useful for investigating a novel system like this. For each of the vessel offset positions and current profiles combination, the FCRs experienced different magnitudes of lateral deflections. The lateral deflection increases for conf-3, conf-6, conf-2, conf-5, conf-1, and conf-4, in that order. This order corresponds with the magnitude of the combined projected area presented in Figure 6-9, indicating the influence the hydrodynamic area of the riser can have on their global deflection under current load. The riser seabed clearances under current drift conditions are expected to be less critical compared with the cases where only vessel offsets are applied. This is because the lateral deflection of the risers will reduce the vertical clearance component from the seabed.

The general conclusion from the lateral deflection behaviour of the FCRs is that they may be functionally limited in an environment where there exist intensive current profiles close to the seabed. This is because the largest projected area of the riser to current flow and largest current drag force exists on FCR sections close to the seabed. However, the FCR should be feasible in an environment with a minimum current profile close to the seabed, such as current profile-2 investigated in this study. Riser interference may be less of a problem since little difference in the riser plane (angular deviation on the horizontal plane) will result in a large gap of the FCR wave bends close to the seabed, considering deepwater. Also, the current load impact on neighbouring FCRs will result in a drift of the risers in the same direction, keeping their nominal distance almost unchanged, except in cases where the risers undergo large amplitude motions under VIV. This can be designed out following practical design recommendations [105].

6.3.2.4 Seabed clearance under extreme and damaged vessel condition

In addition to the extreme offsets, excess vessel heel caused by vessel damage condition may also impact the seabed clearance of the FCRs wave bends. The vessel damaged condition is modelled by imposing static vessel heel of 8deg in the direction of riser azimuth on the extreme vessel offsets, storm wave load and the current profile-2. Both the FCRs' seabed clearances under extreme and damaged conditions are compared with those of the static nominal FCRs configurations to observe their influence on the FCRs.

The FCRs' minimum seabed clearances under extreme condition (storm wave load, vessel offsets and current profile-2) are presented in Figure 6-11. The minimum seabed clearances under vessel damaged conditions (storm wave load, vessel offsets, current profile-2 and vessel heel of 8deg) are presented in Figure 6-12. For the FCRs considered in this study, the nominal and far vessel offset conditions for both extreme and damage scenarios provide no threat to the seabed clearance of the FCRs. However, the near vessel offset condition can significantly negatively impact the FCRs' seabed clearances under these conditions.

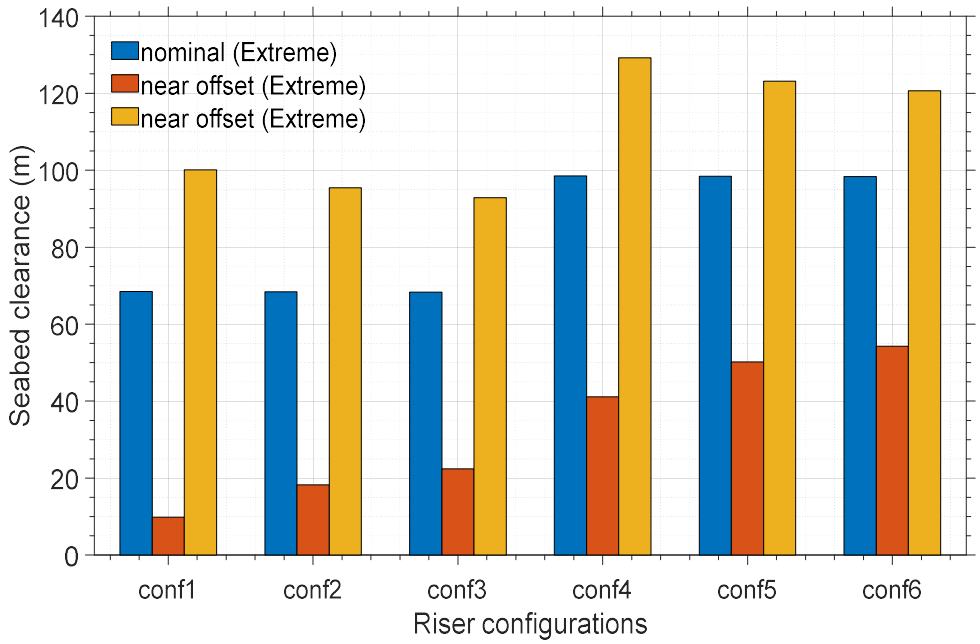

Figure 6-11. Minimum seabed clearances of FCRs during combined load extreme conditions (storm wave, current profile-2, and vessel offsets)

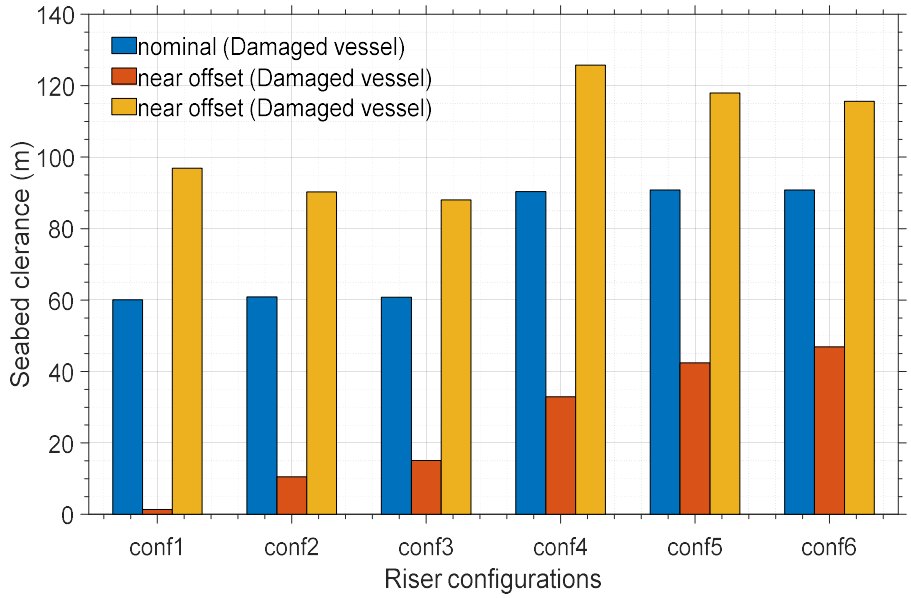

Figure 6-12. Minimum seabed clearances of FCRs during combined load and vessel damaged conditions (storm wave, current profile-2, vessel offsets and vessel damaged condition)

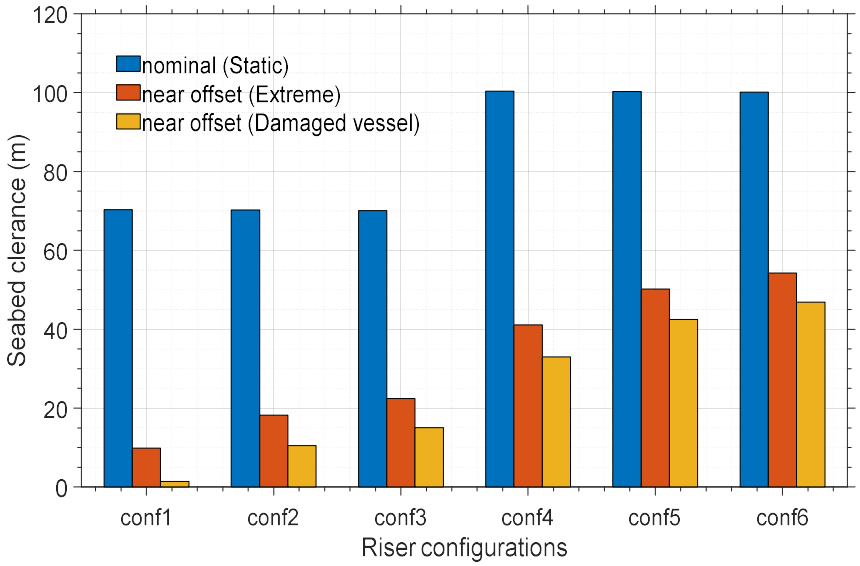

Figure 6-13. Minimum seabed clearance of FCRs in static nominal vessel position compared with the seabed clearance of FCRs in near vessel offset for extreme and vessel damaged conditions.

The minimum seabed clearances for the near vessel offsets for both the extreme and the damaged conditions are compared with seabed clearances of the static nominal FCR configuration in Figure 6-13. It could be observed from Figure 6-13 that the seabed clearance requirement can be violated when the vessel is damaged and in its near offset configurations. Hence, the damaged condition at the preliminary stage of FCR configuration selection must be put into consideration to select suitable static FCR profiles that give the required seabed

clearance for all design scenarios. Similar behaviour of seabed clearance reduction is observed for the extreme response, as seen in Figure 6-13. However, the damaged conditions, as expected, is more critical and should be the driver or determining factor that limits the minimum seabed clearance during the FCR design.

6.3.2.5 Dynamic stress utilisation

The storm wave load in Table 6-3, each of the three-vessel offset conditions, and the current profile-2 are jointly imposed on the risers. The wave loads and vessel offsets are applied in the riser azimuth direction, while the current load is applied perpendicular to the riser plane. As a result, there will be time-varying bending moments and resulting stresses, as well as tension generated in the risers. The resulting stresses in the risers are expressed as the stress utilisation computed based on the DNV-OS-F201 combined load criteria [4]. The stress utilisation for the risers in the nominal, near and far offset conditions are presented in in Figure 6-14 (a), (b) and (c), respectively. The highest stress utilisation is observed close to the dynamic TDP of the SCR (conf-0), where a sharp peak of the stress is observed. The reduction in the FCRs' stress utilisation (compared with SCR) is attributed to the decoupling capability of the wave bends of the risers from the vessel motions. This results in the reduced and more regular distribution of the bending stresses along the wave bends and the FCRs' TDZs. A general inspection of the plotted stress utilisation distribution in the FCR wave bend section shows that conf-2 and conf-5 (with $AMR \approx$ -1) have the least stress response in the three vessel offsets condition. It could also be observed that conf-1 and conf-4 (with the shorter Δh) possess higher stress utilisation peaks around the wave bend section and the TDZ as seen in Figure 6-14 (a), (b), (c) and (d). This indicates that the decoupling of the FCR TDZ by the wave bends is dependent on Δh. This stress response behaviour dependency on Δh is similar to that of the SLWR [51]. However, as mentioned earlier, higher Δh will require higher buoyancy capacity and an increased associated riser cost. A balance between the stress response and buoyancy cost need to be considered during the optimisation of such a system. Generally, as observed from the results, the peak stress of FCRs appear to be less sensitive to the different vessel offset conditions under dynamic loading, when compared with those of the SCR.

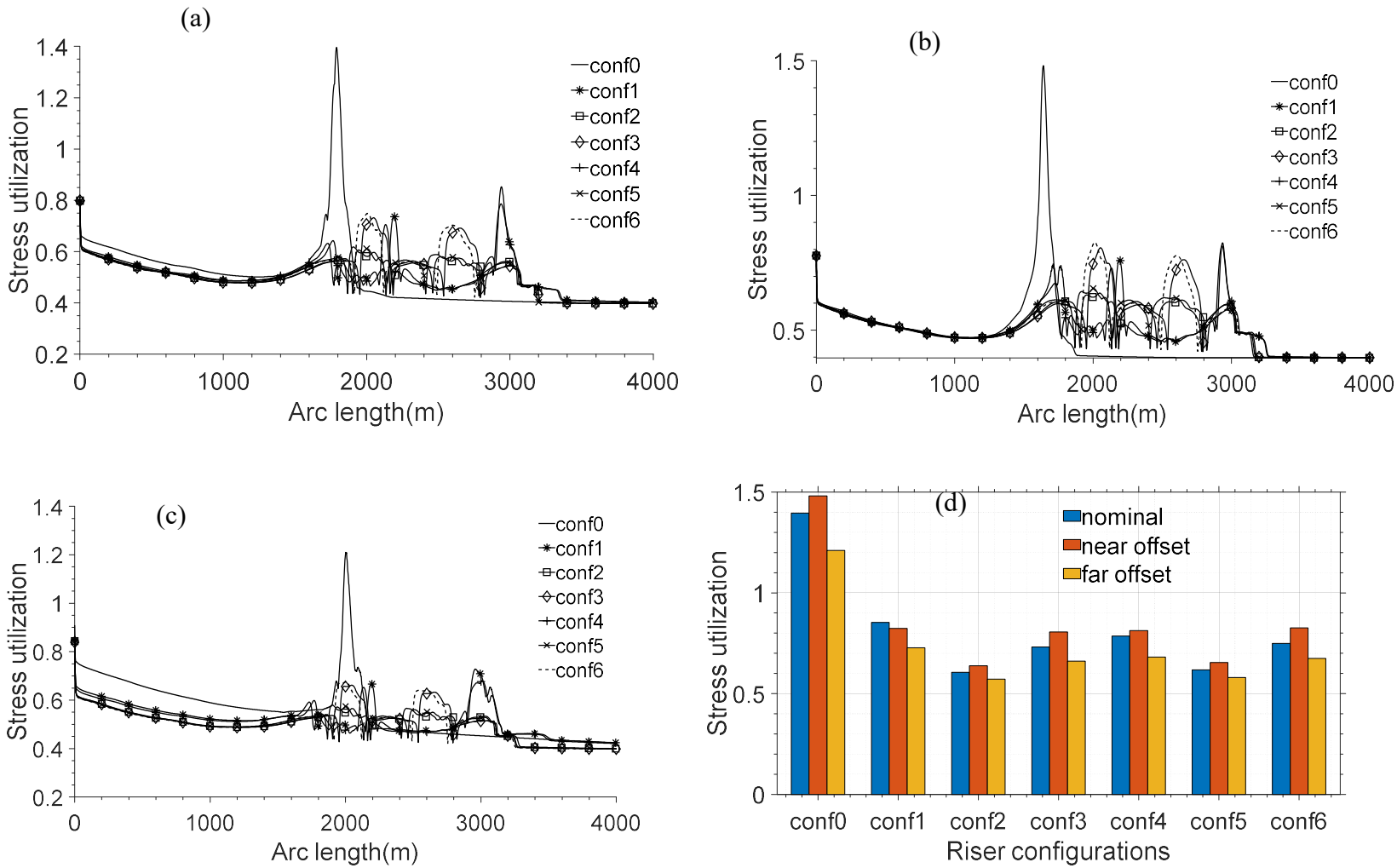

Figure 6-14. (a) Risers stress utilisation (storm wave load, nominal offset, and current profile-2), (b) Risers stress utilisation (storm wave load, near offset, and current profile-2), (c) Risers stress utilisation (storm wave load, far offset, and current profile-2), (d) Bar chart plot comparing stress utilisation for the three combined load scenarios.

6.3.2.6 Dynamic maximum and minimum tension

A characteristic response of the SCR is its high-top dynamic tension, which is higher for larger hang-off angle and deeper water column. The highest top tension is expected to be seen for risers in their far configurations since the longer section of the riser will be hanging for this condition. Therefore, only the dynamic tensions in the risers far offsets are presented in Figure 6-15 (a). However, a comparison of the maximum dynamic top tensions for the riser in the three offsets conditions are presented in Figure 6-15 (c). One of the benefits of the SLWR is the reduced top tension due to the upward pull of a section of the riser. Increased submerged weight reduction is achievable when the buoyancy section is installed on the higher sections of the riser from the seabed. However, for the FCR, the buoyancy modules are installed at the possible lower parts of the riser close to the seabed. Hence, the weight reduction may not be as significant as that of the SLWR. It is worth noting that the FCRs can still achieve an appreciable level of reduction in the dynamic top tensions. As seen in Figure 6-15 (a) and (c), more than 300kN reduction is observed for all FCRs compared with the SCR.

Buckling is one of the challenges of SCR around its TDZ. The global buckling tendencies of the SCR around its TDZ can be characterised by effective negative tension. Since the near offset condition contributes more to the global riser compression at the TDZ than the nominal and far vessel offsets, the near offset configuration is expected to increase the buckling tendencies or cause increased negative tensions in the risers. Therefore, only the minimum effective tensions of the risers in their near offset conditions are presented in Figure 6-15 (b). However, a comparison of the minimum effective tension for the three-vessel offset conditions is presented in Figure 6-15 (d). The SCR is seen to be in higher compression under the combined loading conditions. Nevertheless, all FCRs have positive minimum effective tension, although FCR configurations with shorter values of Δh such as conf-1 and conf-4 are seen to be in higher compression around the wave bends than other FCR configurations. This behaviour is also typical with the steel lazy wave riser [51].

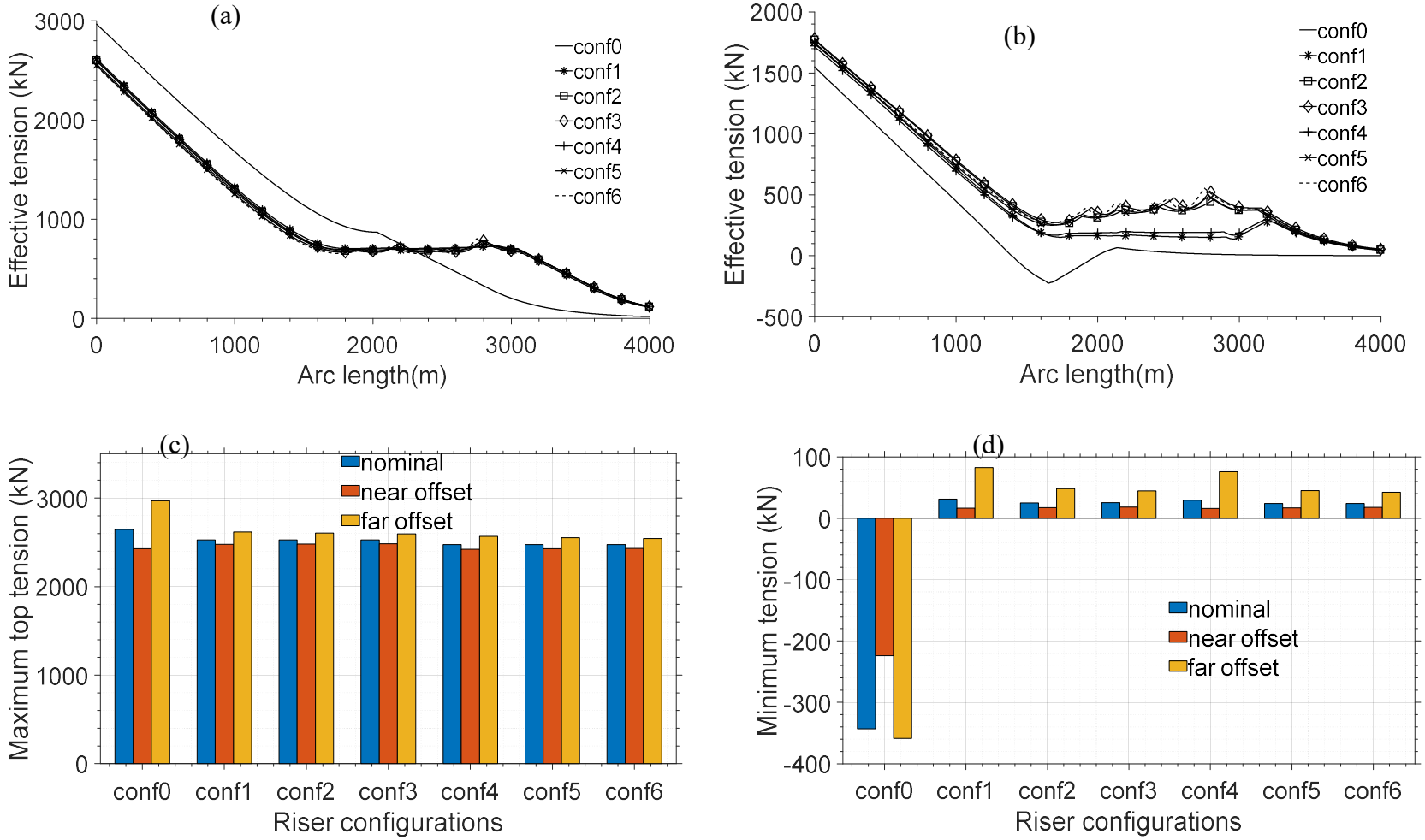

Figure 6-15. (a) Risers maximum effective tension (storm wave load, far offset, and current profile-2), (b) Risers minimum effective tension (storm wave load, near offset, and current profile-2), (c) Bar chart plot comparing maximum effective tension for the three combined load conditions, (d) Bar chart plot comparing minimum effective tension for the three combined load conditions.

1.1. Fatigue load analysis

The fatigue analyses for the risers are conducted with the risers in their nominal position, with the wave load acting in the riser azimuth direction. No current load was applied for the fatigue analysis. The fatigue damage responses along the risers are plotted on a semi-log scale in Figure 6-16, the peak fatigue damage responses are plotted on a log scale in the bar chart presented in Figure 6-17 (a), and the peak fatigue damage of the FCRs normalised by the peak fatigue damage of the SCR (conf-0) are plotted in normal scale in Figure 6-17 (b). Generally, the fatigue damages are observed from Figure 6-16 to be highest around the wave bends and the TDZ as expected for all riser configurations. The SCR possesses the most serious fatigue damage compared with all FCRs. However, as shown in Figure 6-16 and Figure 6-17 (a), conf-1 and conf-4 have a comparative damage response with that of the SCR (conf-0). This is due to their characteristic shorter Δh, which reduces their compliance to fluctuating bending moment and stresses caused by the vessel response to the fatigue wave load. In fact, as the Δh approaches zero, the FCRs behaves like the SCR in terms of the fatigue damage response. Hence, shorter arc heights (Δh) of the FCR wave bends are not favourable for both stress utilisation and the fatigue damage responses. The conf-2, conf-3, conf-5 and conf-6 with the highest Δh are seen to have good performers in terms of the fatigue damage response. One can also observe from Figure 6-16 and Figure 6-17 (a) that the fatigue performance can be improved by increasing y_{sag}. For FCRs with equal Δh, the configuration with higher y_{sag} have better performance (in terms of fatigue damage) than configuration with lower y_{sag}. For example, conf-5 which has higher y_{sag} than conf-2 possess smaller peak fatigue damage than conf-2, although both of them have equal Δh. Higher values of Δh and y_{sag} will therefore improve the fatigue performance of the FCR. However, higher buoyancy capacity and associated cost of the buoyancy modules will be required to achieve higher Δh and y_{sag}. Hence, an optimum FCR configuration should be able to achieve the desired ΔX_{TDP}, maintain the require minimum seabed clearance in the extreme and damaged near offset conditions, and be able to cut down significantly on the stress utilisation and fatigue damage responses, at a minimum cost of the riser and its buoyancy system.

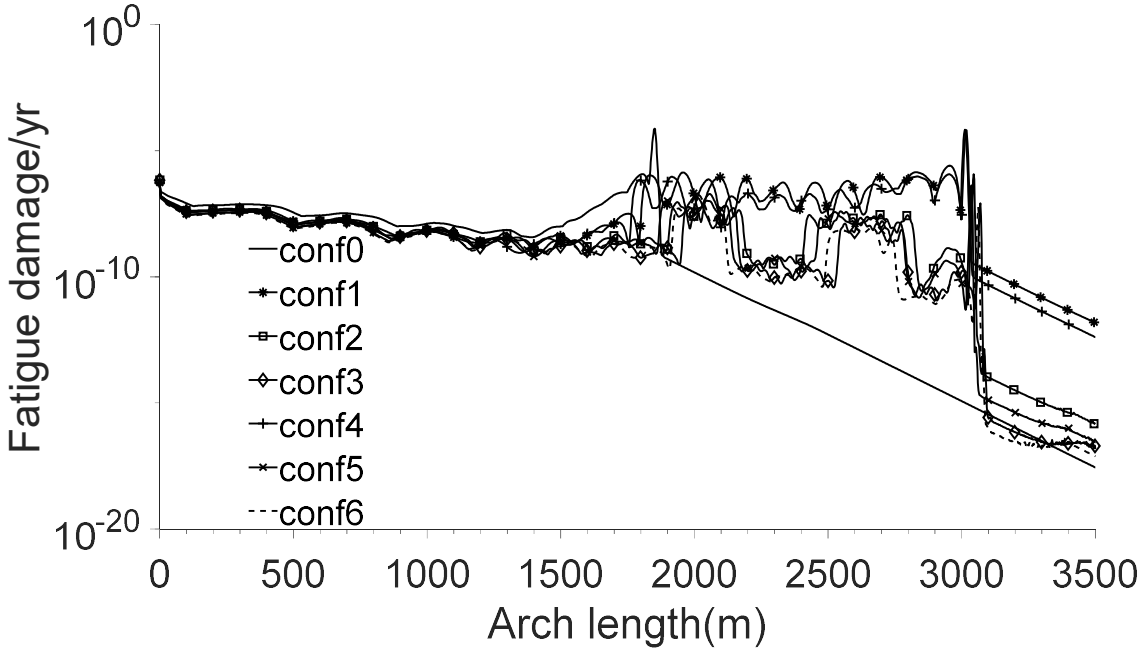

Figure 6-16. Fatigue damage response for risers

(a)

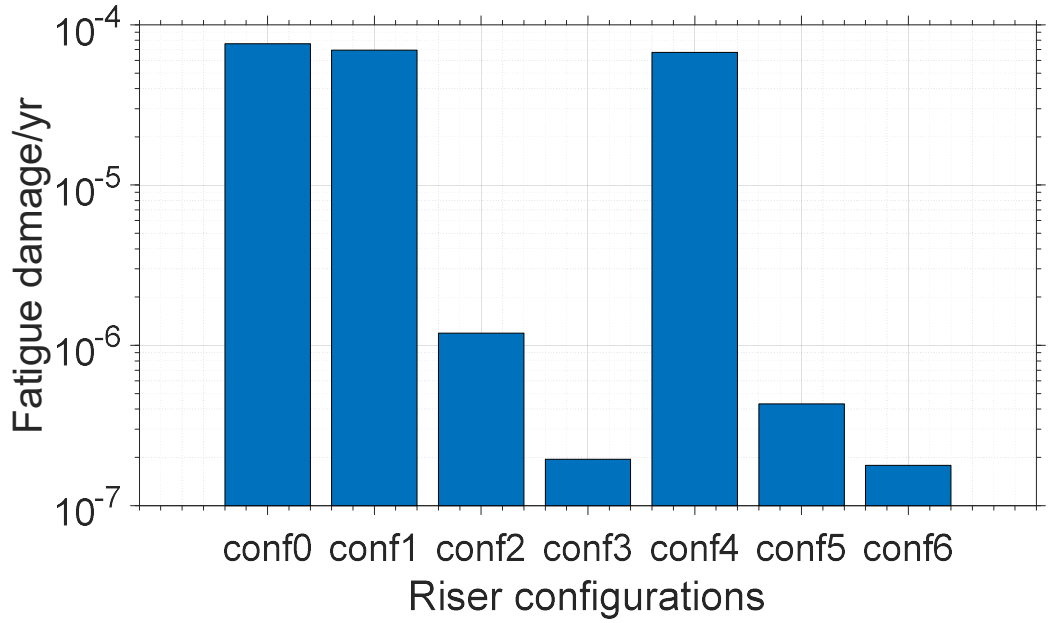

(b)

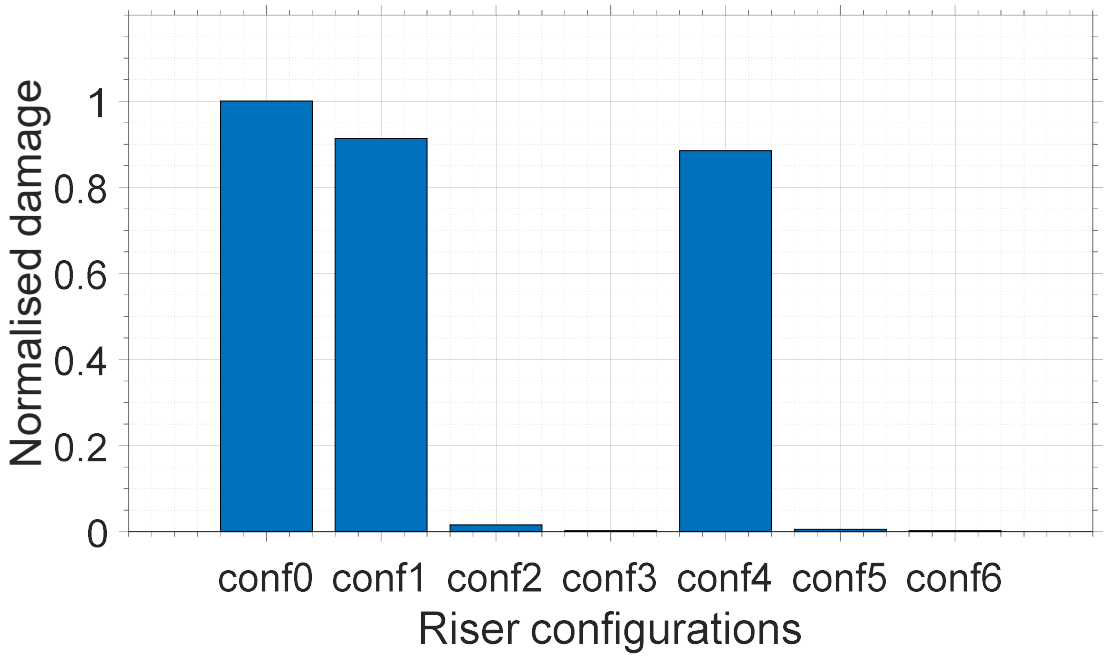

Figure 6-17. (a) peak fatigue damage response, (b) peak fatigue damage response normalised by SCR peak fatigue

6.4 Global optimisation of FCR

The FCR configuration is defined by a unique combination of the apparent mass ratio (AMR), the sag elevation (y_{sag}) and the arc height (Δh). A change in any of these variables will result in a different FCR configuration affecting its global stress and fatigue responses, its span length and minimum seabed clearance, and its cost represented by the riser length and volume of buoyancy material. The following are the objective function for the optimisation problem:

- The fatigue damage around the wave bends, including the touchdown zone, D. The wave bend and touch down-zone with smaller curvature are hot spots for the riser's fatigue damage. These curvatures are highly dependent on the FCR configurations. Hence, it will be an objective to obtain an FCR configuration that minimises the fatigue damage.

- The maximum tension at the riser connecting the interface to the vessel, T_{top}. In most cases for the FCR system, the top tension will not exceed the maximum design limit. However, the cost of the top connecting structure of the riser to the vessel depends on its weight capacity. The AMR, y_{sag} and Δh all have an impact on the magnitude of the

weight of the riser hanging section. An objective of the optimisation will be to obtain suitable combinations of these design variables to achieve minimum top tension.

- The lateral riser deflection under out of riser plane current load, L. The most critical current load causing larger lateral deflection will be the out of riser plane current load (90deg to the riser plane). A design functional requirement for risers will be to minimise the lateral deflections that may cause interference with neighbouring risers and structures or stress in the line. Therefore, it will be objective to minimise obtain a configuration that minimises the lateral riser deflection.

- The total hanging length of the riser, S. The longer the length of the FCR, the higher will the riser cost be. Therefore, it will be a cost minimisation objective to minimise the overall hanging length of the riser.

- The material volume of the buoyancy module installed to induce the wave bend sections, V_b. The higher the total amount of buoyancy material required to cause a given configuration, the higher the cost of the buoyancy system, hence the cost of the riser. Minimising the amount of buoyancy module will therefore mean minimising the riser cost, which will be an objective function

Note that the cost of the riser is implicitly optimised by the optimisation of the hanging length, S, and the required buoyancy material volume, V_b for a given FCR configuration. While searching for optimum FCR configurations, some design limits will be imposed on the optimisation design space. These are the constraint functions which are as follows:

- The stress utilisation, U in the curved sections of the FCR, including the touchdown zone. The stress utilisation ratio is the combined stress ratio in the riser bends, calculated based on DNV F201, to the allowable stress limit for the riser pipe material. The FCR configurations with stress utilisation responses greater than one will be eliminated from the family of configuration solutions.

- The minimum effective tension, T_{min}. The minimum effective tension indicates the level of compressions in the riser, especially at the bends and the TDZ. Negative minimum effective tension is not allowed as such values will indicate the higher buckling tendencies of the riser.

- The minimum seabed clearance, c. The minimum seabed clearance is the vertical distance between the minimum point on the wave bend section and the seabed, it is relevant for the wave bend sections, which should be engineered to be sufficiently higher than the subsea pipelines and structures the FCR spans over on the seabed. The limiting values for c will be user-specified values to be investigated in this work.
- The touchdown point offset, ΔX_{TDP}. As have been earlier mentioned, this is the increase in the touchdown point of the FCR compared with the SCR TDP of the same hang off-angle. A major proposed application of the FCR is to increase the nominal TDP of SCR to create a span over the congested seabed. Hence, the suitable FCR configurations must be able to provide these TDP offsets. Just like ΔX_{TDP}, different user-specified values of ΔX_{TDP} will be set for the optimisation process.

These objective and constraint functions for the FCR optimisation problem can be elegantly presented as follows:

Find:

$$\mathrm{X} = \begin{Bmatrix} AMR \\ y_{sag} \\ \Delta h \end{Bmatrix} \text{ which minimises Y} = \begin{Bmatrix} D \\ T_{top} \\ L \\ S \\ V_b \end{Bmatrix} \tag{6-13}$$

Subject to the following constraints, g:

$$\mathrm{g} = \begin{Bmatrix} U < 1 \\ T_{min} > 0 \\ (\Delta X_{TDP}, c) < A_{mn} \end{Bmatrix} \tag{6-14}$$

Where:

AMR = Apparent mass ratio.

y_{sag} = Sag elevation.

Δh = Arc height (difference between y_{hog} and y_{sag}).

D = Fatigue damage in wave bend sections, including the TDZ.

L = Lateral deflection of FCR under lateral current load.

S = Hanging length of the riser.

V_b = Material volume of installed buoyancy module.

U = Stress utilisation in riser bends, including the TDZ.

T_{min} = Minimum effective tension in riser bends, including the TDZ.

c = Minimum seabed clearance of FCR wave bands from the seabed.

ΔX_{TDP} = FCR touchdown point offset from the SCR TDP.

A_{mn} = Pair of values of constraint variables c and ΔX_{TDP}.

m = Counter for values in ΔX_{TDP}.

n = Counter for values in c.

Since this problem is a multi-objective type, there is no single unique optimum FCR configuration or solution that will serve to minimise all objective functions. However, a group or a family of optimum solutions can be obtained which will suitably meet the optimisation design criteria. Two methods were applied in section 4.3 for multi-objective optimisation, both based on the index matching technique but applied differently. We will employ method -1 for the optimisation of the FCR.

6.4.1 Numerical modelling and analysis methodology

OrcaFlex finite element software package is applied to conduct the modelling and analysis in this study. The modelling, pre-processing, simulations and post-processing are automated using MATLAB programs integrated with the OrcaFlex programming interface, OrcFxAPI [114]. The developed MATLAB program creates the initial OrcaFlex model configurations for each design point in the optimisation design space, considering the different buoyancy section dimensions, pipe unit weights, hang off angles, the apparent mass ratio, sag elevation, arch height, water depth, vessel offsets conditions, etc. These initial configurations for the SCR are calculated implementing the double wave configuration equations developed in 3.1. Models corresponding to the optimisation design points are developed for the design storm conditions with the vessel in the extreme near and far conditions, and for the fatigue analysis scenario where the vessel remains in its nominal position. Both the design storm and fatigue wave load are modelled using the Dean Stream theory, with the wave load acting on the vessel beam to

effect maximum roll motions on the SCR. The simulations are performed in the time domain, implementing an implicit integration scheme during the numerical solution process. Results post-processing from the simulated models are also automated, from which the constraint and objective functions are evaluated. The DNV-OS-F201 combined load (bending, tension, and pressure) resistance factor design criteria is used for the post-processing of the stress utilisation. Detailed information about the DNV-OS-F201 criteria can be found in [115]. For the fatigue post-processing, with Miner's rule, uses the S-N D-curve in seawater with cathodic protection is used [116]. Once the objective and the constraints functions are evaluated, the index matching optimisation technique is applied to obtain the optimum indices which represents a family of the optimum configurations.

6.4.2 Analysis data

6.4.2.1 Riser pipe data, vessel data and soil data

Since there are numerous locations, water depths, environmental conditions and ranges of seabed distance that could need protection from risers, the optimum FCR configurations will be determined on a case-by-case basis and for constraints set by the project specifications. However, some considerations and simplification are made to demonstrate the general procedure of obtaining optimum FCR configurations. These include:

- A fixed water depth.
- A singe representative regular storm wave load.
- A single representation regular fatigue wave load.
- A given range of values of seabed distance to span over.
- A given range of minimum FCR wave bend height values above the congested or protected seabed sections.

The FCR pipe used in this study is a 12-inch X70 grade pipe, hosted by a generic floating production, storage, and offloading unit at an azimuth of 90deg to the vessel heading. The minimum required pipe wall thickness is calculated using DNV-OS-F201 burst and collapse resistance criteria [4]. Table 4-7 presents the riser data. A generic response amplitude operator (RAOs) for the floating production unit is implemented. Two vessel offset conditions in the far and near directions are considered. The hysteretic nonlinear riser soil interaction model is

implemented. Details of the soil model and its default data can be found in [56]. The current profile applied during the optimisation analysis is presented in Figure 6-4. The direction of the current is perpendicular to the riser plane to impose the highest lateral drift effect on the risers. The selected current profile is a 10years return period current with a surface velocity of 1.6m/s [113]. This decreases to 0.1m/s close to the seabed. The two regular beam wave loads simulated for the combined load and fatigue analysis are presented in Table 6-3. The drag coefficients presented in Table 4-7 are chosen with reference to the smooth pipe outer diameter. For practical purposes, this value ranges between 0.7 and 1.0 [112], and a value of 0.7 is selected for the bare pipe section in this study. However, due to the increased diameter of the smeared buoyancy system over the bare pipe section, a conservative drag coefficient of 1.2 is applied for the buoyancy section.

Table 6-5. Riser data.

Riser data	**Values**
Pipe size (D_o)	12inch
Internal Design pressure	10ksi
Pipe thickness	27.5mm
Hang off angle with the vertical ($90 - \theta$)	12^o
Content density	600kg/m^3
Buoyancy material density (ρ_b)	500kg/m^3
Water depth (h)	1500m
Drag coefficient for the bare pipe section	0.7
Drag coefficient for the smeared buoyant section	1.2
Vessel offsets (far and near offset conditions)	$\pm$10 % of water depth

6.4.2.2 Environmental data

Table 6-6. Combined and fatigue wave load data.

Analyses	**Wave type**	**Data**	**Values**
Storm	regular wave	H(m)	8
		T(sec)	12
		Dir (deg)	180
Fatigue	regular wave	H(m)	3
		T(sec)	7
		Dir (deg)	180

There are two aspects of investigation in this work. These are the optimisation stage where the optimum FCR configuration is searched for and the detailed analysis investigation stage where a few selected optimum FCR configurations are subjected to detailed and varying directions of the design storm wave load, fatigue wave load, vessel offsets and current loads analysis. To manage the huge computational resource requirement for the optimisation process, we apply a regular design storm and fatigue wave loads in the riser azimuth direction, which is also the beam of the vessel, to effect maximum heave and roll vessel response impact on the riser. The two regular wave load data are presented in Table 6-3. The current profile -2 presented in Figure 6-4 is applied for the optimisation analysis. The current direction is perpendicular to the riser plane to impose the highest lateral drift effect on the risers.

6.4.2.3 Design optimisation variable data

The FCR is a replacement riser tieback for an SCR, which may unfortunately not be possible due to the seabed congestions. The basis for the FCR configuration will be such as to make its hang-off angle (HOA, θ) equal to a supposed SCR, whose HOA may have already been determined from preliminary design. So, the important parameters in such a case for the FCR will be the variation in the "wave bends" configurations close to the seabed rather than the HOA to achieve its "spanned" purpose. Hence the HOA for the FCR is fixed during the optimisation or screening process.. The range of the variable space and the discretisations are presented in Table 6-7. The discretisation of these design dimensions are reasonable for a large scale global FCR system in a water depth of 1500m.

Table 6-7. Optimisation design configuration variables

Variables	**Symbol**	**unit**	**Range for variable**		**Number of discrete values**
			Limit	Interval	
Hang off angle	θ	deg	12	-	1
Apparent mass ratio	AMR	-	(-3,-0.2)	0.1	29
Sag elevation	y_{sag}	m	(20,150)	5	27
Arc height	Δh	m	(10,100)	5	19
Number of design point	-	-	-	-	14877

6.4.2.4 Constraint function data

The constraints imposed on the optimisation problem are expressed in equation (8-17). The constrained variables are the stress utilisation around the wave bend including the TDZ, U, the minimum effective tension around the wave bend including the TDZ, the TDP offsets of the FCR relative to that of the base SCR, ΔX_{TDP}, and the minimum seabed clearance of the wave bend sections, c. The limits of the constraint functions are imposed on the optimisation problem under extreme conditions of combined design wave, current and vessel offsets conditions in the far and near directions. Nine (9) constraint limits combinations, $(U, T_{min}, \Delta X_{TDP}, c)$, are investigated in this work, with maximum limit of U is set to 1 i.e., $U < 1$, minimum limit of T_{min} set to 1 i.e. $T_{min} < 1$, and varying minimum limits of ΔX_{TDP} and c set to values presented in Table 6-8.

Table 6-8. Limits for the constraint functions

$\boldsymbol{A = (U, T_{min}, \Delta X_{TDP}, c)}$				
		Min seabed clearance, c (m)		
		20	50	70
ΔX_{TDP}(m)	500	(1,0,500,20)	(1,0,500,50)	(1,0,500,70)
	1000	(1,0,1000,20)	(1,0,1000,50)	(1,0,1000,70)
	1500	(1,0,1500,20)	(1,0,1500,50)	(1,0,1500,70)

Table 6-9. Limits for the constraint functions

$\boldsymbol{A = (U, T_{min}, \Delta X_{TDP}, c)}$			
		Min seabed clearance, c (m)	
		50	100
ΔX_{TDP}(m)	500	(1,0,500,50)	(1,0,500,100)
	1000	(1,0,1000,50)	(1,0,1000,100)
	1500	(1,0,1500,50)	(1,0,1500,100)

6.4.3 Analyses, results and discussions

In this section, the ideal and global optimum configurations are obtained and presented, considering the nine constraint function sets presented in Table 6-8 imposed on the design

optimisation space. The configurations at the top of the lists of the family of ideal and optimum configurations will be selected and used for comparative purposes during the detailed analysis investigation that will be conducted.

We can recall from Table 6-7 that the number of discrete points within the optimisation design space is defined by all unique combinations of the optimisation design variables $(AMR, y_{sag}, \Delta h)$, which is 14877 design points in this work. Also, there are three categories of analysis (see Table 6-3) conducted during the optimisation stage. These are the design storm analysis, the configuration, and the fatigue analyses. These are detailed in Table 6-10:

Table 6-10. Analysis conducted at the optimisation stage

Analysis type	**Vessel position**	**Purpose**	**Number of FE models**
Design storm + Current load	Nominal, far, near	- Constraint function evaluation $(U, T_{min}, \Delta X_{TDP}, c)$ - Objective function evaluation (T_{top}, L)	14877×2= 44631
Configuration	Nominal	- Objective function evaluation (S, V_b)	14877×1= 14877
Fatigue	Nominal	- Objective function evaluation (D, T_{top})	14877×1= 14877

Hence, the design indices representing the design points for each of the three analyses will range from 1 to 14877, with the overall relevant extreme values (maximum or minimum) for each variable obtained at these points. For example:

- The maximum stress utilisation, U, at say design point with index k, will be the maximum values for both the riser in its nominal, far and near configurations, under design storm loading.
- The smeared buoyancy material volume, V_b, at design point with index k, will be the calculated value to achieve the required nominal configuration at that design point.

- The fatigue damage, D, at the critical wave bend section (including the TDZ), is the maximum fatigue damage obtained within this riser region, for the riser in its nominal configuration and under fatigue loading.

Considering the application of each of the nine constraint sets presented in Table 6-8, the design optimisation space will reduce from 14877 to the feasible design space as presented in Table 6-11.

Table 6-11. Number of feasible design points when the constraint sets are imposed on the design space

$\boldsymbol{A = (U, T_{min}, \Delta X_{TDP}, c)}$				
		Min seabed clearance, c (m)		
		20	50	70
ΔX_{TDP}(m)	500	7513	4537	2609
	1000	5594	3451	2008
	1500	1348	836	486

A cursory look at the variation in the number of the feasible design space indicate that as the desired design horizontal span, ΔX_{TDP}, increases, the number of feasible design points satisfying this constraint decreases. Similarly, as the desired design minimum clearance, c, from seabed increases, the number of feasible design points also decreases. A joint increase in both ΔX_{TDP} and c result in significant squeezing of the number of feasible design points. These imply that it becomes increasingly challenging to find feasible FCR configurations that will satisfy the constraint functions' higher limiting values. However, while our interest is to maintain a minimum seabed clearance, c, it can be more expensive in terms of the amount of buoyancy material (volume) required to maintain higher seabed clearance well as an increased lateral deflection from the current load. Out of the number of feasible design points (configurations) for the constraint sets presented in Table 6-8, the first five configurations will be presented for both the global optimums and the ideal optimum configuration scenarios.

6.4.3.1 Ideal optimum configurations

An ideal solution is an optimum solution for an objective function when it is considered exclusively, i.e., without the consideration of other objective functions. This means that the

optimum design points only minimise that objective function, with associated values of other objective functions which may not be optimum. Since we have five objective functions for the problem, there will be five sets of objective functions evaluated for each of the nine constraint sets in Table 6-11. The first four (4) ideal optimum configurations for each set of the constraint function are obtained and presented in Table 6-12. The associated values of the five objective functions are also presented. The designer implementing this optimisation technique can use such a table as a lookup table to obtain suitable FCR configuration considering the design constraint imposed and a particular objective function. However, such consideration will mean that other objective functions are disregarded. If, for example, we selected the fifth constraint function, $[U, T_{min}, \Delta X_{TDP}, c]$ = [1,0,1000,50], the corresponding ideal solution indices for the five objective function will be 888, 14877, 12161 and 12161 respectively. These configurations are highlighted in grey in Table 6-12. For each of the configurations represented by these indices, we can obtain the associated values of other objective functions. These have been presented in

Table 6-13, from where we can see that except for the L, S and V_b which have the same best solution, the associated values of the objective functions are not the optimum at the points where other objective functions have optimum values. Hence, there is a need to obtain a global objective function.

Table 6-12. Ideal optimum solutions for the individual objective function

Constraint sets $[U, T_{min}, \Delta X_{TDP}, c]$	S/N	Ideal optimum design Indices, I					Associated ideal values of objective functions, Y				
		$I'(D)$	$I'(T_{top})$	$I'(L)$	$I'(S)$	$I'(V_b)$	D	T_{top}	L	S	V_b
		[-]	[-]	[-]	[-]	[-]	[/year]	[kN]	[m]	[m]	[m^3]
[1,0,500,20]	1	280	14877	12560	12560	12560	2.43E-09	2845.59	31.86	2383.83	172.01
	2	261	14364	12047	12579	12047	2.44E-09	2845.84	32.07	2385.68	172.92
	3	242	13851	12579	12047	11534	2.45E-09	2846.12	32.24	2386.87	173.90
	4	299	13338	11534	12598	12579	2.46E-09	2846.37	32.29	2387.39	174.23
(1,0,1000,20)	1	280	14877	14602	1483	2321	2.43E-09	2845.59	52.37	2788.93	293.16
	2	261	14364	14621	1502	1883	2.44E-09	2845.84	52.72	2793.32	294.65
	3	242	13851	14089	1521	4394	2.45E-09	2846.12	52.77	2794.70	295.03
	4	299	13338	12055	3043	5383	2.46E-09	2846.37	52.83	2796.90	295.11
(1,0,1500,20)	1	280	6156	5871	477	803	2.43E-09	2854.82	88.77	3281.22	429.09
	2	261	5643	5890	496	1337	2.44E-09	2854.96	89.20	3285.66	431.36
	3	242	5130	5376	803	822	2.45E-09	2855.42	89.31	3318.24	431.94
	4	299	4617	4862	1337	1833	2.46E-09	2855.43	89.61	3318.81	433.48
(1,0,500,50)	1	280	2052	1881	368	368	2.43E-09	2861.93	138.91	3810.39	570.00
	2	261	1539	1270	387	772	2.44E-09	2864.04	139.06	3814.30	570.33
	3	242	1538	1900	406	791	2.45E-09	2866.36	139.57	3817.98	572.68
	4	299	1026	1289	425	387	2.46E-09	2867.03	139.89	3821.46	572.75
(1,0,1000,50)	1	888	14877	12161	12161	12161	2.57E-09	2845.59	34.21	2396.47	185.53
	2	869	14364	11648	12180	11648	2.58E-09	2845.84	34.47	2397.70	186.56
	3	341	13851	12180	12199	12180	2.58E-09	2846.12	34.53	2397.89	187.48
	4	4973	13338	11135	12218	11135	2.59E-09	2846.37	34.76	2398.94	187.67
(1,0,1500,50)	1	888	14877	12663	1483	1921	2.57E-09	2845.59	54.05	2788.93	299.67
	2	869	14364	12682	1502	1483	2.58E-09	2845.84	54.38	2793.32	300.68
	3	341	13851	12150	1521	6010	2.58E-09	2846.12	54.57	2794.70	301.72
	4	4973	13338	12701	3043	3443	2.59E-09	2846.37	54.70	2796.90	301.89
(1,0,500,70)	1	888	6156	5985	477	477	2.57E-09	2854.82	91.26	3281.22	435.75
	2	869	5643	5471	496	1394	2.58E-09	2854.96	91.46	3285.66	438.31
	3	341	5130	6004	1394	496	2.58E-09	2855.42	91.66	3327.40	438.64
	4	399	4617	5490	1413	1413	2.60E-09	2855.43	91.87	3328.02	440.52
(1,0,1000,70)	1	888	2052	1881	387	387	2.57E-09	2861.93	138.91	3814.30	572.75
	2	869	1539	1900	406	406	2.58E-09	2864.04	139.57	3817.98	575.44
	3	341	1538	1919	425	425	2.58E-09	2866.36	140.21	3821.46	578.07
	4	399	1026	1938	444	444	2.60E-09	2867.03	140.85	3824.74	580.63
(1,0,1500,70)	1	1970	14877	12218	12218	12218	2.69E-09	2845.59	35.16	2398.94	191.27
	2	948	14364	11705	11705	11705	2.69E-09	2845.84	35.45	2402.75	192.32
	3	929	13851	11192	11724	11192	2.70E-09	2846.12	35.75	2403.76	193.46
	4	5031	13338	11724	11743	11724	2.70E-09	2846.37	35.76	2403.77	194.17

Table 6-13. Associated values of the other objective functions to ideal solutions

Variables	Index				
	$I'(D)$ = 888	$I'(T_{top})$ = 14877	$I'(L)$ = 12161	$I'(S)$ = 12161	$I'(V_b)$= 12161
D[/yr]	2.6E-09	2.38E-08	4.97E-07	4.97E-07	4.97E-07
$T_{top}[kN]$	2947.14	2845.59	3072.25	3072.25	3072.25
L[m]	159.47	73.52	34.21	34.21	34.21
S[m]	3986.70	3187.48	2396.47	2396.47	2396.47
V_b[m^3]	618.02	412.42	185.53	185.53	185.53
U[-]	0.60	1.00	0.99	0.99	0.99
T_{min}[kN]	325.77	274.81	29.99	29.99	29.99
ΔX_{TDP}[m]	2156.10	1289.92	588.90	588.90	588.90
c [m]	56.68	102.06	55.29	55.29	55.29

6.4.3.2 Global optimum configurations

The normalised global objective function, F^{nom}, is a linear combination of the five objective functions factored by their wights, $a_i = a_i^{max}$ or $a_i = a_i^{min}$ which are calculated using expressions already presented in section 4.3.1. These parameters have been computed from the post-processing results of the objective functions, Y_i.

Table 6-14. Parameters used to calculate the global normalised objective function

Parameters	$\boldsymbol{D}$ [/year]	$\boldsymbol{T_{top}}$ [kN]	$\boldsymbol{L}$ [m]	$\boldsymbol{S}$ [m]	$\boldsymbol{V_b}$ [m^3]
Y_i^{max}	8.7E-06	3.3E+03	2.5E+02	4.7E+03	8.3E+02
	$\sum_{i=1}^{5} Y_i^{max} = 9.1\text{E}+03$				
a_i^{max}[-]	9.6E-10	3.6E-01	2.7E-02	5.2E-01	9.1E-02

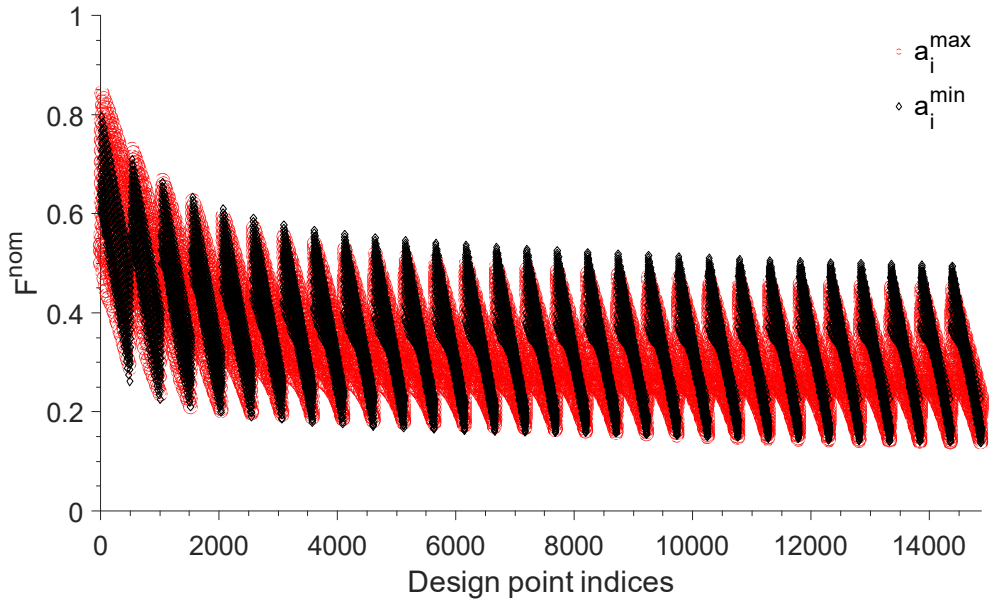

Figure 6-18. Normalised global objective function for the unconstrained design optimisation space

Table 6-15. Comparing $\boldsymbol{F^{nom}}$ calculated based on $\boldsymbol{a_i = a_i^{max}}$ and $\boldsymbol{a_i = a_i^{min}}$

	F^{nom} with $a_i = a_i^{max}$			F^{nom} with $a_i = a_i^{max}$		
S/N	Index	F_{nom} [-]	$[\Delta h, y_{sag}, AMR]$ [m, m,-]	Index	F_{nom} [-]	$[\Delta h, y_{sag}, AMR]$ [m, m,-]
1	12810	0.142435	[25,150,-2.6]	13838	0.139981886	[35,150,-2.8]
2	13324	0.143386	[30,150,-2.7]	13325	0.141034669	[35,150,-2.7]
3	12297	0.143656	[25,150,-2.5]	13839	0.141522795	[40,150,-2.8]
4	12811	0.144842	[30,150,-2.6]	13324	0.141549697	[30,150,-2.7]
5	11784	0.145043	[25,150,-2.4]	12812	0.142425763	[35,150,-2.6]
6	12298	0.146402	[30,150,-2.5]	12811	0.142805111	[30,150,-2.6]
7	12296	0.146678	[20,150,-2.5]	13326	0.142842048	[40,150,-2.7]
8	11271	0.146699	[25,150,-2.3]	12299	0.143618294	[35,150,-2.5]
9	11783	0.147564	[20,150,-2.4]	12298	0.144139779	[30,150,-2.5]
10	13838	0.148188	[35,150,-2.8]	12813	0.144268193	[40,150,-2.6]
11	11785	0.148287	[30,150,-2.4]	13840	0.145241125	[45,150,-2.8]
12	10758	0.148502	[25,150,-2.2]	11786	0.145336002	[35,150,-2.4]
13	11270	0.148713	[20,150,-2.3]	11785	0.14587122	[30,150,-2.4]
14	13325	0.149492	[35,150,-2.7]	12300	0.145886314	[40,150,-2.5]
15	10757	0.149794	[20,150,-2.2]	13327	0.146365822	[45,150,-2.7]
16	11272	0.150276	[30,150,-2.3]	11273	0.14679649	[35,150,-2.3]
17	12791	0.150378	[25,145,-2.6]	11787	0.147502726	[40,150,-2.4]
18	10245	0.150605	[25,150,-2.1]	11272	0.14766565	[30,150,-2.3]
19	12812	0.151073	[35,150,-2.6]	12814	0.147702124	[45,150,-2.6]
20	10244	0.151263	[20,150,-2.1]	10760	0.148480336	[35,150,-2.2]

A comparison of F^{nom} calculated based on a_i^{max} and a_i^{min} can be made across the unconstrained design optimisation space, as shown in Figure 6-4. The peaks and troughs of the F^{nom} response for both cases appear to follow same patterns and match closely with each other. This indicates that both options can be used for the computation of F^{nom} and the global optimum configurations. This is confirmed by comparing the first 20 optimum configurations for the constrained design optimisation space using both options, as presented in Table 6-16. The first constraint set (1,1) from Table 6-8 has been applied for this case, for which there are 7513 feasible design point or configurations (see Table 6-11), with the first best 40 reported in Table 6-16. We can see from the two groups that the design indices and design variables match closely with one another, although the values of the F^{nom} for the two options are different.

Using the option: $a_i = a_i^{max}$, for the calculation of F^{nom}, details of the first 20 optimum configurations obtained when the first constraint set (1,1) is applied is presented in Table 6-16. The table contains the index representation, the normalised function values, the coordinates of the optimisation design point (design variables), the values of the objective and the constraint functions. We can observe that the constraint functions for these configurations satisfy the first constraint set imposed on the optimisation design space, an indication that the solutions are within the feasible design space for this constraint set.

Recall that index 13324 is index representative of the optimum FCR configuration considering calculations based on $a_i = a_i^{max}$ and $a_i = a_i^{min}$. Table 6-17 presents the performance of these global optimum FCR configurations in comparison with the ideal solutions. The values of the objective and the constraint functions are presented. It could be seen that the selected global optimum configurations provide performance that captures the interest of each of the objective functio (see note for Table 6-17)

Table 6-16. The first 40 global optimum FCR configurations based on $\boldsymbol{a_i = a_i^{max}}$

S/N	Index	F_{nom}	$[\Delta h, y_{sag}, AMR]$	D	T_{top}	L	S	V_b	U	T_{min}	ΔX_{TDP}	c
		[-]	[m, m,-]	[/year]	[kN]	[m]	[m]	[m^3]	[-]	[kN]	[m]	[m]
1	12810	0.142435	[25,150,-2.6]	1.34E-07	2923.88	44.76	2596.40	251.77	0.98	51.93	786.78	92.77
2	13324	0.143386	[30,150,-2.7]	8.42E-08	2909.31	46.95	2646.17	265.22	0.99	59.90	831.85	93.07
3	12297	0.143656	[25,150,-2.5]	1.19E-07	2923.87	45.16	2601.11	253.04	0.96	53.17	791.77	92.68
4	12811	0.144842	[30,150,-2.6]	7.78E-08	2909.61	47.34	2650.77	266.47	0.97	61.29	836.73	92.99
5	11784	0.145043	[25,150,-2.4]	1.08E-07	2923.92	45.58	2606.24	254.41	0.94	54.33	797.20	92.59
6	12298	0.146402	[30,150,-2.5]	7.20E-08	2909.92	47.76	2655.76	267.82	0.94	62.49	842.02	92.91
7	12296	0.146678	[20,150,-2.5]	1.76E-07	2946.14	42.37	2542.67	236.99	0.98	44.52	737.47	92.58
8	11271	0.146699	[25,150,-2.3]	9.90E-08	2924.16	46.03	2611.84	255.90	0.92	53.94	803.12	92.48
9	11783	0.147564	[20,150,-2.4]	1.54E-07	2945.69	42.77	2547.47	238.28	0.96	45.60	742.54	92.47
10	13838	0.148188	[35,150,-2.8]	6.83E-08	2900.61	48.97	2692.33	277.69	1.00	69.69	873.05	93.50
11	11785	0.148287	[30,150,-2.4]	6.79E-08	2910.49	48.21	2661.19	269.27	0.92	62.93	847.78	92.82
12	10758	0.148502	[25,150,-2.2]	9.26E-08	2924.41	46.51	2617.97	257.51	0.89	55.30	809.59	92.37
13	11270	0.148713	[20,150,-2.3]	1.38E-07	2945.42	43.19	2552.71	239.67	0.94	46.01	748.08	92.36
14	13325	0.149492	[35,150,-2.7]	6.24E-08	2900.77	49.36	2696.80	278.91	0.98	68.88	877.80	93.44
15	10757	0.149794	[20,150,-2.2]	1.25E-07	2945.14	43.64	2557.58	241.18	0.91	46.91	753.26	92.23
16	11272	0.150276	[30,150,-2.3]	6.71E-08	2911.03	48.70	2667.12	270.84	0.91	64.38	854.05	92.72
17	12791	0.150378	[25,145,-2.6]	1.22E-07	2933.77	44.46	2597.07	250.17	0.98	52.09	786.26	87.38
18	10245	0.150605	[25,150,-2.1]	8.04E-08	2924.84	47.04	2624.70	259.26	0.87	56.12	816.68	92.24
19	12812	0.151073	[35,150,-2.6]	5.42E-08	2901.15	49.78	2701.64	280.23	0.96	70.48	882.95	93.37
20	10244	0.151263	[20,150,-2.1]	1.15E-07	2944.93	44.13	2563.88	242.82	0.89	47.26	759.90	92.10

Table 6-17. Performance comparison of the global and the ideal optimum solutions

	Variables	Global Optimum	Ideal optimum				
		$I'(D)$ = 13324	$I'(D)$ = 888	$I'(T_{top})$ =14877	$I'(L)$ = 12161	$I'(S)$ =12161	$I'(V_b)$=12161
Objective functions	D[/yr]	8E-08	2.6E-09	2E-08	5E-07	5E-07	5E-07
	$T_{top}[kN]$	2909.31	2947.14	2845.59	3072.25	3072.25	3072.25
	L[m]	46.95	159.47	73.52	34.21	34.21	34.21
	S[m]	2646.17	3986.70	3187.48	2396.47	2396.47	2396.47
	V_b[m^3]	265.22	618.02	412.42	185.53	185.53	185.53
Constraint functions	U[-]	0.99	0.60	0.99	0.99	0.99	0.99
	T_{min}[kN]	59.90	325.77	274.81	29.99	29.99	29.99
	ΔX_{TDP}[m]	831.85	2156.10	1289.92	588.90	588.90	588.90
	c [m]	93.07	56.68	102.06	55.29	55.29	55.29

Note: Table 6-17 combines the ideal solution in

Table 6-13 and the selected global solution (index 13324) in Table 6-16.

- Fatigue damage, D, of the ideal solutions is between 2.6E-09/yr to 5E-07/yr; it is 8E-08/yr for the global solution
- Riser lateral deflection, L, of the ideal solutions is between 34.2m to 159.47m; it is 46.95m for the global solution
- The hanging riser length, S, of the ideal solutions is between 2396.47m to 3986.70m; it is 2646.17m for the global solutions
- The material volume of the buoyancy module, v_b, of ideal solutions are between 185.53m^3 to 618.02 m^3; it is 265.22m^3 for the global solution

It could be seen from the comparison of the results that the values of the objective functions in the global optimum solution are within the range of values of the ideal solutions for the respective objective functions and closer to the minimum ideal values within the range.

6.5 Chapter summary

The development and feasibility investigation of a novel riser, the floating catenary riser (FCR), is presented in this chapter The FCR concept is being developed to address the challenges associated with additional SCR tiebacks during a brownfield expansion. Expanding a brownfield may be necessary when the production capacity of the field is to be ramped up. However, if the potential seabed path of the SCR is congested, the tie back can be impossible. The FCR can provide the opportunity to extend the SCR nominal TDP far beyond the congested seabed zone by an offset (ΔX_{TDP}). The FCR is characterised by two-wave bends of equal sag and arc height elevation, created by the installation of buoyancy modules on the seabed section of the SCR. The buoyant section provides an uplift to the SCR seabed section, ensuring that that desired minimum seabed clearance between the riser and the congested seabed is achieved in all loading conditions. The two-wave buoyant sections also provide the FCR with the capability to decouple its TDZ from the floating platform motion. This can result in a significant reduction in the stress and fatigue damage around the riser bends and TDZ. To demonstrate the feasibility of the FCR concept, configuration variables, responses under static vessel offsets, responses under combined loading conditions, and fatigue damage responses under fatigue wave loading are investigated in this study. The following features are observed for the FCR:

- Three configuration variables, the sag or hog elevation (y_{sag} or y_{hog}), the arch height (Δh) and the apparent mass ratio (AMR) are important for the easy control of the FCR configuration or profile. A combination of these three variables can result in an infinite number of configurations. However, an optimum configuration will be required to achieve the design seabed clearance and touch down point extension (ΔX_{TDP})

- Increasing values of AMR result in reduced smeared buoyancy thickness and a longer buoyancy section for a given required buoyancy capacity. An $AMR \approx$ -1 provides an FCR configuration with increased performance in stress utilisation.

- The y_{sag} and Δh controls the elevation of the FCR wave bends from the seabed. Increased values of the two variables increase the compliancy of the FCR and can help to significantly reduce the fatigue damage response when compare with the conventional SCR. As Δh values approach zero, the FCR fatigue damage can be as serious as those of the conventional SCR.

- The vertical minimum seabed clearance of the FCR above the congested seabed is an important output variable that must be looked out for if the FCR must achieve its purpose. This clearance can become very critical for vessel near offset conditions where the riser is in global compression resulting in a significant reduction in the clearance between the FCR wave bends and the seabed. However, suitable design values of y_{sag} and Δh can help to address this problem.

- Because the buoyancy sections are quite close to the seabed, the reduced top tension provided by the FCR concept compared to those of the SLWR can be moderate. However, when compared with the dynamic top tension of the SCR, the FCR can be said to provide an appreciable reduction in the top tension. The compression in the FCRs, measure by the negativity of the minimum effective tension is seen to be lower for the FCR compare with the SCR under dynamic condition. This indicates improved performance against global buckling when compared with those of the SCR.

- The FCR, because of its longer buoyancy section, can be prone to significant lateral deflection under intensive current loads. This limits the FCR application to regions where the current profile towards the seabed is minimum.

In general, the seabed clearance, the top tension, the compression, the stress, and the fatigue response can be improved by higher values of y_{sag} and Δh. However, the required buoyancy capacity to achieve higher values Δh and y_{sag} can introduce negative cost implication. Hence, an optimum FCR configuration required to be able to achieve the desired ΔX_{TDP}, maintain the required minimum seabed clearance in the extreme near offset condition, and be able to cut down significantly on the stress utilisation and fatigue damage responses, at a minimum cost of the riser and its buoyancy system.

The FCR optimisation process is demonstrated using the index matching optimisation technique developed in section 4. Here, the objective functions were set to be the fatigue damage in the FCR wave bends (including TDZ), the total FCR length, the length of the buoyancy section, and the volume of the buoyancy material and the lateral deflection of the FCR under current loading. The length of the buoyancy section and the volume of the buoyancy material are the cost representative objective functions. The design variables for the optimisation problems are the configuration variables for the FCR, which are the AMR, y_{sag} and Δh. The constraint functions are the top tension, the compressions in the curved sections, the TDP offsets and the seabed clearance. The multi-objective optimisation technique developed in chapter 4 proved efficient to obtaining family of global optimum solutions which puts into consideration all the objective functions' s interest. The FCR optimisation demonstration in his chapter provides a template to designers of this riser concept.

7 SCR SEABED INTERACTION

As discussed in the literature review in chapter 2, one of the challenges with the design of the SCR is its complex interactions with the seabed. Less understanding of this subject may result in either over-designing or under-designing of the SCR, which can result in some cost implications for the riser. In this chapter, two areas of studies on SCR soil interactions were conducted. These are the investigating the impact of sloped seabed on SCR touch down response and the development of seabed pre-trenching. The numerical pre-trenching technique is called the simulation stage-based pre-trenching technique (SSBPT). The technique is developed and applied to investigate the impact pre-trench would have on the SCR TDZ fatigue responses.

The chapter is sectioned as follows.

- Section 7.1 - Impact of seabed slope on SCR strength and fatigue damage
- Section 7.2 – The simulation stage-based pre-trenching technique (SSBPT)
- Section 7.3 – Chapter summary

7.1 Impact of seabed slope on steel catenary riser strength and fatigue response

7.1.1 Background

It is a common practice during the design of SCR to assume a flat seabed [112]. Realistically, seabed can hardly be flat. Bathymetric data reveal complexities in the topography of the seabed and the variation of the seabed profiles along riser azimuth. Sloped seabed, especially in the immediate region surrounding TDZ, may impact SCR

configurations calculated based on the flat seabed assumption, leading to SCR TDP mismatch [117]. The mismatch is the distance between the SCR TDP on an assumed flat seabed and the SCR TDP on realistic sloped seabeds. This work does not only investigate the influence of seabed slope on the static riser configurations of SCRs but also the impact sloped seabed can have on the strength and fatigue response around the SCR TDZ. The impact of seabed slope on SCR response is investigated, considering the hysteretic nonlinear soil interaction model developed by Randolph and Quiggin [56]. The sloped seabeds in this investigation extend linearly from before the TDP to after the riser seabed termination. The linear seabed profiles considered are 0deg (flat seabed), ± 2deg, ± 4deg, ± 7deg and ± 10deg. Three groups of SCRs with hang-off angles of 8deg, 12deg and 16deg rest on theses profiled seabed. The SCRs static, dynamic and fatigue responses are calculated considering nominal configurations of the risers, i.e. no vessel offsets. Findings from this study will provide not only relevant information about SCRs behaviour on the sloping seabed but also possible seabed modifications to improve SCR response.

7.1.2 Analysis methodology

In this study, we conducted the analysis calculations using the OrcaFlex finite element (FE) software package. The initial SCRs' configurations for the FE modelling is calculated using the catenary equations developed in chapter 3. A core objective of this study is to investigate the impact of the sloped seabed on SCR responses, compared with SCR response on the flat seabed. When developing the models for this study, we assume an initial flat seabed to obtain a base SCR configuration. Then, we rotate the seabed about the base SCR TDP to impact the influence of sloped seabed on the base configuration. The modelling approach for the three groups of the SCRs of different HO angles, considering the nine seabed slopes (see

Table 7-1). The following conventions were adopted for the sloped seabed modelling:

- The seabed slope is positive when the seabed increases in the positive direction (upward relative to the TDP) from the SCR TDP to the riser seabed termination.
- The seabed slope is negative when the seabed increases in the negative direction (downward relative to the TDP), from the SCR TDP to the seabed termination.

Consider a flat seabed (AE), as shown in Figure 7-1. We will need to determine the coordinates of point B and C to be able to define the linear sloped seabed profile BC. The coordinates of B and C will be such that the line joining them passes through the static TDP of the SCR on a flat seabed. By doing this, we can impose the effect of the sloping seabed on the SCR configuration. This approach represents the scenario during riser preliminary layout design where the static TDP is known for an assumed flat seabed, which is eventually found not to be.

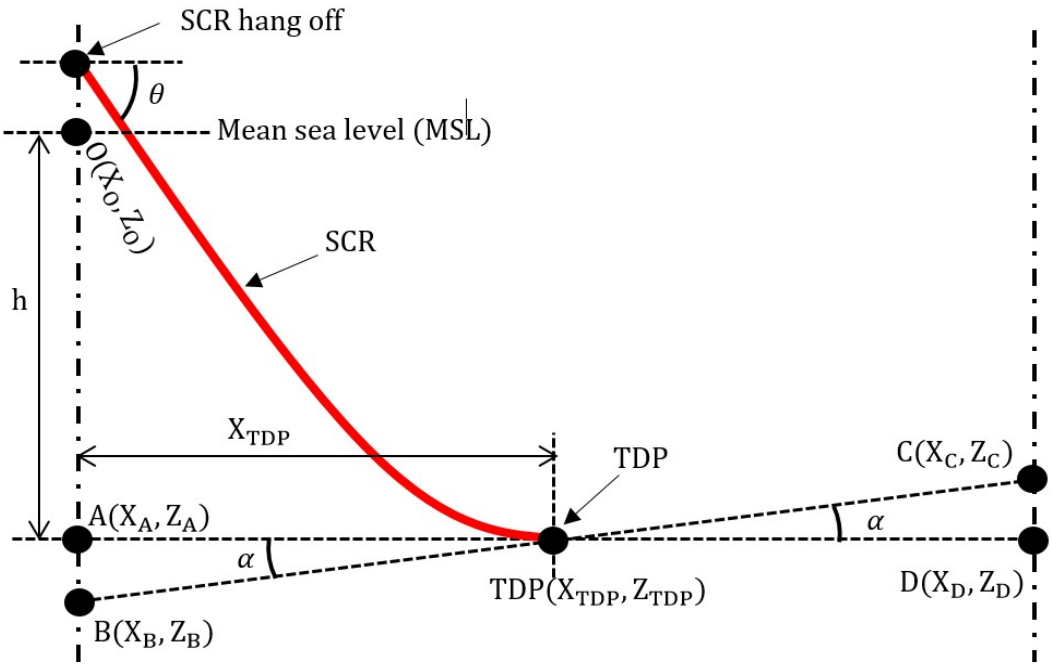

Figure 7-1 – Schematic of a linearly sloped seabed profile (BC)

Referencing all points from O on the mean sea level (MSL) in Figure 7-1, z coordinates of point B and C can be expressed as:

$$\boldsymbol{Z_B = Z_A + (X_A - X_{TDP})\, tan\, \alpha} \quad (7\text{-}1)$$

$$Z_C = Z_D + (X_D - X_{TDP})\, tan\, \alpha \quad (7\text{-}2)$$

Where:

$X_A = X_O = X_B$ = x coordinate of reference point O on the MSL.

$Z_A = Z_{TDP} = ZD$ = Elevation of the seabed referenced from the MSL.

X_{TDP} = x coordinate of the TDP from static configuration calculation.

α = Seabed slope

With the coordinates of point B and C calculated from equation (7-1) and (7-2), the seabed profile can be defined in OrcaFlex. Examples of SCRs configurations on the flat, positive, and negative sloped seabed are shown in Figure 7-2 (a), (b) and (c). The seabed incidence angle, β is the angle the riser makes with the vertical at the TDP. Under dynamic conditions, the dynamic incidence angle ($\beta_{dynamic}$) varies about the static incidence angle (β_{static}). Increasing the HO angle and the angle of the positively sloped seabed will result in increasing β_{static}, vice versa as observed in Figure 7-2 (a), (b) and (c), where $\beta_1 > \beta_2 > \beta_3$. β is an essential SCR geometric parameter, influenced by the HO angle, seabed slope and riser motion. It will be shown later how β correlates with the SCR TDZ response under dynamic loading.

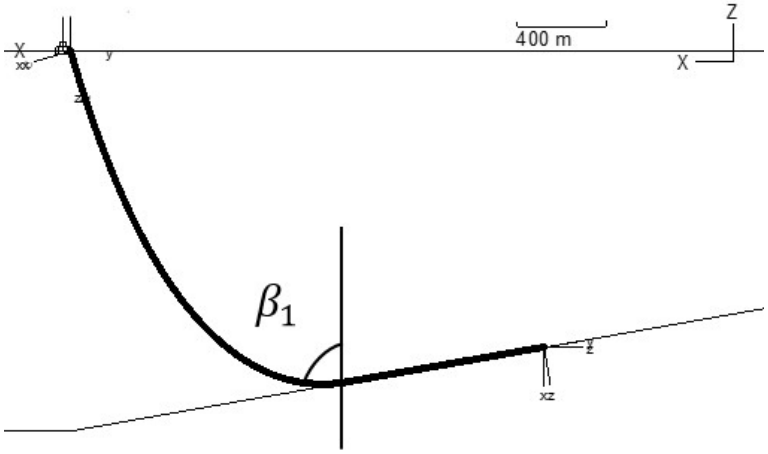

(a)

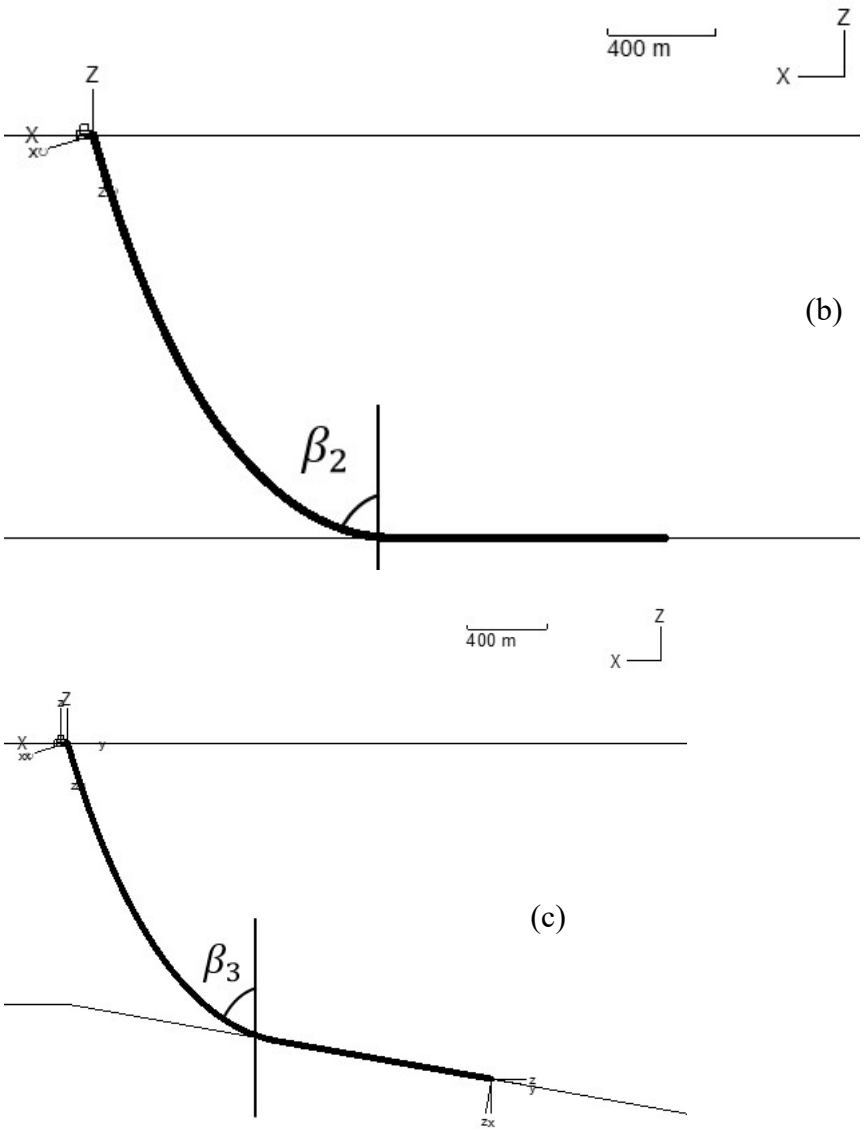

Figure 7-2 – Example: OrcaFlex SCR model with HO angle = 16deg on (a) flat seabed (0deg), (b) positive slopped seabed (+10deg) and (c) negative sloped seabed (-10deg)

The modelling, simulation and post-processing are automated using MATLAB programs integrated with the OrcaFlex high-level programming interface (OrcFxAPI [102]). The program calculates the initial SCR configurations using the catenary equations and creates the OrcaFlex SCRs models on flat seabed. The static calculation is then conducted to obtain the SCRs TDP coordinate on the flat seabed. The TDP coordinate and the seabed slope are then used to calculate point B and C using equations (7-1) and (7-2), such that the straight line from B to C passes through the calculated flat seabed TDP coordinate (see Figure 7-1). The linear profile defined by line BC is then

used to develop and update the seabed profile, inducing the sloped seabed profile on the configurations of SCR initially resting on the flat seabed. This translate to rotating the flat seabed about the SCR flat seabed TDP in the positive and negative senses as the rotation angle may be. The program repeats this for other SCRs across the three groups, generating models ready to be simulated. The storm and fatigue irregular wave loads (see Table 7-2) are modelled using the JONSWAP spectrum and simulated for all SCRs throughout 1200sec. The vessel RAOs and riser pipe content are set as well. A simulation buildup period of 50sec is allowed before the beginning of the main simulation to ensure the application of fully developed wave loads. The simulation period of 1200sec was sufficient since the study is a comparative one, same wave loads are imposed on all SCR models across the three groups, and the possibility of resonance in the SCRs are not considered. Numerical results post-processed by the program include the SCR node positions and motions, effective tensions, stress utilisation, stress ranges, and fatigue damage along the SCRs.

7.1.3 Analysis data for investigation

There are three groups of SCRs characterised by their hang-off angles (with the vertical), which are 8deg, 12deg and 16deg respectively. Each group consists of the SCR resting on nine linear profiled seabeds with seabed slopes of 0deg (flat seabed), ± 2deg, ± 4deg, ± 7deg and ± 10deg as presented in

Table 7-1. The SCRs are made up of 12inch pipe joints, hosted by a floating production system in a water depth of 1500m, and are conveying fluid of density 600kg/m^3. The SCRs wall-thickness (27.5mm) are calculated based on DNV-OS-F201 criteria [4], considering burst and collapse requirements for a design pressure of 10ksi. The hang-off connection stiffness of each SCRs has a linear value of 12kN.m/deg. Note that the HO angles given in

Table 7-1 are the angle the riser makes with the vertical.

Table 7-1 – Riser group for analysis

Group	HO angle (deg)	Seabed Slope (deg)
1	8	
2	12	0, ±2, ±4, ±7, ±10
3	16	

Presented in Table 7-2 are the selected storm and fatigue wave loads under which we investigate the responses of the groups of SCRs. Since the study is comparative rather than project design-based, we consider here a total exposure time of the SCRs to the fatigue load to be 20 years, neglecting stress concentration factors and other safety factors.

The nonlinear hysteretic riser-soil interaction model developed by Randolph and Quiggin (R&Q) is applied for this investigation.

Table 7-3 presents the default model data for the R&Q model. Details of the NL model can be found in [56]. Recall that the seabed profiles investigated in this study are 0deg (flat seabed), ± 2deg, ± 4deg, ± 7deg and ± 10deg. The vessel motion response to first-order beam sea wave is defined by its response amplitude operator (RAO) at 50% draft as presented in Figure 7-3.

We show here only the relevant RAOs to beam wave since the wave load are applied along the riser plane, which is at 90deg azimuth from the vessel's heading. This

direction is expected to impose the most significant vessel heave and roll motions on the risers. The RAOs are symmetric about the vessel's longitudinal and transverse axes.

Table 7-2 – Storm and fatigue wave load

Analysis	**Hs(m)**	**Tp (sec)**	**gamma**
Storm	8.0	13	1.6
Fatigue	4.5	9.5	1.8

Table 7-3 –Non-linear soil model data [56]

Model Parameter	**Value**
Mudline shear strength	5kPa
Shear strength gradient	1.5 kPa/m
Power law parameters (a, b)	(6, 0.25)
Normalised maximum stiffness	200
Suction ratio	0.6
Suction decay parameter	0.4
Penetration parameter	0.2

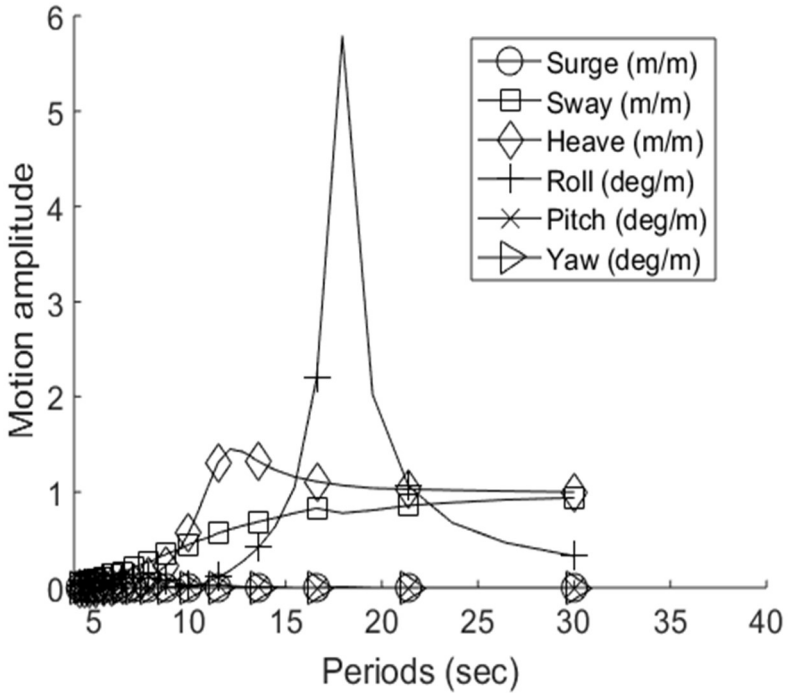

Figure 7-3 – Vessel RAOs in 90deg and 270deg direction

7.1.4 Analysis, results, and discussion

7.1.4.1 Static configuration

Static configurations for the three groups of SCRs are presented in Figure 7-4 (a), (b) and (c). A visual inspection of the global configurations of SCRs in each group indicates a minimum difference in their shapes. This is because the initial theoretical configurations defined during the FE modelling for each group was set to the same TDP. However, the TDPs of SCRs in each group are not the same in the FE static configurations, owing to the influence of the seabed slope and global stiffness of the risers. The impact of the seabed slope on the TDP locations, referred to as TDP offsets or errors in TDP location will be presented shortly.

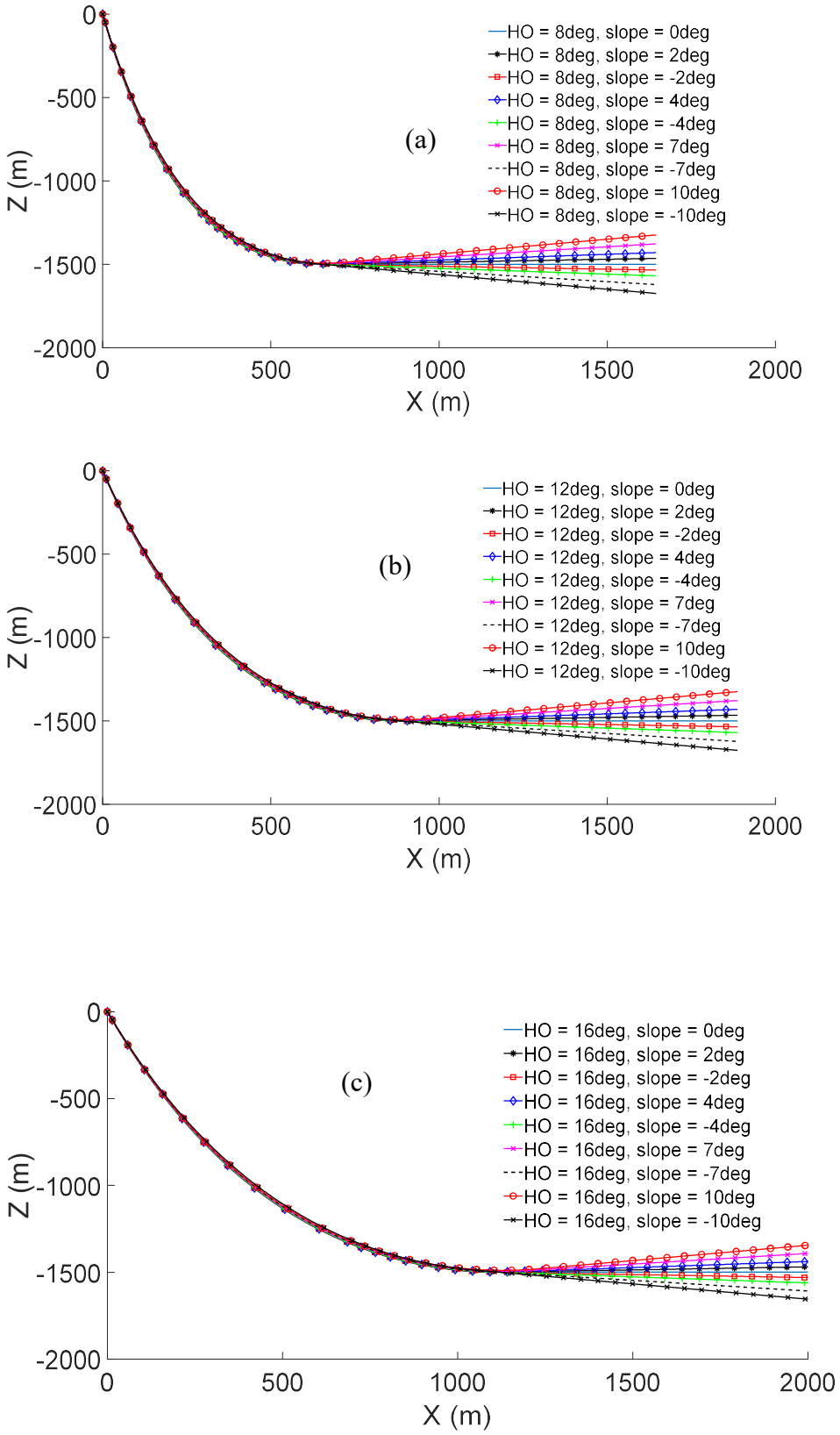

Figure 7-4 – Global FE static configuration of SCRs of different sloped seabed (a) HO angle = 8deg (b) HO angle = 12deg (c) HO angle = 16deg

7.1.4.2 Static touch down point offsets

Figure 7-5 presents the positions of the static TDP of risers in each group relative to their corresponding flat seabed SCR configurations. The abscissa indicates the difference between TDP arc length of SCRs on the sloped seabed (s_α) and those on the flat seabed (s_{0deg}). Positive and negative values indicate longer, and shorter TDP arc lengths compare with flat seabed risers, respectively.

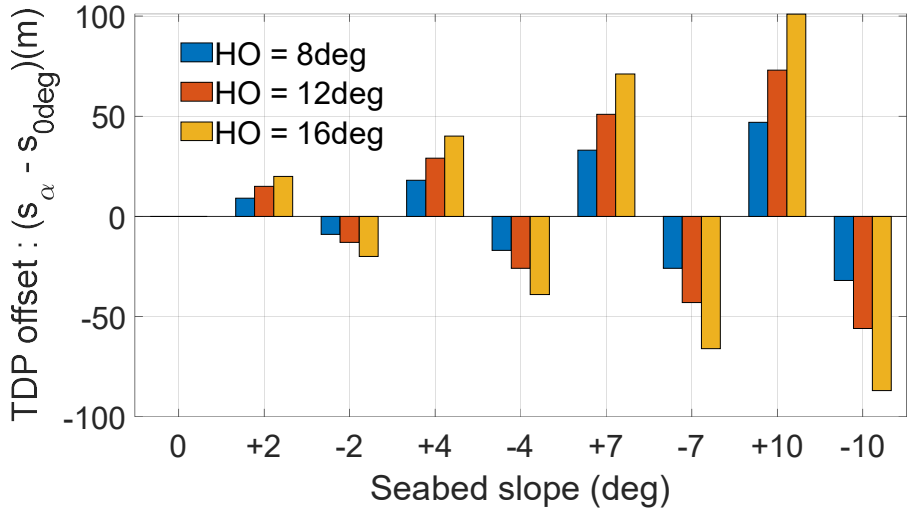

Figure 7-5 –TDP offsets of SCRs TDP on sloped from SCRs TDP on the flat seabed (0deg slope)

In each group, it is generally observed that the SCRs will first touch the seabed (i.e. at shorter arc length from HO) on the negatively sloped seabed, follow by on the flat seabed and then the positively slope seabed. The trend shows a progressive increase in TDP offset as the riser hang-off angle increases, and as the seabed slope increases in both positive and negative sense. TDP offset between 40m and 100m is possible for seabed slope between ±4deg and ±10deg. For deeper water where the SCR TDP is farther from the HO, the TDP offset can be even more significant. The SCR TDP offsets offset errors occur when a flat seabed is assumed during riser design rather than the realistic sloped seabed. Such errors can impact on the design of SCRs whose touch down sections are to be cladded with carbon resistive alloys (CRA), for corrosion induced fatigue mitigation. Coating of the internal riser section with CRA is expensive.

Hence, the arc length region to be cladded should correctly be estimated as best as possible. This underpins the importance of seabed slope consideration at the preliminary stage of the SCR design.

7.1.4.3 Static stress utilisation

The static stress utilisation of the SCRs for each group are presented in Figure 7-6 (a), (b), and (c). The static stress utilisations around the TDZ are observed to decrease with increasing HO angles. This is understandable since increasing HO angle implies reduced bending moments and bending stress around the TDZ. Also, the region of maximum static stress utilisation spreads over longer riser sections as the HO angle increases. Increasing HO angle translates to increasing β, causing gentler static riser contact with the seabed. As the seabed slope increases positively, it can be observed that the arc length (measured from the HO) at which the maximum stress utilisation occurs moves further towards the riser seabed anchor location. The reverse is the case for increasing negatively sloped seabed. This indicates that under dynamic conditions the location of peak stress withing the TDZ will likely be seen to move towards the direction of the riser seabed anchor with increasing positive slope seabed, and towards the HO direction for the negatively sloped seabed. This trend can be observed in the dynamic results presented later in this work.

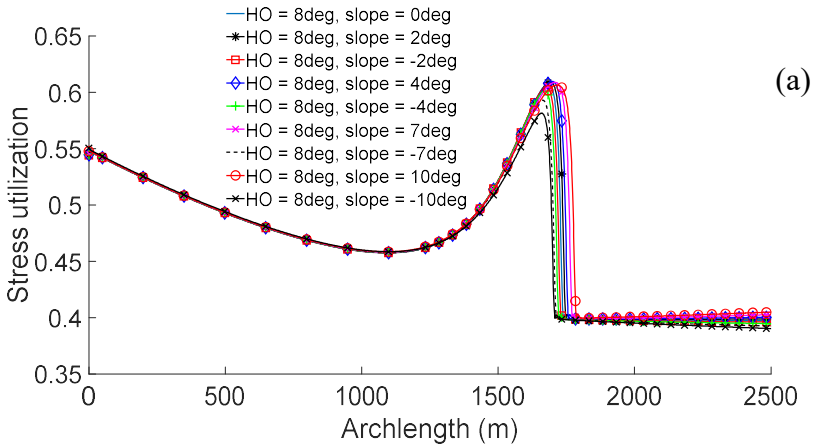

(a)

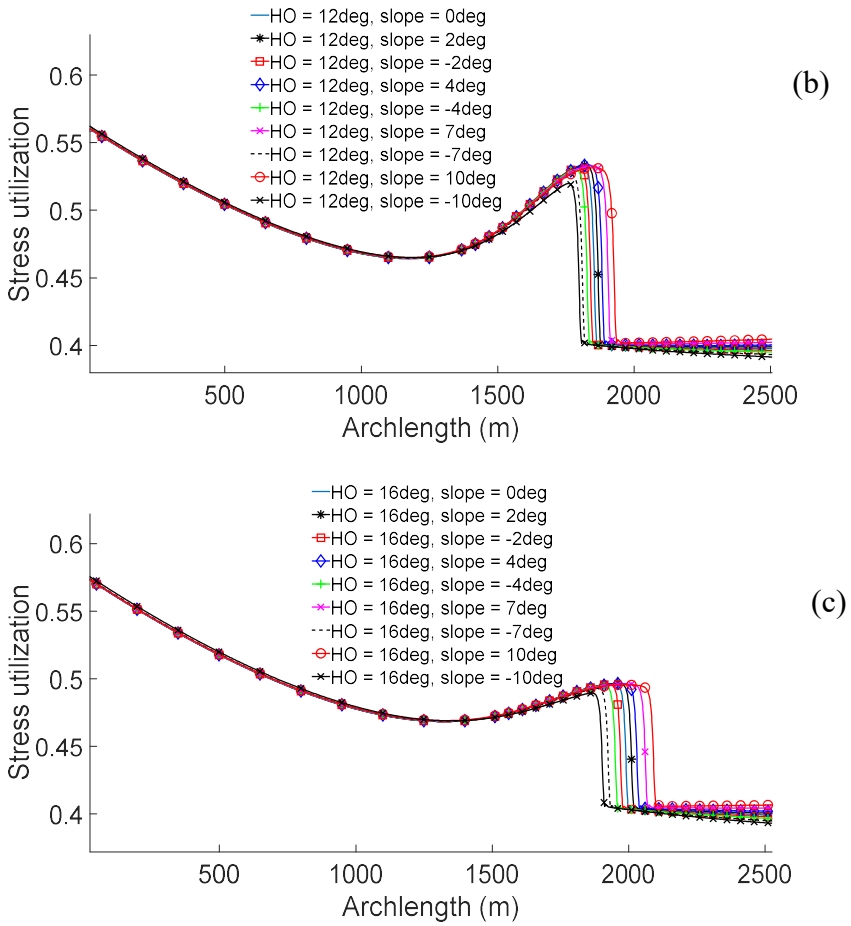

Figure 7-6 – Static stress utilization of SCRs of different sloped seabed (a) HO angle = 8deg (b) HO angle = 12deg (c) HO angle = 16deg

7.1.4.4 Static curvatures around the hang-off region

The SCRs curvatures around the HO region are presented in Figure 7-7 (a),(b) and (c). In the HO region, the axial stress component usually dominates stress utilisation. However, as observed in Figure 7-7 (a),(b) and (c), there could be small impacts on curvatures around the HO and hence bending moments and stresses caused by the seabed slope. The seabed slope impact on the riser curvature around HO region is observed to be more significant with increasing riser HO angle with the vertical. This influence can be amplified in dynamic conditions.

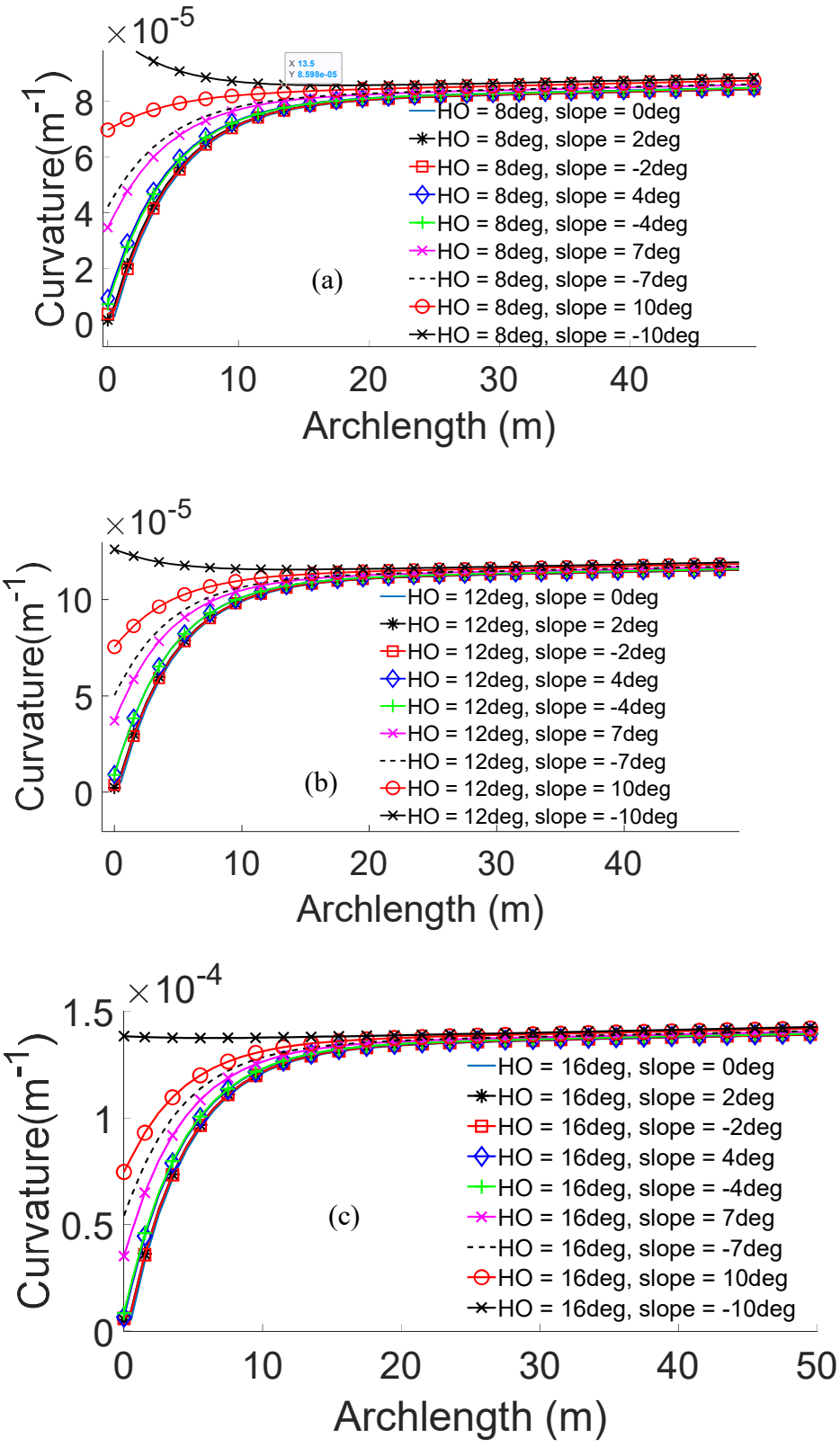

Figure 7-7 – Riser curvature around the HO region (a) HO angle = 8deg (b) HO angle = 12deg, (c) HO angle = 16deg.

7.1.4.5 Static top tension

The static top tension of SCR is a combination of the weight of its hanging section, including content (600kg/m^3 in this study), less its displacement. The external and internal pressures effect are accounted for in the case of effective tension calculation. The difference in the lengths of the hanging SCR section (from HO and TDP) results in a difference in the static top tension. The difference between the static top tension of SCR on the sloping seabed and those of SCR on the flat seabed, across the riser groups, are presented in Table 7-4 and the bar chart in Figure 7-8. It could be seen that both positively and negatively sloped seabed profiles around the SCR TDZ can increase static top tension with respect to top tension of SCR on the flat seabed. For seabed slope up to -2deg, there is a negligible change in top tension. The difference, however, becomes significant as the seabed slope increases in the negative sense beyond -4deg, with higher differences occurring for higher HO angles. For example, with seabed slope of -10deg, the static top tension of SCR on the flat seabed can be increased by more than 20kN if the seabed is inaccurately assumed to be flat (0deg). On the other hand, the positively sloped seabed affects the top tension less than what was observed for the negatively sloped seabed. Not more than 10kN increase in flat seabed SCR top tension is observed if seabed slope of up to +10deg around TDZ is inaccurately assumed to be flat. The change in top tension of sloped seabed SCRs with their corresponding flat seabed SCRs reduces with increasing HO angles for increasing positively sloped seabed.

Table 7-4 – Effect on SCR static top tension for sloped and flat seabed

Seabed slope (deg)	**Static top tension T_{eff} (kN)**			**Change in top tension ΔT_{eff} ($T_{\alpha} - T_{0deg}$)(kN)**		
	HO = 8deg	HO = 12deg	HO = 16deg	HO = 8deg	HO = 12deg	HO = 16deg
0	2436.0	2646.5	2892.4	0.0	0.0	0.0
2	2437.1	2647.5	2893.2	1.1	1.0	0.8
-2	2435.9	2646.6	2892.7	-0.1	0.1	0.3

4	2438.7	2649.0	2894.5	2.7	2.5	2.1
-4	2437.3	2648.5	2895.1	1.3	2.1	2.7
7	2441.2	2651.3	2896.1	5.2	4.8	3.7
-7	2444.2	2657.2	2905.2	8.2	10.7	12.8
10	2442.8	2652.5	2896.3	6.8	6.0	3.9
-10	2460.2	2677.1	2928.7	24.1	30.6	36.3

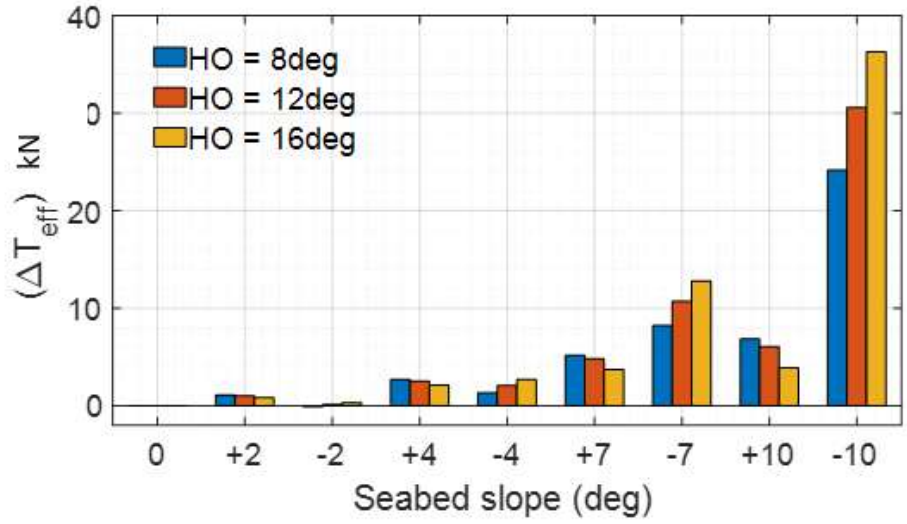

Figure 7-8 – Percentage change in static top tension of SCRs on sloped seabed relative to SCR on a flat seabed

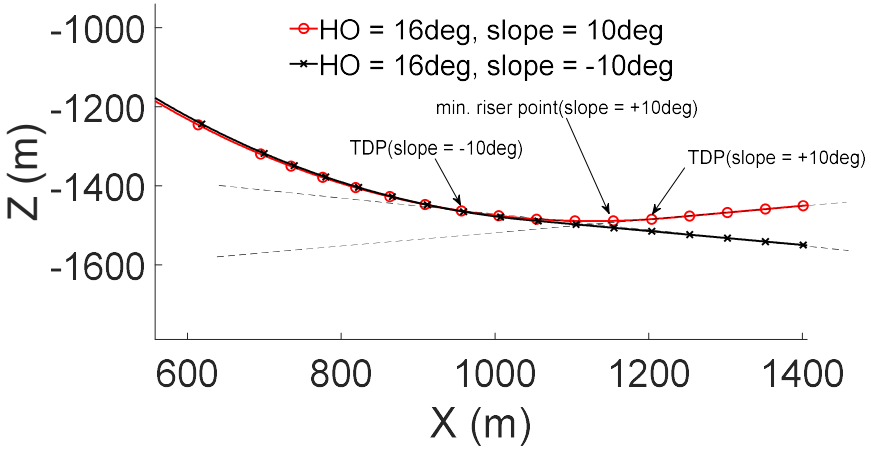

Figure 7-9 – Expanded view of TDZ sections for SCR with HO angle = 16deg, seabed slope = -10deg and +10deg.

Recall that the SCRs on negatively sloped seabed touched down first (i.e. TDP occurs at shorter arc length from HO) before those of positively sloped seabed, with the flat

seabed SCRs in between (see Figure 7-5). This is supposed to mean that the top tension of SCR on the negatively sloped seabed will be smaller than the same SCR on the positively sloped seabed. However, as can be seen in Figure 7-8, the static top tensions for SCRs on the negatively sloped seabed are higher than those of positively sloped seabed. This appears contradictory. A detailed look at Figure 7-9 which is the configuration plot for SCR with 16deg HO angle resting on ± 10deg sloped seabed, reveals the reason why it is so. Although the TDP of the riser on negative seabed touches down first, the riser section beyond the TDP on the seabed still contributes to the vertical weight component to the hanging weight of the SCR until the riser seabed frictional force cancels it. On the other hand, the weight beyond the TDP of the SCR resting on positively sloped seabed rests solely on the seabed. Hence, the top tension only dependent on the length of the hanging section rather than additional contributions from seabed section, i.e.the hanging section weight is only contributing to by the riser section from the hang off to the minimum point (just before its TDP)(see Figure 7-9).

7.1.4.6 Dynamic analysis – Maximum top effective tension

The three groups of risers are subjected to storm wave load presented in see Table 7-2. The range graph maximum effective tension is the vector of nodal maximums over the simulation time. The range graph maximum results are presented in Figure 7-10(a),(b) and (c). Maximum top tension occurs during the upward motion of the vessel where the SCRs are pulled upward, and a longer section of the SCRs are hanging. It is observed from Figure 7-10 that the negatively sloped seabed SCRs have higher top tension when compared with the flat and positively sloped seabed SCRs. Top tensions of positively sloped seabed SCRs have values slightly less than SCRs on the flat seabed. SCRs top tensions are seen to be more sensitive to increasing negatively sloped seabed than positively sloped seabed SCRs. The results presented in Table 7-5 and Figure 7-11 indicate more than 10% increase in SCR top tension for SCRs on the sloped seabed that of -10deg compared with SCRs on the flat seabed. These observations translate to significantly impact on the design of topside supporting structures for the SCRs if a flat

seabed is assumed during design, rather than the actual sloped seabed profile around the TDZ. As the water gets deeper, the top tension increases and hence the increase in the impact on top tension of SCRs on the negatively sloped seabed. While this is disadvantageous to SCRs resting on the negatively sloped seabed, it is an advantage for SCRs resting on the positively sloped seabed since their top tensions are reduced relative to SCR on assumed flat seabed. Table 7-5 and Figure 7-11. However, such improvement is small but can be relevant for deeper water, higher positively sloped seabed, and for SCRs with higher HO angles.

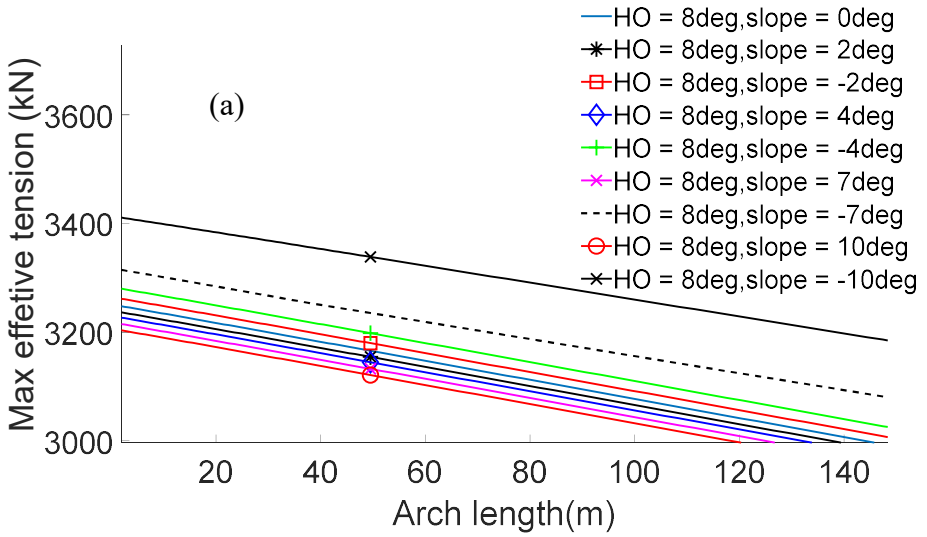

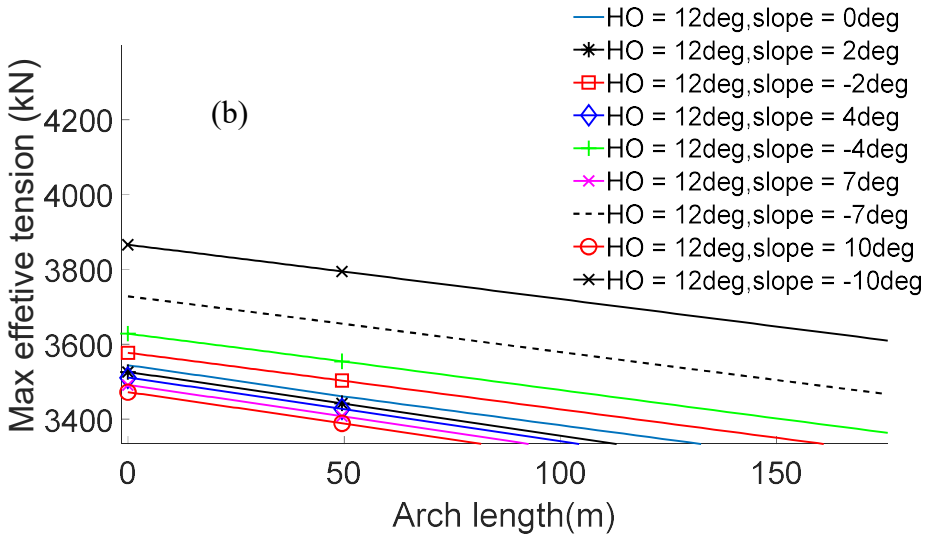

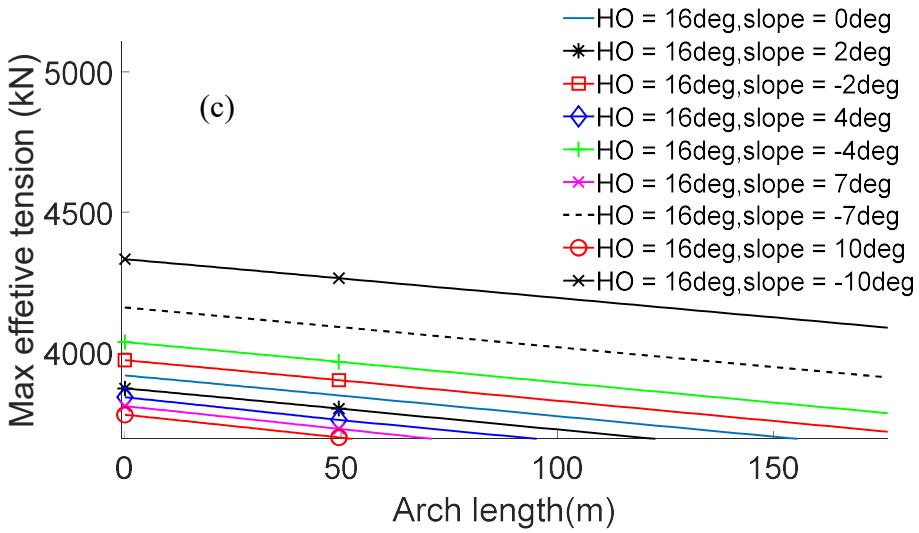

Figure 7-10 – Riser maximum effective tension: (a) HO angle = 8deg, (b) HO angle = 12deg, (c) HO angle= 16deg.

Table 7-5 – Maximum top tension of SCRs on the sloping seabed, and their percentage differences from SCRs on the flat seabed.

Seabed slope (deg)	**Maximum T_{eff} (kN)**			**% change in max. top T_{eff} relative with flat seabed risers**		
	HO = 8deg	HO = 12deg	HO = 16deg	HO = 8deg	HO = 12deg	HO = 16deg
0	3250.9	3543.8	3918.2	0.0	0.0	0.0
2	3239.7	3525.5	3872.1	-0.3	-0.5	-1.2
-2	3264.6	3577.1	3972.5	0.4	0.9	1.4
4	3229.8	3510.6	3840.5	-0.6	-0.9	-2.0
-4	3283.1	3628.0	4037.2	1.0	2.4	3.0
7	3218.0	3490.9	3808.7	-1.0	-1.5	-2.8
-7	3317.7	3727.9	4160.4	2.1	5.2	6.2
10	3206.5	3471.9	3778.0	-1.4	-2.0	-3.6
-10	3413.7	3865.7	4332.4	5.0	9.1	10.6

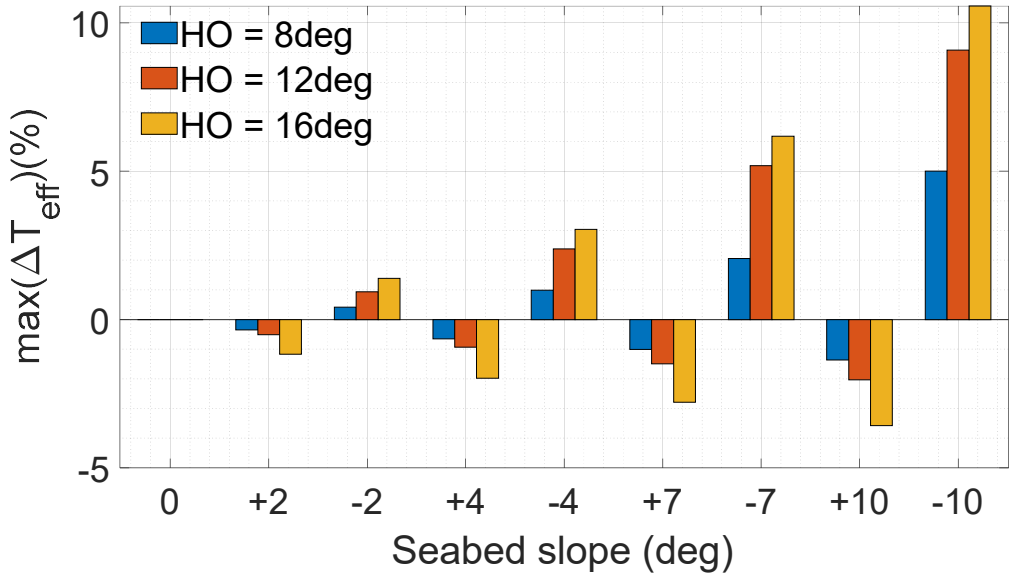

Figure 7-11 – Percentage change in maximum dynamic top tension of sloped seabed SCRs relative to SCRs on a flat seabed

7.1.4.7 Dynamic analysis – TDZ compression

The effective negative tension around the riser TDZ is an indication of riser compression. In general, for risers resting on the same sloped seabed, the compression increases with decreasing hang off-angle. SCR TDZ compression is highly sensitive to seabed slope around the TDZ. The range graph minimum effective tension in the SCRs are presented in Figure 7-12 (a), (b), and (c). From Figure 7-12, all SCRs resting on the flat seabed are in compression. The level of compression observed for flat seabed SCRs are significantly amplified for even smaller change in the inclination of the negatively sloped seabed as seen in Table 7-6 and Figure 7-13. Note that in Figure 7-13, the positive abscissa values indicate an increase in compression (increased negativity of effective tension relative with the flat seabed SCRs). The reverse is the case for negative abscissa values which indicate a reduction in TDZ compression. Compression observed for flat seabed SCRs is improved upon significantly when the seabed becomes positively sloped. Note that SCRs resting on negatively and positively sloped seabed respectively have smaller and larger seabed incidence angle (β) than SCRs resting on the flat seabed. The observations translate to higher SCR TDZ compressions or higher

buckling tendencies for SCRs having smaller β. Increased compression for negatively sloped seabed SCRs may be critical for SCRs designs where TDZ buckling is majorly a challenge. The results show that we underpredict TDZ buckling when we assume a flat seabed rather than the profiled seabed around the SCR TDZ. For example, SCR of HO angle 16deg, encountering -4deg seabed slope around its TDP, can have up to 500% increase in TDZ compression unaccounted for if we assumed a flat seabed profile for the design. On the other hand, with a positively sloped seabed profile, a significant benefit in the form of reduced TDP compression or buckling is observed.

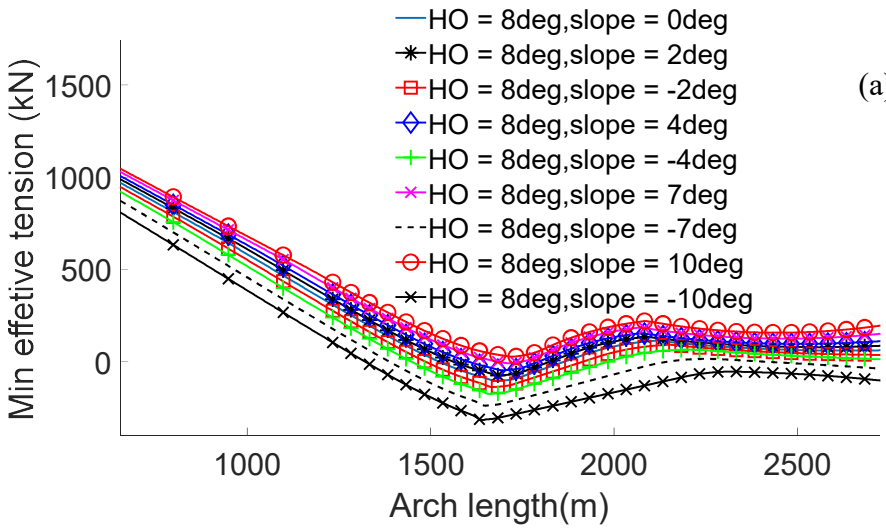

(a)

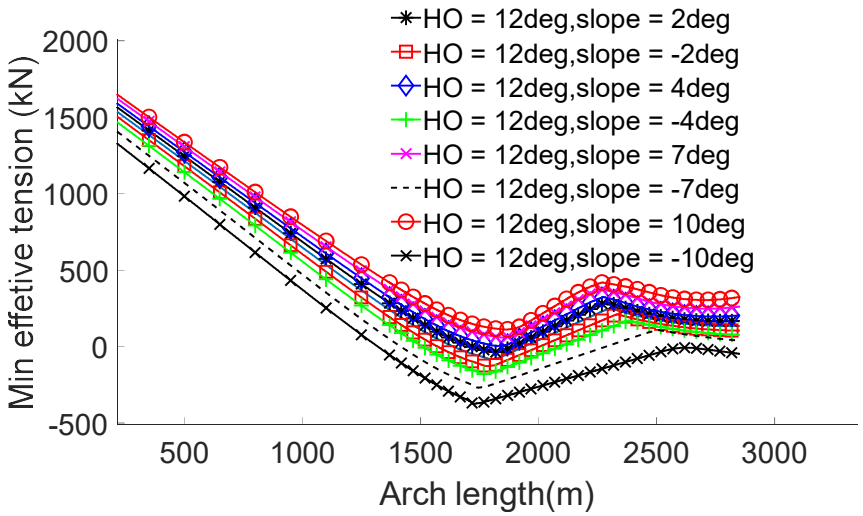

(b)

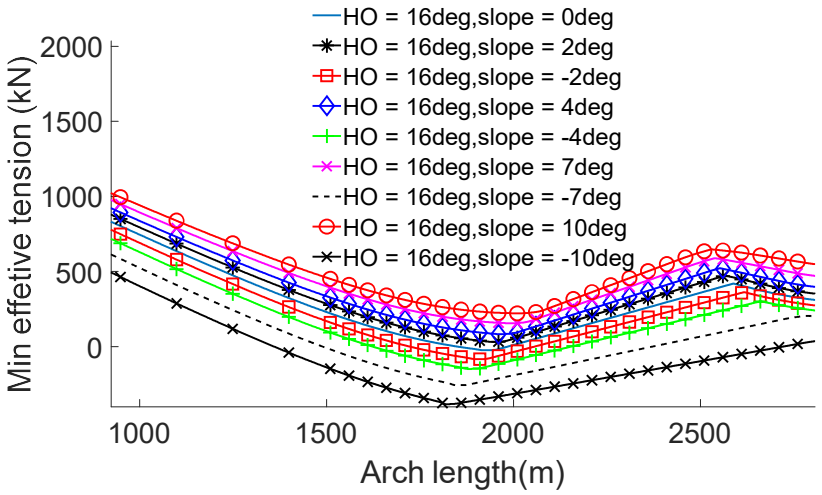

(c)

Figure 7-12 –Minimum effective tension in SCR TDZs: (a) HO angle = 8deg, (b) HO angle= 12deg, (c) HO angle= 16deg.

Table 7-6 – Percentage change in SCRs TDZ compression relative to their respective flat seabed configuration

Seabed slope (deg)	**Minimum T_{eff} (kN)**			**% Change in min. T_{eff} relative with flat seabed (compression)**		
	HO = 8deg	HO = 12deg	HO = 16deg	HO = 8deg	HO = 12deg	HO = 16deg
0	-106	-80	-25	0.0	0.0	0.0
2	-75	-37	31	-29.2	-53.8	-224.0
-2	-138	-127	-84	30.2	58.8	236.0
4	-48	4	83	-54.7	-105.0	-432.0
-4	-175	-179	-149	65.1	123.8	496.0
7	-9	60	155	-91.5	-175.0	-720.0
-7	-239	-268	-258	125.5	235.0	932.0
10	27	112	222	-125.5	-240.0	-988.0
-10	-317	-374	-384	199.1	367.5	1436.0

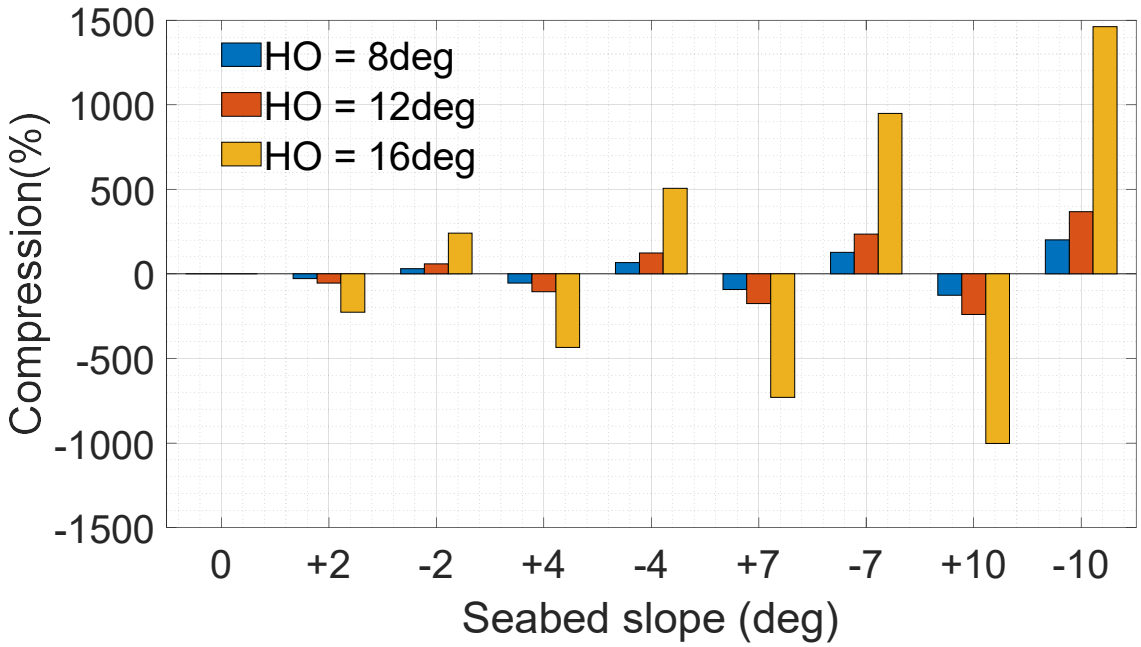

Figure 7-13 – Percentage change in SCR TDZ compression relative to SCRs on a flat seabed

7.1.4.8 Dynamic analysis – Stress utilisation

The DNV-OS-F201 dynamic stress utilisation in the SCR TDZ for risers in the three groups are presented in Figure 7-14 (a), (b) and (c) respectively.

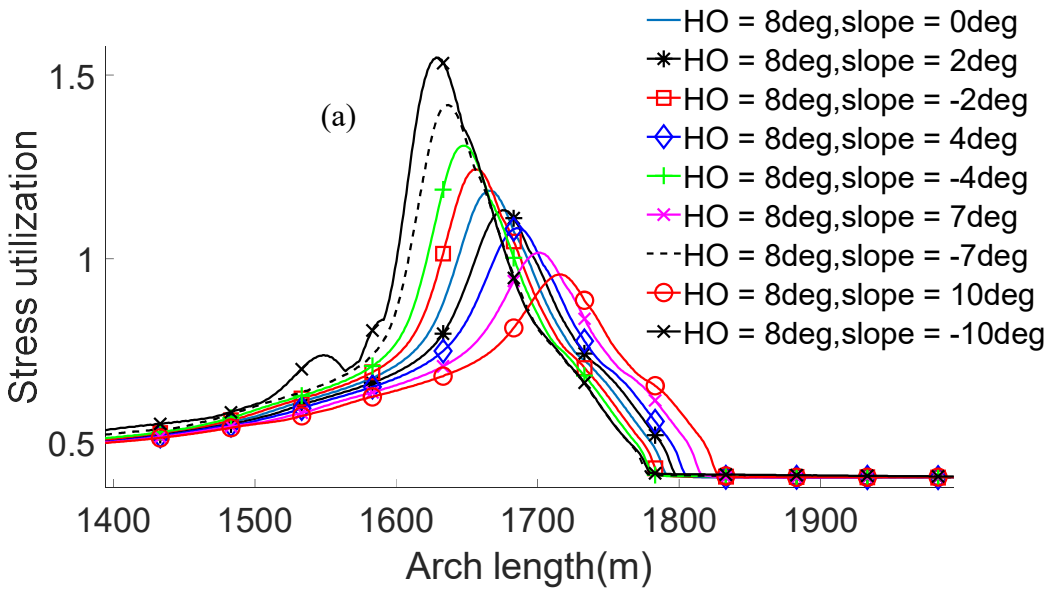

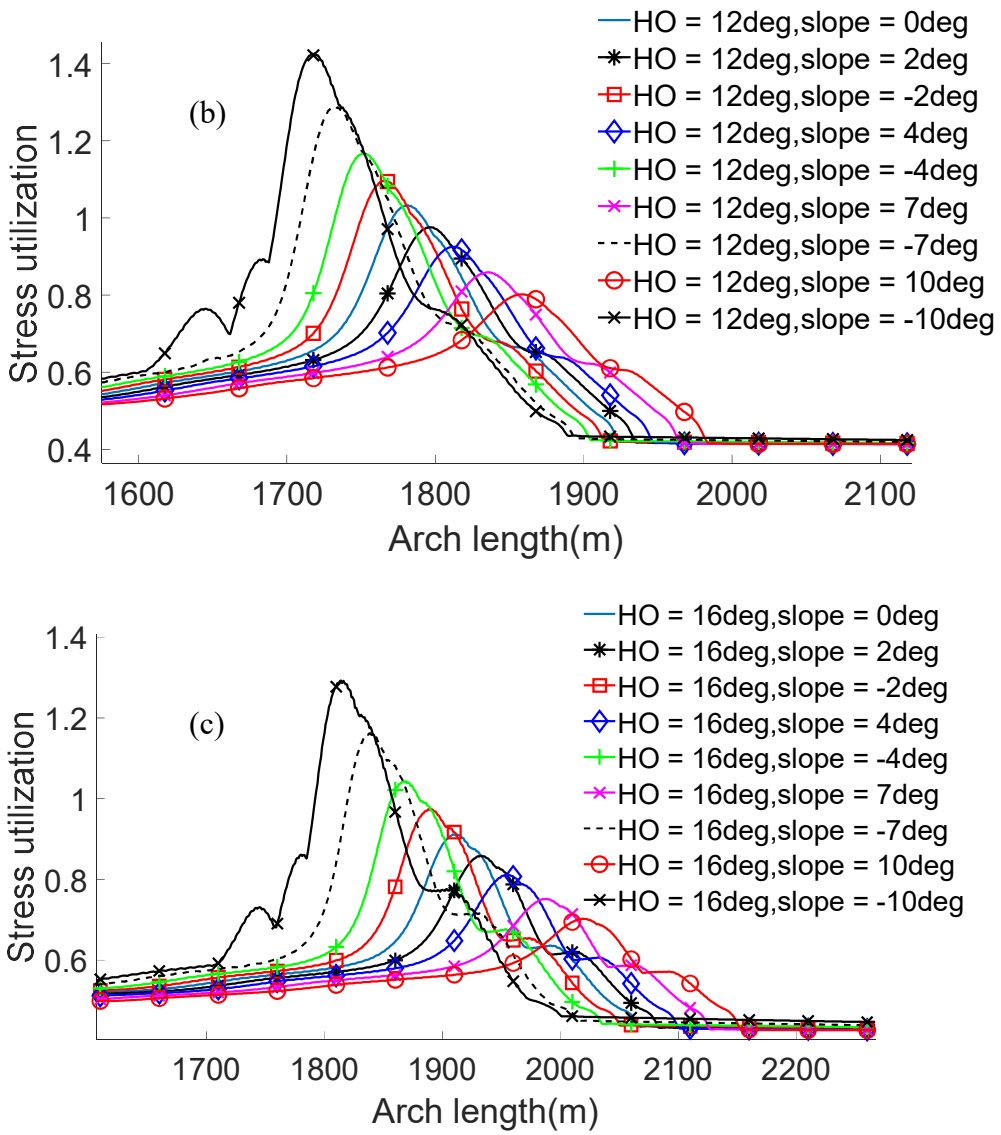

Figure 7-14 – Maximum DNVF201 stress utilization in TDZ for risers: (a) HO angle = 8deg, (b) HO angle= 12deg, (c) HO angle= 16deg.

The TDZ stress utilisation is a combination of stress component contributed to by the axial tension, bending moment and pressure loads. The most dominating component of the stress utilisation around the TDZ is with the bending stress component. Since higher buckling tendencies were observed in the TDZ of SCRs resting on the negatively sloped seabed, it is expected that the stress utilisation within this region is higher for the negatively sloped seabed. This is confirmed by the results presented in Figure 7-14 (a), (b), and (c). It can indeed be observed that SCRs resting on negatively sloped seabed incur higher TDZ stress utilisation compared with same SCRs resting on the flat seabed.

The converse is the case for the positively sloped seabed. It is also observed in general (both static and dynamic cases) that the point of highest TDZ stress utilisations shifts towards the HO direction for increasing negatively sloped seabed and towards the seabed anchor direction for the positively sloped seabed. For SCRs on the flat seabed, the TDZ stress utilisation is observed to be higher for risers with smaller HO angles since this implies smaller β. However, it is possible to have higher TDZ stress utilisation for SCRs with larger HO angle compared with SCRs with smaller hang off-angle if the seabed slope on which the former risers rest result in smaller β than the later risers.

Table 7-7 – Percentage change in SCRs stress utilisation (U) relative to their respective flat seabed configuration

Seabed slope (deg)	**Maximum U**			**% change in U relative with the flat seabed**		
	HO = 8deg	HO = 12deg	HO = 16deg	HO = 8deg	HO = 12deg	HO = 16deg
0	1.2	1.0	0.9	0.0	0.0	0.0
2	1.1	1.0	0.9	-8.3	0.0	0.0
-2	1.2	1.1	1.0	0.0	10.0	11.1
4	1.1	0.9	0.8	-8.3	-10.0	-11.1
-4	1.3	1.2	1.0	8.3	20.0	11.1
7	1.0	0.9	0.8	-16.7	-10.0	-11.1
-7	1.4	1.3	1.2	16.7	30.0	33.3
10	1.0	0.8	0.7	-16.7	-20.0	-22.2
-10	1.5	1.4	1.3	25.0	40.0	44.4

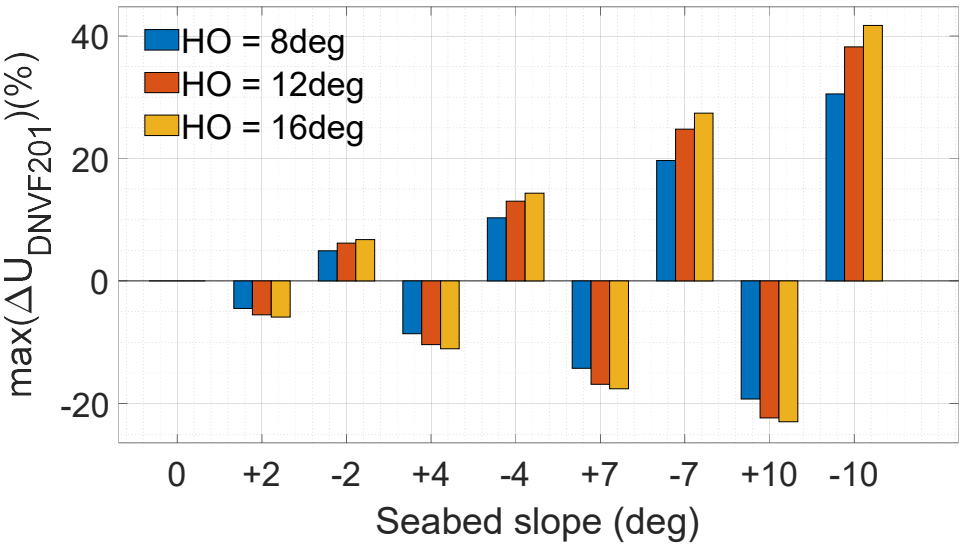

Figure 7-15 – Percentage change in SCRs TDZ stress utilisation relative to SCRs on a flat seabed

Again, similar to observations made on results for SCRs maximum top tensions and TDZ compressions, the positively sloped seabed provides benefits in the form of the reduction in stress utilisation. On the other hand, assuming a flat seabed in design, when the seabed is indeed sloped negatively can result in underestimation of the stress utilisation in the SCR TDZ.

7.1.4.9 Dynamic analysis - Time history of the most critical point

Compression or buckling in the SCR TDZ depends on the velocity of the TDZ section during riser excitations. TDZ compression can occur when the difference between the downward velocity of the riser TDZ section are higher compared with the section terminal velocity, and when the TDZ section impact on the seabed at higher acceleration. The time history of the seabed incidence angle (β), the absolute velocity, the compression (effective negative tension) and stress utilisation at critical points within the TDZ regions are presented in Figure 7-16(a), (b), (c) and (d) respectively. The critical points are the arc lengths along the SCRs from the HO, where the highest stress utilisation occur for the different SCRs in the three groups. It is observed that β have the smallest values at the time when the absolute values of velocities are highest. This indicates a correlation between the impact velocity and the resulting SCR curvature characterised by β. On the other hand, value of β are higher for lower absolute values of velocities. Hence, higher impact velocities at these points on the seabed resulting in lower values of β cause higher dynamic bending curvature, bending moments, compressions and stress utilisations. Again, SCRs on the positively sloped seabed are seen to have higher β than SCRs on negatively sloped seabed, hence reduced time history responses.

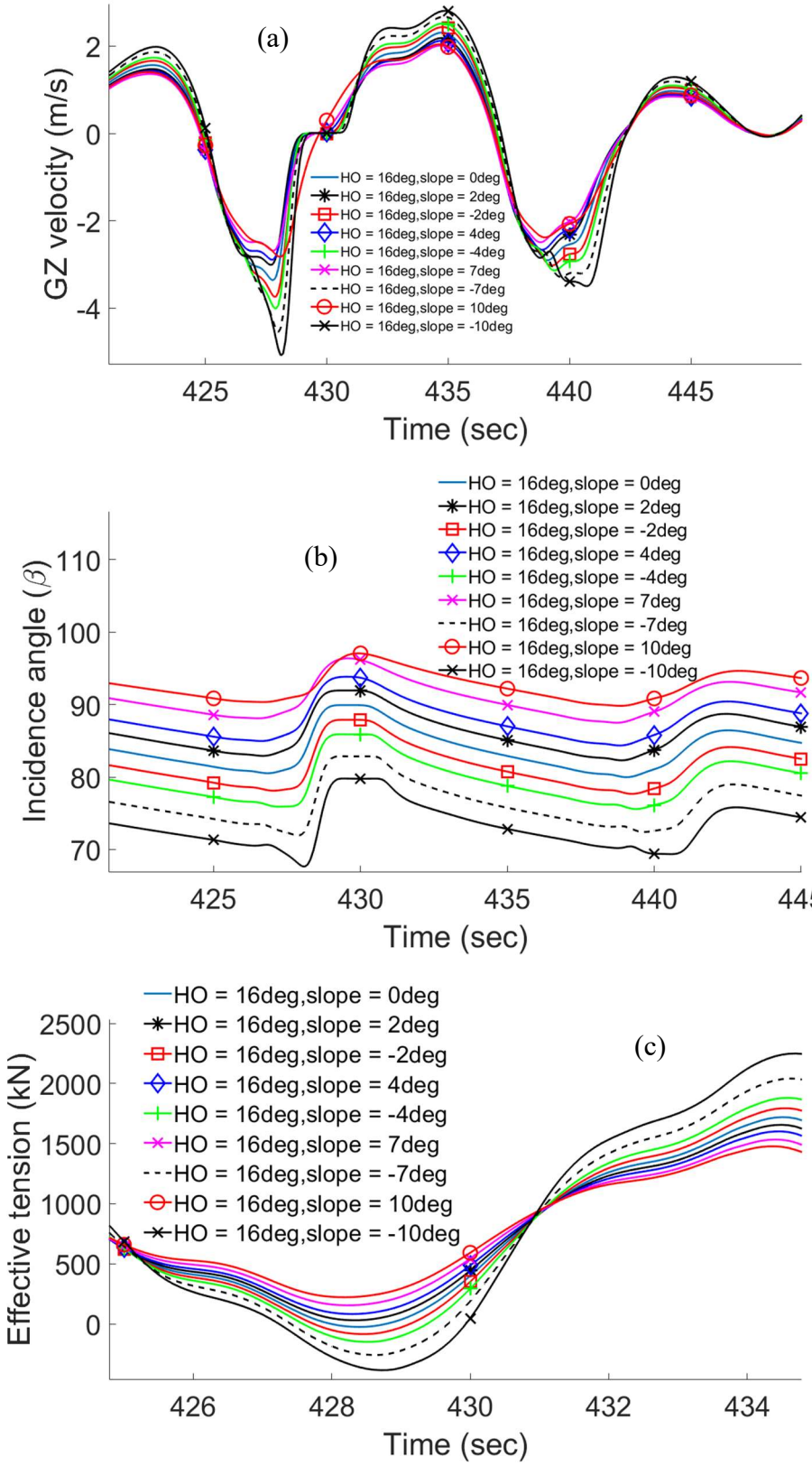
(a)
GZ velocity (m/s)
Time (sec)
HO = 16deg,slope = 0deg
HO = 16deg,slope = 2deg
HO = 16deg,slope = -2deg
HO = 16deg,slope = 4deg
HO = 16deg,slope = -4deg
HO = 16deg,slope = 7deg
HO = 16deg,slope = -7deg
HO = 16deg,slope = 10deg
HO = 16deg,slope = -10deg
(b)
Incidence angle (β)
Time (sec)
(c)
Effective tension (kN)
Time (sec)

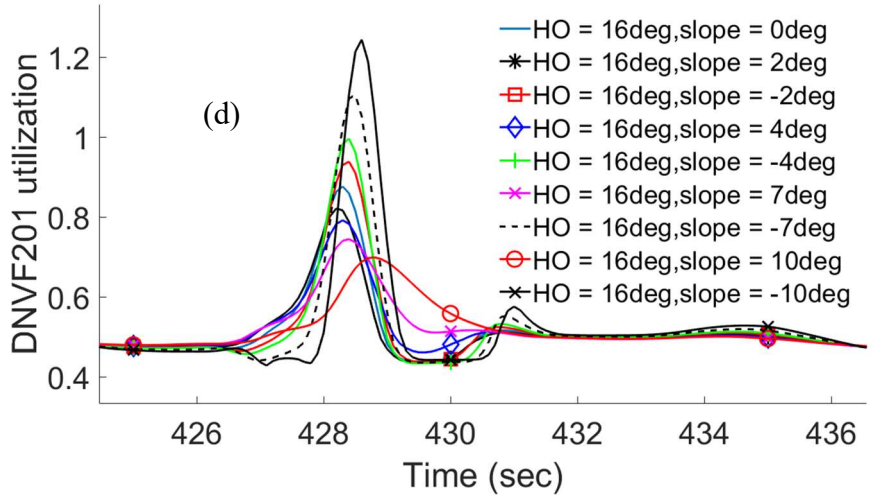

Figure 7-16 –Critical TDZ point time history (a) GZ velocity, (b) seabed incidence angle($\boldsymbol{\beta}$), (c) Effective tension, (d) DNV-OS-F201stress utilisation

7.1.4.10 Fatigue analysis – stress range

The three groups of risers are subjected to fatigue load presented in Table 7-2. The maximum stress range within the stress histogram is presented in Figure 7-17 (a), (b) and (c). The active TDZ session is the TDZ region were the stress range is significant. During SCR design, it is important to know the start and endpoint of this region for a number of reasons. As observed from the results, the arc lengths at which the maximum stress range occur in each riser moves in the direction of the HO for increasing negatively sloped seabed and move in the direction of the seabed anchor for increasing positively sloped seabed. With increasing SCR HO angles, the spread of active TDZ for SCR on sloped seabed deviates more from the active TDZ for SCR on the flat seabed. As a result, a higher error can be incurred in the estimation of the active TDZ section when the seabed is assumed flat rather than considering the actual sloped profile.

Considering SCRs resting on the flat seabed for each group, one can observe from Figure 7-17 that SCRs are having smaller HO angle incur higher maximum stress range compared with those having higher hang off-angle. This means that higher fluctuating bending stress occurs for riser with smaller β since smaller hang off-angle on flat

seabed translates to smaller β. As the seabed slope increases in the positive sense, β increases resulting in a reduction in the maximum stress range value in the TDZ. Conversely, as the seabed slope increases in the negative sense, β decreases and the maximum stress range values increases. This again indicates the benefits of having a positively sloped seabed in the SCR TDZ vicinity as it improves or reduces the SCR TDZ maximum stress range. A summary of the maximum stress range results for SCR on sloped seabed compared with SCR on the flat seabed are presented in Table 7-8 and Figure 7-18.

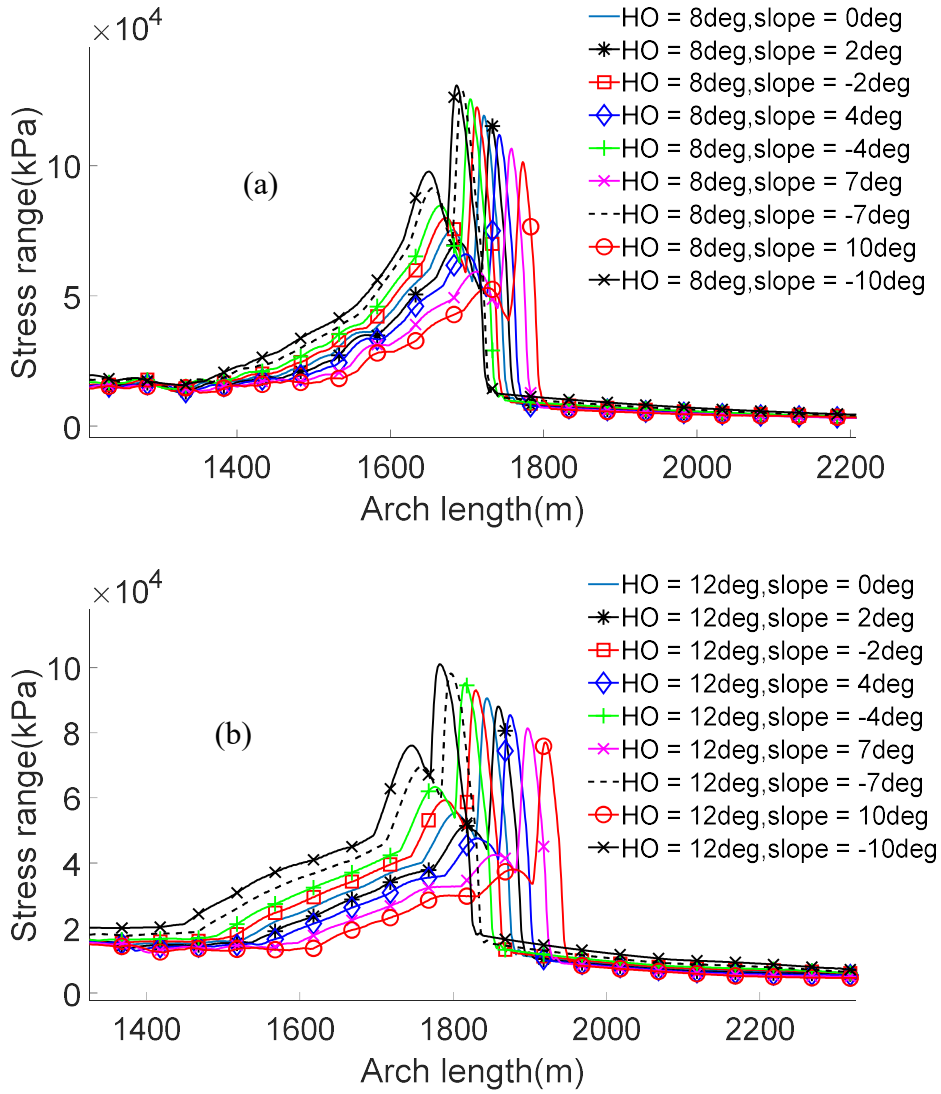

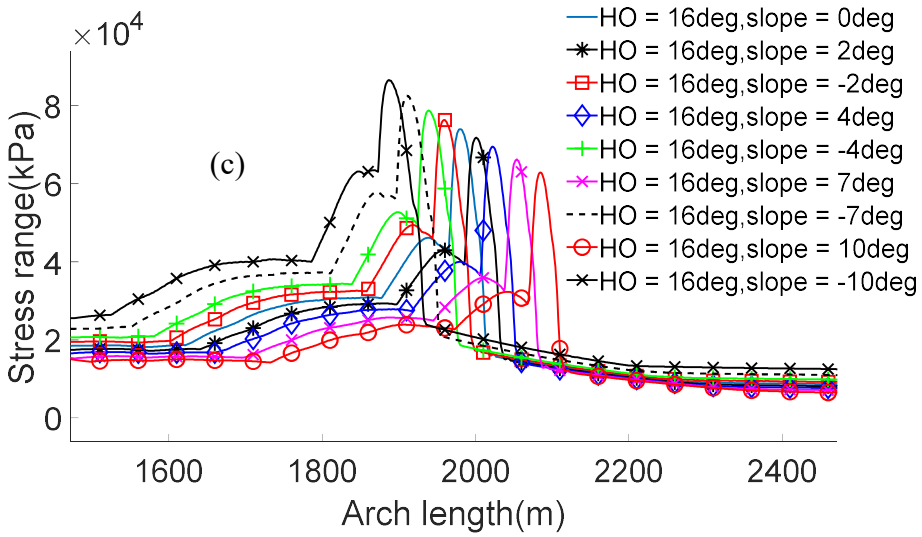

Figure 7-17 – Maximum stress range around riser TDZ for riser groups: (a) HO angle = 8deg, (b) HO angle= 12deg, (c) HO angle= 16deg

Table 7-8 – Percentage change in SCRs maximum stress range relative to their respective flat seabed configuration

Seabed slope (deg)	**Maximum Δσ (kPa)**			**% change in Δσ relative with the flat seabed**		
	HO = 8deg	HO = 12deg	HO = 16deg	HO = 8deg	HO = 12deg	HO = 16deg
0	119314	90695	73987	0.0	0.0	0.0
2	115798	88141	71805	-2.9	-2.8	-2.9
-2	122480	93079	76362	2.7	2.6	3.2
4	111949	85486	69491	-6.2	-5.7	-6.1
-4	125560	95248	78773	5.2	5.0	6.5
7	106615	81449	66209	-10.6	-10.2	-10.5
-7	128844	98270	82590	8.0	8.4	11.6
10	101487	77132	62903	-14.9	-15.0	-15.0
-10	130929	101107	86613	9.7	11.5	17.1

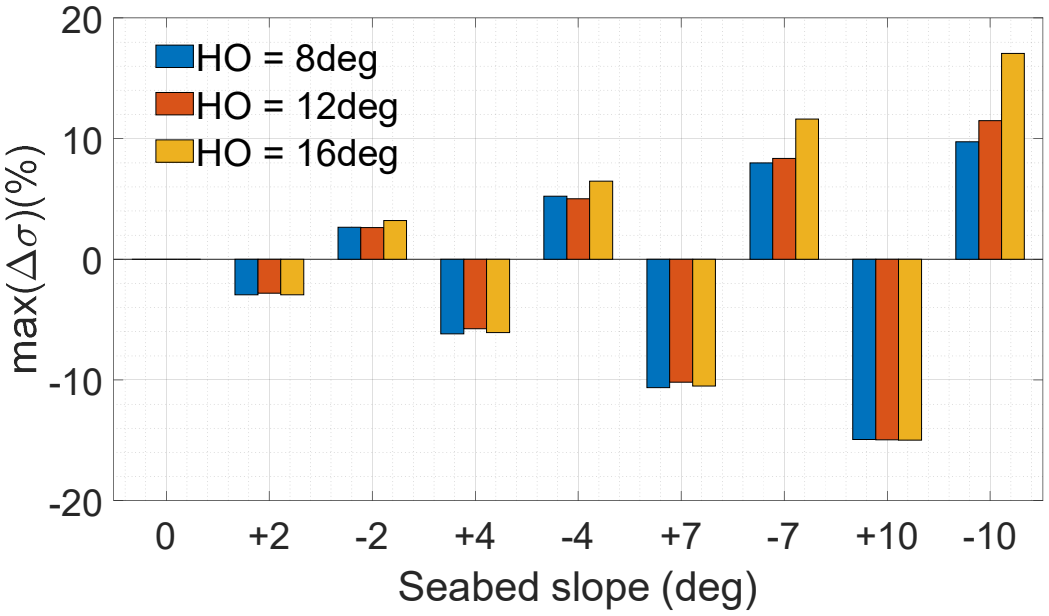

Figure 7-18 – Percentage change in SCRs TDZ maximum stress range relative to their respective flat seabed configuration

7.1.4.11 Fatigue analysis – fatigue damage

Although the maximum stress range is a subset of the stress histogram, the general contributions of the totality of the stress range to fatigue damage will follow similar trends as observed for maximum stress range response, for positively and negatively sloped seabed. However, the relative percentage increase of damage in SCRs on sloped seabed relative to those on the flat seabed can be different since the total fatigue damage will be contributed to by all stress ranges in the stress histogram. The SCRs fatigue damage results are presented in Figure 7-19 (a), (b) and (c). The damage computation is performed using the RFC technique, which combines the whole histogram of stress ranges at each nodal location along the riser string. The results reveal that with increasing positively sloped seabed (increasing β), the fatigue damage reduces compared with same SCRs on the flat seabed. The converse is the case for negatively sloped seabed with higher β. Summary results of fatigue damage are presented in

Table 7-9. The results further indicate benefits to SCRs fatigue lives by the positively sloped seabed and drawbacks for SCRs resting on the negatively sloped seabed, for which flat seabed was assumed during their design.

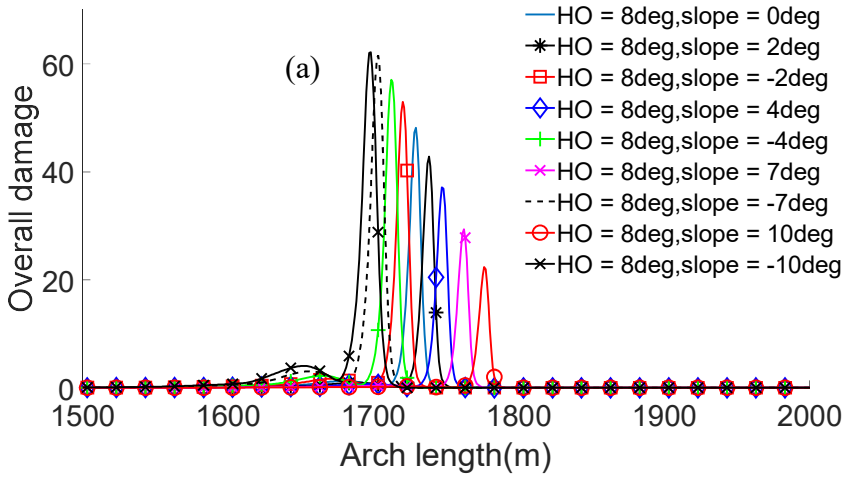

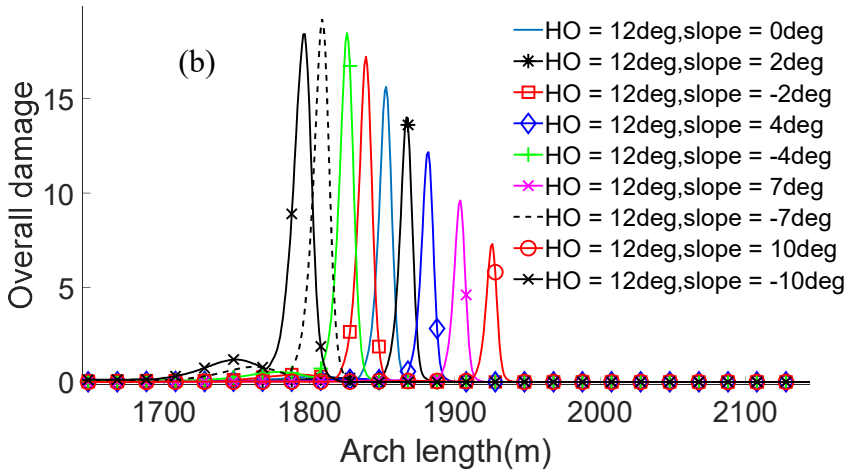

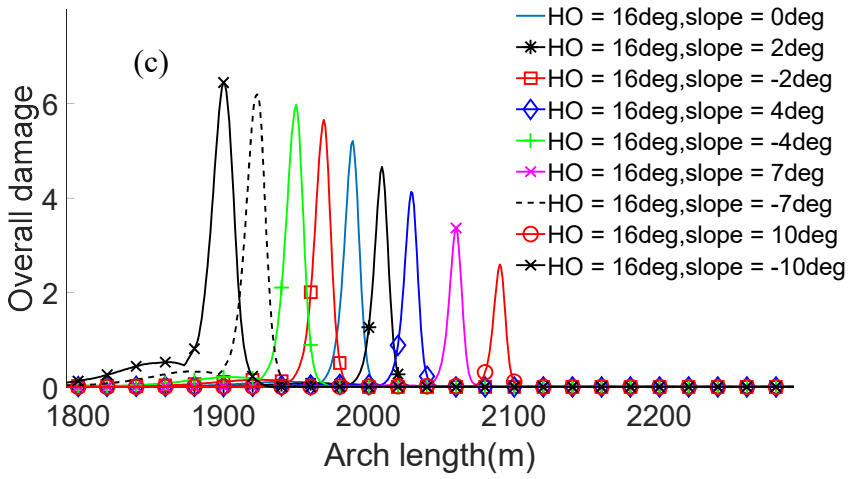

Figure 7-19 – Fatigue damage around riser TDZ for riser configuration groups: (a) HO angle = 8deg, (b) HO angle= 12deg, (c) HO angle= 16deg.

Table 7-9 – Percentage change in fatigue damage of sloped seabed risers relative to flat seabed riser configuration

Seabed slope (deg)	**Fatigue damage/year**			**% change in fatigue damage relative with the flat seabed**		
	HO = 8deg	HO = 12deg	HO = 16deg	HO = 8deg	HO = 12deg	HO = 16deg
0	48	16	5	0.0	0.0	0.0
2	43	14	5	-10.4	-12.5	0.0
-2	53	17	6	10.4	6.3	20.0

4	37	12	4	-22.9	-25.0	-20.0
-4	57	18	6	18.8	12.5	20.0
7	29	10	3	-39.6	-37.5	-40.0
-7	62	19	6	29.2	18.8	20.0
10	22	7	3	-54.2	-56.3	-40.0
-10	62	18	6	29.2	12.5	20.0

7.1.5 Concluding remarks on analysis

The impact of seabed slope on riser TDZ stress and fatigue response have been investigated in this work. The studies consider SCR design scenarios where flat seabed are assumed rather than the realistic profiled seabed around the TDZ. The positively and negatively sloped seabed of different slopes in degrees, $\alpha = 0, \pm 2, \pm 4 \pm 7 \pm 10$, were imposed on SCR configurations modelled on the flat seabed. Three SCRs groups were considered with HO angles of 8deg, 12deg and 16deg. For flat seabed, it is easy to relate the SCR HO angle with the stress and fatigue response at the TDZ since smaller HO angle will cause higher TDZ stress utilisation and fatigue damage than higher HO angle. However, when the seabed is sloped, comparison based on the SCR incidence angle (β) on the seabed is suitable since it represents a combination of the HO angle and the seabed slope.

For each group of risers considered, negatively sloped seabed resulted in smaller β while the converse was the case for the positively sloped seabed. The negatively sloped seabed with smaller β induces higher stress utilisation, higher compression (buckling tendencies), higher top tension, higher maximum stress range, and more significant fatigue damage than SCRs on the flat seabed. On the other hand, positively sloped seabed with smaller β resulted in SCR having reduced stress utilisation, maximum top tension, compressions, maximum stress range, and fatigue damage than SCRs on the flat seabed. For small seabed slope up to ± 2deg where SCR response impacts are

minimal and flat seabed assumptions is sufficient during the SCR design. However, for designs where SCRs stress utilisation and fatigue damage are mostly utilised, it is important to include the influence of correct seabed profile around the SCR TDZ.

There could be possibilities of introducing the structural form to impose a positively sloped seabed-like profile within the SCR TDZ can be considered to take advantage of the positive influence contributed by the positively sloped seabed to SCR responses

7.2 Simulation stage pre-trenching technique

7.2.1 Background

The development of seabed trench by the steel catenary riser (SCR) touch down zone (TDZ) in its early life can be caused by installation loads, direct hydrodynamic loads and vessel first and second-order motion imposed on the SCR during and after its installation. Several studies have been conducted to investigate the SCR TDZ fatigue response as the excited SCR TDZ progressively trench itself into the seabed, while other studies have investigated the impact of existing trench or pre-trench on the SCR fatigue response. However, most of these investigations were conducted using a series of regular wave loads through quasi-static simulations. Also, though important information on the trench effect on SCR TDZ fatigue response is known in the research domain, little has been said about how to incorporate them in the actual riser design process. This work is a numerical technique by which pre-trench can be initiated for fatigue response calculations during SCR detailed design analysis. Examples are presented to demonstrate the new approach and how the SCR fatigue response can be calculated in the presence of the created pre-trench. The SCR (after the pre-trenching process) is allowed to respond to the vessel first order six degrees of freedom motions about its nominal position in the presence of the created pre-trench. As demonstrated in this work, the pre-trenching technique makes it possible to conduct a full time-

domain, irregular wave simulations of the SCR in the presence of a pre-trench created using the hysteretic non-linear pipe soil interaction model.

7.2.2 The simulation stage-based pre-trenching technique (SSBPT)

The early method of conducting fatigue analysis assumes that the SCR TDZ lie on infinite stiff soil. This means no seabed penetration during the SCR TDZ excitations, but only pipe stress generated due to the active contact between SCR TDZ and the seabed. This assumption, although conservative, is not correct, hence the development of the linear (Spring model) and subsequently the more advanced non-linear SCR-soil interaction model (e.g. the RQ model). The RQ model represents finite soil stiffnesses and models the pipe inversions in the seabed. The model is developed on the backbone curve, which provides considerable stiffness resistance to the pipe penetration at the beginning of the loading cycle. Hence, small vessel excitations (typical of fatigue loads) can only cause negligible pipe penetration. This is a limitation of the RQ model and makes it challenging to create a pre-trench explicitly. However, even within these negligible penetrations, the hysteretic pipe - soil interactions are still represented. The pipe either remains in contact with the seabed, where the hysteretic stiffness exists or breaks out from the seabed contact for large enough upward riser motions. The SSBPT provided in this work to generate deeper trenches is built on the RQ model's capabilities. This is achieved using large regular wave loads, the first-order vessel motions and oscillatory vessel offsets (second-order drifts).

For the SSBPT, the simulation stage is decomposed into three stages, namely the trenching stage, the rest stage and the main stage, as shown in Figure 7-20. The load applied during the trenching stage is referred to as the trenching load, and the length of time over which the load is applied is referred to as the trenching period. Once the desired trench envelope is reached, the trenching load is discontinued, and the system is allowed to transit through a resting stage where the system achieves dynamic calmness prior to the main stage simulation. The fatigue load is then imposed during

the main stage simulation. In each of the stages, the vessel motion responses are expressed as time histories. The time histories of the three stages are then composed as single time history and imposed on the vessel in a single simulation run.

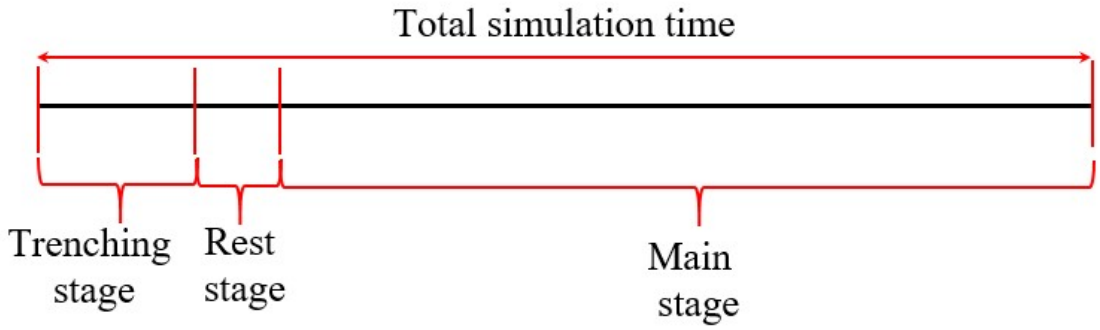

Figure 7-20 – Simulation stages in the new pre-trenching technique (SSBPT)

7.2.2.1 Pre-trenching stage

In this stage, the desired pre-trench envelope is created by imposing a suitable trenching wave load on the SCR-vessel system. The vessel response to the trenching load, based on the vessel's response amplitude operators (RAOs) and second-order motions (represented as oscillatory vessel offset in the riser plane), is transferred to the SCR TDZ from the riser top. The SCR TDZ under this motion creates trench progressively. The period for this stage is taken to be the period sufficient to achieve a desired design trench envelope. Hence, several runs may be needed at this stage to decide on suitable pre-trenching load characteristics. The wave loads applied in this stage can be a regular or irregular wave load. However, since many parametric analyses may be needed to determine the suitable load required to create the desired trench envelope, regular wave loads will be ideal for this stage. The RQ model would naturally not provide sufficient depth and span length for trench under normal loading conditions. Hence, the regular trenching load is coupled with the vessel's second-order motion (offsets) to significantly enhance the pre-trench profile creation process. It will be seen in this work that the pre-trench created in this stage with vessel offset included is significantly different from the trench created without vessel offsets. Once a suitable trenching load

characteristic (load amplitude and period) have been decided, the load time history for the vessel over the trenching stage period is then generated and stored.

7.2.2.2 Rest stage

The rest stage is the transition from the pre-trenching stage to the main stage. Transitioning from the pre-trenching to the main stage can result in turbulent responses transmitted to the SCR TDZ that can distort the created pre-trench envelope created at the pre-trenching stage. This can result in a severe distortion of the SCR TDZ fatigue response during the main stage. Hence, there is the need to dampen the pre-trench response and to set the SCR system to its nominal configuration just before the main stage simulation starts. To achieve the dampening process, the time history of the pre-trenching stage is examined, and the simulation times of the peak responses of the last motion cycles of the vessel are obtained. The time at which these peaks occur matches with the zero-velocity point for their motions but may not match when the SCR assumes its nominal configuration. Hence, the vessel needs to be smoothly brought back to its nominal position before starting the main stage simulation. If this process is not conducted smoothly, there is a high tendency that the pre trench already created will be numerically distorted. Therefore, it is important to check the state of the created pre-trench at the end of the rest stage to ensure that its profile is successfully retained into the main stage simulation where it is needed. Exponential, sinusoidal and linear damping functions were tested. Only the linear damping process preserved the pre-trench profile and hence is applied to the rest stage time history. Equation (7-3) presents the linear model used, where x is the rest stage time history profile (linear) for any of the 6DOF motion, x_1 is the peak value of the response in the last load cycle of the trenching stage, t_1 is the simulation time at which x_1 occur, x_2 is the final response value (the nominal configuration at the start of the main stage), t_2 is the end of the rest stage (coinciding with the start of the main stage). Hence t_2 must be selected long enough to make the slope (velocity) small. In this study, a rest stage $(t_2 - t_1)$ of 600sec

was sufficient for all 6DOF. The vessel time history during the rest stage is generated and stored.

$$x = x_1 + \frac{x_2 - x_1}{t_2 - t_1}(t - t_1) \tag{7-3}$$

7.2.2.3 The main stage

The main stage is the major stage of interest, where the realistic irregular storm and fatigue wave loads are applied. This stage can be an irregular wave simulation of the riser-vessel system or a simplified simulation of an equivalent regular wave. The wave loads are applied to the vessel, and the resulting vessel 6DOF motions are generated and stored. This pre-trenching technique provides the opportunity to include the second-order vessel motions (or vessel excursions) in this stage. Usually, SCR fatigue simulation is conducted with the vessel in nominal position (no vessel offset). This is conservative since particular sections of the active SCR TDZ maintain longer seabed contact while in nominal position, compared with the case where the vessel's offsets are included during the main stage simulation. The vessel's second-order drift during the main stage will cause the spreading and consequent reduction in the fatigue damage over the longer riser TDZ section, resulting in an overall reduction in the fatigue damage. However, for the demonstrated example in this work, while the vessel's second-order motion (implemented as oscillatory offsets about the mean vessel position) is included at the pre-trenching stage, it is discontinued at the main stage.

7.2.2.4 Composing simulation stage time histories

Once each of the above stages is completed independently, the generated motion time histories from the three stages are then composed to a single load time history as depicted in Figure 7-20. This single time history is then imposed on the vessel in a single simulation run. The resulting fatigue responses in the SCR TDZ are post-processed in the main stage. The impact of pre-trench conditions can then be evaluated and compared with the no-pre-trench (flat seabed) condition. Note that the trenching stage simulation should be sufficient for the desired pre-trench profile envelope to be

created. Simulating the vessel-riser systems under the pre-trenching load beyond the trenching period can result in further incremental or a stabilised trench envelope. The rest stage's simulation time should be sufficient for the riser's transient response to dampen out successfully to avoid distortion of the created pre-trench envelope. The main stage simulation time is the numerical time adequate to achieve considerable confidence in the fatigue results. This depends on the balance between available computation power, result convergencies, and correctness. The main stage simulation period of 7200sec is used in this work.

7.2.3 Analysis methodology

Figure 4 presents the analysis flowchart for the SSBPT. For the demonstration example in this work, the OrcaFlex FE software package is used to conduct the numerical computation. Simulations are performed in the time domain, and the implicit integration scheme is applied in the numerical solution process. The modelling, pre-processing, simulations and post-processing are automated using MATLAB programs integrated with the OrcaFlex programming interface, OrcFxAPI [114]. The MATLAB program is used to create the initial OrcaFlex SCR model using the catenary equations. The vessel model, RQ soil model, the selected pre-trenching loads, and the fatigue wave loads are modelled through the MATLAB program as needed, depending on the simulation stage as described by the flow chart in Figure 7-21. The pre-trenching regular wave load are modelled with the Dean Stream theory, while the irregular wave fatigue loads for the main stage simulation are modelled using the JONSWAP spectrum.

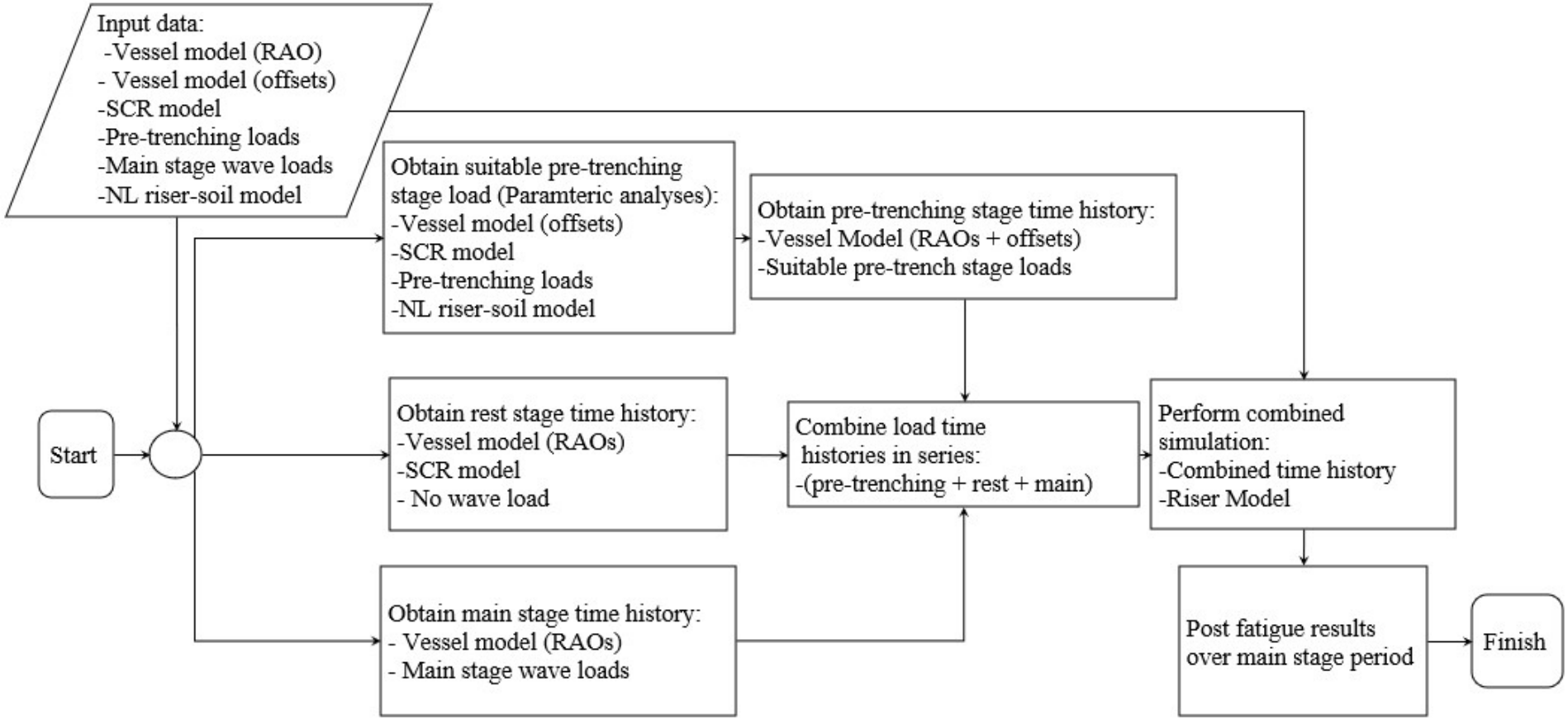

Figure 7-21 – Analysis flowchart

The oscillatory vessel offsets about the vessel mean position, representative of the vessel excursions is only imposed on the vessel during the pre-trenching stage. The length of simulation time for each stage are presented in Table 7-10. The S-N fatigue D-curve in seawater with cathodic protection [118] is applied for the fatigue damage calculation. Numerical fatigue responses are only post-processed during the main stage, using the Rain flow counting technique [98].

Table 7-10 –Simulation stages and associated time lengths

Analysis steps	**Simulation time (sec)**
Trenching Stage	1000
Rest Stage	600
Main Stage	7200
Single run (combined time history)	8800

7.2.4 Comparing the SSBPT with existing literature

The simulation stage-based pre-trenching technique (SSBPT) is developed based on the potentials of the hysteretic non-linear SCR soil interaction model (RQ model)[56]. It is expedient to compare the capability of this technique to other techniques developed on the same model (like for like comparison). The study with which the SSBPT is compared is available in [119]. In that work, the authors conducted qualitative comparisons of fatigue damage response of the SCR TDZ in three different mathematical adjusted trench profiles presented in Figure 7-22. These are the linear-exponential trench, the quadratic-exponential trench obtained from [120], and a polynomial trench obtained from [88]. The technique uses the RQ model in OrcaFlex but with adjusted values of the penetration factor and suction ratio to create initial numerical trenches. The adjusted soil data are then reset to their nominal values once the desired pre-trench has been made. These created trench profiles are modified based on the aforementioned mathematical profiles and then modelled through a specially developed in-house routine in Abacus for the fatigue simulation. These processes are

understandable since, in OrcaFlex, the restart facility does not provide the capability for resetting the RQ model data in a single fatigue simulation run once the simulation is initiated. Hence, it is not yet directly possible to create these trenches and conduct the fatigue damage analysis in the same process unless an incremental trenching process is considered (no soil data modification), which is the default no pre-trench scenario. Also, the resulting trenches developed by the authors' technique may not provide a sufficiently longer span typical with observed field data. This may have necessitated further modifications of similar trenches through the stepped trench profile technique developed by Mekha, Randolph, Bhat and Jain 2013 (see Figure 2-17). However, the SSBPT technique uses the actual soil data, but with a large regular wave, vessel motions, and oscillatory vessel offsets in a single simulation run, without the need for external modification of the numerical trenches or its data. The technique takes advantage of other powerful features that OrcaFlex provide in handling such non-linear interactions for the penetrating SCR TDZ under complex loading in the presence of the created pre-trench.

The SSBPT pre-trench parametric study is conducted in search of trench profiles that have similar depth as the three profiles from Shoghi and Shiri 2019. Regular wave loads with height ranging from 1m to 10m, with corresponding periods around the spar peak heave period (23sec to 35sec) (see Figure 7-23 (b)), and vessel oscillatory offset of 0%, 2%, 6%, 8% and 10% of the water depth were applied for this purpose. The pre-trenching process was conducted over a period of 1000sec with an oscillatory vessel offset period of 100sec. Among the pre-trenches created and investigated, attention is drawn to two pre-trench envelopes that are similar in depths to those used by Shoghi and Shiri 2019. These two pre-trenches are included in Figure 7-22 and are created using the following pre-trenching load:

- SSBPT Trench1: pre-trench envelope created from H = 19m, T = 32sec, vessel offset = 2%

- SSBPT Trench2: pre-trench envelope created from H = 20m, T = 31sec, vessel offset = 0%

The general data obtained from [119] used for the fatigue analysis are summarised in Table 7-11. The joint fatigue wave data, the spar vessel RAO and the RQ model data used are presented in Figure 7-23 (a), (b) and (c), respectively. Note that these data are only used to obtain results with the SSBPT for comparison purposes. The data applied for the main investigation in this work are presented in section 7.2.5.

Table 7-11 – Analysis data used for the comparative analysis

Data	**Values**
SCR pipe outer diameter - OD (m)	0.324
SCR in service weight (kg/m)	100
Pipe bending stiffness (N.m^2)	4.67E7
SCR total length (m)	2333
Hydrodynamic coefficients $[C_d, C_M, C_a]$	[0.7,1.5,1.0]
SCR nominal TDP from vessel hull centre (m)	949.4
SCR seabed anchor from hull centre (m)	1306.6
SCR hang off-angle (with vertical) (deg)	12
SCR hanging length (m)	1975.8
Fatigue S-N curve $[m_1, log\bar{a}_1, log\bar{a}_2]$	E-class in seawater [118]
Fatigue wave data [H_s(m), T_z(sec), N]	See manipulated
Pre-trench depth (4.63OD) (m)	1.5
Water depth (m)	1600
Spar COG below MSL (m)	110
RAO symmetry (see Figure 1)	Circular
SCR connection to hull below COG (m)	90

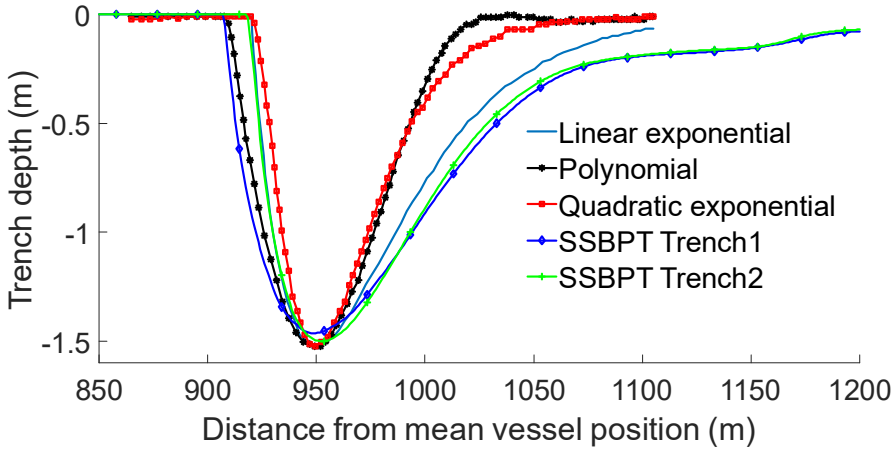

Figure 7-22. Pre-trench envelopes for comparison purposes

The fatigue analyses are conducted for the SCR for the pre-trench-2 condition as the riser is exposed to the 30 wave loads presented in Figure 7-23 (a). The joint fatigues damage response is obtained from the main simulation stage of the SSBPT, to be compared with the results based on the three pre-trench envelopes from [119]. It is noteworthy here that authors of the validating literature [119] have indicated that their results are intended for qualitative purposes rather than quantitative assessments. A qualitative comparison of the fatigue damage results from the validating literature and the SSBPT are presented in Figure 7-24. For this comparison, the fatigue damages from the pre-trenched cases in the respective studies are normalised by the maximum fatigue damage from the flat seabed or no pre-trench case. In general, the pre-trench fatigue damage is greater than the flat seabed cases, as is in the validating results. Although the fatigue damage peaks occur around the same arc length, the SSBPT technique provides greater fatigue damage on SCR TDZ sections neighbouring the peak damage arc length. This makes some sense since the 30 wave loads applied have a wide range of significant wave heights and zero up crossing periods, and the impact of these waves on the vessel may result in a more spreaded fatigue damage within the SCR TDZ. Also, the SCR TDZ sections beyond the trench surface points are expected to incur some level of damage from these combined wave loads excitations.

(a)

S/N	Hs	Tz	Cycles	S/N	Hs	Tz	Cycles
1	0.5	4.2	18011291	16	8	9.1	3389
2	1	4.6	71370445	17	8.5	9.3	3011
3	1.5	5	48449608	18	9	9.5	1822
4	2	5.4	25187856	19	9.5	9.7	1395
5	2.5	5.8	13529335	20	10	9.9	1070
6	3	6.1	7473660	21	10.5	10.1	1246
7	3.5	6.5	3080495	22	11	10.2	566
8	4	6.9	1631014	23	11.5	10.4	928
9	4.5	7.3	583770	24	12	10.6	544
10	5	7.7	363725	25	12.5	10.7	813
11	5.5	8	114700	26	13	10.9	712
12	6	8.4	33676	27	13.5	11	877
13	6.5	8.5	16907	28	14	11.2	262
14	7	8.7	10864	29	14.5	11.3	343
15	7.5	8.9	5421	30	15	11.5	420

(b)

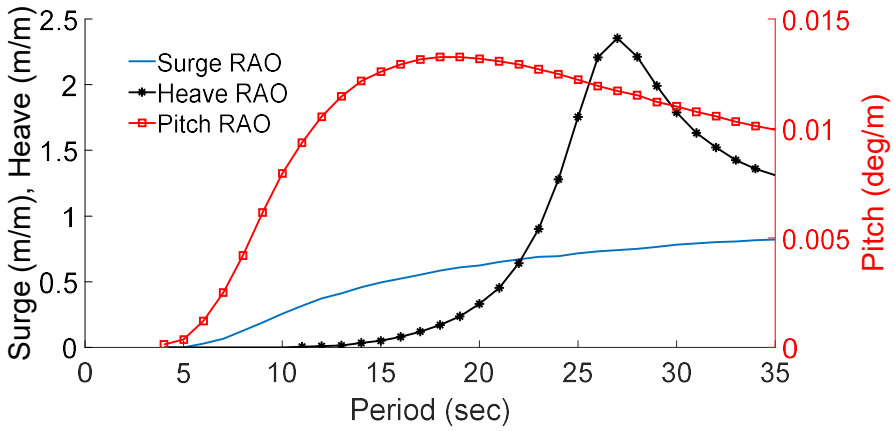

(c)

Parameter	Symbol	Value
Mudline shear strength	s_{u0}	0.65 kPa
Shear strength gradient	ρ	1.5 kPa/m
Power law parameter	a	6
Power law parameter	b	0.25
Normalized maximum stiffness	K_{max}	200
Suction ratio	f_{suc}	0.3
Suction decay parameter	λ_{suc}	0.5
Repenetration parameter	λ_{rep}	0.5

Figure 7-23. (a) Fatigue wave data; (b) Spar vessel response amplitude operators (RAO); (c) NL hysteretic soil interaction model (RQ model) data.

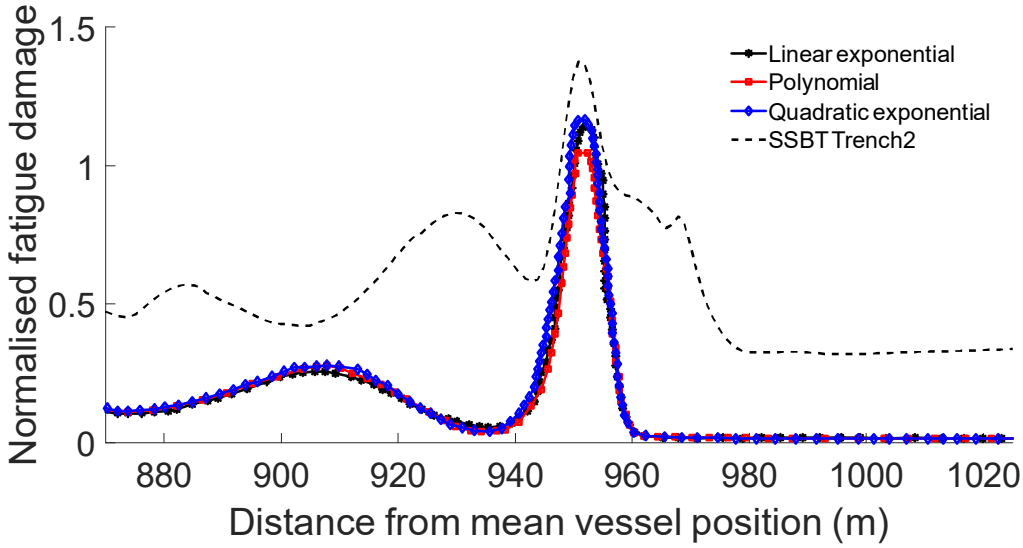

Figure 7-24. Normalised fatigue damage response of the SCR for the validating literature and the SSBPT.

It is expected that as the excitation in the SCR dampens out towards the SCR seabed anchor, the fatigue damage along it will reduce accordingly as observed from the SSBPT result. The authors would like to summarise at this point that this comparison is by no means a conclusion on whether the pre-trench induces greater fatigue damage or not as that will depend on a wider range of variables, which we believe the SSBPT provide opportunities to model and to investigate.

7.2.5 Main Analysis Data

The general analysis data for the main investigation in this work is presented in Figure 7-20. The most relevant vessel RAOs, considering the direction of wave load application, are presented in Figure 7-25. Three pre-trench conditions are considered in this investigation. They are the no-pre trench (flat seabed), pre-trench-1 of depth 2.04OD and pre-trench-2 of depth 4.49OD. The significance of selecting these three pre-trench conditions in this study is to demonstrate the different SCR TDZ fatigue damage responses in the different scenarios of pre-trench conditions. Further justification for selecting these pre-trench conditions is discussed in Section 7.2.6.2. Note that 1OD = 0.232m as presented in Figure 7-20. The SCR pipe considered for this

study is a bare steel pipe with no insulation and internal coating layers. The insulation layers (if included) is usually not considered stress-bearing layers for the SCR. For the interaction of the riser TDZ with the seabed, the stiffness provided by the riser pipe is taken to be the axial stiffness, EA_s, and bending stiffness, EI of the steel layer, where E is the young's modulus, A_s is the steel pipe cross sectional area (single wall steel pipe in this case), and I is the second moment of area of the SCR pipe.

For the main stage, the simulated fatigue wave loads are presented in

Table 7-13. The wave loads are applied to the vessel-riser system in the riser azimuth direction, which happens to be beam waves for the vessel. This wave load direction is set to induce maximum vessel roll and heave, which impact high motions on the SCR TDZ. The five-wave loads from

Table 7-13 and the three pre-trenching conditions are combined to derive fifteen analysis cases presented in Table 7-16 of section 7.2.6.3.

The nonlinear hysteretic SCR-seabed interaction model (RQ model) is used in this study. The seabed model possesses the capability for incremental seabed trenching, which is employed in the SSBPT to create longer and deeper pre-trenches under high SCR excitations. The RQ model penetration modes and characteristics were presented in Figure 2-15. Details of the RQ model can be found in [56]. The default soil parameters for the RQ model for clay soil used are presented in Table 7-14.

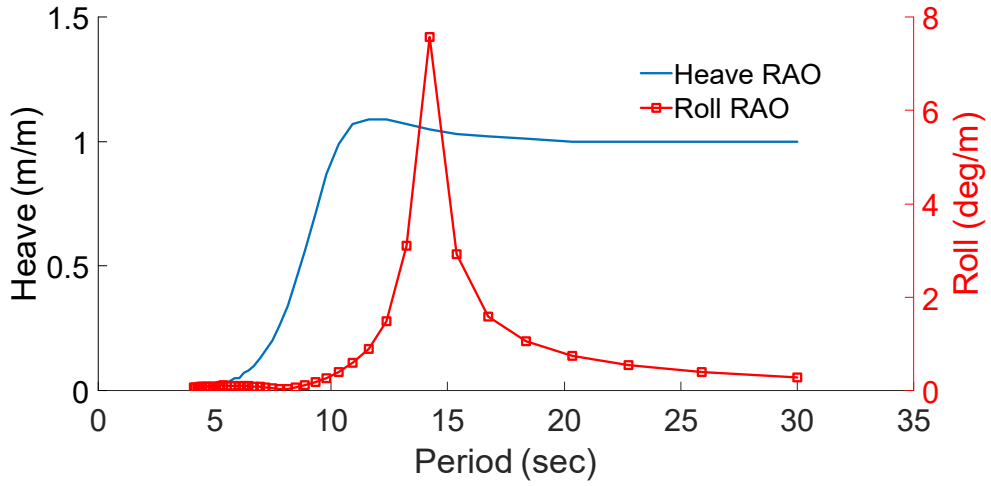

Figure 7-25. FPSO response amplitude operators (RAO).

Table 7-12 – Main analysis data

Data	**Values**
SCR pipe outer diameter - OD (m)	0.2032
Wall thickness (single wall) (mm)	0.0183
In service weight (kg/m)	63.3
Young modulus of pipe material (E) (kPa)	2.12E+08
Axial and bending stiffness [EA_s (kN), EI (kN.m^2)]	[2.3E6, 9.7E3]
Hydrodynamic coefficients [C_d, C_M, C_a]	[0.7,2.0,1.0]
SCR content density and pressure [ρ (kg/m), P(ksi)]	[600,10]
SCR hang off with the vertical (deg)	12
Nominal height of SCR (m) = Water depth (m)	1500
Fatigue S-N curve (with cathodic protection)	D-class in seawater (Veritas 2010)
Fatigue wave data [H_s(m), T_z (sec), N]	See Table 7-13
Pre-trench depths (OD)	No trench≈ 0OD, trench1≈ $2OD$, trench2≈ $4.5OD$
FPSO RAOs (Heave and roll responses)	See Figure 7-25
FPSO RAOs symmetry (see Figure 1)	The longitudinal and transverse axes
SCR connection to FPSO hull	Mean sea level, transverse axis

Table 7-13 –Fatigue wave data to be applied during the main stage

Wave No	**Irregular wave loads**		
	Hs (m)	Tp (sec)	$\boldsymbol{\gamma}$
1	1.5	5.5	1.8
2	3	8.8	1.0
3	4.5	9.5	1.6
4	8	13	1.6
5	15.8	16.9	2.4

Table 7-14 – The nominal hysteretic non-linear soil data [56]

Data	**Units**	**Values.**
Soil model parameters:		
Penetration resistance parameters (a, b)	-	(6.00, 0.25)
Soil Buoyancy factor (f_b)	-	0.25
Normalised maximum stiffness $(K_{max}$)	-	1.50
Shear strength at mudline	kPa	5.0
Shear strength gradient	kPa/m	1.5
Saturated soil density	te/m^3	1.5
Suction resistance ratio (f_{suc})	-	200.00
Normalised suction decay distance (γ_{suc})	-	0.60
Normalised re-penetration offsets after uplift (λ_{rep})	-	0.3

7.2.6 Main Analysis, Results and Discussions

7.2.6.1 Pre-trenching parametric analysis

The selection process of an appropriate regular wave load to create a desired design pre-trench envelope requires a parametric study. Regular wave loads ranging from 1 m to 10 m, with corresponding periods above their breaking wave limit, are simulated up to 1000 sec. The regular trenching wave load investigated is presented in

Table 7-15

The wave-table is simulated along with oscillatory vessel offsets of 2%, 4%, 6% and 8% water depth. 400 pre-trenched envelop were examined, but a few of the resulting trench profile envelopes are presented in Figure 7-26 to Figure 7-28

Table 7-15 – Regular wave load for pre-trenching parametric study

H (m)	T (sec)									
1	3	5	7	9	11	13	15	17	19	21
2	4	6	8	10	12	14	16	18	20	22
3	4	6	8	10	12	14	16	18	20	22
4	5	7	9	11	13	15	17	19	21	23
5	5	7	9	11	13	15	17	19	21	23
6	6	8	10	12	14	16	18	20	22	24
7	6	8	10	12	14	16	18	20	22	24
8	7	9	11	13	15	17	19	21	23	25
9	7	9	11	13	15	17	19	21	23	25
10	7	9	11	13	15	17	19	21	23	25

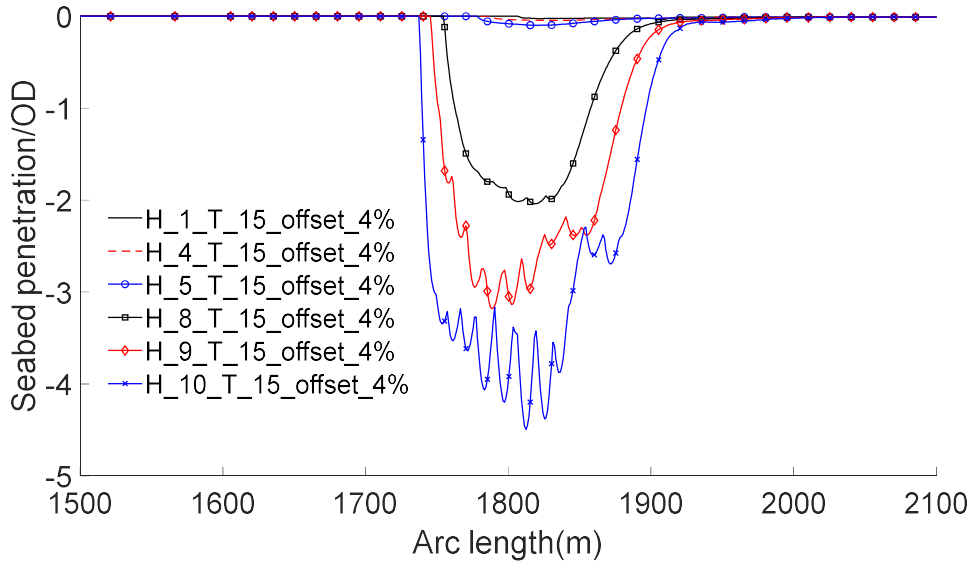

Figure 7-26 –Pre-trench profile envelopes for increasing trenching load amplitude with 4% vessel oscillatory offsets

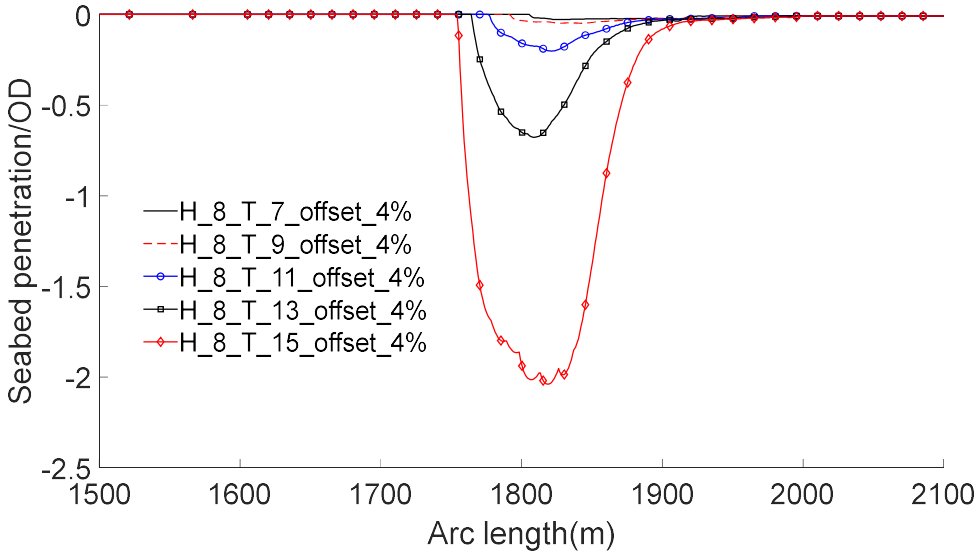

Figure 7-27 – Pre-trench profile envelopes for increasing trenching load period with 4% vessel oscillatory offsets

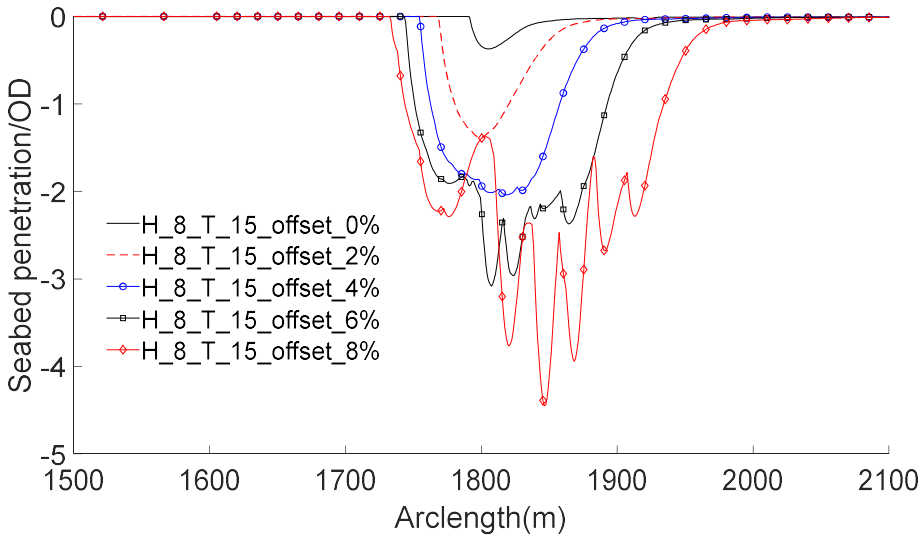

Figure 7-28 – Pre-trench profile envelopes for increasing oscillatory vessel offset

The following are observed for the pre-trench profile envelope in Figure 7-26 to Figure 7-28

- The pre-trench envelopes, characterised by their depths and lengths, expands and deepens with increasing regular trenching load amplitude, as seen in Figure 7-26. However, it can be observed that higher values of H result in a more irregular trench profile pattern. This may be attributed to the combined response of the seabed and the riser under the trenching load. If the riser TDZ is infinitely stiff globally, higher trenching load amplitude will result in deeper and smoother pre-trench envelope boundaries. However, because the riser TDZ is globally deformable, its shape can rapidly deform under higher load amplitude in the presence of the seabed resistance, resulting in rougher pre-trench envelop boundaries.

- The pre-trench envelopes expand with increasing regular trenching load period, as seen in Figure 7-27. It can be observed that periods between 13sec and 15sec provide deeper and longer span pre-trench envelopes. This could be because the joint vessel heave and roll responses are more significant within this range, as shown in Figure 7-25. Similar observations were also made for the pre-

trenching parametric study for the comparative analysis in section 7.2.4. It should be noted that the trenching stage is the stage where the designed trench profile is created, and no fatigue damage responses should be post-processed from it. Fatigue damage response should only be post-processed from the main stage where the system's actual fatigue wave load is applied. Hence, we can take advantage of the resonance period of the vessel excitations to enhance the pre-trench creation process.

- The pre-trench envelopes expand with increasing oscillatory vessel offsets, as seen in Figure 7-28. It can be observed that for larger vessel oscillatory offsets (e.g. 10% of the water depth), the trench profile envelope starts to become irregular. This behaviour may be associated with the large range in the change of the SCR TDZ curvatures due to larger vessel offsets. Such large-amplitude vessel offsets are only mentioned here to understand the created pre-trench profiles under them but are not practicable considering fatigue loading conditions.

7.2.6.2 Selected pre-trenching conditions for fatigue analysis

Figure 7-28 shows that the trench-envelope created in the vessel offset condition and that created in the no-vessel offset conditions are significantly different. This indicates that the vessel offsets or excursions during SCR installation and operations may substantially impact the trench evolution process as numerically observed during the pre-trenching parametric analysis. The three pre-trenched conditions presented in Figure 7-29 are those selected for this study, derived from the trench parametric analyses conducted in section 7.2.6.1. According to Figure 7-16, these three selected pre-trench conditions for which the five fatigue wave loads (also see

Table 7-13) will be investigated were created with the following pre-trenching excitation conditions at the pre-trenching stage.

- No pre-trench (flat seabed): H = NA, T = NA, oscillatory vessel offset amplitude = NA
- Pre-trench 1: H = 8m, T = 15sec, oscillatory vessel offset amplitude = 4%
- Pre-trench 2: H = 10m, T = 15sec, oscillatory vessel offsets amplitude = 4%

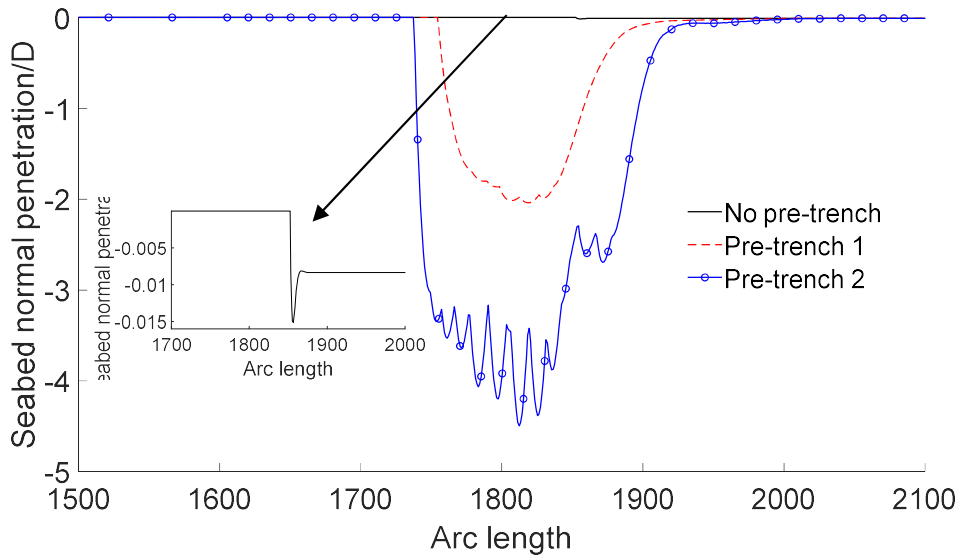

Figure 7-29 – Pre-trench profile envelope selected for fatigue analysis

The justifications for the selected three pre-trench conditions are discussed as follows:

- No pre-trench condition: The "No pre-trench" condition represents a "flat seabed" at the beginning of the main stage simulation. This is usually the case for fatigue analysis with the NL SCR-soil interaction model when no pre-trench conditions are considered. The initial trench depth for the flat seabed case is negligible, based on the RQ model. The depth corresponds with the static SCR TDZ penetration, which is about $0.015OD$ in this study, as seen in Figure 7-29. Under fatigue loading, the SCR TDZ incrementally creates a trench from the flat seabed and embeds itself into it. There is a need to include this case in the analysis for comparison purposes with the cases where an initial trench is imposed at the beginning of the main stage simulation.

- Moderate pre-trench envelope: When moderate pre-trenches are subject to large SCR TDZ excitation, their trench envelopes are exceeded, and a deeper and stabilised trench will be created within a short time under such high riser motion conditions [77]. As observed from field data [83], a trench in trench scenario may also result. It is relevant to have such pre-trench depth to understand how the SCR TDZ fatigue damage behaves when the pre-trench envelope is exceeded. This pre-trench envelope of ≈2OD deep is considered to model and investigate this scenario.

- Deeper pre-trench envelope: Since it is believed that the existing trench created during the riser installation and other environmental influences should be large enough to contain all SCR TDZ motions [92], this relatively deeper trench of ≈ $4\boldsymbol{OD}$ is considered. For this pre-trench conditions, the pre-trench envelope is large enough to contain the motions of the SCR TDZ under moderate SCR excitations typical of fatigue load.

7.2.6.3 Load case table and vessel time history for fatigue analysis

Based on the five fatigue wave load data in

Table 7-13 and the selected three pre-trench conditions, the created analysis cases are detailed in Table 7-16. There will be fifteen groups of 6DOF motion time histories composed from the three stages (see Figure 7-20). Only two groups of the composed vessel 6DOF time histories are presented in Figure 7-30 and Figure 7-31 to provide a visual sense of what they will look like. These are the time histories for case3 and case8, respectively. Note that in the numerical model built for this study, the X-DOF vessel motion is centred about the nominal position (X = 34 m). The X-DOF for case8 in Figure 7-31 appears to be constant at 34m after the pre-trenching stage. In contrast, it is not, as the vessel oscillations about the X = 34m are negligible compared with the large offsets during the pre-trenching stage (see a different plot scale for case3 in Figure 7-30. The linear motion dampening for all 6DOF through the resting stage can be seen in Figure 7-31.

Table 7-16 – Load case table for the analyses. Note the case numbers (1-15) as referenced in the results discussion section.

Pre-trench conditions + Fatigue wave loads		
No pre-trench	Pre-trench 1	Pre-trench 2
Case No: 1 Pre-trench= (0.015OD) Pre-trench load: H = NA T = NA Offset = NA Fatigue wave loads (main stage): - Case No 1: Plus Wave1 - Case No 2: Plus Wave2 - Case No 3: Plus Wave3 - Case No 4: Plus Wave4 - Case No 5: Plus Wave5	Case No: 6 Pre-trench = 2.04OD Pre-trench load: H = 8m T = 15sec Offset = 4% Fatigue wave loads (main stage): Case No 6: Plus Wave1 Case No 7: Plus Wave2 Case No 8: Plus Wave3 Case No 9: Plus Wave4 Case No 10: Plus Wave5	Case No:11 Pre-trench =4.49OD Pre-trench load: H = 10m T = 15sec Offset = 4% Fatigue wave loads (main stage): Case No 11: Plus Wave1 Case No 12: Plus Wave2 Case No 13: Plus Wave3 Case No 14: Plus Wave4 Case No1 5: Plus Wave5

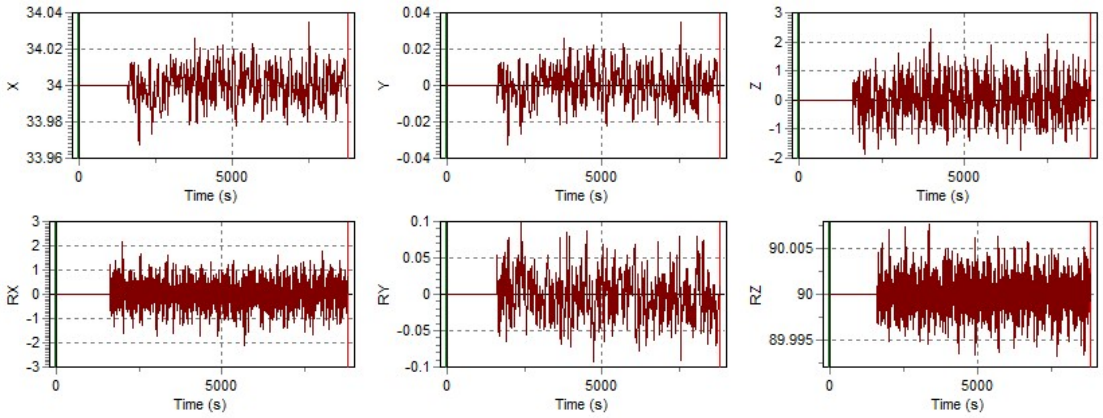

Figure 7-30 – 6DOF motion time history for case3 in Table 7-16.

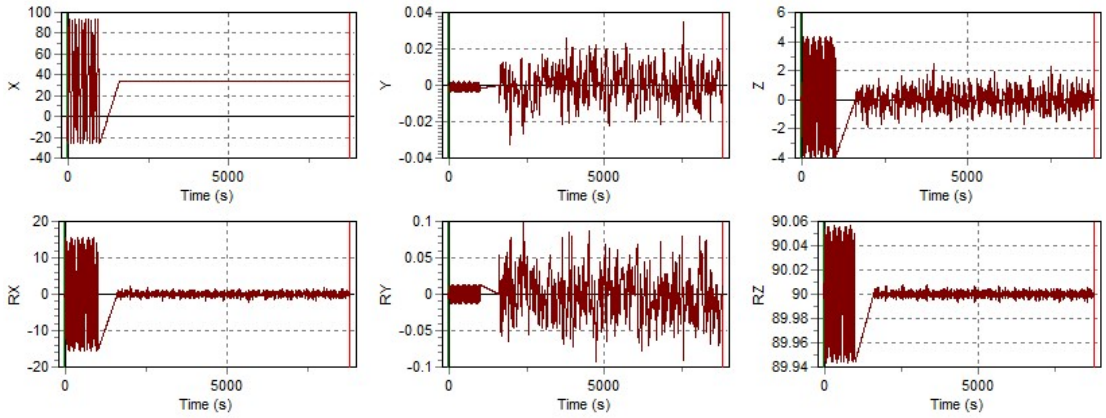

Figure 7-31 – 6DOF motion time history for case8 in Table 7-16. (Ordinate units are in meters)

7.2.6.4 Pre-trench envelope integrity verification

Refer to Table 7-10, the main stage simulation starts at (1000sec + 600sec = 1600sec) and ends at 8800sec, which is the sum of the time in all the three simulation stages. First, it is essential to verify that the integrity (profile shape) of the pre-trench envelope created in the pre-trenching stage is preserved by proper dampening out of the trenching loads in the rest stage. To verify this, we present the pre-trench envelopes present at the beginning of the main stage (at 1600sec) for the no pre-trench, the pre-trench1 and the pre-trench2 cases in Figure 7-32 (a),(b) and (c), respectively. The trench envelopes for all the cases match those presented in Figure 7-29. This verifies that the desired pre-trench envelope conditions created at the pre-trench stage are available or 'remembered' at the beginning of the main stage for fatigue calculations. This is also an indication that the rest stage linear motion dampening of the vessel 6DOF was effective.

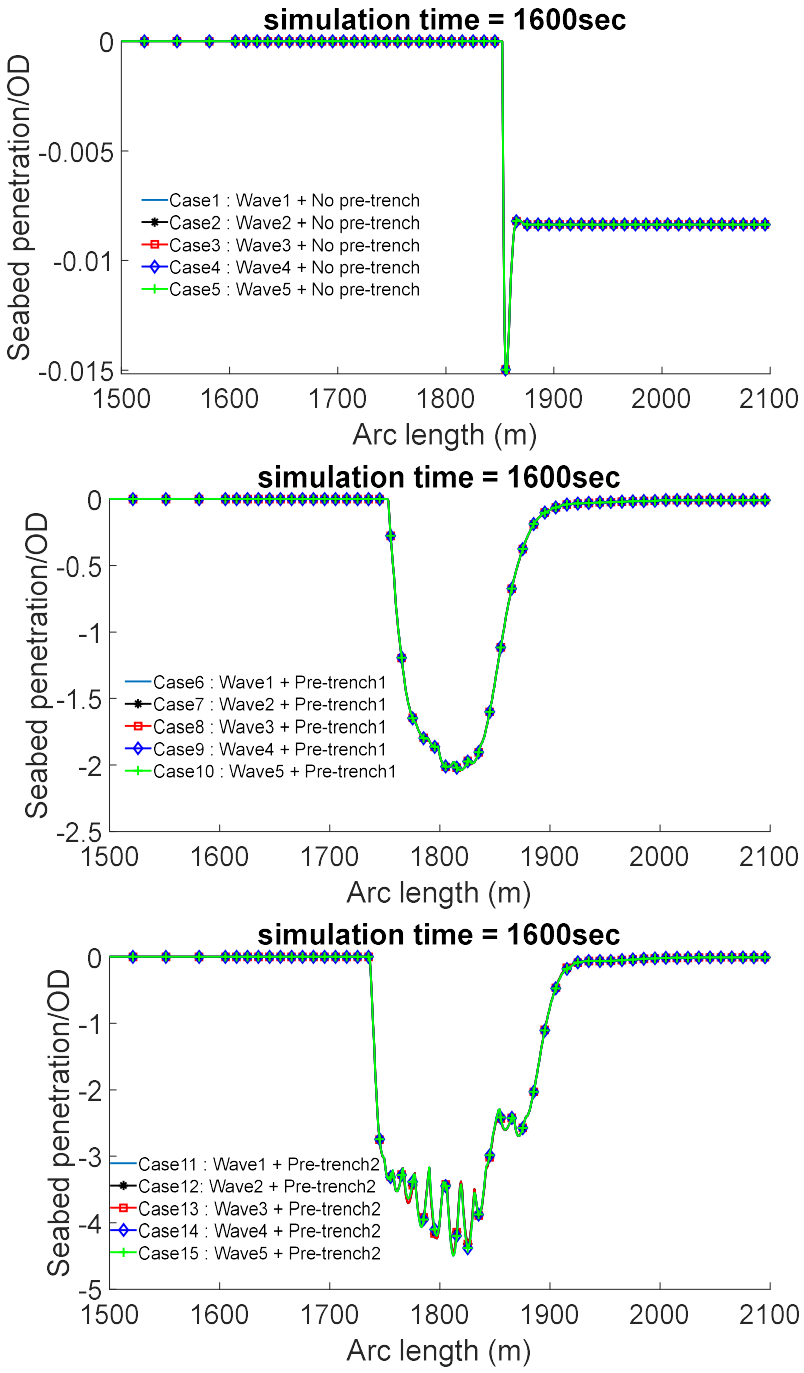

Figure 7-32 – Pre-trench conditions at the beginning of the main stage simulation for (a) No pre-trench envelope: case1 to case5, (b) Pre-trench1 envelope: case6 to case10, (c) Pre-trench2 envelope: case11 to case15

7.2.6.5 Pre-trench envelope and final trench profile

It is important at this point to distinguish between the pre-trench envelope and the final trench profile developed at the end of the main stage simulation. The pre-trench envelope is the trench introduced prior to the main stage simulation, effected in this study using suitable regular wave loads, the vessel motion (RAOs) and the vessel's oscillatory offsets. It can also be referred to as the design trench condition. On the other hand, the final trench is the range graph maximum of the profile created by the SCR TDZ while undergoing motions within the pre-trench envelope during the main stage. The main stage motions are caused only by the fatigue wave load applied to the vessel, defined by the vessel's RAOs. In this study, the vessel 6DOF motion during the main stage is about its mean (nominal) position, i.e., no second-order drift effect is included.

Consider the no pre-trench cases during the main stage, continuous motions of the SCR TDZ cause incremental embedment into the virgin soil until the trench is stabilised at the final trench profile. The final trench profiles for the no pre-trench cases at the end of the main stage are plotted in Figure 7-33 (a). Recall that the pre-trench envelope for these cases is the static penetration of the riser into the soil ($0.015OD$), which is negligible. It could be observed that as the wave loads increase (implying higher motion amplitude of the SCR TDZ), deeper final trench profiles are created at the end of the main stage, as seen in Figure 7-33 (a). For example, it is observed in Figure 7-33 (a) that penetration into the virgin seabed can reach a depth up to 8 times the riser pipe diameter (OD) for wave5 (H = 15.8m, Tp = 16.9sec).

For the pre-trench cases, continuous embedment of the excited SCR TDZ is also experienced but into an already penetrated or softened soil defined by the pre-trench envelope. The SCR TDZ will continue to embed itself deeper into or beyond the pre-trench envelope until the trench profile created stabilises under the applied fatigue load. The final stabilised trench profile in these cases can be less than the pre-trench envelop for cases with relatively lower wave load or motion amplitude (case6, case7, case8 in Figure 7-33 (b) and case11, case12, case13 in Figure 7-33(c)). The final trench may

also have some of its profile section shallower or deeper than the pre-trench envelop as observed for case9 in Figure 7-33(b) and case14 in Figure 7-33(c). Lastly, the final stabilised trench envelope can exceed the pre-trench envelope under high motion amplitudes, as seen for case10 in Figure 7-33(b) and case15 in Figure 7-33(c). Therefore, it should be noted that an existing pre-trench envelope can be exceeded if the riser TDZ are excited so much that they penetrate deeper and longer beyond an existing trench wall. The RQ model, which provides the capability for these trenching processes, is developed on the backbone curve, which offers large stiffness resistance to the pipe penetration at the beginning of the loading cycle. This high soil resistance to SCR TDZ penetration is defined by the ultimate penetration resistance curve in Figure 2-15(b). Hence, small vessel excitations, such as those caused by smaller waves 1,2,3, as observed in Figure 7-33 (a), (b) and (c), can only result in negligible SCR TDZ penetration. However, once large-amplitude SCR excitations caused by larger waves overcome this high resistance in its first penetration, subsequent soil resistance, defined by the re-penetrations curves, provide less soil resistance and deeper trenches.

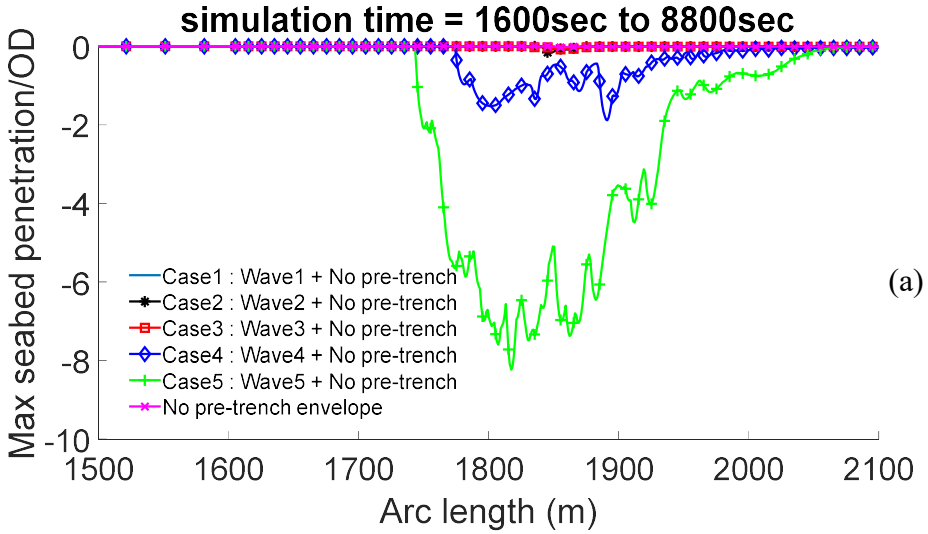

(a)

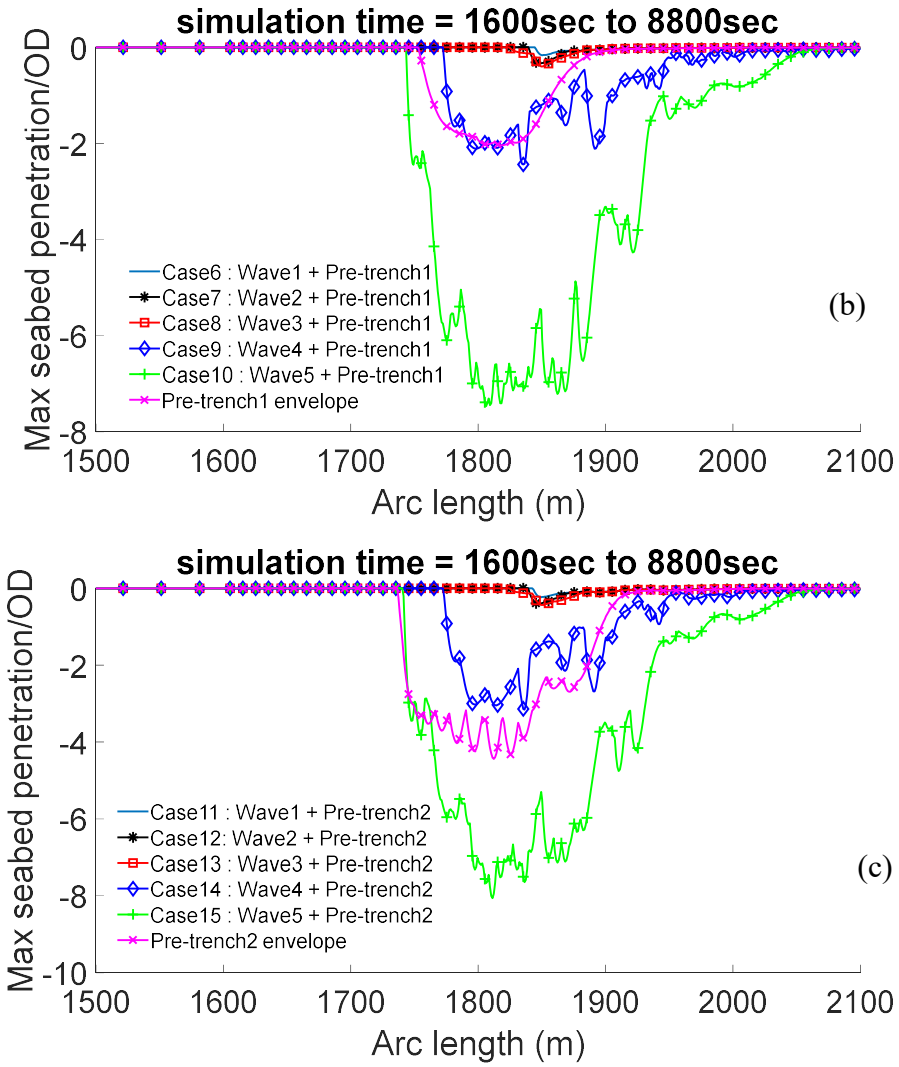

Figure 7-33 – Final trench profile for pre-trenched cases – (a) No pre-trench (b) pre-trench1 (c) pre-trench2, at the end of the main stage

7.2.6.6 Investigating pre-trench envelope impact on SCR TDZ fatigue damage response

To investigate the impact of pre-trench on the fatigue damage response of the SCR TDZ. Each of the five fatigue wave loads (Wave1, Wave2, Wave3, Wave4 and Wave5) is applied across the three pre-trench conditions (No pre-trench, pre-trench1, and pre-trench2). The final trench profile and the corresponding fatigue damage responses of the SCR TDZ are presented in Figure 7-34 to Figure 7-38. A summary of the fatigue damage response is presented in Table 7-17. Figure 7-39 presents the percentage

increase or decrease of the SCR TDZ fatigue damage response for the pre-trench cases relative to the no pre-trench cases.

Generally, it could be observed from the results that irrespective of the presence of a pre-trench or no pre-trench conditions, SCR fatigue damage increases with increasing applied wave load. As the pre-trench envelop gets deeper, and the fatigue wave load amplitude increases, the fatigue damage incurred by the SCR TDZ increases, as long as the motion of the SCR TDZ does not result in a final trench profile that is equal to or exceeds the pre-trench envelope. The increasing trend can be seen for wave1, wave2 and wave3 cases in Figure 7-34(b), Figure 7-35(b), Figure 7-36(b), the first three result rows of Table 7-17 and Figure 7-39. Also, see Figure 7-33(b) and Figure 7-33(c) to compare the final trench profile caused by wave1,wave2 and wave3 relative to the pre-trench1 and pre-trench2 envelope. For example, it could be seen from Figure 7-39 that wave3 + pre- trench1 (case8) and wave3 + pre-trench2 (case13) resulted in up to 60% and 70% increase in fatigue damage compared with their respective no pre-trench cases. As the wave load amplitudes decrease from wave3 through wave2 to wave1, increase fatigue damage relative to respective no pre-trench cases are observed (for both pre-trench1 and pre-trench2) but in decreasing order of the wave amplitudes as seen in Figure 7-39.

When the final trench profile matches or exceeds the pre-trench envelope, irrespective of the wave load amplitude in action, there will be less difference between the SCR fatigue response in the pre-trenched case and the no pre-trench case. This can be seen for wave4 and wave5 for pre-trench1 and pre-trench2 conditions in Figure 7-37(b), Figure 7-38 (b), and Figure 7-39. For example, consider a high sea state condition typical of the North Sea. If the existing pre-trench caused by extreme events cannot accommodate the SCR TDZ motions under the fatigue load, further trenching beyond the pre-trench envelop results and the corresponding fatigue damage of the pre-trench case will be of equal magnitude as that of the no pre-trench condition. This may also be true for low sea states plus an existing smaller pre-trench that can be exceeded by the

SCR motions caused by the low sea conditions. This indicates that the relevance of pre-trench or no pre-trench in the design analysis of SCRs should be a joint consideration of the available design trench envelope and the motion amplitudes of the SCR TDZ caused by the wave loads and the vessel RAOs.

When the applied wave loads result in SCR TDZ motion amplitudes that are just contained within or exceed the pre-trench envelope, the SCR TDZ nodes will interact closely with some or all parts of the pre-trench envelop boundaries over the loading cycles. This was observed for the Wave4, which created final trench profiles that are either shallower or deeper than parts of the boundaries of the pre-trench envelope, as seen in Figure 7-33(b) and Figure 7-33(c). There will be regular pressure hot spots created between the pre-trench envelope boundaries and the SCR TDZ nodes for such wave conditions and design pre-trench envelope. These hotspots are not artificial in this case since the pre-trench envelope wall is not constrained to a fixed envelope (as done in most studies) but allowed to be trenched through by higher amplitude SCR TDZ. Hence, these are natural SCR TDZ interactions with trench walls as captured by the SSBPT. Such a combination of wave load and pre-trench condition results in a random trenching response of the SCR TDZ, as seen in the final trench profile in Figure 7-37(a). For cases like this, it is not obvious whether the pre-trench cases induce greater fatigue damage than the no pre-trench cases. In fact, as can be seen in Figure 7-37 (b), the pre-trench conditions and the no pre-trench conditions induces greater fatigue damages than the other at different sections of the SCR TDZ. However, the difference in peak fatigue damage between the trenched and the no trenched conditions for this type of combined wave load and pre-trench conditions is small, even with the higher amplitude wave5 as observed in Figure 7-39. It could be seen from Figure 7-39 that while pre-trench1 resulted in about a 3.7% decrease in fatigue damage, pre-trench2 resulted in about a 2.3% increase in the fatigue damage compared with the no pre-trench case for wave5. Hence, the fatigue damage patterns for these conditions are difficult to predict.

Consider a calm sea state condition. The SCR TDZ profile may closely match the profile of the wall of a very shallow trench. However, for deeper trenches, the SCR TDZ, due to its high axial stiffness, cannot stretch enough to assume the trench wall profiles but follows its natural shape in equilibrium with the soft resistance provided by the loosed soil material in the trench, or overhangs if the loosed soil material are eroded from the trench. If the wave loads are high, the heave motions of the vessel will force the SCR TDZ deeper into the existing pre-trench, where the TDZ either follows the predefined trench shape upon having contact with the trench [120] or digs deeper beyond the trench envelope. The deformation rate of the SCR TDZ will depend on a balance between the resistance of the loosed soil material in the trench or the resistance of virgin (unpenetrated) soil beyond the trench envelope and the global bending stiffness of the SCR TDZ. When the riser digs beyond the trench envelop under high amplitude motions, the trench tends to stabilise very quickly [77], defining a new/modified trench envelop. These interactions are very complex and drive the fluctuating SCR TDZ curvatures and the resulting fatigue damage. However, allowing these natural interactions of the SCR TDZ and the soil through comprehensive NL SCR-interaction models will provide more reliable results than enforcing a constrained artificial trenches envelope as is done in many studies.

Although efforts are made in this work to track these behaviours of the SCR TDZ fatigue damage in the considered pre-trench conditions, under the considered single applied wave load and direction, for the considered vessel motions, riser geometry, riser configurations, etc., the behaviours are quite complex and difficult to predict when any of these variables changed. For example, for a fully combined sea state fatigue wave conditions, typical of fatigue analysis plus second-order vessel effects, a simple prediction of the fatigue damage response in different pre-trench conditions is potentially elusive to common sense. However, with numerical tools and reliable methods, further investigation of the impact of these design variables can be conducted. For SCR design purposes, different scenarios involving combinations of varying design

variables should be considered in sensitivity studies to increase design confidence that the presence of pre-trenches does not negatively impact the SCR response computed by the traditional method of SCR analysis with no pre-trench conditions.

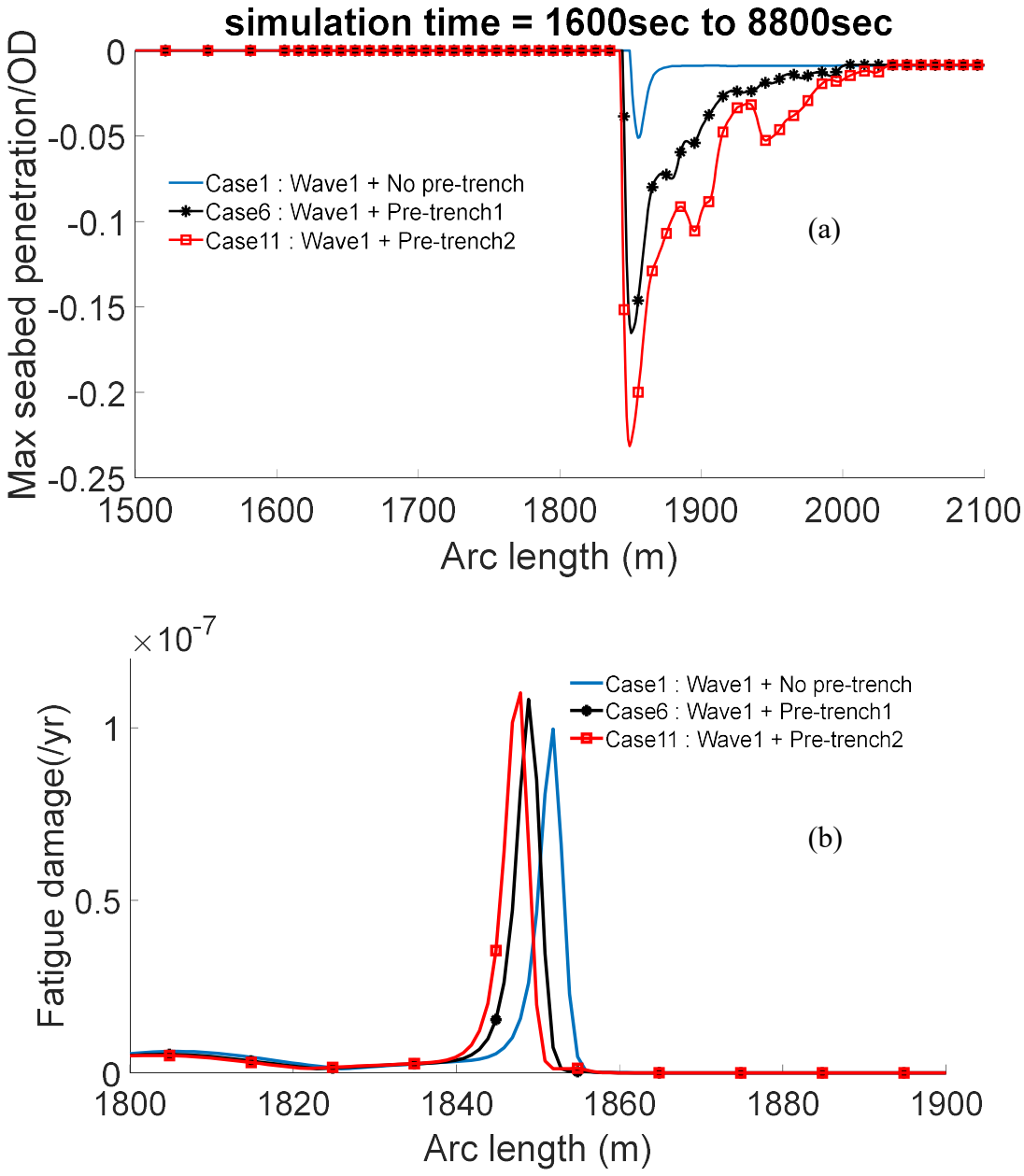

Figure 7-34 – (a) Final trench profile at the end of the main stage, (b) Fatigue damage response during the main stage for the three pre-trench conditions under wave1

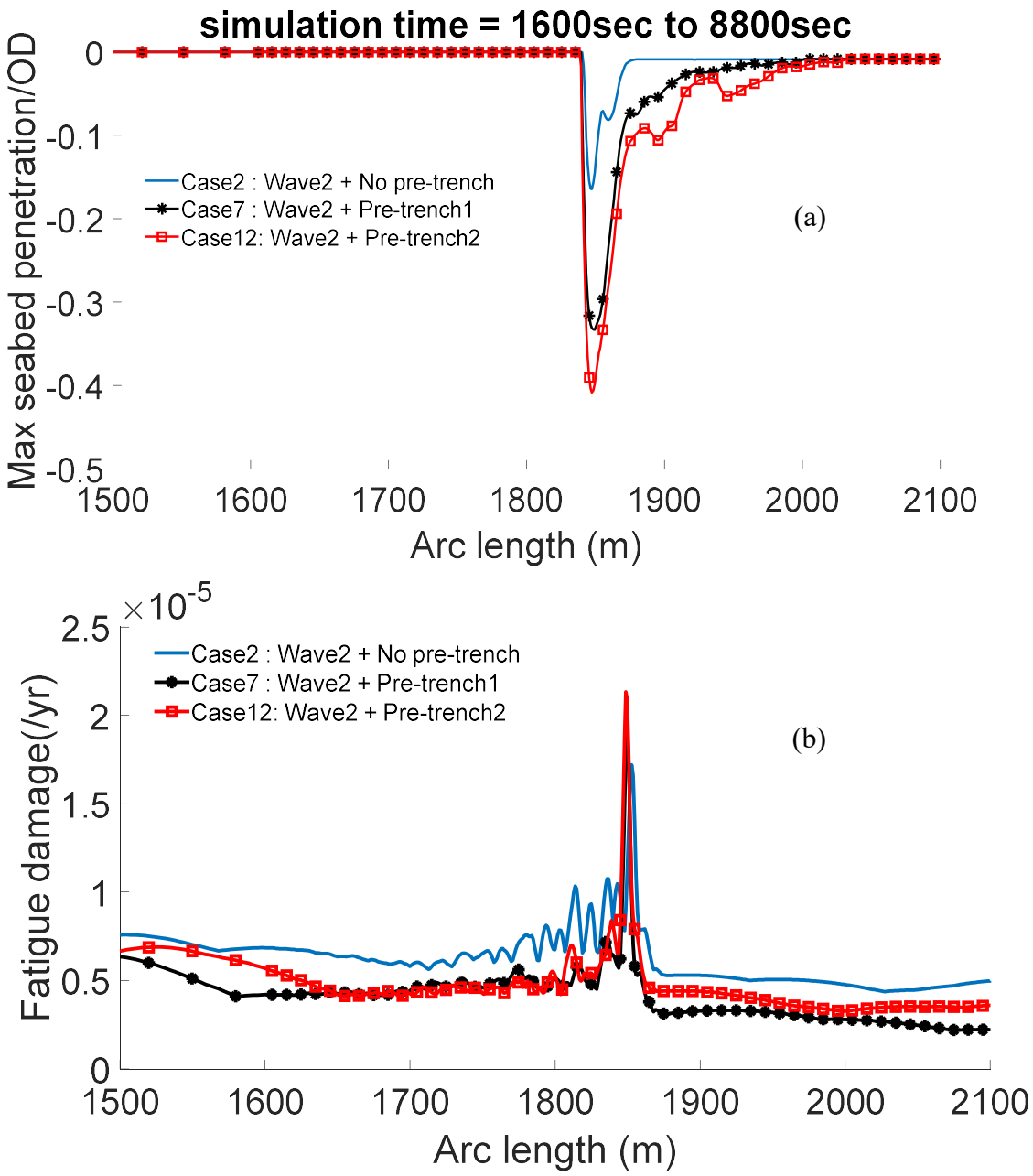

Figure 7-35 - (a) Final trench profile at the end of the main stage, (b) Fatigue damage response during the main stage for the three pre-trench conditions under wave2

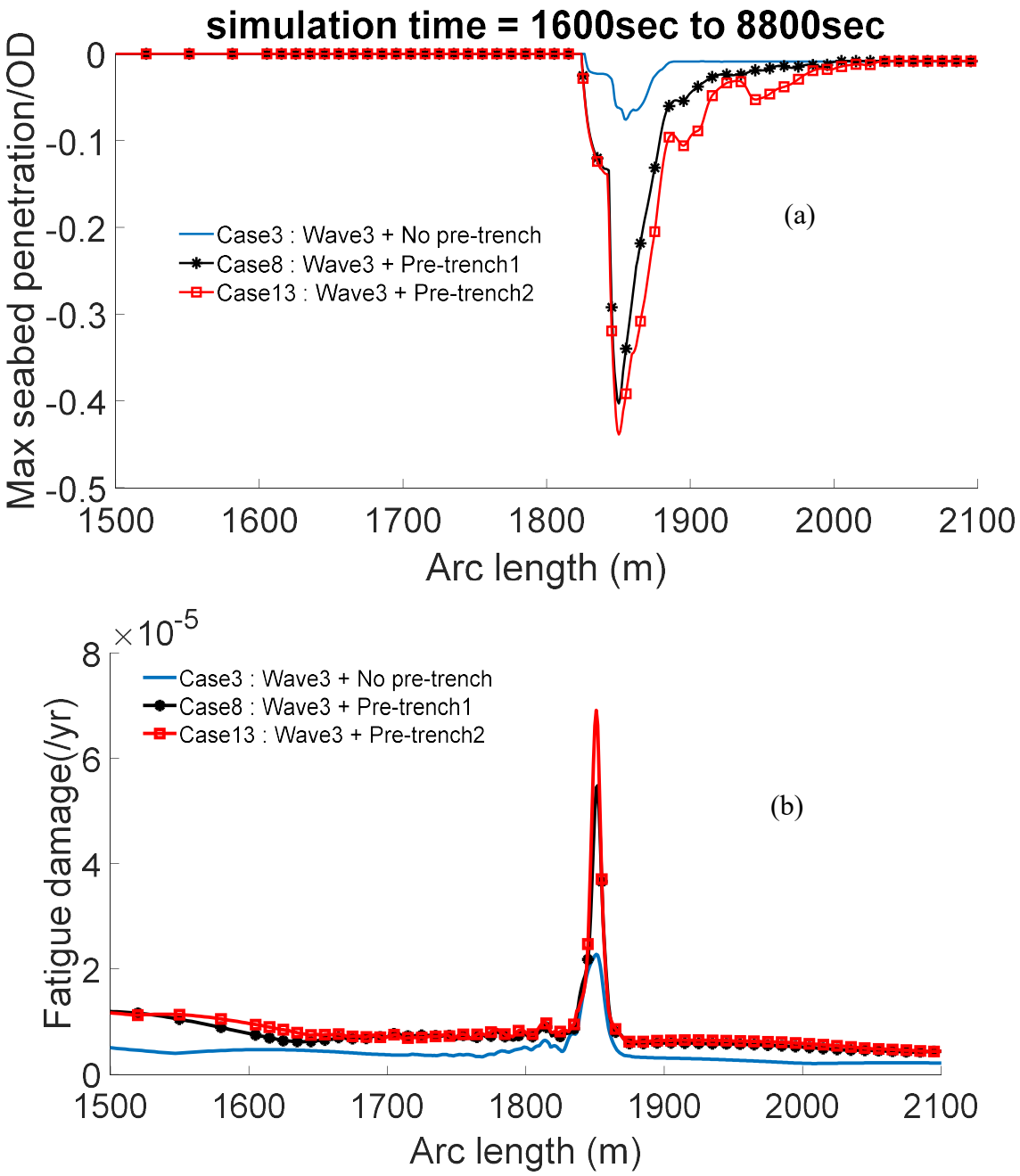

Figure 7-36 – (a) Final trench profile at the end of the main stage, (b) Fatigue damage response during the main stage for the three pre-trench conditions under wave3

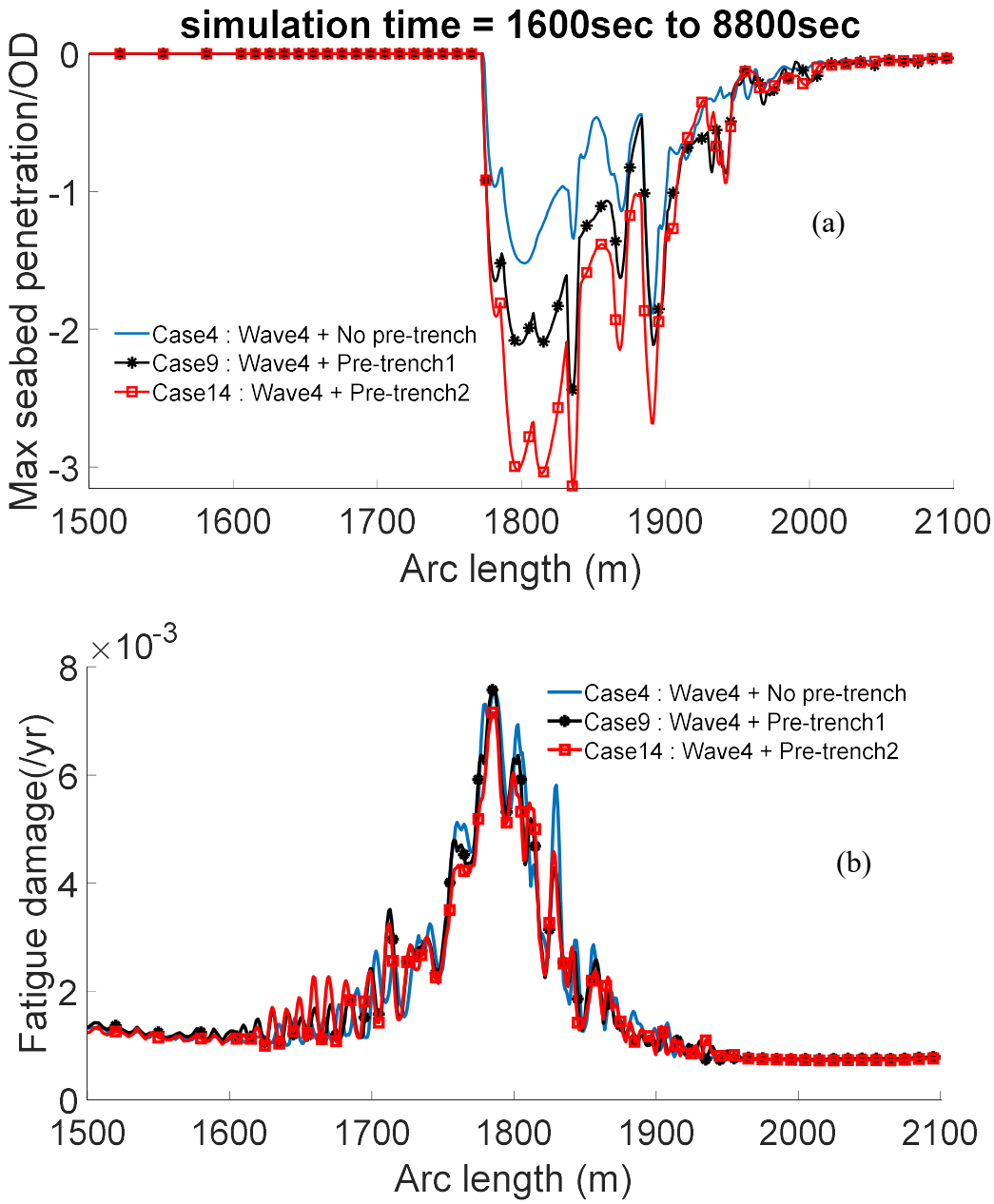

Figure 7-37 – (a) Final trench profile at the end of the main stage, (b) Fatigue damage response during the main stage for the three pre-trench conditions under wave4

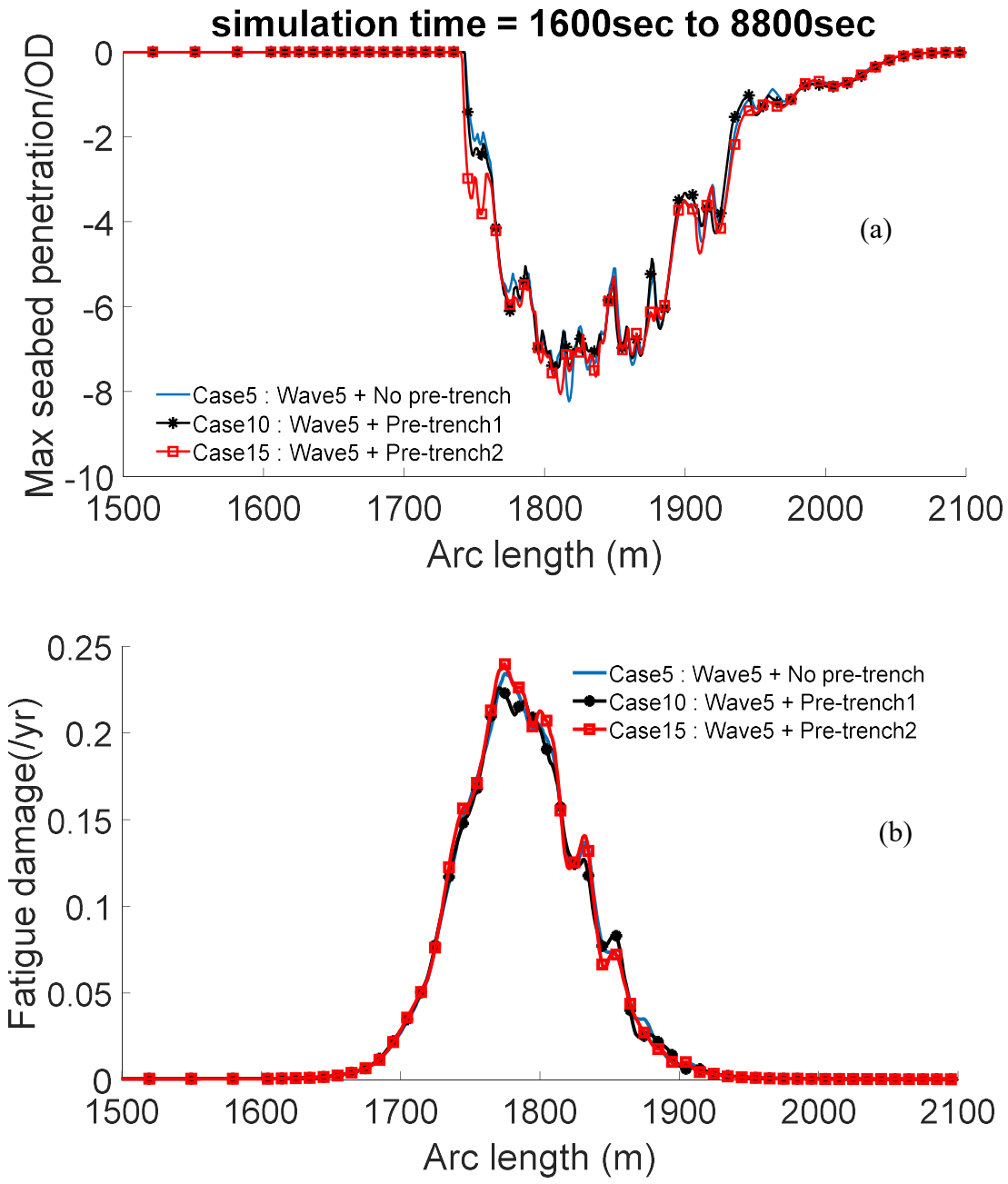

Figure 7-38 – (a) Final trench profile at the end of the main stage, (b) Fatigue damage response during the main stage for the three pre-trench conditions under wave5.

Table 7-17 – Summary of maximum SCR TDZ fatigue damage for the 15 analyses cases

	Pre-trench conditions		
Fatigue Loads	**No pre-trench**	**Pre-trench 1**	**Pre-trench 2**
Wave1 (Hs, Tp) = (1.5,5.5)	Case No: 1 Pre-trench = Static penetration Fatigue damage (/yr) = 9.97E-08	Case No: 6 Pre-trench = 2.04OD Fatigue damage (/yr) = 1.08E-07	Case No:11 Pre-trench = 4.49OD Fatigue damage (/yr) = 1.10E-07
Wave2 (Hs, Tp) = (3,8.8)	Case No: 2 Pre-trench = Static penetration Fatigue damage (/yr) = 1.72E-05	Case No: 7 Pre-trench = 2.04OD Fatigue damage (/yr) = 1.90E-05	Case No: 12 Pre-trench = 4.49OD Fatigue damage (/yr) = 2.13E-05
Wave3 (Hs, Tp) = (4.5,9.5)	Case No: 3 Pre-trench = Static penetration Fatigue damage (/yr) = 2.28E-05	Case No: 8 Pre-trench = 2.04OD Fatigue damage (/yr) = 5.48E-05	Case No: 13 Pre-trench = 4.49OD Fatigue damage (/yr) = 6.91E-05
Wave4 (Hs, Tp) = (8,13)	Case No: 4 Pre-trench = Static penetration Fatigue damage (/yr) = 7.58E-03	Case No: 9 Pre-trench = 2.04OD Fatigue damage (/yr) = 7.61E-03	Case No:14 Pre-trench = 4.49OD Fatigue damage (/yr) = 7.16E-03
Wave5 (Hs, Tp) = (15.8,16.9)	Case No: 5 Pre-trench = Static penetration Fatigue damage (/yr) = 2.34E-01	Case No:10 Pre-trench = 2.04OD Fatigue damage (/yr) = 2.26E-01	Case No: 15 Pre-trench = 4.49OD Fatigue damage (/yr) = 2.40E-01

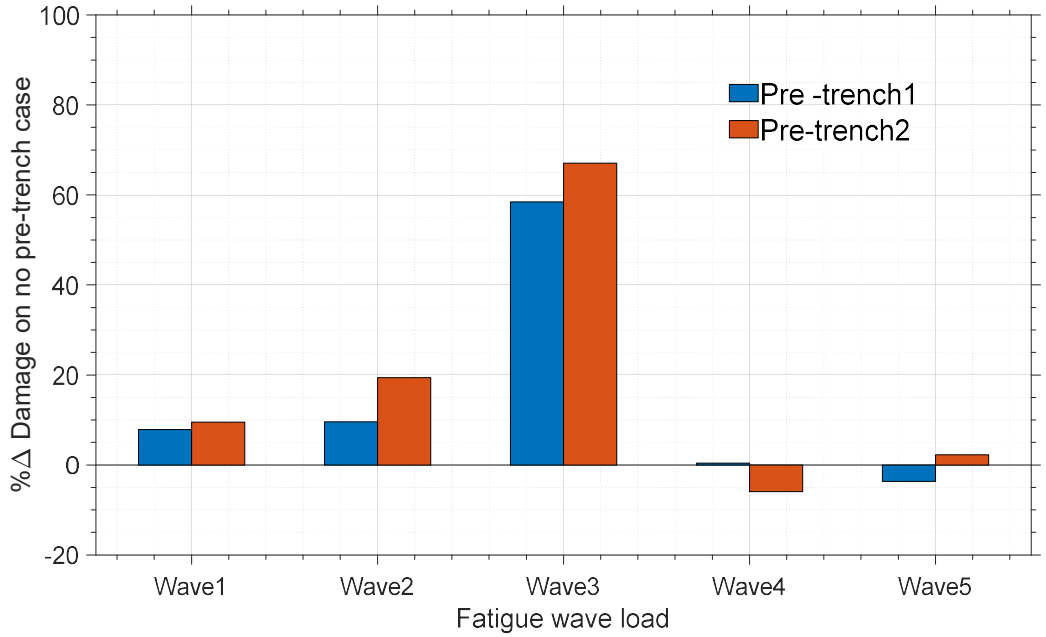

Figure 7-39 –Percentage change in fatigue damage of the pre-trench1 and pre-trench2 cases relative to the no pre-trench cases.

7.2.6.7 Pre-trench resistance and SCR TDZ bending moments

The pre-trench envelope is not an empty space or vacuum but contains softened soil caused by several cycles of SCR TDZ penetrations. Some of the loosed soil may be eroded and forced out of the trench by hydraulic- erosional processes from high water velocities as the pipe moves up and down into the trench [78]. In such a case, overhanging of the SCR TDZ over a deep trench for calm conditions is a possibility. The strength of the soft soil is degraded compared to a virgin seabed that has not been penetrated. Although some authors indicate that the loosed soil, if left for a long period, can reconsolidate and regain appreciable strength [121, 122], other authors suggested that the strength regained is significantly less than that before the seabed was penetrated [123, 124]. However, the degradation of the seabed strength in stiffness and suction is captured by the RQ model [56].

To demonstrate that the soil materials within the pre-trench provide some form of resistance to the SCR TDZ motion, the range graph maximum of the seabed normal

resistance per pipe diameter (OD) corresponding to the penetrations for case3 (wave3 + no pre-trench) and case8 (wave3 + pre-trench1) are presented in Figure 7-40 (a). Note that wave3 ($H_s = 4.5$m, $T_p = 9.5$sec) does not cause the SCR TDZ to exceed the pre trench1 envelope. This can be seen in Figure 7-33 (b), which is also presented in Figure 7-40 (a). It could be observed that the resistance imposed on the SCR TDZ by the pre-trench1 condition is significantly reduced compared to the seabed resistance imposed on the SCR TDZ for the no pre-trench condition (case3) under the same wave condition (wave3). This indicates that the pre-trench resistance is weakened after several penetrations of the pipe into the soil during the pre-trench stage. However, the maximum bending moments for these two cases are comparable, as seen in Figure 7-40 (b). The peak bending moment for case3 and case8 occur before the maximum penetrated point in the SCR TDZ. Although the maximum bending moment for both cases closely matched each other, the spatial variation of the bending moment along the SCR TDZ appears more random for the SCR TDZ section of the no pre-trench case (case3) and for the SCR TDZ section outside the pre-trench envelop for the pre-trenched case (case8), compared with section within the pre-trench envelope. This is the natural hot spots interactions of the SCR and seabed. Figure 7-40 (c) present the variation of fatigue damage with penetrations of the SCR TDZ section for both case3 and case8. Here it could be seen that since the SCR penetrated deeper into the pre-trench envelope for case8, compared with the no-pre-trench case (case3), more bending will be experienced by the SCR TDZ section of case 8 within the trench. Considering in Figure 7-40 (b), alongside within Figure 7-40 (c), it could be observed that the point of maximum bending moments (in these cases) do not coincide exactly with points of maximum fatigue damage. For both case3 and case8, the maximum fatigue damages occur at the most penetrated point of the SCR TDZ. This may imply that variation in the bending moment at the maximum fatigue damage point may have more influence on the fatigue damage than the amplitudes of the bending moments.

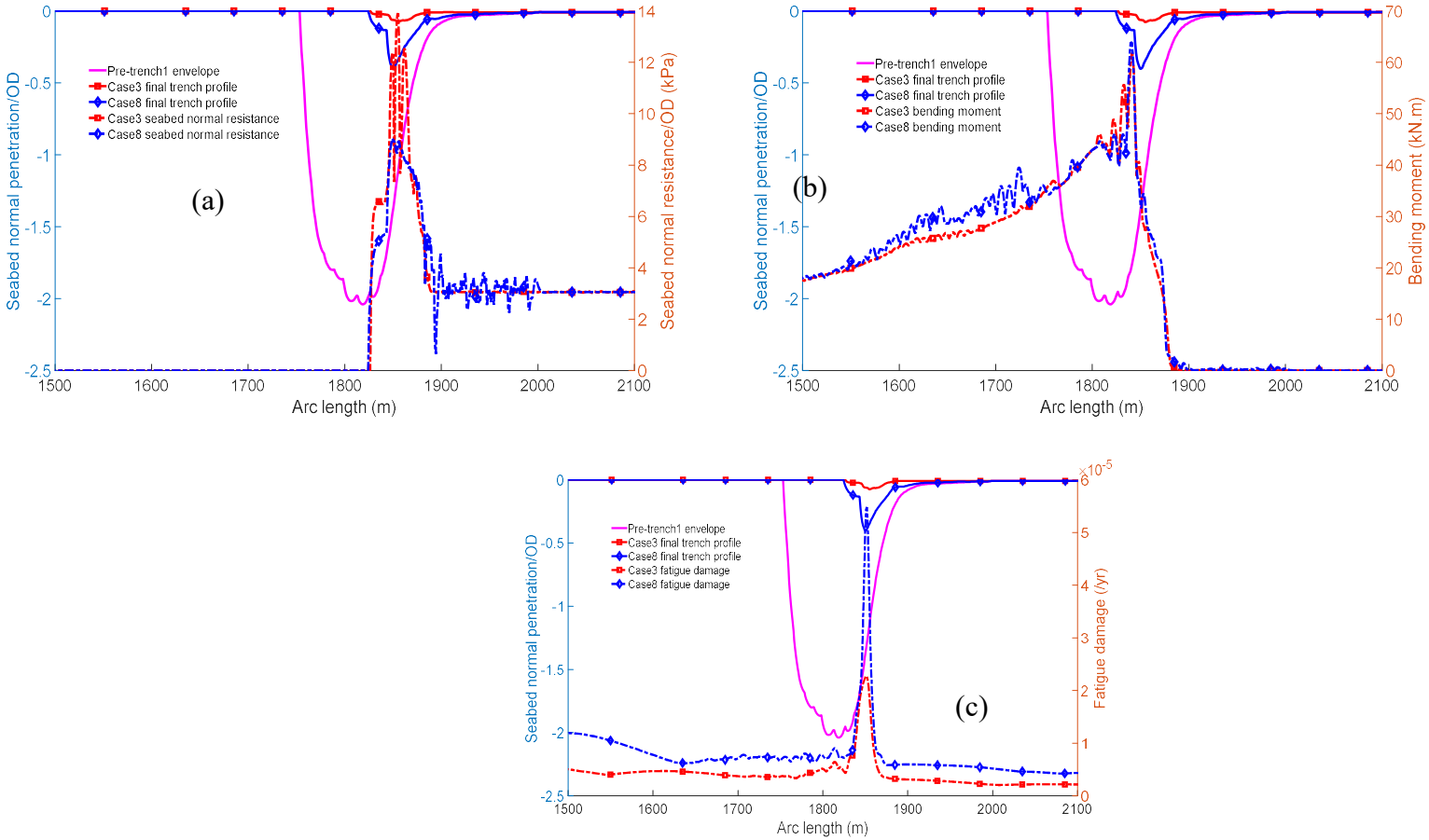

Figure 7-40 – (a) Seabed normal resistance to pipe penetration in the trench, (b) seabed normal penetration in comparison with SC TDZ bending moment.

7.2.7 Concluding remarks on analysis

It is essential to the riser industry to be able to qualify and quantify the fatigue damage response of the SCR TDZ in the presence of existing trench (pre-trench condition), complex fatigue wave load, vessel first order motions and vessel offsets in a full time-domain simulation. This knowledge will help the riser designer mitigate uncertainties surrounding the complex interactions between the SCR TDZ and the seabed. A new numerical pre-trenching technique, referred to as the simulation stage-based pre-trenching technique (SSBPT), is introduced in this work to achieve this goal. The SSBPT decomposes the usual single simulation period into three stages which are the trenching stage (in which the pre-trench envelope is created), the rest stage (in which the pre-trenching load response are dampened out), and the main stage (in which the main fatigue wave load is imposed on the vessel-riser system in the presence of the created pre-trench). The SSBPT has been compared with similar studies developed on the same hysteretic non-linear soil interaction model but with a different pre-trenching approach. Although the two methods can provide pre-trenches, the SSBPT offers the opportunities to obtain longer span pre-trenches typical of those observed from field data by the imposition of oscillatory vessel offsets. This is possible due to the inclusion of oscillatory vessel offsets at the pre-trenching stage of the SSBPT. Also, though the peak fatigue damage occurs at a similar location for both techniques, the SSBPT can capture more spreading of the fatigue damage in the SCR TDZ neighbourhood resulting from a combination of multiple fatigue wave loads of a broader range of amplitudes and periods.

The SSBPT has been demonstrated with an SCR example on which different random fatigue wave load conditions are imposed in the presence of different pre-trench conditions. The results indicate that the pre-trench can increase the SCR TDZ fatigue damage if the fatigue wave loads applied do not cause the SCR TDZ motions to exceed the existing pre-trench envelope. However, if the motions of the SCR TDZ caused by a combination of the wave load and the vessel response resulted in a trench, which exceeds the pre-trench envelope (longer and deeper), the resulting fatigue damage response will be similar (either larger or smaller) compared with the cases where a flat seabed or no pre-trench is assumed prior to the fatigue simulation. Since the trenching process is caused by other factors apart from the wave and vessel excitations, it is believed that the existing pre-trench envelope can fully accommodate the riser TDZ motions during the fatigue loading. Hence the pre-trench will likely cause an increase in the fatigue damage of the SCR TDZ section. However, if the pre-trench envelope

is not able to accommodate the SCR TDZ large excitation, further trenching can be observed (referred to as trench in trench from the field observation study). The impact of this process can be captured by the SSBPT.

The fatigue load applied in this study is for one direction (along the riser azimuth), while the host vessel remains in its nominal position. Although the comparative study and the main analysis in this work showed that pre-trenching increases the SCR fatigue damage, these interactions are too complex to make absolute conclusions. It is preferable to have suitable methods of accessing these interactions for a case-by-case investigation, which may not provide similar qualitative conclusions. A more robust understanding can be obtained with the SSBPT to investigate other variable conditions, such as different vessel motions, the vessel second-order offsets, the SCR global configurations, the SCR TDZ stiffness, different soil model data different wave loads and directions etc.

7.3 Chapter summary

This chapter presents the impact of the seabed slope on the strength and fatigue damage responses of the SCR TDZ. It was found that the seabed slope around the SCR TDZ could positively or negatively affect the TDZ response. Inface, positive slope increases the life of the SCR TDZ, while the converse is that case for positive sloped seabed. In line with this, it is recommended that a parametric study with the final SCR design should be conducted during SCR design to quantify the benefits or additional design restrictions that may be encountered caused by error

s in the seabed profile data available during the SCR design. Also, a new technique to evaluate the impact of seabed trench on SCR TDZ is presented. The method provides robustness to SCR design computation involving complex loads typical of real-life projects. For the example presented in this research, the presence of a pre-trench is observed to cause increase in the fatigue damage response of the SCR TDZ. However, the investigation of the SCR TDZ with this technique showed that the effect of the pre-trench should be conducted on a case-by-case basis as many factors ranging from the riser configuration to the vessel offset and motions can impact the SCR TDZ responses in seabed trenches. It is noted here that including the trench impact investigation during screening or optimisation analysis of the SCR could be challenging. Hence, such investigation can be conducted on the final SCR design as parametric analyses.

8 VESSEL RELOCATION STRATEGY

This Chapter is focused on developing a formal optimisation approach to the vessel relocation program for steel catenary riser (SCR) touch down zone (TDZ) fatigue management. Vessel relocation is the planned repositioning of the vessel within the acceptable limit of the riser design to help spread and reduce the fatigue damage over the SCR TDZ. There is a need to obtain an optimum vessel relocation program that best reduces the SCR TDZ fatigue damage. Hence, the facility operator will need to know the optimum combination of the following: the number of stations along the relocation axis, the distance limits for the relocation, and the relocation axis direction. The constraints on the problem are imposed by the stress utilisation, TDZ compression and top tension. The index-matching optimisation technique is applied to solve the optimisation problem. Here, we first consider symmetrical vessel relocation programs for a single SCR hosted by a production platform. The fatigue damage responses of the SCR with the optimum vessel relocation programs are compared with those without vessel relocation. The results obtained indicate that a considerable fatigue reduction can be achieved through a well-planned and optimum vessel relocation program. In reality, vessel host several SCRs, not one as considered in Section 8.1. An extended vessel relocation strategy for multiple SCRs is developed based on the technique for. Here, the symmetrical relocation strategy for single SCR was extended to accommodate non symmetrical relocation programs and for multiple SCR systems. Also, a screening methodology is developed to cut down significantly on the computation resources required for the simulations. This chapter is sectioned as follows:

- Section 8.1 – Vessel relocation strategy for single SCR
- Section 8.2 – Vessel relocation strategy for multiple SCRs
- Section 8.3 – Chapter summary

8.1 vessel relocation strategy for single SCR

Steel catenary riser systems are used for the transportation of hydrocarbon production-related materials between the seabed and the host floating platform. Steel catenary risers are the most attractive riser solution because of their simplicity, robustness, and lower procurement costs [9, 28, 52, 112, 125, 126]. A major challenge with SCR application is the high stress and fatigue damage incurred around its critical sections, which are the hang off (HO) and the TDZ [7-9, 127]. The high fatigue response in the SCR HO region is relatively easier to control compared with those occurring at the TDZ. A suitable material of high strength can be employed at the HO region to reduce the high stress and fatigue damage experienced. However, at the touchdown zone, a longer section of the SCR interacts in a complex way with the non-linear seabed, resulting in high and intricate fatigue response patterns that pose great challenges to manage.

Several efforts have been committed by research institutions and the offshore industries to increase the application of SCRs for deepwater hydrocarbon extraction [31-33]. These solutions include the SCR configuration change such as steel lazy wave and shaped riser solutions [13, 34-51], the alternative material application for SCR design such as high strength material including titanium for the riser pipe joint [31, 52-55], the advancement in riser soil interaction modelling such as the development of non-linear riser soil interaction models [56-58], the decoupling of SCR from vessel motion such as the uncoupled steel catenary riser systems [59-62], the vessel relocation to effect fatigue damage spreading along the SCR TDZ [32, 63-65], the use of upset pipe end and titanium welding connection to improve the life of the riser at welded joints [31, 55, 63-70], the use of hydrodynamic dampers which enhances the damping of stress wave propagated from vessel motion to the SCR TDZ [67], etc. The vessel relocation solution for fatigue mitigation in the SCR TDZ has been referenced in literature and has been implemented in real-life projects [32, 63-65]. However, the methodology for investigating and conducting an optimum vessel relocation program is still absent from open literature. This section is set to present and demonstrate the development and application of the vessel relocation technique using a single SCR-vessel system case. The approach presented here can be useful for both new risers and brown field risers for life extension purposes.

8.1.1 Basis for the vessel relocation strategy

The fatigue damage in the active SCR TDZ is proportional to its exposure time to the applied fatigue load, which in turn depends on the variation in the SCR global position and configuration. The relocation of the vessel is a planned variation of the riser host platform from its mean position to effect changes in the global riser configuration, resulting in the spatial (arc length) variation of the SCR fatigue hot spots. The wider the variation or spread of the active seabed section, the higher will be the reduction of the fatigue exposure time and a consequent spread or reduction in the SCR TDZ effective fatigue damage.

To demonstrate this variation, we monitor the offsets of SCR touchdown points (TDPs) by conducting vessel movement in their azimuth direction or riser planes, as shown in Figure 8-1. Figure 8-1 (a) presents the SCR TDP offsets from their nominal positions for different SCR configurations with hang-off angles ranging from 8deg to 20deg in a fixed water depth of 1500m, while Figure 8-1 (b) presents the SCR TDP offset from its nominal position for an SCR with a hang-off angle of 12deg (with the vertical), in various water depths ranging from 1000m to 3000m. For both scenarios, the vessel offsets are expressed as percentages of the water depths. The negative vessel offsets values are the near vessel offsets where the vessel is relocated towards the SCR TDP along the riser plane. On the other hand, the positive vessel offsets values are for the vessel far offset where the vessel is moved away from the SCR TDP along the riser plane. Note that the vessel in its nominal position (0% offset), incurs no SCR TDP offsets. It could be observed from the plots that the vessel relocation in the far direction imposes larger riser TDP offsets than those of the near vessel offsets. This implies that the SCR TDP horizontal movement is more sensitive to the vessel far offsets. A combination of 10% vessel offsets in both direction for the riser in a water depth of 1500m can be seen to provide more than 200m TDP offset for the SCR with a 12deg hang-off angle (Figure 8-1 (a)). The TDP offsets are seen to increase with increasing SCR hang-off angle and water depths. For example, it could be observed in Figure 8-1 (b) that more than 700m of SCR TDP horizontal travel is possible for an SCR with a 12deg hang-off angle, hosted in a water depth of 3000m, and subjected to 10% vessel offset in the far and near directions. These TDP offsets translate to the spreading of the SCR TDZ fatigue hot spots and a consequent fatigue damage reduction. So, with the relocation program, longer sections of the SCR on seabed share the period of intensive contact with the seabed over the design life of the riser, meaning different fatigue hotspots along the SCR TDZ now receive a reduced number of fatigue load cycles due to the vessel relocation scheme. While the vessel relocation strategy is helpful for brownfield SCRs

for life extension purposes [32, 63-65], pre-planning for vessel relocation for a new field development can reduce the stringent requirement for the SCR fatigue design. This can reduce the wall thickness specification, reduce the riser weight and the required design load capacities of the vessel and the hang-off structures and removes the need for SCR TDZ redesign, such as cladded pipe section (e.g. corrosion resistive alloys (CRA)). These potential positive contributions of the vessel relocation technique can significantly reduce the overall cost of the greenfield SCRs.

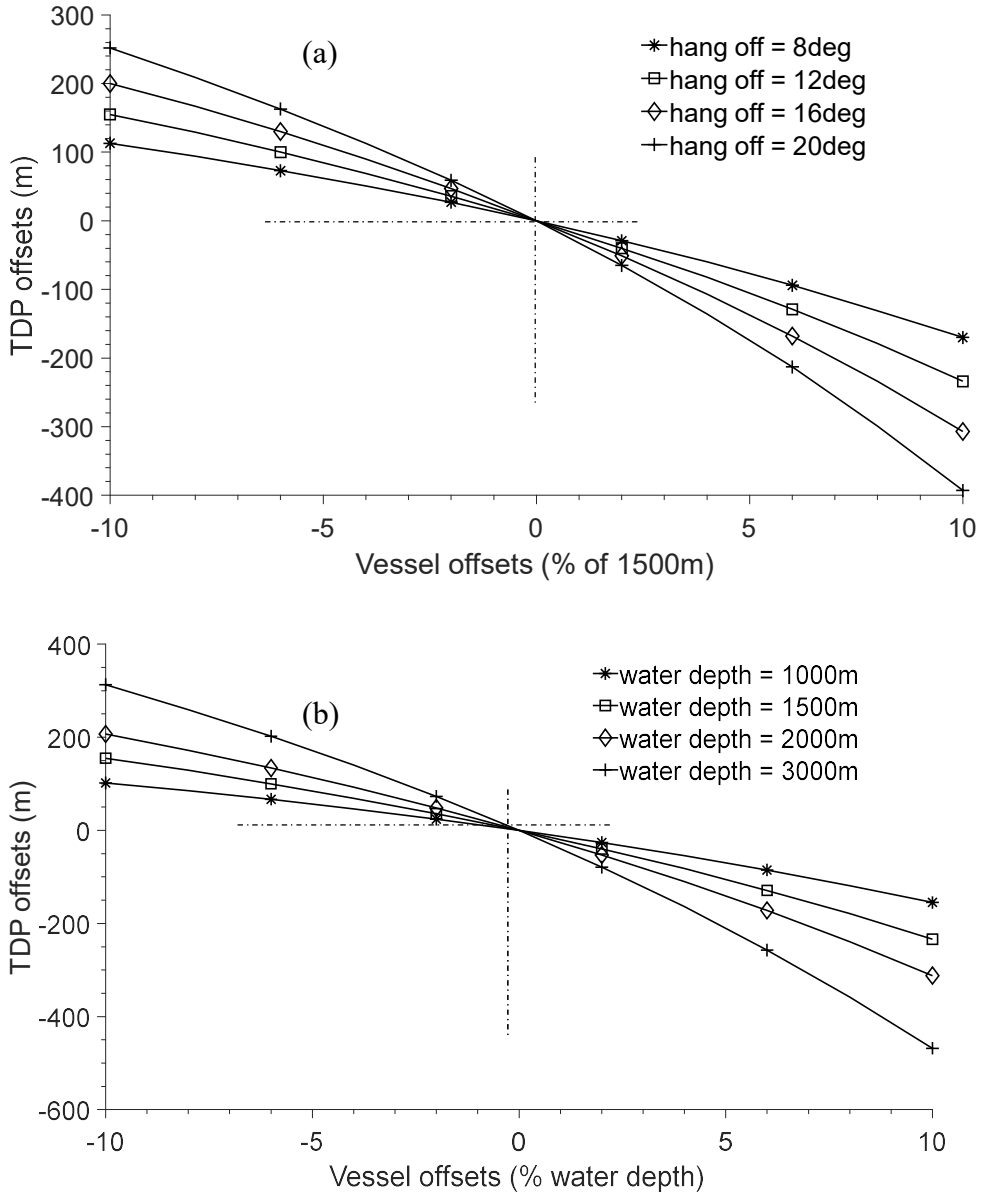

Figure 8-1. SCR touch down point relocation (a) risers with different hang-off angle and different vessel offset conditions in 1500m water depth (b) a 12deg hang off riser in different water depths and different vessel offset conditions.

The planned vessel relocation is a complex operation requiring several inputs, and it is mainly feasible for host platforms with catenary shaped sea keeping systems rather than tension leg platform (TLP). The input to the vessel relocation operation includes but not limited to the directions of the relocation, the number of relocations over the design life of the riser, the number of relocation points or stations, the personnel and equipment required for each relocation operation, the temporary shutdown of production during relocation operation, etc. An appropriate or optimum combination of these variables is required to minimise the fatigue damage of the risers. In this section, we develop and demonstrate a method to achieve an optimum vessel relocation for a single SCR.

8.1.2 Development of symmetric vessel relocation strategy for single SCR

8.1.2.1 Definition of terms and SCR TDZ effective fatigue damage

Vessel relocation program - All the variables, parameters, activities, and plans involved in the movement of the vessel from one point to another to enhance the spreading of fatigue damage over longer sections of the SCR TDZ are embodied in the *relocation program*. However, in this section, the relocation program term is used to refer to a unique set of combinations of *the relocation axis,* the *relocation span,* and the *number of relocation stations.* These are the inputs variables for the vessel relocation optimisation analysis in this section.

Vessel relocation axis – From the operational and analysis point of view, it may be relatively easier to conduct a vessel relocation program in a straight line known as the *relocation axis*, as shown in Figure 8-2. A direction characterises the relocation axis (α) measured from a suitable referenced line. The axis extends from one limit on the riser nearside to the other limit on the riser far side, with the relocation stations equally distributed in between the limits. The optimum relocation axis is one of the design variables for the vessel relocation optimisation problem.

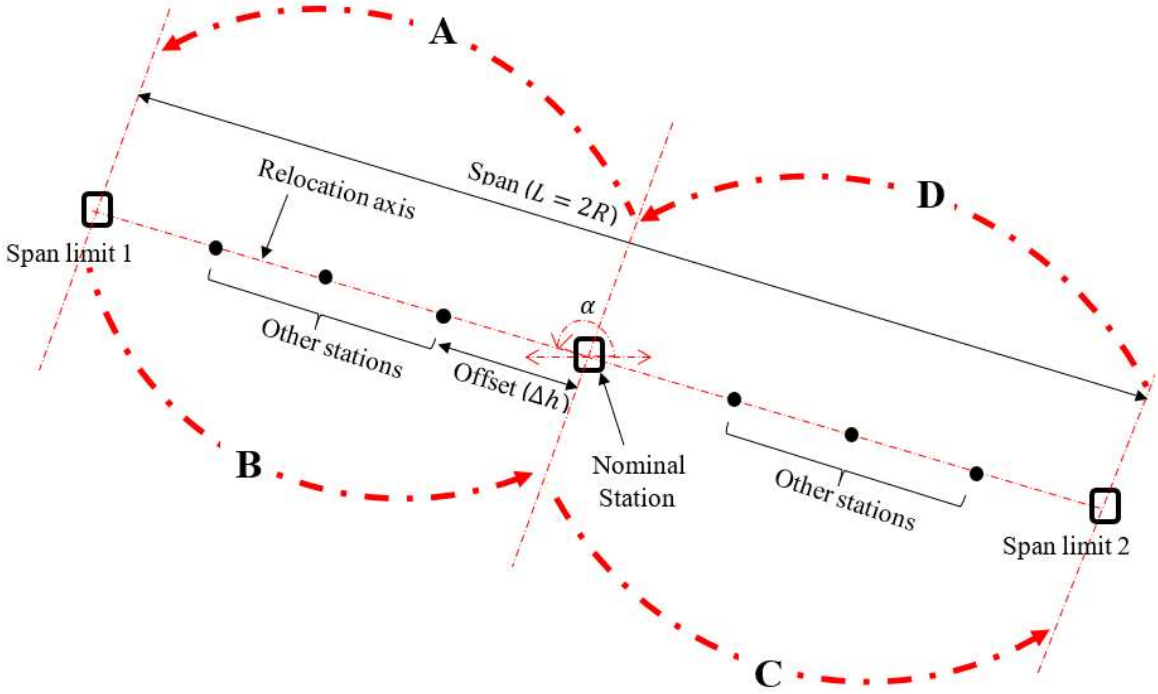

Figure 8-2. A symmetric vessel relocation program layout, depicting equally spaced relocation stations ($\boldsymbol{p}$) between the relocation span limits ($\boldsymbol{L}$) along a relocation axis ($\boldsymbol{\alpha}$).

Relocation span limits - The limit on the extent to which the vessel can be moved on either side of the nominal station, along the relocation axis, is constrained by factors including the stress utilisation, the top tension, and the compression around the TDZ of the SCR. The allowable limits within which the relocation program is feasible is referred to as the *span limit,* L, as seen in Figure 8-2. For the symmetric relocation program considered in this study, the distance of any of the two-span limits from the nominal station is referred to as the span radius of relocation, $R = L/2$. The span radius is expressed as percentage of the water depth in this study, and it's one of the design variables for the vessel relocation optimisation.

Relocation stations - In any relocation program, the vessel is moved intermittently from one position to another, starting from the nominal position (mean or nominal station). These positions are referred to as the *relocation stations,* p. For a symmetric vessel relocation program depicted in Figure 8-2, p will have to be odd, e.g. $p = 3, 5, 7, 9$ etc., as seen in Table 8-1. For $p = 1$, the vessel is in its nominal station.

Relocation cycle - Considering the relocation program in Figure 8-2, a *relocation cycle* will be the complete movement of the vessel from its nominal station to and from both span limits. The planned journey of the vessel between these span limits involves relocation from one station to another on both sides of the nominal station as indicated by the arrow on A, B, C and

D. Each of A, B, C, and D represents a quarter of one relocation cycle and each consist of relocation stations as shown in Figure 8-2. For example, considering the nine-relocation station program ($p = 9$) in Table 8-1, one cycle of relocation will consist of the quarter cycles (A, B, C and D) with the following relocation patterns:

Table 8-1. A symmetric vessel relocation program pattern.

No of stations	Station index (m)																	
(p)	Nearside							Nominal		Farside								
No relocation								1										
3							2	1		3								
5						3	2	1		4	5							
7					4	3	2	1		5	6	7						
9				5	4	3	2	1		6	7	8	9					
…			…	…	…	…	…		…	…	…	…	…	…				
k	$(k+1)/2$		…	5	4	3	2	1		6	7	8	9	…	k			

$$1 \text{ relocation cycle} = \begin{cases} A: 1 \rightarrow 2 \rightarrow 3 \rightarrow 4 \rightarrow 5. \\ B: 5 \rightarrow 4 \rightarrow 3 \rightarrow 2 \rightarrow 1 \\ C: 1 \rightarrow 6 \rightarrow 7 \rightarrow 8 \rightarrow 9 \\ D: 9 \rightarrow 8 \rightarrow 7 \rightarrow 6 \rightarrow 1 \end{cases} \quad (8\text{-}1)$$

Note that the spread of the fatigue hotspots (fatigue reduction) around the SCR TDZ is related to the time spent at each relocation station and will be independent of the number of relocation cycles. Hence, the methods presented in this section is based on one relocation cycle.

Number of relocations - The number of times the vessel is moved from one station to another is referred to as the *number of relocations* (n). Referring to the 9-station ($p = 9$) relocation program depicted in equation (8-1), each quarter of the relocation cycle contains 4 vessel movement. The total number of movements of the vessel for the symmetric 9-station relocation program will be 16. Generally, the number of relocations can be related to the number of relocation station, p, as follows:

$$n = 2(p - 1) \quad (8\text{-}2)$$

When $p = 1$ as seen in Table 8-1, $n = 0$ i.e., no vessel relocation. This is the case representing the traditional approach layout for fatigue analysis where no vessel relocation is considered.

Relocation offsets - The direct distance between two neighbouring stations is referred to as the *relocation offset* (Δh) (see Figure 8-2). This is the distance over which the vessel is moved during each of the n relocations. For equally spaced relocation stations, the relocation offsets can be obtained from the relocation span, L, and the number of relocation stations, p, as follows:

$$\Delta h = \frac{L}{p-1} = \frac{2R}{p-1} \tag{8-3}$$

Rest and transition time during relocation - The time spent by the vessel at each of the stations before being moved to a neighbouring station is referred to as the *rest time* (T_r). The time it takes to move the vessel from one station to another is referred to as the *transition time* (T_t). The following can be observed for the 9-relocation station example from equation (8-1):

- The nominal station (1) is reached 3 times. This means that the vessel spends a rest time of $3T_r$ at the nominal station.
- Each of the two span limit stations (5 and 9) are reached once. This means the vessel spends a cumulative rest time of T_r each at station 5 and 9.
- The other relocation station ($9 - 3 = 2$) are each reached two times. This means that the vessel spends a rest time of $2T_r$ at each of these other ($p - 3$) stations.

This pattern can be generalised for p number of stations ($m = 1$ to p) as follows:

$$T_{r_m} = \begin{cases} 3T_r & m = \text{nominal station} \\ T_r & m = \text{span limit1 station} \\ T_r & m = \text{span limit2 station} \\ 2T_r & m = \text{other } (p-3)\text{stations} \end{cases} \tag{8-4}$$

Where m is the station count ranging from $m = 1$ to p, hence, the cumulated rest times across all stations can then be expressed as:

$$T_{r_{cumm}} = \sum_{m=1}^{p} T_{r_m} = 3T_r + T_r + T_r + 2T_r(p-3)$$

$$T_{r_{cumm}} = T_r(2p-1) \tag{8-5}$$

For n number of relocations, the cumulative transition time will be:

$$T_{t_{cumm}} = nT_t \tag{8-6}$$

The total exposure time, T_{cumm}, can then be expressed as:

$$T_{cumm} = T_{r_{cumm}} + T_{t_{cumm}} = T_r(2p-1) + nT_t \tag{8-7}$$

The time in transit, T_t, is negligible compared with the rest time T_r. Operationally, the movement of the vessel from one station to another may take less than a day or a few days, compared with the rest time, which can run into years. Hence, we can rewrite (8-7) as:

$$T_{cumm} = T_r(2p-1) \tag{8-8}$$

The total exposure time, T_{cumm} is equal to the design life of the SCR, i.e., $T_{cumm} = T_D$. Hence,

$$T_r = \frac{T_D}{(2p-1)} \tag{8-9}$$

Substituting equation (8-9) into equation (8-4), the resulting coefficient of T_D is expressed in equation (8-10). This is referred to as the fatigue damage fraction, f_m.

$$f_m = \begin{cases} \dfrac{3}{(2p-1)} & m = nominal\ station. \\ \dfrac{1}{(2p-1)} & m = span\ limit1\ station \\ \dfrac{1}{(2p-1)} & m = span\ limit2\ station \\ \dfrac{2}{(2p-1)} & m = other\ (p-3)\ stations \end{cases} \tag{8-10}$$

Where:

$$\sum_{m=1}^{p} f_m = 1 \tag{8-11}$$

The resulting (effective) fatigue damage (D_{eff}) at any fatigue hotspot in the SCR TDZ for the relocation program can then be expressed as follow:

$$D_{eff} = \sum_{m=1}^{p} f_m D_m \tag{8-12}$$

Where:

D_m = fatigue damage at station m.

p = number of relocation station for the program

m = relocation station counter from 1 to p

8.1.2.2 Fatigue damage for Greenfields and Brownfields

For a new field (greenfield) with an included vessel relocation plan, the fatigue damage of the SCR at the relocation stations, D_m, can be obtained considering the design life of the riser T_D, appropriate safety factors and other design variables and factors. For example, considering a single occurrence fatigue load case, the Rain flow counting technique [98] can be used to express the varying SCR TDZ stress spectrum as a histogram of stress reversals. The Miner's rule presented in equation (8-13) can then be applied to cumulate the fatigue damage for the SCR at each of the m^{th} station, where n_i is the number of cycles of the i^{th} stress range components at (station m) and N_i is the number of cycles to failure associated with the i^{th} stress range (at station m) as obtained from the S-N curve.

$$D_m = \sum_i \frac{n_i}{N_i} \tag{8-13}$$

For an existing field (brownfield), the objective of the vessel relocation program will be to extend the life of the SCR. Let the remaining or residue fatigue life of the SCR be T_{rem} and the remaining design life of the SCR be $T_{D_{rem}}$. The effective fatigue damage can be calculated

using the expressions already presented in equation (8-12) but with design factors appropriate for existing risers. Also, for brownfield fatigue calculation, T_D will be replaced by $T_{D_{rem}}$ i.e.:

$$T_D = T_{D_{rem}} \tag{8-14}$$

The life extension, T_{ext}, of the SCR can then be obtained as:

$$T_{ext} = \frac{1}{D_{eff}} - T_{rem} \tag{8-15}$$

8.1.2.3 Vessel relocation optimisation

Each of the relocation programs consists of a unique combination of the axis of relocation (α), the span radius ($R = L/2$) and the number of stations (p). These are the vessel relocation design variables. A change in any of these variables will result in a different relocation program. Therefore, there is the need to obtain an optimum relocation program that will yield the minimum effective damage (D_{eff}) around the SCR TDZ. However, the resulting SCR configuration obtained from any combination of the design variables (α, R and p) must satisfy the design limit for the SCR design storm responses. The vessel relocation optimisation problem can, therefore, be cast as follow:

$$\text{find X} = \begin{Bmatrix} \alpha \\ R \\ p \end{Bmatrix} \text{ which minimises } D_{eff} \tag{8-16}$$

Subject to the following constraints, g:

$$\text{g} = \begin{cases} U_{TDZ} < 1 \\ T_{top} < T_y \\ T_{TDZ} > 0 \end{cases} \tag{8-17}$$

Where:

α = relocation axis measured from a reference axis.

R = span radius.

p = number of relocation station.

D_{eff} = effective fatigue damage per relocation program.

U_{TDZ} = stress utilisation in the SCR TDZ.

T_{top} = maximum effective tension at the riser top.

T_{TDZ} = minimum effective tension around the riser TDZ.

T_y = yield tension of the riser pipe = $0.9SA$.

S = Specified minimum yield strength.

A = SCR pipe cross-section area.

Once the design space (α, R, p) is defined for the problem, any suitable optimisation technique can be applied, using the result data obtained for the evaluated objective and constraint functions. In this work, the index matching optimisation technique is used. Details of the index matching technique are provided in Chapter 4.

8.1.3 Numerical modelling and analysis data

8.1.3.1 Numerical modelling

The OrcaFlex numerical software package is used to conduct the analysis for this study. The analysis simulations are performed in the time domain, applying the implicit integration scheme in the numerical solution process. The pre-processing, modelling, simulations and post-processing are automated using MATLAB programs integrated with the OrcaFlex programming interface, OrcFxAPI [114]. The developed MATLAB program pre-processes analysis data and computes additional data required for the numerical modelling in OrcaFlex. The program then generates OrcaFlex models for the relocation programs based on equations developed in this section. The regular design storm and fatigue wave loads are modelled with the Dean Stream theory, with the wave load acting on the vessel beam to effect maximum roll motions on the SCR.

The storm response analysis is conducted using a single representative regular (design) wave to evaluate the constraint functions. The SCR TDZ stress utilisations, TDZ compressions and top tensions are calculated from the simulated design storm numerical models. The stress utilisation is post-processed using the DNV-OS-F201 combined load (bending, tension, and pressure) resistance factor design criteria. Detailed information about the DNV-OS-F201 criteria can be found in [115]. Similarly, the fatigue analyses for the relocation programs are also conducted using a single regular fatigue wave load to evaluate the SCR TDZ fatigue

damage. The objective function (effective fatigue damage, D_{eff}) is then post-processed from the SCR TDZ fatigue damage results. For the fatigue calculation, the S-N D-curve in seawater with cathodic protection is used [116]. Once the design storm and effective fatigue damage responses are calculated, the index matching optimisation technique is applied to obtain the indices representing the optimum solutions lying within the shaded region depicted in Figure 8-3. The applied procedure for the analysis is presented in Figure 8-4 and summarised as follows:

- Assemble all possible combinations of the design variables (α, R, p).
- Run numerical analyses (for each combination) to determine the values of the constraints (U, T_{TDZ}, T_{top}).
- Run numerical analyses (for each combination) to determine the values of the objective function (effective fatigue damage).
- Eliminate combinations that do not satisfy the constraints.
- Order the remaining combinations in ascending order of the objective function to find the combination that minimises the objective function while satisfying the constraints.

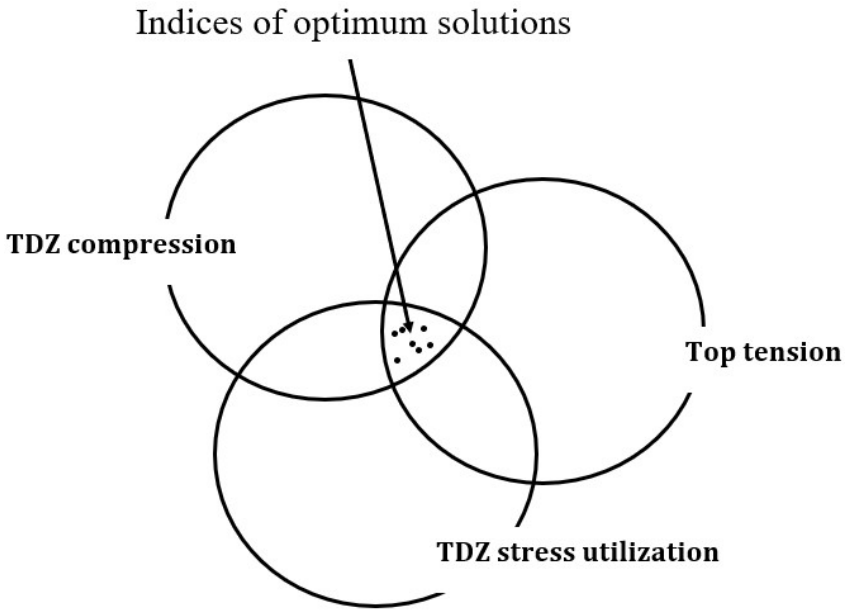

Figure 8-3. Optimum configuration index space.

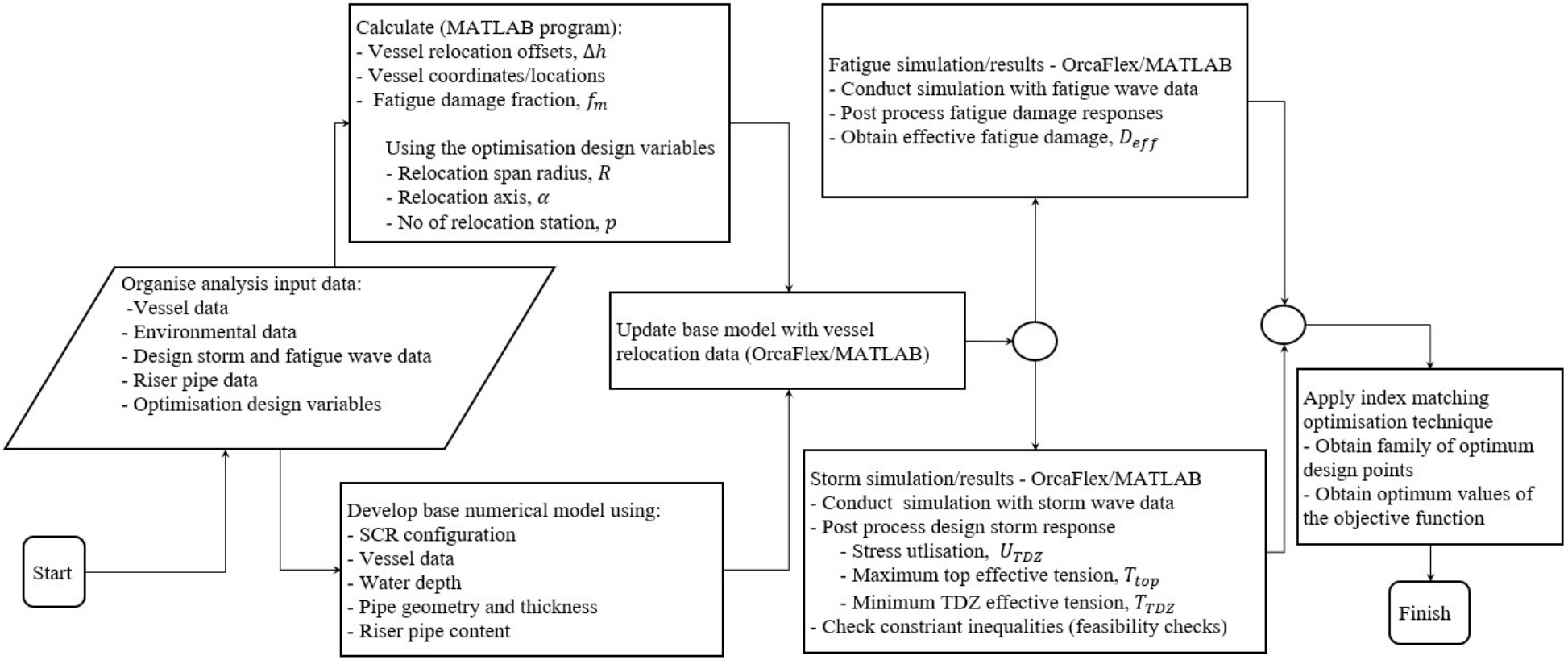

Figure 8-4. Analysis flow chart

8.1.3.2 Riser pipe data and relocation design variables

The SCR investigated in this work is an 8-inch X70 steel grade pipe hosted by a generic floating production, storage, and offloading (FPSO) unit at an azimuth of 90deg to the vessel heading, as shown in Figure 8-5. The SCR is connected to the FPSO via a flex joint. The SCR minimum wall thickness required for burst and collapse pressure resistance is calculated based on DNV-OS-F201 criteria [4]. Table 8-2 presents the analysis data for the study.

Table 8-2. Analysis data.

SCR data	**Values**
Pipe size	8inch
Internal Design pressure	10ksi
Pipe thickness (fixed)	16.7mm
SMYS	482 MPa
Hang off angle with the vertical	12^o
Content density	600kg/m^3
Flex joint stiffness (linear)	12kN.m/deg
Water depth	1500m
S-N curve (seawater plus cathodic protection)	D-Curve [116]
Riser design life (T_D) (greenfield)	30 years
Relocation axis(α)	[0,30,60] deg
Span radius (R)(%water depth)	$\{R$:$1 \leq R \leq 20\}$
Number of station (p)	$\{p$:$3 \leq p \leq 19\}$

The range of values for the optimisation design variables (α, R, p) presented in Table 8-2 are briefly discussed as follows:

Axes of relocation (α) – To cover the full range of relocation directions, six axes are considered. The axes are at 30deg offset from each other and are measured relative to the positive x-axis. As seen in Figure 8-5, five out of the six axes extend from one side (portside) of the vessel to the other side (starboard), which in this analysis are the SCR nearside and the far side, respectively. The axis-4 aligns with the heading of the vessel. The single SCR system is hosted on the port side and at 90deg to the vessel heading. Since the SCR is perpendicular to the vessel heading, vessel relocation along the axis-4 will cause little variation of the SCR

TDZ fatigue hotspots. Hence, axis-4 will not be included in the analysis. The floating production vessel implemented for this study has response amplitude operators (RAOs) that are symmetric about the axis-1 and axis-4. That means, with the SCR orientation, vessel relocation along axis-2 and axis-6 as well as vessel relocation along axis-3 and axis-5 will result in the same response at the SCR TDZ. Hence, vessel relocation along axis-5 and axis-6 will be excluded from the analysis, leaving us with three discrete values of α which are axes-1, axis-2 and axis-3. These axes correspond respectively with 0deg, 30deg, and 60deg measured from the reference axis, as have been presented in Table 8-2.

Span radius (R) – Different span radii are considered for the analysis and are expressed as percentages of the water depth. As shown in Table 8-2, R ranges from 1% to 20% of the water depth on each of the far and near side of the SCR, i.e., on both side of the nominal station. The span radius is discretised at 1% interval, resulting in 20 discrete values for R.

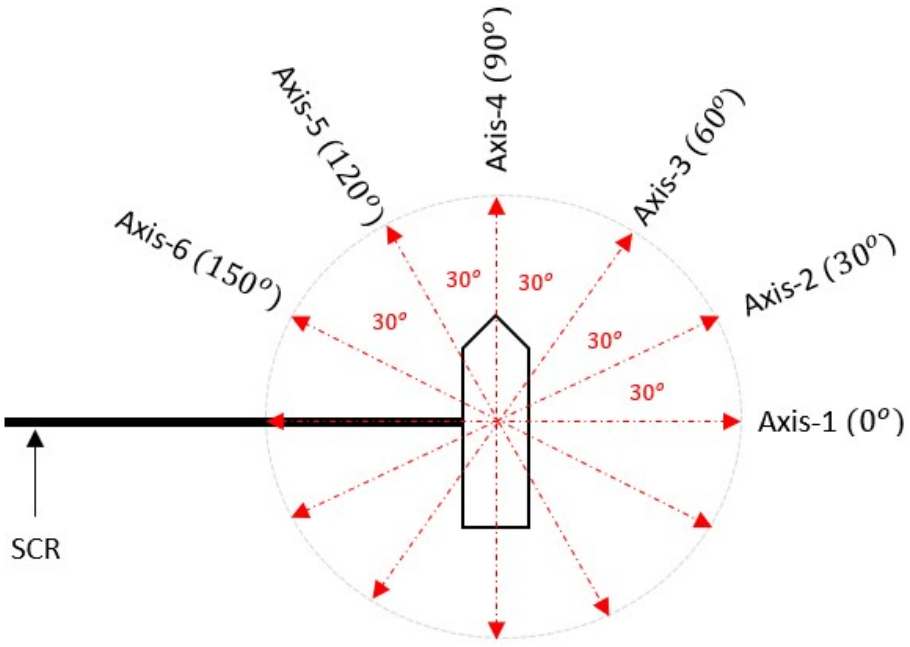

Figure 8-5. The layout of the vessel relocation axes for this study.

Number of relocation stations $(\boldsymbol{p})$ – The number of the equally spaced relocation stations along each axis (α) and for each span radius (R) is an odd number, considering a symmetric vessel relocation pattern. As presented in Table 8-2, the number of stations ranges from 3 to 19 at intervals of 2. This gives 9 discrete values of p.

8.1.3.3 Vessel motion data

A generic response amplitude operator (RAOs) for the FPSO is implemented. Considering the SCR azimuth and connection to the vessel mid-length, the heave and roll RAOs are the most relevant vessel responses to the beam wave acting on the vessel and are presented in Figure 8-6. The RAOs are symmetrical about the central longitudinal and lateral axes of the FPSO

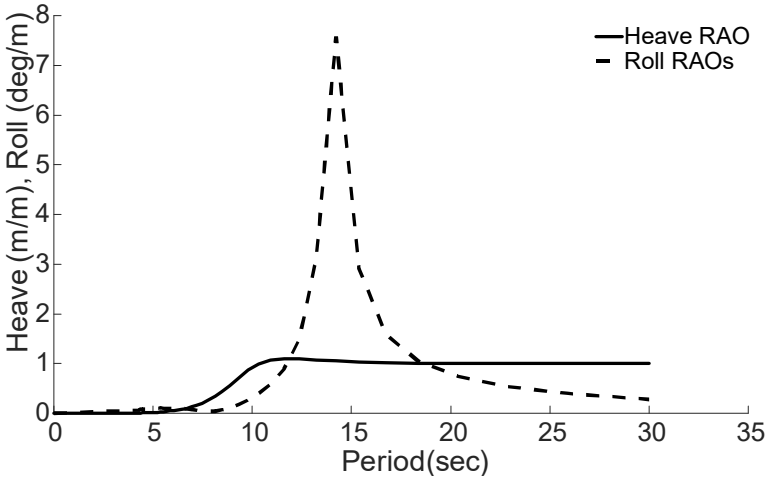

Figure 8-6. Vessel heave and roll RAOs to wave load in the beam sea direction (90deg and 270deg)

Table 8-3. Single wave load data for storm and fatigue analysis

Analyses	**Wave type**	**Data**	**Values**
Extreme	Regular	H	8m
		T	13sec
Fatigue	Regular	H	4.5m
		T	9.5ec

8.1.3.4 Environmental data

The non-linear hysteretic riser soil interaction model detailed in [56] is used in this study. A single regular design storm wave and fatigue sea state are applied during the numerical storm and fatigue analyses. This means the probability of occurrence of the fatigue sea state is 100%. All wave loads are Beam Sea to impact maximum roll motions on the SCR. Both the fatigue and the extreme wave sea state used are presented in Table 8-3.

The main objective of this study is to develop and demonstrate the vessel relocation methodology. Hence the single wave loads for design storm conditions and fatigue analysis are selected arbitrarily, with periods around the peak of the heave RAO, for demonstration

purposes. However, a single representative regular storm and fatigue wave load can be obtained from the irregular wave data available through preliminary screening of the riser hang-off motion at the vessel interface by conducting vessel spectral response calculations [128]. We can use the wave height and associated period causing significant hang-off vertical velocity to represent the design storm wave data. This is reasonable since the SCR vertical hang off velocities correlate with the stress response and compressions of the SCR at the TDZ [129-131] and that different SCR configuration will respond proportionately to different design wave with resulting excitation periods not matching the SCR natural periods. Also, the SCR TDZ fatigue damage correlates with the vertical hang off root mean square (rms) velocity values. With such correlation, a screening of the fatigue wavetable can be conducted to obtain the most effective wave height and associated period that will represent the fatigue wavetable for the optimisation simulations. Note that the single wave data are representative. It will be essential to confirm the performance of the derived optimum riser solution through detailed analysis using the actual storm and the full sea state fatigue wave data.

8.1.4 Analysis, results, and discussion

8.1.4.1 Obtaining optimum objective function

Recall from Table 8-2 that there are 3 discrete values of α, and 20 discrete values of R. These 2 variables provide 60 α-R design points i.e., 2-D design space bordered by α and R. Each of these 60 points relates to the 9 discrete values of p, with p ranging from 3 to 19 stations at an interval of 2. This gives 540 design points or relocation programs for this study. Now, each of the 540-design points will consist of a varying number of numerical models ranging from $m = 1$ to p as seen in the relocation pattern provided in the annotated Table 8-4. Hence, the index matching technique index system will have indices ranging from 1 to 540 relocation programs, each containing several models ranging from $m = 1$ to p. An alternative way of considering the number of numerical models is to associate the 99 stations in Table 8-4 to each of the α-R 60 design points resulting in 5940 models. Since the storm and the fatigue wave load are different (see Table 8-3), the number of models simulated for the problems for both the design storm and the fatigue wave load is 11880. For the 540-relocation programs, if any constraint function is not satisfied at any of the $m = 1$ to p station, that relocation program or design point will be deemed infeasible and eliminated from the solution process. For comparison purposes with the optimum relocation programs, Table 8-5 presents the TDZ maximum fatigue damage, the stress utilisation, the top effective tension and the TDZ compression for the no-

relocation case. For this case, the vessel is kept in the nominal station over the design period, T_D.

Table 8-4. Vessel relocation patterns

Number of station (p)	**Vessel relocation patterns (m)**																	
3								2	1	3								
5							3	2	1	4	5							
7						4	3	2	1	5	6	7						
9					5	4	3	2	1	6	7	8	9					
11				6	5	4	3	2	1	7	8	9	10	11				
13			7	6	5	4	3	2	1	8	9	10	11	12	13			
15		8	7	6	5	4	3	2	1	9	10	11	12	13	14	15		
17	9	8	7	6	5	4	3	2	1	10	11	12	13	14	15	16	17	
19	10	9	8	7	6	5	4	3	2	1	11	12	13	14	15	16	17	18	19

Station ID

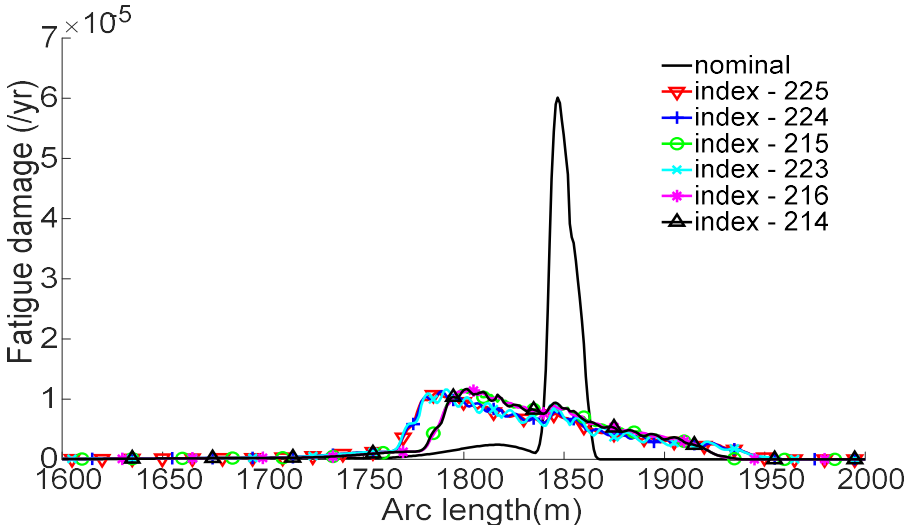

Figure 8-7. The layout of the vessel relocation axes for this study.

Table 8-5. Fatigue damage and storm responses of SCR for the no-relocation case.

S/N	Index	$[p, R, \alpha]$ [(-), (%), (deg)]	D_{eff} (/year)	Damage reduction (%)	U	T_{top} (kN)	min T_{TDZ} (kN)
0	NA	[NA, NA, NA]	6.0134E-05	NA	0.792	1532.3	12.40

Table 8-6. The first 35 members of the optimum relocation programs (design points).

S/N	Index	$[p, R, \alpha]$ [(-), (%), (deg)]	D_{eff} (/year)	Damage reduction (%)	U_{TDZ}	T_{top} (kN)	min T_{TDZ} (kN)
1	225	[19, 5, 30]	1.1148E-05	81.46	0.84	1677.74	6.15
2	224	[17, 5, 30]	1.1306E-05	81.20	0.84	1677.74	6.15
3	215	[17, 4, 30]	1.1611E-05	80.69	0.82	1645.62	7.38
4	223	[15, 5, 30]	1.1618E-05	80.68	0.84	1677.74	6.15
5	216	[19, 4, 30]	1.1619E-05	80.68	0.82	1645.62	7.38
6	214	[15, 4, 30]	1.1683E-05	80.57	0.82	1645.62	7.38
7	36	[19, 4, 0]	1.1805E-05	80.37	0.83	1664.32	6.65
8	234	[19, 6, 30]	1.1897E-05	80.22	0.84	1711.68	5.02
9	222	[13, 5, 30]	1.1945E-05	80.14	0.84	1677.74	6.15
10	35	[17, 4, 0]	1.1947E-05	80.13	0.83	1664.32	6.65
11	213	[13, 4, 30]	1.1977E-05	80.08	0.82	1645.62	7.38
12	34	[15, 4, 0]	1.2148E-05	79.80	0.83	1664.32	6.65
13	45	[19, 5, 0]	1.2305E-05	79.54	0.84	1702.33	5.35
14	44	[17, 5,0]	1.2332E-05	79.49	0.84	1702.33	5.35
15	221	[11, 5, 30]	1.2395E-05	79.39	0.84	1677.74	6.15
16	232	[15, 6, 30]	1.2468E-05	79.27	0.84	1711.68	5.02
17	233	[17, 6, 30]	1.2584E-05	79.07	0.84	1711.68	5.02
18	33	[13, 4, 0]	1.2587E-05	79.07	0.83	1664.32	6.65
19	43	[15, 5, 0]	1.2633E-05	78.99	0.84	1702.33	5.35
20	25	[15, 3, 0]	1.2669E-05	78.93	0.82	1628.42	8.01
21	27	[19,3,0]	1.2671E-05	78.93	0.82	1628.42	8.01
22	212	[11, 4, 30]	1.2743E-05	78.81	0.82	1645.62	7.38
23	243	[19, 7, 30]	1.2751E-05	78.80	0.85	1747.49	4.01
24	26	[17, 3, 0]	1.2755E-05	78.79	0.82	1628.42	8.01
25	441	[19, 9, 0]	1.2834E-05	78.66	0.83	1693.05	6.52
26	24	[13, 3, 0]	1.2861E-05	78.61	0.82	1628.42	8.01
27	54	[19, 6, 0]	1.2864E-05	78.61	0.85	1742.42	4.16
28	431	[17, 8, 0]	1.2971E-05	78.43	0.83	1672.23	6.98
29	432	[19, 8, 0]	1.2979E-05	78.42	0.83	1672.23	6.98
30	242	[17, 7, 30]	1.3034E-05	78.33	0.85	1747.49	4.01
31	231	[13, 6, 30]	1.3042E-05	78.31	0.84	1711.68	5.02
32	422	[17, 7, 0]	1.3083E-05	78.24	0.82	1651.90	7.50
33	421	[15, 7, 0]	1.3115E-05	78.19	0.82	1651.90	7.50
34	32	[11, 4, 0]	1.3120E-05	78.18	0.83	1664.32	6.65
35	211	[9, 4, 30]	1.3163E-05	78.11	0.82	1645.62	7.38

The first 35 members of the feasible optimum relocation programs are presented in

Table 8-6 in their order of performance in terms of D_{eff}. The following are data columns reported in the table.

- The index representation of the optimum family members.
- The sets of optimum input design variables (p, R, α) for the optimum design points.
- The effective fatigue damage $\left(D_{eff}\right)$ in the active SCR TDZ, which is the objective function for the problem.
- The percentage reduction in D_{eff} in the SCR TDZ compared with the no vessel relocation case.
- The maximum stress utilisation (U_{TDZ}) in the active SCR TDZ. This is a constraint function on the optimisation problem, which must be less than 1 (see equation (8-17)).
- The maximum top tension (T_{top}) around the SCR hang off region. This is a constraint function whose value must be less than 90% of the yield tension of the riser pipe (see equation (8-17)).
- The compression in the active SCR TDZ measured as the minimum effective tension (T_{TDZ}). This is a constraint function on the optimisation problem, which must be positive, i.e., greater than 0 (see equation (8-17)). For values less than zero, the riser TDZ is said to be in compression, which is unacceptable during the solution process.

A comparison of the fatigue damage response of the first six optimum relocation programs (index-225, 224, 215, 223, 216, 214) with the no-vessel relocation case is presented in Table 8-5 It could be observed for these optimum relocation programs that the D_{eff} are at least 78% lower than the fatigue damage for the no vessel relocation case. This significant reduction is attributed to the effective spreading of the SCR TDZ fatigue hotspot region over a longer riser TDZ section. The redistribution or spreading of the fatigue damage can be seen for each relocation program in Figure 8-7 compared with the no-relocation case where the fatigue damage is concentrated over a shorter section of the TDZ. It can also be seen that the relocation programs are more effective in reducing the fatigue damage towards the riser anchor rather

than towards the riser hang off. The higher reduction in fatigue damage towards the anchor side is caused by the vessel relocation in stations at the riser far side, which causes higher variation in the active TDZ section than vessel relocations on the riser near side. This SCR TDZ hotspot region variation difference is also demonstrated in Figure 8-7. From the analysis result in

Table 8-6, it is observed that the best relocation program (index-225) is not necessarily along the riser plane axis ($\alpha = 0$deg) as is generally expected, but along the ($\alpha = 30$deg) axis. However, a relocation program along the riser plane axis (index-36) also provided a significant improvement in the fatigue damage response. It appeared as the seventh-best relocation program with 80.37% fatigue damage reduction. Index-225 and index-36 are similar in terms of the number of station (p =19) but different in terms of the span radius ($R = 5\%$ and 4% respectively), and relocation axis ($\alpha = 0$deg and 30deg respectively). To compare the relocation programs for these different R and α, the D_{eff} range graph maximum is plotted in Figure 8-8 (a) for index 45, index-225 and index-405 ($p = 19, R = 5\%$, $\alpha = 0$deg, 30deg and 60deg respectively), and index-36, index-216 and index-396 ($p = 19, R = 4\%, \alpha = 0$deg, 30deg and 60deg respectively). The maximum values of the D_{eff} are presented in Figure 8-8 (b). Here, the D_{eff} along the 30deg axis for $R = 4\%$ and $R = 5\%$ are lower than D_{eff} along 0deg.

To explore why the relocation program along other axes could have higher performance than relocation along the SCR plane axis, a three-station vessel relocation program is considered, with 5% vessel offset from the mean station. Instead of the three-axis (0deg, 30deg and 60deg) considered during the optimisation solution process, we conduct the vessel relocation analysis along 180 directions ranging from 2deg to 358deg at 2deg interval. The maximum fatigue damage around the SCR TDZ at each station (apart from the mean station) along each relocation axis follows the behaviour presented in Figure 8-9(a). The figure shows that the most significant fatigue damage is experienced when the vessel is relocated towards the SCR TDZ (near-near offset, 180deg), causing higher fluctuating bending stress response and more significant TDZ fatigue damage. However, when the vessel is relocated in the direct opposite direction (far-far offset, 0deg), the fatigue damage is minimum, resulting from the stretching and associated reduced fluctuating bending stress around the TDZ. Since the relocation station in both directions of any axis plus the nominal station makes up the number of station ($p = 3$)

along that axis, the effective damage, D_{eff}, will be a sum of the stations' fatigue damages factored by their damage fractions. Similar consideration can be made for all axes consisting of vessel offset in both directions, as shown in Figure 8-9(b). It is evident from Figure 8-9(b) that there will be some axes of relocation that provide reduced D_{eff} than the axis coinciding with the riser plane (α = 0deg/180deg). This indicates that the optimum relocation program may not be along the riser plane. Extending the same for the optimum case in this study (index-225, see **Table 8-6** with a higher number of stations (p =19), similar findings are applicable

(a)

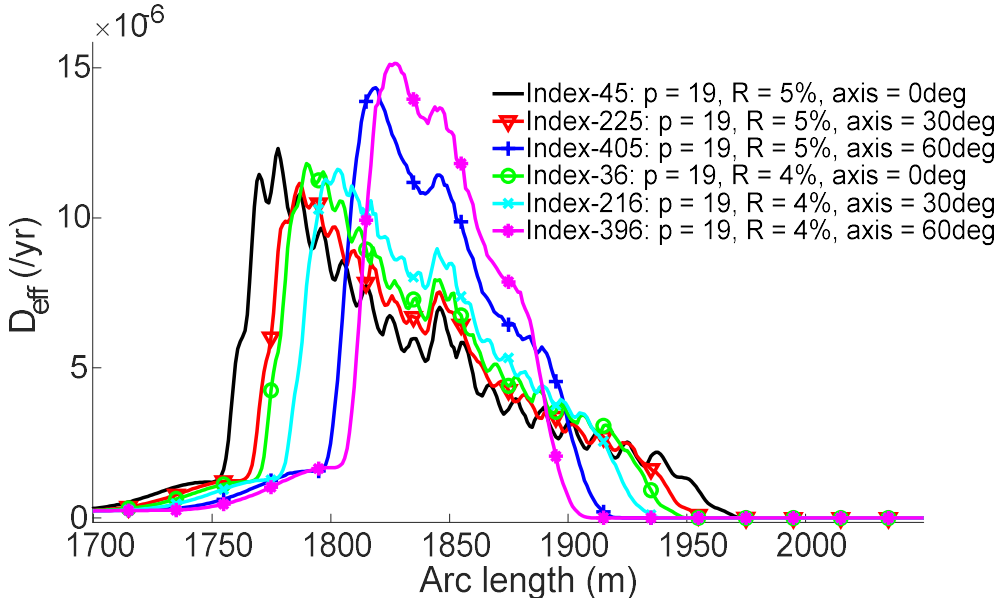

(b)

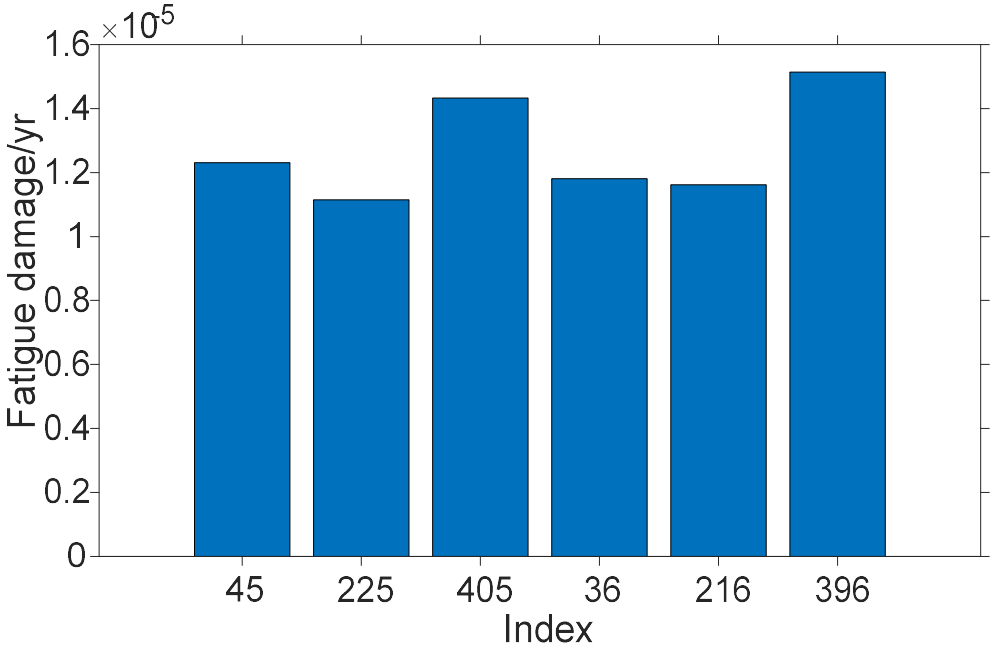

Figure 8-8. (a) D_{eff} range graph maximum for relocation program along the three axes for ($p = 19, R = 5\%, R = 4\%$), (b) Maximum D_{eff} for relocation program along the three axes for ($p = 19, R = 5\%, R = 4\%$),

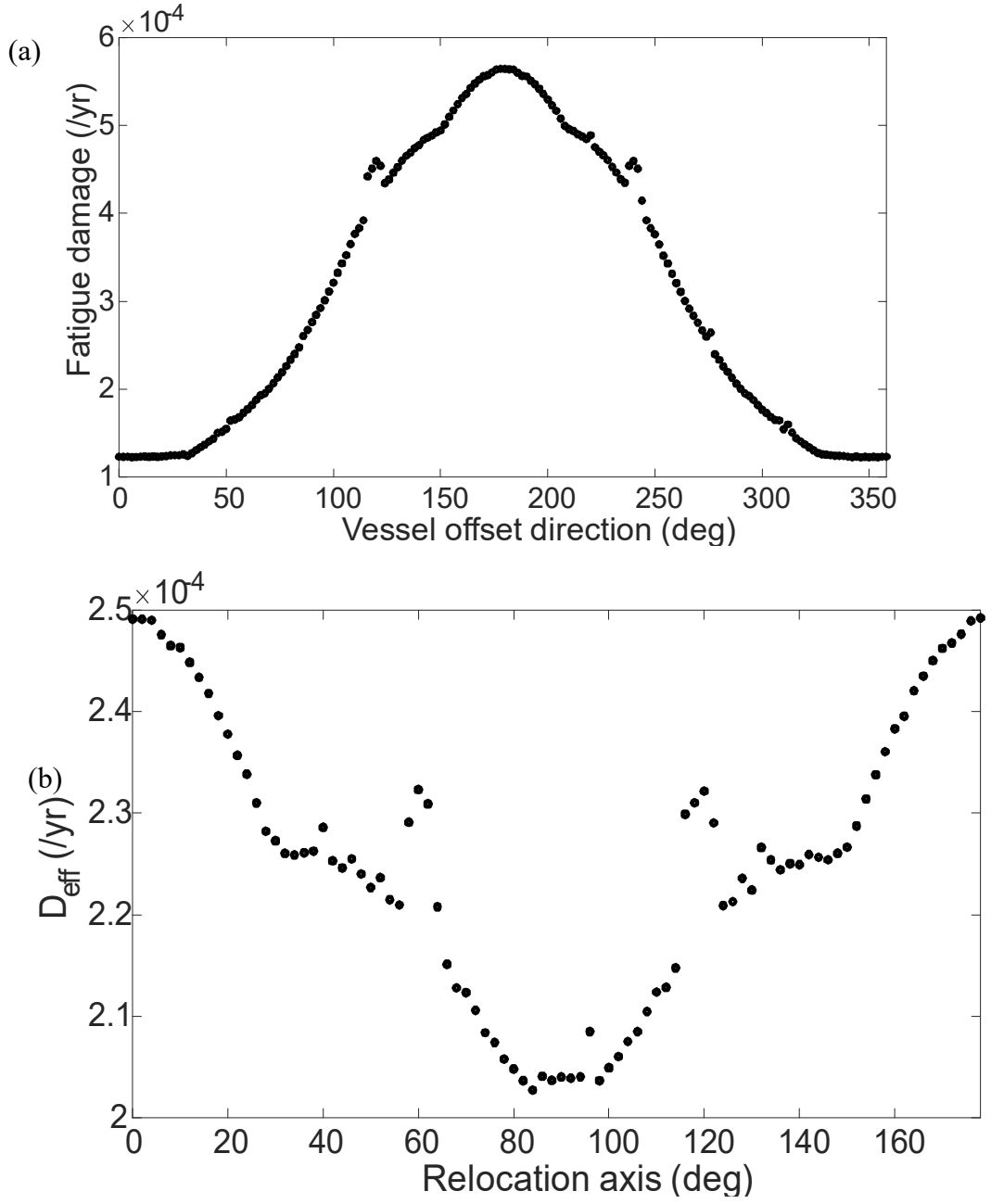

Figure 8-9. Maximum SCR TDZ fatigue damage response for 3-station relocation program ($\boldsymbol{p = 3}$) with vessel offset of 5% (from nominal station) in all direction, (b) Resulting maximum effective fatigue damage for the 3-station relocation program ($\boldsymbol{p = 3}$) with vessel 5% along all axes.

Revisiting

Table 8-6 it can also be observed that the improvement in fatigue damage response increases with increasing p. For a given p, the fatigue exposure time over the design life (T_D) does not (in general) change with respect to α and R. However, α and R affect the configuration of the SCR, which in turn influence the configuration of the fatigue hotspots and a consequential impact on the fatigue damage. Larger R will result in higher TDZ fluctuating bending moments for stations in the riser near directions, causing more significant fatigue damage. It can be observed from

Table 8-6 that the first 22 best relocation programs are limited to about $R = 6\%$ of the water depth. Relocation programs with higher values of R such as index-243 ($R = 7\%$ of water depth) and index - 441 ($R = 9\%$ of water depth) perform less than the best six relocation programs. However, it is noted that their performances are still significantly higher than those of the SCR for the no-relocation case. For even higher values of R, the fatigue performances for the corresponding relocation programs decreases and are located down the performance list or removed from the solution process for violation of the constraint functions (especially the U_{TDZ} and T_{TDZ}).

8.1.4.2 Constraint function responses

The index matching technique retains the relocation programs which satisfy the constraint function, as seen in the constraint function columns in

Table 8-6. All the values of the three-constraint functions (U_{TDZ}, T_{top} and T_{TDZ}) for the optimum relocation programs are within the constraint's limits (see equation (8-17)). The order of performance of the SCR response to the design storm wave condition does not necessarily have to be in the order of fatigue performance if the constraint inequalities are satisfied. Updating any of the constraint limits in equation (8-17) will result in new sets of optimum relocation programs. For example, if it should be considered that the SCR TDZ minimum tension (compression) must be greater than 8kN, then the best relocation program becomes index-25, while others before and after it that do not satisfy this new constraint are eliminated.

This indicates how sensitive the relocation program is to the constraint functions imposed by the SCR storm responses and the designer's choice. The index matching technique can capture these changes when constraint functions are updated without the need to rerun the simulations.

The range graph maximum of the stress utilisation (U_{TDZ}) for the first six best relocation programs from

Table 8-6 and that of the no-relocation case are presented in Figure 8-10. Note that these response profiles connect the nodal maximum across the stations ($m = 1$ to p) for each relocation program, with an observable spread of higher U_{TDZ} over longer section of the SCR TDZ. However, for the no-relocation case, the riser range graph is maximum within short sections of the TDZ since the SCR remains in the nominal station (station-1) all through its design life. It is observed from Figure 8-10 for the six optimum programs that the stress utilisation resulting from the combined load can be higher than that of the no-relocation case, especially in the TDZ section towards the vessel. Higher U_{TDZ} occur during vessel positions in stations on the near side of the riser, as these impose higher bending stress around the TDZ, hence higher U_{TDZ} than that of the no-relocation case. Index-215, 216 and 214 relocation programs with $R = 4\%$ have equal U_{TDZ} although they have different p. Similarly, equal U_{TDZ} is observed for index-225, 224 and 223 relocation programs with $R = 5\%$. As expected, U_{TDZ} increases with increasing R as the vessel is relocated towards the SCR anchor as observed with relocation programs with $R = 5\%$ compared with relocation programs with $R = 4\%$.

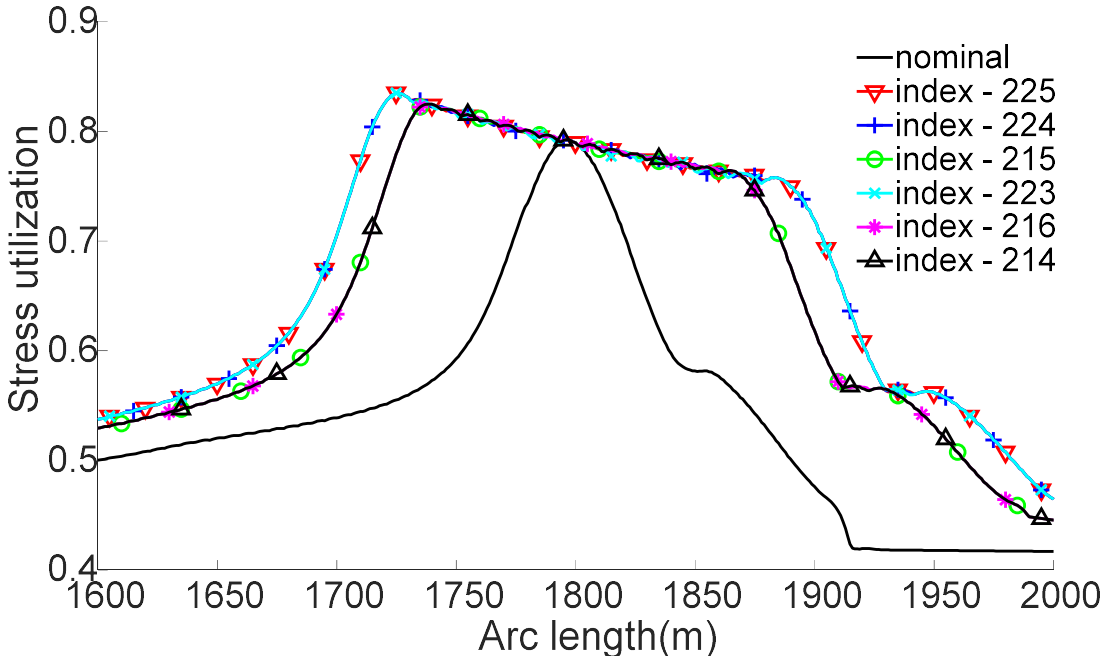

Figure 8-10. Maximum stress utilisation in the active SCR TDZ across the stations for the best 6 relocation programs.

The range graph maximum of the second constraint function (T_{top}) for the first six best relocation programs from

Table 8-6 and that of the no-relocation case is presented in Figure 8-11. Again, it should be noted that these values are the maximum across the relocation stations contained in each of the relocation programs, except that of the no-relocation case where the riser remains in nominal position throughout the design life. All the six best relocation programs give maximum tension around SCR hang off that is higher than that of the no-relocation case but are, however, below 90% of the yield tension (see equation (8-17)). Higher top tension than the no-relocation case occurs when the vessel is in stations on the far side of the SCR. This results in a more extended hanging riser section and a consequent increased in top tension. Index-215, 216 and 214 relocation programs have equal maximum top tension as should be expected since their span radii ($R = 4\%$) are equal, although they contain different stations (p), which are 17 19, 15, respectively. Similar behavior is seen for the top tension of index-225, 224 and 223 relocation programs, where they possess the same R value of 5%. The relocation programs with R = 5% are expected to have higher top tension than those with $R = 4\%$ as observed from Figure 8-11.

This is because farther vessel position from the nominal station in the riser far direction causes a longer hanging riser section resulting in higher top tension.

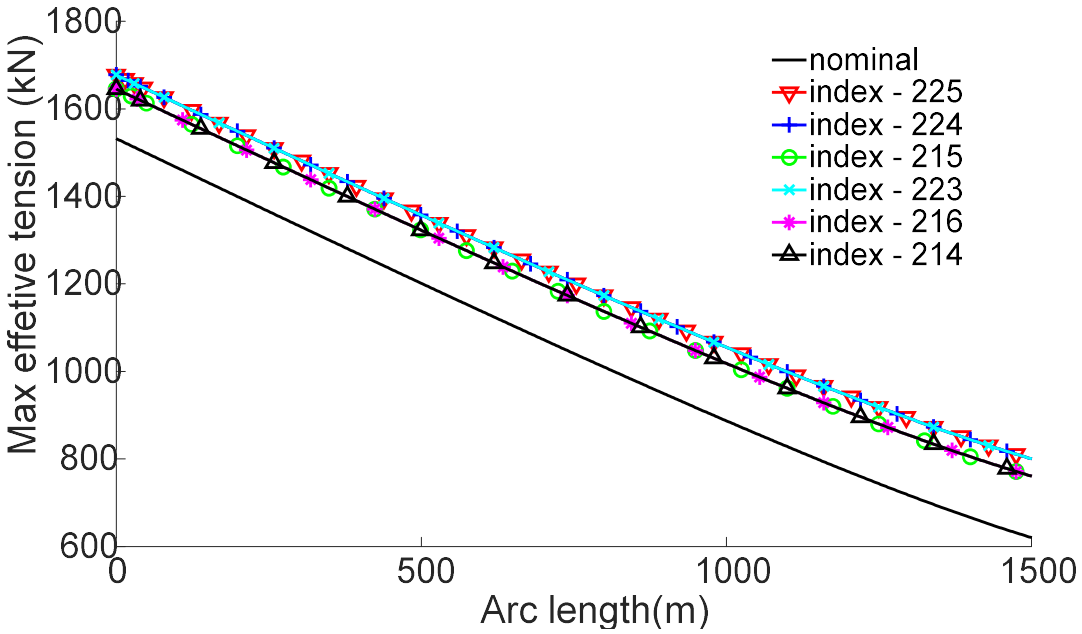

Figure 8-11. Maximum effective tension in the SCR hang-off region across the relocation stations for the best 6 relocation program.

The range graph minimum of the third constraint function (T_{TDZ}) for the first six best relocation programs from

Table 8-6 and that of the no-relocation case are presented in Figure 8-12. Like the SCR TDZ stress utilisation, we expect higher compression in the active TDZ for these six relocation programs when compared with the no-relocation case. This is because the SCR experiences higher compression around the TDZ when the vessel occupies stations on the nearside of the riser. The TDZ compression response for index-215, 216 and 214 relocation programs have a common span radius, $R = 4\,\%$, and hence same TDZ compression responses. A similar behaviour is observed for index-225, 224 and 223 relocation programs with $R = 5\%$. For the same reason given for U_{TDZ}, considering equal number of stations p, the compression for relocation programs with $R = 5\%$ will be (slightly) higher than those with $R = 4\%$ as can be seen from

Table 8-6 and Figure 8-12.

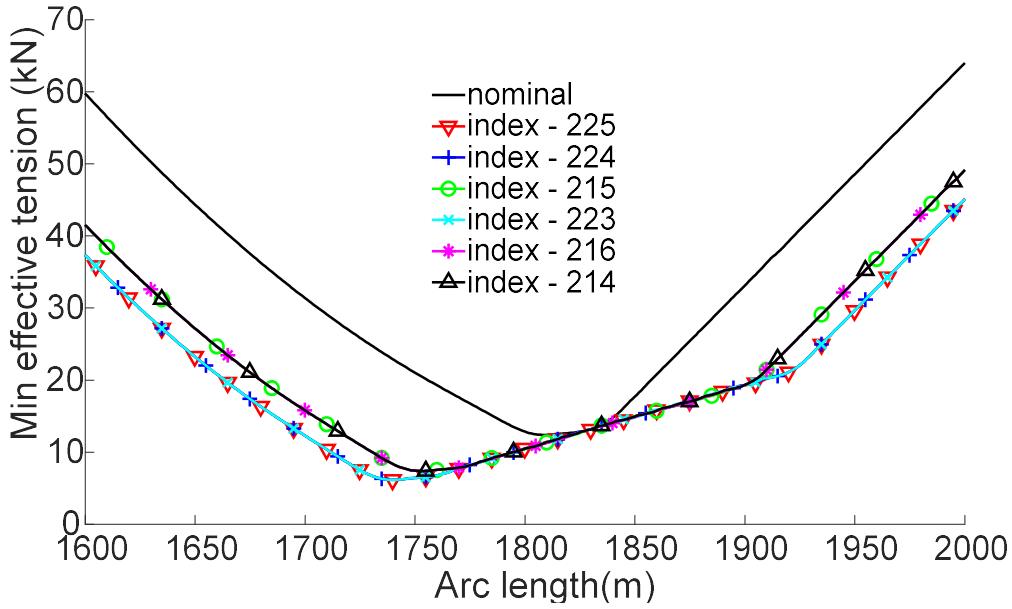

Figure 8-12. Maximum compression (minimum effective tension) in the active SCR TDZ across the stations in the best 6 relocation programs.

8.1.4.3 A detailed discussion of the Index-225 relocation program.

The index-225 represents the best relocation program for the vessel relocation optimisation analyses in this section. A detailed consideration of this first and best optimum program (the first row in

Table 8-6 shows that there are $p = 19$ equally spaced stations, with relocations limited to a span radius, $R = 5\%$ of the water depth in both the far and the near direction of the SCR. This means that to satisfy the constraint functions and obtain minimum fatigue damage, the vessel movement is limited within 75m (5% ×1500m), each in the far and the near direction along the axis, $\alpha = 30$deg. This gives a relocation span ($L = 2R$) of 150m. The relocation offset (Δh), i.e., the distance between two neighbouring stations is 8.33m, obtained using equation (8-18) and the number of times (n) that the vessel is relocated over the SCR design life T_D, is 36 times, obtained using equation (8-2). For the p =19 stations in this relocation program, the cumulative exposure time over the SCR design life (T_D =30yrs.) at each station will follow the pattern depicted by the damage fraction (f_m) presented in Figure 8-13. It should be recalled that the exposure time is T_D factored by f_m, where the f_m at each of the stations ($m = 1\ to\ p$) are calculated from equation (8-10). The exposure times at each of the 19 stations are presented in Table 8-7. The unfactored fatigue damage responses of the active SCR TDZ at each of the

19 stations are shown in Figure 8-14, and the corresponding constraint function responses $(U_{TDZ}, T_{top}, T_{TDZ})$ at each of the 19 stations are presented in Figure 8-15, Figure 8-16 and Figure 8-17, respectively.

Table 8-7. Fatigue damage fraction (f_m) and exposure time (T_{rm}) for the 19 stations of the index-225 relocation program over the SCR design life (T_D) of 30yrs.

Station ID $(\boldsymbol{m} =)$	**Station Description**	**Damage fraction**	**Exposure Time (yrs.)**
1	Nominal	0.081	2.43
10	Span limit1	0.027	0.81
19	Span limit2	0.027	0.81
Others	$(p-3)$ stations	0.054	1.62

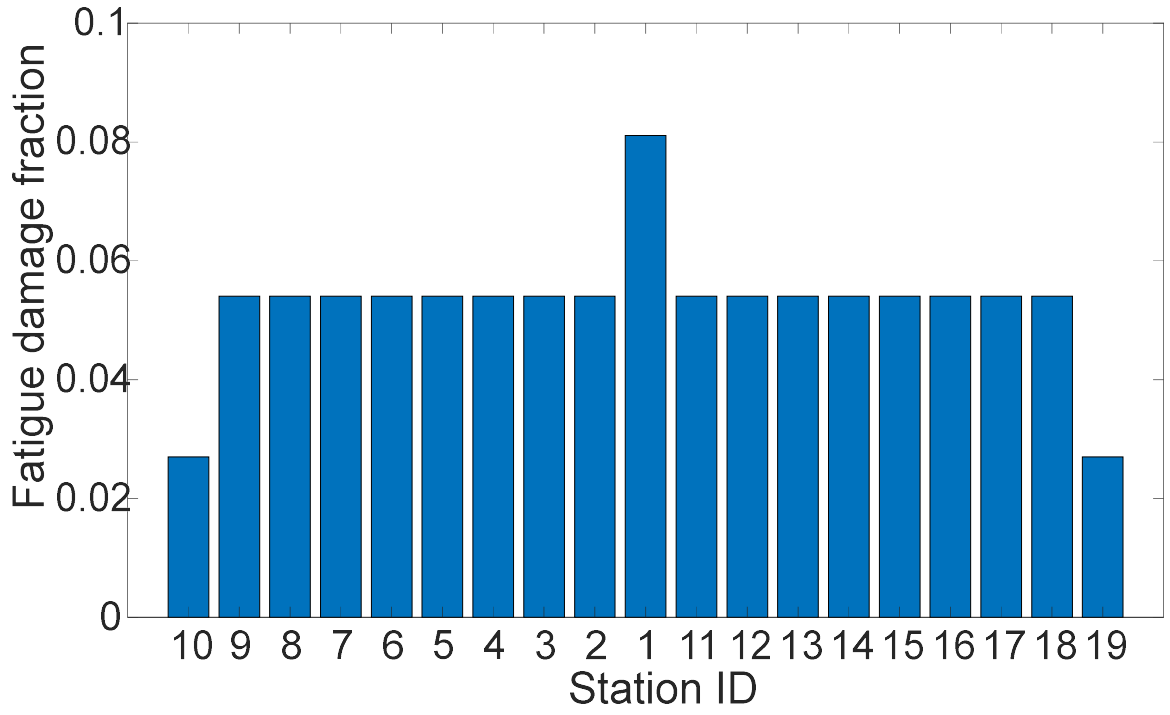

Figure 8-13. Fatigue damage fraction for the 19 relocation stations in the index-225 vessel relocation program.

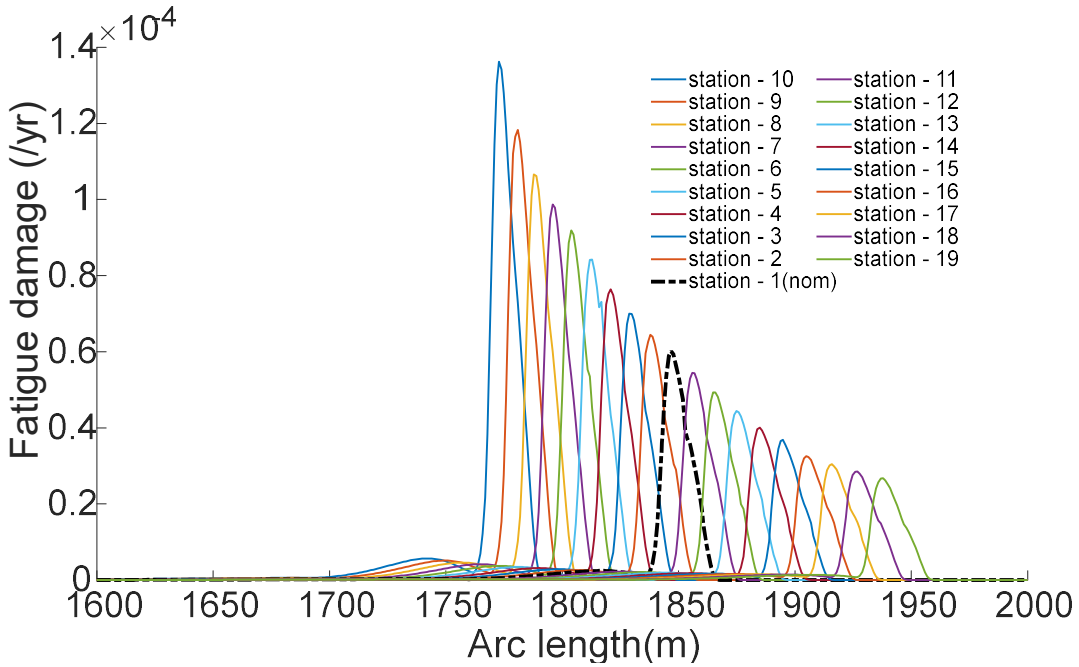

Figure 8-14. SCR TDZ fatigue damage at the 19 stations for index-225 relocation program: $p = 19, \alpha = 30^o, R = 5\%$

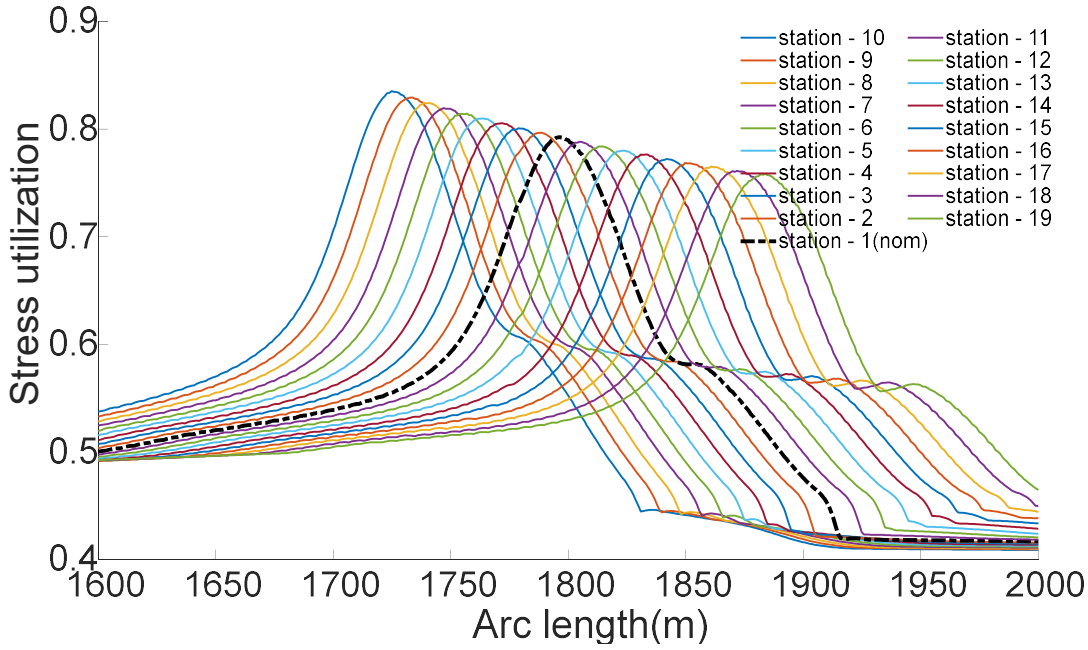

Figure 8-15. SCR TDZ stress utilisation at the 19 stations for index-225 relocation program: $p = 19, \alpha = 30^o, R = 5\%$

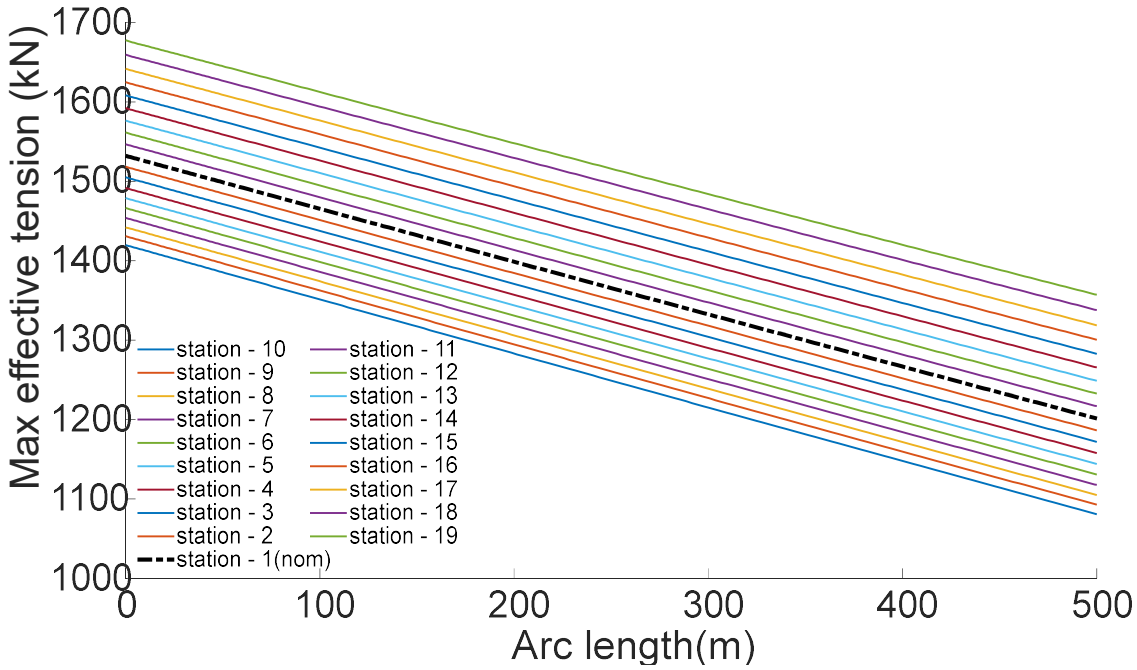

Figure 8-16. SCR maximum top tension at the 19 stations for index-225 relocation program: $p = 19, \alpha = 30^o, R = 5\%$

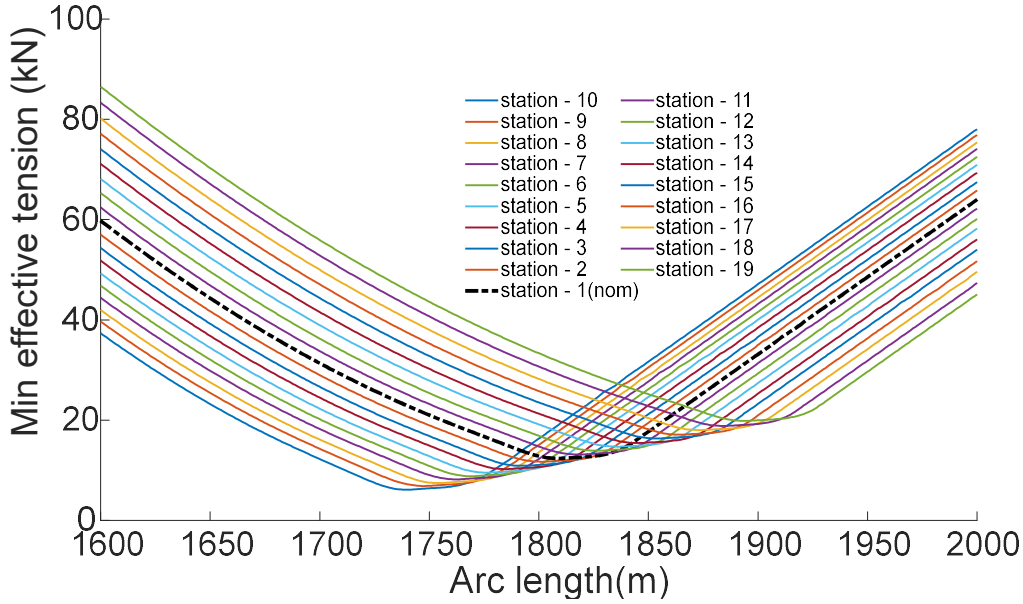

Figure 8-17. SCR TDZ compression (min. effective tension) at the 19 stations for index-225 relocation program: $p = 19, \alpha = 30^o R = 5\%$

It could be seen from Figure 8-14 that the highest of the maximum fatigue damage occur at station-10, which is the span limit station on the SCR near side (towards seabed anchor). The vessel position in station-10 causes significant global compression and higher fluctuating

bending moments in the SCR TDZ compared with configurations at other relocation stations. This result in a higher fatigue damage response, as seen in Figure 8-14. The reverse is the case for station-19, where the SCR global configuration is stretched, and less fluctuating bending occurs at the TDZ resulting in minimum fatigue damage compared with other stations. The vessel in station-1 (nominal station) imposes fatigue damage of magnitude between the above extreme configuration conditions.

The effectiveness of any vessel relocation program is measured by its ability to level out the peakedness of the fatigue damage response in the active SCR TDZ, i.e., the capacity to impose a wider spread of the fatigue hotspot region. It could be seen from Figure 8-14 that the fatigue damage is concentrated within short regions of the SCR TDZ with the vessel in each of the 19 stations. Table 8 presents the maximum fatigue damage responses and the arc length where they occur within the active SCR TDZ for the 19 stations in the index-225 relocation program. The leading diagonal terms are the maximum fatigue damage at the respective 19 stations, with the corresponding critical arc lengths in the first column of the table. The off-diagonal terms are the associated damages occurring at other stations' critical arc lengths. For example, the critical damage arc length when the vessel is at station-1 is 1846.8m, and the critical damage arc length when the vessel is at station-19 is 1937.8m. When the vessel is at station-1, the fatigue damage at arc length 1937.8m is about 60000 times smaller than the fatigue damage at arclength 1846.8m. On the other hand, at station-19, the fatigue damage at arc length 1846.8m is about 115 times smaller than the fatigue damage at arclength 1937.8m. The maximum fatigue damage when the vessel is at stations 1 and 19, with the associated fatigue damage occurring at other stations' critical arc lengths, are presented in Figure 8-18 and Figure 8-19, respectively.

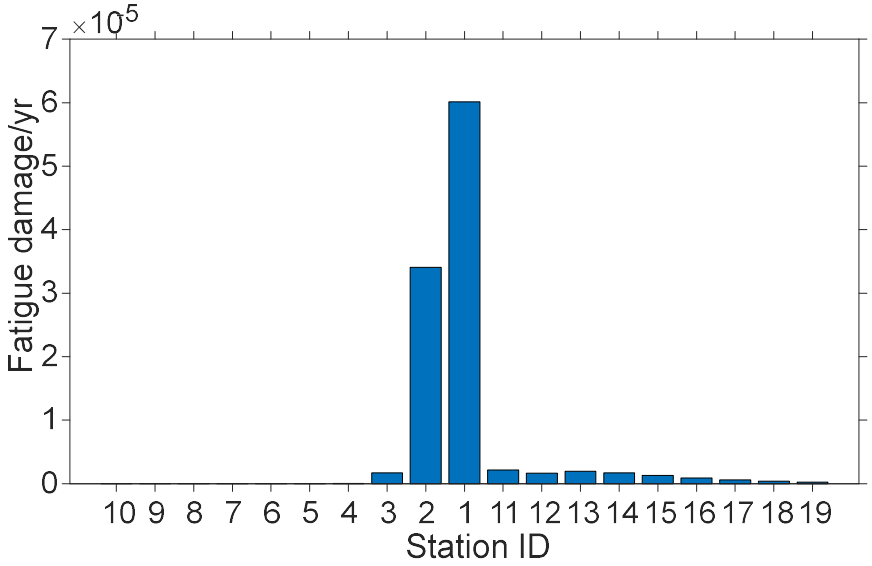

Figure 8-18. Fatigue damage at station-1 with the associated fatigue damage at other stations' critical arc lengths

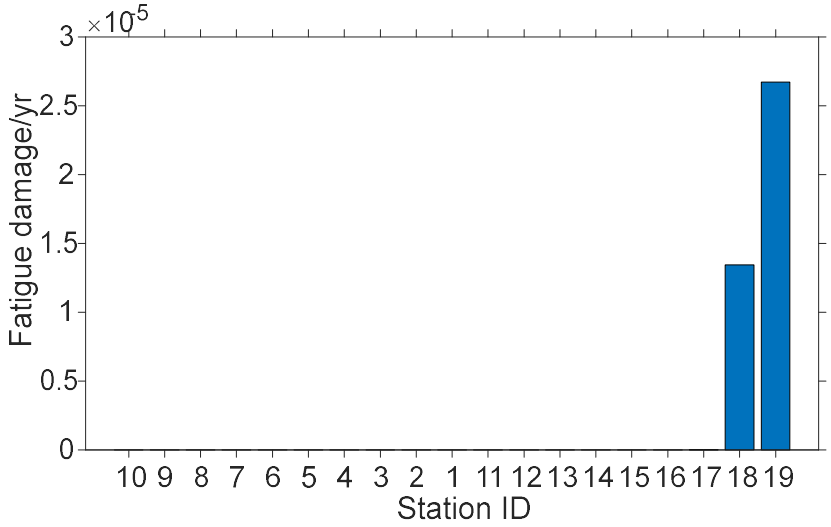

Figure 8-19. Fatigue damage at station-19 with the associated fatigue damage at other stations' critical arc lengths

Relocation stations

Arc lengths (m)	10	9	8	7	6	5	4	3	2	1	11	12	13	14	15	16	17	18	19
1772.846	136.173	8.788	2.411	3.650	3.757	3.106	2.187	1.425	0.867	0.505	0.279	0.186	0.178	0.173	0.178	0.182	0.182	0.181	0.190
1780.846	72.864	118.278	10.178	2.154	3.302	3.436	2.805	1.991	1.287	0.791	0.458	0.256	0.167	0.162	0.170	0.175	0.180	0.179	0.187
1787.846	11.376	68.971	106.601	5.633	2.239	3.199	3.145	2.474	1.717	1.116	0.680	0.396	0.214	0.152	0.159	0.168	0.174	0.175	0.182
1795.846	0.012	8.158	59.995	98.685	5.331	2.078	2.945	2.834	2.216	1.554	1.006	0.615	0.351	0.195	0.145	0.158	0.165	0.168	0.174
1803.846	0.014	0.012	6.495	53.551	91.839	4.609	2.006	2.731	2.597	2.002	1.398	0.904	0.547	0.318	0.177	0.144	0.153	0.160	0.164
1812.846	0.006	0.010	0.012	2.574	45.209	84.236	6.230	1.823	2.516	2.378	1.854	1.294	0.843	0.519	0.305	0.171	0.138	0.146	0.152
1820.846	0.006	0.005	0.008	0.011	2.865	43.398	76.413	4.318	1.805	2.353	2.169	1.675	1.160	0.758	0.465	0.272	0.160	0.132	0.141
1828.846	0.003	0.006	0.005	0.006	0.009	3.600	42.310	70.013	2.645	1.793	2.218	1.989	1.510	1.043	0.678	0.413	0.253	0.147	0.128
1837.846	0.001	0.002	0.004	0.006	0.005	0.008	2.316	37.423	64.420	2.550	1.693	2.067	1.838	1.391	0.967	0.627	0.400	0.242	0.144
1846.846	0.001	0.001	0.001	0.002	0.004	0.004	0.006	1.700	34.059	60.134	2.156	1.628	1.924	1.696	1.286	0.894	0.595	0.376	0.232
1855.846	0.001	0.001	0.001	0.002	0.002	0.003	0.003	0.005	1.530	32.987	54.477	1.652	1.573	1.828	1.569	1.198	0.835	0.552	0.354
1865.846	0.001	0.001	0.001	0.001	0.001	0.002	0.003	0.003	0.004	0.520	27.936	49.346	1.863	1.465	1.710	1.492	1.128	0.799	0.537
1874.846	0.000	0.001	0.001	0.001	0.001	0.002	0.002	0.003	0.003	0.004	0.828	26.623	44.468	1.054	1.462	1.607	1.374	1.049	0.742
1884.846	0.000	0.001	0.001	0.001	0.001	0.001	0.002	0.002	0.003	0.003	0.005	0.446	23.188	40.037	0.978	1.383	1.537	1.311	0.995
1894.846	0.000	0.000	0.001	0.001	0.001	0.001	0.001	0.002	0.002	0.003	0.004	0.006	0.308	20.706	36.886	0.851	1.349	1.465	1.239
1904.846	0.000	0.000	0.000	0.001	0.001	0.001	0.001	0.002	0.002	0.002	0.003	0.005	0.009	0.259	18.600	32.565	0.792	1.311	1.394
1915.846	0.000	0.000	0.000	0.001	0.001	0.001	0.001	0.001	0.002	0.002	0.003	0.004	0.005	0.012	0.083	16.569	30.461	0.762	1.268
1926.846	0.000	0.000	0.000	0.000	0.001	0.001	0.001	0.001	0.001	0.002	0.002	0.003	0.004	0.006	0.014	0.039	15.141	28.534	0.756
1937.846	0.000	0.000	0.000	0.000	0.000	0.001	0.001	0.001	0.001	0.001	0.002	0.003	0.003	0.005	0.007	0.017	0.027	13.443	26.728

Fatigue damage/yr ($\times 10^{-5}$) in SCR TDZ

Figure 8-20. Fatigue damage in SCR TDZ at the 19 relocation stations for index - 225 relocation program: Shaded diagonal terms are the maximum damage, and the corresponding arc length is the point the maximum damage occurs; The off-diagonal terms are the associated damage at other arc lengths where the critical damages occur for other relocation stations.

For the vessel positioned in any of these stations, it could be seen that the associated fatigue damage occurring at other stations' critical arclength are quite negligible except for the immediate neighbouring station's critical arc length. This is the general behaviour of the fatigue damage responses considering other stations in any given relocation program. The effective fatigue damage (D_{eff}) is obtained by summing the SCR fatigue damage at each station (D_m) factored by the corresponding fatigue damage fraction (f_m) across all stations as presented in equation (8-12). For the index-225 relocation program, the D_{eff} range graph maximum has already been presented in Figure 8-7. Figure 8-7, it could be observed for the index-225 relocation program that the arc length where the maximum D_{eff} occur is 1786.8m, which never appear as a critical arc length for any of the 19 stations in Figure 8-20. However, this arch length is very close to 1787.85m, which is the SCR TDZ critical fatigue damage arc length when the vessel is at station-8. It should be noted that this arclength is not the point that experienced the maximum fatigue damage across the stations. The maximum fatigue damage occurred at arclength 1772.8m when the vessel was at station-10 (see Figure 8-20 and Figure 8-14). It is therefore evident that the point of maximum D_{eff} for the relocation program is most likely not the point which experienced the highest fatigue damage across the stations. This generally applies to all relocation programs and presents the fatigue damage spreading basis either for a newly designed SCR or an existing SCR (for life extension purpose).

8.1.4.4 Vessel relocation cost

Although no cost objective function was included in the optimisation analysis in this work, it is worth mentioning that the higher the number of relocation station (p), the lower will be the effective fatigue damage (D_{eff}), and the higher will be the number of vessel relocations (n) (see equation (8-2)). The cost of vessel relocation operations will be expected to increase with n over the SCR design life. Hence, the objective function to reduce D_{eff} will be in competition with the cost objective function. A balance can be reached to maximise the benefit of the program in terms of D_{eff} at optimum operation cost.

Table 8-8. Order of performance of relocation programs with varying number of relocation stations, p

Index	Order of Performance*	R (%)	α (deg)	p
No relocation	-	-	-	1
217	311	5	30	3
218	195	5	30	5
219	122	5	30	7
220	43	5	30	9
221	15	5	30	11
222	9	5	30	13
223	4	5	30	15
224	2	5	30	17
225	1	5	30	19

*The order of performance is the relocation program's position (S/N)

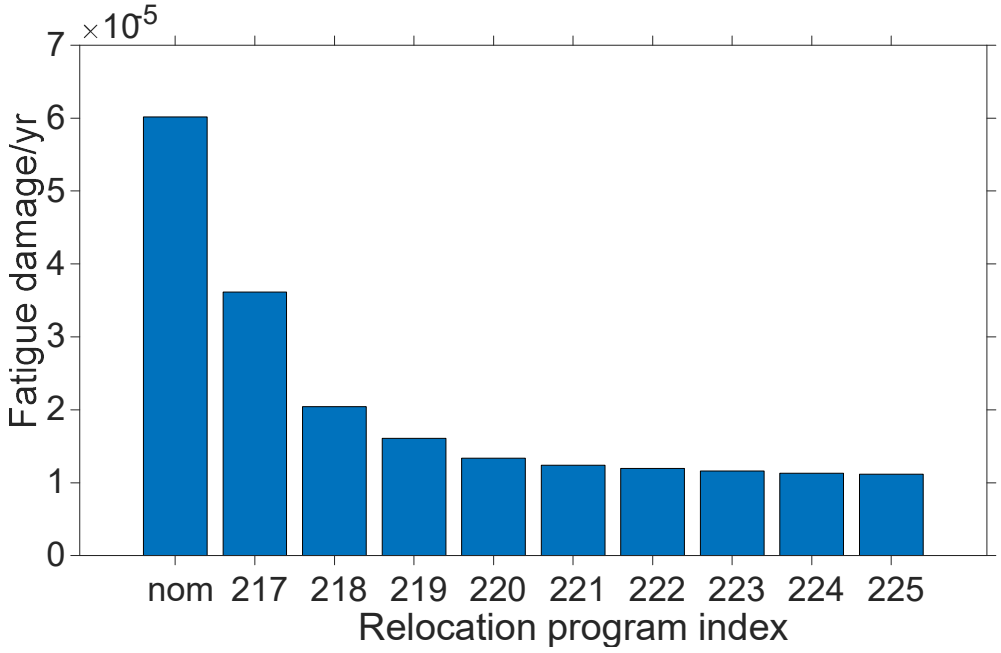

Figure 8-21. Maximum fatigue damage response with an increasing number of relocation station, $\boldsymbol{p}$

The index-225 relocation program, which is the best program in the analysis example in this section, will not be the best if an objective cost function were to be included in the problem. In Table 8-8, we present a group of other feasible relocation programs (index-217, 218, 219, 220,

221, 222, 223, 224) having the same relocation axis (α) and span radius (R) as index-225, but with varying number of stations (p) . The maximum effective fatigue damage in the SCR TDZ for these programs have been presented in Figure 8-21. We can see from Figure 8-21 that the relocation programs with higher p are more effective for fatigue damage reduction than those with lower p. However, it should be noted that the SCR TDZ fatigue performance dropped very quickly with increasing p, as seen in Figure 8-21. The range graph maximum of D_{eff} for these programs are presented in Figure 8-22.

These result plots show that the increasing cost associated with increasing p will not be justified in terms of the fatigue performance when p exceeds certain values. For example, for $p > 9$ (beyond index-220 relocation program), there is no appreciable improvement in the fatigue performance for the programs. Increasing the number of stations, p, beyond 9 will result in increased operating cost, but with no appreciable benefits to fatigue damage reduction in the SCR TDZ. Hence, an optimum relocation program should be selected vis-à-vis the associated vessel relocation operating cost during actual project relocation program design.

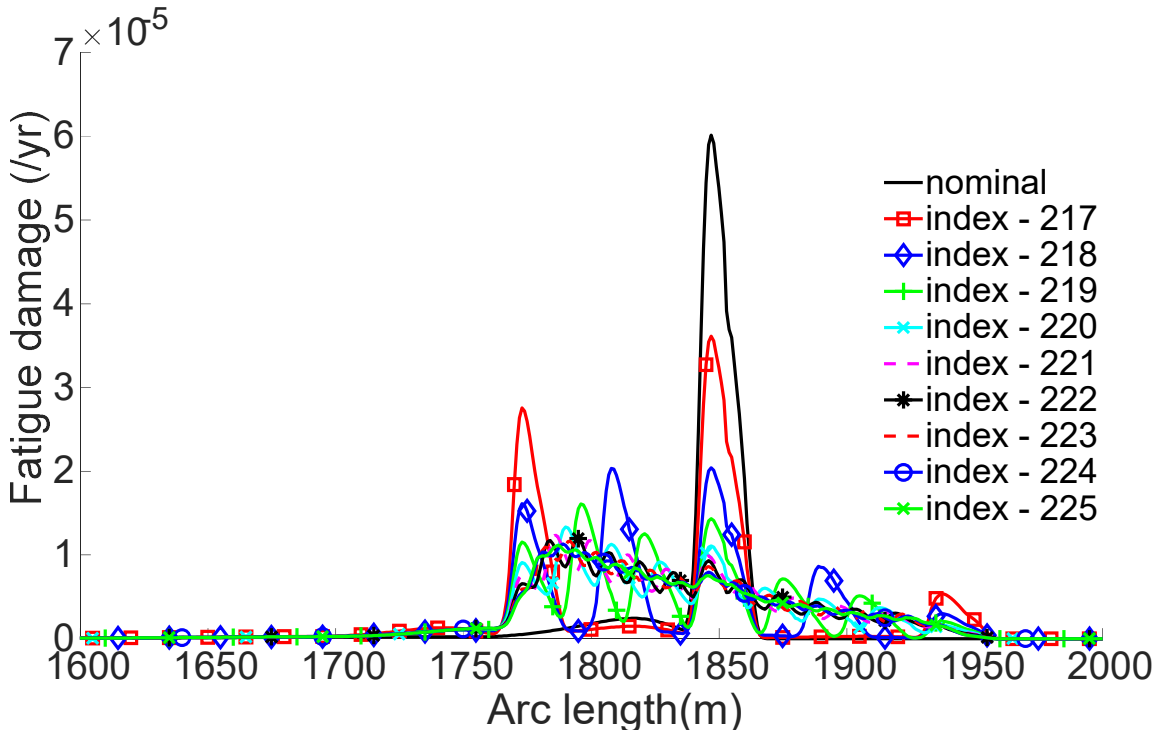

Figure 8-22. Range graph maximum of a family of relocation programs differing only in the number of relocation stations $\boldsymbol{p}$.

8.1.5 Concluding remarks for analysis

The vessel relocation program involves managing, engineering, and operating the riser host floating vessel from one location or station to another. This may be required to enhance the spread of fatigue damage over a longer section of the SCR TDZ, resulting in effective reduction of the fatigue damage when compared with those of the SCRs with the host vessel not relocated. An approach to modelling vessel relocation is developed and presented in this section. The relocation programs are modelled in terms of three optimisation design variables, which are the axis of relocation (α), the span radius of relocation (R) and the number of relocation stations (p). An optimum combination of these variables can be obtained by casting the problem as an optimisation type, where the effective fatigue damage (D_{eff}) is the objective function and the SCR design storm responses (stress utilisation around TDZ (U), top tension (T_{top}) and TDZ compression (T_{TDZ})) serve as the constraint function. In this section, the index matching technique is applied to solve the optimisation problem. The methodology developed here is demonstrated using a single SCR hosted by an FPSO relocated symmetrically about the mean vessel position (nominal station).

- The following can be deduced from the exampled vessel relocation optimisation analyses:
- The resulting SCR TDZ fatigue damage (effective damage, D_{eff}) from any relocation program depend on the exposure time and the configurations of the SCR. The configuration of the SCR is influenced by the combination of the design variables (α, R, p)
- For a given p, the exposure time over the design life of the riser does not change irrespective of the α and the R. However, both α and R affect the configuration of the risers, which in turn impacts the fatigue damage in the active SCR TDZ.
- Increasing R will result in increased variation in the position of the fatigue hotspots in the active SCR TDZ, which will enhance the fatigue damage spreading and reduction in D_{eff}. However, R is significantly limited by the constraint functions, which are the design storm responses of the SCR. Higher R values can cause large compression, stress utilisation and fatigue damage in the SCR TDZ when the vessel is relocated to stations on the extreme near side of the riser.

- The optimum relocation axis (α) may not necessarily be along the SCR plane axis as is generally expected.
- The reduction in the SCR TDZ fatigue damage increases with increasing p. However, the higher the value of p, the higher will be the number of relocations (n) of the vessel over the riser design life, and hence the increased cost of the relocation program. Therefore, a practical p value should be selected with relocation cost consideration.

The analysis result for the single SCR case study shows that an SCR fatigue damage reduction up to 81% can be achieved with the vessel relocation program compared with the case where the vessel is not relocated. This indicates that the vessel relocation technique can provide significant fatigue performance for the SCRs if properly planned through optimisation. This benefit may not easily be achieved from the redesign (modification) of the TDZ section of the SCR. The vessel relocation technique provides ample opportunities to extend the life of the SCRs for brownfields. If considered during greenfield development, it can result in SCRs with reduced wall thickness and a consequent weight reduction. These benefits directly impact the vessel and hang-off structure holding required capacities and the SCR cost. However, the operating cost associated with the vessel relocation program and the cost associated with the SCR TDZ modification need to be compared to inform the final decision on the SCR fatigue improvement options.

Although a single SCR case is used to demonstrate the technique presented in this section, this technique can be extended to multiple SCR of different azimuth, hang-off angle, and pipe geometry. Also in this section, a symmetric vessel relocation about the nominal station along the relocation axes is considered. However, a non-symmetric vessel relocation about the vessel's nominal station will allow candidate relocation programs that are not centered on the nominal FPSO position to be considered. This may provide further improvement of the effective fatigue damage performance. The non-symmetric vessel relocation strategy for multiple SCRs is the subject of discussion in the following section.

8.2 Vessel relocation strategy for multiple SCRs

8.2.1 Background

In previous section, the vessel relocation methodology for a single steel catenary riser (SCR) was developed to extend the fatigue life of the SCR touchdown zone (TDZ). The method was

developed considering symmetrical vessel relocation programs, where the vessel offsets about the nominal station in all directions is equal. However, in actual field applications, the production platform hosts multiple SCRs of different azimuth, cross-section geometry and global configurations. Also, the symmetrical relocation consideration eliminates the potentials of exploring non-symmetrical relocation patterns that may be suitable candidate solutions. These considerations add complexity to the problem since, for example, each of the SCR may have unique optimum relocation programs (ideal solutions), but one global optimum solution is required. In this work, we extend the symmetrical relocation method and apply the index matching technique to solve the multi-objective optimization problem. The non-symmetrical relocation of this methodology for multiple SCRs is demonstrated by comparing the global optimum solutions with those of the no-relocation case. The developed approach can be applied to new and existing SCRs for life extension purposes.

A real scenario involves relocating a floating platform hosting several riser systems, like the vessel-SCR layout in Figure 8-23 (b), causing complex SCR TDZ offsets. To demonstrate this, we monitor the SCR TDP as the vessel is relocated from the nominal station to stations at distances of 7% of the water depth, along the six relocation axes shown in Figure 8-23 (b). The resulting TDPs locations due to the vessel offset are compared with the TDPs when no vessel relocation is applied. The 7% vessel offset selected here is for demonstration purposes. As will be seen in the main analysis part of this study, the vessel offset values are limited or decided by the constraint function defined by the SCR TDZ stress utilisation, compression, and top tension. In this demonstration, the risers have the same cross-section properties and hang off angles (12^{o}) and are hosted by the vessel in a water depth of 1500 m. The numerical analyses in this demonstration and other parts of this study are conducted using the OrcaFlex software, with modelling and post-processing often automated using MATLAB scripts. As a result of the vessel movement, the active seabed sections of the six SCRs will experience different degrees of spatial variation compared to the nominal configuration. The six SCR TDP offsets from their nominal position when the vessel is relocated towards the vessel portside for relocation axes (1,2,3,5,6) and towards the stern (axis 4) are presented in Figure 8-24 (a). Similarly, the six SCR TDP offsets from their nominal position when the vessel is relocated towards the vessel starboard for relocation axes (1,2,3,5,6) and towards the bow (axis 4) are presented in Figure 8-24 (b). For both sets of vessel relocation directions, it is observed that if the axis of relocation relative to a given riser is in the riser far direction, a longer section of the riser will be hanging, meaning the TDP arc length position will be longer than the nominal TDP arc length. For this

condition, the TDP offsets ($L_{TDP} - L_{nom}$) will be positive. This is observed for SCR-4,5,6 for vessel offset towards the vessel port side and SCR 1, 2, 3 for vessel offset towards the starboard side. The converse is the case when the vessel is relocated in the near direction of the risers, where more sections of the riser will rest on the seabed with a resulting shorter TDP arclength compared with the nominal. For this case, ($L_{TDP} - L_{nom}$) will be negative as observed for SCR-1,2,3 for vessel relocation towards the portside, and SCR-4,5,6 for vessel relocation towards the starboard. It is also observed that for vessel relocations in the riser far direction, $|L_{TDP} - L_{nom}|$ values are higher than $|L_{nom} - L_{TDP}|$ for vessel offsets in the risers near direction. Also, if the relocation axis is close to or out of the riser plane direction, there is insignificant variation in the TDP location compared with the nominal TDP. This is observed for SCR-4 for relocations along the 60^0 axis, SCR-2 for relocations along the 90^0 axis and SCR-3 for relocations along the 120^0 relocation axis. The overall variation in the TDP location (ΔTDP) caused by the vessel offset in both the far and near directions of the risers are presented in Figure 8-25 (a) – (d). One could see, in general, that while the TDP variation for the SCR is maximum for some relocation axis, it can even be zero for another axis. For example, SCR-2, SCR-3 and SCR-4 experience maximum variations in TDP location for relocation axis-1 (0^0), axis-2 (30^0), and axis-6 (150^0) respectively, but each experience no variation of TDP for vessel relocation along axis-4 (90^0), axis-5 (120^0) and axis-3 (60^0) respectively. This implies that for a given relocation axis, while some risers enjoy the maximum variation in TDZ fatigue hot spot, other risers may benefit very little in TDZ hots spot variation. It is, therefore, obvious that the influence on SCR TDZ fatigue hots spot spreading for this simple demonstrated relocation pattern is not directly apparent.

Considering risers with different hang off angles, different azimuths, and vessel offsets patterns, it becomes clear that determining the best relocation program will not be an easy task. However, this study addresses this challenge by providing a methodology to assess a group of optimum relocations programs from which all risers benefit best in terms of the SCR TDZ fatigue damage reduction. For such a scenario, the objective and constraint functions are multiples of the number of risers. Hence, there will not be a unique relocation program or combination of (α, R, p) that will be the optimal solution, but a family of optimum relocation programs, which will best satisfy the objective function for all the risers.

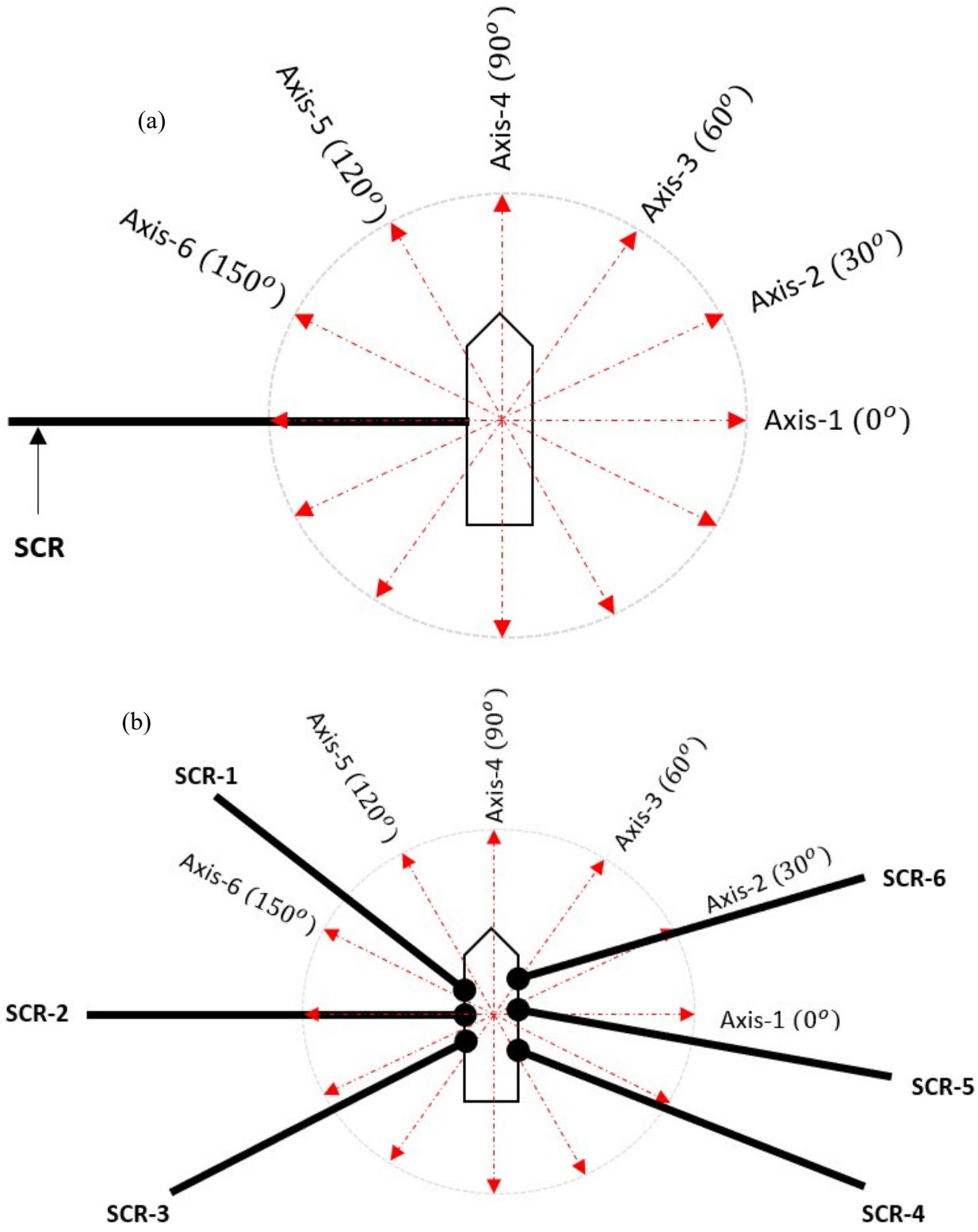

Figure 8-23. (a) Vessel relocation axes for (a) single SCR system, (b) Multiple SCR systems.

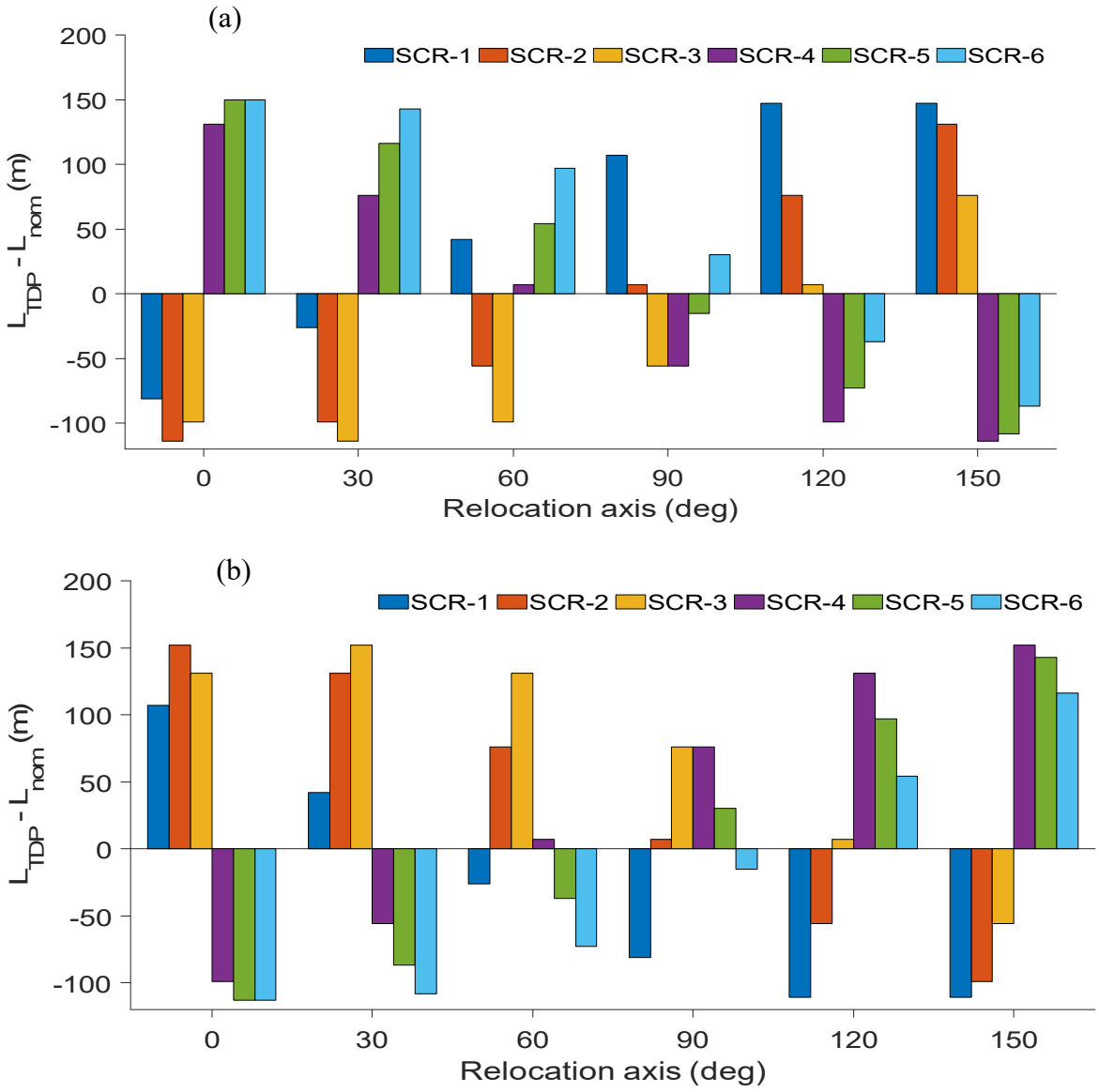

Figure 8-24. SCR TDP offsets from their nominal position for 7% vessel offset (a) towards the portside (along axes-1,2,3,5,6), and stern (along axis-4); (b) towards the starboard (along axes-1,2,3,5,6, and bow (along axis-4).

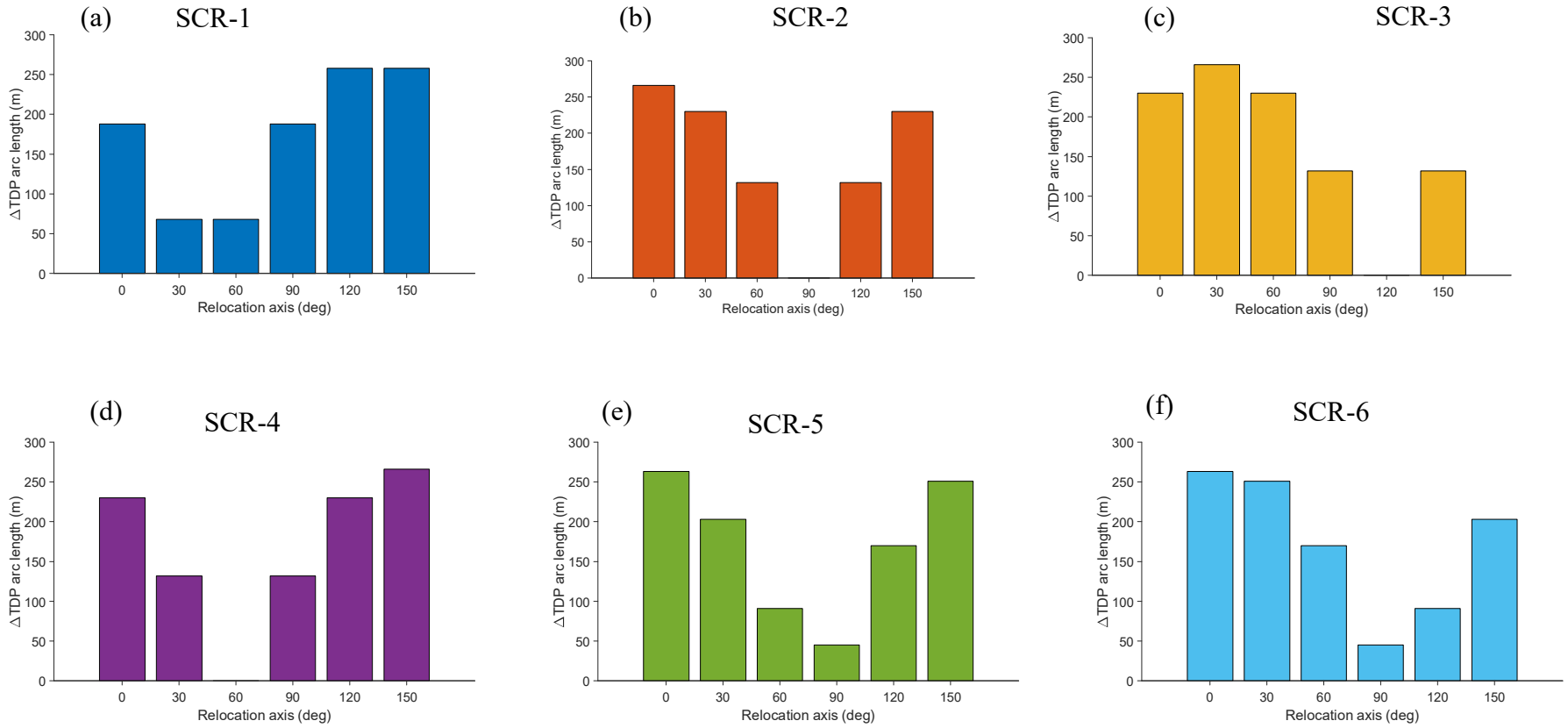

Figure 8-25. Resulting overall change in SCRs' TDP between vessel far and near offsets for (a) SCR-1, (b) SCR-2, (c) SCR-3, (d) SCR-4, (e) SCR-5, (f) SCR-6.

8.2.2 Vessel Relocation Strategy

8.2.2.1 Definition of terms relevant to the modelling of vessel relocation programs for multiple SCRs.

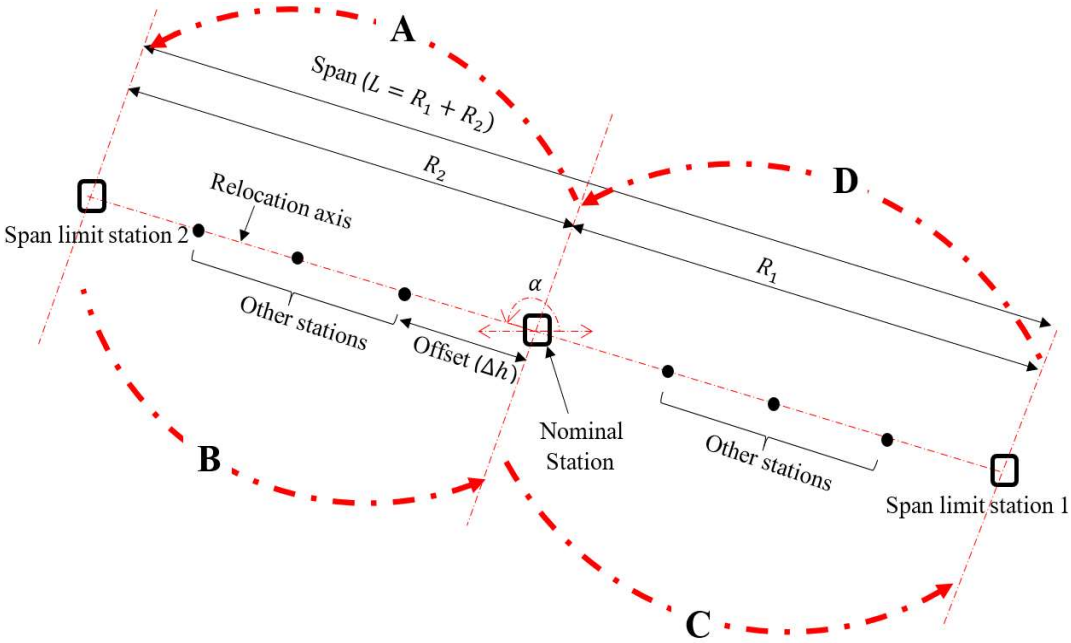

Figure 8-26. A vessel relocation program layout, depicting $\boldsymbol{p}$ relocation stations along a relocation axis, $\boldsymbol{\alpha}$, with span limit stations (extreme stations) positioned at $\boldsymbol{R_1}$ and $\boldsymbol{R_2}$ from the nominal station.

8.2.2.1.1 Relocation program

A relocation program in the context of this study is the combination of vessel relocation variables, namely: the axis of relocation (α), the relocation span radii $(R: R_1, R_2)$ and the number of relocation stations (p). The relocation programs can also be referred to as the design points in the optimisation design space for the problem. The number of numerical models representing the design points simulated to evaluate the objective and constraint functions will depend on the size and the discretisation of the optimisation design space.

8.2.2.1.2 Vessel relocation axis

In this work, we consider vessel relocation programs in straight lines known as the *relocation axes.* A relocation axis is characterised by angle α measured from a suitable referenced line, as shown in Figure 8-2. The axis extends from one limit to another on the respective sides of the vessel.

8.2.2.1.3 Relocation span limits and span radius

The limit on the extent to which the vessel can be moved on either side of the nominal station, along the relocation axis, is constrained by factors including the TDZ stress utilisation, the top tension, and the TDZ compression of the SCR. The span of relocation ($L = R_1 + R_2$) is the distance between both span limit stations. For symmetric relocation patterns, the distance of the two-span limit stations from the nominal station are equal, $R_1 = R_2 = L/2$. For non-symmetric relocation patterns, $R_1 \neq R_2$.

8.2.2.1.4 Relocation offsets

The direct distance between two neighbouring stations is referred to as the *relocation offset* (Δh) (see Figure 8-2). For equally spaced relocation stations, the relocation offsets can be obtained from the relocation span, L, and the number of relocation stations, p, as expressed in equation (8-18). However, equal distance between stations cannot be guaranteed for non-symmetric relocation patterns if the nominal station's location is fixed.

$$\Delta h = \frac{L}{p-1} = \frac{R_1 + R_2}{p-1} \tag{8-18}$$

8.2.2.1.5 Station coordinates

The initial configurations of all SCRs are calculated for the vessel positioned at the nominal station, with coordinate (0,0). The risers' configurations will change from the nominal configurations as the vessel moves from one station to another. The relocation programs are defined by a given combination of α, R_1, R_2, p, bounded by a pair of span limit stations at R_1 and R_2 from the nominal station, as seen in Figure 8-2. Consider a symmetric relocation program's span limit stations with coordinates (x_1, y_1) and (x_2, y_2) along a given relocation axis. The coordinates of p equidistant stations (within and including the span limits stations) can be expressed as:

$$(x, y) = \big(x_1 + r(x_2 - x_1), y_1 + r(y_2 - y_1)\big) \tag{8-19}$$

where r is the fractional part of each division within the span limit stations, which can be expressed in terms of the relocation offsets (Δh) and a station counter (i), where $i = 0$ to $p - 1$ as shown in equation (8-20).

$$r = \frac{i\Delta h}{R_1 + R_2} = \frac{i}{p-1} \tag{8-20}$$

8.2.3 Analysis Data and Methodology

8.2.3.1 Analysis data

Riser data: The SCRs used in this study are made of X70 steel grade material. The risers are hosted by a generic floating production, storage, and offloading (FPSO) unit at different azimuths (riser planes) shown in Figure 8-27. The cross-section dimensions of the SCRs, their hang off angles (HO) measure relative with the downward vertical, and their azimuth angles measure relative to the vessel heading (AZ) are presented in Table 8-9.

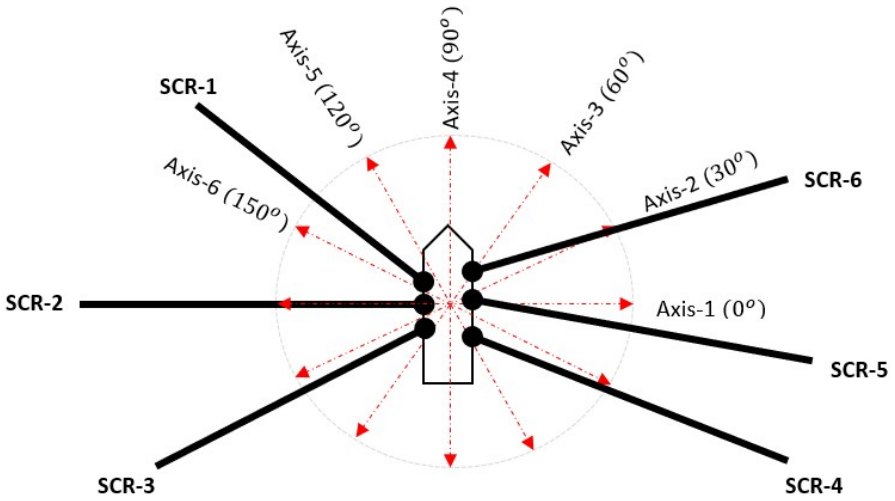

Figure 8-27. The layout of the vessel relocation axes.

Table 8-9. SCRs' cross-section geometry and configuration data.

SCR ID	**HO angle** (deg)	**AZ** (deg)	**OD** (m)	**WT** (m)
SCR-1	12	65	0.2540	0.0212
SCR-2	15	90	0.3556	0.0297
SCR-3	14	100	0.3048	0.0254
SCR-4	15	240	0.3556	0.0297
SCR-5	12	260	0.2540	0.0212
SCR-6	14	280	0.3048	0.0254

The SCRs (WT) minimum wall thicknesses are calculated based on the burst and collapse pressure resistance criteria in DNV-OS-F201 [4]. Other common data applied to the SCRs, including the optimisation design variables for the vessel relocation programs, are presented in Table 8-2. Note that the vessel relocation axes (red dotted lines) are measured from the positive vessel x-axis.

Table 8-10. Operational data for the SCRs.

SCR data	**Values**
Internal Design pressure	10 ksi
SMTS	565 MPa
Content density	600 kg/m^3
Hang off rotational stiffness (linear)	12 kN.m/deg
Water depth	1500 m
S-N curve (seawater plus cathodic protection)	D-Curve [116]
Riser design life (T_D) (greenfield)	30 years
Relocation axis(α)	[0,30,60,90,120,150] deg
Span radii (R: R_1, R_2)(%water depth)	$\{R_1$:$1 \leq R \leq 20\}$,$\{R_2$:$1 \leq R \leq 20\}$
Number of station (p)	$\{p$:$3 \leq p \leq 9\}$

The optimisation design variables are the axes of relocation (α), the span radii (R) and the number of relocation stations (p). The ranges of values for these variables have been presented in Table 8-2.

- **The axes of relocation ($\boldsymbol{\alpha}$)** – The relocation axes are at 30^o from each other, resulting in 6 discrete values for the 360^o coverage. Five out of the six axes extend from one side (portside) to the other side (starboard). The axis-4 aligns with the heading of the vessel.

- **The span radius ($\boldsymbol{R}$: $\boldsymbol{R_1, R_2}$)** – The span radii (measured from the nominal station) are expressed in percentage of the water depths and are discretized at 1% interval, resulting in 20 discrete values for R.

- **The number of relocation stations ($\boldsymbol{p}$)** – The number of relocation stations ranges from 3 to 9 at intervals of 2, resulting in 4 discrete values of p. For symmetric relocation programs, the station patterns are obtained by expanding values of p as shown in Figure 8-28, where "1" is the nominal station. However, for non-symmetrical relocation programs, the patterns will be skewed about the nominal station.

Number of station (p)	Vessel relocation patterns (m)																	
3								2	1	3								
5							3	2	1	4	5							
7						4	3	2	1	5	6	7						
9					5	4	3	2	1	6	7	8	9					

Station ID

Figure 8-28. Station arrangement in symmetric relocation programs.

In previous work for symmetric relocation optimisation for single SCR [132], it was found that the optimum relocation program (α, R, p) was (30deg, 5%, 19). A further investigation of this relocation program showed that although 19 stations gave the least effective fatigue damage, the number of stations beyond $p = 9$ along $\alpha = 30$deg, for R =5% contributed very little reduction to the effective damage of the SCR TDZ as shown in Table 8-8 and Figure 8-21. Hence, we can generalise that increasing the number of stations beyond a certain number of p will only increase the associated operating cost for the relocation program, with minimal reduction to the effective damage. Although we cannot yet generalise this behaviour for multiple SCR vessel relocation optimisations, considering the required computational resource requirements, it is only rational to consider a maximum of nine (9) relocation stations for this study. The suitability of $p = 9$, wil be discussed in the result section.

Environmental data: To demonstrate the vessel relocation strategy for multiple SCRs, one regular wave load is considered for the storm (constraint function evaluation) and fatigue (objective function evaluation) analyses, as presented in Table 8-3. This means the probability of occurrence for the single fatigue sea state is 100%. The wave loads are considered Beam Seas (perpendicular to vessel heading) to impact the largest combined roll and heave FPSO motions on the risers.

Table 8-11. Wave load data representative of fatigue and design storm sea state conditions.

Analyses	Wave type	Data	Values
Extreme	Regular	H	8 m
		T	12 sec
Fatigue	Regular	H	4.5 m
		T	9.5 sec

The vessel's response amplitude operators are symmetrical about the longitudinal vessel axis. Since Beam Seas are applied, the most relevant vessel response amplitude operators (RAOs), the heave and roll RAOs, are presented in Figure 8-6. The non-linear hysteretic seabed model for catenary pipeline contact is implemented to model the SCR TDZ soil interactions. The soil model data used are presented in Table 8-12.

Table 8-12. Non-linear catenary pipeline soil interaction model data [56].

Parameter	**Symbol**	**Value**
Mudline shear strength	s_{u0}	5 kPa
Shear strength gradient	ρ	1.5 kPa/m
Power law parameter	$[a, b]$	[6,0.25]
Normalised maximum stiffness	K_{max}	200
Suction ratio	f_{suc}	0.6
Suction decay parameter	λ_{suc}	0.4
Repenetration parameter	λ_{rep}	0.2

8.2.3.2 Vessel relocation optimization

The objective of the vessel relocation optimisation analysis is to determine optimum combinations of the design variables, α, R and p, which result in the least effective fatigue damage in the SCR TDZ. The optimum relocation programs must satisfy constraint functions, which are the design limit set for the SCR design storm responses. The vessel relocation optimization problem can be expressed as follows:

$$\text{find X} = \begin{Bmatrix} \alpha \\ R \\ p \end{Bmatrix} \text{ which minimizes } D_{eff} \tag{8-21}$$

Subject to the following constraints, g:

$$\text{g} = \begin{cases} U_{TDZ} < 1 \\ T_{top} < T_y \\ T_{TDZ} > T_{min} \end{cases} \tag{8-22}$$

where:

α = Relocation axis measured from a reference axis.

R: = Span radii (R_1, R_2).

p = Number of relocation stations.

D_{eff} = Effective fatigue damage per relocation program.

U_{TDZ} = Stress utilization in the SCR TDZ.

T_{top} = Maximum effective tension at the riser top.

T_{TDZ} = Minimum effective tension around the riser TDZ.

T_y = Yield tension of the riser pipe = $0.9SA$.

S = Specified minimum yield strength.

A = SCR pipe cross-section area.

T_{min} = Minimum allowable effective tension (T_{min} =85 kN in this work).

The above optimisation model is applied for each of the six SCRs hosted by the vessel. This implies that there will be six objective functions, $\left(D_{eff}\right)_j$, where j =1 to 6 and eighteen (3 × 6 = 18) constraints functions to be evaluated for the problem. In section 8.2.3.3, two approaches are presented to organise these objective functions and conduct the optimization step. Any suitable optimization technique can be applied to solve the problem. However, the index matching optimization technique is used in this study. Details of the index matching technique are provided in Chapter 4. The flow chart for the index matching optimization process is presented in Figure 4-2. Index matching optimisation technique flowchart. and summarised as follows:

- Assemble all possible combinations of the design variables.
- Run numerical analyses (for each combination) to determine the values of the constraint functions.
- Run numerical analyses (for each combination) to determine the values of the objective function.
- Eliminate the combinations that do not satisfy the constraints.

- Order the remaining combinations in ascending order of the objective function to find the combination that minimises the objective function while satisfying the constraints.

For the vessel relocation example in this study, the six objective functions are the effective fatigue damage in the TDZ of the six SCR. These objective functions are evaluated within the feasible constraint region for the 18 constraint functions.

8.2.3.3 Procedure to obtain global fatigue damage function.

There is a need to determine the optimal global solutions to provide optimum D_{eff} for the six SCRs. These techniques are based on the multip-objective optimisation methods presented in Chapter 4. The two technique applied in this study, both based on the index matching technique but applied differently. Results comparison for both methods will be discussed in the results section.

8.2.3.3.1 Method 1 - Constructing a global objective function

The global objective function, F, is created through a linear combination of the six objective functions, weighted by their contributions to F. This is expressed in equation (8-23).

$$F = \sum_{j=1}^{6} a_j \left(D_{eff}\right)_j \tag{8-23}$$

where j is the number of SCRs, which in this analysis example ranges from 1 to 6. Although the components of F have the same unit (yr^{-1}), the six SCR configurations are different. This implies differences in the fatigue damage scale. Hence, there is the need to standardise or normalize the effective damage, D_{eff}, of each of the SCRs before computing their linear sum, to obtain the normalised joint objective function, F^{nom}. The following are steps taken to obtain F^{nom}:

- Evaluate D_{eff} in the six SCRs for the feasible relocation programs using equation (8-12).
- For each program, obtain the maximum and minimum D_{eff} in the six SCR TDZs. These are $\left(D_{eff}\right)_j^{max}$ and $\left(D_{eff}\right)_j^{min}$ respectively.
- Obtain the normalised or standardized D_{eff} as expressed in equation (8-24).

- $\left(D_{eff}\right)_j^{nom} = \frac{(D_{eff})_j - (D_{eff})_j^{min}}{(D_{eff})_j^{max} - (D_{eff})_j^{min}}$, $j = 1$ to 6 (8-24)

- Obtain the weight contributions, a_j, of the six SCRs ($j = 1$ to 6) based on maximum or minimum values of $\left(D_{eff}\right)_j$. This means the higher the maximum effective damage for a given SCR, the higher will be its weight contributions to the global fatigue damage function, and the less favourable its contributions will be to the minimisation of the global fatigue damage function. The weight calculations options are presented in equations (8-25) and (8-26).

$$a_j = a_j^{max} = \frac{\left(D_{eff}\right)_j^{max}}{\sum_{j=1}^{6}\left(D_{eff}\right)_j^{max}} \quad (8\text{-}25)$$

$$a_j = a_j^{min} = \frac{\left(D_{eff}\right)_j^{min}}{\sum_{j=1}^{6}\left(D_{eff}\right)_j^{min}} \quad (8\text{-}26)$$

The combined normalised D_{eff} is then obtained using equation (8-27).

$$F^{nom} = \sum_{j=1}^{6} a_j \left(D_{eff}\right)_j^{nom} \quad (8\text{-}27)$$

The index optimisation technique can then be applied to obtain the optimum solutions for this single global objective function.

8.2.3.3.2 Method 2 – Intersection of the index systems of the Ideal solutions

The individual ideal solutions are the family of optimum relocation programs obtained considering each objective function exclusively. This means, within the feasible design space, the best family of optimum relocation programs are obtained for each SCR without considering the influence of the other SCRs objective functions. Recall from th eindex matching technique that the reordered index system representing each of the objective functions can be written as:

$$\mathrm{I}' = (\mathrm{I}_{\mathrm{FDS}})_{\mathrm{reordered}} = \{I_1', I_2', \ldots, I_6'\}^{\mathrm{T}} \quad (8\text{-}28)$$

A direct intersection of the columns of $\mathbf{I}'$, taken q rows at a time, provides the family of joint optimum solutions for the six SCRs. Figure 8-29 (a) shows a common region where the family of global optimum solutions lie, while Figure 8-29 (b) demonstrates the intersection operation process for the columns of $\mathbf{I}'$ taken q rows at a time. As will be seen later in the result section, the first values of q, may yield no intersected indices, resulting in an empty set. However, as q increases i.e., as we go further down the columns, the number intersected indices increase. The maximum value of q, denoted as Q in Figure 8-29 (b), is the number of feasible design points or relocation program within the optimisation designs space.

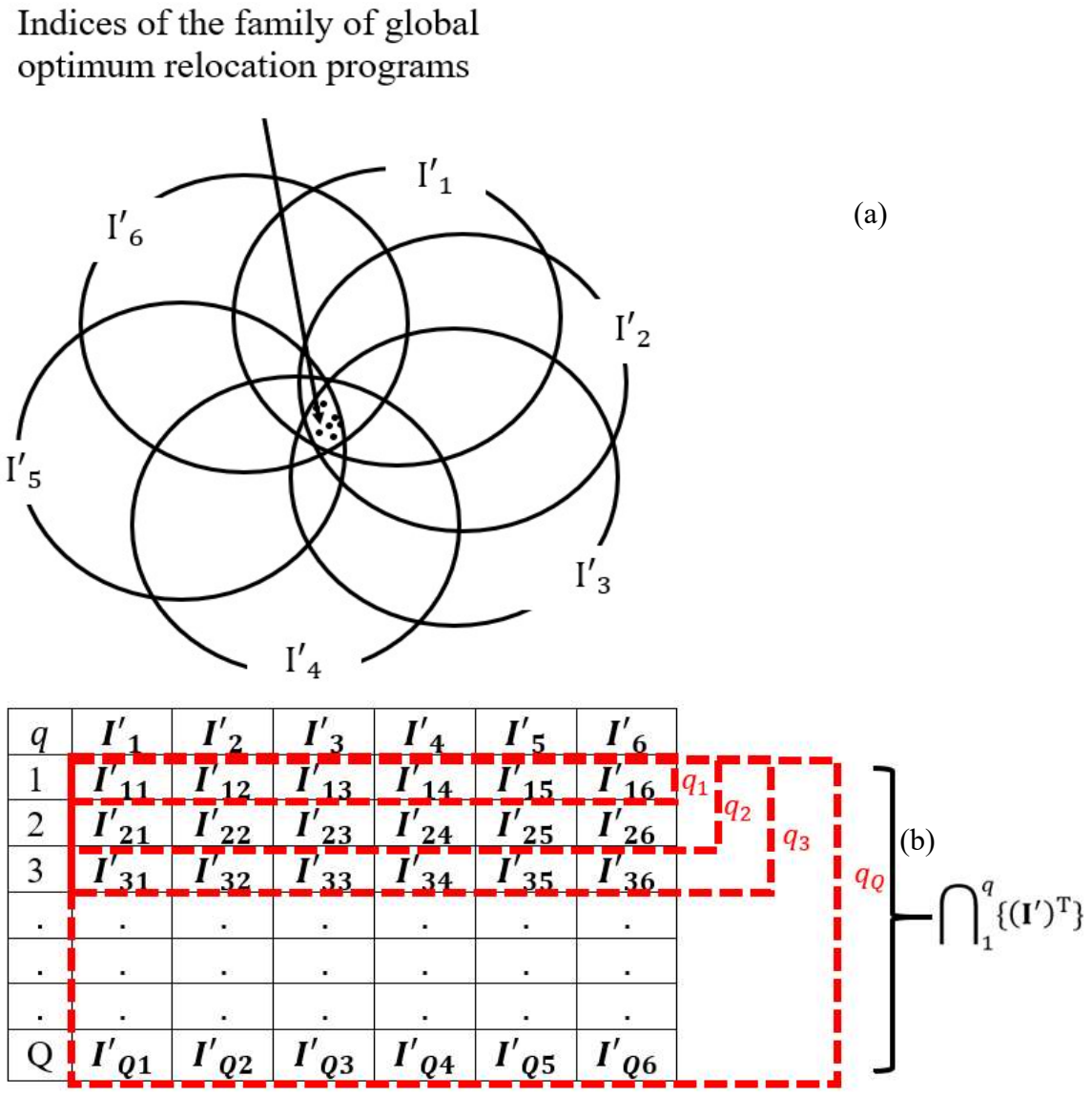

Figure 8-29. (a) Intersection region containing the family of global optimum relocation programs, (b) Conducting intersection operation on the index columns of the ideal solutions, $\boldsymbol{q}$ row at a time.

8.2.3.4 Screening methodology based on SCR storm constraint analysis

This section provides a screening analysis methodology to help reduce the computational resource requirements by identifying and eliminating unfeasible relocation stations during the storm and fatigue analysis. The constraint function defined in equation (8-17) is imposed on the vessel optimisation relocation problem to determine feasible span limits for all relocation programs. Constraint function evaluation requires numerical modelling and simulations of all constituent stations of every candidate relocation program. There are three constraints inequalities for any of the six SCRs ($j = 1$ to 6). This result in 18 constraints to be evaluated for each constituent station of any relocation program. Conducting the full constraint function evaluation (storm response analysis) and objective function evaluation (fatigue analysis) at every station (both feasible and non-feasible) of every candidate relocation program can be very expensive computationally. If any of the 18 SCRs' constraint functions is violated in any station of a relocation program, that relocation program becomes unfeasible and should be eliminated from the process. Hence, it is expected that no fatigue analysis should be conducted for that program. However, instead of eliminating an unfeasible initially considered symmetric relocation program, the program can degenerate to a non-symmetrical feasible program. Hence, the screening exercise removes the need for unnecessary simulation and expands the optimisation design space within which good non-symmetrical relocation programs can be captured. The screening procedure is as follows:

- Make an initial consideration of symmetric pattern for the relocation programs, with the span limits equidistant from the nominal station ($R = R_1 = R_2$).
- Conduct numerical modelling and analysis of the SCRs and evaluate the constraint functions at the span limits stations to determine their feasibilities. This means that if the span limit stations are feasible, the remaining $p - 2$ relocation stations in between the span limit stations will also be feasible and fall within the feasible region depicted in Figure 8-30. Hence, no need to conduct storm responses for all p stations between these limits. This implies a huge computation saving.
- If the span limit stations for a relocation program is feasible, then the relocation program will stay symmetrical, as depicted in Figure 8-31 (a). We calculate r using equation (8-20) and then calculate the coordinates of the p stations using equation (8-19).

- Suppose any or both span limit stations of the relocation program are not feasible. In that case, the relocation pattern can degenerate to the next lower feasible span limit(s), which may be non-symmetrical, as depicted in Figure 8-31 (b). For this scenario, we calculate r using p' in place of p in equation (8-20), where $p' = p - 1$, to remove the nominal station coordinate (0,0) from the list of the equidistant station coordinates. The stations' coordinates are then calculated using equation (8-19). The resulting coordinate list is then modified by inserting the nominal station coordinate (0,0) at the appropriate location (transition from one side of the relocation axis to the other side). In this case, the distance between the nominal station and its nearest neighbours will not have equal distance, Δh, like other stations, but $\Delta h/2$.
- Calculate the fatigue damage fraction, f, for the stations in the relocation programs using equation (8-10).
- Conduct numerical modelling and fatigue analysis for the feasible relocation programs to evaluate the objective function, D_{eff}, using equation (8-12).

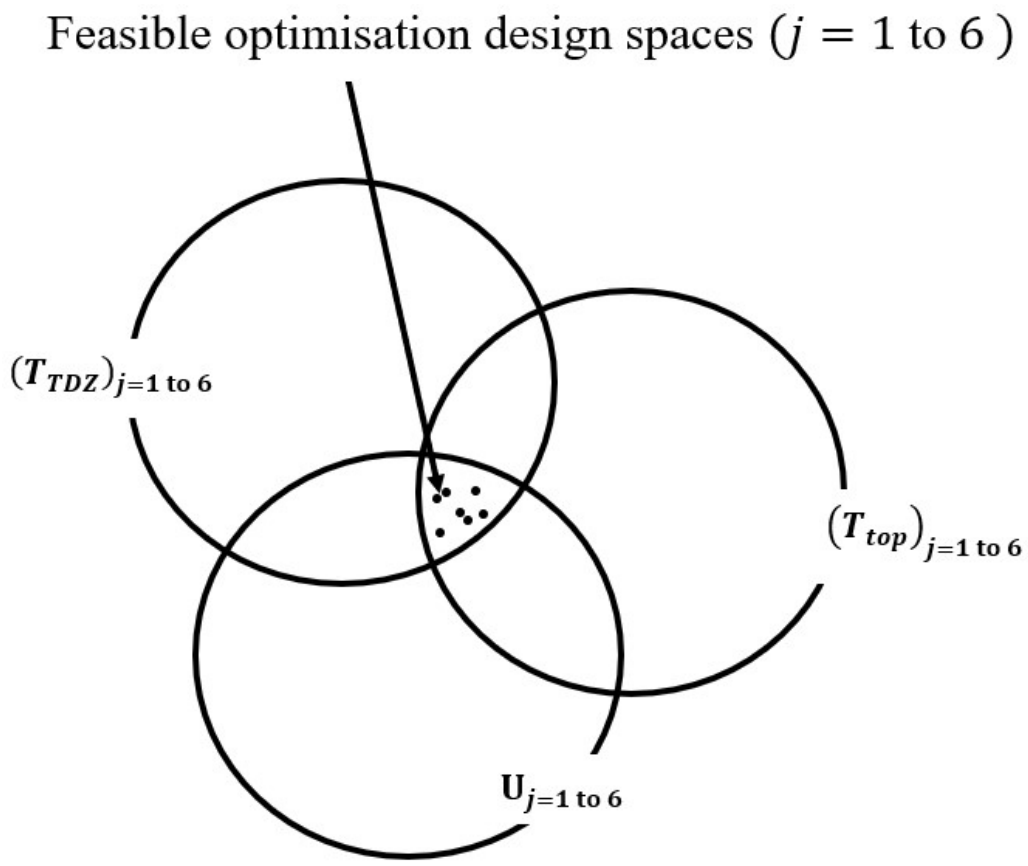

Figure 8-30. Feasible region for relocation programs.

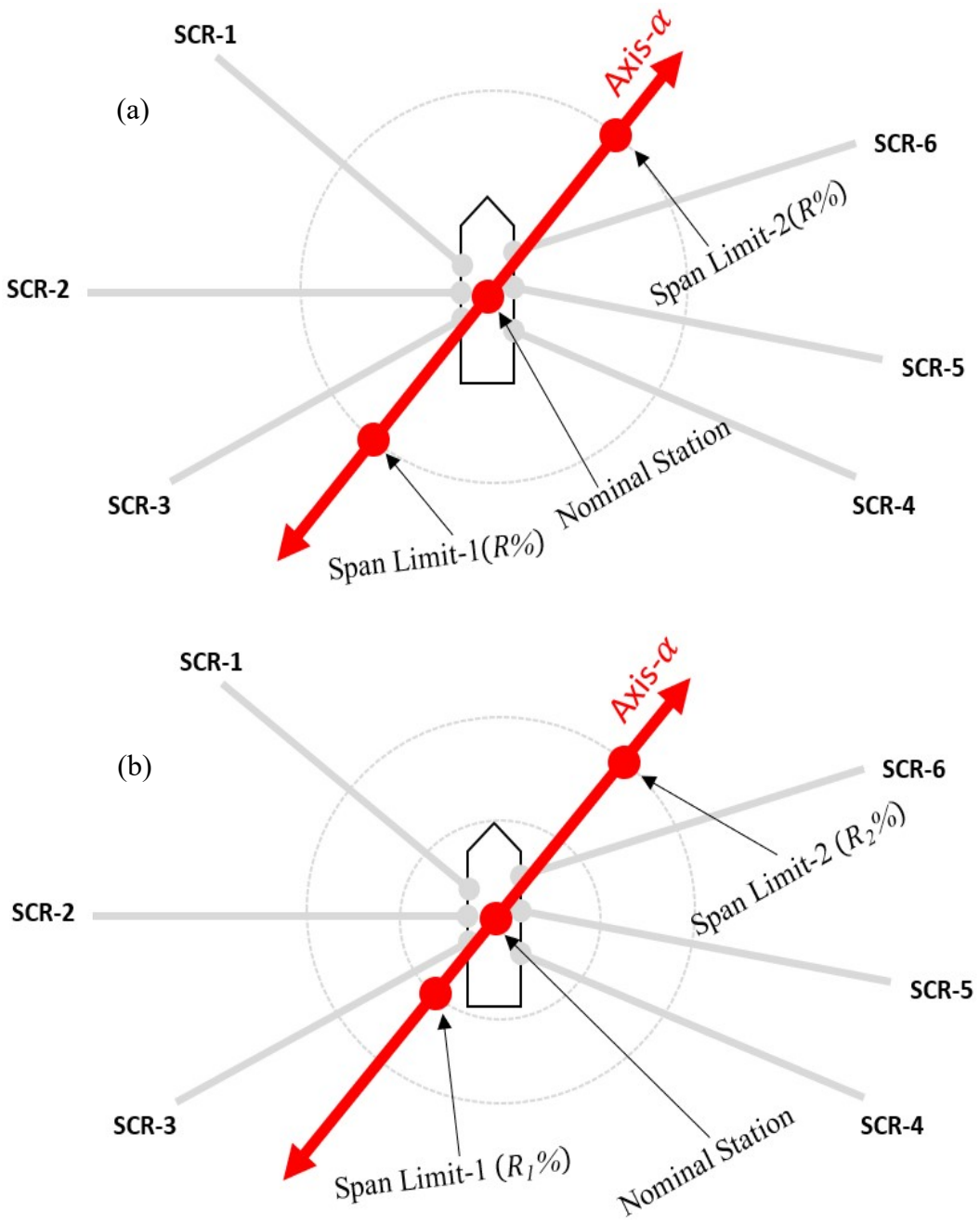

Figure 8-31. Depiction of the span limits and nominal stations in (a) a symmetric vessel relocation program layout, (b) a non-symmetrical vessel relocation program layout.

The key consideration during the screening analysis, as mentioned in the second bullet point, is that if the span limit stations are feasible, the remaining $p-2$ relocation stations in between the span limit stations will also be feasible and fall within the feasible region the design optimisation space. This consideration is correct as long at there is no incidence at any of the stations, and no resonance occurring for any of the risers during the vessel relocations. To

demonstrate this, Consider the example of the 6 SCRs hosted by the vessel in section 8.2.1. The span limit stations are considered symmetrical and at radii of 7% of the water depth (105 m) from the nominal station, as depicted in Figure 8-32 (a). The relocation axes for this example are axis-1 (0 º), axis-2 (45 º), axis-3 (90 º), and axis-4 (135 º). There are five relocation stations (1,2,3,4,5), including the span limit stations (1 and 5) along each relocation axis. Hence, there are 20 relocation stations for this example. All stations along each relocation axes are equidistant from each other. For the visual understanding of this example set up and interpretation of results, Figure 8-31 (a), which depicted a generic symmetrical relocation pattern, is put side by side with Figure 8-32 (a) as Figure 8-32 (b). With the orientations of the SCRs in Figure 8-32 (b), one would be able to match the riser responses to the sense of their locations and configurations during the vessel relocations along any of the four axes and across the relocation stations. The Beam Sea regular storm wave load in Table 8-3 is applied on the vessel-riser systems at each relocation station.

The constraint functions which are the stress utilization at the SCRs' TDZ (U_{TDZ}), the minimum effective tension representative of SCRs' TDZ compression (T_{TDZ}) and the maximum top tensions for the SCRs at each of the relocation stations along each relocation axis are post-processed from the simulations and presented in Table 8-13. The highest and lowest values of these responses within the SCR region of interest for the relocation station per relocation axes are highlighted in Table 8-13. One could observe that for all the axis of relocation, the critical value occurs at the span limit stations (1 and 5), while the response at stations in between the span limits station falls within the response value obtained for the SCR at the span limit stations. An exception is only observed for SCR-2 for the relocation program along the 90 º axis. Recall from Figure 8-32 (b) that SCR-2 is at an azimuth of 90 º and that the relocation of the vessel along the vessel heading, which is perpendicular to the azimuth of SCR-2, will induce small SCR TDZ offsets on the SCR-2 TDZ, as seen in the results presented in Figure 8-24 and Figure 8-25. This is not a problem to achieving the optimum relocation program in the primary analyses of the study since relocation along 90 º provides the least TDZ spreading. Without detailed optimisation of the relocation program, it is evident from perceived and a physical sense that this axis will give negligible fatigue damage spreading and will not even appear among the optimum solutions. However, as will be seen in the detailed optimisation analysis in this study, we included relocation along this axis in the design optimisation space for the sake of completeness. We can conclude from these results that the extreme responses of the SCRs will most likely be at the extreme station (span limit-1 and 2)

unless resonance or an incidence occurs. This is the basis for the screening exercise, based on the vessel-SCRs systems at span limits-1 and 2. If the SCRs failed the constrained function at any of these span limit stations, that symmetric relocation program is unfeasible and would need to be modified or degenerated to a feasible nonsymmetrical relocation program. With this approach, there is no need to conduct simulations in the stations that lie between the span limit stations for the evaluation of the objective function. However, for any feasible relocation program determined based on the feasibility of the span limit station, all relocation stations between the span limit stations must be included in the fatigue calculations during the evaluation of the objective functions (D_{eff}) for the problem.

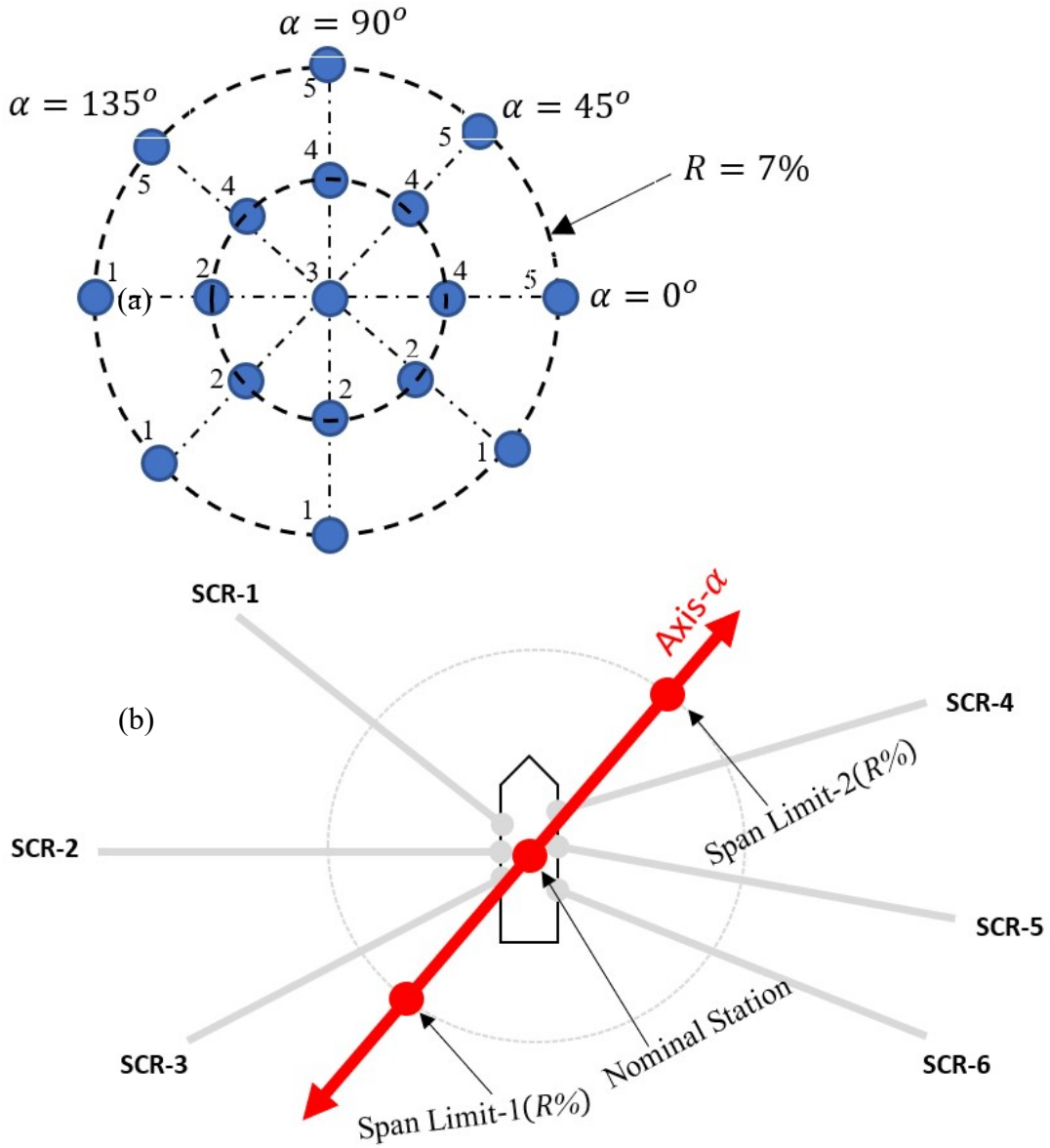

Figure 8-32. (a) – Layout of vessel relocation stations showing both span limit stations (1 and 5) with three intermediate stations (2,3,4) for each of the four relocation axes (b) A generic symmetric vessel relocation layout showing the directions or azimuth of the six SCRs

Table 8-13. Table of constraint functions' values showing maximum and minimum values occur at span limit stations.

SCR Responses	SCR	Axis - 1 (0 °)					Axis - 2 (45 °)					Axis - 3 (90 °)					Axis - 4 (135 °)				
		Stations					Stations					Stations					Stations				
		1	2	3	4	5	1	2	3	4	5	1	2	3	4	5	1	2	3	4	5
U_{TDZ}	SCR-1	0.81	0.77	0.74	0.71	0.68	0.76	0.75	0.74	0.73	0.71	0.71	0.72	0.74	0.75	0.77	0.68	0.71	0.74	0.77	0.82
	SCR-2	0.70	0.67	0.63	0.61	0.60	0.68	0.66	0.63	0.62	0.60	0.63	0.63	0.63	0.63	0.63	0.60	0.62	0.63	0.65	0.68
	SCR-3	0.73	0.69	0.66	0.64	0.61	0.72	0.69	0.66	0.64	0.62	0.67	0.67	0.66	0.66	0.65	0.63	0.65	0.66	0.68	0.70
	SCR-4	0.68	0.71	0.74	0.77	0.81	0.72	0.73	0.74	0.75	0.76	0.78	0.76	0.74	0.72	0.70	0.82	0.78	0.74	0.71	0.68
	SCR-5	0.59	0.61	0.63	0.66	0.70	0.60	0.62	0.63	0.65	0.67	0.64	0.64	0.63	0.63	0.62	0.69	0.66	0.63	0.61	0.59
	SCR-6	0.59	0.60	0.63	0.66	0.70	0.59	0.61	0.63	0.65	0.68	0.62	0.62	0.63	0.63	0.64	0.66	0.64	0.63	0.61	0.60
T_{TDZ}	SCR-1	75.31	96.38	121.07	149.21	180.97	106.05	112.79	121.07	131.38	142.52	151.33	135.57	121.07	108.93	98.88	185.79	151.01	121.07	94.97	72.71
	SCR-2	187.87	312.82	515.37	762.63	1008.27	295.63	381.51	515.37	706.62	903.57	607.68	547.02	515.37	547.80	608.63	901.86	705.98	515.37	381.85	295.38
	SCR-3	124.07	218.94	352.43	428.49	517.98	169.72	241.58	352.43	417.34	492.39	329.09	339.26	352.43	368.73	388.40	441.53	394.13	352.43	281.05	238.20
	SCR-4	536.93	439.37	361.14	295.59	239.22	410.21	382.53	361.14	342.48	327.86	285.83	320.79	361.14	407.44	463.77	224.47	287.28	361.14	451.54	567.94
	SCR-5	364.46	297.00	239.67	192.86	152.44	310.75	273.16	239.67	212.83	189.48	226.99	231.75	239.67	251.04	265.24	167.13	200.44	239.67	287.36	342.55
	SCR-6	648.12	530.35	432.98	351.20	282.18	611.42	514.54	432.98	363.84	305.24	476.65	452.70	432.98	418.29	408.63	346.26	385.94	432.98	487.80	551.78
T_{top}	SCR-1	1991.84	2070.90	2163.45	2271.80	2399.93	2097.51	2127.56	2163.45	2206.47	2254.93	2265.38	2211.72	2163.45	2122.97	2088.55	2404.72	2274.17	2163.45	2068.94	1988.41
	SCR-2	3633.24	3809.38	4019.38	4271.88	4584.36	3743.17	3870.57	4019.38	4194.88	4402.46	4041.09	4026.39	4019.38	4024.37	4037.90	4405.09	4196.35	4019.38	3869.61	3740.88
	SCR-3	2764.22	2890.84	3043.20	3228.01	3449.86	2814.55	2918.34	3043.20	3192.93	3367.57	3010.35	3023.01	3043.20	3072.83	3113.81	3280.79	3151.70	3043.20	2950.58	2873.32
	SCR-4	5074.90	4792.20	4549.81	4344.20	4171.05	4713.24	4624.28	4549.81	4484.30	4439.03	4336.30	4431.47	4549.81	4684.16	4834.28	4133.56	4322.89	4549.81	4818.17	5131.78
	SCR-5	2147.22	2031.86	1935.93	1855.26	1786.62	2057.98	1991.63	1935.93	1888.94	1849.13	1915.18	1923.88	1935.93	1954.23	1976.69	1811.49	1868.75	1935.93	2015.13	2109.73
	SCR-6	3279.64	3072.90	2904.82	2764.63	2647.70	3205.38	3041.60	2904.82	2789.27	2692.46	2969.62	2933.66	2904.82	2884.50	2871.53	2749.87	2821.09	2904.82	3003.40	3117.70

8.2.3.5 Numerical modelling and analysis procedure

The OrcaFlex numerical software package is used to conduct the analyses for this study. The analysis simulations are performed in the time domain, applying the implicit integration scheme in the numerical solution process. The pre-processing, modelling, simulations and post-processing are automated using MATLAB programs integrated with the OrcaFlex programming interface, OrcFxAPI [114]. The developed MATLAB program pre-processes analysis data and computes additional data required for the numerical modelling in OrcaFlex. The program then generates OrcaFlex models for the relocation programs. The regular design storm and fatigue wave loads are modelled with the Dean Stream theory. The stress utilisation is post-processed using the DNV-OS-F201 combined load (bending, tension, and pressure) resistance factor design criteria [115]. For the fatigue calculation, the S-N D-curve in seawater with cathodic protection is used [116]. The Rain flow counting technique [98] expresses the varying SCR TDZ stress spectrum as a histogram of stress reversals. Miner's rule is then applied to cumulate the fatigue damage for the SCR. The flow chart for the analysis is summarised in Figure 8-34.

It is mentioned in section 8.2.3.1 that the wave loads are considered Beam Seas (perpendicular to the vessel heading) to impact the largest combined roll and heave FPSO motions on the risers. The two directions for the beam sea are 0^o and 180^o along the global X-axis, considering a vessel heading of 90^o. Although the vessel response is symmetric about its longitudinal axis, wave application in these two directions will not result in the same responses in the 6 SCRs. This is because the SCRs configuration and orientations are different, with different hydrodynamic loads for the two wave directions. As a result, the storm and fatigue wave loads are applied in both the screening analysis and optimisation simulation stages. Our interest in these two directional wave applications is to capture the extreme values of the storm responses and the worse fatigue damage for each of the 6 SCRs. Any of the critical storm responses, $R_{extreme}$, can be obtained using equation (8-29). The combined fatigue damage, $D_{combined}$, in each of the SCR can be obtained using equation (8-30), assuming a probability of occurrence of 50% for each of the two wave directions. The $D_{combined}$ across the relocation stations of a relocation program can then be factored by the corresponding set of the fatigue damage fraction, f, to obtain D_{eff} (see equation (8-12)).

$$R_{extreme} = \max(R_{waveDir=0^o}, R_{waveDir=180^o}), R = \{U_{TDZ}, T_{TDZ}, T_{top}\} \quad (8\text{-}29)$$

$$D_{combined} = \frac{D_{waveDir=0^o} + D_{waveDir=180^o}}{2} \tag{8-30}$$

The span limit station conventions are presented in Figure 8-33. The conventions will be helpful to visualise the positions of these limit stations relative to the nominal station. They will also help to understand the expected strength and fatigue behaviours of the SCRs at these stations.

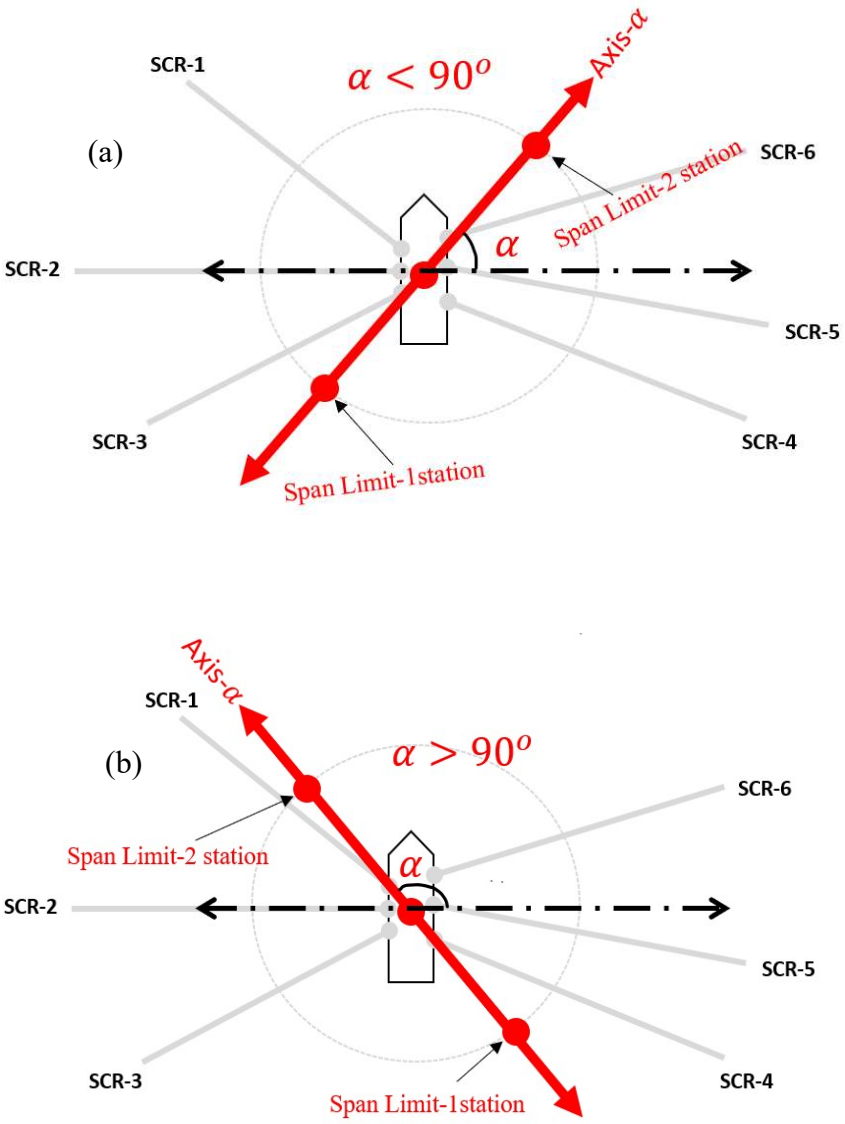

Figure 8-33. Span limit station convention: (a) span limit station-1 on the portside and span limit station-2 on the starboard side for $\boldsymbol{\alpha < 90}$, (b) span limit station-1 on the starboard side and span limit station-2 on the portside for $\boldsymbol{\alpha > 90}$; for $\boldsymbol{\alpha = 90^o}$, span limit station-1 on the aft side, span limit station-2 on the forward side.

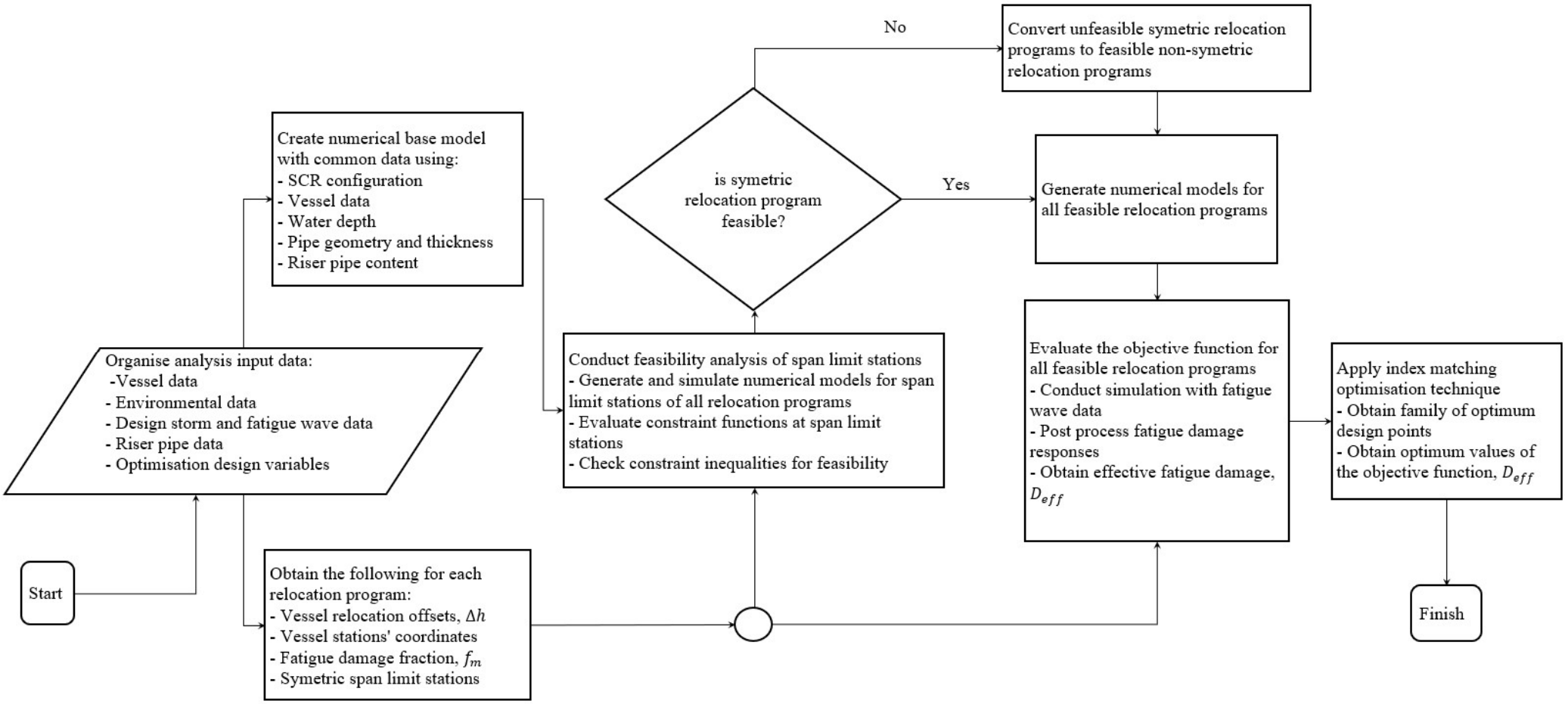

Figure 8-34. Analysis flow chart.

8.2.4 Analyses, results and discussions.

8.2.4.1 Screening (storm constraint analysis) results

Referring to the screening procedure outlined in section 8.2.3.4, we initially consider symmetric vessel relocation patterns on which the relocation programs will be developed. Recall that we have 6 discrete points for α, and 20 discrete points each for R_1 and R_2. The coordinate sets of the span limit stations calculated based on the combination of α and R_1 and α and R_2 on both sides of the nominal relocation station are respectively presented in Table 8-14 (a) and Table 8-14 (b). For brevity, the decimal parts of the coordinates have been truncated. Each table has 120 elements, which should not be taken as equal to the number of relocation programs since varying the value of p for the same pair of span limits stations results in different relocation programs. A combination of corresponding coordinates from the two tables provides the span limit station pairs ({span limit-1 station, span limit-2 station}) as have been demonstrated in Figure 8-31 (a). So, if we assign the same integer ID (from 1 to 120) as shown in Table 8-14 (c) to corresponding stations on Table 8-14 (a) and Table 8-14 (b), we will obtain the span limit ID pairs as presented in Table 8-14 (d).

Following the steps in section 8.2.3.4, the screening analysis is conducted for each of these symmetric span limit station pairs, i.e., two numerical models are built to represent each span limit station in a pair. Storm response analyses are conducted for these pairs and the constraint function in equation (10) is evaluated for the six SCRs. It should be noted that each SCR has three constraint functions to be satisfied, meaning that 18 constraint functions must be satisfied at both stations of each span limit pair for that relocation pattern to be feasible (see Figure 8-30). When a relocation pattern is unfeasible, all dependent relocation programs will also be unfeasible. The resulting feasibility matrices for the sets of the span limit stations for (R_1, α) and (R_2, α) are presented in Table 8-15 (a) and Table 8-15 (b) respectively. Any of the 6 SCRs at any of the span limit stations having a zero (0) implies that SCR failed or violated at least one of the storm response constraints in equation (8-17). If we combine the feasibility matrix in Table 8-15 (a) and Table 8-15 (b) and express the outcome in terms of the span limit pair IDs, we will obtain Table 8-15 (c), which demonstrate the feasibility and unfeasibility of the symmetrical relocation patterns shaded in green and red respectively. For example, consider the span limit station pair ID {95,95} in Table 8-15 (c) characterised by α =120°, $R_1 = 16\%$ and $R_2 = 16\%$. Although all the SCRs passed the constraint test for span limit-1 station i.e. [1,1,1,1,1,1] in Table 8-15 (a), ID {95,95} is unfeasible because SCR-1 failed to satisfy at least

one of the 3 constraint functions at span limit-2 station i.e. [0,1,1,1,1,1] in Table 8-15 (b). This is no surprise since the relocation axis, $\alpha = 120^{o}$ falls within the azimuth sector of SCR-1 as depicted in Figure 8-33, and the vessel at span limit-2 position will induce significant compression on SCR-1. For demonstration purposes, the 6 SCRs' range graph maximums for the three constraint functions and their corresponding bar chart of peak values when the vessel is at the span limit stations pair ID {95,95} are presented in Figure 8-35, Figure 8-36 and Figure 8-37:

- Figure 8-35 (a) and (b) show the graph of the TDZ stress utilization response at span limit-1 and span limit-2 stations. Figure 8-35 (c) and (d) are the bar chart representation of the maximum value of the stress utilisation around the SCR TDZ.
- Figure 8-36 (a) and (b) show the range graph compression (T_{TDZ}) around the 6 SCR TDZ for the vessel positioned at span limit-1 and span limit -2 stations.
- Figure 8-36 (c) and (d) present bar charts of the highest compressions around the SCR TDZ.
- Figure 8-37 (a) and (b) shows the range graph maximums of the 6 SCR top tensions (T_{top}) at span limit-1 and span limit-2 station.
- Figure 8-37 (c) and (d) are bar chart representations of the maximum value of the SCRs T_{top}.

It could be observed that all constraint functions are satisfied except the compression limit for SCR-1 at span limit-2 station as shown in Figure 8-36 (b) and (d), where the T_{TDZ} in the SCR-1 TDZ was less than 85kN. $T_{TDZ} \geq 0$ kN can be specified as the compression limit around the SCR TDZ, but to allow for safety margins, we have set this limit to $T_{TDZ} \geq 85$ kN. Once the results have been post-processed, the index matching technique (applied for the optimisation process) provides the flexibility to the user or the design engineer to reset these constraint limits based on design standards and client specifications, without the need for re-simulation.

The relocation programs dependent on the unfeasible symmetric relocation patterns (shaded red) are supposed to be eliminated from the solution process if only symmetric relocation patterns were to be considered for the problem. However, in this screening analysis, we explore the opportunity to identify the infeasible symmetric relocation patterns and modify their span limits, thereby converting or degenerating them to non-symmetric but feasible relocation

patterns. This increases the potential of obtaining non-symmetric relocation programs that could be a good solution to the problem. To conduct this conversion process, if any symmetric span limit station pair is unfeasible, the next possible lower span limit pair are considered. For example, consider the unfeasible symmetric span limit pair ID {95,95} in Table 8-15 (c); this pair being feasible at span limit-1, will retain its ID {95,...}. However, because it is unfeasible at span limit 2, the ID {…,95} will be degenerated to the next lower feasible span radius along the same relocation axis ($\alpha = 120^o$), which in this case is ID {...,29}. Hence the unfeasible symmetric span limit pair ID {95,95} is now converted to a feasible non-symmetric span limit pair ID {95,29}, which corresponds to $\alpha = 120^o$, $R_1 = 16\%$, $R_2 = 5\%$. The same modification is applied for all unfeasible span limit pairs to derive the feasible span limit pair matrix presented in Table 8-15 (d). It is observed from Table 8-15 (d) that after the reduction process, some span limit station pairs are repeated (see the 16 cells shaded grey). Hence, we remove these duplicates from the design space to avoid repetition of simulation of relocation programs developed from them in the fatigue analysis stage.

The cells in Table 8-15 (d) (excluding the greyed cells) define the feasible span limit pairs for which the vessel relocation programs are generated, and optimisation simulations are conducted. The screening analysis removes the need to include the storm simulation during the optimisation process, where all candidate stations of all relocation programs are supposed to be simulated. Instead, with the feasible relocation patterns obtained from the screening process, only fatigue calculation (evaluation of the objective function) will be conducted. Recall from Figure 8-28, that for each span limit pair, there are four dependent relocation programs (p =3,5,7,9), with a total of 24 stations. By conducting the storm response analysis only for the span limit stations and removing 16 duplicated limit pairs after the modification, we eliminate the need to simulate (16 span limit pair duplications × 24 stations × 2 wave directions = 768) numerical fatigue models. Also, instead of the (120 span limits pairs × 24 stations × 2 wave directions = 5760) numerical storm models that would have been simulated during the optimisation simulation stage, only (2 × 120 span limit pairs × 2 storm wave direction = 480) numerical storm models are simulated at the screening stage. Hence, the screening exercise provides the opportunity to enlarge the optimisation space by including non-symmetric relocation programs and provide up to 47.5% reduction in the computation resource required for the vessel relocation optimisation problem.

Table 8-14. Coordinates and station IDs for symmetric relocation patterns: (a) Set of span limit-1 coordinates, (b) Set of span limit-2 coordinates, (c) integer ID representation for both sets of span limit-1 and span limit-2 stations, (d) ID pairs for span limit-1 and span limit-2 stations ((span limit-1, span limit-2)).

(a)

Axis (deg) \ R(%)	1	2	3	4	5	6	7	8	9	10	11	12	13	14	15	16	17	18	19	20
0	[-15,0]	[-30,0]	[-45,0]	[-60,0]	[-75,0]	[-90,0]	[-105,0]	[-120,0]	[-135,0]	[-150,0]	[-165,0]	[-180,0]	[-195,0]	[-210,0]	[-225,0]	[-240,0]	[-255,0]	[-270,0]	[-285,0]	[-300,0]
30	[-13,-8]	[-26,-15]	[-39,-23]	[-52,-30]	[-65,-38]	[-78,-45]	[-91,-53]	[-104,-60]	[-117,-68]	[-130,-75]	[-143,-83]	[-156,-90]	[-169,-98]	[-182,-105]	[-195,-113]	[-208,-120]	[-221,-128]	[-234,-135]	[-247,-143]	[-260,-150]
60	[-8,-13]	[-15,-26]	[-23,-39]	[-30,-52]	[-38,-65]	[-45,-78]	[-53,-91]	[-60,-104]	[-68,-117]	[-75,-130]	[-83,-143]	[-90,-156]	[-98,-169]	[-105,-182]	[-113,-195]	[-120,-208]	[-128,-221]	[-135,-234]	[-143,-247]	[-150,-260]
90	[-0,-15]	[-0,-30]	[-0,-45]	[-0,-60]	[-0,-75]	[-0,-90]	[-0,-105]	[-0,-120]	[-0,-135]	[-0,-150]	[-0,-165]	[-0,-180]	[-0,-195]	[-0,-210]	[-0,-225]	[-0,-240]	[-0,-255]	[-0,-270]	[-0,-285]	[-0,-300]
120	[8,-13]	[15,-26]	[23,-39]	[30,-52]	[38,-65]	[45,-78]	[53,-91]	[60,-104]	[68,-117]	[75,-130]	[83,-143]	[90,-156]	[98,-169]	[105,-182]	[113,-195]	[120,-208]	[128,-221]	[135,-234]	[143,-247]	[150,-260]
150	[13,-8]	[26,-15]	[39,-23]	[52,-30]	[65,-38]	[78,-45]	[91,-53]	[104,-60]	[117,-68]	[130,-75]	[143,-83]	[156,-90]	[169,-98]	[182,-105]	[195,-113]	[208,-120]	[221,-128]	[234,-135]	[247,-143]	[260,-150]

(b)

Axes (deg) \ R(%)	1	2	3	4	5	6	7	8	9	10	11	12	13	14	15	16	17	18	19	20
0	[15,0]	[30,0]	[45,0]	[60,0]	[75,0]	[90,0]	[105,0]	[120,0]	[135,0]	[150,0]	[165,0]	[180,0]	[195,0]	[210,0]	[225,0]	[240,0]	[255,0]	[270,0]	[285,0]	[300,0]
30	[13,8]	[26,15]	[39,23]	[52,30]	[65,38]	[78,45]	[91,53]	[104,60]	[117,68]	[130,75]	[143,83]	[156,90]	[169,98]	[182,105]	[195,113]	[208,120]	[221,128]	[234,135]	[247,143]	[260,150]
60	[8,13]	[15,26]	[23,39]	[30,52]	[38,65]	[45,78]	[53,91]	[60,104]	[68,117]	[75,130]	[83,143]	[90,156]	[98,169]	[105,182]	[113,195]	[120,208]	[128,221]	[135,234]	[143,247]	[150,260]
90	[0,15]	[0,30]	[0,45]	[0,60]	[0,75]	[0,90]	[0,105]	[0,120]	[0,135]	[0,150]	[0,165]	[0,180]	[0,195]	[0,210]	[0,225]	[0,240]	[0,255]	[0,270]	[0,285]	[0,300]
120	[-8,13]	[-15,26]	[-23,39]	[-30,52]	[-38,65]	[-45,78]	[-53,91]	[-60,104]	[-68,117]	[-75,130]	[-83,143]	[-90,156]	[-98,169]	[-105,182]	[-113,195]	[-120,208]	[-128,221]	[-135,234]	[-143,247]	[-150,260]
150	[-13,8]	[-26,15]	[-39,23]	[-52,30]	[-65,38]	[-78,45]	[-91,53]	[-104,60]	[-117,68]	[-130,75]	[-143,83]	[-156,90]	[-169,98]	[-182,105]	[-195,113]	[-208,120]	[-221,128]	[-234,135]	[-247,143]	[-260,150]

(c)

Axes (deg)	1	2	3	4	5	6	7	8	9	10	11	12	13	14	15	16	17	18	19	20
0	{1}	{7}	{13}	{19}	{25}	{31}	{37}	{43}	{49}	{55}	{61}	{67}	{73}	{79}	{85}	{91}	{97}	{103}	{109}	{115}
30	{2}	{8}	{14}	{20}	{26}	{32}	{38}	{44}	{50}	{56}	{62}	{68}	{74}	{80}	{86}	{92}	{98}	{104}	{110}	{116}
60	{3}	{9}	{15}	{21}	{27}	{33}	{39}	{45}	{51}	{57}	{63}	{69}	{75}	{81}	{87}	{93}	{99}	{105}	{111}	{117}
90	{4}	{10}	{16}	{22}	{28}	{34}	{40}	{46}	{52}	{58}	{64}	{70}	{76}	{82}	{88}	{94}	{100}	{106}	{112}	{118}
120	{5}	{11}	{17}	{23}	{29}	{35}	{41}	{47}	{53}	{59}	{65}	{71}	{77}	{83}	{89}	{95}	{101}	{107}	{113}	{119}
150	{6}	{12}	{18}	{24}	{30}	{36}	{42}	{48}	{54}	{60}	{66}	{72}	{78}	{84}	{90}	{96}	{102}	{108}	{114}	{120}

(d)

Axes (deg) \ R(%)	1	2	3	4	5	6	7	8	9	10	11	12	13	14	15	16	17	18	19	20
0	{1,1}	{7,7}	{13,13}	{19,19}	{25,25}	{31,31}	{37,37}	{43,43}	{49,49}	{55,55}	{61,61}	{67,67}	{73,73}	{79,79}	{85,85}	{91,91}	{97,97}	{103,103}	{109,109}	{115,115}
30	{2,2}	{8,8}	{14,14}	{20,20}	{26,26}	{32,32}	{38,38}	{44,44}	{50,50}	{56,56}	{62,62}	{68,68}	{74,74}	{80,80}	{86,86}	{92,92}	{98,98}	{104,104}	{110,110}	{116,116}
60	{3,3}	{9,9}	{15,15}	{21,21}	{27,27}	{33,33}	{39,39}	{45,45}	{51,51}	{57,57}	{63,63}	{69,69}	{75,75}	{81,81}	{87,87}	{93,93}	{99,99}	{105,105}	{111,111}	{117,117}
90	{4,4}	{10,10}	{16,16}	{22,22}	{28,28}	{34,34}	{40,40}	{46,46}	{52,52}	{58,58}	{64,64}	{70,70}	{76,76}	{82,82}	{88,88}	{94,94}	{100,100}	{106,106}	{112,112}	{118,118}
120	{5,5}	{11,11}	{17,17}	{23,23}	{29,29}	{35,35}	{41,41}	{47,47}	{53,53}	{59,59}	{65,65}	{71,71}	{77,77}	{83,83}	{89,89}	{95,95}	{101,101}	{107,107}	{113,113}	{119,119}
150	{6,6}	{12,12}	{18,18}	{24,24}	{30,30}	{36,36}	{42,42}	{48,48}	{54,54}	{60,60}	{66,66}	{72,72}	{78,78}	{84,84}	{90,90}	{96,96}	{102,102}	{108,108}	{114,114}	{120,120}

Table 8-15. Relocation pattern feasibility matrices: (a)Feasibility matrix for the 6 SCRs at span limit-1 stations, (b) Feasibility matrix for the 6 SCRs at span limit-2 stations, (c) Span limit ID pair feasibility matrix for symmetric relocation patterns, (d) Modified symmetric span limit ID pair now containing non-symmetric relocation patterns.

(a)

Axes (deg) \ R(%)	1	2	3	4	5	6	7	8	9	10	11	12	13	14	15	16	17	18	19	20
0	[1,1,1,1,1,1]	[1,1,1,1,1,1]	[1,1,1,1,1,1]	[1,1,1,1,1,1]	[1,1,1,1,1,1]	[0,1,1,1,1,1]	[0,1,1,1,1,1]	[0,1,1,1,1,1]	[0,1,1,1,1,1]	[0,1,0,1,1,1]	[0,1,0,1,1,1]	[0,1,0,1,1,1]	[0,0,0,1,1,1]	[0,0,0,1,1,1]	[0,0,0,1,1,1]	[0,0,0,1,1,1]	[0,0,0,1,1,1]	[0,0,0,1,1,1]	[0,0,0,1,1,1]	[0,0,0,1,1,1]
30	[1,1,1,1,1,1]	[1,1,1,1,1,1]	[1,1,1,1,1,1]	[1,1,1,1,1,1]	[1,1,1,1,1,1]	[1,1,1,1,1,1]	[1,1,1,1,1,1]	[1,1,1,1,1,1]	[1,1,1,1,1,1]	[0,1,1,1,1,1]	[0,1,0,1,1,1]	[0,1,0,1,1,1]	[0,1,0,1,1,1]	[0,1,0,1,1,1]	[0,1,0,1,1,1]	[0,1,0,1,1,1]	[0,1,0,1,1,1]	[0,0,0,1,1,1]	[0,0,0,1,1,1]	[0,0,0,1,1,1]
60	[1,1,1,1,1,1]	[1,1,1,1,1,1]	[1,1,1,1,1,1]	[1,1,1,1,1,1]	[1,1,1,1,1,1]	[1,1,1,1,1,1]	[1,1,1,1,1,1]	[1,1,1,1,1,1]	[1,1,1,1,1,1]	[1,1,1,1,1,1]	[1,1,1,1,1,1]	[1,1,1,1,1,1]	[1,1,1,1,1,1]	[1,1,1,1,1,1]	[1,1,1,1,1,1]	[1,1,1,1,1,1]	[1,1,1,1,1,1]	[1,1,0,1,1,1]	[1,1,0,1,1,1]	[1,1,0,1,1,1]
90	[1,1,1,1,1,1]	[1,1,1,1,1,1]	[1,1,1,1,1,1]	[1,1,1,1,1,1]	[1,1,1,1,1,1]	[1,1,1,1,1,1]	[1,1,1,1,1,1]	[1,1,1,1,1,1]	[1,1,1,1,1,1]	[1,1,1,1,1,1]	[1,1,1,1,1,1]	[1,1,1,1,1,1]	[1,1,1,1,1,1]	[1,1,1,1,1,1]	[1,1,1,1,1,1]	[1,1,1,1,1,1]	[1,1,1,1,1,1]	[1,1,1,1,1,1]	[1,1,1,1,1,1]	[1,1,1,1,1,1]
120	[1,1,1,1,1,1]	[1,1,1,1,1,1]	[1,1,1,1,1,1]	[1,1,1,1,1,1]	[1,1,1,1,1,1]	[1,1,1,1,1,1]	[1,1,1,1,1,1]	[1,1,1,1,1,1]	[1,1,1,1,1,1]	[1,1,1,1,1,1]	[1,1,1,1,1,1]	[1,1,1,1,1,1]	[1,1,1,1,1,1]	[1,1,1,1,1,1]	[1,1,1,1,1,1]	[1,1,1,1,1,1]	[1,1,1,1,1,1]	[1,1,1,1,1,1]	[1,1,1,1,1,1]	[1,1,1,1,1,1]
150	[1,1,1,1,1,1]	[1,1,1,1,1,1]	[1,1,1,1,1,1]	[1,1,1,1,1,1]	[1,1,1,1,1,1]	[1,1,1,1,1,1]	[1,1,1,1,1,1]	[1,1,1,1,1,1]	[1,1,1,1,1,1]	[1,1,1,1,1,1]	[1,1,1,1,1,1]	[1,1,1,1,1,1]	[1,1,1,1,1,1]	[1,1,1,1,1,1]	[1,1,1,1,1,1]	[1,1,1,1,0,1]	[1,1,1,0,0,1]	[1,1,1,0,0,1]	[1,1,1,0,0,1]	[1,1,1,0,0,1]

(b)

Axes (deg) \ R(%)	1	2	3	4	5	6	7	8	9	10	11	12	13	14	15	16	17	18	19	20
0	[1,1,1,1,1,1]	[1,1,1,1,1,1]	[1,1,1,1,1,1]	[1,1,1,1,1,1]	[1,1,1,1,1,1]	[1,1,1,1,1,1]	[1,1,1,1,1,1]	[1,1,1,1,1,1]	[1,1,1,1,1,1]	[1,1,1,1,1,1]	[1,1,1,1,1,1]	[1,1,1,1,1,1]	[1,1,1,1,1,1]	[1,1,1,1,1,1]	[1,1,1,1,0,0]	[1,1,1,1,0,0]	[1,1,1,1,0,0]	[1,1,1,1,0,0]	[1,1,1,1,0,0]	[1,1,1,1,0,0]
30	[1,1,1,1,1,1]	[1,1,1,1,1,1]	[1,1,1,1,1,1]	[1,1,1,1,1,1]	[1,1,1,1,1,1]	[1,1,1,1,1,1]	[1,1,1,1,1,1]	[1,1,1,1,1,1]	[1,1,1,1,1,1]	[1,1,1,1,1,1]	[1,1,1,1,1,1]	[1,1,1,1,1,1]	[1,1,1,1,1,1]	[1,1,1,1,1,1]	[1,1,1,1,1,1]	[1,1,1,1,1,0]	[1,1,1,1,1,0]	[1,1,1,1,1,0]	[1,1,1,1,1,0]	[1,1,1,1,1,0]
60	[1,1,1,1,1,1]	[1,1,1,1,1,1]	[1,1,1,1,1,1]	[1,1,1,1,1,1]	[1,1,1,1,1,1]	[1,1,1,1,1,1]	[1,1,1,1,1,1]	[1,1,1,1,1,1]	[1,1,1,1,1,1]	[1,1,1,1,1,1]	[1,1,1,1,1,1]	[1,1,1,1,1,1]	[1,1,1,1,1,1]	[1,1,1,1,1,1]	[1,1,1,1,1,1]	[1,1,1,1,1,1]	[1,1,1,1,1,1]	[1,1,1,1,1,1]	[1,1,1,1,1,1]	[1,1,1,1,1,1]
90	[1,1,1,1,1,1]	[1,1,1,1,1,1]	[1,1,1,1,1,1]	[1,1,1,1,1,1]	[1,1,1,1,1,1]	[1,1,1,1,1,1]	[1,1,1,1,1,1]	[1,1,1,1,1,1]	[1,1,1,1,1,1]	[1,1,1,1,1,1]	[1,1,1,1,1,1]	[1,1,1,1,1,1]	[0,1,1,1,1,1]	[0,1,1,1,1,1]	[0,1,1,1,1,1]	[0,1,1,1,1,1]	[0,1,1,1,1,1]	[0,1,1,1,1,1]	[0,1,1,1,1,1]	[0,1,1,1,1,1]
120	[1,1,1,1,1,1]	[1,1,1,1,1,1]	[1,1,1,1,1,1]	[1,1,1,1,1,1]	[1,1,1,1,1,1]	[0,1,1,1,1,1]	[0,1,1,1,1,1]	[0,1,1,1,1,1]	[0,1,1,1,1,1]	[0,1,1,1,1,1]	[0,1,1,1,1,1]	[0,1,1,1,1,1]	[0,1,1,1,1,1]	[0,1,1,1,1,1]	[0,1,1,1,1,1]	[0,1,1,1,1,1]	[0,1,1,1,1,1]	[0,1,1,1,1,1]	[0,1,1,1,1,1]	[0,1,1,1,1,1]
150	[1,1,1,1,1,1]	[1,1,1,1,1,1]	[1,1,1,1,1,1]	[1,1,1,1,1,1]	[0,1,1,1,1,1]	[0,1,1,1,1,1]	[0,1,1,1,1,1]	[0,1,1,1,1,1]	[0,1,1,1,1,1]	[0,1,1,1,1,1]	[0,1,1,1,1,1]	[0,1,1,1,1,1]	[0,1,1,1,1,1]	[0,1,1,1,1,1]	[0,1,0,1,1,1]	[0,1,0,1,1,1]	[0,1,0,1,1,1]	[0,0,0,1,1,1]	[0,0,0,1,1,1]	[0,0,0,1,1,1]

(c)

Axes (deg) \ R(%)	1	2	3	4	5	6	7	8	9	10	11	12	13	14	15	16	17	18	19	20
0	{1,1}	{7,7}	{13,13}	{19,19}	{25,25}	{31,31}	{37,37}	{43,43}	{49,49}	{55,55}	{61,61}	{67,67}	{73,73}	{79,79}	{85,85}	{91,91}	{97,97}	{103,103}	{109,109}	{115,115}
30	{2,2}	{8,8}	{14,14}	{20,20}	{26,26}	{32,32}	{38,38}	{44,44}	{50,50}	{56,56}	{62,62}	{68,68}	{74,74}	{80,80}	{86,86}	{92,92}	{98,98}	{104,104}	{110,110}	{116,116}
60	{3,3}	{9,9}	{15,15}	{21,21}	{27,27}	{33,33}	{39,39}	{45,45}	{51,51}	{57,57}	{63,63}	{69,69}	{75,75}	{81,81}	{87,87}	{93,93}	{99,99}	{105,105}	{111,111}	{117,117}
90	{4,4}	{10,10}	{16,16}	{22,22}	{28,28}	{34,34}	{40,40}	{46,46}	{52,52}	{58,58}	{64,64}	{70,70}	{76,76}	{82,82}	{88,88}	{94,94}	{100,100}	{106,106}	{112,112}	{118,118}
120	{5,5}	{11,11}	{17,17}	{23,23}	{29,29}	{35,35}	{41,41}	{47,47}	{53,53}	{59,59}	{65,65}	{71,71}	{77,77}	{83,83}	{89,89}	{95,95}	{101,101}	{107,107}	{113,113}	{119,119}
150	{6,6}	{12,12}	{18,18}	{24,24}	{30,30}	{36,36}	{42,42}	{48,48}	{54,54}	{60,60}	{66,66}	{72,72}	{78,78}	{84,84}	{90,90}	{96,96}	{102,102}	{108,108}	{114,114}	{120,120}

(d)

Axes (deg) \ R(%)	1	2	3	4	5	6	7	8	9	10	11	12	13	14	15	16	17	18	19	20
0	{1,1}	{7,7}	{13,13}	{19,19}	{25,25}	{25,31}	{25,37}	{25,43}	{25,49}	{25,55}	{25,61}	{25,67}	{25,73}	{25,79}	{25,25}	{25,25}	{25,25}	{25,25}	{25,25}	{25,25}
30	{2,2}	{8,8}	{14,14}	{20,20}	{26,26}	{32,32}	{38,38}	{44,44}	{50,50}	{50,56}	{50,62}	{50,68}	{50,74}	{50,80}	{50,86}	{50,50}	{50,50}	{50,50}	{50,50}	{50,50}
60	{3,3}	{9,9}	{15,15}	{21,21}	{27,27}	{33,33}	{39,39}	{45,45}	{51,51}	{57,57}	{63,63}	{69,69}	{75,75}	{81,81}	{87,87}	{93,93}	{99,99}	{99,105}	{99,111}	{99,117}
90	{4,4}	{10,10}	{16,16}	{22,22}	{28,28}	{34,34}	{40,40}	{46,46}	{52,52}	{58,58}	{64,64}	{70,70}	{76,64}	{82,64}	{88,64}	{94,64}	{100,64}	{106,64}	{112,64}	{118,64}
120	{5,5}	{11,11}	{17,17}	{23,23}	{29,29}	{35,29}	{41,29}	{47,29}	{53,29}	{59,29}	{65,29}	{71,29}	{77,29}	{83,29}	{89,29}	{95,29}	{101,29}	{107,29}	{113,29}	{119,29}
150	{6,6}	{12,12}	{18,18}	{24,24}	{30,24}	{36,24}	{42,24}	{48,24}	{54,24}	{60,24}	{66,24}	{72,24}	{78,24}	{84,24}	{90,24}	{90,24}	{90,24}	{90,24}	{90,24}	{90,24}

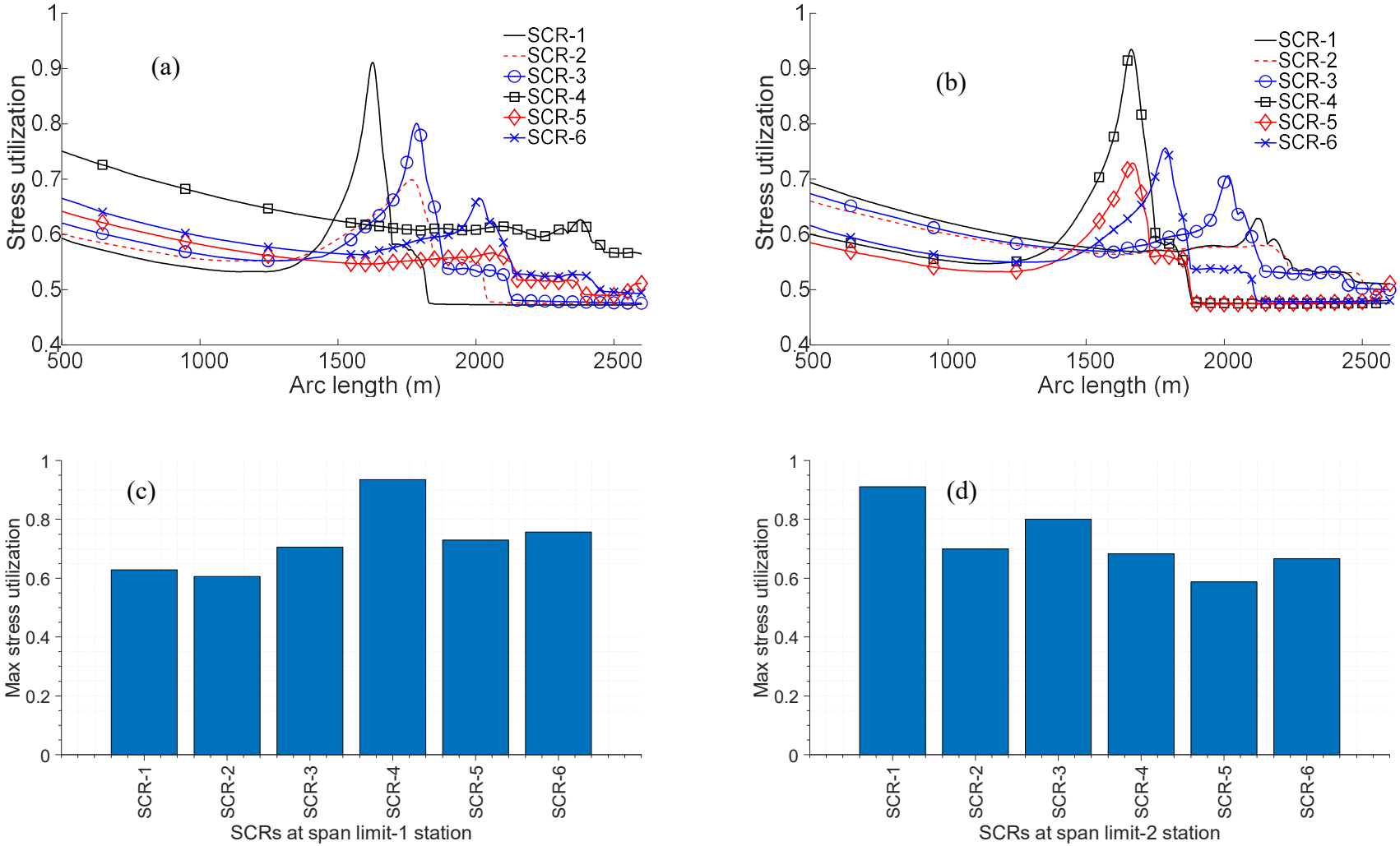

Figure 8-35. TDZ stress utilization at span limit station pair (station pair ID {95,95}): (a) range graph maximum at span limit-1 station, (b) range graph maximum at span limit-2 station, (c) Maximum values at span limit-1 station, (d) Maximum values at span limit-2 station.

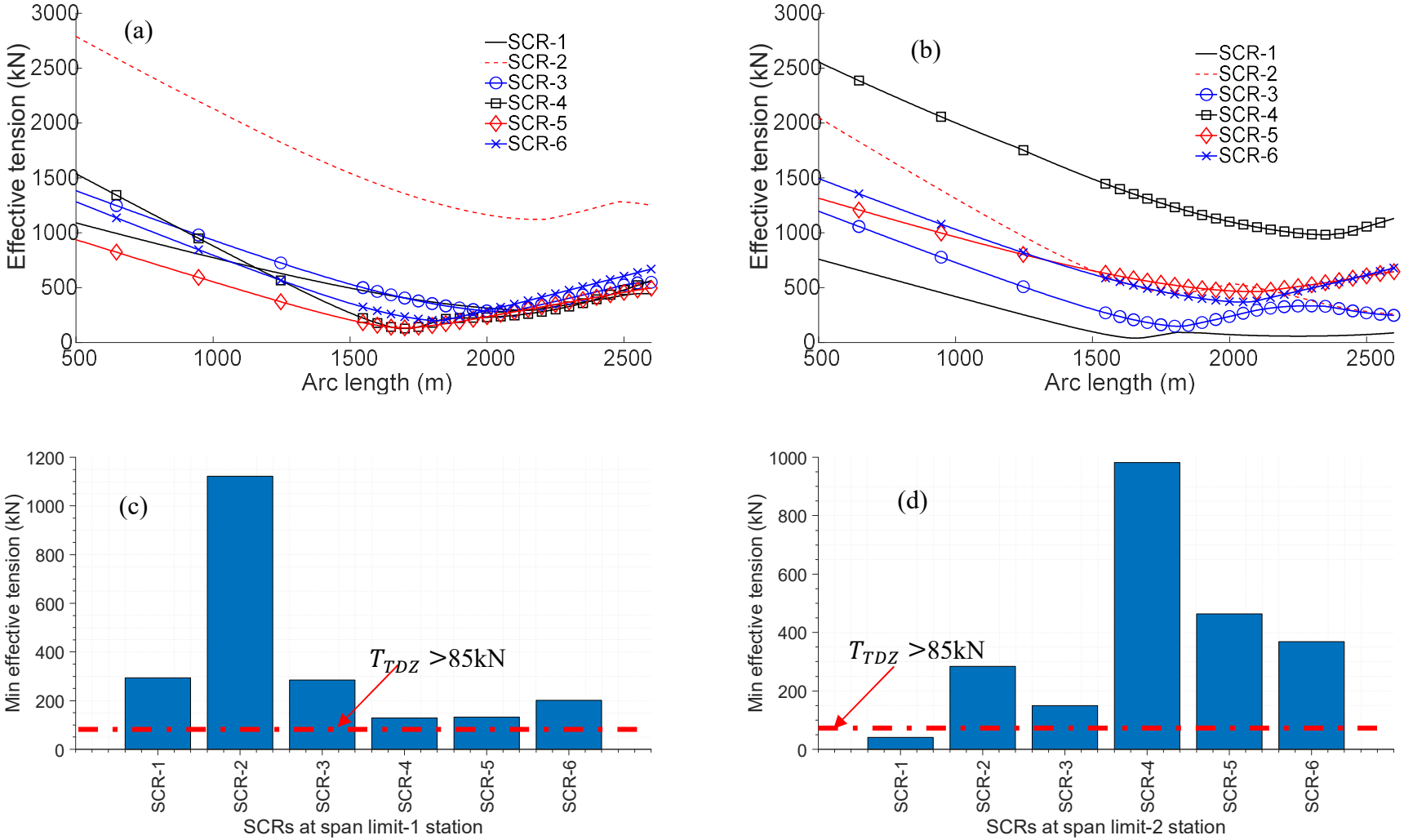

Figure 8-36. TDZ compression at span limit station pair (station pair ID {95,95}): (a) range graph minimum at span limit-1 station, (b) range graph minimum at span limit-2 station, (c) Minimum values at span limit-1 station, (d) Minimum values at span limit-2 station.

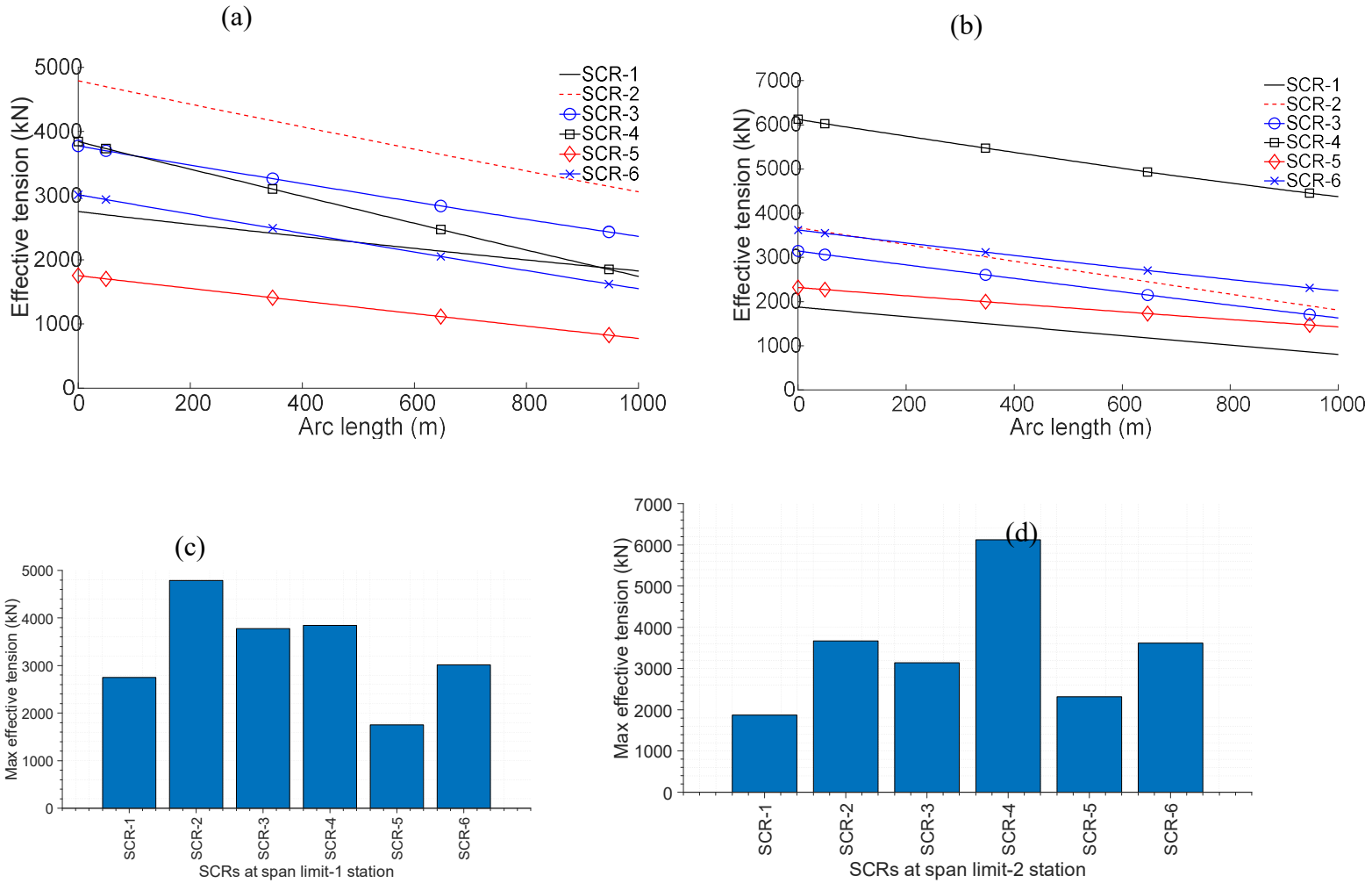

Figure 8-37. Top tension at span limit station pair (station pair ID {95,95}): (a) range graph maximum at span limit-1 station, (b) range graph maximum at span limit-2 station, (c) Maximum values at span limit-1 station, (d) Maximum values at span limit-2 station.

*Note from equation (8-17) that the limit on the maximum top tension constraints for the 6 SCRs are ≈ [7883,15450,11351,15450,7883,11351] kN

8.2.4.2 The global and ideal optimum relocation programs

In section 3.4, two methods were developed for the index matching optimisation technique to obtain families of optimum relocation programs. The global optimum relocation programs presented in this section are computed based on these two methods. Results obtained by the two methods are also compared in this section.

8.2.4.2.1 Method 1 solutions – Construction of a global objective function

The solution method detailed in section 8.2.3.3.1 creates a normalised global objective function (F^{nom}), which jointly represents the six SCR objective functions, $\left(D_{eff}\right)_j$, where *j*=1 to 6. The normalised effective fatigue damage, F^{nom}, is only representative of the effective fatigue damage for the SCRs' TDZ. It is used by the index matching optimisation technique to track the optimum relocation programs' indices. From the obtained index set, the actual effective damage response of the 6 SCRs can then be matched and reported. For this study, the parameters required to calculate F^{nom} are obtained and presented in Table 8-16.

Table 8-16. Parameters for calculating the normalised global objective function ($\boldsymbol{F^{nom}}$).

Parameters	**SCR-1** ($j=1$)	**SCR-2** ($j=2$)	**SCR-3** ($j=3$)	**SCR-4** ($j=4$)	**SCR-5** ($j=5$)	**SCR-6** ($j=6$)
$\left(D_{eff}\right)_j^{max}$(/yr)	4.76E-05	2.64E-06	1.15E-04	1.39E-04	1.63E-06	4.57E-05
$\left(D_{eff}\right)_j^{min}$(/yr)	7.89E-06	4.17E-07	2.26E-05	2.70E-05	3.56E-07	8.38E-06
$\sum_{j=1}^{6}\left(D_{eff}\right)_j^{max}$ (/yr)	3.52E-04					
$\sum_{j=1}^{6}\left(D_{eff}\right)_j^{min}$ (/yr)	6.66E-05					
a_j^{max}	0.1353	0.0075	0.3271	0.3957	0.0046	0.129845
a_j^{min}	0.1184	0.0063	0.3393	0.4049	0.0054	0.125821

Applying the index matching optimisation technique on the computed F^{nom} based on the two options of $a_j^{max}$and a_j^{min}, the first 20 global optimum relocation programs are obtained and presented in Table 8-18. Fatigue damage in the six SCR TDZ for the "no vessel relocation" case.

S/N	Index	$[\alpha, R_1, R_2, p]$ [(-), (%), (%), (deg)]	F^{nom} (/yr)	Fatigue damage for each SCRs' TDZ					
				SCR-1	SCR-2	SCR-3	SCR-4	SCR-5	SCR-6
1	NA	NA	NA	4.96E-05	2.63E-06	1.21E-04	1.39E-04	2.26E-06	4.68E-05

Table 8-19. The following are details of the columns of Table 8-18. Fatigue damage in the six SCR TDZ for the "no vessel relocation" case.

S/N	Index	$[\alpha, R_1, R_2, p]$ [(-), (%), (%), (deg)]	F^{nom} (/yr)	Fatigue damage for each SCRs' TDZ					
				SCR-1	SCR-2	SCR-3	SCR-4	SCR-5	SCR-6
1	NA	NA	NA	4.96E-05	2.63E-06	1.21E-04	1.39E-04	2.26E-06	4.68E-05

Table 8-19.

- The "S/N" column indicates the position of each of the relocation programs in decreasing order of performance of the normalised global objective function, F^{nom}.
- The "Index" column is the unique index representation of the relocation programs used to track the family members of the global optimum relocation programs.
- The "$[p, R_1, R_2, \alpha]$" column contains the coordinates or design points of the relocation programs. These are the optimisation design variables for the vessel relocation optimisation analysis. Recall that the span limit of any relocation program is defined by the span radii R_1 and R_2 on both sides of the nominal station. For $R_1 = R_2$ the relocation program is symmetrical, i.e., the span limit stations are equidistant from the nominal station. For $R_1 \neq R_2$, the relocation program is non-symmetrical, i.e., the span limit stations for the relocation program are not equidistant from the nominal station.
- The "F^{nom}" column is the normalised joint global objective function. As seen in Table 8-17, the values of F^{nom} appear in increasing order, with the minimum at the top.

It could be observed that the index representation of the global optimum solutions matches closely for the F^{nom} calculated based on a_j^{max} and a_j^{min}, with a few mismatches as one

progresses down the index columns. A more intuitive comparison of F^{nom} from the two weighting options is presented in Figure 8-38, where it is seen that the order of index solutions for the first 20 global optimum relocation programs matches, except S/N 4 and 5 (relocation program index-72 and index-100). From Table 8-17 and Figure 8-38, it could be seen that the solutions are less sensitive to which options of a_j^{max} or a_j^{min} is used for the calculation process in method-1. Hence, the F^{nom} calculated from a_j^{max} will be considered. The effective damage $(D_{eff})_j$ of the six SCRs are obtained by matching corresponding indices of F^{nom} to the effective fatigue damage data. These are presented in Table 8-18. Fatigue damage in the six SCR TDZ for the "no vessel relocation" case.

S/N	Index	$[\alpha, R_1, R_2, p]$ [(-), (%), (%), (deg)]	F^{nom} (/yr)	Fatigue damage for each SCRs' TDZ					
				SCR-1	SCR-2	SCR-3	SCR-4	SCR-5	SCR-6
1	NA	NA	NA	4.96E-05	2.63E-06	1.21E-04	1.39E-04	2.26E-06	4.68E-05

Table 8-19. It could be seen from Table 8-18. Fatigue damage in the six SCR TDZ for the "no vessel relocation" case.

S/N	Index	$[\alpha, R_1, R_2, p]$ [(-), (%), (%), (deg)]	F^{nom} (/yr)	Fatigue damage for each SCRs' TDZ					
				SCR-1	SCR-2	SCR-3	SCR-4	SCR-5	SCR-6
1	NA	NA	NA	4.96E-05	2.63E-06	1.21E-04	1.39E-04	2.26E-06	4.68E-05

Table 8-19 that while the F^{nom} column contains values in increasing order (the minimum at the top), this is not guaranteed for the D_{eff} columns of the 6 SCRs. This of course is a peculiar feature of a multi-objective optimisation problem, where a good global solution is likely not to be the best solution across all the objectives but one that assigns weighted consideration to them. However, the performance of these D_{eff} values compared with the no vessel relocation case will prove the effectiveness of the vessel relocation strategy for multiple SCRs. This will be discussed shortly. The fatigue damage for the 6 SCRs for the no vessel relocation case is presented in Table 8-18. The "no vessel relocation" is where the vessel is kept at the nominal

station without vessel offsets. It represents the traditional way of conducting SCR fatigue analysis.

8.2.4.2.2 Method 2 solutions – Intersection of the index systems of the Ideal solutions

The results obtain using method-2 is presented in Table 8-20, which contains the ideal optimum solutions for each of the 6 SCRs with their corresponding design variables, $[\alpha, R_1, R_2, p]$ and effective fatigue damage, D_{eff}. The individual ideal solutions are the family of optimum relocation programs obtained considering each objective function, $\left(D_{eff}\right)_j$ exclusively. This means, within the feasible design, a given $\left(D_{eff}\right)_j$ is obtained without considerations of the influence from other objective functions. Technically, this is a single objective optimisation problem for the objective function in question. As such, there will be 6 independent families of ideal solutions for the six SCRs presented in the columns of Table 8-20. It is observed from Table 8-20 that the best (top) ideal optimum relocation program for each objective function is different except for SCR- 1 and SCR-3, which have a common best ideal optimum relocation program (index-356) characterised by the design variables, $[\alpha, R_1, R_2, p] = [150^o, 15\%, 4\%, 9]$. However, as we progress down the columns, order of members of ideal solutions for SCR-1 and SCR-3 differs. The family of global optimum relocation programs are obtained by conducting the intersections of the index columns $[I_1', I_2', I_3', I_4', I_5', I_6']$, q row at a time, as discussed in section 8.2.3.3.2 and demonstrated in Figure 8-29 (b). As one progresses down the columns, there appear not to be any intersection until q =34, where index-148 appeared. Going further down the columns result in more intersection of relocation program indices. However, we truncate the table after the first 20 intersections where obtained. Please note that the table's text size has been reduced to fit on one page, and some rows containing repetitions of intersected indices have been removed from the presented q rows for brevity. It is of interest to investigate the performance comparison of the global optimum relocation programs with the ideal optimum relocation program and the "no vessel relocation" case. This will be discussed shortly.

Table 8-17. The first 20 family of global optimum relocation programs.

F^{nom} calculated using a_j^{max}	F^{nom} calculated using a_j^{min}

S/N	Index	$[\alpha, R_1, R_2, p]$ [(-), (%), (%), (deg)]	F^{nom} (/yr)	Index	$[\alpha, R_1, R_2, p]$ [(-), (%), (%), (deg)]	F^{nom} (/yr)
1	76	[0,4,4,9]	0.018362	76	[0,4,4,9]	0.018413
2	96	[150,4,4,9]	0.026558	96	[150,4,4,9]	0.026776
3	52	[0,3,3,9]	0.036916	52	[0,3,3,9]	0.036366
4	100	[0,5,5,9]	0.039671	72	[150,3,3,9]	0.039625
5	72	[150,3,3,9]	0.040425	100	[0,5,5,9]	0.03989
6	124	[0,5,6,9]	0.04144	124	[0,5,6,9]	0.041289
7	104	[30,5,5,9]	0.044943	104	[30,5,5,9]	0.044615
8	148	[0,5,7,9]	0.047302	148	[0,5,7,9]	0.046814
9	80	[30,4,4,9]	0.048734	80	[30,4,4,9]	0.0482
10	128	[30,6,6,9]	0.049725	128	[30,6,6,9]	0.049464
11	120	[150,5,4,9]	0.053831	120	[150,5,4,9]	0.052608
12	152	[30,7,7,9]	0.064608	152	[30,7,7,9]	0.064302
13	116	[120,5,5,9]	0.068294	116	[120,5,5,9]	0.067108
14	51	[0,3,3,7]	0.074796	51	[0,3,3,7]	0.075049
15	95	[150,4,4,7]	0.078031	95	[150,4,4,7]	0.078536
16	75	[0,4,4,7]	0.078471	75	[0,4,4,7]	0.078555
17	192	[150,8,4,9]	0.082259	192	[150,8,4,9]	0.080732
18	144	[150,6,4,9]	0.082992	144	[150,6,4,9]	0.082813
19	147	[0,5,7,7]	0.083254	147	[0,5,7,7]	0.083076
20	176	[30,8,8,9]	0.084187	176	[30,8,8,9]	0.083529

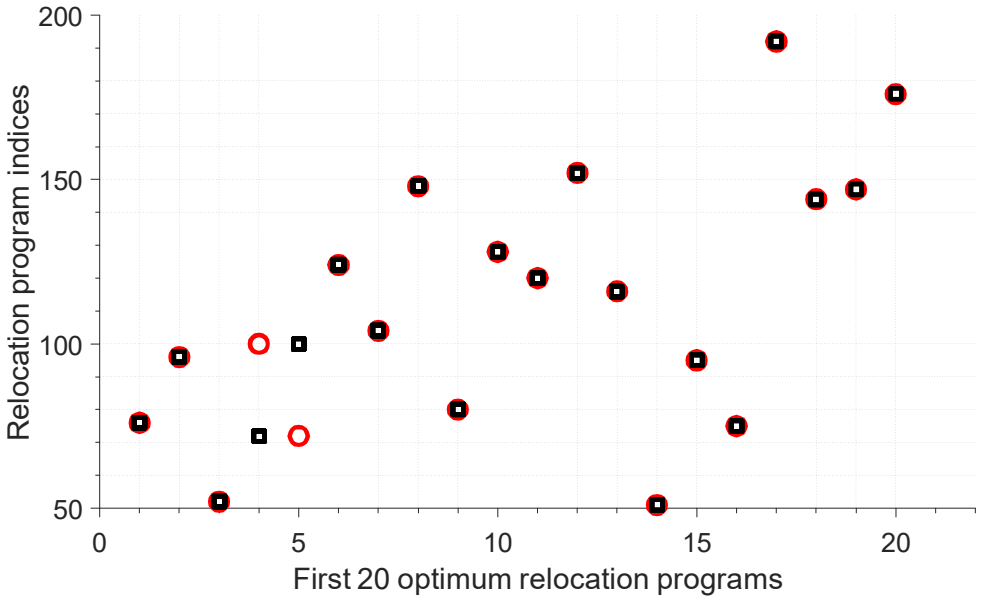

Figure 8-38. A matching plot of the first 20 members of the global optimum relocation program calculated based on the two weighting options, $\boldsymbol{a_j^{max}}$ and $\boldsymbol{a_j^{min}}$.

Table 8-18. Fatigue damage in the six SCR TDZ for the "no vessel relocation" case.

S/N	Index	$[\alpha, R_1, R_2, p]$ [(-), (%), (%), (deg)]	F^{nom} (/yr)	Fatigue damage for each SCRs' TDZ					
				SCR-1	SCR-2	SCR-3	SCR-4	SCR-5	SCR-6
1	NA	NA	NA	4.96E-05	2.63E-06	1.21E-04	1.39E-04	2.26E-06	4.68E-05

Table 8-19. Effective fatigue damage in the 6 SCR TDZ for the first 20 members of the optimum relocation programs (calculated from method 1).

S/N	Index	$[\alpha, R_1, R_2, p]$ [(-), (%), (%), (deg)]	F^{nom} (/yr)	Corresponding D_{eff} (/yr) for each SCRs' TDZ					
				SCR-1	SCR-2	SCR-3	SCR-4	SCR-5	SCR-6
1	76	[0,4,4,9]	0.018362	9.01E-06	4.66E-07	2.62E-05	2.70E-05	3.99E-07	8.81E-06
2	96	[150,4,4,9]	0.026558	9.89E-06	4.66E-07	2.62E-05	2.89E-05	3.99E-07	8.39E-06
3	52	[0,3,3,9]	0.036916	8.86E-06	4.66E-07	2.67E-05	3.21E-05	3.99E-07	8.38E-06
4	100	[0,5,5,9]	0.039671	1.02E-05	4.66E-07	2.87E-05	2.84E-05	3.99E-07	9.87E-06
5	72	[150,3,3,9]	0.040425	8.85E-06	4.66E-07	3.04E-05	2.93E-05	3.99E-07	8.45E-06
6	124	[0,5,6,9]	0.04144	9.25E-06	4.20E-07	2.55E-05	3.31E-05	3.57E-07	9.77E-06
7	104	[30,5,5,9]	0.044943	9.01E-06	4.66E-07	2.64E-05	3.29E-05	3.99E-07	1.01E-05
8	148	[0,5,7,9]	0.047302	8.65E-06	4.18E-07	2.79E-05	3.17E-05	3.58E-07	1.09E-05
9	80	[30,4,4,9]	0.048734	8.96E-06	4.66E-07	2.47E-05	3.66E-05	3.99E-07	9.13E-06
10	128	[30,6,6,9]	0.049725	9.21E-06	4.66E-07	2.93E-05	3.00E-05	3.99E-07	1.13E-05
11	120	[150,5,4,9]	0.053831	8.66E-06	4.23E-07	3.16E-05	3.19E-05	3.57E-07	8.67E-06
12	152	[30,7,7,9]	0.064608	9.74E-06	4.66E-07	3.26E-05	2.94E-05	3.99E-07	1.23E-05
13	116	[120,5,5,9]	0.068294	9.69E-06	4.67E-07	3.73E-05	2.85E-05	3.99E-07	9.36E-06
14	51	[0,3,3,7]	0.074796	1.15E-05	6.09E-07	2.97E-05	3.47E-05	5.21E-07	1.09E-05
15	95	[150,4,4,7]	0.078031	1.22E-05	6.09E-07	2.96E-05	3.52E-05	5.21E-07	1.09E-05
16	75	[0,4,4,7]	0.078471	1.15E-05	6.09E-07	3.17E-05	3.37E-05	5.21E-07	1.10E-05
17	192	[150,8,4,9]	0.082259	8.17E-06	4.23E-07	2.74E-05	4.24E-05	3.57E-07	1.07E-05
18	144	[150,6,4,9]	0.082992	1.14E-05	4.74E-07	3.26E-05	3.45E-05	3.90E-07	1.08E-05
19	147	[0,5,7,7]	0.083254	1.02E-05	5.29E-07	2.90E-05	3.70E-05	4.52E-07	1.31E-05
20	176	[30,8,8,9]	0.084187	9.89E-06	4.66E-07	3.68E-05	2.93E-05	3.99E-07	1.35E-05

Table 8-20. First 20 global optimum solutions obtained by conducting intersections of the index columns for the ideal solutions

	SCR-1			SCR-2			SCR-3			SCR-4			SCR-5			SCR-6			$\mathbf{I}_{opt} = \bigcap_{1}^{q}\{(\mathbf{I}')\}$ $\mathbf{I}' = [I'_1, I'_2, I'_3, I'_4, I'_5, I'_6]$
q	Index (I'_1)	$[\alpha, R_1, R_2, p]$ [(-), (%), (%), (deg)]	D_{eff}	Index (I'_2)	$[\alpha, R_1, R_2, p]$ [(-), (%), (%), (deg)]	D_{eff}	Index (I'_3)	$[\alpha, R_1, R_2, p]$ [(-), (%), (%), (deg)]	D_{eff}	Index (I'_3)	$[\alpha, R_1, R_2, p]$ [(-), (%), (%), (deg)]	D_{eff}	Index (I'_3)	$[\alpha, R_1, R_2, p]$ [(-), (%), (%), (deg)]	D_{eff}	Index (I'_3)	$[\alpha, R_1, R_2, p]$ [(-), (%), (%), (deg)]	D_{eff}	
1	356	[150,15,4,9]	7.89E-06	272	[30,9,12,9]	4.17E-07	356	[150,15,4,9]	2.26E-05	76	[0,4,4,9]	2.70E-05	404	[120,19,5,9]	3.56E-07	52	[0,3,3,9]	8.38E-06	[]
26	68	[120,3,3,9]	8.90E-06	316	[0,5,14,9]	4.43E-07	416	[120,20,5,9]	2.83E-05	280	[90,12,12,9]	3.22E-05	264	[150,11,4,9]	3.90E-07	119	[150,5,4,7]	1.08E-05	[]
32	296	[30,9,13,9]	9.06E-06	380	[120,17,5,9]	4.62E-07	128	[30,6,6,9]	2.93E-05	159	[90,7,7,7]	3.36E-05	96	[150,4,4,9]	3.99E-07	71	[150,3,3,7]	1.09E-05	[]
33	184	[90,8,8,9]	9.09E-06	360	[60,16,16,9]	4.66E-07	107	[60,5,5,7]	2.96E-05	75	[0,4,4,7]	3.37E-05	116	[120,5,5,9]	3.99E-07	95	[150,4,4,7]	1.09E-05	[]
34	308	[120,13,5,9]	9.10E-06	372	[60,17,17,9]	4.66E-07	95	[150,4,4,7]	2.96E-05	71	[150,3,3,7]	3.37E-05	76	[0,4,4,9]	3.99E-07	148	[0,5,7,9]	1.09E-05	[148]
37	272	[30,9,12,9]	9.16E-06	80	[30,4,4,9]	4.66E-07	240	[150,10,4,9]	2.99E-05	140	[120,6,5,9]	3.40E-05	104	[30,5,5,9]	3.99E-07	31	[30,2,2,7]	1.09E-05	[148]
38	128	[30,6,6,9]	9.21E-06	204	[60,9,9,9]	4.66E-07	79	[30,4,4,7]	2.99E-05	127	[30,6,6,7]	3.41E-05	72	[150,3,3,9]	3.99E-07	75	[0,4,4,7]	1.10E-05	[148]
39	124	[0,5,6,9]	9.25E-06	180	[60,8,8,9]	4.66E-07	55	[30,3,3,7]	3.01E-05	112	[90,5,5,9]	3.43E-05	80	[30,4,4,9]	3.99E-07	351	[120,15,5,7]	1.10E-05	[124,148]
40	48	[150,2,2,9]	9.27E-06	324	[60,14,14,9]	4.66E-07	196	[0,5,9,9]	3.01E-05	99	[0,5,5,7]	3.44E-05	128	[30,6,6,9]	3.99E-07	115	[120,5,5,7]	1.10E-05	[124,148]
41	208	[90,9,9,9]	9.30E-06	132	[60,6,6,9]	4.66E-07	404	[120,19,5,9]	3.02E-05	144	[150,6,4,9]	3.45E-05	152	[30,7,7,9]	3.99E-07	204	[60,9,9,9]	1.10E-05	[124,148]
42	232	[90,10,10,9]	9.32E-06	300	[60,13,13,9]	4.66E-07	72	[150,3,3,9]	3.04E-05	271	[30,9,12,7]	3.46E-05	92	[120,4,4,9]	3.99E-07	236	[120,10,5,9]	1.11E-05	[124,148]
43	248	[30,9,11,9]	9.36E-06	52	[0,3,3,9]	4.66E-07	123	[0,5,6,7]	3.04E-05	175	[30,8,8,7]	3.46E-05	176	[30,8,8,9]	3.99E-07	131	[60,6,6,7]	1.11E-05	[52,124,148]
46	116	[120,5,5,9]	9.69E-06	252	[60,11,11,9]	4.66E-07	171	[0,5,8,7]	3.14E-05	348	[90,15,11,9]	3.48E-05	228	[60,10,10,9]	3.99E-07	143	[150,6,4,7]	1.12E-05	[52,124,148]
47	152	[30,7,7,9]	9.74E-06	200	[30,9,9,9]	4.66E-07	312	[150,13,4,9]	3.14E-05	115	[120,5,5,7]	3.49E-05	252	[60,11,11,9]	3.99E-07	47	[150,2,2,7]	1.12E-05	[52,124,148]
48	364	[90,16,11,9]	9.75E-06	76	[0,4,4,9]	4.66E-07	316	[0,5,14,9]	3.14E-05	207	[90,9,9,7]	3.49E-05	180	[60,8,8,9]	3.99E-07	36	[60,2,2,9]	1.13E-05	[52,76,124,148]
49	96	[150,4,4,9]	9.89E-06	104	[30,5,5,9]	4.66E-07	120	[150,5,4,9]	3.16E-05	95	[150,4,4,7]	3.52E-05	276	[60,12,12,9]	3.99E-07	128	[30,6,6,9]	1.13E-05	[52,76,104,120,124,148]
50	176	[30,8,8,9]	9.89E-06	56	[30,3,3,9]	4.66E-07	83	[60,4,4,7]	3.16E-05	103	[30,5,5,7]	3.56E-05	300	[60,13,13,9]	3.99E-07	79	[30,4,4,7]	1.13E-05	[52,76,104,120,124,148]
51	291	[0,5,13,7]	9.97E-06	96	[150,4,4,9]	4.66E-07	75	[0,4,4,7]	3.17E-05	111	[90,5,5,7]	3.57E-05	324	[60,14,14,9]	3.99E-07	380	[120,17,5,9]	1.14E-05	[52,76,96,104,120,124,148]
52	263	[150,11,4,7]	9.97E-06	128	[30,6,6,9]	4.66E-07	103	[30,5,5,7]	3.20E-05	320	[30,9,14,9]	3.60E-05	56	[30,3,3,9]	3.99E-07	216	[150,9,4,9]	1.14E-05	[52,76,96,104,120,124,128,148]
53	355	[150,15,4,7]	9.97E-06	176	[30,8,8,9]	4.66E-07	228	[60,10,10,9]	3.21E-05	199	[30,9,9,7]	3.61E-05	344	[60,15,15,9]	3.99E-07	367	[120,16,5,7]	1.15E-05	[52,76,96,104,120,124,128,148]
54	287	[150,12,4,7]	9.98E-06	152	[30,7,7,9]	4.66E-07	355	[150,15,4,7]	3.22E-05	231	[90,10,10,7]	3.64E-05	156	[60,7,7,9]	3.99E-07	404	[120,19,5,9]	1.15E-05	[52,76,96,104,120,124,128,148]
55	315	[0,5,14,7]	9.98E-06	72	[150,3,3,9]	4.66E-07	392	[120,18,5,9]	3.22E-05	48	[150,2,2,9]	3.65E-05	372	[60,17,17,9]	3.99E-07	155	[60,7,7,7]	1.15E-05	[52,72,76,96,104,120,124,128,148]
56	335	[150,14,4,7]	9.98E-06	100	[0,5,5,9]	4.66E-07	264	[150,11,4,9]	3.25E-05	80	[30,4,4,9]	3.66E-05	360	[60,16,16,9]	3.99E-07	328	[90,14,11,9]	1.16E-05	[52,72,76,80,96,104,120,124,128,148]
86	347	[90,15,11,7]	1.05E-05	395	[60,17,19,7]	5.30E-07	351	[120,15,5,7]	3.50E-05	44	[120,2,2,9]	4.13E-05	247	[30,9,11,7]	4.52E-07	327	[90,14,11,7]	1.24E-05	[52,72,76,80,96,104,120,124,128,148]
87	327	[90,14,11,7]	1.05E-05	239	[150,10,4,7]	5.30E-07	272	[30,9,12,9]	3.50E-05	87	[90,4,4,7]	4.14E-05	171	[0,5,8,7]	4.52E-07	388	[90,18,11,9]	1.25E-05	[52,72,76,80,96,104,120,124,128,148]
88	139	[120,6,5,7]	1.05E-05	367	[120,16,5,7]	5.31E-07	368	[120,16,5,9]	3.50E-05	187	[120,8,5,7]	4.14E-05	143	[150,6,4,7]	4.52E-07	363	[90,16,11,7]	1.25E-05	[52,72,76,80,96,100,104,120,124,128,148]
89	303	[90,13,11,7]	1.06E-05	123	[0,5,6,7]	5.31E-07	179	[60,8,8,7]	3.51E-05	123	[0,5,6,7]	4.15E-05	163	[120,7,5,7]	4.52E-07	103	[30,5,5,7]	1.25E-05	[52,72,76,80,96,100,104,120,124,128,148]
90	200	[30,9,9,9]	1.06E-05	351	[120,15,5,7]	5.31E-07	143	[150,6,4,7]	3.51E-05	192	[150,8,4,9]	4.24E-05	123	[0,5,6,7]	4.52E-07	415	[120,20,5,7]	1.25E-05	[28,52,72,76,80,96,100,104,120,124,128,148]
92	319	[30,9,14,7]	1.07E-05	331	[120,14,5,7]	5.31E-07	276	[60,12,12,9]	3.55E-05	139	[120,6,5,7]	4.27E-05	283	[120,12,5,7]	4.52E-07	172	[0,5,8,9]	1.25E-05	[28,52,72,76,80,96,100,104,120,124,128,148]
93	339	[30,9,15,7]	1.08E-05	391	[120,18,5,7]	5.31E-07	319	[30,9,14,7]	3.55E-05	412	[90,20,11,9]	4.36E-05	415	[120,20,5,7]	4.52E-07	252	[60,11,11,9]	1.29E-05	[28,52,72,76,80,96,100,104,120,124,128,148]
94	295	[30,9,13,7]	1.08E-05	163	[120,7,5,7]	5.32E-07	243	[0,5,11,7]	3.55E-05	27	[0,2,2,7]	4.37E-05	407	[60,17,20,7]	4.53E-07	386	[90,18,11,5]	1.30E-05	[28,52,72,76,80,96,100,104,120,124,128,148,152]
101	399	[90,19,11,7]	1.14E-05	44	[120,2,2,9]	5.35E-07	27	[0,2,2,7]	3.65E-05	236	[120,10,5,9]	4.46E-05	24	[150,1,1,9]	4.59E-07	410	[90,20,11,5]	1.31E-05	[28,52,72,76,80,96,100,104,120,124,128,148,152]
102	212	[120,9,5,9]	1.14E-05	187	[120,8,5,7]	5.35E-07	59	[60,3,3,7]	3.67E-05	294	[30,9,13,5]	4.46E-05	368	[120,16,5,9]	4.61E-07	203	[60,9,9,7]	1.32E-05	[28,52,72,76,80,96,100,104,120,124,128,148,152]
103	75	[0,4,4,7]	1.15E-05	4	[0,1,1,9]	5.37E-07	176	[30,8,8,9]	3.68E-05	375	[90,17,11,7]	4.47E-05	212	[120,9,5,9]	4.62E-07	362	[90,16,11,5]	1.32E-05	[28,52,72,76,80,96,100,104,120,123,124,128,143,148,152,192]
110	103	[30,5,5,7]	1.15E-05	383	[60,17,18,7]	5.83E-07	354	[150,15,4,5]	3.77E-05	223	[30,9,10,7]	4.64E-05	256	[90,11,11,9]	4.73E-07	276	[60,12,12,9]	1.35E-05	[28,52,72,76,80,96,100,104,120,123,124,128,143,148,152,192]
111	183	[90,8,8,7]	1.15E-05	24	[150,1,1,9]	5.83E-07	215	[150,9,4,7]	3.79E-05	346	[90,15,11,5]	4.64E-05	295	[30,9,13,7]	4.76E-07	231	[90,10,10,7]	1.35E-05	[28,52,72,76,80,96,100,104,120,123,124,128,143,148,152,192]
112	135	[90,6,6,7]	1.15E-05	8	[30,1,1,9]	5.84E-07	300	[60,13,13,9]	3.80E-05	195	[0,5,9,7]	4.65E-05	355	[150,15,4,7]	4.80E-07	255	[90,11,11,7]	1.35E-05	[28,52,56,72,76,80,96,100,104,119,120,123,124,128,143,144,148,152,192]
113	159	[90,7,7,7]	1.15E-05	212	[120,9,5,9]	6.00E-07	195	[0,5,9,7]	3.81E-05	338	[30,9,15,5]	4.67E-05	319	[30,9,14,7]	4.91E-07	176	[30,8,8,9]	1.35E-05	[28,52,56,72,76,80,96,100,104,119,120,123,124,128,143,144,147,148,152,192]
118	55	[30,3,3,7]	1.17E-05	55	[30,3,3,7]	6.09E-07	227	[60,10,10,7]	3.89E-05	230	[90,10,10,5]	4.74E-05	291	[0,5,13,7]	4.99E-07	127	[30,6,6,7]	1.37E-05	[28,52,56,72,76,80,96,100,104,119,120,123,124,128,143,144,147,148,152,192]
119	87	[90,4,4,7]	1.17E-05	79	[30,4,4,7]	6.09E-07	48	[150,2,2,9]	3.92E-05	399	[90,19,11,7]	4.75E-05	280	[90,12,12,9]	5.06E-07	208	[90,9,9,9]	1.38E-05	[28,52,56,72,76,80,96,100,104,119,120,123,124,128,143,144,147,148,152,192]

.

Note: The texts size in the Figure 8-22 have been scaled down to fit into one page. For brevity, there are jumps in q column to avoid repetitions of a set of intersected indices in the $\mathbf{I_{opt}}$ column. $q = 119$ provides 20 global optimums in the $\mathbf{I_{opt}}$ column

8.2.4.2.3 Comparison of global optimum solutions for method-1 and method-2

For multi-objective optimisation engineering problems, there is no unique best solution for the problem, but a family of optimum solutions that the engineer can choose from, based on the design requirements. A matching comparison for the first 20 members of the family of optimum vessel relocation programs from method-1 and method-2 are compared through a matching plot shown in Figure 8-38. This matching plot shows which of the optimum relocation program are common for the family of solutions obtained by method-1 and method-2. Note that only the first 20 members are considered here and that the order in which these relocation program indices occur from the two methods is not considered. As the number of members considered increases (beyond 20), more matches will be obtained, but we believe that the list of these first 20 members is sufficient for demonstration. As observed from Figure 8-39, there are 15 matches out of the 20 first optimum relocation programs from method-1 and method-2. This indicates that the two methods sufficiently capture a good number of optimum relocation programs for the problem.

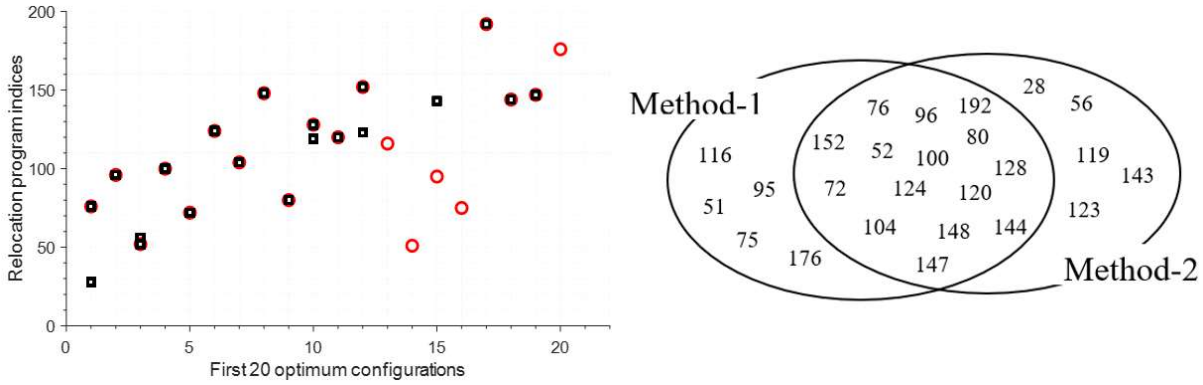

Figure 8-39. Matching plot for the first 20 global optimum relocation programs from method-1 and method-2.

Considering the 15 common optimum relocation programs between method-1 and method-2, the fatigue performance measured as percentage reductions in fatigue damage relative to the "no relocation case" are presented in Table 8-21. A bar chart representation of these percentage reductions is presented in Figure 8-40. It is observed from Table 8-21 and Figure 8-40 that the overall improvements in fatigue damage

across all SCR are quite close to each other, indicating that in the solution process, we achieved a balanced interest to reduce the fatigue in the six SCR TDZ. Among these 15 global optimum programs, the relocation program index-76 provides the largest combined reduction in fatigue damage of 486.5% for all SCRs, while index-147 provide the least reduction in fatigue damage of 460.7%. However, the contributions to the damage reduction of the programs considering individual SCR may be slightly different. This is measured in terms of the standard deviation (σ) from the mean percentage fatigue damage reduction for each SCR as presented in Table 8-21. From Table 8-21, it could be seen that index-76 has the smallest σ indicating that this relocation program provides a more equally distributed fatigue damage reduction across all SCRs. For this reason, we select the index-76 relocation program for further results discussions. A general observation of the performance of these optimum relocation programs from Table 8-21 and Figure 8-40 indicate the significance of the vessel relocation strategy to achieve longer lives for new SCRs and extend the lives of existing SCRs. Including vessel relocation programs for existing SCRs can result in significant life extension. For new risers, apart from higher fatigue lives, the design requirements such as the pipe wall thickness, internal cladding of pipe to mitigate corrosion, etc., can be reduced, resulting in significant improvement in the design cost of the risers. However, these benefits must be compared with the cost incurred for the vessel relocation operation, to make appropriate, cost-effective decisions during the SCR design and relocation plan. It should be noted that out of these 15-relocation programs, 5 of them are non-symmetric ($R1 \neq R_2$). This emphasises the importance of the screening methodology presented in section 8.2.4.1 and the modification/conversion of unfeasible symmetric relocation programs to feasible non-symmetric programs. If only symmetric relocation programs were considered, these good non-symmetric vessel relocations programs would not be captured.

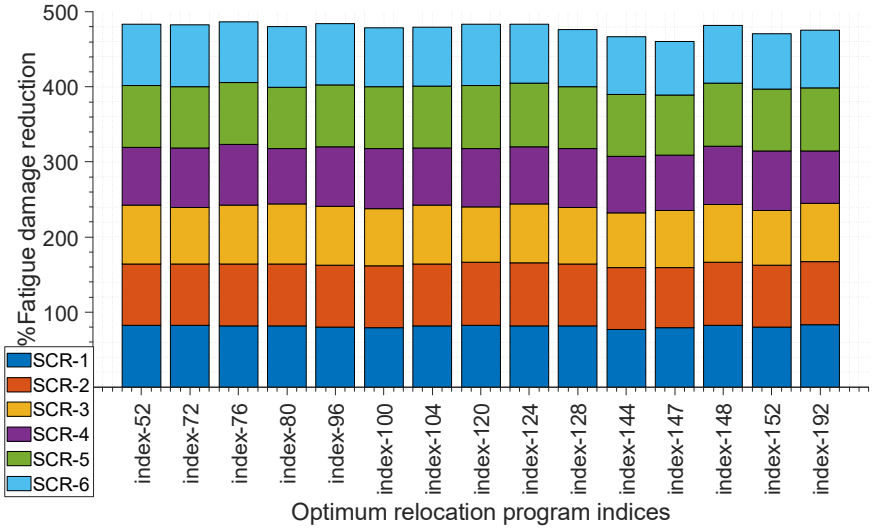

Figure 8-40. Bar chart representation of the percentage reduction in SCR TDZ $\boldsymbol{D_{eff}}$ compared with the no relocation fatigue damage

Table 8-21. Percentage reduction in SCR TDZ $\boldsymbol{D_{eff}}$ compared with the no relocation fatigue damage.

Index	$[\alpha, R_1, R_2, p]$ [(-), (%), (%), (deg)]	Reduction in Fatigue damage (%)						σ
		SCR-1	SCR-2	SCR-3	SCR-4	SCR-5	SCR-6	
52	[0,3,3,9]	82.1	82.3	77.9	76.9	82.3	82.1	2.5
72	[150,3,3,9]	82.2	82.3	74.9	78.9	82.3	81.9	3.0
76	[0,4,4,9]	81.8	82.3	78.3	80.6	82.3	81.2	1.5
80	[30,4,4,9]	81.9	82.3	79.5	73.7	82.3	80.5	3.3
96	[150,4,4,9]	80.1	82.3	78.3	79.2	82.3	82.1	1.8
100	[0,5,5,9]	79.5	82.3	76.2	79.6	82.3	78.9	2.3
104	[30,5,5,9]	81.8	82.3	78.1	76.4	82.3	78.4	2.6
120	[150,5,4,9]	82.5	84.0	73.9	77.1	84.2	81.5	4.1
124	[0,5,6,9]	81.3	84.1	78.9	76.2	84.2	79.1	3.2
128	[30,6,6,9]	81.4	82.3	75.7	78.4	82.3	75.9	3.1
144	[150,6,4,9]	77.0	82.0	73.0	75.2	82.7	76.8	3.8
147	[0,5,7,7]	79.5	79.9	76.0	73.4	80.0	72.0	3.5
148	[0,5,7,9]	82.6	84.1	76.9	77.2	84.1	76.7	3.7
152	[30,7,7,9]	80.4	82.3	73.0	78.9	82.3	73.7	4.1
192	[150,8,4,9]	83.5	83.9	77.3	69.5	84.2	77.1	5.8

8.2.4.3 Result discussions for the selected global optimum configuration (index-76)

8.2.4.3.1 Comparison of the index-76 program with the ideal optimum relocation program.

Table 8-22 compares the selected global optimum relocation program (index-76) with the ideal optimum relocation programs for the 6 SCRs, obtained from method-2. These comparisons are conducted with respect to the no relocation case, also included in Table 8-22. Recall from Table 8-20 that the ideal solutions for the individual SCRs (if each objective function is considered exclusively) are : index-356 for SCR-1, index-272 for SCR-2, index-356 for SCR-3, index-76 for SCR-4, index-404 for SCR-5 and index-52 for SCR-6 respectively. Consider the best optimal relocation program for a given SCR; that relocation program will provide the least value of its objective function and have associated objective functions' values for the other 5 SCRs, which are not necessarily minimum for them. Each best ideal solution and its associated relocation programs for other SCRs are presented in Table 8-22. Note that index-76, which is the selected global optimum relocation program happens to be the best relocation program for SCR-4, and hence appears two times in Table 8-22. Each ideal optimum relocation program is greyed, and the associated values of the other five objective functions are presented on the same row with it. From the computed percentages of fatigue damage reduction with respect to the no vessel relocation case, it could be observed that the ideal relocation programs (except index-76 and index-52) do not provide a balanced reduction of fatigue damage across all SCRs. A more intuitive view of the percentage fatigue damage reduction potentials of the relocation programs is presented in Figure 8-41 (a). The orientations of the SCRs and the axes of relocations have been included in Figure 8-41 (b) to provide the reader with the sense of configuration change of the SCRs for the different relocation programs. Note that the directions of the relocation programs presented in Figure 8-41 (a) are also provided as α in the fourth column of Table 8-22. It could be seen easily from Figure 8-41 (a) that index-76 (also ideal solution for SCR-4) and index-52 (ideal solution for SCR-6) both provide a good level of balance of fatigue damage reduction in all SCRs compared with the no vessel relocation case. Both are seen in Table 8-22 to have the least standard deviations from the mean of the percentage fatigue reduction. It should be noted that these two relocation programs (index-76 and index-52) are also in the list of top members of the global optimum relocation programs obtained from both method-1 and method-2 (see Figure 8-39).

.

Table 8-22. Comparison of the selected global optimum program, the first ideal optimum programs for the respective SCRs and the no vessel relocation case.

Result Type	SCRs	Index	$[\alpha, R_1, R_2, p]$ [(-), (%), (%), (deg)]	$(D_{eff})_j, j = 1$ to 6						Percentage reduction in fatigue damage (%) (Relative to fatigue damage for no-relocation)						σ
				SCR-1	SCR-2	SCR-3	SCR-4	SCR-5	SCR-6	SCR-1	SCR-2	SCR-3	SCR-4	SCR-5	SCR-6	
No relocation	NA	-	[NA, NA, NA]	4.96E-05	2.63E-06	1.21E-04	1.39E-04	2.26E-06	4.68E-05	-	-	-	-	-	-	-
Selected optimum	All	Index-76	[0,4,4,9]	9.01E-06	4.66E-07	2.62E-05	2.70E-05	3.99E-07	8.81E-06	81.8	82.3	78.3	80.6	82.3	81.2	1.5
Ideal optimum	SCR-1	Index-356	[150,15,4,9]	7.89E-06	4.19E-07	2.26E-05	8.16E-05	3.89E-07	1.91E-05	84.1	84.1	81.3	41.3	82.8	59.1	17.9
	SCR-2	Index-272	[30,9,12,9]	9.16E-06	4.17E-07	3.50E-05	3.19E-05	3.93E-07	1.71E-05	81.5	84.2	71.0	77.1	82.6	63.5	8.0
	SCR-3	Index-356	[150,15,4,9]	7.89E-06	4.19E-07	2.26E-05	8.16E-05	3.89E-07	1.91E-05	84.1	84.1	81.3	41.3	82.8	59.1	17.9
	SCR-4	Index-76	[0,4,4,9]	9.01E-06	4.66E-07	2.62E-05	2.70E-05	3.99E-07	8.81E-06	81.8	82.3	78.3	80.6	82.3	81.2	1.5
	SCR-5	Index-404	[120,19,5,9]	7.90E-06	4.22E-07	3.02E-05	8.07E-05	3.56E-07	1.15E-05	84.1	84.0	75.0	42.0	84.2	75.4	16.3
	SCR-6	Index-52	[0,3,3,9]	8.86E-06	4.66E-07	2.67E-05	3.21E-05	3.99E-07	8.38E-06	82.1	82.3	77.9	76.9	82.3	82.1	2.5

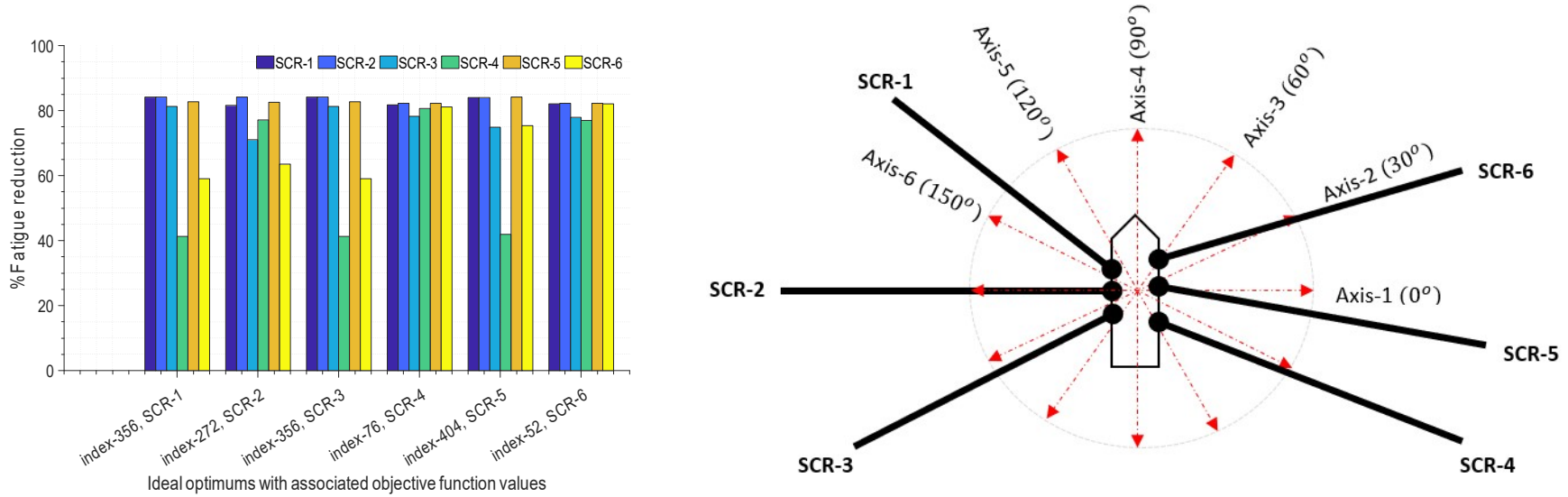

Figure 8-41. (a) Percentage fatigue damage reduction for individual SCR's ideal optimum relocation program, with associated percentage fatigue damage reduction for other SCRs, (b) Vessel-SCR layout showing the risers' orientations (azimuth) and the relocation axes, $\boldsymbol{\alpha}$

The relevance of comparing the global performances and the ideal solutions may be obvious from a scenario where there are a large number of SCRs hosted by the vessel. Consider, for example, a vessel hosting 30 or more SCRs, vessel relocation optimisation for such configuration with all SCRs included in each simulation model can be prohibitive numerically, especially when thousands of models need to be simulated to evaluate the objective functions. However, this example analysis shows that some ideal solutions can provide good fatigue reduction across other SCRs, like index-76 and index-52. A recommended approach for such a scenario will be to conduct an exclusive optimisation analysis for carefully selected SCR(s). The ideal solutions obtained are then investigated to determine their balanced contributions to fatigue damage reduction across other SCRs. Perhaps a good global optimum solution may be detected that will effectively reduce fatigue damage across all SCRs. The number of design variables can also be reduced for the problem, such as selecting the likely best axis of relocation. As could be seen in this example, index -76 has an axis of relocation of 0^o, which is close to a line of symmetry for all the azimuths of the SCRs (see Figure 8-27). The number of relocation stations can also be reduced for the problem, below the number at which no significant fatigue reduction benefits to relocation cost ratios are achieved. This will be discussed shortly

8.2.4.3.2 Further discussion on relocation program (index-76)

The optimisation design variables for index-76 are $[\alpha, R_1, R_2, p]$ = [0,4,4,9], as seen in Table 8-21. The values of the span radii ($R_1 = R_2 = 4\%$) indicate that this relocation program is symmetric with the axis of relocation, $\alpha = 0^o$, the number of stations, $p = 9$. For this relocation program, the vessel span limit stations are at 60 m (4% of water depth (1500 m)) equidistance from the nominal stations along the relocation axis. Since there are 9 stations, the relocation offsets calculated from equation (8-18), Δh , will be 15 m. This means the vessel is relocated 15 m at each relocation step from one station to another, which is also the distance between neighbouring stations. The fatigue damage fraction computed using equation (8-10) is presented in Figure 8-42. It could be seen that the nominal station, which received the highest number of vessel presence (exposure) during the vessel relocation, has the highest damage fraction. The span limit stations received the vessel presence once per relocation cycle, while the other 6 stations received the vessel presence twice per relocation cycle.

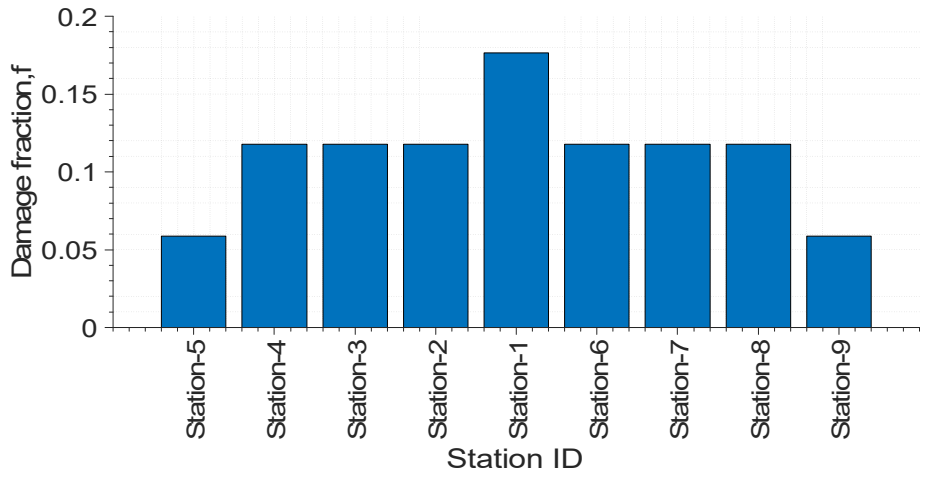

Figure 8-42. Damage fraction, $\boldsymbol{f}$, for index-76 relocation program.

For illustration purposes, Figure 8-43 presents the unfactored fatigue damage for the 6 SCRs for the vessel at stations 1 to 9 in index-76 relocation program. The unfactored fatigue damage plots are made on a y-logarithm scale. The maximum fatigue damage values and the point in the SCR TDZ where they occur (critical arc lengths) are presented in Table 8-23. It could be seen from Figure 8-43 and Table 8-23 that the maximum fatigue damages are concentrated around a short section of each SCR TDZ but with different critical arc lengths along the TDZ sections of the 6 SCRs due to different vessel locations. When the unfactored fatigue damages across the nine stations of the index-76 relocation program are factored by the fatigue damage fraction in Figure 8-42, the resulting effective fatigue damage (D_{eff}) along the SCRs are presented in Figure 8-44. It could be seen by comparing Figure 8-43 and Figure 8-44 that the relocation program is effective in spreading the fatigue damage over more extended sections of each of the SCR TDZ, as well as reducing the peak fatigue damage response by a large percentage as discussed in previous results. These underline the relevance of the vessel relocation and the need to optimally conduct such operation to maximise fatigue damage reduction across multiple SCRs hosted by a floating production platform.

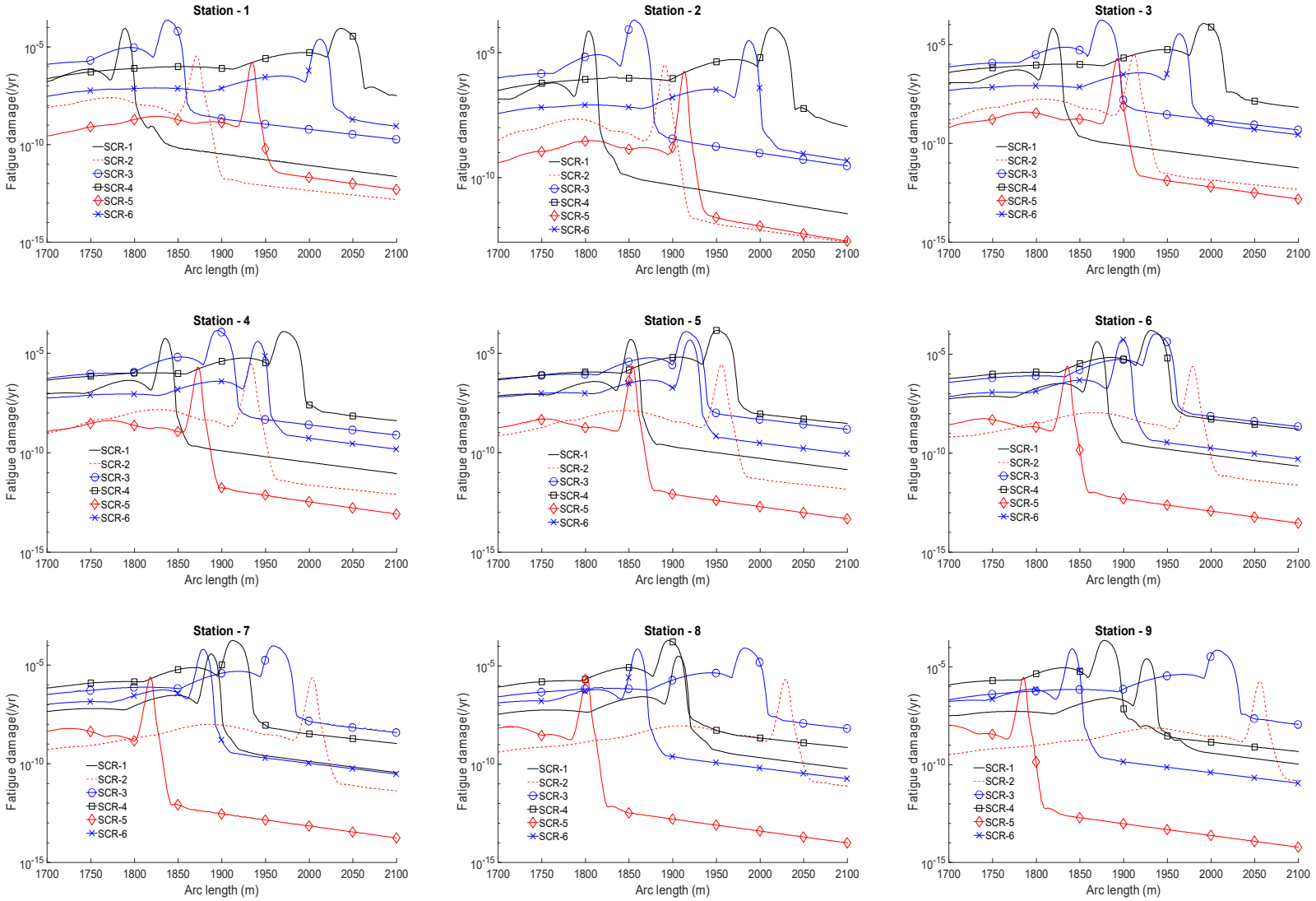

Figure 8-43. Unfactored SCR TDZ fatigue damage at station 1 to 9 for the index 76 relocation program.

Table 8-23. Unfactored maximum fatigue damage and points where they occur (critical points) in the SCR TDZ across the relocation stations in index-76 relocation program.

SCRs	Station-1		Station-2		Station-3		Station-4		Station-5 (nominal)		Station-6		Station-7		Station-8		Station-9	
	Unfactored Damage (/yr)	Critical Arc length (m)	Unfactored Damage (/yr)	Critical Arc length (m)	Unfactored Damage (/yr)	Critical Arc length (m)	Unfactored Damage (/yr)	Critical Arc length (m)	Unfactored Damage (/yr)	Critical Arc length (m)	Unfactored Damage (/yr)	Critical Arc length (m)	Unfactored Damage (/yr)	Critical Arc length (m)	Unfactored Damage (/yr)	Critical Arc length (m)	Unfactored Damage (/yr)	Critical Arc length (m)
SCR-1	8.94E-05	1789	7.51E-05	1804	6.43E-05	1819	5.68E-05	1836	4.96E-05	1851.7	4.28E-05	1870	3.68E-05	1888	3.15E-05	1907	2.62E-05	1927
SCR-2	3.47E-06	1871	3.35E-06	1891	3.10E-06	1912	2.88E-06	1933	2.63E-06	1956	2.40E-06	1979	2.23E-06	2004	2.06E-06	2029	1.84E-06	2056
SCR-3	2.38E-04	1837	2.00E-04	1855	1.69E-04	1874	1.43E-04	1894	1.21E-04	1914.4	1.05E-04	1936	9.38E-05	1959	8.12E-05	1982	7.21E-05	2007
SCR-4	9.03E-05	2036	1.01E-04	2014	1.14E-04	1992	1.25E-04	1971	1.39E-04	1951	1.57E-04	1932	1.77E-04	1912	1.98E-04	1895	2.28E-04	1878
SCR-5	1.66E-06	1935	1.78E-06	1913	1.95E-06	1893	2.08E-06	1873	2.26E-06	1853.7	2.45E-06	1836	2.47E-06	1818	2.77E-06	1802	2.91E-06	1786
SCR-6	2.54E-05	2012	3.05E-05	1987	3.40E-05	1963	3.99E-05	1941	4.68E-05	1919.4	5.47E-05	1898	6.36E-05	1878	7.32E-05	1859	8.48E-05	1841

.

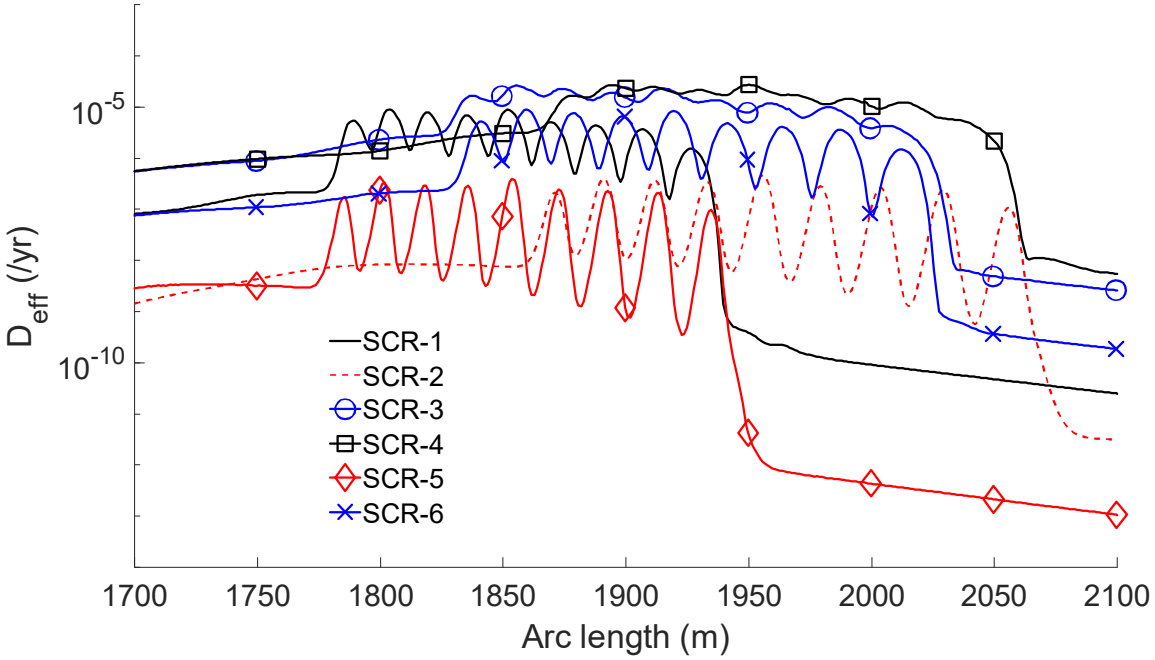

Figure 8-44. SCR TDZ effective fatigue damage obtained from the sum of factored fatigue damages across the 9 stations of the index-76 relocation program

One cycle of relocation is considered for the analyses in this study, as multiple cycles of relocations do not further reduce the fatigue damage of the SCR [132]. The number of times the vessel is moved from one station to another per relocation cycle is the number of relocations (n). The number of relocations, n, depends on the number of relocation station, p, as follows:

$$n = 2(p - 1) \tag{8-31}$$

When $p = 1$, $n = 0$ meaning which is the no vessel relocation case. The cost associated with the relocation program over the life span of the SCRs depends on n. The D_{eff} presented in Figure 8-44 were obtained for the $p = 9$ station relocation program (index-76). We can investigate the resulting D_{eff} if the number of stations is reduced from $p = 9$. This will demonstrate if the choice of maximum $p = 9$ for this example was sufficient to achieve the best reduction in the fatigue damage without a significant increase in the associated cost of relocation. The investigation will also tell if $p = 9$ was an optimum limiting number of stations for the analysis considering the balance between the fatigue damage reduction and associated

cost of vessel relocation operations. For this demonstration, we acquire relocation programs with the same α, R_1, R_2 with index-76 relocation program, but with different values of p i.e $p = 3, 5, 7$. The effective fatigue damage of these programs , including index-76, are presented in Table 8-24. The percentage fatigue reductions relative to the no vessel relocation case are shown in Figure 8-45.

Table 8-24. Influence of varying $\boldsymbol{p}$ on the effective fatigue damage of the SCRs.

Index	$[\alpha, R_1, R_2, p]$	**Effective fatigue damage (D_{eff})**					
		SCR-1	SCR-2	SCR-3	SCR-4	SCR-5	SCR-6
76	[0,4,4,9]	2.98E-05	1.58E-06	7.27E-05	8.40E-05	1.35E-06	2.81E-05
75	[0,4,4,7]	1.66E-05	8.79E-07	4.15E-05	4.79E-05	7.52E-07	1.57E-05
74	[0,4,4,5]	1.15E-05	6.09E-07	3.17E-05	3.37E-05	5.21E-07	1.10E-05
73	[0,4,4,3]	9.01E-06	4.66E-07	2.62E-05	2.70E-05	3.99E-07	8.81E-06

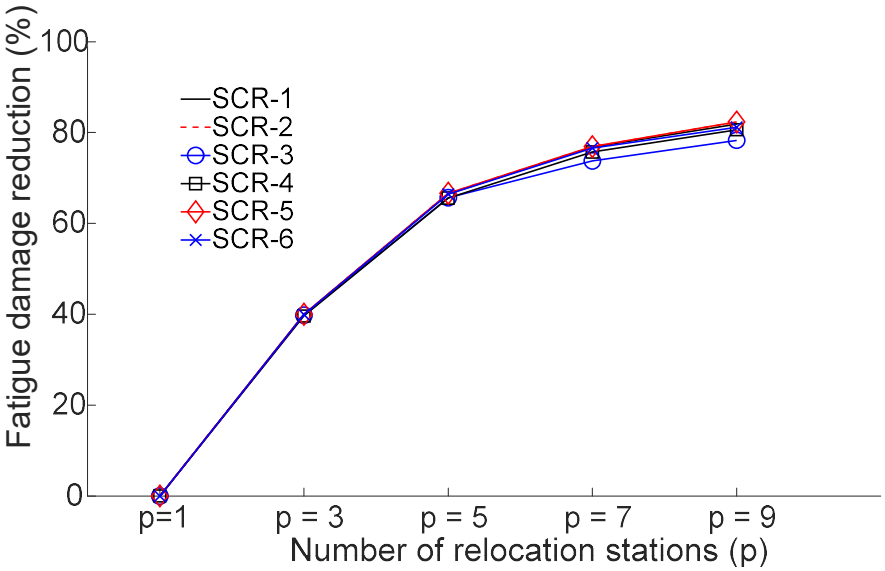

Figure 8-45. (a) Variation of fatigue damage reduction (%) with number of location stations, p

From Figure 8-45, it could be observed that significant reductions in fatigue damage can be achieved for all SCRs when the number of stations of the relocation program ranges from 1 to 5. The slope of each line segment drops quickly after $p = 5$ implying that additional stations beyond 9 will only slightly reduce fatigue damage for the SCRs with cost implications for the

relocation operations. The significance of this variation of fatigue damage reduction with p is that if the vessel relocation optimisation analyses are conducted without the operation cost included, these curves will help determine an appropriate cut-off point for p. .

8.2.5 Concluding remarks on multiple SCR vessel relocation Analysis

The vessel relocation program involves the management, engineering, and operations required to move a floating production platform from one location or station to another. Vessel relocation operation can be conducted to enhance the spreading and consequent reduction in fatigue damage over a longer section of the SCR TDZ. In the previous work [132], a vessel relocation optimisation technique was developed for a single SCR system to access the best relocation program. However, since the riser vessel system consists of multiple risers, there is the need to extend the previous method to solve the multiple SCR vessel relocation problems. The multiple SCR vessel relocation optimization technique is developed based on four optimization design variables, which are the axis of relocation (α), the span radii of relocation (R_1 and R_2) and the number of relocation stations (p). The effective fatigue damages, D_{eff}, for the SCR are the objective functions. The limiting values on the SCR design storm responses, which are the stress utilization around TDZ (U_{TDZ}), the top tension (T_{top}) and the TDZ compression (T_{TDZ}) are the imposed constraints on the optimisation design space. The span limits of any relocation program are defined by the distances of the extreme stations (span limit stations) from the nominal station ($R_1$and R_2). The relocation patterns are symmetrical if $R_1 = R_2$ and are not symmetrical if $R_1 \neq R_2$. Two optimisation methods based on the index matching optimisation technique are presented to solve the resulting multi-objective optimisation problem. The methods are either developing a normalised joint objective function or conducting direct intersections of the sorted columns of indices representing the families of ideal optimum solutions to the 6 objective functions. The methods provided good results with up to 75% match considering the first 20 family members of the global optimum relocation programs obtained from both methods.

To reduce the huge computation resource in the study, a screening analysis process is developed. The SCRs strength feasibilities based on the satisfaction of the constraint functions

are evaluated only at the two-span limit stations. The initial consideration of the screening analyses were relocation programs with symmetric relocation patterns $(R_1 = R_2)$. If at least one of the constraint functions is not satisfied at any of the span limit stations, the non-feasible symmetric relocation pattern degenerates to a feasible non-symmetric relocation pattern $(R_1 \neq R_2)$ instead of it being eliminated. This screening analysis stage reduced the computation need by up to 47% (in this work) and expanded the solution space by including non-symmetric relocation programs. The feasible relocation programs are then modelled and simulated for the fatigue wave load to evaluate the objective functions. To demonstrate the approach, a vessel hosting 6 SCRs is considered. The risers are characterized by different cross-section geometry as well as azimuths and configurations. For demonstration purposes, a single representative regular storm wave load is simulated during the screening stage, while the single regular fatigue wave load is simulated for the evaluation of the objective function, D_{eff}. The performances of the optimum global relocation programs are compared with the no-vessel relocation case and the ideal optimum relocation programs for the SCRs. The following can be deduced from the analyses:

- The vessel relocation technique, if optimally implemented, can significantly reduce the fatigue damage of newly designed SCRs, and provide good life extension for existing SCRs. These benefits can reduce the costs associated with required additional material strength and wall thickness for fatigue mitigation.

- For single SCR vessel relocation problem, the objective could be to minimise fatigue damage i.e., to increase the reduction in the SCR TDZ fatigue response compared with the no vessel relocation case. For multiple SCRs, while minimisation of the fatigue damage across all SCRs is crucial, it is also important to search for a relocation program that will provide a balanced contributions to all SCR TDZ fatigue damage reduction. This can be measured (as in this study) in terms of the standard deviations of the percentage damage reductions relative to the fatigue damage of the no vessel relocation case.

- The reduction in the SCR TDZ fatigue damage increases with an increasing number of relocation stations, p for any relocation program. As p goes beyond certain values, the

fatigue reduction contributions may not sufficiently justify the cost implications associated with the number of relocations of the vessel ($n = 2(p-1)$). Hence, fatigue reduction performance should be considered along with the associated cost incurred during the vessel relocation operation.

- It is possible for some ideal optimum relocation programs, exclusive to individual SCR, to provide a good fatigue reduction performance across all SCRs. For example, in this study, index-76 and index-52 relocation programs are ideal optimum programs for SCR-4 and SCR-6, respectively. However, they are also members of the best 20 global optimum relocation programs. Exploring this possibility may significantly reduce the computation that would have been conducted if all SCRs are included in the models and simulated for the design points.

- It is observed from this study that the best relocation axes are those which are close or equal to the line of symmetry for all SCR azimuths, which in this study was $\alpha = 0^{o}$. With this information, fewer relocation axes can be selected for the optimisation analysis process. Also, a preliminary analysis of a single SCR effective fatigue damage response variation with p can provide a good idea of what suitably low number of p to apply for the problem. In addition, with the screening analysis prior to the evaluation of the objective function, simulation of unfeasible relocation stations can be avoided. With these observations carefully incorporated into the vessel relocation optimisation process, computational resources can be hugely saved, especially when a high number of SCRs are involved.

8.3 Chapter summary

The vessel relocation strategy has been developed and demonstrated in this chapter. A formal approach for this assessment is absent from open literature, and there is need to develop such strategy for possible application during the design of new or life extensions of existing SCRs. The chapter is started with the development of the method for single SCR, with symmetric vessel relocation pattern. However, a limitation of the approach is that there could be non-symmetric vessel relocation programs that could be candidate optimum solutions for the vessel

relocation problems. Also, the single SCR vessel relocation technique need to be extended to accommodate multiple SCR cases, which represent the real scenario. With many SCRs involved, the computation resource required is quite significant. We introduced and developed a screening methodology prior to the multiple SCR fatigue simulation during the optimisation. This screening technique could be seen to have resulted in huge saving in the computation resource required for the problem's simulations. The vessel relocation technique, when properly conducted can contribute significantly to the reductions in fatigue damage across all SCRs hosted by the floating production platform.

9 CONCLUSIONS AND RECOMMENDATIONS

The conventional steel catenary risers (SCR) are limited in their application for deep and harsh water environments due to their critical sections' high stresses and fatigue response. In line with the aims and objectives of this research, novel riser solutions for SCR are developed and investigated in this thesis. These solutions include the branched riser system (BRS), the floating catenary riser system (FCR), the vessel relocation strategy (VRS) and the simulation stage-based pre-trenching technique (SSBPT). The index matching optimisation technique (IMT) is developed to optimise some of the novel riser solutions. This chapter presents a summary review of the work conducted in this thesis. It discusses the benefits of the riser solutions presented in this thesis and identifies their limitations and possible future work to enhance these solutions. The chapter is sectioned as follows:

- Section 9.1– Thesis chapters overview
- Section 9.2 – Research recommendations

9.1 Research review by chapters

The following are are summary of the work conducted by chapters in this thesis:

- In chapter 1, deepwater steel catenary risers and their current challenges were introduced. The factors mitigating the design responses and design processes of these risers were highlighted. The research goals and objectives for this thesis were presented, and the thesis chapter organisation were outlined.
- In chapter 2, the literature survey was conducted to dientify areas of focus and knowledge contributions by this research. This inlcuded four key areas namely: SCR

design/analysis methodology, SCR seabed ineteractions, SCR configuraion change and operational optimisation.

- In chapter 3 the framework for the numerical modelling of catenary shaped risers, including the proposed risers' configurations was presented. The data, procedures, design limits, and methods presented in this chapter were applied across the thesis during the investigations of proposed solutions.
- In chapter 4, the index matching optimisation method was presented. The technique provides a straightforward assessment of the design optimisation space for the proposed risers solutions. The methods of development, validation, and demonstration were demonstrated using the SLWR.
- In chapter 5, the branched riser system (BRS) solution concept was developed on the basis of comparative stress and fatigue responses of SCRs with different diameters. The BRS concept combines opportunities provided by small and large pipe SCRs while jointly mitigating their respective limitations. The global optimisation of the BRS conducted was also presented in this chapter.
- In chapter 6, the floating catenary riser (FCR) global analysis, and optimisation. The FCR concept allows spanning of risers over congested or environmentally protected seabed sections. The FCR stresses, fatigue responses, and cost can be affected by its configuration variables. Hence, the need for the FCR configuration optimisation.
- In chapter 7, studies conducted on SCR TDZ soil interactions were presented. The chapter presents the impact sloped seabed has on SCR TDZ responses. The chapter also contains the development of the simulation stage-based pre-trenching technique (SSBPT) for conducting assessment of the SCR TDZ fatigue response in a pre-trench. SCR is observed from field data to embed themselves into trenches of varying depth shortly after installation. Therefore, it is important to understand how these trenches affect the fatigue damage of the riser TDZ. The SSBPT technique was proposed and demonstrated to address this challenge.

- In chapter 8, the vessel relocation strategy for SCR TDZ fatigue mitigation was developed. Vessel relocation aids the fatigue damage spreading over a longer section of the SCR TDZ, resulting in extended fatigue lives for the risers. A formal, symmetrical vessel relocation strategy is developed for a single SCR, which is further advanced by introducing nonsymmetrical relocation programs for multiple SCR systems.

- In chapter 9, the summary review of the work conducted in this thesis. It restates the benefits of the riser solutions presented in this thesis and highlights their limitations and possible future work to enhance these solutions.

9.2 Research recommendations

The following are recommendations and future work for the index matching technique (IMT)

- The SSBPT approach is descriptive rather than inferential and hence will require the simulation of all design points within the optimisation design space. For very large problems, the method may be prohibitive to apply with large design space. It is believed that this approach can be incorporated into any optimisation techniques such as GA to enhance speed and accuracy as well as obtain quick convergence. This is an aspect of this technique that need to be explored in further study.

- The tabular optimisation technique is a type of the IMT, which reduces the three-dimensional problem to two dimensions. It was found that the technique significantly improves the efficiency of the 3 dimensional SLWR optimisation problem for which it was applied in this thesis. A potential limitation with the technique is the reduction of higher dimensional space to that of two dimensions, a transformation that needs further investigation. Future work will be to extend this technique to a higher dimensional riser optimisation problems.

The following are recommendations and future work for the BRS

- The only type of BRS investigated in this thesis is the BSCR. Future work is open to exploration of other BRS concepts such as the BSLWR, and the BLWHR.

- Currently, branching a steel riser at made water depth is something the riser industry is risk-averse towards. The connector interface structure is still a challenge, and more justification of the potentials of this riser concept based on the feasibility of the branching will be required.
- The transition of a large bore pipe to a small bore pipe will pose maintenance operations such as pigging operation. Pigging of variable size pipe in the offshore industry is still an area under development, and the technology has not fully matured. This is an area that required further research vis-a-vis the BRS

The following are recommendations for future work on the FCR concept.

- The current code does not allow the crossing of dynamic risers over pipelines and subsea structures. There is a need to conduct safety feasibility of the FCR for deepwater application when it spans across seabed congested with other structures.
- The FCR is characterised by a long-span section close to the seabed. The long span section is susceptible to large lateral global deflection under current loads. This limits the FCR use in regions with intensive current profiles close to the seabed.
- For the FCR, the wave bend section under the intensive current profile can be a “hot region” for vortex-induced vibration (VIV) fatigue damage. The VIV fatigue damage response needs to be investigated in future work as part of the feasibility study for the FCR.
- The FCR, similar to the SLWR, can be susceptible to heave induced vibration in response to the vessel's heave motions. This is a potential challenge for the FCR application and should be investigated in future work.
- The slug induced vibration can also be a limitation for the FCR, as the multiple wave bends are potential slugging sites for transported hydrocarbons. This should also be a subject of future investigation for the FCR.

The following are recommendations and future work for the vessel relocation strategy

- The offshore industry currently risks adverse to vessel relocation operations, and further demonstrations of its feasibility and effectiveness are required to convince the industry of the potential this may present to extending the lives of SCR.
- Vessel relocation still stands a complex operation as the risers and other connected dynamic systems such as umbilical and mooring are moved along with the vessel. Future work is required to assess the impact of these relocations on other dynamic systems. Therefore, an integrated optimisation needs to be investigated for this purpose.
- In this study, we have used a single design storm and a single fatigue wave load representative of the sea state conditions. However, a large wave database will require constructing better representative wave loads for the strength and fatigue analysis. The technique presented in this study can be scaled up to accommodate such wider load cases. However, a balance between accuracy and computational resource requirement will play an imperative role in deciding the number of representative wave loads to apply. This is a potential subject of future investigation.
- In this study, the coupled interactions between the fatigue damages during the vessel transition period and the period spent at each station are not considered. This is an interesting problem to consider for future work.

The following are recommendations and future work for the SSBPT

- This technique is difficult to apply when conducting screening analysis for the riser's system as very many models need to be involved in such analysis. It is recommended that the riser should be considered on a flat seabed (no pre-trench) during optimisation or screening design. Once one of a few configurations has been chosen for full detail design, a parametric study of the impact of different pre-trench depth can then be investigated for them
- It is still challenging to determine the design trench profile for a given riser system. The created trench profile is project-specific as it depends on the riser configuration, vessel motions, wave environment, seabed properties, etc. More field data need to be collected

worldwide and across the different fields to improve numerical trench modelling and validation. In the meantime, parametric analysis of different trench profiles needs to be investigated for newly designed SCR.

- The fatigue load applied in this study is for one direction (along the riser azimuth), while the host vessel remains in its nominal position. However, the comparative study and the main analysis in this study showed that pre-trenching increases the SCR fatigue damage. These interactions are too complex to make absolute conclusions. Future work can investigate the impact of other variable conditions, such as different vessel motions, second-order vessel offsets, SCR global configurations, SCR TDZ stiffness, different soil model data, wave loads and wav directions.

- A simplified linear seabed profile is assumed in this study, and a one-directional wave load is imposed on the model in the riser azimuth direction (beam sea), where the roll and heave components of the vessel response is expected to be highest. However, the seabed profile can be more complex than the assumed linear and contains local undulations within the SCR TDZ. This is worth investigating in future work.

REFERENCES

[1] Y. Bai and Q. Bai, *Subsea pipelines and risers*. Elsevier, 2005.

[2] C. P. Sparks, *Fundamentals of marine riser mechanics: basic principles and simplified analyses*. PennWell Books, 2007.

[3] A. P. I. Standard, "2RD, 2013,“," *Dynamic Risers for Floating Production Systems-Second Edition” American Petroleum Institute, Washington, DC*.

[4] D.-O. Standard, "F201, 2010," *Dynamic Risers. DNV: Norway*.

[5] J. K. BSEE, "Deepwater Riser Design, Fatigue Life and Standards Study," *Project. Report for MMS,* 2007.

[6] R. Song and P. Stanton, "Advances in Deepwater Steel Catenary Riser Technology State-of-the-Art: Part I—Design," 2007: American Society of Mechanical Engineers, pp. 331-344.

[7] H. Quintin, J.-L. Legras, K. Huang, and M. Wu, "Steel catenary riser challenges and solutions for deepwater applications," in *Offshore technology conference*, 2007: Offshore Technology Conference.

[8] L. M. Quéau, M. Kimiaei, and M. F. Randolph, "Sensitivity studies of SCR fatigue damage in the touchdown zone using an efficient simplified framework for stress range evaluation," *Ocean Engineering,* vol. 96, pp. 295-311, 2015.

[9] E. Clukey, R. Ghosh, P. Mokarala, and M. Dixon, "Steel catenary riser (SCR) design issues at touch down area," 2007: International Society of Offshore and Polar Engineers.

[10] C. T. Gore and B. B. Mekha, "Common Sense Requirements (CSRs) for Steel Catenary Risers (SCRs)," presented at the Offshore Technology Conference, Houston, Texas, 2002/1/1/, 2002. [Online]. Available: https://doi.org/10.4043/14153-MS.

[11] Z. Wang, W. Qin, X. Zhang, J. Zhao, and Y. Bai, "Study on the Design Method of Deepwater Steel Lazy Wave Riser," in *International Conference on Offshore Mechanics and Arctic Engineering*, 2019, vol. 58813: American Society of Mechanical Engineers, p. V05BT04A035.

[12] J. Hoffman, H. Yun, A. Modi, and R. Pearce, "Parque das Conchas Pipeline, Flowline and Riser System Design, Installation and Challenges," in *Offshore Technology Conference*, 2010: OnePetro.

[13] B. Thomas, A. Benirschke, and T. Sarkar, "Parque das Conchas (BC-10) Steel Lazy Wave Riser Installation: Pre-Abandonment, Recovery and Transfer Challenges," in *Offshore Technology Conference*, 2010, vol. All Days, OTC-20605-MS, doi: 10.4043/20605-ms. [Online]. Available: https://doi.org/10.4043/20605-MS

[14] "2017 Deepwater Solutions & Records for Concept Selection," in *Enabling Technologies for Deepwater Production* O. Magazine, Ed., ed: Offshore Magazine, 2017.

[15] Chevron, "Am Operator's View on Deepwater Floating Systems and Technology Development," ed, 2011.

[16] RIGZONE. "How Do FPSO Work?" https://www.rigzone.com/training/insight.asp?insight_id=299 (accessed Febraury, 3rd, 2017).

[17] B. Ronalds and E. Lim, "FPSO trends," in *SPE Annual Technical Conference and Exhibition*, 1999: Society of Petroleum Engineers.

[18] G. Rowles. "Keppel scores SBM Offshore FPSO Conversion Contract." http://splash247.com/keppel-scores-sbm-offshore-fpso-conversion-contract/ (accessed Februry, 3rd, 2018).

[19] A. Sworn, "Hybrid riser towers from an operator's perspective," in *Offshore Technology Conference*, 2005: Offshore Technology Conference.

[20] C.-A. Zimmermann, D. Petruska, and A. S. Duggal, "Effective Riser Solutions for a Deepwater FPSO," in *ASME 2002 21st International Conference on Offshore Mechanics and Arctic Engineering*, 2002: American Society of Mechanical Engineers, pp. 667-677.

[21] D. Petruska, C. Zimmermann, K. Krafft, B. Thurmond, and A. Duggal, "Riser System Selection and Design for a Deepwater FSO in the Gulf of Mexico," in *Offshore Technology Conference*, 2002: Offshore Technology Conference.

[22] B. Carter and B. Ronalds, "Deepwater riser technology," in *SPE Asia Pacific Oil and Gas Conference and Exhibition*, 1998: Society of Petroleum Engineers.

[23] "2015 Deepwater Production Riser Systsems & Components," in *Status of the Technology From Seabed to Surface*, ed: Offshore Magazine, 2015.

[24] J. Watson, "Advantage of an FPSO," 2021. [Online]. Available: https://www.watsonpost.com/advantages-of-an-fpso.

[25] H. Howells, "AAdvances in Steel Catenary Riser Design@," in *The 2nd Annual International Forum on Deepwater Technology, DEEPTEC*, 1995, vol. 95.

[26] Y. Wang *et al.*, "SCR Hang-Off System Selection Considerations and Criteria," in *The Twenty-first International Offshore and Polar Engineering Conference*, 2011: International Society of Offshore and Polar Engineers.

[27] G. Chaudhury and J. Kennefick, "Design, testing, and installation of steel catenary risers," in *Offshore Technology Conference*, 1999: Offshore Technology Conference.

[28] S. A. Hatton, "Update on the design of steel catenary riser systems," *TRANSACTIONS-INSTITUTE OF MARINE ENGINEERS-SERIES C-,* vol. 111, pp. 127-138, 1999.

[29] V. Alliot, J. Legras, and D. Perinet, "A comparison between steel catenary risers and hybrid riser towers for deepwater field developments," in *Deep Offshore Technology Conference. New Orleans*, 2004.

[30] R. Shankaran, H. Howells, M. Lopes, and A. Anaturk, "Application of Steel Lazy Wave Riser Solution in Deepwater and Comparison to Other Riser Types," in *SPE Offshore Europe Conference & Exhibition*, 2017: Society of Petroleum Engineers.

[31] R. K. Aggarwal *et al.*, "Development and Qualification of Alternative Solutions for Improved Fatigue Performance of Deepwater Steel Catenary Risers," in *ASME 2007 26th International Conference on Offshore Mechanics and Arctic Engineering*, 2007, vol. Volume 1: Offshore Technology; Special Symposium on Ocean Measurements and Their Influence on Design, pp. 315-329, doi: 10.1115/omae2007-29325. [Online]. Available: https://doi.org/10.1115/OMAE2007-29325

[32] S. Bhat, A. Dutta, J. Wu, and I. Sarkar, "Pragmatic Solutions to Touch-Down Zone Fatigue Challenges in Steel Catenary Risers," in *Offshore Technology Conference*, 2004: Offshore Technology Conference.

[33] R. K. Aggarwal, S. U. Bhat, T. S. Meling, C. van der Linden, M. M. Mourelle, and M. Else, "Qualification of enhanced SCR design solutions for improving fatigue life at touch down zone," in *The Sixteenth International Offshore and Polar Engineering Conference*, 2006: International Society of Offshore and Polar Engineers.

[34] A. M. Mansour, S. Bhat, D. Pasala, and D. Kumar, "Field Development using Semisubmersible Floating Production System with Steel Catenary Risers in Western Australia Harsh Environment," in *Offshore Technology Conference*, 2014, vol. Day 4 Thu, May 08, 2014, D041S052R007, doi: 10.4043/25265-ms. [Online]. Available: https://doi.org/10.4043/25265-MS

[35] P. Cao and J. Cheng, "Design of Steel Lazy Wave Riser for Disconnectable FPSO," in *Offshore Technology Conference*, 2013, vol. All Days, OTC-24166-MS, doi: 10.4043/24166-ms. [Online]. Available: https://doi.org/10.4043/24166-MS

[36] B. P. Jacob, M. C. Reyes, B. S. de Lima, A. L. Torres, M. M. Mourelle, and R. Silva, "Alternative configurations for steel catenary risers for turret-moored FPSOs," in *The Ninth International Offshore and Polar Engineering Conference*, 1999: International Society of Offshore and Polar Engineers.

[37] N. Alderton and R. Thethi, "Choosing the most appropriate rigid catenary riser design for various deepwater and harsh environments," *Advances in Riser Systems & Subsea Technologies for Deepwater Euroforum,* 1998.

[38] W. L. Alexander, M. Wu, and S.-H. M. Chang, "Dynamic Performance Comparison of Deepwater Riser Systems for A Turret-Moored FPS," in *Offshore Technology Conference*, 1999, vol. All Days, OTC-10934-MS, doi: 10.4043/10934-ms. [Online]. Available: https://doi.org/10.4043/10934-MS

[39] E. Q. De Andrade, L. L. de Aguiar, S. F. Senra, E. F. N. Siqueira, A. L. F. L. Torres, and M. M. Mourelle, "Optimization Procedure of Steel Lazy Wave Riser Configuration for Spread Moored FPSOs in Deepwater Offshore Brazil," in *Offshore Technology Conference*, 2010, vol. All Days, OTC-20777-MS, doi: 10.4043/20777-ms. [Online]. Available: https://doi.org/10.4043/20777-MS

[40] R. Franciss and E. Ribeiro, "Analyses of a Large Diameter Steel Lazy Wave Riser for Ultra Deepwater in Campos Basin," in *ASME 2004 23rd International Conference on Offshore Mechanics and Arctic Engineering*, 2004, vol. 23rd International Conference on Offshore Mechanics and Arctic Engineering, Volume 1, Parts A and B, pp. 355-361, doi: 10.1115/omae2004-51176. [Online]. Available: https://doi.org/10.1115/OMAE2004-51176

[41] A. L. c. F. Lima Torres, E. C. Gonzalez, M. Q. de Siqueira, C. M. Silva Dantas, M. M. Mourelle, and R. M. Correia da Silva, "Lazy-Wave Steel Rigid Risers for Turret-Moored FPSO," in *ASME 2002 21st International Conference on Offshore Mechanics and Arctic Engineering*, 2002, vol. 21st International Conference on Offshore Mechanics and Arctic Engineering, Volume 1, pp. 203-209, doi: 10.1115/omae2002-28124. [Online]. Available: https://doi.org/10.1115/OMAE2002-28124

[42] M. M. Mourelle, M. Q. de Siqueira, G. G. de Avila, and A. L. F. L. Torres, "Methodology for Analysis of Installation of a Steel Lazy Wave Riser," in *2004 International Pipeline Conference*, 2004, vol. 2004 International Pipeline Conference, Volumes 1, 2, and 3, pp. 1945-1950, doi: 10.1115/ipc2004-0110. [Online]. Available: https://doi.org/10.1115/IPC2004-0110

[43] L. V. Sudati Sagrilo, E. Castro Prates de Lima, F. J. Mendes de Sousa, C. M. Silva Dantas, M. Q. de Siqueira, and A. L. c. Fernandes Lima Torres, "Steel Lazy Wave Riser Design: API-RP-2RD and DNV-OS-F201 Criteria," in *ASME 2005 24th International Conference on Offshore Mechanics and Arctic Engineering*, 2005, vol. 24th International Conference on Offshore Mechanics and Arctic Engineering: Volume 1, Parts A and B, pp. 107-113, doi: 10.1115/omae2005-67040. [Online]. Available: https://doi.org/10.1115/OMAE2005-67040

[44] F. E. Roveri, C. v. de Arruda Martins, and R. Balena, "Parametric Analysis of a Lazy-Wave Steel Riser," in *ASME 2005 24th International Conference on Offshore Mechanics and Arctic Engineering*, 2005, vol. 24th International Conference on Offshore Mechanics and Arctic Engineering: Volume 1, Parts A and B, pp. 289-295, doi: 10.1115/omae2005-67128. [Online]. Available: https://doi.org/10.1115/OMAE2005-67128

[45] A. L. c. F. Lima Torres, E. C. Gonzalez, M. D. A. da S. Ferreira, M. Q. de Siqueira, M. M. Mourelle, and R. M. Correia da Silva, "Lazy-Wave Steel Rigid Risers for FSO With Spread Mooring Anchoring System," in *ASME 2003 22nd International Conference on Offshore Mechanics and Arctic Engineering*, 2003, vol. Volume 2: Safety and Reliability; Pipeline Technology, pp. 547-555, doi: 10.1115/omae2003-37068. [Online]. Available: https://doi.org/10.1115/OMAE2003-37068

[46] P. A. Trapper, "Feasible numerical analysis of steel lazy-wave riser," *Ocean Engineering,* vol. 195, p. 106643, 2020.

[47] B. J. Elliott, A. Zakeri, A. Macneill, R. Phillips, E. C. Clukey, and G. Li, "Centrifuge modeling of steel catenary risers at touchdown zone part I: Development of novel

centrifuge experimental apparatus," *Ocean Engineering,* vol. 60, pp. 200-207, 2013/03/01/ 2013, doi: https://doi.org/10.1016/j.oceaneng.2012.11.012.

[48] J. Wang, M. Duan, J. Fan, and Y. Liu, "Static Equilibrium Configuration of Deepwater Steel Lazy-Wave Riser," in *The Twenty-third International Offshore and Polar Engineering Conference*, 2013, vol. All Days, ISOPE-I-13-063.

[49] V. Jhingran, H. Zhang, H. Lie, H. Braaten, and J. K. Vandiver, "Buoyancy spacing implications for fatigue damage due to vortex-induced vibrations on a steel lazy wave riser (SLWR)," in *Offshore Technology Conference*, 2012: Offshore Technology Conference.

[50] A. Felisita, O. T. Gudmestad, D. Karunakaran, and L. O. Martinsen, "A Review of VIV Responses of Steel Lazy Wave Riser," no. 49934, p. V002T08A031, 2016, doi: 10.1115/OMAE2016-54321.

[51] A. Felisita, O. T. Gudmestad, D. Karunakaran, and L. O. Martinsen, "Review of steel lazy wave riser concepts for the north Sea," *Journal of Offshore Mechanics and Arctic Engineering,* vol. 139, no. 1, p. 011702, 2017.

[52] B. A. Carter and B. F. Ronalds, "Deepwater Riser Technology," in *SPE Asia Pacific Oil and Gas Conference and Exhibition*, 1998, vol. All Days, SPE-50140-MS, doi: 10.2118/50140-ms. [Online]. Available: https://doi.org/10.2118/50140-MS

[53] J. Murali and M. W. Joosten, "Titanium Drilling Risers—Application and Qualification," 2000.

[54] C. F. Baxter, R. W. Schutz, and C. S. Caldwell, "Experience and Guidance in the Use of Titanium Components in Steel Catenary Riser Systems," in *Offshore Technology Conference*, 2007, vol. All Days, OTC-18624-MS, doi: 10.4043/18624-ms. [Online]. Available: https://doi.org/10.4043/18624-MS

[55] M. Nygård, A. Sele, and K. Lund, "Design of a 25.5-in Titanium Catenary Riser for the Åsgard B Platform," in *Offshore Technology Conference*, 2000: Offshore Technology Conference.

[56] M. Randolph and P. Quiggin, "Non-linear hysteretic seabed model for catenary pipeline contact," in *ASME 2009 28th International Conference on Ocean, Offshore and Arctic Engineering*, 2009: American Society of Mechanical Engineers, pp. 145-154.

[57] E. Zargar, M. Kimiaei, and M. Randolph, "A new hysteretic seabed model for riser-soil interaction," *Marine Structures,* vol. 64, pp. 360-378, 2019.

[58] C. P. Aubeny and G. Biscontin, "Seafloor-riser interaction model," *International Journal of Geomechanics,* vol. 9, no. 3, pp. 133-141, 2009.

[59] F. Jamaludin and J. Koto, "Catenary Offset Buoyant Riser Assembly for Malaysian Deepwater," *Science and Engineering,* vol. 12, 2017.

[60] D. N. Karunakaran and R. Baarholm, "COBRA: An Uncoupled Riser System for Ultradeep Water in Harsh Environment," in *Offshore Technology Conference*, 2013: Offshore Technology Conference.

[61] T. Nurwanto, D. Karunakaran, and R. Franciss, "COBRA Riser Concept for Ultra Deepwater Condition," in *ASME 2013 32nd International Conference on Ocean, Offshore and Arctic Engineering*, 2013, vol. Volume 4B: Pipeline and Riser Technology, V04BT04A030, doi: 10.1115/omae2013-11161. [Online]. Available: https://doi.org/10.1115/OMAE2013-11161

[62] D. Karunakaran, H. Aasen, and R. Baarholm, "New Un-coupled Deepwater Riser Concept for Harsh Environment–Catenary Offset Buoyant Riser Assembly (COBRA)," in *Deepwater Offshore Technology Conference. New Orleans, USA*, 2011, pp. 11-13.

[63] C. E. Haveman, A. R. Cribbs, and J. D. Miller, "Global Benefits and Operational Challenges of Vessel Relocation," in *ASME 2015 34th International Conference on Ocean, Offshore and Arctic Engineering*: American Society of Mechanical Engineers Digital Collection.

[64] B. Yue, M. Campbell, D. Walters, H. Thompson, and K. Raghavan, "Improved SCR design for dynamic vessel applications," in *International Conference on Offshore Mechanics and Arctic Engineering*, 2010, vol. 49132, pp. 495-504.

[65] V. Vijayaraghavan *et al.*, "Large diameter steel catenary riser solutions for semi-submersible platforms in offshore Northwest Australia," in *Offshore Technology Conference*, 2015: Offshore Technology Conference.

[66] A. Izquierdo *et al.*, "Qualification of Weldable X65 Grade Riser Sections with Upset Ends to Improve Fatigue Performance of Deepwater Steel Catenary Risers," in *The Eighteenth International Offshore and Polar Engineering Conference*, 2008: International Society of Offshore and Polar Engineers.

[67] R. Brito, L. Aguiar, and V. Prado, "Technical Feasibility Study of Steel Catenary Risers for Pre-Salt Field Developments," presented at the OTC Brasil, Rio de Janeiro, Brazil, 2017/10/24/, 2017.

[68] A. G. Garmbis, P. Zumpano Jr, L. L. Aguiar, R. M. Brito, and D. A. Rade, "A Fracture Mechanics-Based Feasibility Study of Damped Steel Catenary Risers for Pre-Salt Field Developments," in *International Conference on Offshore Mechanics and Arctic Engineering*, 2019, vol. 58813: American Society of Mechanical Engineers, p. V05BT04A042.

[69] A. I. Garcia and H. M. Q. Carmona, "Seamless steel tube for use as a steel catenary riser in the touch down zone," ed: Google Patents, 2008.

[70] A. M. Horn, M. Hauge, P.-A. Rø stadsand, B. Bjø rnbakk, P. Dahlberg, and T. Fossesholm, "Cost Effective Fabrication of Large Diameter High Strength Titanium Catenary Riser," in *ASME 2002 21st International Conference on Offshore Mechanics and Arctic Engineering*, 2002, vol. 21st International Conference on Offshore Mechanics and Arctic Engineering, Volume 3, pp. 331-337, doi: 10.1115/omae2002-28445. [Online]. Available: https://doi.org/10.1115/OMAE2002-28445

[71] S. Li and C. Nguyen, "Dynamic response of deepwater lazy-wave catenary riser," *Deep Offshore Technology International, Amsterdam, The Netherlands,* 2010.

[72] M. Hariharan, "Lazy Wave SCRs: The 4 Biggest Design Challenges and How to Address Them," vol. 2018, ed, 2017.

[73] H.-z. Yang, H.-j. Li, and H.-i. Park, "Optimization design for steel catenary riser with fatigue constraints," *International Journal of Offshore and Polar Engineering,* vol. 21, no. 04, 2011.

[74] J. Gouveia *et al.*, "The Buoy Supporting Risers (BSR) System: Steel Catenary Risers (SCRs) From Design to Installation of the First Reel CRA Lined Pipes," in *OTC Brasil*, 2015: Offshore Technology Conference.

[75] I. Cruz, C. Claro, D. Sahonero, L. Otani, and J. Pagot, "The Buoy Supporting Risers (BSR) System: A Novel Riser Solution for Ultra-Deep Water Subsea Developments in Harsh Environments," presented at the OTC Brasil, Rio de Janeiro, Brazil, 2015/10/27/, 2015.

[76] J.-L. Legras, "Tethered Catenary Riser: A Novel Concept for Ultradeep Water," presented at the Offshore Technology Conference, Houston, Texas, USA, 2013/5/6/, 2013. [Online]. Available: https://www.onepetro.org/conference-paper/OTC-23972-MS

https://www.onepetro.org:443/download/conference-paper/OTC-23972-MS?id=conference-paper%2FOTC-23972-MS.

[77] B. Mekha, M. Randolph, S. Bhat, and S. Jain, "Modeling the Touchdown Zone Trench and Its Impact on SCR Fatigue Life," in *Offshore Technology Conference*, 2013: Offshore Technology Conference.

[78] E. C. Clukey *et al.*, "A Perspective on the State of Knowledge Regarding Soil-Pipe Interaction for SCR Fatigue Assessments," 2017: Offshore Technology Conference.

[79] R. Theti, "Soil interaction effects on simple-catenary riser response," *Pipes & pipelines international,* vol. 46, no. 3, pp. 15-24, 2001.

[80] C. P. Aubeny, G. Biscontin, and J. Zhang, "Seafloor interaction with steel catenary risers," *Final Project Report to Minerals Management Service, Offshore Technology*

Research Centre Industry Consortium, Texas A&M University, College Station, Houston, TX, OTRC Library, no. 9/06A173, 2006.

[81] C. Bridge, K. Laver, E. Clukey, and T. Evans, "Steel catenary riser touchdown point vertical interaction models," in *Offshore Technology Conference*, 2004: Offshore Technology Conference.

[82] L. Orcina, "OrcaFlex User Manual: OrcaFlex Version 10.2 c," *Daltongate Ulverston Cumbria, UK,* 2018.

[83] C. D. Bridge and H. A. Howells, "Observations and modeling of steel catenary riser trenches," in *The Seventeenth International Offshore and Polar Engineering Conference*, 2007: International Society of Offshore and Polar Engineers.

[84] C. Bridge, H. Howells, N. Toy, G. A. R. Parke, and R. Woods, "Full-scale model tests of a steel catenary riser," (in English), *Adv Fluid Mech Ser,* vol. 36, pp. 107-116, 2003. [Online]. Available: <Go to ISI>://WOS:000189462200011.

[85] E. Giertsen, R. Verley, and K. Schroder, "CARISIMA: A catenary riser/soil interaction model for global riser analysis," in *ASME 2004 23rd International Conference on Offshore Mechanics and Arctic Engineering*, 2004: American Society of Mechanical Engineers Digital Collection, pp. 633-640.

[86] K. Wang and Y. M. Low, "Study of seabed trench induced by steel catenary riser and seabed interaction," in *ASME 2016 35th International Conference on Ocean, Offshore and Arctic Engineering*, 2016: American Society of Mechanical Engineers Digital Collection.

[87] P. P. Sharma and C. P. Aubeny, "Advances in pipe-soil interaction methodology and application for SCR fatigue design," in *Offshore Technology Conference*, 2011: Offshore Technology Conference.

[88] C. G. Langner, "Fatigue Life Improvement of Steel Catenary Risers due to Self-Trenching at the Touchdown Point," presented at the Offshore Technology Conference, Houston, Texas, 2003/1/1/, 2003.

[89] H. Shiri and M. Randolph, "The Influence of Seabed Response on Fatigue Performance of Steel Catenary Risers in Touchdown Zone," no. 49132, pp. 63-72, 2010, doi: 10.1115/OMAE2010-20051.

[90] B. J. Elliott, A. Zakeri, J. Barrett, B. Hawlader, G. Li, and E. C. Clukey, "Centrifuge modeling of steel catenary risers at touchdown zone part II: Assessment of centrifuge test results using kaolin clay," *Ocean Engineering,* vol. 60, pp. 208-218, 2013/03/01/ 2013, doi: https://doi.org/10.1016/j.oceaneng.2012.11.013.

[91] A. Nakhaee and J. Zhang, "Effects of the Interaction With the Seafloor On the Fatigue Life of a SCR," presented at the The Eighteenth International Offshore and Polar Engineering Conference, Vancouver, Canada, 2008/1/1/, 2008.

[92] R. Shoghi and H. Shiri, "Re-assessment of trench effect on fatigue performance of steel catenary risers in the touchdown zone," *Applied Ocean Research,* vol. 94, p. 101989, 2020.

[93] J. Liu, "Numerical modelling of seabed trench and its effect on the structural response of steel catenary risers," 2018.

[94] A. P. I. S. 2RD, "Dynamic Risers for Floating Production Systems," 2013.

[95] D. N. Veritas, "Offshore Standard DnV OS F201—Dynamic Risers," *DNV Services, Research and Publications, Hovik, Norway,* 2001.

[96] D. N. Veritas, "DNV-RP-C205 Environmental conditions and environmental loads," *Det Norske Veritas: Oslo, Norway,* 2010.

[97] D. N. V. As, "DNV RP C203 Fatigue Design of Offshore Steel Structures," ed: Norway, 2010.

[98] M. Matsuishi and T. Endo, "Fatigue of metals subjected to varying stress," *Japan Society of Mechanical Engineers, Fukuoka, Japan,* vol. 68, no. 2, pp. 37-40, 1968.

[99] S. S. Rao, *Engineering optimization: theory and practice*. John Wiley & Sons, 2009.

[100] D. N. Veritas, "Modelling and analysis of marine operations," *Offshore Standard,* 2011.

[101] O. Manual, "Online at http://www. orcina. com/SoftwareProducts/OrcaFlex/Documentation," *OrcaFlex. pdf,* 2012.

[102] D. Heffernan, "An introduction to the Python interface to OrcaFlex," Orcina, Tech. Rep, 2016.

[103] P. Hopkins, H. Salah, and G. Jewell. "Composite riser study confirms weight, fatigue benefits compared with steel." Offshore. http://www.offshore-mag.com/articles/print/volume-75/issue-9/subsea/composite-riser-study-confirms-weight-fatigue-benefits-compared-with-steel.html (accessed February, 4th, 2018).

[104] W. Toh, L. B. Tan, R. K. Jaiman, T. E. Tay, and V. B. C. Tan, "A comprehensive study on composite risers: Material solution, local end fitting design and global response," *Marine Structures,* vol. 61, pp. 155-169, 2018.

[105] D. N. Veritas, "Riser Interference," *DNV Recommended Practice F,* vol. 203, 2009.

[106] S. Chakrabarti, *Handbook of Offshore Engineering (2-volume set)*. Elsevier, 2005.

[107] D. Cébron, B. Gaurier, and G. Germain, "Vortex-induced vibrations using wake oscillator model: comparison on 2d response with experiments," *Flow-Induced Vibrations*.

[108] W. Iwan and R. Blevins, "A model for vortex induced oscillation of structures," *Journal of Applied Mechanics,* vol. 41, no. 3, pp. 581-586, 1974.

[109] M. Triantafyllou, G. Triantafyllou, Y. Tein, and B. D. Ambrose, "Pragmatic riser VIV analysis," in *Offshore technology conference*, 1999: Offshore Technology Conference.

[110] R. Song and P. Stanton, "Advances in Deepwater Steel Catenary Riser Technology State-of-the-Art: Part II—Analysis," 2009: American Society of Mechanical Engineers, pp. 285-296.

[111] B. Yue, D. Walters, W. Yu, K. Raghavan, and H. Thompson, "Lazy wave SCR on turret moored FPSO," in *The Twenty-first International Offshore and Polar*

Engineering Conference, 2011: International Society of Offshore and Polar Engineers.

[112] R. Song and P. Stanton, "Advances in Deepwater Steel Catenary Riser Technology State-of-the-Art: Part II—Analysis," in *ASME 2009 28th International Conference on Ocean, Offshore and Arctic Engineering*, 2009: American Society of Mechanical Engineers Digital Collection, pp. 285-296.

[113] G. DNV, "DNVGL-OS-E301 Position Mooring," *DNV GL, Oslo,* 2015.

[114] D. Heffernan, "An introduction to the Python interface to OrcaFlex," *Orcina, Tech. Rep2016,* 2016.

[115] D. N. Veritas, "Offshore standard dnv-os-f101," *Submarine pipeline systems,* 2010.

[116] D. N. Veritas, "Recommended practice DNV-C203: Fatigue design of offshore steel structures," ed: DNV Oslo, 2010.

[117] C. Huang, G. Hu, and F. Yin, "Investigation of touchdown point mismatch during installation for catenary risers," *Ocean Systems Engineering,* vol. 8, no. 3, pp. 313-327, 2018.

[118] D. N. V. AS, "Fatigue design of offshore steel structures," *Rev. 3,* 2011.

[119] R. Shoghi and H. Shiri, "Modeling touchdown point oscillation and its relationship with fatigue response of steel catenary risers," *Applied Ocean Research,* vol. 87, pp. 142-154, 2019.

[120] H. Shiri, "Influence of seabed trench formation on fatigue performance of steel catenary risers in touchdown zone," *Marine Structures,* vol. 36, pp. 1-20, 2014.

[121] M. Hodder, D. White, and M. Cassidy, "Effect of remolding and reconsolidation on the touchdown stiffness of a steel catenary riser: observations from centrifuge modeling," in *Effect of remolding and reconsolidation on the touchdown stiffness of a steel catenary riser: observations from centrifuge modeling*, 2009: Offshore Technology Conference, p. OTC 19871.

[122] F. Yuan, D. White, and C. O'Loughlin, "The evolution of seabed stiffness during cyclic movement in a riser touchdown zone on soft clay," *Géotechnique,* vol. 67, no. 2, pp. 127-137, 2017.

[123] C. Aubeny, T. White, T. Langford, V. Meyer, and E. Clukey, "Seabed stiffness model for steel catenary risers," *Frontiers in offshore geotechnics III,* pp. 351-356, 2015.

[124] E. C. Clukey, A. G. Young, J. Dobias, and S. Garmon, "Soil response and stiffness laboratory measurements of SCR pipe/soil interaction," in *Offshore Technology Conference*, 2008: Offshore Technology Conference.

[125] C. M. Larsen and T. Hanson, "Optimization of catenary risers," 1999.

[126] R. Song and P. Stanton, "Advances in Deepwater Steel Catenary Riser Technology State-of-the-Art: Part I—Design," in *International Conference on Offshore Mechanics and Arctic Engineering*, 2007, vol. 42673, pp. 331-344.

[127] J. R. Maison and J. F. Lea, "Sensitivity Analysis Of Parameters Affecting Riser Performance," presented at the Offshore Technology Conference, Houston, Texas, 1977/1/1/, 1977.

[128] Orcina, "Knowledge Based Article - Generating Spectral RAOs," 2018. [Online]. Available: www.orcina.com.

[129] W. Ruan, W. Dai, and J. Wu, "Study on motion transfer rule and extreme dynamic response of SCR's top-end heave excitation," *Journal of Marine Engineering & Technology,* pp. 1-14, 2019.

[130] B. Yue, M. Campbell, D. Walters, H. Thompson, and K. Raghavan, "Novel Technique for SCR Porch Location Screening," in *International Conference on Offshore Mechanics and Arctic Engineering*, 2010, vol. 49132, pp. 411-418.

[131] Y. Cheng, R. Song, B. Mekha, A. Torstrick, and H. Liu, "Compression assessment of deepwater steel catenary risers at touch down zone," in *International Conference on Offshore Mechanics and Arctic Engineering*, 2007, vol. 42673, pp. 345-353.

[132] A. M. Ogbeifun *et al.*, "Vessel relocation solution for steel catenary riser touch down fatigue management," *Ocean Engineering,* vol. 237, p. 109632, 2021.